

SHORT PAPERS IN—

Analytical methods

Astrogeology

Economic geology

Geochemistry

Geophysics

Glacial geology

Ground water

Hydrologic techniques

Isotope studies

Marine geology

Paleontology and
stratigraphy

Petrology and
mineralogy

Remote sensing

Structural geology

Surface water

Urban hydrology

GEOLOGICAL SURVEY RESEARCH 1972

Chapter B



GEOLOGICAL SURVEY RESEARCH 1972

Chapter B

GEOLOGICAL SURVEY PROFESSIONAL PAPER 800-B

*Scientific notes and summaries of investigations
in geology, hydrology, and related fields*



UNITED STATES GOVERNMENT PRINTING OFFICE, WASHINGTON: 1972

UNITED STATES DEPARTMENT OF THE INTERIOR

ROGERS C. B. MORTON, Secretary

GEOLOGICAL SURVEY

V. E. McKelvey, Director

CONTENTS

GEOLOGIC STUDIES

	Page
Marine geology	
Structural features of the continental margin, northeastern Gulf of Mexico, by R. G. Martin, Jr.	B1
Marine geology of Yakutat Bay, Alaska, by F. F. Wright	9
Paleontology and stratigraphy	
<i>Leiosphaeridia</i> (Acritarcha) in the Mesozoic oil shales of northern Alaska, by R. F. Boneham and I. L. Tailleir	17
Quartz-sand-bearing zone and Early Silurian age of upper part of the Hanson Creek Formation in Eureka County, Nev., by T. E. Mullens and F. G. Poole	21
Trend-surface analysis of the thickness of the High Bridge Group (Middle Ordovician) of central Kentucky and its bearing on the nature of the post-Knox unconformity, by D. E. Wolcott, E. R. Cressman, and J. J. Connor	25
Glacial geology	
The Ingraham esker, Chazy, N.Y., by C. S. Denny	35
Economic geology	
High-purity veins of soda-niter, NaNO ₃ , and associated saline minerals in the Chilean nitrate deposits, by G. E. Ericksen and M. E. Mrose	43
Thorium distribution in a granite stock near Bull Canyon, Lemhi County, Idaho, by M. H. Staatz, C. M. Bunker, and C. A. Bush	51
White clay deposits of Centre, Blair, Huntingdon, and Bedford Counties, Pa., by J. W. Hosterman	57
Reconnaissance geology and mineral potential of Thomas, Keg, and Desert calderas, central Juab County, Utah, by D. R. Shawe	67
Petrology and mineralogy	
A classification of igneous rocks by their history of crystallization and emplacement, by T. P. Thayer and E. D. Jackson	79
Tertiary basalts in the Feather River area, California, by Anna Hietanen	85
Mafic and ultramafic inclusions, Crater 160, San Francisco volcanic field, Arizona, by David Cummings	95
Some genetic implications of the phase composition of a simple New England pegmatite, by R. O. Castle and T. G. Theodore	105
New X-ray data on natural atacamite, by A. L. Larson and R. B. Tripp	119
Zonal distribution of montmorillonite and zeolites in the Laney Shale Member of the Green River Formation in the Washakie Basin, Wyo., by H. W. Roehler	121
Geochemistry	
Geochemical factor analysis of intrusion breccia and reconstituted rocks of Mule Ear diatreme, San Juan County, Utah, by R. A. Cadigan and D. E. Stuart-Alexander	125
Analytical methods	
An automated spectrophotometer, by Leonard Shapiro and C. J. Massoni	137
Electrolytic cells for cleaning crystals before fluid inclusion analysis, by D. M. Pinckney	141
X-ray fluorescence determination of arsenic, antimony, nickel, rubidium, scandium, vanadium, and zinc in rock standards and other rock samples, by B. P. Fabbi and L. F. Espos	147
Determination of mercury in geologic materials by flameless atomic absorption spectrometry, by John Marinenko, Irving May, and J. I. Dinnin	151
Chemical analysis of rutile—Direct spectrophotometric determination of titanium, total iron, niobium, phosphorus, and vanadium, by Robert Meyrowitz	157
Astrogeology	
Boulder tracks on the Moon and Earth, by H. J. Moore, W. A. Vischer, and G. L. Martin	165
Remote sensing	
Long-wavelength radar images of northern Arizona—A geologic evaluation, by G. G. Schaber and W. E. Brown, Jr.	175

	Page
Geophysics	
Gravity study of the San Juan Mountains, Colo., by Donald Plouff and L. C. Pakiser	B183
Isotope studies	
Rb-Sr and fission-track age determinations in the Precambrian plutonic basement around the Superstition volcanic field, Arizona, by J. S. Stuckless and C. W. Naeser	191
Structural geology	
Permian(?) to Jurassic(?) metavolcanic and related rocks that mark a major structural break in the northern White Mountains, Calif.—Nev., by D. F. Crowder and D. C. Ross	195
A conspicuous flexure in regional structural trend in the Puna of northwestern Argentina, by Kenneth Segerstrom and J. C. M. Turner	205
Southeastern Alaska—A displaced continental fragment?, by D. L. Jones, W. P. Irwin, and A. T. Ovenshine	211

HYDROLOGIC STUDIES

Urban hydrology	
Population density as an indirect indicator of urban and suburban land-surface modifications, by S. J. Stankowski	219
Preliminary hydrogeologic appraisal of nitrate in ground water and streams, southern Nassau County, Long Island, N.Y., by N. M. Perlmutter and Ellis Koch	225
Ground water	
Travel of pollution-indicator bacteria through the Magothy aquifer, Long Island, N.Y., by John Vecchioli, G. G. Ehrlich, and T. A. Ehlke	237
Microbiological aspects of ground-water recharge—Injection of purified chlorinated sewage effluent, by G. G. Ehrlich, T. A. Ehlke, and John Vecchioli	241
Corrosion of well-casing and screen metals in water from the Magothy aquifer and in injected reclaimed water, Bay Park, Long Island, N.Y., by John Vecchioli and A. A. Giaimo	247
Surface water	
Hurricane Camille—Effect on stages in Ross Barnett Reservoir, Mississippi, by K. V. Wilson	253
Unusual temperature variations in two small streams in northern Virginia, by E. J. Pluhowski	255
Tree rings, stream runoff, and precipitation in central New York—A reevaluation, by R. L. Phipps	259
Isotope hydrology	
Tritium in pine trees from selected locations in the United States, including areas near nuclear facilities, by G. L. Stewart, T. A. Wyerman, Max Sherman, and Robert Schneider	265
Hydrologic techniques	
The upper bound of a log-Pearson type III random variable with negatively skewed logarithms, by E. J. Gilroy	273

INDEXES

Subject	277
Author	281

GEOLOGICAL SURVEY RESEARCH 1972

This collection of 39 short papers is the first published chapter of "Geological Survey Research 1972." The papers report on scientific and economic results of current work by members of the Geologic and Water Resources Divisions of the U.S. Geological Survey.

Chapter A, to be published later in the year, will present a summary of significant results of work done in fiscal year 1972, together with lists of investigations in progress, cooperating agencies, and Geological Survey offices.

"Geological Survey Research 1972" is the thirteenth volume of the annual series Geological Survey Research. The twelve volumes already published are listed below, with their series designations.

<i>Geological Survey Research</i>	<i>Prof. Paper</i>
1960	400
1961	424
1962	450
1963	475
1964	501
1965	525
1966	550
1967	575
1968	600
1969	650
1970	700
1971	750

STRUCTURAL FEATURES OF THE CONTINENTAL MARGIN, NORTHEASTERN GULF OF MEXICO

By RAY G. MARTIN, JR., Corpus Christi, Tex.

Abstract.—Seismic reflection profiles were recorded along five traverses across the continental slope of the northeastern Gulf of Mexico during joint U.S. Geological Survey—U.S. Naval Oceanographic Office investigations in spring 1969. On the basis of these profiles, the sedimentary character and structural framework of the northeastern Gulf are described, and the surfaces of Lower and Upper Cretaceous units are delineated. A structure map contoured on the uppermost Cretaceous unit discloses a westward extension of the Apalachicola embayment beneath the continental shelf and slope and suggests a genetic relationship between the embayment and the Gulf Coast geosyncline. The embayment merges on the north into the structural gradient of the Coastal Plain and is bounded on the south by the Middle Ground arch. The structural framework of this part of the continental margin is postulated to have developed in response to tectonic movements involving the elevation of the Peninsular arch and subsidence of the Gulf Coast geosyncline.

The continental margin of the Gulf of Mexico can be divided into two distinct provinces: (1) the thick terrigenous embankments that border the northern and western Gulf from De Soto canyon into the Bay of Campeche, and (2) the massive carbonate platforms of Florida and Yucatan. The northeastern corner of the Gulf, where these two provinces join, is an area of transition, both structurally and sedimentologically. Similar transitional complexities are believed to occur in the Bay of Campeche where a sedimentary embankment adjoins the Yucatan platform. This report describes the structural framework of the transitional area in the northeastern Gulf as deduced from seismic reflection profiles.

PREVIOUS INVESTIGATIONS

The rather unusual physiographic characteristics of the northeastern Gulf of Mexico—for example, the precipitous western slope of the Florida platform, the incised De Soto canyon, and the abrupt change from Florida's north-south trend to the east-west strike of the northern Gulf coast—have attracted numerous geologic investigations. Jordan (1951) presented the first detailed bathymetric chart of this area; the map (fig. 1) used in this report is largely based on his work. Seismic refraction studies in the De Soto canyon area and in the bight of Florida by Antoine and Harding (1963, 1965)

delineated pre-Cretaceous and Upper Cretaceous surfaces and suggested the existence of a lateral facies change from clastic to carbonate materials, a change equivalent to that known in the subsurface of northern Florida. Antoine, Bryant, and Jones (1967) reported that seismic reflection profiles and a core sample indicate that the Florida escarpment is underlain by a Lower Cretaceous limestone reef. Subsequent reflection profiling (Antoine and Jones, 1967; Uchupi and Emery, 1968; Pyle and others, 1968) has shown the reef to be best developed in the area of the present investigation but discontinuous and less well defined south of lat 27° N. A Lower Cretaceous reef fronting the Florida escarpment suggests a connection with known reef trends of equivalent age in the subsurface of Louisiana and Texas (Antoine and others, 1967; Meyerhoff, 1967; Uchupi and Emery, 1968; Bryant and others, 1969).

PRESENT STUDY

In spring 1969, the U.S. Geological Survey, in a joint program with the U.S. Naval Oceanographic Office aboard the USNS *Elisha Kane*, made five seismic reflection traverses across the continental slope south of Pensacola, Fla., to approximately lat 28° N. (fig. 1). The resulting data provide a more detailed look at the structural relationships of this region than has heretofore been available.

The survey utilized a Teledyne Seismic Section Profiler (SSP)¹ programed to discharge 160,000 joules of electrical energy at 6-second intervals through four sets of electrodes towed approximately 75 m behind the ship at an average speed of 9 knots. Acoustic returns were detected through a hydrostreamer 66 m long, consisting of 100 Geospace MP-7 crystal hydrophones and two preamplifiers towed approximately 180 m behind the ship at a depth of 6 m. The acoustic signals were recorded on a modified Raytheon PFR-196B dry-paper recorder after being amplified and filtered to pass only those frequencies between 17 and 47 hertz.

The ship's position was determined by a satellite navigation

¹Use of brand names in this report does not necessarily indicate endorsement by the U.S. Geological Survey.

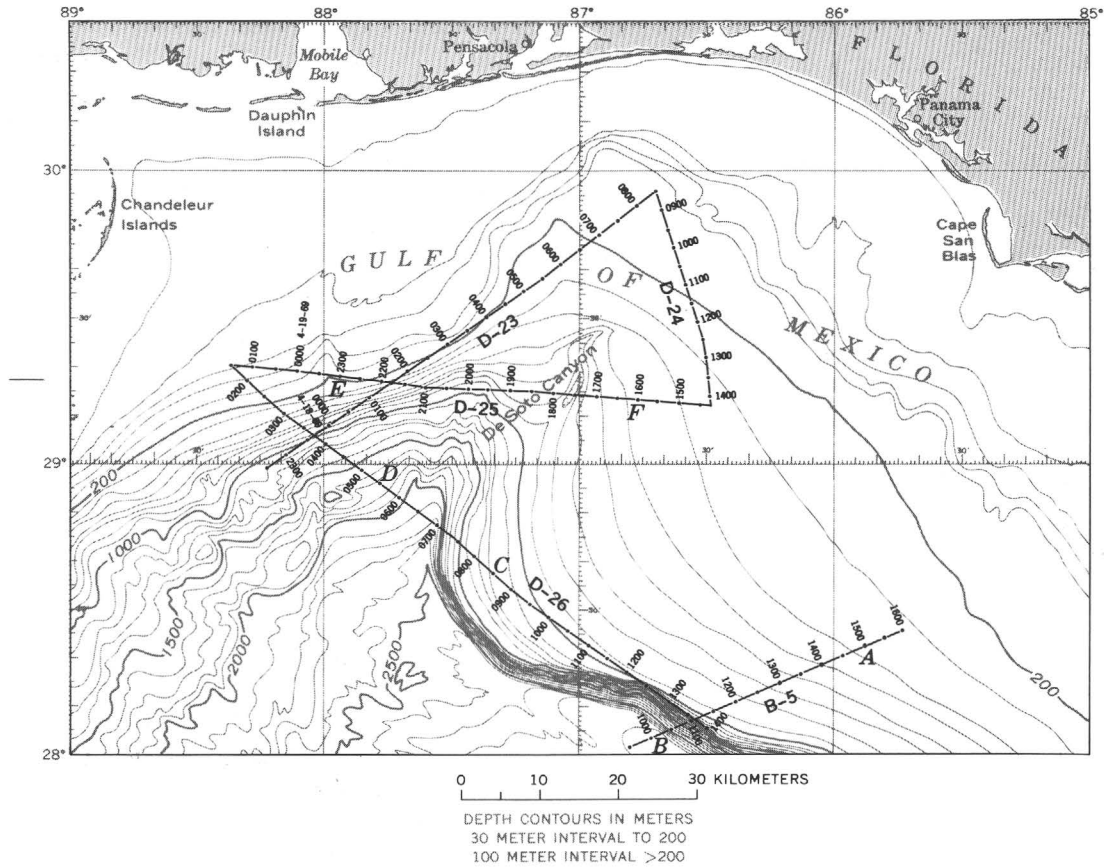


Figure 1.—Bottom-contour chart of the northeastern Gulf of Mexico, showing seismic reflection traverses made by the USNS *Kane* and locations of profiles presented in this report. Base map adapted from Jordan (1951), Uchupi (1967), and U.S. Naval Chart BC 0905.

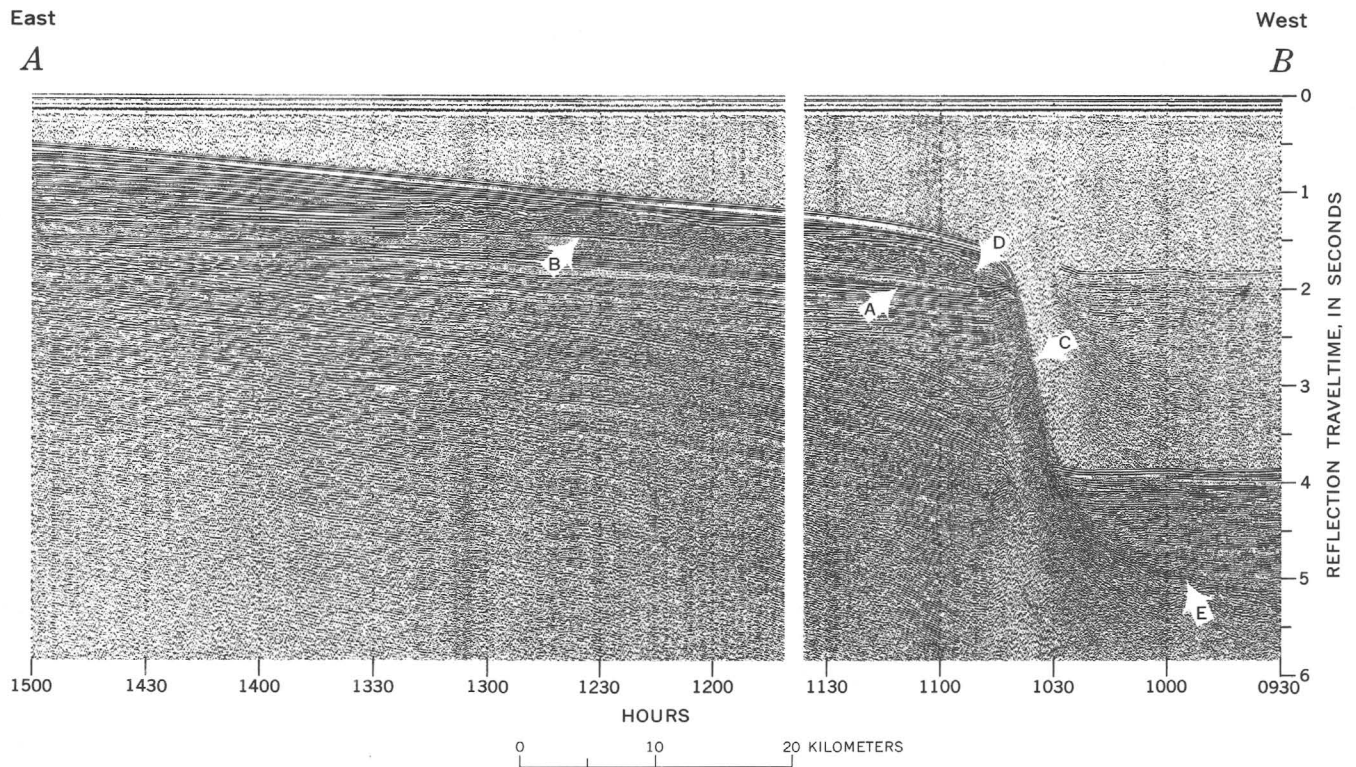


Figure 2.

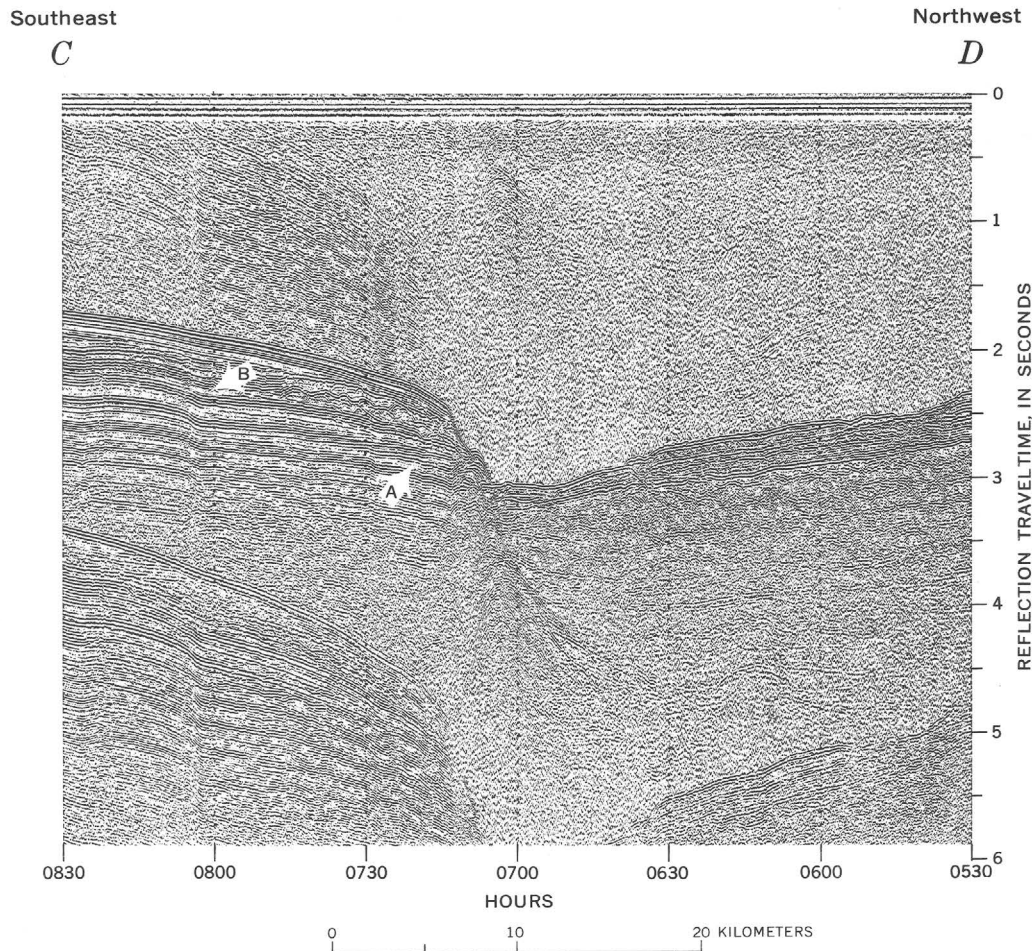


Figure 3.—Profile C–D, showing the partly buried Florida escarpment at the De Soto valley. See figure 1 for location. A, top of Lower Cretaceous (reflector A); B, top of Upper Cretaceous (reflector B).

system (Magnavox, Mx/702/HP) for all tracks used in this report, with the exception of line B-5 where fixes were made utilizing Loran-A and Omega systems.

SEISMIC REFLECTION PROFILES

The structural and stratigraphic characteristics which distinguish the Florida platform from the great terrigenous embankment of the northern Gulf margin are strikingly shown on continuous seismic reflection profiles. The platform appears in these profiles as a uniform sequence of parallel

reflections, two of which are picked as the probable tops of Lower and Upper Cretaceous formations. These reflectors can be traced over an area of 21,000 sq km. The thick sequence of consolidated and unconsolidated sediments composing the terrigenous embankment to the north and west, however, presents a less orderly sequence of subbottom reflectors, and, except for reflectors in the upper few meters, none can be traced over great distances.

Profile A–B (fig. 2) crosses the upper slope and escarpment southwest of Panama City, Fla., where the character and position of reflectors A and B correlate with horizons representing the tops of the Lower and Upper Cretaceous formations (Antoine and others, 1967; Bryant and others, 1969). The Lower Cretaceous reef appears on the profile as a zone of hyperbolic reflectors centered below the ship's position near 1040 hours. The stratigraphic interval between A and B pinches out over the crest of the reef, suggesting that it ceased to be an effective barrier to the open sea after Early Cretaceous time.

Figure 2.—Profile A–B, illustrating characteristic features of the Florida platform and escarpment in the northeastern Gulf of Mexico. See figure 1 for location, A, postulated top of Lower Cretaceous (reflector A); B, approximate top of Upper Cretaceous (reflector B); C, postulated Lower Cretaceous reef. Lenticular zone of disorganized reflectors, D, may represent post-Cretaceous reef development. Note well-defined scarp-face reflector, E, passing beneath sediments of the Mississippi cone.

The zone of disorganized reflectors which overlies reflector B can be traced landward approximately 15 km into more coherent bedding. This zone has been described elsewhere as a possible reef and reef talus complex of Maestrichtian to early Eocene age, equivalent to the Cedar Keys Limestone (mainly Paleocene) of west-central and southern Florida (Bryant and others, 1969). Its presence on each scarp-crossing north of about lat $27^{\circ}45'$ N. indicates that it is a characteristic feature of the lowermost Tertiary deposits along the outer edge of the Cretaceous platform. Two cycles of deposition separated by a conspicuous unconformity are recognized above this zone.

Seaward of the escarpment, the scarp-face reflector zone dips steeply, at first, then more gently basinward beneath the thick cover of abyssal sediments. The hummocky and discontinuous nature of this reflector zone is suggestive of sea-floor roughness due to talus deposits.

Profile *C-D* (fig. 3) crosses the escarpment in the De Soto canyon near the area where the terrigenous embankment joins and advances over the Florida platform. In this area, the canyon is formed between the steep carbonate escarpment and the gentler slope of prograding clastic deposits of the Mississippi and adjacent river systems. The records suggest that the uppermost sequence of the clastic embankment has been thinned by nondeposition; no indications of canyon cutting on the lower slope are disclosed. Thus, the lower slope part of De Soto canyon is constructional and has originated through depositional processes. However, a narrow S-shaped channel described by Harbison (1968) from the upper continental slope does appear to be erosional. The term "canyon" should be restricted to the erosional channel of Harbison; the writer prefers to call the conspicuous physiographic feature on the lower slope between the platform and the embankment the De Soto valley.

As in profile *A-B*, profile *C-D* shows Lower Cretaceous beds lapping against the reef structure and the Upper Cretaceous sequence thinning basinward over it. Cenozoic units deposited on the Cretaceous platform correlate with those in profile *A-B*. Lower and perhaps middle Tertiary beds on the platform were warped, displaced by minor down-to-the-north faults, and truncated during the last major erosional period to affect this part of the slope. Presumably this erosional episode was contemporaneous with the cutting of De Soto canyon.

The acoustic character of the embankment of terrigenous sediment to the west differs sharply from that of the carbonate bank. The profiles indicate that the terrigenous deposits include a thin upper unit of well-stratified material, marked by some erosional channels and minor slump structures, and a thick lower sequence characterized by disorganized reflectors and less well defined horizons. The thickness of the upper unit shown on figure 3 decreases from about 0630 hours to the face of the escarpment. This thinning may be due to either nondeposition or slight erosion which, in either case, could have resulted from currents flowing down the De Soto valley.

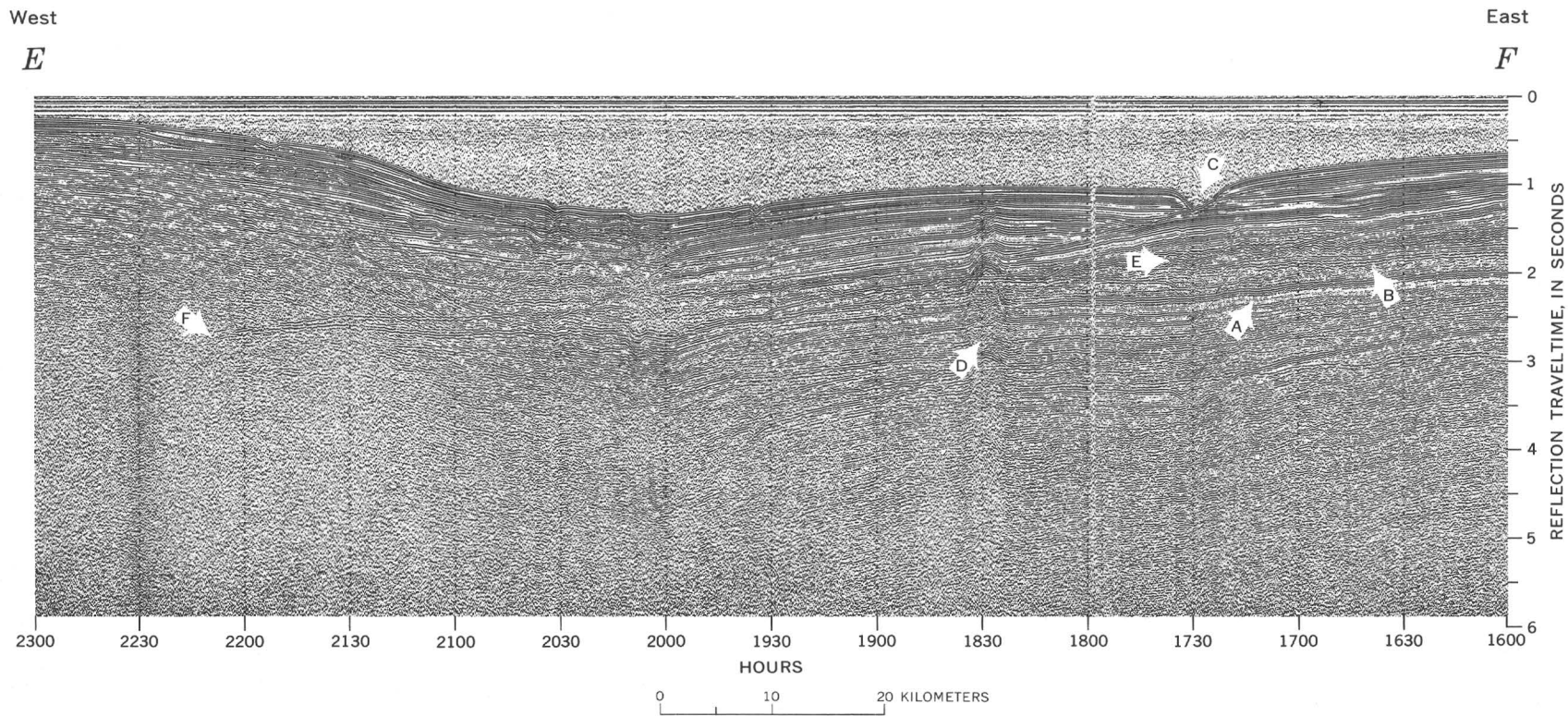
The doming of beds shown on figure 3 at a depth of 4.5 seconds near 0615 hours is probably the result of differential compaction over the reef-talus buildup which is commonly present at the base of the escarpment.

Profile *E-F* (fig. 4) traverses the upper continental slope from the Mississippi-Alabama shelf eastward to the vicinity of the De Soto canyon. The position of reflector B on this profile and on traverse D-24 (fig. 1) correlates with the top of the Upper Cretaceous, as defined on the basis of seismic refraction studies by Antoine and Harding (1963). The lowermost zone of conspicuous reflectors is correlated with the top of the Lower Cretaceous (reflector A), principally on the basis of the acoustical character of this zone and its position relative to the overlying reflector B. This horizon is discernible on each of the traverses in the northeastern Gulf, with two noteworthy exceptions: westward of 2215 hours on profile *E-F* (fig. 4) and on the nearby traverse D-23 (fig. 1). On both, the reflector shows a marked change in slope and appears to trace the outer edge of the buried Florida platform.

Either because the reef is absent or discontinuous north of the De Soto valley or because the seismic system was unable to detect it, the hyperbolic reflectors which normally characterize the Lower Cretaceous reef are absent in this area. There is an indication that the Upper Cretaceous surface has been eroded, as shown on figure 4, particularly at 1930 and 2000 hours where channel cutting is evidenced.

Localized discontinuities within the Cenozoic sequence along profile *E-F* suggest a complex depositional history for the Florida platform after Cretaceous time. Initial upbuilding above the Cretaceous surface by sediment derived from the east probably lasted through the middle Tertiary and was succeeded by the onlap of the southeasterly prograding terrigenous embankment. The zone of jumbled reflectors shown overlying reflector B on figure 4 near 1630 hours may represent a reef complex related to those noted on profiles *A-B* and *C-D*. Erosional and slump features appear to be present within the terrigenous embankment in the area shown on figure 4 between 2000 and 2130 hours; these features account for the marked change in the wavy and discontinuous bedding characteristics of the Cenozoic sequence along this part of the traverse. The latest major cycle of deposition is shown on figure 4 as the uppermost 0.15 seconds of the record, in which the reflectors generally lie concordant to the sea floor.

Late Cenozoic sea-floor erosion is indicated on figure 4 by channels between 1930 and 2200 hours and by the broader (2.5 km) and more deeply incised (about 150 m) De Soto canyon at 1730 hours. This canyon was probably cut during a time of lower sea level; its S-shaped course has been attributed by Harbison (1968) to a combination of erosion, deposition, and the influence of buried domes such as the one shown at 1830 hours. This dome may be a salt diapir. Diapirs are reportedly numerous in the vicinity of the canyon and may represent the easternmost limit of salt domes along the northern Gulf margin (Antoine and Gilmore, 1970; Harbison, 1967, 1968; Antoine and others, 1967).



MARTIN

Figure 4.—Profile *E-F*, showing the thinly capped Florida platform surface dipping westward (to the left) beneath the terrigenous Mississippi embankment. See figure 1 for location. A, postulated top of Lower Cretaceous (reflector A); B, approximate top of Upper Cretaceous (reflector B). De Soto canyon, C, has been cut deeply into upper-slope sediments. Note the effects of a nearby piercement dome, D, and possible post-Cretaceous reef development, E. Buried edge of Florida platform postulated at F.

STRUCTURE OF THE SURFACE OF THE CRETACEOUS

Structure contours on the uppermost Cretaceous shown on figure 5 are based on data reported here and from published sources. Depths to reflector B were obtained from the profiles by correcting for variations in sound velocities by use of data from Antoine and Harding (1963). Structural features of regional significance are shown on the inset.

Contours on the uppermost Cretaceous surface reveal the gulfward extension of the Apalachicola embayment, the principal negative structural element of the northeastern Gulf margin. The embayment merges on the north into the structural gradient of the Coastal Plain and is bounded on the south by the Middle Ground arch. The contours reveal that the embayment broadens and deepens westward beneath the Mississippi-Alabama shelf and slope, suggesting a genetic relationship to the Gulf Coast geosyncline.

A pronounced domal uplift south of the Florida Panhandle has divided the Apalachicola embayment (fig. 5) into two troughs. One parallels the northern coastline from Cape San Blas to the vicinity of Mobile Bay; the other generally coincides with the trend of the De Soto valley. The channel-like configuration of the southern trough is perhaps due in

part to post-Cretaceous erosion, as noted in figure 4. Seismic reflection profiles that cross the western and southern flanks of the uplift show a pronounced increase in the rates of dip of lower Tertiary and older beds, indicating that the uplift of the dome continued from late Mesozoic into early Tertiary time.

Although the existence of this dome is well documented, explanations of its origin are inconclusive. Because of a nearby magnetic anomaly of +500 gammas reported by Gough (1967), Antoine, Bryant, and Jones (1967) related the feature to deep-seated igneous activity. King (1959) suggested that similar anomalies along the Apalachicola River in northern Florida may have resulted from post-Paleozoic diabase intrusions. The possible occurrence of Louann Salt beneath the Florida Panhandle and the Florida platform (Winston, 1969; Marsh, 1967) and the demonstrated presence of numerous shallow piercement domes in the terrigenous embayment between the Mississippi River Delta and De Soto canyon (Harbison, 1968; Antoine and Gilmore, 1970; Uchupi and Emery, 1968), however, make appealing the hypothesis that the uplifted area has been produced by the growth of a nonpiercement salt swell (Antoine, 1965).

The structure contours disclose that the two troughlike areas are separated by a low ridge extending northwest from the

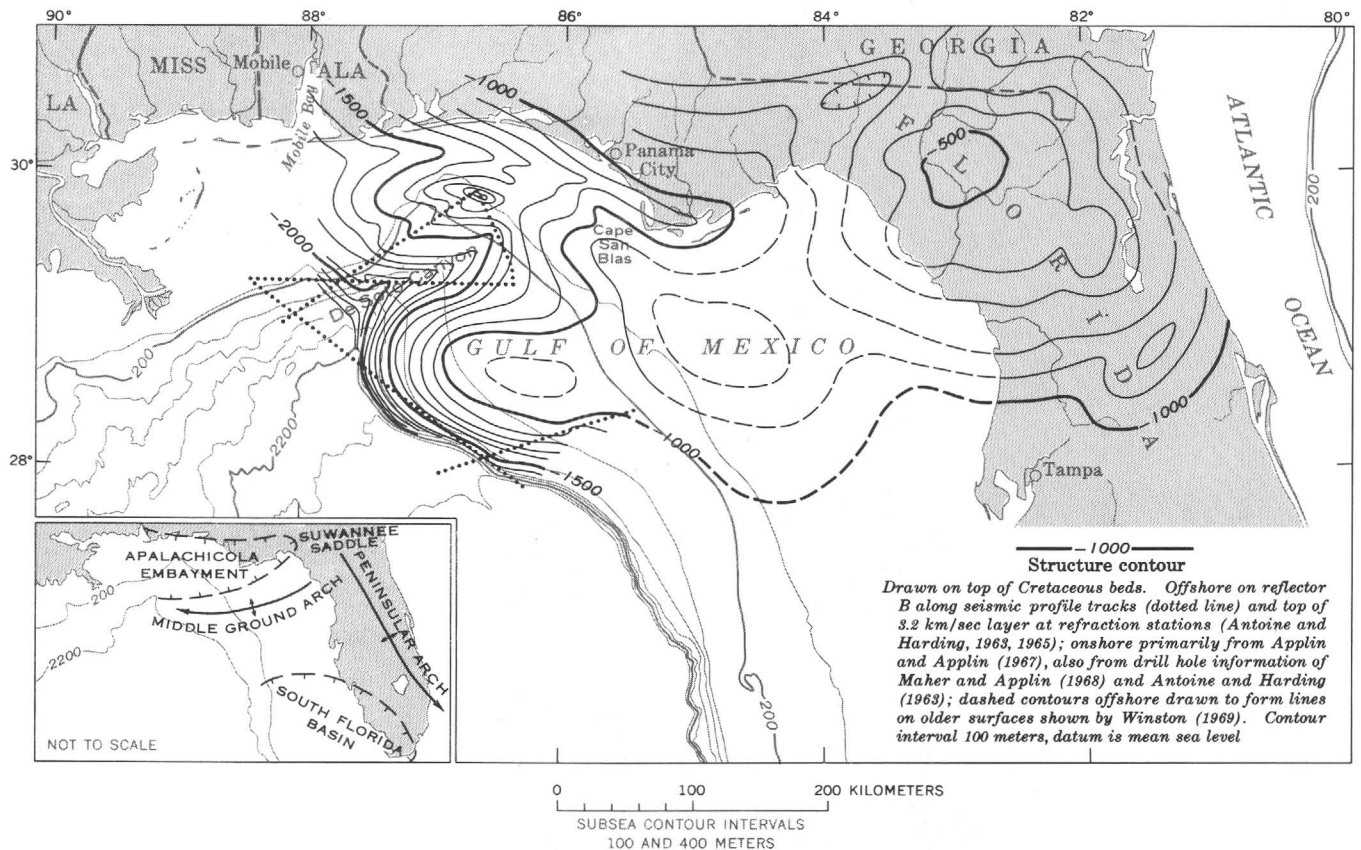


Figure 5.—Structure contour map on the top of the Cretaceous surface in the northeastern Gulf of Mexico and northern Florida. Major structural axes of the eastern Gulf of Mexico shown on inset map.

Middle Ground arch. This barrier probably promoted infilling in the northern trough while limiting or altogether preventing terrigenous sedimentation in the southern trough. The southern flank of this ridge is possibly the east-west-trending "erosional slope" or shoreline which, according to Harbison (1968), strongly influenced the trend of the northernmost part of the erosional De Soto canyon.

The Middle Ground arch, principally a subsurface structure, is an irregular ridge that extends southwest from the crest of the Peninsular arch and separates the Apalachicola embayment from the South Florida basin. The structural relief of the uplift increases downward into older strata, suggesting continued uplift contemporaneous with deposition. The arch was firmly established in its present location and form by middle Early Cretaceous time and provided a favorable setting for the development of the reef (fig. 2), as indicated by the smooth bulge of the escarpment (fig. 1) outlining the western terminus of the arch. The irregular outline of the arch and apparent centers of local uplift along its axis are perhaps due to stratigraphic thickening in Upper Cretaceous carbonate units such as the one that produced an axial shift of the Peninsular arch in northern Florida (Applin and Applin, 1967).

The development of the Middle Ground arch is probably associated with the tectonic movements that caused the elevation of the Peninsular arch and the subsidence of the adjacent Apalachicola embayment and South Florida basin during Mesozoic and Tertiary time. However, it is suspected that the arch is more a product of differential subsidence of the Florida platform than of active upwarping. The trend of the arch may have been determined along preexisting "Appalachian" tectonic trends discussed by King (1959) and Gough (1967).

CONCLUDING REMARKS

The structural framework of the continental margin of the northeastern Gulf of Mexico probably began to evolve during late Paleozoic and early Mesozoic time as a result of moderate tectonic warpings of a Paleozoic foreland. The principal elements of this framework are the Apalachicola embayment and the Middle Ground arch.

Evidence presented in this report and in earlier studies suggests that differential subsidence of the eastern Gulf of Mexico in Mesozoic and Cenozoic time produced the Middle Ground arch. The position of this low positive area was possibly localized along older tectonic trends and was firmly established by middle Early Cretaceous time, as indicated by the development of the reef about its western terminus. The actively subsiding Apalachicola embayment between the arch and the Coastal Plain has been filled largely with terrigenous detritus since the Jurassic; Winston (1969) estimated that more than 20,000 feet (6.1 km) of sediments has accumulated there. In contrast, refraction studies and stratigraphic evidence indicate that carbonate deposition prevailed on the Middle

Ground arch and in the South Florida basin during the Mesozoic and Cenozoic Eras. The transition between clastic and carbonate regimes on the Florida platform is believed to have occurred over a broad zone along the northern flank of the arch. The structural high provided by the Middle Ground and Peninsular arches, therefore, is postulated to have provided a barrier to clastic sedimentation into the South Florida basin in a manner comparable to that provided by the Suwannee saddle (Applin and Applin, 1967) in southern Georgia and northern Florida. Thus, the tectonic behavior of the Middle Ground arch and Apalachicola embayment has not only directed the course of the geological evolution of this corner of the Gulf of Mexico, but also has exercised significant control over the sedimentary development of the western part of the Florida platform.

Absence of the acoustic signature of the Lower Cretaceous barrier reef beneath the terrigenous flank of the De Soto valley presents a challenge to earlier postulations of reef continuity between the Florida escarpment and the subsurface of Louisiana and east Texas. Evidence of predominantly clastic sedimentation in the Apalachicola embayment during this period (Winston, 1969) may mean that the reef terminates in the vicinity of the De Soto valley.

Significant modifications to the structure of the Apalachicola embayment have been imposed by the growth of diapirs whose cores have been postulated to be Louann Salt. It is estimated that more than 2 km of clastic sediments were deposited in the embayment during Cretaceous time, certainly enough overburden to produce mobility within an underlying salt bed. The seismic profiles taken in the northeastern Gulf indicate that the prominent dome, postulated to be a salt swell, began to be uplifted sometime during the Late Cretaceous. Diapirism in the vicinity of the De Soto canyon probably also was initiated at this time but was not to manifest itself until later in Tertiary time. Evidence from this study and from Harbison (1968) suggests that diapirism greatly controlled the depositional pattern of Tertiary sequences in the northeastern Gulf and was primarily responsible for localizing the course of the De Soto canyon.

The present morphology of the northeastern Gulf margin was shaped during late Tertiary time when the center of maximum deposition shifted along the northern Gulf to the vicinity of the present Mississippi River Delta. The shift of depocenter resulted in a rapid increase in the rate of seaward progradation of the terrigenous embankment in the area basinward of the delta front. As shown in profiles *A-B* and *C-D* (figs. 2 and 3), the voluminous detritus brought to the northeast Gulf by the Mississippi and adjacent drainage systems was spread over the older sediments in the Apalachicola embayment and on the northern flank of the Middle Ground arch as a thick terrigenous mantle. Downslope, the embankment abutted the Florida escarpment and formed the pronounced valley, into which were later channeled the currents that cut the S-shaped course of the De Soto canyon on the upper slope.

REFERENCES

- Antoine, J. W., 1965, Structural features under continental shelf of Florida panhandle revealed by seismic reflection measurements [abs.]: *Geophysics*, v. 30, no. 6, p. 1228.
- Antoine, J. W., Bryant, W. R., and Jones, B. R., 1967, Structural features of continental shelf, slope, and scarp, northeastern Gulf of Mexico: *Am. Assoc. Petroleum Geologists Bull.*, v. 51, no. 2, p. 257-262.
- Antoine, J. W., and Gilmore, J. C., 1970, Geology of the Gulf of Mexico: *Ocean Industry*, v. 5, no. 5, p. 34-38.
- Antoine, J. W., and Harding, J. L., 1963, Structure of the continental shelf, northeastern Gulf of Mexico: *Texas A&M Univ. Tech. Rept.* 63-13T, 18 p.
- 1965, Structure beneath continental shelf, northeastern Gulf of Mexico: *Am. Assoc. Petroleum Geologists Bull.*, v. 49, no. 2, p. 157-171.
- Antoine, J. W., and Jones, B. R., 1967, Geophysical studies of the continental slope, scarp, and basin, eastern Gulf of Mexico: *Gulf Coast Assoc. Geol. Socs. Trans.*, v. 17, p. 268-277.
- Applin, P. L., and Applin, E. R., 1967, The Gulf Series in the subsurface in northern Florida and southern Georgia: *U.S. Geol. Survey Prof. Paper* 524-G, 34 p.
- Bryant, W. R., Meyerhoff, A. A., Brown, N. K., Jr., Furrer, M. A., Pyle, T. E., and Antoine, J. W., 1969, Escarpments, reef trends, and diapiric structures, eastern Gulf of Mexico: *Am. Assoc. Petroleum Geologists Bull.*, v. 53, no. 12, p. 2506-2542.
- Gough, D. I., 1967, Magnetic anomalies and crustal structure in eastern Gulf of Mexico: *Am. Assoc. Petroleum Geologists Bull.*, v. 51, no. 2, p. 200-211.
- Harbison, R. N., 1967, De Soto Canyon reveals salt trends: *Oil and Gas Jour.*, v. 65, no. 8, p. 124-128.
- 1968, Geology of De Soto Canyon: *Jour Geophys. Research*, v. 73, no. 16, p. 5175-5185.
- Jordan, G. F., 1951, Continental slope off Apalachicola River, Florida: *Am. Assoc. Petroleum Geologists Bull.*, v. 35, no. 9, p. 1978-1993.
- King, E. R., 1959, Regional magnetic map of Florida: *Am. Assoc. Petroleum Geologists Bull.*, v. 43, no. 12, p. 2844-2854.
- Maher, J. C., and Applin, E. R., 1968, Correlation of subsurface Mesozoic and Cenozoic rocks along the eastern Gulf Coast: *Am. Assoc. Petroleum Geologists Cross Sec. Pub.* 6, 29 p.
- Marsh, O. T., 1967, Evidence for deep salt deposits in western Florida panhandle: *Am. Assoc. Petroleum Geologists Bull.*, v. 51, no. 2, p. 212-222.
- Meyerhoff, A. A., 1967, Future hydrocarbon provinces of Gulf of Mexico-Caribbean region: *Gulf Coast Assoc. Geol. Socs. Trans.*, v. 17, p. 217-260.
- Pyle, T. E., Antoine, J. W., and Bryant, W. R., 1968, Geophysical studies of south Florida continental margin and western Straits of Florida [abs.]: *Am. Assoc. Petroleum Geologists Bull.*, v. 52, no. 9, p. 1830; *Gulf Coast Assoc. Geol. Socs. Trans.*, v. 18, p. 50.
- Uchupi, Elazar, 1967, Bathymetry of the Gulf of Mexico: *Gulf Coast Assoc. Geol. Socs. Trans.*, v. 17, p. 161-172.
- Uchupi, Elazar, and Emery, K. O., 1968, Structure of continental margin off Gulf Coast of United States: *Am. Assoc. Petroleum Geologists Bull.*, v. 52, no. 7, p. 1162-1193.
- Winston, G. O., 1969, A deep glimpse of west Florida's platform: *Oil and Gas Jour.*, v. 67, no. 48, p. 128-129, 132-133.



MARINE GEOLOGY OF YAKUTAT BAY, ALASKA

By F. F. WRIGHT¹, College, Alaska

Abstract.—Yakutat Bay is a broad, locally shallow coastal embayment exposed by the recession of a piedmont glacier. The morphology and sediments of the bay reflect the complex interaction of glacial, climatic, and marine agents. The bathymetry is dominated by an irregular series of relatively recent moraines left by deglaciation. These moraines are presently being winnowed by tide- and wave-generated currents. Fine sediment, especially mud, is accumulating in the deeper, more sheltered parts of the system. Sand occurs only on modern beaches and in the immediate nearshore zone; gravel occurs on morainal ridges. Values of potential placer accumulations of heavy minerals are low, particularly in the head of the bay.

The University of Alaska and the U.S. Geological Survey have jointly conducted reconnaissance geologic surveys for deposits of heavy minerals in the surficial sediments on parts of the Gulf of Alaska Continental Shelf. This report describes the sediment in the broad, locally shallow embayment of Yakutat Bay near the distal end of the Malaspina Glacier on the Alaskan coast (fig. 1). Other reports discuss similar areas both on the nearby Continental Shelf and in the Nuka Bay area (Reimnitz and others, 1970; Valencia and Wright, 1968; Wright and others, 1968; Wright, 1970).

Acknowledgments.—Many people contributed to various phases of this study. At the University of Alaska, these included Dr. C. M. Hoskin, Department of Geology, and Dr. D. J. Cook, Mineral Industries Research Laboratory, who supervised most of the sediment-size and heavy-minerals analyses, and Cmdr. A. H. Clough (U.S. Coast Guard, retired) and the crew of the RV *Acona*, whose cooperation and efficiency during shipboard operations were outstanding. The study was performed under Office of Marine Geology contract 14-08-001-10885 and was directed by E. H. Lathram and R. E. von Huene, U.S. Geological Survey. The encouragement and critical review of D. M. Hopkins, also of the Geological Survey, are gratefully acknowledged.

METHODS OF INVESTIGATION

Sediment samples, bathymetric records, and seismic profiles were obtained using the University of Alaska's Research Vessel

Acona. Sediment samples were taken primarily with a Shipek grab to a depth of 10 to 12 cm (4 to 5 inches) in the sea floor; three gravel samples were collected with a small dredge; and four beach samples were taken from the surface at midtide level. Depth records were made with a precision depth recorder (PDR), and acoustic profiles were obtained with a sparkler system provided by the Geological Survey. The spark arrays were operated at an approximate energy level of 5 kilojoules; the filters were adjusted to accept acoustic returns in the range 20–200 hertz. Radar was the primary navigational tool, but sextant angles and occasional loran fixes were also used during the survey. Precision of location is estimated to average 0.6 km (0.3 nautical mile).

The sediment samples were processed for size distribution and general mineralogic composition at the University of Alaska. Samples that contained a significant sand and gravel fraction were processed by size. Specific-gravity and magnetic-separation techniques were used for heavy-mineral content, and atomic-absorption procedures were used for specific elements. A sink–float separation with tetrabromoethane (specific gravity 2.96) was used to divide these samples into light and heavy fractions. All samples were analyzed by sieve and pipet techniques to yield percentages of gravel (>2mm), sand (2mm–62 μ), silt (62–4 μ), and clay (<4 μ).

GEOGRAPHIC SETTING

Yakutat Bay is the largest embayment in the Alaskan coast between the fiord areas of Prince William Sound and the Alexander Archipelago of the southeastern Alaska panhandle. The Yakutat Bay area has a maritime-alpine climatic regime typical of the southern Alaska coast. This climate is influenced both by the relatively warm North Pacific Current that flows southeastward along the shelf and by the extensive icefields of the nearby Chugach and St. Elias Mountains (Johnson and Hartman, 1969). The velocity of the North Pacific Current in the Yakutat area is commonly between 77 and 103 cm/second (1.5 and 2 knots); tidal range averages 3.3 m (10.1 feet).

The temperature is generally cool throughout the year, with an annual mean of 40°F (4.4°C). Sea ice does not form in Yakutat Bay, but large quantities of small bergs are produced by the Hubbard and Turner Glaciers, which empty into

¹ University of Alaska, Institute of Marine Science.

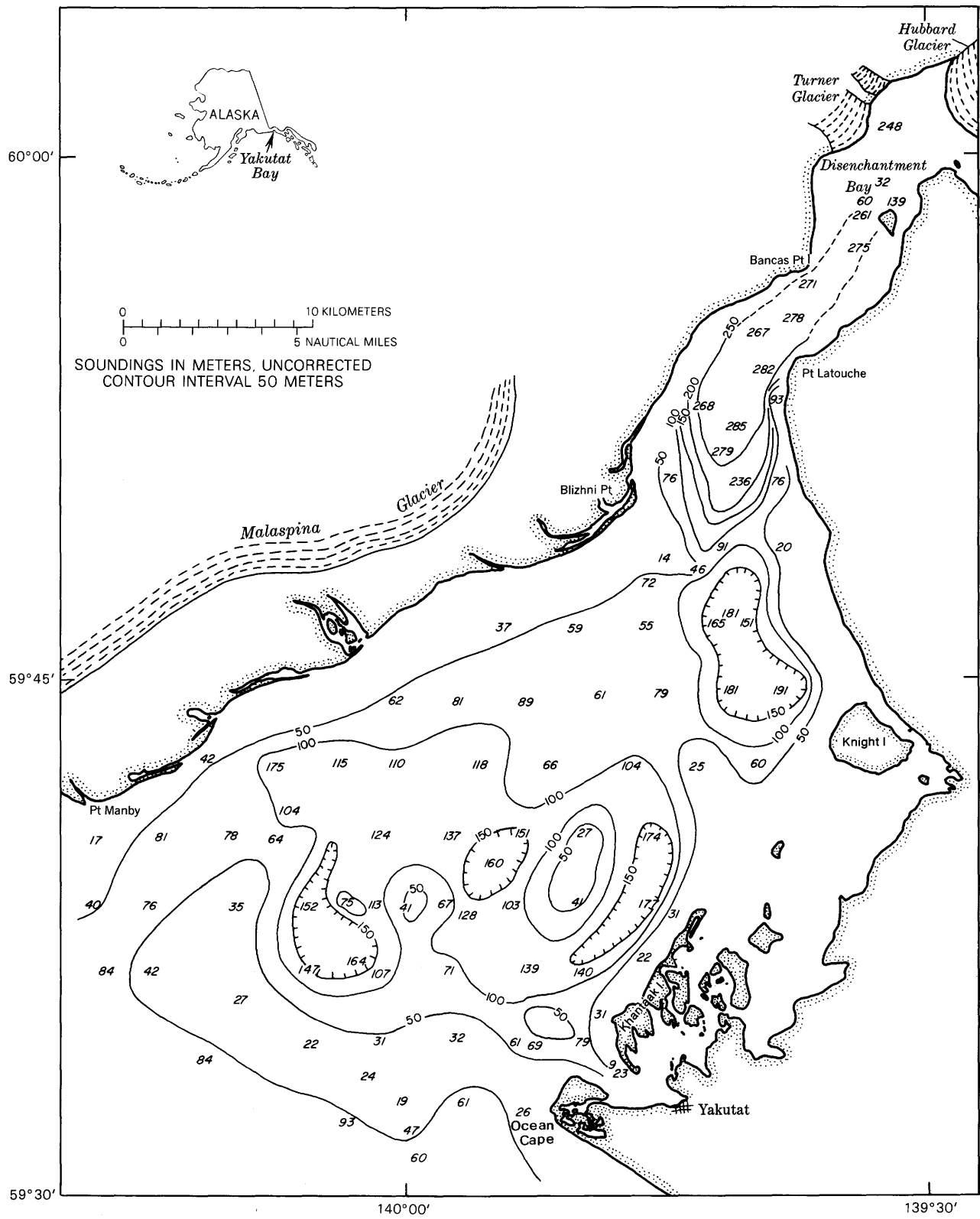


Figure 1.—Bathymetric map of Yakutat Bay, Alaska.

Disenchantment Bay at the head of Yakutat Bay (fig. 1). These small bergs are generally found only in the northern part of the bay (as far south as Blizhni Point), but some have been seen at the mouth of the bay.

Storms occur frequently during the fall, winter, and spring. They are commonly associated with low-pressure cells that are generated in the Aleutian Islands and travel eastward between the continental high and the North Pacific low. These storms dissipate much of their energy in the immediate vicinity of Yakutat Bay and contribute much precipitation to the neighboring icefields. Mean annual precipitation is the highest of any reporting station in the State—over 330 cm (130 inches), including about 546 cm (215 inches) of snow and sleet. The limited fetch available to the intense local storms results in the generation of steep short-period waves, which are undoubtedly an important factor in shallow-water sedimentation in the area. Major long-period waves only occasionally come to the Yakutat area; breakers are then observed along the entire length of the submerged moraine at the mouth of the bay (U.S. Coast and Geodetic Survey, 1964). During the summer there are occasional periods of clear weather along the coast, usually found when a stable low-pressure area in the Gulf of Alaska permits the development of katabatic winds from the St. Elias icefields (U.S. Environmental Science Services Administration, 1967).

Contemporary glaciers in the St. Elias Mountains near Yakutat Bay appear to be predominantly in retreat (Miller, 1964). Miller reported that 82 percent of the glaciers observed in the area were shrinking, 15 percent were in equilibrium, and only 3 percent showed signs of persistent advance. In the immediate area of Yakutat Bay, however, there seems to be a state of quasi-equilibrium. The Turner and Hubbard Glaciers at the head of Yakutat Bay have been advancing steadily into tidewater since 1890 (Miller, 1964). These glaciers have relatively high-elevation névés and have been able to maintain a steady advance into tidewater despite the accelerated wastage associated with a submerged snout (Miller, 1964). In marked contrast, a piedmont glacier, the Malaspina, which is perhaps the largest nonpolar glacier today (Sharp, 1958), appears to be waning. The Malaspina is presently retreating from its most extensive late Quaternary advance, which culminated roughly 1,000 years ago (Plafker and Miller, 1958). This irregular glacial activity appears to have characterized the Gulf of Alaska coastal mountains and shoreline since about late Miocene time (Miller, 1958; Bandy and others, 1969).

GEOLOGIC SETTING

The head of Yakutat Bay penetrates the St. Elias Mountains, a crystalline complex of Mesozoic and older metasediments with minor mafic and quartz monzonitic intrusions (Miller, 1961; Plafker, 1967). Upper Mesozoic and Tertiary sediments, unmetamorphosed but extensively deformed by a series of major thrust faults, underlie the coastal plain and possibly the Continental Shelf (Stoneley, 1967). The bay and its associated

seavalley cross the entire coastal plain and Continental Shelf, possibly in a zone of structural transition (Wright and others, 1968).

The coastal plain and some of the coastal mountains are separated by the largest of the faults, the Chugach—St. Elias—Fairweather system, a branch of which forms part of the structural control for the fiords at the head of Yakutat Bay. Movement on this system appears to have included both vertical and right-lateral displacement (Stoneley, 1967).

Another fault, whose presence is inferred from the mapping of a series of uplifted strandlines, was named the Mountain-Front and East Shore fault by Tarr and Martin (1912), who noted that the strandlines were uplifted more than 5 m (17 feet) along the east shore of Disenchantment Bay. The uplift presumably occurred during the Yakutat earthquake of 1899. A later earthquake with major topographic readjustment occurred in 1958 (Miller, 1964).

BATHYMETRY AND SEDIMENTATION

The detailed bathymetric map (fig. 1), which was constructed from data obtained along 160 nautical miles (290 km) of bathymetric profiles during the cruise of the RV *Acona*, shows moderately irregular submarine topography with small-scale hummocks and closed depressions partly smoothed by deposition of contemporary sediment. Relief on the bay floor and on the surrounding coastal plain is largely due to morainal hills left from the most recent advances and retreats of Malaspina Glacier (Plafker, 1967). At the head of the bay is a well-defined closed depression, Disenchantment Basin, with water depths greater than 280 m (919 feet).

South of Disenchantment Bay, three sets of ridges occur within the bay proper. The innermost set extends eastward from Blizhni Point to a position not quite halfway across the bay. Because of the occurrence of gravel at its surface, it is assumed to be a moraine and has been termed the bayhead moraine. This feature has a distinct, apparently unbreached sill with a maximum depth of about 90 m (295 feet). A second but less obvious group of gravel-covered topographic highs extends southwest from Knight Island to the central part of the bay. It includes many depressions and may possibly represent drowned “kettle and kame” topography developed during deglaciation. The largest rise of this group, about 15 km (8.3 nautical miles) north of Ocean Cape, has an elongate streamlined shape suggestive of a drumlin. However, because of the association with other morainal forms, this group of bathymetric highs is also believed to be of morainal origin and has been termed the mid-bay moraine. The third and most clearly defined ridge extends in an arcuate pattern across the mouth of Yakutat Bay from Ocean Cape near Yakutat village toward Point Manby. Most of this ridge, which is designated the baymouth moraine, lies at depths less than 30 m (98 feet). The ridge is breached near its western end by a channel with a maximum depth of 76 m (249 feet). A few miles offshore, within the sedimentary fill of Yakutat Seavalley,

there is at least one probable moraine buried in outwash (Wright and others, 1968).

In order to determine the bedding characteristics within the ridge sets and other sedimentary units, about 290 km (160 nautical miles) of subbottom acoustic profiles were obtained in Yakutat Bay and its tributary fiords. The subbottom profiles were studied not only for thickness and sedimentary features of unconsolidated sediments but also for data concerning the underlying geologic structure. Because the water in Yakutat Bay is shallow and acoustic reflections from the ridge highs are poor, structural features observed in the bay were largely superficial, and analysis was limited to the identification of coherent reflecting horizons.

Subbottom profiles in the broad part of the bay show a distinctive pattern of irregular acoustically opaque rises separated by patches of poorly stratified fill in the deeps (fig. 2). The highs absorb or reflect most of the sonic energy without showing any signs of stratification. The lack of good stratification virtually rules out kame-deposit origin and suggests that the highs are composed of loose heterogeneous material typical of moraines.

In Disenchantment Basin at the head of Yakutat Bay, the acoustical profiles show that the sedimentary fill reaches a thickness of at least 250 m (820 feet) (fig. 2) if a minimum

acoustic velocity of 1.5 km/second is assumed in the sediments. The basin serves as a sediment trap, capturing a large amount of the materials being introduced at the head of the bay and from the subsidiary fiords.

Other data concerning the sediments that underlie Yakutat Bay were obtained from 73 surface-sediment stations approximately 3.6 km (2 nautical miles) apart (fig. 3). These sediment samples were taken from the RV *Acona* during the survey and show that gravel-size material is a particularly conspicuous constituent of the topographic highs in Yakutat Bay (fig. 3 and table 1). On the bayhead moraine the gravel occurs in discrete zones and constitutes 89 to 94 percent of the samples. In the area of the mid-bay moraine, only two samples (Nos. 26 and 38) contained significant quantities of gravel (44 and 90 percent). Samples from the baymouth moraine contained the highest gravel concentrations (100 percent in two dredge samples, 74 to 99 percent in three Shipek samples).

Excluding the presumably relict gravel of the morainal ridges, two classes of strictly contemporary sediment are found in the bay: (1) sand, and (2) mud (silt and clay). Sand is a ubiquitous constituent in samples containing gravel (except dredge samples). In eight samples, sand constituted more than 40 percent; in nine samples, sand-size constituents amounted to between 20 and 40 percent. Nearly all these samples came

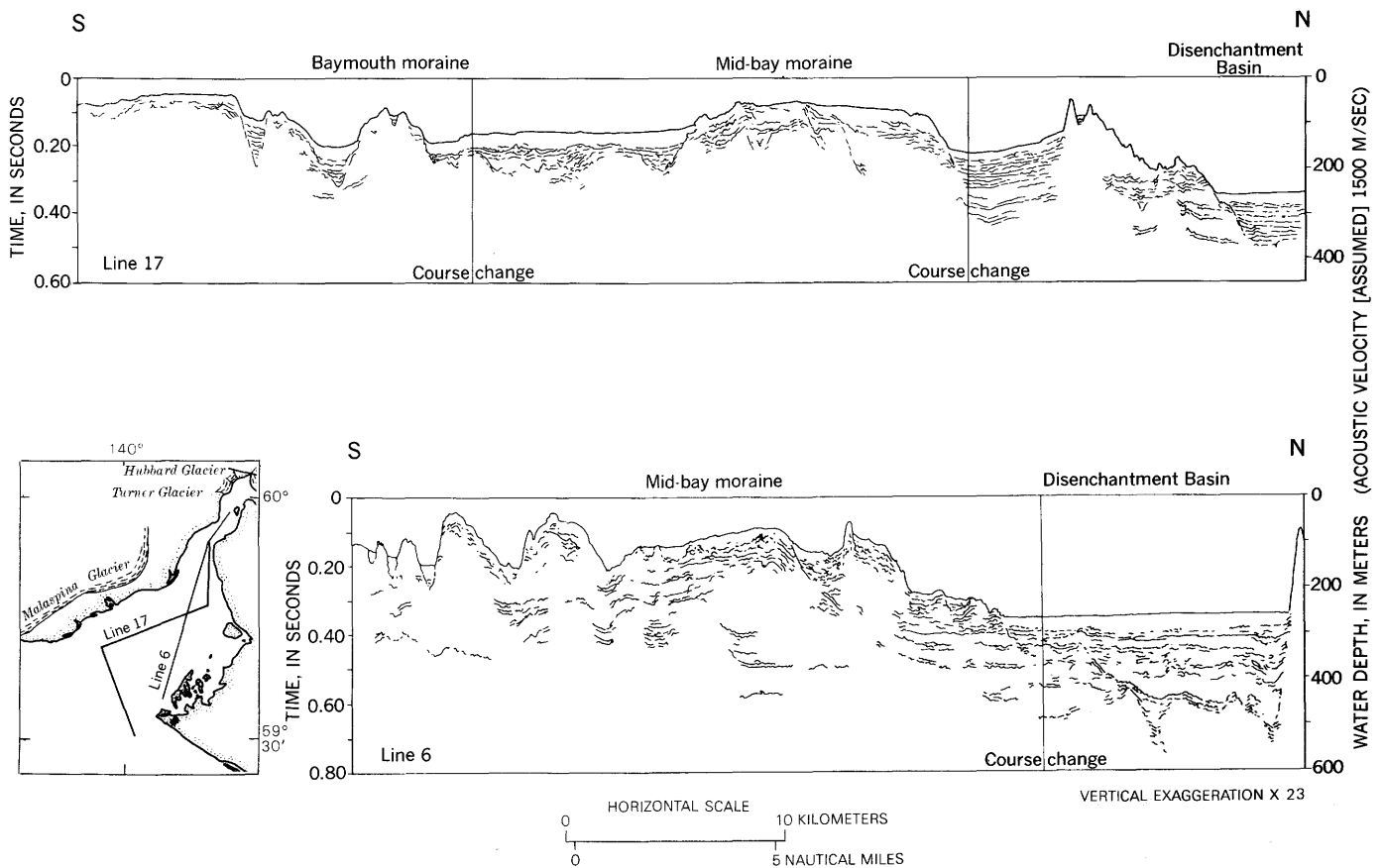


Figure 2.—Subbottom acoustic profiles in Yakutat Bay, Alaska.

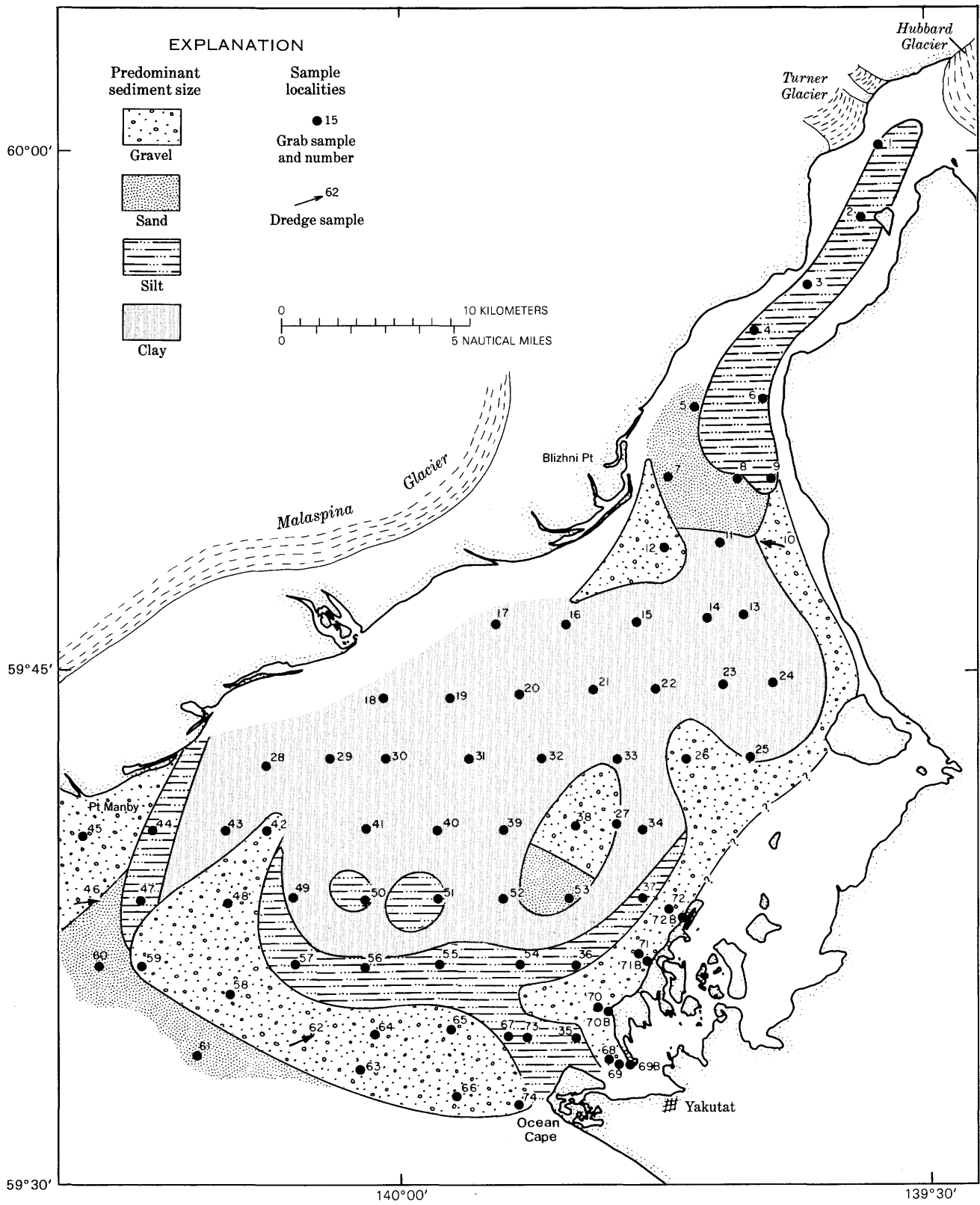


Figure 3.—Sediment distribution and sample localities, Yakutat Bay, Alaska.

Table 1.—Sediment parameters, in percent, Yakutat Bay, Alaska

[Analysts: S. M. Valencia, Sally Short, and Richard Nelson]

Station	Gravel	Sand	Silt	Clay	Heavy minerals ¹
1	0	14.37	53.80	31.83	
2	.02	.92	50.70	48.36	
3	.92	3.58	48.20	47.29	17.2
4	2.22	4.85	46.08	46.85	18.1
5	.02	.80	44.20	54.99	
6	.75	1.76	48.49	48.50	18.3
7	.86	47.48	35.26	16.39	
8	.41	42.32	34.24	23.03	
9	1.75	4.71	46.20	47.34	
10	94.18	3.18	1.27	1.37	
11	0	25.15	31.23	43.62	16.0
12	88.98	8.07	1.84	1.10	
13	.95	1.06	31.27	66.73	
14	.72	1.21	33.21	64.86	
15	1.12	2.68	41.08	55.11	
16	.55	2.22	37.95	59.28	
17	.44	1.11	34.23	64.22	
18	1.70	1.85	33.17	63.27	
19	1.12	1.16	29.72	68.00	
20	1.08	.92	13.79	84.21	
21	6.17	4.37	32.75	56.71	16.9
22	0	1.36	39.16	59.48	
23	.56	.83	33.41	65.20	
24	.20	.39	33.60	65.81	
25	11.72	6.50	33.92	47.86	
26	43.92	17.05	18.01	21.02	
27		No recovery			
28	.60	1.21	39.41	58.78	
29	.67	.36	13.74	85.23	
30	.09	.48	30.57	68.86	
31	.10	.47	28.30	71.13	
32	1.22	2.42	40.13	56.22	11.0
33	.03	.42	38.17	61.38	
34	0	2.01	40.33	57.66	
35	0.06	40.36	46.03	13.54	19.5
36	0	22.26	48.16	29.57	
37	0	4.83	52.26	42.90	
38	89.88	9.27	.39	.46	
39	0	1.09	42.54	56.38	
40	.02	1.68	42.74	55.50	
41	0	.70	35.07	64.23	
42	65.33	2.75	17.03	14.89	
43	.71	1.03	32.38	65.88	
44	.06	5.66	53.94	40.34	1.3
45		No recovery			
46	100.00	0	0	0	
47	0	37.98	47.77	14.26	16.6
48	98.79	1.20	0	0	
49	0	.88	32.76	66.35	
50	0	4.60	41.78	53.61	
51	20.80	24.99	31.22	22.98	
52	0	4.50	39.87	55.63	
53	20.57	28.08	27.42	23.92	
54	0	7.15	55.80	37.05	17.1
55	0	24.33	55.49	20.18	19.8
56	0	3.44	48.18	48.37	
57	0	5.63	87.06	7.32	12.0
58	82.25	17.75	0	0	
59		No recovery			
60	.37	49.31	30.78	19.53	13.0

Table 1.—Sediment parameters, in percent, Yakutat Bay, Alaska—Continued

[Analysts: S. M. Valencia, Sally Short, and Richard Nelson]

Station	Gravel	Sand	Silt	Clay	Heavy Minerals ¹
61	.04	53.95	38.59	17.24	11.6
62	100.00	0	0	0	
63		No recovery			
64		No recovery			
65	34.95	65.05	0	0	
66	74.10	23.21	2.33	0	12.8
67	0	30.09	50.93	18.99	18.2
68	61.24	27.53	9.19	2.05	
69	.90	77.10	10.24	11.76	15.5
69B	32.43	67.08	.47	0	28.8
70	75.68	19.58	3.76	0.87	
70B	88.82	11.16	0	0	36.1
71	76.29	15.63	1.56	6.66	13.8
71B	80.23	17.98	2.07	0	26.5
72	23.72	10.97	40.20	25.10	
72B	87.70	13.23	0	0	16.5
73	0	48.26	40.78	10.96	20.7
74	66.38	33.22	1.02	0	23.1

¹Percentage of sand-size fraction.

from locations on or related to topographic highs. The one exception is a sandy silt from the south end of Disenchantment Bay. Across the mouth of Yakutat Bay, just seaward of the morainal gravels, a sand zone is apparently part of the material in active alongshore transport.

The characteristic sediment of the deeper part of the bay is mud made up of roughly equivalent quantities of silt and clay and locally an appreciable admixture of sand with a trace of gravel (table 1). This mud is accumulating as stratified deposits throughout the Yakutat Bay system presently protected from tidal currents or wave action. In the Disenchantment Bay area, close to the tidal glaciers, the mud grades into silt, but the material still closely resembles the mud of the main bay.

Heavy-mineral concentrations observed in the sands of the Yakutat Bay area were moderate to low. They included chlorite, amphibole, and pyroxene, with usually minor quantities of magnetite and ilmenite. Zircon was found in trace amounts. The highest concentrations were in the immediate vicinity of Yakutat village from Ocean Cape to Khantaak Island. The survey did not extend into the shallows eastward of the line between Khantaak and Knight Islands, and sands in this area might also be expected to yield moderate concentrations of heavy minerals. Since the Shipek sampler can collect only relatively small quantities of surficial sediment, this sampling technique is not ideal for heavy-mineral studies. However, the heavy-mineral concentrations summarized in table 1 may be used for preliminary assessments. Additional data are contained in reports by Tarr and Butler (1909) and Thomas and Berryhill (1962).

ECONOMIC GEOLOGY

No significant deposits of economic minerals have been found in the study area, although during the gold rush in the late 1800's there were sporadic efforts to produce gold from the black sands of the local beaches, and various prospectors investigated the neighboring St. Elias Mountains. Beach placers continue to be of potential interest for exploitation, most recently for magnetite and ilmenite as well as for gold and platinum, but no large-scale strikes have been reported in the study area (Tarr and Butler, 1909; Thomas and Berryhill, 1962). The sources of heavy minerals and metals found in the beach sands are presumed to be associated with intrusive bodies of the St. Elias crystalline complex and may well lie beneath the extensive icefields of the coastal mountains (Maddren, 1914).

Oil and gas seeps are found in various parts of the coastal plain centered on Yakutat Bay, and a small oil field of Katalla, 240 km (150 miles) west of Yakutat, was exploited from 1902 to 1933 (Stoneley, 1967). Thirty or more exploratory wells have been drilled on the coastal plain, including several in the immediate vicinity of Yakutat Bay, but no commercial production has been developed (Plafker, 1967).

SUMMARY AND CONCLUSIONS

The marine geology of Yakutat Bay closely reflects the recent glacial and glacial marine history of the area. There is only limited direct contact now with the glaciers of the St. Elias Mountains, but the bay and surrounding coastal plain are dominated by evidence of glacial activity. The entire present bay system has formed since A.D. 1400, the approximate date of the older recession in the region (Plafker and Miller, 1958). Both subbottom records and sediment distribution show the bay to be a pattern of morainal material somewhat modified by contemporary sedimentation and wave and current action.

Sedimentation is very active in the deeper parts of the Yakutat Bay system. Despite the possibility that coarse debris was iceberg rafted, most of the minerals are muds, possibly transported as turbid layers either on the bottom or within the water column (Moore, 1966). Such muds have been termed "periglacial muds" and are thought to be the typical marine sediment associated with active deglaciation (Wright and Sharma, 1969). Sedimentation rates appear to be very high within the entire system, presumably because of the availability of sediments and the activity of the various sedimentary agents (Jordan, 1962).

Heavy minerals are present in the glacial sediments of the Yakutat Bay area. The percentages are highest where contemporary sorting mechanisms, particularly wave attack, have winnowed and concentrated the heavy minerals. The lowest percentages are found toward the head of the bay where sedimentation is so rapid that the heavy minerals are masked by other sediments.

REFERENCES

- Bandy, O. L., Butler, E. A., and Wright, R. C., 1969, Alaskan Upper Miocene marine glacial deposits and the *Turborotalia pachyderma* datum plane: *Science*, v. 166, p. 607-609.
- Johnson, P. R., and Hartman, C. W., 1969, Environmental atlas of Alaska: College, Alaska, Alaska Univ. Inst. of Arctic Environmental Eng., 111 p.
- Jordan, G. F., 1962, Redistribution of sediments in Alaskan bays and inlets: *Geog. Rev.*, v. 52, p. 548-558.
- Maddren, A. G., 1914, Mineral resources of the Yakataga district, Alaska: U.S. Geol. Survey Bull. 592-E, p. 119-153.
- Miller, D. J., 1958, Anomalous glacial history of the northeastern Gulf of Alaska region: *Geol. Soc. America Bull.*, v. 69, no. 12, pt. 2, p. 1613-1614.
- 1961, Geology of the Yakutat district, Gulf of Alaska Tertiary Province, Alaska: U.S. Geol. Survey open-file map.
- Miller, M. M., 1964, Inventory of terminal position changes in Alaskan coastal glaciers since the 1750's: *Am. Philos. Soc. Proc.* v. 108, p. 257-273.
- Moore, D. G., 1966, Structure, litho-orogenic units, and postorogenic basin fill by reflection profiling, California Continental Borderland: Unpub. Ph. D. dissert., Groningen Univ., the Netherlands, 151 p.
- Plafker, George, 1967, Geologic map of the Gulf of Alaska Tertiary Province, Alaska: U.S. Geol. Survey Misc. Geol. Inv. Map I-484, scale 1:500,000.
- Plafker, George, and Miller, D. J., 1958, Glacial features and surficial deposits of the Malaspina district, Alaska: U.S. Geol. Survey Misc. Geol. Inv. Map I-271, scale 1:125,000.
- Reimnitz, Erk, von Huene, Roland, and Wright, F. F., 1970, Detrital gold and sediments in Nuka Bay, Alaska, in *Geological Survey Research 1970*: U.S. Geol. Survey Prof. Paper 700-C, p. C35-C42.
- Sharp, R. P., 1958, Malaspina Glacier, Alaska: *Geol. Soc. America Bull.*, v. 69, p. 617-646.
- Stoneley, Robert 1967, The structural development of the Gulf of Alaska sedimentary province in southern Alaska: *Geol. Soc. London Quart. Jour.*, v. 123, p. 25-57.
- Tarr, R. S., and Butler, B. S., 1909, The Yakutat Bay region, Alaska: U.S. Geol. Survey Prof. Paper 64, 183 p.
- Tarr, R. S., and Martin, Lawrence, 1912, The earthquakes at Yakutat Bay, Alaska, in September, 1899: U.S. Geol. Survey Prof. Paper 69, 135 p.
- Thomas, B. I., and Berryhill, R. V., 1962, Reconnaissance studies of Alaskan beach sands, eastern gulf of Alaska: U.S. Bur. Mines Rept. Inv. 5986, 40 p.
- U.S. Coast and Geodetic Survey, 1964, U.S. Coast Pilot 9, Pacific and Arctic Coasts, Alaska, Cape Spencer to Beaufort Sea [7th ed.]: Washington, D.C., U.S. Government Printing Office.
- U.S. Environmental Science Services Administration, 1967, Annual summary of local climatological data, 1966: U.S. Dept. Commerce, 4 p.
- Valencia, S. M., and Wright, F. F., 1968, Sediments of Yakutat Bay and the eastern Gulf of Alaska continental shelf [abs.]: 19th Alaska Sci. Conf., Program, Am. Assoc. Adv. Sci., Whitehorse, Yukon Territory, p. 66.
- Wright, F. F., 1970, Turbid layer sedimentation in Alaskan fiords [abs.]: EOS (Am. Geophys. Union Trans.), v. 51, p. 335.
- Wright, F. F., and Sharma, G. D., 1969, Periglacial marine sedimentation in southeastern Alaska [abs.]: Internat. Assoc. for Quaternary Research, 8th Cong., Paris, Proc., p. 73.
- Wright, F. F., von Huene, Roland, and Lathram, E. H., 1968, Tectonic features of the continental shelf in the northeastern Gulf of Alaska [abs.]: *Am. Geophys. Union Trans.*, v. 49, p. 207.



LEIOSPHAERIDIA (ACRITARCHA) IN THE MESOZOIC OIL SHALES OF NORTHERN ALASKA

By ROGER F. BONEHAM¹, and IRVIN L. TAILLEUR,
Kokomo, Ind., Menlo Park, Calif.

Abstract.—Three collection sites in northern Alaska have yielded *Leiosphaeridia borealis* n. sp. and *L. rugosa* n. sp. from a type of oil shale known as tasmanite. The age of the strata is presumably Jurassic.

A number of reports on the oil shales of northern Alaska have noted that the alga *Tasmanites* makes an oil-rich rock called tasmanite. On microscopic examination, Boneham has found that tasmanite from three different localities also contains the *Leiosphaeridia* genus of Acritarcha, an artificial group of microfossils with uncertain (but undoubtedly both animal and plant) affinities (Evitt, 1963). He describes herein two new species that appear to have contributed to the rich accumulation of organic remains in the tasmanite. The geology on which the Jurassic age is based is summarized by Tailleux.

OIL SHALES

The extensive occurrence of oil shale in northern Alaska has been known for some time (Collier, 1906; Smith and Mertie, 1930). With support from the U.S. Navy through the Office of Petroleum and Oil Shale Reserves and the Naval Arctic Research Laboratory (Office of Naval Research), the U.S. Geological Survey recently began a systematic investigation of the oil yield and areal extent of the oil shale (Tailleur, 1964; Duncan and Swanson, 1965; Tourtelot and Tailleux, 1966; Tourtelot and others, 1967).

Organically rich shales were found in rock units ranging in age from Mississippian to Late Cretaceous (Donnell and others, 1967). The oil yield of the Paleozoic shales is low, however, and attention has been focused on the oil shales of probable Mesozoic age.

Most of the oil shales crop out in terranes of complexly deformed rocks that have not been mapped in enough detail to be defined with confidence. Tasmanite and cannel shale are the richest and most widely distributed types of rock. They are inferred to be Jurassic in age but can be dated with assurance only as post-Mississippian and pre-Cretaceous.

TASMANITE SAMPLES

The three samples of this report were collected by Robert Blair in the west-central part of the southern section of the Arctic Foothills of the Brooks Range (fig. 1). Many of the rocks that form the southern section of the foothills and the western Brooks Range to the south have been strongly dislocated and deformed (Tailleur, 1969a). They appear to have been foreshortened along broad, flat thrusts during the Early Cretaceous to about half their original north-south extent (Snelson and Tailleux, 1968; Tailleux and Snelson, 1969; Tailleux, 1969b).

Tasmanite occurs in two of the several different rock sequences that have been thrust together. The original spatial relation between these two sequences is undetermined. The more widespread sequence (Ipnavik tectonic unit of Snelson and Tailleux, 1968) is characterized by Devonian and Mississip-

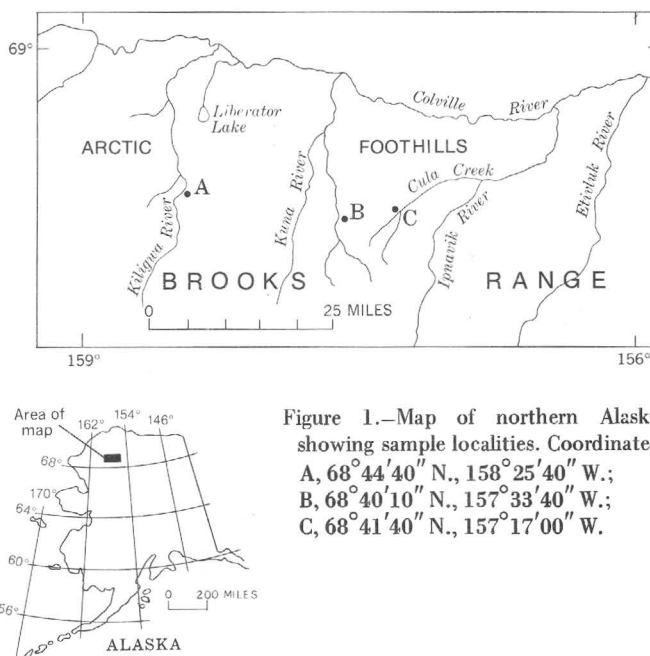


Figure 1.—Map of northern Alaska, showing sample localities. Coordinates: A, $68^{\circ}44'40''$ N., $158^{\circ}25'40''$ W.; B, $68^{\circ}40'10''$ N., $157^{\circ}33'40''$ W.; C, $68^{\circ}41'40''$ N., $157^{\circ}17'00''$ W.

¹ Indiana University.

pian carbonates (Baird and Lisburne Groups), numerous diabase sills, and earliest Cretaceous coarse-grained orogenic deposits (Okpikruak Formation). The other sequence is distinguished by an absence of igneous rocks and by earliest Cretaceous fine-grained orogenic deposits. An unnamed unit of varicolored chert is conspicuous in both sequences; clay shale with boudins or thin layers of tasmanite and cancell shale is interlayered with radiolarian chert in the upper part of this unit.

Paleozoic as well as Mesozoic time is represented by the chert unit, but a Jurassic age is inferred for the upper tasmanite-bearing part. In the Ipnavik tectonic unit, the chert unit lies between the Lisburne Group, which is here of Mississippian age, and the earliest Cretaceous Okpikruak Formation; Late Paleozoic fossils have been collected from the base of the chert, and a foraminifer from the clay shale in the upper part has been identified as a Jurassic and Cretaceous form (H. R. Bergquist, written commun., 1952). Further, the upper part appears volcanogenic; volcanic episodes in northern Alaska have been dated as Jurassic from paleontologic data (Imlay, 1955, p. 77, 86; Patton and Tailleux, 1964, p. 444; Jones and Grantz, 1964, p. 1468) and radiometrically (Tailleur and Brosgé, 1970, p. E5). The interlayered cancell shale is very similar to that containing Jurassic fossils (Imlay, 1967, p. 6) in another of the juxtaposed sequences.

Samples A and B appear to be tasmanite from the Ipnavik tectonic unit, in which the varicolored radiolarian chert is

associated with diabase sills. Sample C likely represents tasmanite in the other sequence because the outcrop is a few miles north of the mapped limit of the Ipnavik tectonic unit, and no igneous rock was exposed in the chaos of rock types in outcrop (table 1).

SYSTEMATIC PALEONTOLOGY

All specimen numbers refer to the Indiana University, Bloomington, Department of Geology fossil collection. Individual specimens are located on a given slide using an England Finder Slide.

Group ACRITARCHA Evitt, 1963

Subgroup SPHAEROMORPHITAE Downie, Evitt, and Sarjeant, 1963

Genus LEIOSPHAERIDIA Eisenack, 1958 Leiosphaeridia borealis n. sp.

Figure 2, a

Description.—Diameter 180μ – 450μ ; 70 specimens measured, 93 percent are in the size range 200μ – 360μ . Wall about 1μ thick. Lunate folds on most of the specimens. None of the specimens has a pylome.

Remarks.—This species resembles *Leiosphaeridia voighti* Eisenack 1958 from the Ordovician of the U.S.S.R. in that they both have lunate folds and thin walls. *L. voighti* has a somewhat smaller size range (190μ – 310μ), and many specimens have a

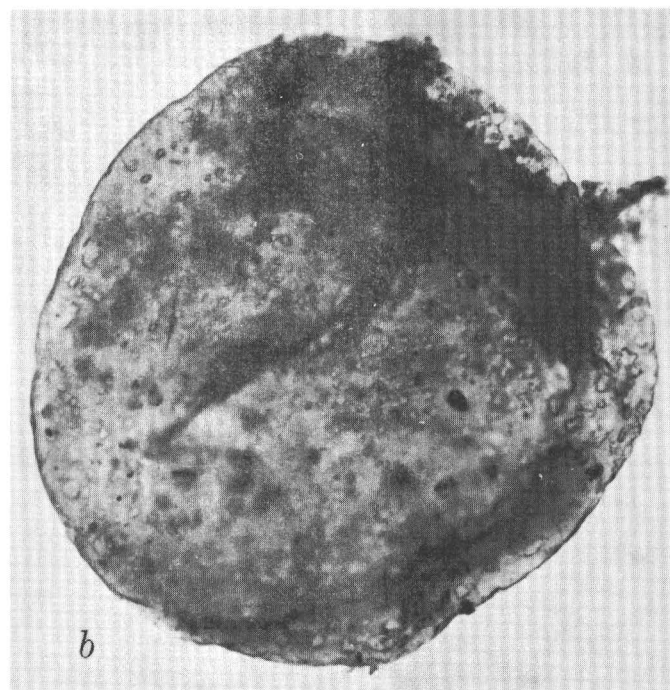
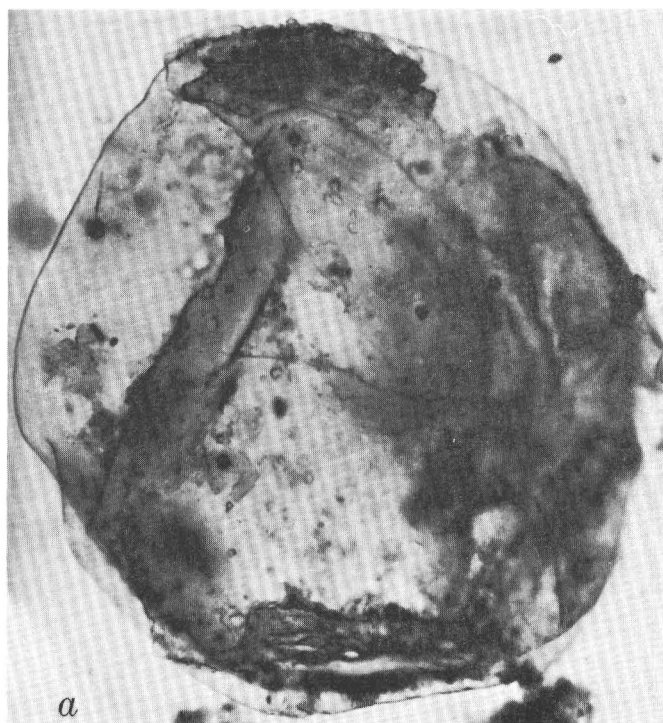


Figure 2.—Two new species of Acritarcha from northern Alaska. Both specimens $\times 260$.

a, *Leiosphaeridia borealis* n. sp. Holotype, IU12132K34/1, locality B.

b, *Leiosphaeridia rugosa* n. sp. Holotype, IU12134H39/4, locality A.

Table 1.—Relative proportions of *Leiosphaeridia* species at the collecting sites

Site	Number of specimens		
	<i>L. rugosa</i>	<i>L. borealis</i>	<i>L. rugosa/L. borealis</i>
A	75	9	8.3
B	89	11	8.1
C	88	12	7.3

pylome. The taxonomic value of the pylome in *Leiosphaeridia* has yet to be decided upon. Apparently in some species it is always present and in others it is rarely, if ever, present; in still other species it may or may not be present on a given individual. Since *L. voighti* usually has a pylome (Eisenack, 1958, p. 392) and since no specimens of *L. borealis* have been found with a pylome (hundreds of individuals were examined in this study), we believe *L. borealis* is distinct from *L. voighti*. *L. plicata* Felix 1965 from the Neogene of southern Louisiana resembles *L. borealis* in the wall folding. However *L. plicata* is smaller (120μ – 200μ) and has a thicker wall (3μ – 7μ) than *L. borealis*.

Leiosphaeridia rugosa n. sp.

Figure 2, b

Description.—Diameter 180μ – 400μ ; 25 specimens measured, 91 percent in the size range 200μ – 380μ . Wall thickness 5μ – 7μ . Wall folded in sinuous curves or not folded. No pylome or puncta.

Remarks.—This species bears a remarkable resemblance to *Tasmanites sinuosus* Winslow 1962 from the Upper Devonian and Lower Mississippian of Ohio. They both have the sinuous wall folds, approximately the same diameter (*T. sinuosus* commonly 150μ – 325μ), and similar wall thickness (*T. sinuosus* commonly 3μ – 10μ). However, as *T. sinuosus* has numerous puncta (a generic character of *Tasmanites*), *Leiosphaeridia rugosa* is easily distinguished from it. The walls of many specimens of *L. rugosa* are somewhat pitted. Because the pitting is irregular on a given specimen and most individuals have rugose walls, we do not believe it is a specific character. The pitting is probably caused by corrosion either from the chemicals used to macerate the rock or by the ground water in the rock. There are some specimens which are gradational between *L. borealis* and *L. rugosa*. They have walls which are 3μ – 4μ thick and have lunate folds. There are few such individuals; apparently populations of *Leiosphaeridia* species contain a few gradational forms which defy exact classification. Winslow (1962, p. 82) noted the presence of such forms in populations of *Tasmanites* species as well.

REFERENCES

- Collier, A. J., 1906, Geology and coal resources of the Cape Lisburne region, Alaska: U.S. Geol. Survey Bull. 278, 54 p.
- Donnell, J. R., Tailleir, I. L., and Tourtelot, H. A., 1967, Alaskan oil shale: Colorado School Mines Quart., v. 62, p. 39–43.
- Downie, Charles, Evitt, W. R., Sarjeant, W. A. S., 1963, Dinoflagellates, hystrichospheres, and the classification of the acritarchs: Stanford Univ. Pubs. Geol. Sci., v. 7, pt. 3, 16 p.
- Duncan, D. C., and Swanson, V. E., 1965, Organic-rich shale of the United States and world land areas: U.S. Geol. Survey Circ. 523, 30 p.
- Eisenack, Alfred, 1958, Mikrofossilien aus dem Ordovizium des Baltikums: Senckenbergiana Lethaea, v. 39, p. 389–405.
- Evitt, W. R., 1963, A discussion and proposals concerning fossil dinoflagellates, hystrichospheres, and acritarchs, II: Natl. Acad. Sci. Proc., v. 49, p. 298–302.
- Felix, C. J., 1965, Neogene *Tasmanites* and leiospheres from southern Louisiana, U.S.A.: Palaeontology, v. 8, p. 16–26.
- Imlay, R. W., 1955, Characteristic Jurassic mollusks from northern Alaska: U.S. Geol. Survey Prof. Paper 274-D, p. 69–96.
- 1967, The Mesozoic pelecypods *Otapiria* Marwick and *Lupherella* Imlay, new genus in the United States: U.S. Geol. Survey Prof. Paper 573-B, p. 1–11.
- Jones, D. L. and Grantz, Arthur, 1964, Stratigraphic and structural significance of Cretaceous fossils from Tigliukpuk Formation, northern Alaska: Am. Assoc. Petroleum Geologists Bull., v. 48, p. 1462–1474.
- Patton, W. W., Jr., and Tailleir, I. L., 1964, Geology of the Killik-Itkilik region, Alaska: U.S. Geol. Survey Prof. Paper 303-G, p. 409–500.
- Smith, P. S., and Mertie, J. B., Jr., 1930, Geology and mineral resources of northwestern Alaska: U.S. Geol. Survey Bull. 815, 315 p.
- Snelson, Sigmund, and Tailleir, I. L., 1968, Large-scale thrusting and migrating Cretaceous foredeeps in the western Brooks Range and adjacent regions of northwestern Alaska [abs.]: Am. Assoc. Petroleum Geologists Bull., v. 52, p. 567.
- Tailleir, I. L., 1964, Rich oil shale from northern Alaska: Art. 148 in U.S. Geol. Survey Prof. Paper 475-D, p. D131–D133.
- 1969a, Speculations on North Slope geology: Oil and Gas Jour., v. 67, no. 38, p. 215–220, 225–226.
- 1969b, Rifting speculation on the geology of Alaska's North Slope: Oil and Gas Jour., v. 67, no. 39, p. 128–130.
- Tailleir, I. L., and Brosge, W. P., 1970, Tectonic history of northern Alaska, in Adkison, W. L., and Brosge, M. M., eds., Proceedings of the geological seminar on the North Slope of Alaska: Los Angeles, Am. Assoc. Petroleum Geologists Pacific Sec., p. E1–E20.
- Tailleir, I. L., and Snelson, Sigmund, 1969, Large-scale thrusting in northwestern Alaska possibly related to rifting of the Arctic Ocean [abs.]: Geol. Soc. America Spec. Paper 121, p. 569.
- Tourtelot, H. A., and Tailleir, I. L., 1966, Oil yield and chemical composition of shale from northern Alaska: U.S. Geol. Survey open-file report 17 p., 5 charts.
- Tourtelot, H. A., Donnell, J. R., and Tailleir, I. L., 1967, Oil yield and chemical composition of shale from northern Alaska: World Petroleum Cong., 7th, Mexico, 1967, Proc., v. 3, p. 707–711.
- Winslow, M. R., 1962, Plant spores and other microfossils from Upper Devonian and Lower Mississippian rocks of Ohio: U.S. Geol. Survey Prof. Paper 364, 93 p., 22 pls.

QUARTZ-SAND-BEARING ZONE AND EARLY SILURIAN AGE OF UPPER PART OF THE HANSON CREEK FORMATION IN EUREKA COUNTY, NEVADA

By THOMAS E. MULLENS and FORREST G. POOLE, Denver, Colo.

Abstract.—The upper part of the Hanson Creek Formation in Eureka County, Nev., contains a widespread quartz-sand-bearing zone. Heretofore the entire Hanson Creek has been assigned to the Ordovician, but conodonts indicate an Early Silurian age for that part of the Hanson Creek above the base of the sand-bearing zone, although the system boundary cannot be precisely placed.

This report has three purposes: (1) to report a quartz-sand-bearing zone in the upper part of the Hanson Creek Formation at seven localities in Eureka County, Nev.; (2) to report that at two of these localities the upper part of the Hanson Creek contains Early Silurian conodonts; and (3) to change the age of the Hanson Creek to include Early Silurian. We do not change the currently accepted mapping contacts of the Hanson Creek. Nor do we try to place the boundary of the Ordovician and Silurian within the Hanson Creek any more precisely than at or below the base of the sandy zone.

STRATIGRAPHY

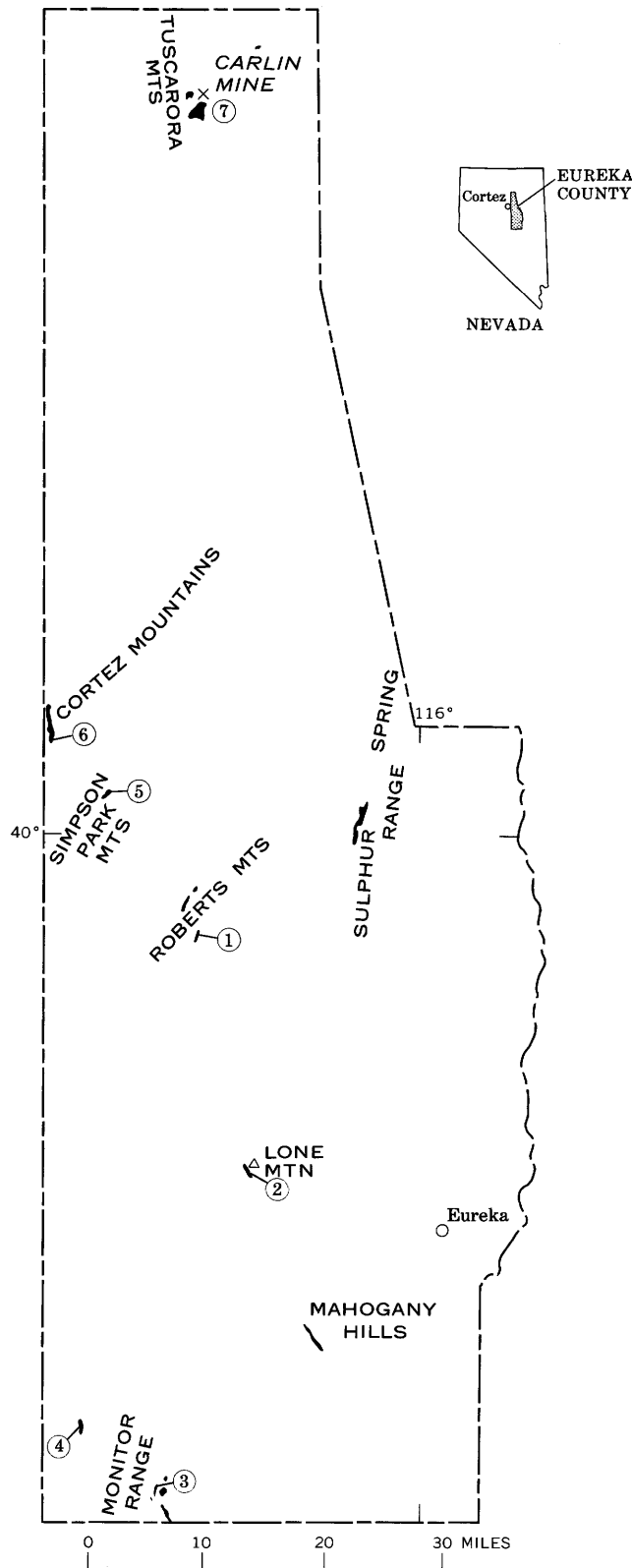
The Hanson Creek Formation was defined by Merriam (1940, p. 10–11) to include those rocks between the Ordovician Eureka Quartzite and the Silurian Roberts Mountains Formation. The type locality consists of about 500 feet of dolomite and limestone exposed along Pete Hanson Creek in the Roberts Mountains, in central Eureka County, Nev. (fig. 1). Merriam considered the Hanson Creek to be Middle and Late Ordovician in age. The contacts of the Hanson Creek with the underlying and overlying formations at the type locality and throughout Eureka County are conspicuous. The basal contact is at the top of light-colored quartzite, and the upper contact is at the base of dark-gray chert and cherty limestone or dolomite. Since being defined by Merriam, the name Hanson Creek has been applied to all strata between the Eureka Quartzite and Roberts Mountains Formation in Eureka County, and a Middle(?) and Late Ordovician age of these strata has been assigned (Roberts and others, 1967). The Hanson Creek is dominantly medium- to dark-gray, medium- to thin-bedded limestone, dolomitic limestone, and dolomite

and ranges in thickness from 300 to 800 feet (Roberts and others, 1967, p. 20). The upper part contains a persistent but locally inconspicuous quartz-sand-bearing zone a few inches to 30 feet thick. The base of this sandy zone is 15 to 68 feet below the top of the Hanson Creek in Eureka County. A similar quartz-sand-bearing-zone has been recognized by Poole in units that correlate with the upper part of the Hanson Creek over a large part of the Great Basin.

A generalized outcrop pattern of the Hanson Creek in Eureka County is shown on figure 1. The formation crops out in eight major areas, and we have found the sandy zone at seven localities indicated by numbers (fig. 1) within the eight areas. The sandy zone was not seen in a brief examination of outcrops in the Sulphur Spring Range, and we have not examined the outcrops in the Mahogany Hills. The sand content ranges from a few grains to about 75 percent. In most places, the zone is inconspicuous and consists of sand grains disseminated in carbonate rock that is similar to other carbonate rock in the upper part of the Hanson Creek. The grains are mostly frosted and clear quartz but include minor amounts of unidentified dark-gray to black mineral or minerals. The grains are mainly subrounded to rounded and range in size from fine to medium coarse. The thickness, distance below the top, and general character of the zone at each of the seven localities are shown in table 1. The localities are places where we examined the upper part of the Hanson Creek Formation as part of our primary interest in studying the overlying Roberts Mountains Formation. The extent, thickness, and character of the zone away from the localities are not known except in the vicinity of the Carlin mine (loc. 7, fig. 1), where its thickness and character are extremely variable. The zone is assumed to be as variable elsewhere.

FOSSILS AND AGE

Eight samples of the Hanson Creek from or above the sandy zone were collected and sent to John W. Huddle, U.S. Geological Survey, for recovery of conodonts. Huddle recovered and identified Early Silurian conodonts from three of



the eight samples; the other five samples contained no conodonts. Two of the conodont-bearing samples (USGS 8488-SD and 8489-SD) are from Copenhagen Canyon (loc. 3, fig. 1). One of these (8488-SD) is a composite sample of 3 feet of strata that includes the sandy zone; the other (8489-SD) is a composite sample of nonsandy dolomite that forms the top 3 feet of the Hanson Creek. The third conodont-bearing sample (USGS 8823-SD) was collected about 1 mile south of the Carlin Mine (loc. 7, fig. 1). It is a grab sample of nonsandy dolomite 5 feet below the top of the Hanson Creek and 15 feet above a 4-foot-thick sandy dolomite that forms the sandy zone. More exact collection localities for the samples and the conodonts that they contained are listed below.

Number of specimens

USGS 8488-SD. 15–18 feet below top of Hanson Creek Formation, Copenhagen Canyon about 1 mile northeast of Rabbit Hill, Monitor Range, E½ SW¼ sec. 36, T. 16 N., R. 49 E., Horse Heaven Mountain 15-minute quadrangle, Eureka County, Nev.

Icriodina cf. I. stenolopata Rexroad 1

USGS 8489-SD. 0–3 feet below top of Hanson Creek Formation, same locality as USGS 8488-SD.

Acodus unicosatus Branson 2
Drepanodus aduncus Nicoll and Rexroad 1
Panderodus sp. 2
Paltodus cf. P. dyscritus Rexroad 2

USGS 8823-SD. 5 feet below top of Hanson Creek Formation, SE¼ NE¼ sec. 23, T. 35 N., R. 50 E., Tuscarora Mountains, Rodeo Creek NE 7½-minute quadrangle, Eureka County, Nev.

Drepanodus aduncus Nicoll and Rexroad 2
Hindeodella sp. 1
Icriodina irregularis Branson and Branson 1
Ligonodina kentuckyensis Branson and Branson 9
Neoprioniodus sp. 3
Ozarkodina sp. 2
Paltodus dyscritus Rexroad 17
Panderodus sp. 60
Synprioniodina sp. 1
Trichonodella aff. *T. papilo* Nicoll and Rexroad 2

The following discussion concerning the age of the conodonts is based on information provided by Huddle (written commun., 1971). All three collections are Early Silurian in

Figure 1.—Map of Eureka County, Nev., showing outcrops of Hanson Creek Formation. Outcrop pattern modified from Roberts, Montgomery, and Lehner (1967, pl. 3). Numbers indicate localities where sandy zone was seen in the upper part of the Hanson Creek Formation.

- | | |
|-------------------------------------|--|
| 1. Pete Hanson Creek. | 5. Coal Canyon. |
| 2. Southwest side of Lone Mountain. | 6. Unnamed canyon 1.5 miles southeast of Cortez. |
| 3. Copenhagen Canyon. | 7. South and west of the Carlin mine. |
| 4. Brock Canyon. | |

Table 1.—*Thickness, distance below top, and character of quartz-sand-bearing zone in upper part of Hanson Creek Formation, Eureka County, Nev.*

Locality	Thickness	Distance between base of zone and top of Hanson Creek Formation (feet)	Character of zone
1. Pete Hanson, Creek, Roberts Mountains (type locality of Hanson Creek Formation).	0.5–3.5	30	Fine to medium quartz grains sparsely disseminated in mottled light-gray fine- to medium-grained dolomite.
2. Southwest side of Lone Mountain.	17	68	Conspicuous dark-gray unidentified mineral grains and frosted clear medium quartz grains common in light-gray fine-grained dolomite.
3. Copenhagen Canyon, Monitor Range.	.1	18	Rounded fine- to medium-coarse quartz grains sparsely disseminated in medium-, to medium-dark-gray fine-grained dolomite.
4. Brock Canyon, Monitor Range.	.1	15	Well-rounded very fine to medium quartz grains in thin-bedded medium-dark-gray limestone matrix. Sand grains form about 75 percent of rock. Scattered coarse phosphatic grains.
5. Coal Canyon, Simpson Park Mountains.	15	22	Subrounded to rounded fine to medium quartz sand forms about 50 percent of rock in medium-bedded gray dolomitic limestone matrix.
6. Unnamed canyon, Cortez Mountains, 1.5 miles southeast of Cortez, Nev.	16	60	Subrounded to rounded fine to medium quartz sand and unidentified dark-gray mineral sparsely disseminated in medium-dark-gray thick-bedded fine-grained limy dolomite that weathers light gray.
7. South and west of Carlin mine, Tuscarora Mountains.	2–30	18–30	Zone extremely variable. Locally as much as 30 feet thick where fine- to medium-coarse quartz grains form as much as 75 percent of rock in dolomite matrix and extend to the upper contact. These places commonly weather light brown. Other places have a 2- to 4-foot zone of disseminated quartz grains in dolomite about 25 feet below top and no quartz grains above.

age. The critical species are *Icriodina irregularis* and *Icriodina stenolopata*, which are confined to the *I. irregularis* Assemblage Zone of Rexroad (1967). The other species and genera listed are common in the Lower Silurian Brassfield Limestone and in the Silurian Salamonie Dolomite of Pinsak and Shaver (1964) along the Cincinnati arch in the Eastern United States, according to Nicoll and Rexroad (1968). They also occur in the Early Silurian in northern Michigan and Ontario, according to Pollock, Rexroad, and Nicoll (1970). The *I. irregularis* Zone is not the lowest Silurian conodont assemblage zone, inasmuch as it lies above the *Panderodus simplex* Assemblage Zone (Pollock and others, 1970) which occurs in the base of the Early Silurian in the Michigan basin area.

These conodonts are the only fossils so far reported from this part of the Hanson Creek. Because of this, the conodonts cannot be correlated directly with graptolite, coral, or brachio-

pod zones that would give a more precise position in the Early Silurian. In Eureka County the upper limits of the age of the conodont faunas can be determined from graptolites found in the overlying Roberts Mountains Formation. The standard British graptolite zones (Elles and Wood, 1901–18) for Lower Silurian and the lower part of Middle Silurian are listed in table 2.

W. B. N. Berry has identified *Climacograptus* cf. *C. rectangularis* (McCoy), *Dimorphograptus confertus* cf. var. *Swanstoni* (Lapworth), and *Glyptograptus* from 102 feet above the base of the Roberts Mountains Formation at the Copenhagen Canyon section. According to Berry (written commun., 1970) these graptolites are indicative of zone 18 of the Great Britain section, although this position in the Great Basin is not firmly established. The conodonts at Copenhagen Canyon, therefore, are possibly no younger than zone 18.

Table 2.—*Graptolite zones for Lower Silurian and lower part of Middle Silurian Series in Great Britain.*
[From Elles and Wood (1901–18)]

SILURIAN	MIDDLE (part)	WENLOCK (part)	27	<i>Monograptus riccartonensis</i>		
			26	<i>Cyrtograptus murchisoni</i>		
	LOWER	LLANDOVERY	UPPER	25	<i>Monograptus crenulatus</i>	
				24	<i>Monograptus griestoniensis</i>	
				23	<i>Monograptus crispus</i>	
				22	<i>Monograptus turriculatus</i>	
				21	<i>Monograptus sedgwicki</i>	
				20	<i>Monograptus convolutus</i>	
			MIDDLE	LOWER	19	<i>Monograptus gregarius</i>
					18	<i>Monograptus cyphus</i>
					17	<i>Orthograptus vesiculosus</i>
					16	<i>Akidograptus acuminatus</i>
UPPER ORDOVICIAN						

The conodont fauna from near the Carlin mine area probably is the same age; there, however, the first graptolite found above the Hanson Creek is *Monograptus spiralis*, which is indicative of uppermost Lower Silurian (zone 25 according to W. B. N. Berry, written commun., 1970). *M. spiralis* is only 35 feet above the conodont collection.

The sandy zone is a good stratigraphic marker in the upper part of the Hanson Creek Formation and has been found from the southern to the northern parts of Eureka County. The Early Silurian age of the conodonts from above the sandy zone indicates that the age of the Hanson Creek Formation should be changed to include Early Silurian as well as Ordovician. The boundary between Silurian and Ordovician rocks likely is at or below the sandy zone, and within the upper part of the Hanson Creek.

REFERENCES

- Elles, G. L., and Wood, E. M. R., 1901–18, A monograph of British graptolites: Palaeont. Soc. London, 539 p., 52 pls.
- Merriam, C. W., 1940, Devonian stratigraphy and paleontology of the Roberts Mountains region, Nevada: Geol. Soc. America Spec. Paper 25, 114 p.
- Nicoll, R. S., and Rexroad, C. B., 1968, Stratigraphy and conodont paleontology of the Salamonie Dolomite and Lee Creek Member of the Brassfield Limestone (Silurian) in southeastern Indiana and adjacent Kentucky: Indiana Geol. Survey Bull. 40, 73 p.
- Pinsak, A. P., and Shaver, R. H., 1964, The Silurian formations of northern Indiana: Indiana Geol. Survey Bull. 32, 87 p.
- Pollock, C. A., Rexroad, C. B., and Nicoll, R. S., 1970, Lower Silurian conodonts from Northern Michigan and Ontario: Jour. Paleontology, v. 44, no. 4, p. 743–764.
- Rexroad, C. B., 1967, Stratigraphy and conodont paleontology of the Brassfield (Silurian) in the Cincinnati Arch area: Indiana Geol. Survey Bull. 36, 64 p.
- Roberts, R. J., Montgomery, K. M., and Lehner, R. E., 1967, Geology and mineral resources of Eureka County, Nevada: Nevada Bur. Mines Bull. 64, 152 p.



TREND-SURFACE ANALYSIS OF THE THICKNESS OF THE HIGH BRIDGE GROUP (MIDDLE ORDOVICIAN) OF CENTRAL KENTUCKY AND ITS BEARING ON THE NATURE OF THE POST-KNOX UNCONFORMITY

By D. E. WOLCOTT, E. R. CRESSMAN, and J. J. CONNOR,
Bandung, Indonesia, Lexington, Ky., Denver, Colo.

Work done in cooperation with the Kentucky Geological Survey

Abstract.—The High Bridge Group (Middle Ordovician) of central Kentucky rests disconformably on the Knox Group. Trend-surface analysis of the thickness of the High Bridge demonstrates that the Cincinnati arch was not present in Middle Ordovician time and that the erosion surface at the top of the Knox Group had a regional slope to the southeast of less than 1 to about 4 feet per mile. Local relief on the erosion surface attains a maximum of about 200 feet but averages about 50 feet. Those fault zones that were active in the Cambrian occupy topographic lows. Petroleum accumulation in the topographic highs and zinc accumulation in paleokarst features in the Knox Group in neighboring areas suggest that trend-surface analysis may aid in exploration.

Thickness data from one deep water well were taken from a gamma-ray log on file with the Kentucky Geological Survey.

STRATIGRAPHY

The erosion surface at the top of the Knox Group is overlain in the southeastern part of the area by quartz sandstone as much as 70 feet thick, which has been generally referred to the St. Peter Sandstone (Freeman, 1953, pl. 6); elsewhere, rocks immediately above the unconformity are brownish-gray very finely crystalline argillaceous dolomite and dolomitic micrite which have been assigned to the Wells Creek Dolomite by most workers (McGuire and Howell, 1963). In many cores, dolomite of the Wells Creek grades upward into micrite and micrite containing dolomite-filled burrows which typify the overlying Camp Nelson Limestone. The contact between the Wells Creek and Camp Nelson is poorly defined and has been placed at widely different positions by different workers. The upper 320 feet of the Camp Nelson is exposed at the surface near the village of Camp Nelson in Jessamine County, Ky., but the basal part of the formation and its contact with the Wells Creek Dolomite are present only in the subsurface.

The unconformity at the top of the Knox Group of Late Cambrian and Early Ordovician age is one of the most conspicuous discontinuities in the stratigraphic section of the continental interior of the Eastern United States and is part of the craton-wide unconformity that separates the Sauk and Tippecanoe sequences of Sloss (1963). The unconformity is of economic as well as scientific interest. In Tennessee, zinc deposits occur in solution-collapse features that formed during development of this unconformity, and oil and gas have been produced from the Knox in topographic highs on the old erosion surface in Indiana (Patton and Dawson, 1969), Ohio (Schmidt and Warner, 1964), and southern Kentucky (McGuire and Howell, 1963, p. 6–8).

The Camp Nelson Limestone is overlain by the Oregon Formation, which is as much as 60 feet thick in parts of Fayette County, Ky., but pinches out near the northern and southern margins of the area. The Oregon is lithologically similar to the Wells Creek Dolomite but is less argillaceous, slightly coarser in crystal size, and lighter in color.

The Knox Group in Kentucky is entirely within the subsurface, but it has been reached by many wells. This paper is based on data from 107 wells within and eight wells marginal to the study area (figs. 1 and 3). Data for 57 holes are from McGuire and Howell (1963, appendix A), and data for 31 wells are from Freeman (1953). In addition, cores from 16 holes and cuttings from 11 holes were examined; the cores and samples are on file with the Kentucky Geological Survey.

The Tyrone Limestone, which overlies the Oregon Formation and ranges from about 60 to 120 feet in thickness, consists of micrite and micrite with dolomite-filled burrows; it resembles much of the Camp Nelson Limestone. The Tyrone contains several bentonite beds; the most extensive, the pencil cave bentonite of drillers, is from as little as 15 to as much as

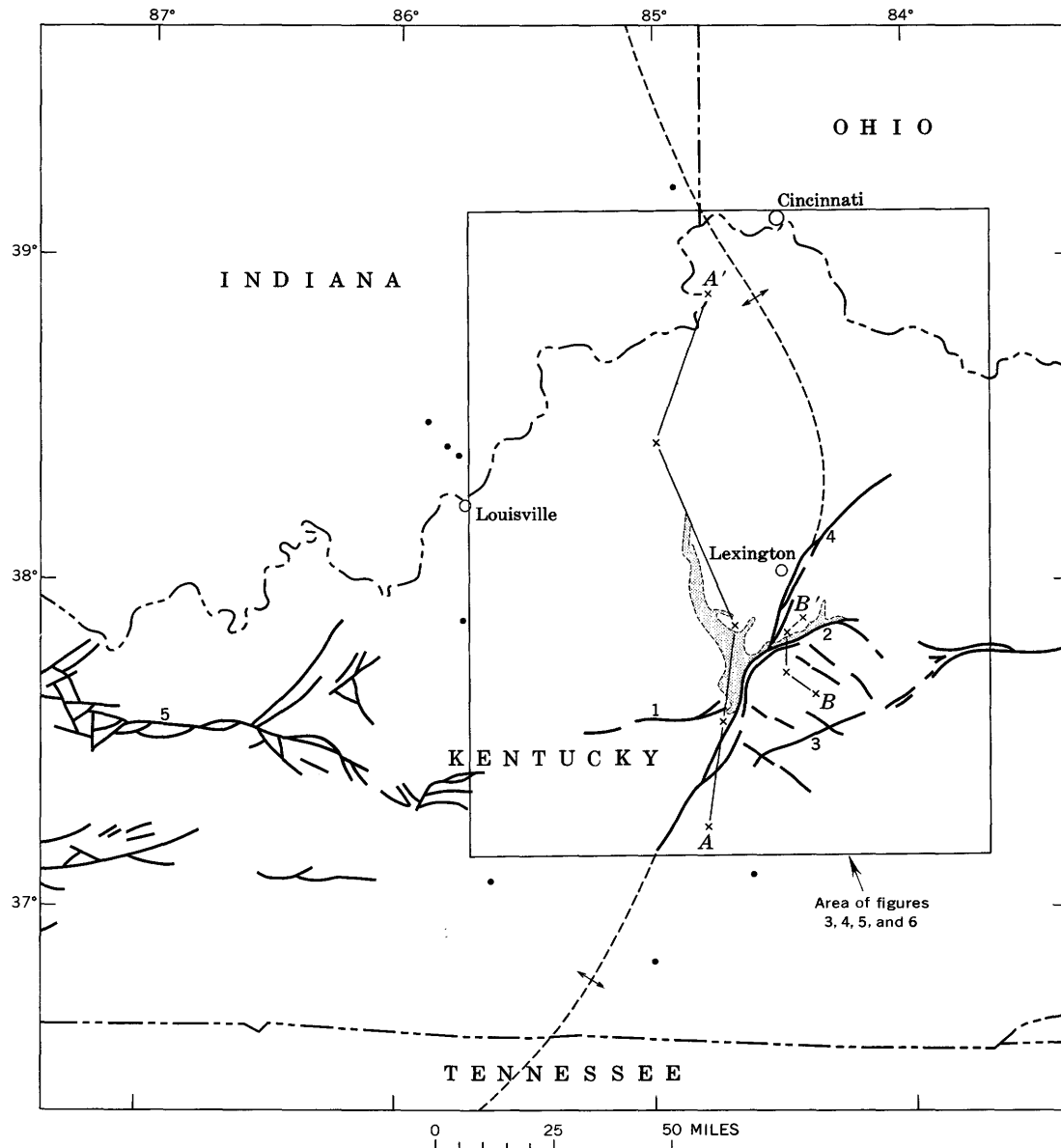


Figure 1.—Map showing area of outcrop of High Bridge Group (shaded) in central Kentucky. Dashed line is approximate axis of Cincinnati arch; *A-A'* is line of sections on figure 2, *B-B'* is line of sections on figure 7; solid lines are faults: 1, Brumfield fault; 2, Kentucky River fault zone; 3, Irvine—Paint Creek fault zone; 4, West Hickman—Bryan Station fault zone; 5, Rough Creek fault zone. Dots are wells used in the study but located outside the report area of figures 3–6.

30 feet below the top of the formation. The Tyrone is overlain by calcarenite and fossiliferous limestone of the Lexington Limestone; the contact is at least locally disconformable.

The Tyrone Limestone, the Oregon Formation, and the Camp Nelson Limestone are generally considered to make up the High Bridge Group. As originally defined (Campbell, 1898), the High Bridge included all the strata in central Kentucky exposed beneath the Lexington Limestone—that is, from the base of the Lexington to 320 feet below the top of the Camp Nelson—and the base of the High Bridge Group was

the base of surface exposures. In the subsurface, however, there is no distinct widespread horizon that could serve as a basal contact of the High Bridge anywhere above the top of the Knox Group, and the Wells Creek is lithologically similar to the Oregon Formation. Therefore, the High Bridge Group, as used in this paper, includes the Wells Creek as well as the Camp Nelson, Oregon, and Tyrone.

Stratigraphic relations within the High Bridge Group from south to north are shown in figure 2. The top of the group is nearly parallel with the pencil cave bentonite of drillers, and

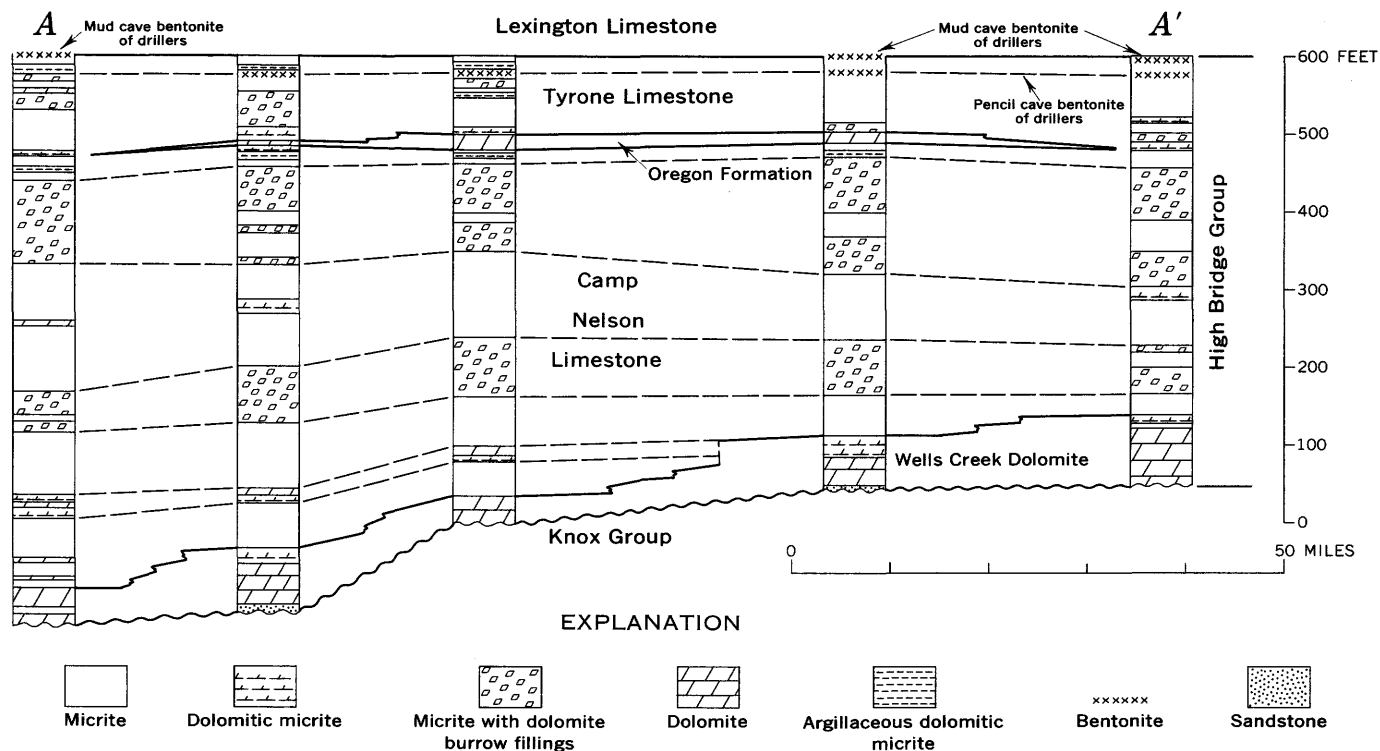


Figure 2.—Generalized columnar sections of High Bridge Group. Location of line of section A—A' is shown on figure 1.

the post-Tyrone disconformity has little relief. There are no obvious time markers in the lower part of the section, but the Wells Creek Dolomite seems to be a transgressive unit deposited as the sea encroached northward on the eroded surface of the Knox Group.

TREND ANALYSIS

The observed thickness of the High Bridge Group in central Kentucky ranges from 434 to 786 feet; the thicker values generally occur in the southeastern part of the area (fig. 3). This variable thickness reflects both a regional thickening to the southeast and a considerable local variation. Inasmuch as Schmidt and Warner (1964, p. 179) reported an erosional relief of 200 feet on the post-Knox unconformity in northern Kentucky, many of the local variations in thickness probably result from deposition on the irregular surface of the Knox.

In an attempt to distinguish the regional and local components of the variation in thickness, the High Bridge isopach data were subjected to stepwise trend-surface analysis, using procedures described by Miesch and Connor (1968). Functions used as potential predictors of thickness are those listed in Miesch and Connor (1968, table 1) and include polynomials, roots, exponents, logarithms, and reciprocals of the geographic coordinate values. Stepwise selection at the 0.01 probability level resulted in the prediction equation:

$$T = 512.9 + 0.4864XY^2. \quad (1)$$

This trend surface is contoured in figure 4; *T* is the predicted

thickness in feet, and *X* and *Y* are the coordinates shown on the map. The trend indicates a rapid increase in thickness of the High Bridge to the southeast and accounts for 76.8 percent of the total variation (sums of squares) in the observed thickness.

The most striking feature of the trend map is the lack of any obvious relation between the regional thickness of the High Bridge Group, as defined by the trend surface, and the location of the Cincinnati arch, thus confirming Woodward's (1961, p. 1654) conclusion that the arch was not present in pre-Trenton time. The line of sections (fig. 2) suggests that most of the regional thinning of the High Bridge is a result of transgression, and we conclude from the trend-surface map that the sea transgressed across the eroded surface of the Knox from southeast to northwest. The post-Knox surface had a gradient of about 4 feet per mile in the southeast and less than 1 foot per mile in the northwest.

Figure 5 is the residual map showing differences between the observed thicknesses and thicknesses predicted by the trend-surface equation; positive values indicate observed thicknesses greater than predicted, and negative values indicate observed thicknesses less than predicted.

Interpretation of the residual map is not so straightforward as that of the trend map. Some of the positive and negative areas, particularly where based on data from single holes, may reflect misidentification of the contact between the Knox and High Bridge Groups, but the general pattern must have geologic significance.

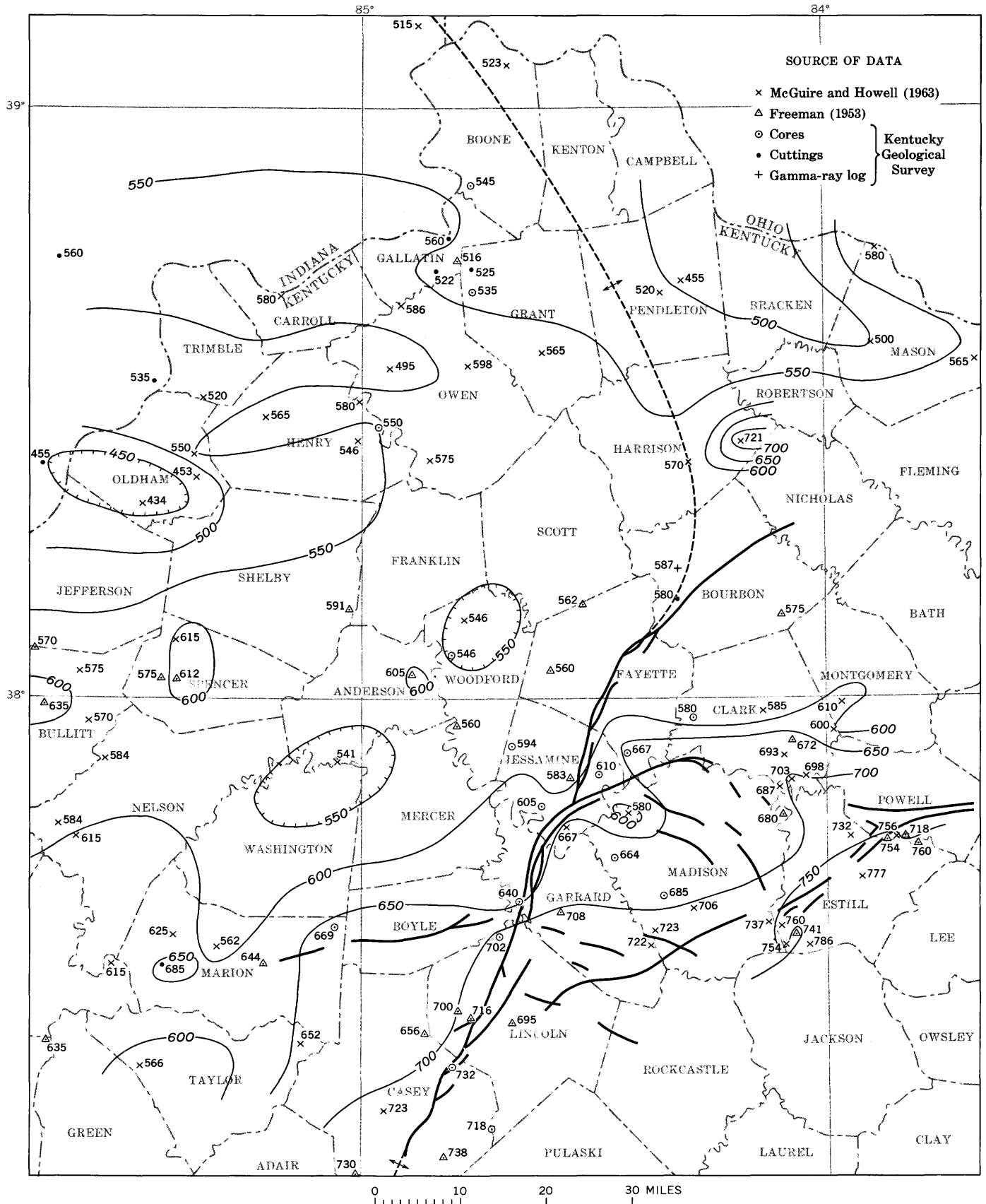


Figure 3.—Isopach map of High Bridge Group. Small numbers by site of each drill hole are thickness, in feet, of High Bridge Group. Heavy lines are faults; dashed line is approximate axis of Cincinnati arch. Fault pattern modified from unpublished compilation by D. F. B. Black. Contour interval 50 feet.

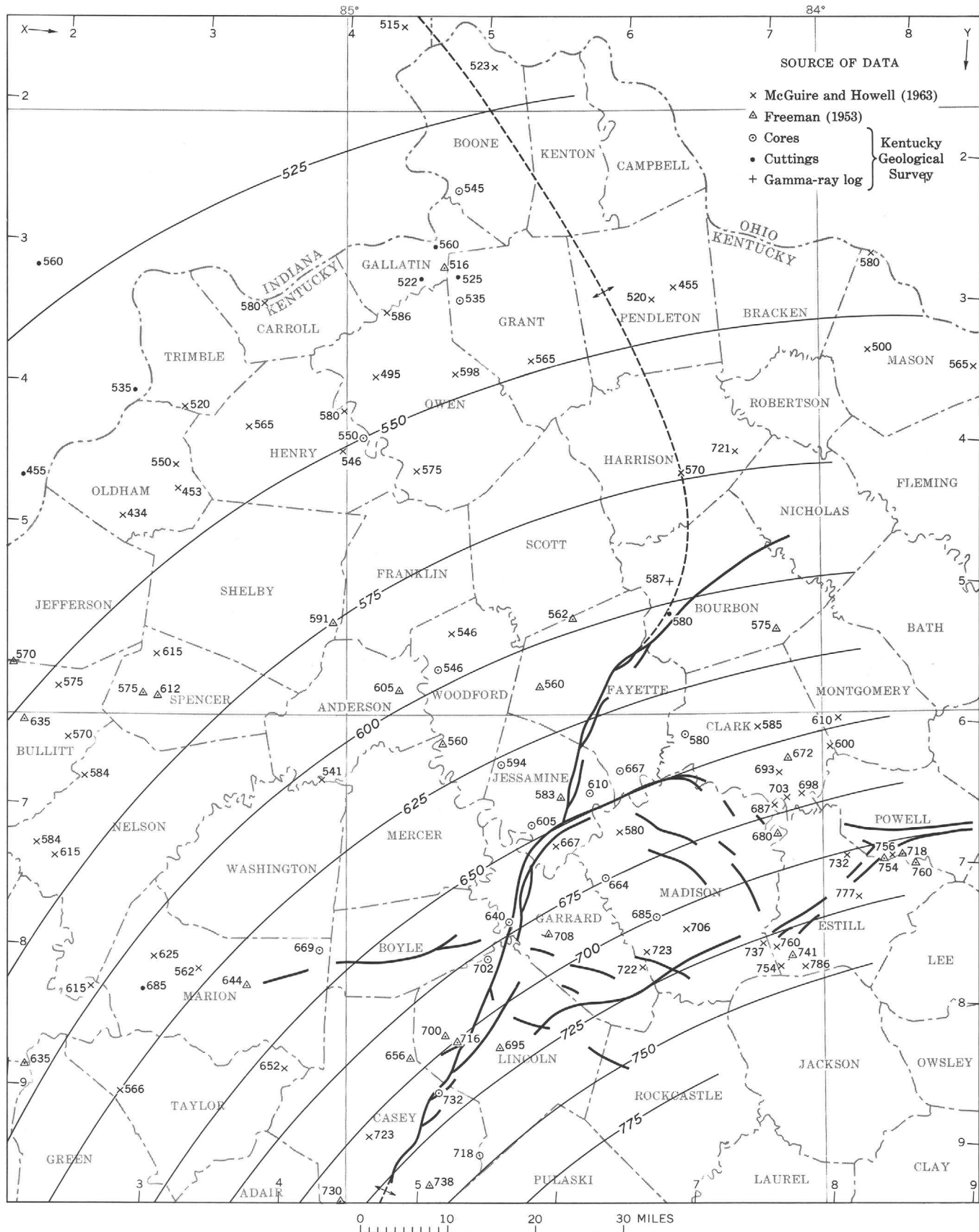
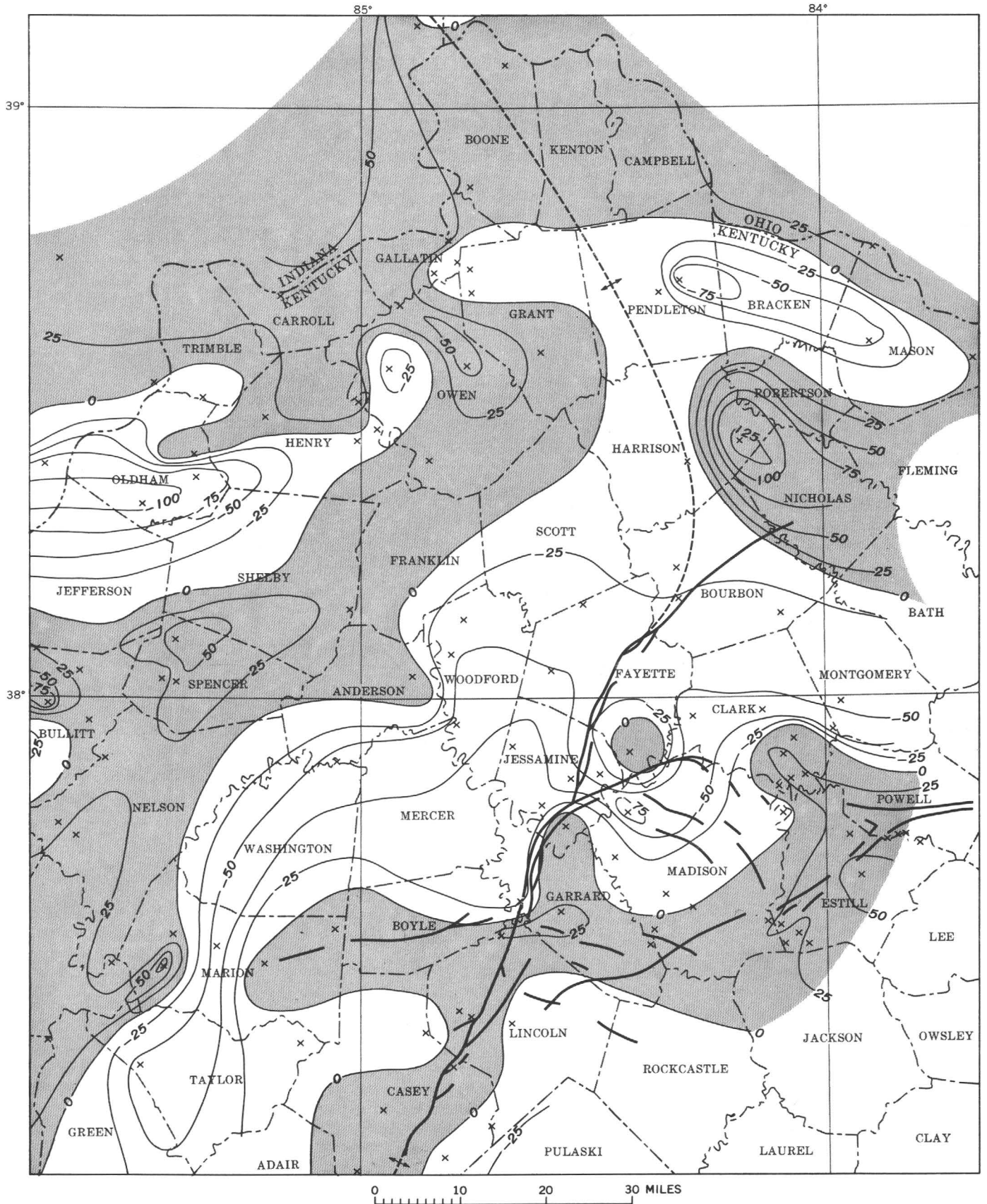


Figure 4.—Trend map of High Bridge Group. Small numbers by site of each drill hole show actual thickness, in feet, of High Bridge Group. Heavy lines are faults; dashed line is approximate axis of Cincinnati arch. Fault pattern modified from unpublished compilation by D. F. B. Black. Contour interval 25 feet.



Relief on the unconformity at the top of the High Bridge Group is no more than about 15 feet, less than the contour interval of the residual map, and gross lithologic units within the group, exclusive of the Wells Creek Dolomite, have considerable continuity and regularity. On the other hand, the unconformity at the top of the Knox Group is known to have much relief, so most of the local thickness variations shown by the residual map result from thickness variations of the basal High Bridge. Thus, the residual map may be viewed as a contour map showing irregularities on the post-Knox erosion surface, the positive values representing local topographic lows and negative values representing local topographic highs. The maximum local relief shown by the residual map is about 200 feet. This value compares favorably with the maximum relief of 200 feet reported by Schmidt and Warner (1964, p. 179) in northern Kentucky and a relief of 125 feet reported by Gilbert and Hoagland (1970) in middle Tennessee. Average local relief shown by the residual map is about 50 feet.

An interesting feature of the residual map is the general correspondence of positive values with the Kentucky River, Irvine–Paint Creek, and Brumfield fault zones. The Kentucky River and Irvine–Paint Creek fault zones were active in the Cambrian, and Middle Cambrian rocks in particular are much thicker on the southeast side of the Kentucky River fault zone than on the northwest side (Webb, 1969). The general correspondence in figure 5 of positive values with the fault zones suggests that the faults may also have been active during deposition of the High Bridge Group.

In order to assess any such fault-related variation, the area of study was arbitrarily divided into two parts along the line of the Kentucky River fault zone, and trend surfaces were fitted to the data on either side independently, using the same functions as before. Stepwise selection at the 0.01 probability level resulted in two prediction equations, one for the area northwest of the zone (T_{NW}) and one for the area to the southeast (T_{SE}):

$$T_{NW} = 532.1 + 0.05166XY^3 \quad (2)$$

$$T_{SE} = 570.9 + 0.006861X^2Y^3 \quad (3)$$

These equations give the predicted thicknesses in feet of the High Bridge Group in the two areas; their configurations are shown in figure 6. The trends collectively account for 78.7 percent of the total variation, an increase of only 1.9 percent over that accounted for by the single equation in equation 1.

In general, the predicted thickness of the High Bridge on either side of the fault zone is similar, and permissible

contemporaneous movement is small—less than about 40 feet. The standard deviation of the residuals about T_{NW} is 42 feet, suggesting that about two-thirds of the time an observed thickness northwest of the zones should fall within a range of 42 feet less than and 42 feet more than the estimated thickness. Similarly, the standard deviation of the residuals about T_{SE} is nearly 27 feet, and about two-thirds of the time an observed thickness to the southeast should fall within the range of 27 feet less than to 27 feet more than the estimated thickness. In the light of such a large expected variation about the predicted values (the trends), the apparent differences in thickness across the zones in figure 6 are probably meaningless.

Furthermore, the difference in predicted thickness indicates scissors movement; in southern Jessamine County the predicted thickness southeast of the fault zone is greater than to the northwest, whereas in Lincoln and Casey Counties it is less on the southeast than on the northwest. This apparent movement contrasts both with Cambrian movement, which was everywhere down on the southeast side of the zones, and with post-Ordovician movement, which was also down to the southeast. It is unlikely that movement along the Kentucky River fault zone would have been of a different type in the Middle Ordovician than before or since. We conclude from these considerations that faulting along these surfaces contemporaneous with High Bridge deposition was nil.

Figure 7 illustrates the stratigraphic relations within the High Bridge Group across the Kentucky River fault zone from Madison County on the south to Jessamine and Fayette Counties on the north. The sections indicate that the local variations in thickness near the fault zone, as elsewhere in the study area, result from differences in thickness of the basal part of the section and that the differences are not the direct result of concurrent faulting. We suspect, then, that the positive residuals near the fault zones were valleys on the post-Knox surface and that the Knox Group was more susceptible to erosion, and particularly to karst solution, along the faults than elsewhere.

This analysis is based on too little data to serve as much of a guide to exploration for gas, oil, or zinc in central Kentucky. However, exploratory holes to and through the Knox Group are being drilled nearly weekly in Kentucky, and with more isopach data, trend analyses like that presented here may help to delineate highs on the post-Knox unconformity that could serve as targets for petroleum exploration and show general trends of paleokarst drainage that might aid in zinc exploration.

Figure 5.—Residual thickness map of the High Bridge Group. Contours show differences between observed thicknesses, in feet, and thicknesses predicted by the trend-surface equation. Areas of positive residuals are shaded. Heavy lines are faults; dashed line is approximate axis of Cincinnati arch. Fault pattern modified from unpublished compilation by D. F. B. Black.

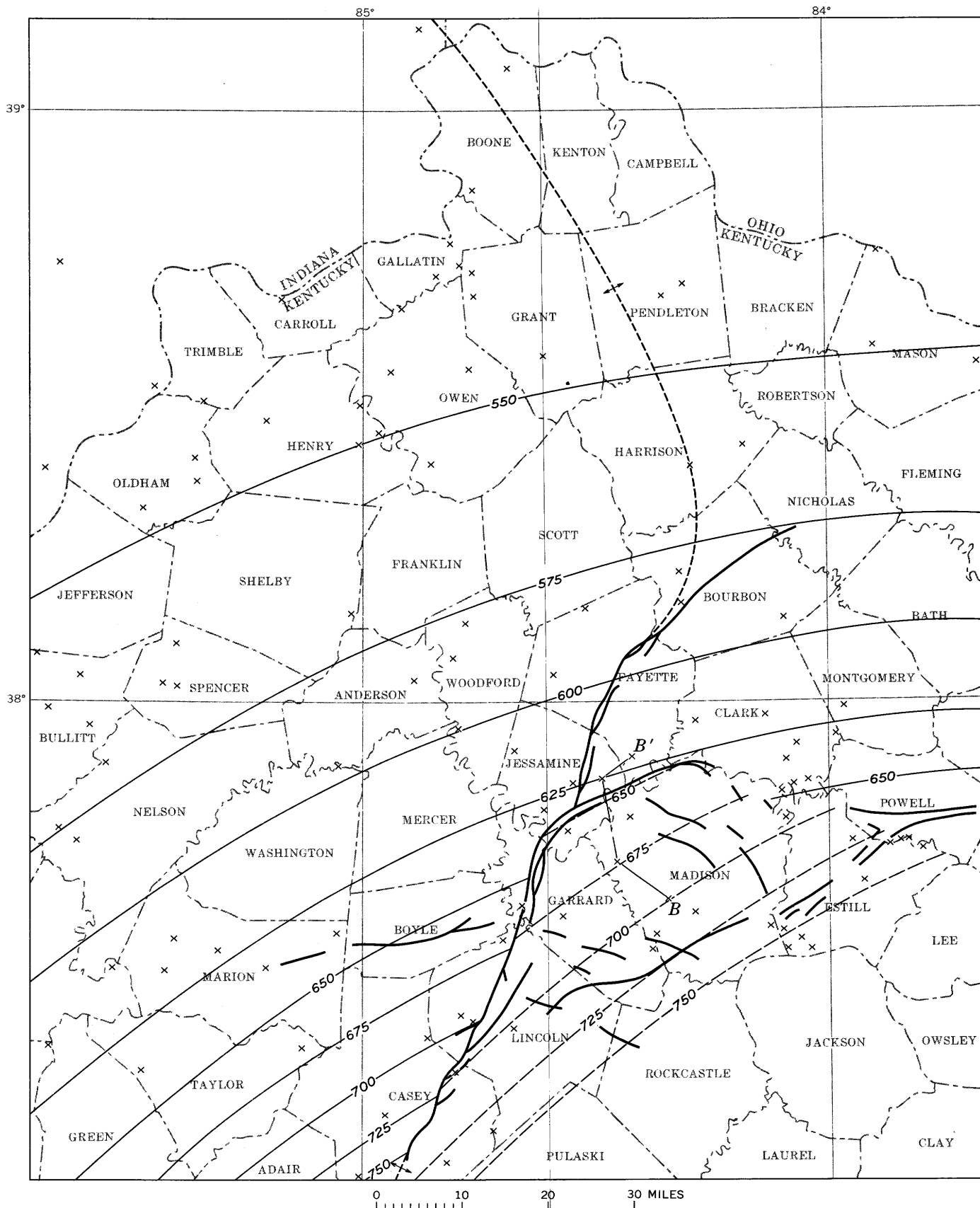


Figure 6.—Comparison of trend surfaces northwest (solid contours) and southeast (dashed contours) of the Kentucky River fault zone. Heavy solid lines are faults; heavy dashed line is approximate axis of Cincinnati arch. Fault pattern modified from unpublished compilation by D. F. B. Black. B-B' is line of sections in figure 7. Contour interval 25 feet.

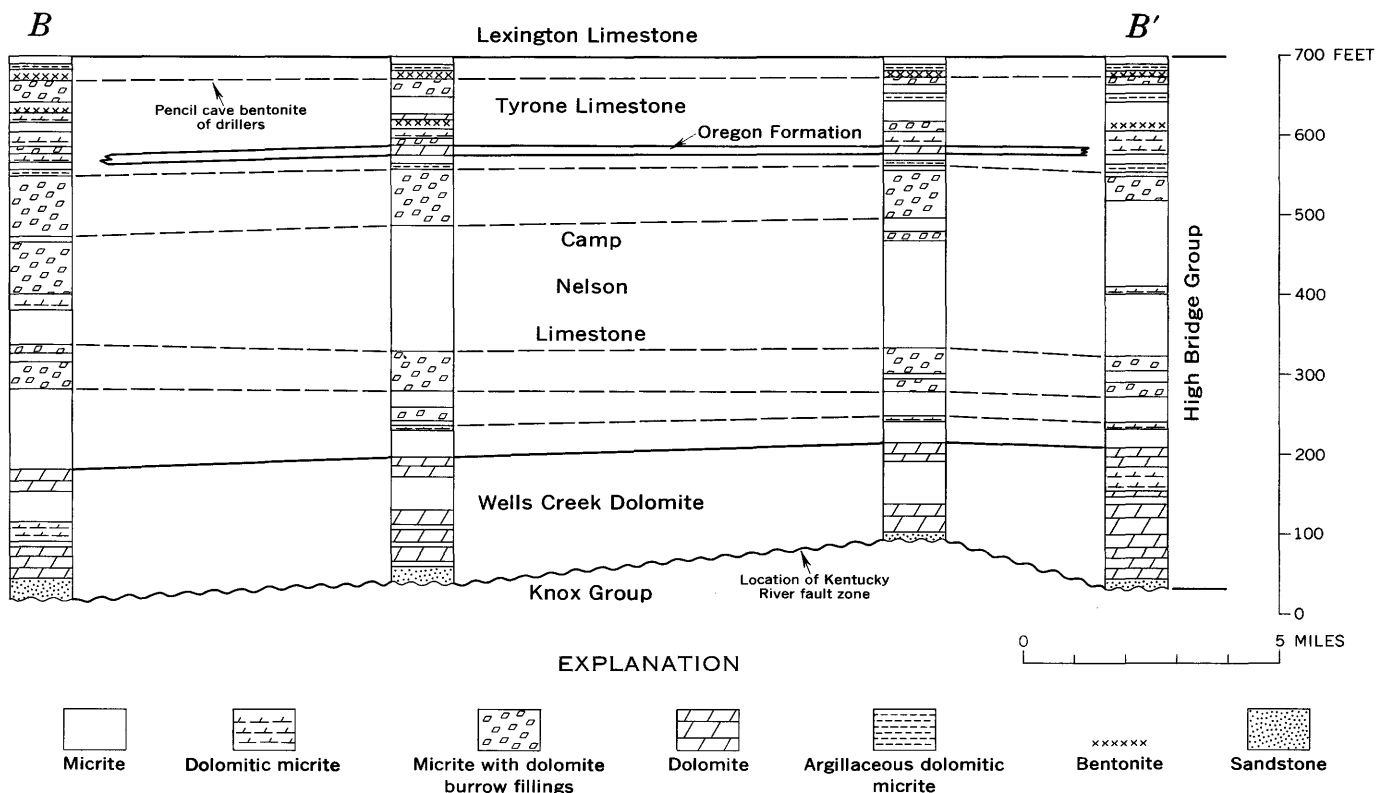


Figure 7.—Stratigraphic relations within the High Bridge Group across the Kentucky River fault zone. See figures 1 and 6 for location of sections.

REFERENCES

Campbell, M. R., 1898, Description of the Richmond quadrangle [Kentucky]: U.S. Geol. Survey Geol. Atlas, Folio 46, 4 p.
 Freeman, L. B., 1953, Regional subsurface stratigraphy of the Cambrian and Ordovician in Kentucky and vicinity: Kentucky Geol. Survey, Ser. 9, Bull. 12, 352 p.
 Gilbert, R. C., and Hoagland, A. D., 1970, Paleokarst phenomena and the post-Knox unconformity of middle Tennessee [abs.]: Geol. Soc. America Abs. with Programs, v. 2, no. 7, p. 558.
 McGuire, W. H., and Howell, Paul, 1963, Oil and gas possibilities of the Cambrian and Lower Ordovician in Kentucky: Lexington, Ky., Spindletop Research Center, [216] p.
 Miesch, A. T., and Connor, J. J., 1968, Stepwise regression and nonpolynomial models in trend analysis: Kansas Geol. Survey

Computer Contr. 27, 40 p.
 Patton, J. B., and Dawson, T. A., 1969, Some petroleum prospects of the Cincinnati arch province, in Kentucky Oil and Gas Assoc. 33d Ann. Mtg., 1969, Proc. Tech. Sess.: Kentucky Geol. Survey, Ser. 10, Spec. Pub. 18, p. 32-39.
 Schmidt, R. G., and Warner, R. A., 1964, Knox is the target for northern Kentucky: Oil and Gas Jour., v. 62, no. 16, p. 178-180.
 Sloss, L. L., 1963, Sequences in the cratonic interior of North America: Geol. Soc. America Bull., v. 74, no. 2, p. 93-114.
 Webb, E. J., 1969, Geologic history of the Cambrian System in the Appalachian basin, in Kentucky Oil and Gas Assoc., 33d Ann. Mtg., 1969, Proc. Tech. Sess.: Kentucky Geol. Survey, Ser. 10, Spec. Pub. 18, p. 7-15.
 Woodward, H. P., 1961, Preliminary subsurface study of southeastern Appalachian interior plateau: Am. Assoc. Petroleum Geologists Bull., v. 45, no. 10, p. 1634-1655.



THE INGRAHAM ESKER, CHAZY, NEW YORK

By CHARLES S. DENNY, Beltsville, Md.

Abstract.—The Ingraham esker near Chazy, Clinton County, N.Y., is composed of ice-contact gravel and sand that are overlain discordantly by deposits of glacial Lake Vermont and the Champlain Sea. The ice-contact deposits were laid down by a subglacial stream that flowed south into Lake Vermont. The overlapping and abutting glacial lake and marine deposits are reworked esker gravel and sand. Erosion and deposition in these water bodies transformed a narrow steep-sided esker into a low broad ridge. In places, more than half of the Ingraham esker is material reworked in these late-glacial water bodies.

In the lowlands west of Lake Champlain near the Canadian border, Woodworth (1905a, pl. 4, p. 13–14) mapped the Ingraham esker, a low broad north-trending ridge about 9 miles long (fig. 1). Excellent longitudinal and transverse exposures, opened in the esker in 1961 during the construction of Interstate Highway 87 which crosses the esker near the town of Ingraham, showed that only about half the ridge-forming material is ice-contact gravel and sand; the rest is deposits of glacial Lake Vermont or the Champlain Sea. Presumably the esker-building stream flowed south under the ice sheet and discharged into Lake Vermont (Woodworth, 1905b, p. 190–206). This ice-dammed lake occupied the Champlain Valley during late-glacial time and overflowed to the south into the Hudson River drainage. Since Woodworth's day, the only descriptions of the lake as a whole have been by Chapman (1937) and by Stewart and MacClintock (1969). Chapman recognized two lake stages; the older he named the Coveville and the younger Fort Ann. When the glacial lake was at the highest stand of the Fort Ann stage, the top of the Ingraham esker was about 475 feet below the surface of the lake. The Champlain Sea (Karrow, 1961; Elson, 1969) invaded the Champlain Valley when the ice front retreated to the northwest from the St. Lawrence Valley near Quebec City (Prest, 1970). During the maximum stand of the sea, the esker was buried by more than 250 feet of water. The marine invasion ended when differential uplift closed the connection to the ocean, and Lake Champlain came into existence.

TOPOGRAPHY

The lowlands surrounding the Ingraham esker range in altitude from 95 feet at the shore of Lake Champlain to about

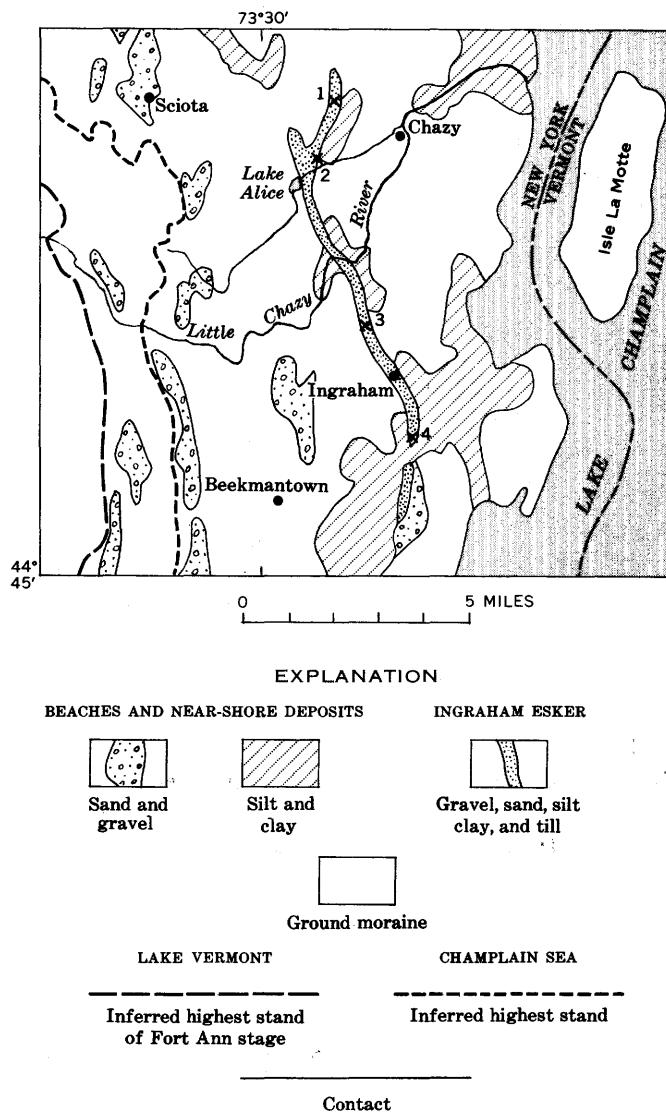


Figure 1.—Surficial geologic map of the Ingraham esker and surrounding area near Chazy, N.Y. (Denny, 1970). Numbered localities are referred to in text.

300 feet. The bedrock is largely sandstone, dolostone, and limestone (Fisher, 1968). The esker is 300 to 800 feet wide and 10 to 30 feet high. The crest is 100 to 300 feet wide. The

maximum angle of slope of the sides of the ridge ranges from about 2° to 15°. Most eskers in the Adirondack region are higher, narrower, and steeper sided than the Ingraham esker (fig. 2).

STRATIGRAPHY

The Ingraham esker is composed of gravel, sand, silt, clay, and till. The abundant pebbles, cobbles, and boulders are chiefly coarse sandstone (Potsdam Sandstone) plus dolostone and limestone, and a few metamorphic and igneous rocks from Precambrian terrane. The finer fraction is largely slightly calcareous sand and silt with subordinate clay. Three stratigraphic units are recognized in the esker: (1) a core of ice-contact stratified drift overlain discordantly by (2) unfossiliferous deposits of Lake Vermont, and (3) fossiliferous deposits of the Champlain Sea.

Ice-contact stratified drift

The ice-contact stratified drift (fig. 3) ranges from boulder gravel to sand within horizontal and vertical distances of only a few feet. The maximum exposed thickness is about 30 feet. There is no uniform change in texture from north to south. Boulder gravel is exposed at many places along the entire length of the esker. Lenses of till were seen at two localities (fig. 4). High-angle faults are common, and vertically dipping beds occur next to mostly undeformed strata, suggesting deposition adjacent to glacial ice and subsequent collapse.

Lake Vermont deposits

These sediments are chiefly well-bedded sand and gravel (fig. 5). The unit includes all material between the typical ice-contact deposits below and the fossiliferous beds above. Masses of clay are present in a few places.

Sediments of the Champlain Sea

The Champlain Sea deposits form the crest and sides of the ridge. They are generally well stratified and contain abundant marine fossils. In many places the crest of the ridge is underlain by a massive pebble to boulder gravel (figs. 4 and 5) that is finer grained and well stratified below. The material on the sides of the ridge is bouldery or is a massive silty clay containing pebbles, boulders, and fragments of marine shells (fig. 6). The silty clay may be a subaqueous mudflow deposit. If the silty clay was laid down when sea level was more than 200 feet above the crest of the ridge, then the mixing with the shells and coarse clastic materials could be the result of subaqueous flowage down the side of the ridge, perhaps when sea level had dropped to a position not far above the crest of the ridge.

PALEONTOLOGY

Macrofossils and microfossils are found in Champlain Sea deposits. They are most abundant in crossbedded sand near the base of the marine unit. Most of the bivalves are represented by disarticulated valves which probably were transported to their present position by currents. However, in some places, whole specimens are present and appear to be in growth position. The pebbly clay and silt on the sides of the esker also contain fossils (fig. 6). Some of the shells are in clusters surrounded by a layer of clay, as if they had been folded into the clay during transport down the submerged slope of the ridge.

A barnacle, three bivalve species, eight species of Foraminifera, and nine species of ostracodes have been identified from four localities (table 1; fig. 1). The identified taxa are listed in

Table 1.—Fossil collection localities, Rouses Point 15-minute quadrangle area, New York

Fossil locality No. (fig. 1)	Location	Approximate altitude (feet)	Zones sampled
1. . . .	Borrow pit about 0.5 mile north of Miner Agricultural Research Institute (loc. 1, fig. 1).	200	4-foot bed of sand containing abundant shells. Sampled strata overlain by 4 feet of fossiliferous pebble and cobble gravel.
2. . . .	Borrow pit, east side of ridge, about 1 mile southwest of Miner Agricultural Research Institute (loc. 2, fig. 1).	215	Coarse-grained crossbedded pebbly sand containing abundant shells.
3. . . .	Borrow pit, west side of ridge, about 1 mile southwest of Miner Agricultural Research Institute (loc. 2, fig. 1).	200	5-foot bed of pebble gravel containing abundant shells in lower 6 inches.
4. . . .	Borrow pit about 1.2 miles south of Ingraham (loc. 4, fig. 1).	150	Pebbly clay at depth of 5 feet below stripped west slope of ridge. Shells abundant in places.

table 2. The barnacle and the bivalves were identified by Joseph Rosewater, of the U.S. National Museum; the Foraminifera were studied by M. Ruth Todd, of the U.S. Geological Survey; and the ostracodes were studied initially by I. G. Sohn and later by J. E. Hazel, of the U.S. Geological Survey.

The fossil assemblage (table 2) indicates shallow cold marine water. Hazel (written commun., 1971) feels that the ostracode assemblage indicates subfrigid or frigid climatic conditions (that is, averaging about 10°C or colder in shallow water during the warmest month). Hazel also states (oral commun.,

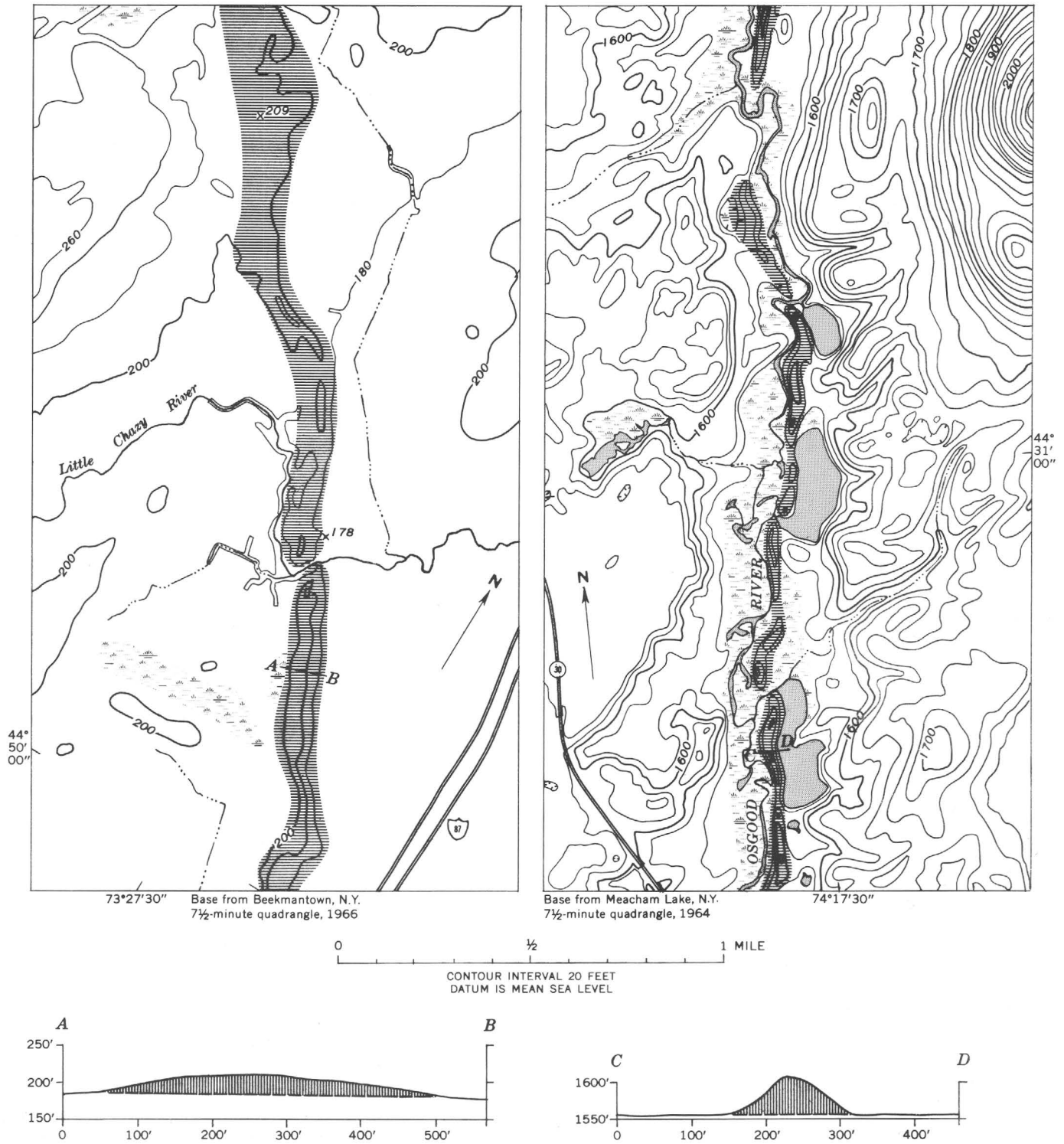


Figure 2.—Topographic maps and profiles showing part of the broad low Ingraham esker (left), and part of a narrow steep-sided esker along Osgood River (right). Eskers patterned. The esker along Osgood River is part of the esker system first described by Chadwick (1928; see also Buddington and Leonard, 1962, fig. 2).

Table 2.—Fossils from Ingraham esker

Species	Fossil locality No.			
	1	2	3	4
Mollusca				
<i>Yoldia</i> sp.	X	X
<i>Macoma balthica</i> (Linne)	X	X	X	X
<i>Hiatella arctica</i> (Linne)	X	X	X	X
Foraminifera				
<i>Buccella frigida</i> (Cushman)	X
<i>Cassidulina teretis</i> Tappan	X	X
<i>Elphidium</i> aff. <i>E. advena</i> (Cushman)	X
<i>E. clavatum</i> Cushman	X	X	...	X
<i>E. incertum</i> (Williamson)	X	X
<i>E. subarcticum</i> Cushman	X
<i>Protelphidium orbiculare</i> (Brady)	X	X
<i>Pseudopolymorphina novangliae</i> (Cushman)	X
Cirripedia				
" <i>Balanus</i> " sp.	X	X	X	...
Ostracoda				
<i>Cytheropteron inflatum</i> Brady, Crosskey and Robertson	X
<i>Cytheropteron</i> sp.	X
<i>Eucytheridea punctillata</i> (Brady)	X
<i>E. macrolaminata</i> (Elofson)	X
<i>E. bradii</i> (Norman)	X
<i>Finmarchinella barenzovoensis</i> (Mandelstam)	X
<i>Heterocyprideis sorbyana</i> (Jones)	X	X
<i>Leptocythere macchesneyi</i> Brady and Crosskey	X	X
<i>Palmanella limicola</i> (Norman)	X

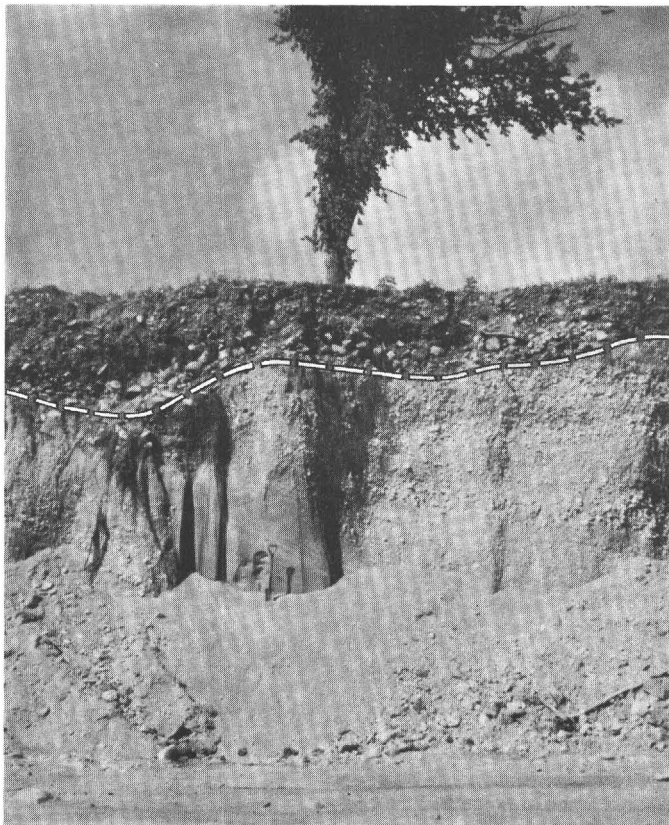


Figure 3.—Ice-contact pebble gravel and sand overlain discordantly by fossiliferous boulder gravel of the Champlain Sea. View looking northwest in borrow pit west of Chazy (loc. 2, fig. 1).

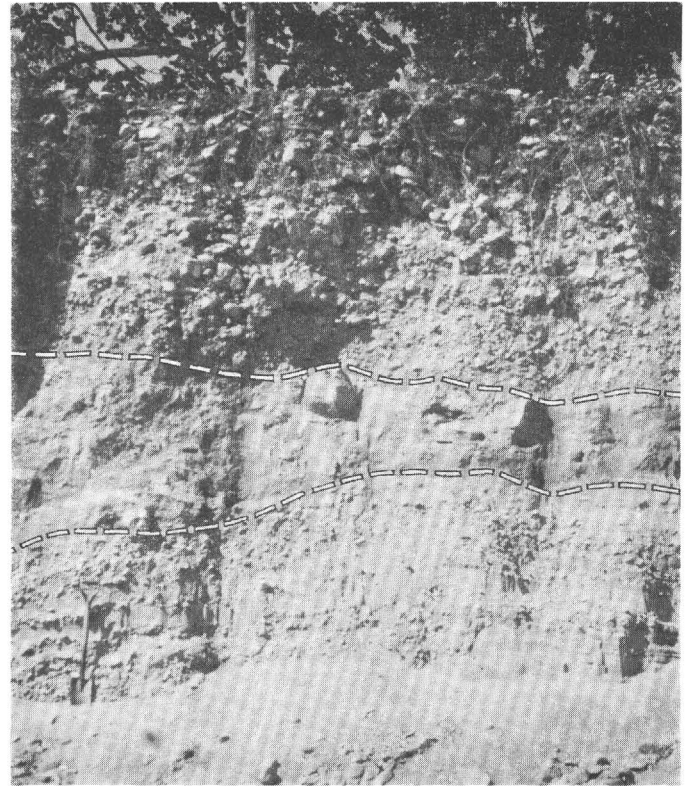


Figure 4.—Fossiliferous pebble and cobble gravel of the Champlain Sea rests on a lens of till(?), a pale-brown massive bouldery fine sand and silt, that has thin wavy clay laminae (not visible in photograph). Pebble gravel and sand below the till(?) are probably ice-contact deposits. View looking west in borrow pit west of Chazy (loc. 2, fig. 1).

1971) that the mean length of the *Hiatella* collected from the Ingraham esker was 20.3 mm for 55 specimens, with an observed range of 14.5–27.1 mm, and that this is very similar to the mean and range of variation observed by Strauch (1968) for *Hiatella arctica* collected from northern Iceland, which is in the subfrigid climatic zone.

STRUCTURE

The internal structure of the Ingraham esker was well exposed in intersecting longitudinal and transverse sections in a borrow pit near the Miner Agricultural Research Institute (fig. 7). Two east-west cross sections (*D–D'* and *A–A'*) show that more than half the ridge is composed of material deposited in the Champlain Sea. West-dipping beds of sand and gravel are highly fossiliferous near the base where they rest unconformably on gravelly ice-contact deposits. The north-south section (*B–B'*) near the road is entirely in well-stratified fossiliferous marine sand and gravel. The section to the east (*C–C'*) is entirely in bouldery ice-contact deposits. Lake Vermont deposits were not recognized in these sections.

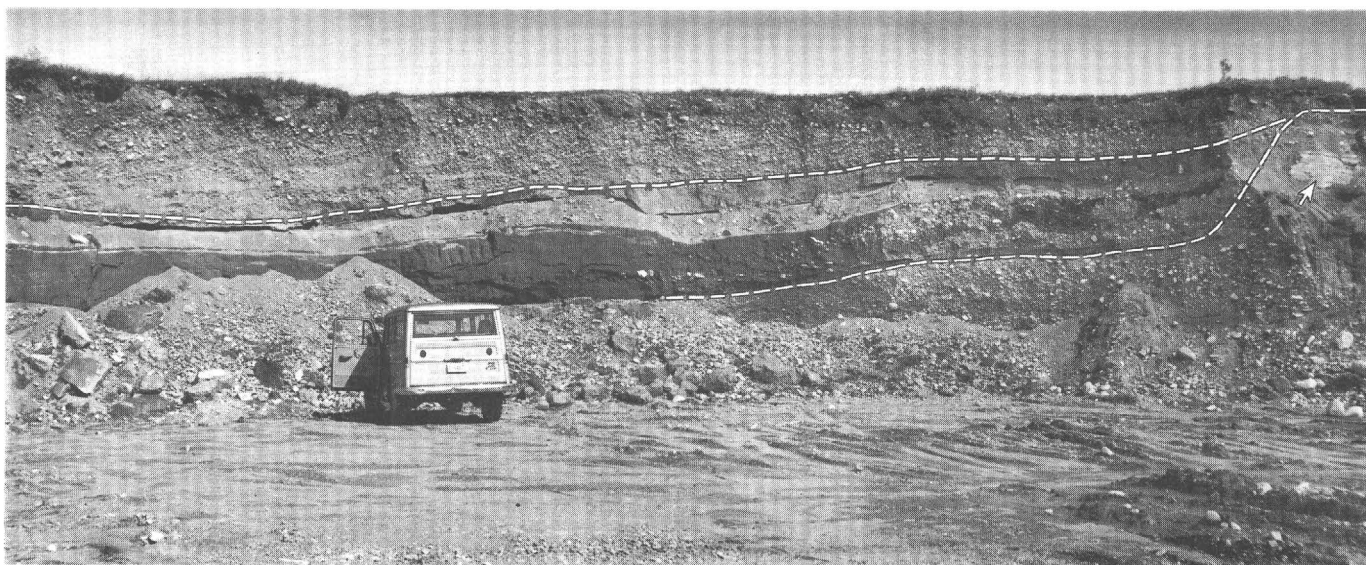


Figure 5.—Fossiliferous gravel and sand of the Champlain Sea form west-dipping beds that overlie massive beds of fine-grained silty sand deposited in Lake Vermont. The sand grades to the right into a pebble and cobble gravel that lies against bouldery ice-contact gravel and till. Large boulder (arrow) lies in till near top of bank at right-hand edge of photograph. View north in borrow pit about 1.1 miles north of Ingraham (loc. 3, fig. 1).



Figure 6.—Mudflow deposit on flanks of ridge. A massive pebbly silty clay containing abundant marine shells rests on a massive cobbly silty clay containing a few shell fragments (not visible in photograph). The materials were probably mixed by subaqueous slumping as a mudflow down the sides of the ridge. Exposure in borrow pit about 0.5 mile south of Ingraham on east side of U.S. Route 9.

AGE

The ice-contact stratified gravel and sand and the till that form the core of the esker were deposited in a tube at or near the bottom of the last (Woodfordian) ice sheet. The tube is presumed to have opened at the ice edge into Lake Vermont some time about 12,400 to 12,200 years B.P.

The marine invasion of the Champlain Sea began about 12,000 years B.P. and lasted to about 10,500 years B.P. (McDonald, 1968; Mott, 1968; Elson, 1969; Prest, 1970). A sample of shells from the borrow pit north of Miner Agricultural Research Institute (loc. 1, fig. 1) gave a radiocarbon age of $10,560 \pm 350$ years B.P. (W-1109, Ives and others, 1964). This date suggests that deposition and reworking of the marine sediments on the ridge took place late in the marine episode, probably as sea level was falling.

ORIGIN

I do not know whether the esker was built during one stand of the ice front or whether, as the front retreated, the ice tunnel also migrated northward. If the entire esker formed at one time, then the "frontal outwash plain or esker fan" (Woodworth 1905a, p. 14) at its south end may have been buried by Champlain Sea and Lake Vermont deposits (fig. 1). Borrow pits just south of the southern end of the esker expose ice-contact gravel beneath sand, silt, and clay of the Champlain Sea (Denny, 1970).

On the other hand, if the esker was built in several episodes, then the ice-contact deposits are progressively younger from south to north. The Lake Vermont deposits were spread over the ice-contact deposits as the mouth of the ice-tunnel migrated northward with the retreating ice front. According to this hypothesis, the Lake Vermont deposits form a subaqueous delta whose apex, the mouth of the ice tunnel, was several hundred feet below the surface of the glacial lake. I favor this alternative. There is no indication of a decrease in grain size of the ice-contact deposits from north to south, as might be expected if they were all deposited during one stand of the ice-front.

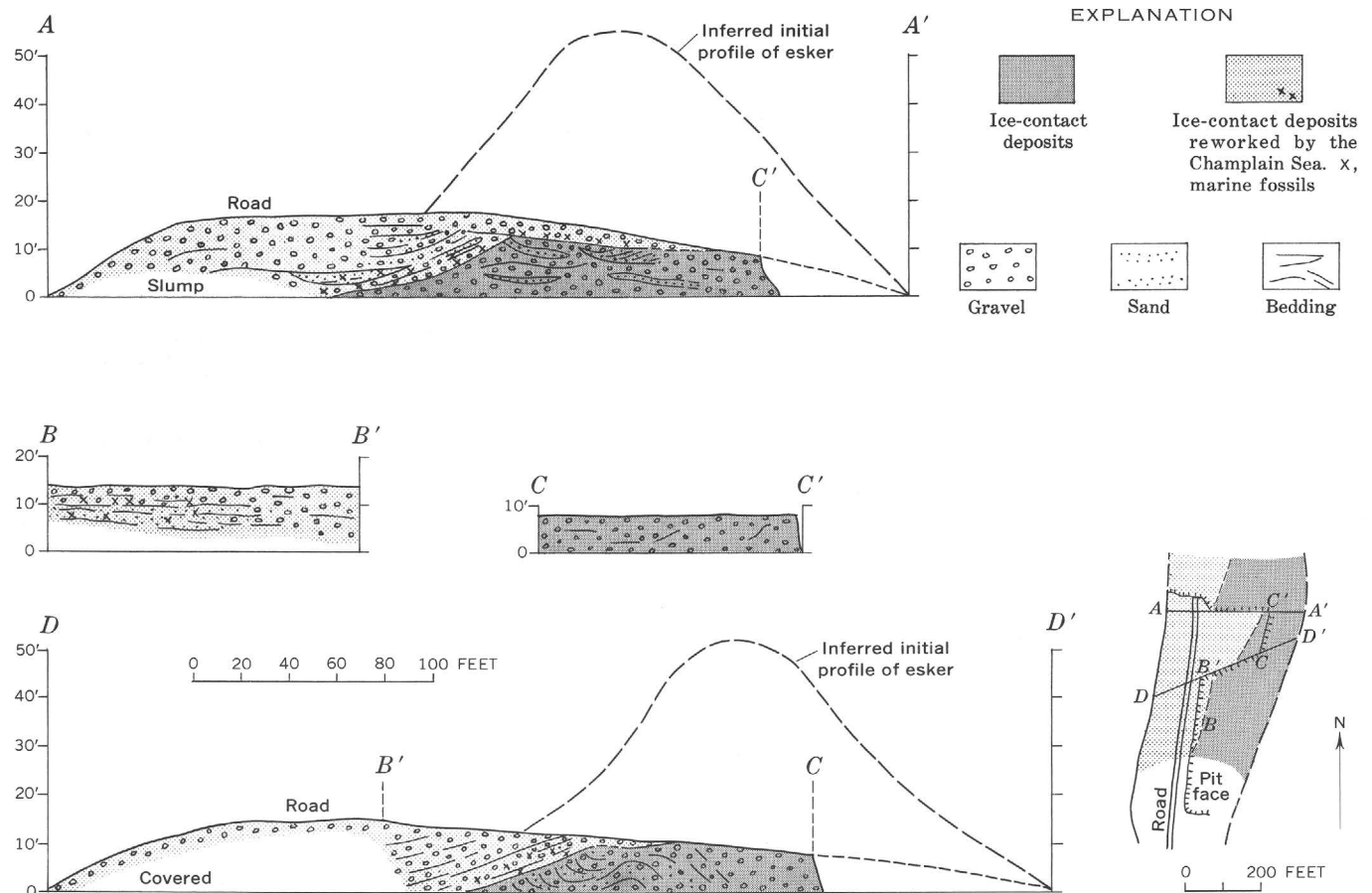


Figure 7.—Map and cross sections of the Ingraham esker exposed in borrow pit about 0.5 mile north of Miner Agricultural Research Institute (loc. 1, fig. 1). Vertical exaggeration $\times 2$; scale given in feet above pit floor.

The Ingraham esker has been greatly modified by wave action. It is lower and broader than most other eskers in the Adirondack region (fig. 2). Initially, the esker was probably a steep-sided ridge, perhaps two or three times higher than the present one. The map and cross sections on figure 7 show that the ice-contact deposits form the eastern part of the esker and the Champlain Sea deposits form the center and western parts. This distribution suggests that the tunnel in which the ice-contact deposits were formed was centered over the eastern part of the modern ridge. The gravel and sand of the Champlain Sea were deposited largely on the west side of a ridge of ice-contact deposits that was considerably reduced in height by erosion in the sea. Cross sections $D-D'$ and $A-A'$ of figure 7 show the inferred initial profile of the ridge of ice-contact deposits prior to modification in the late-glacial water bodies. The crestline of the ancestral ridge was east of the summit of the modern ridge. Erosion and deposition caused the crest to migrate westward a few hundred feet. The existing ridge is, in part, the eroded remnant of an older one and, in part, material derived from the older ridge and deposited on its western slope. In contrast to the conclusion of Stephens and Synge (1966, fig. 12), the side slopes of the

Ingraham esker appear to have been greatly reduced by wave action.

ACKNOWLEDGMENTS

My interpretation of the Ingraham esker stems in part from discussions with the late Paul MacClintock. The comments and assistance of J. A. Elson, J. B. Epstein, L. B. Gillett, J. E. Hazel, Carl Koteff, H. S. Ladd, L. L. Ray, Joseph Rosewater, Meyer Rubin, I. G. Sohn, M. Ruth Todd, and the late G. W. Holmes, are much appreciated. The radiocarbon age measurement (W-1109) of shells was done in the laboratory of the U.S. Geological Survey.

REFERENCES

- Buddington, A. F., and Leonard, B. F., 1962, Regional geology of the St. Lawrence County magnetite district, northwest Adirondacks, New York: U.S. Geol. Survey Prof. Paper 376, 145 p.
 Chadwick, G. H., 1928, Adirondack eskers: Geol. Soc. America Bull., v. 39, no. 4, p. 923-929.
 Chapman, D. H., 1937, Late-glacial and postglacial history of the Champlain Valley: Am. Jour. Sci., 5th ser., v. 34, no. 200, p. 89-124.

- Denny, C. S., 1970, Surficial geologic map of the Mooers quadrangle and part of the Rouses Point quadrangle, Clinton County, New York: U.S. Geol. Survey Misc. Geol. Inv. Map I-630.
- Elson, J. A., 1969, Late Quaternary marine submergence of Quebec: *Rev. Géographie Montréal*, v. 23, no. 3, p. 247-258.
- Fisher, D. W., 1968, Geology of the Plattsburgh and Rouses Point, New York-Vermont, quadrangles: New York State Mus. and Sci. Service, Geol. Survey Map and Chart Ser. 10, 51 p.
- Ives, P. C., Levin, Betsy, Robinson, R. D., and Rubin, Meyer, 1964, U.S. Geological Survey radiocarbon dates VII: *Radiocarbon*, v. 6, p. 37-76.
- Karrow, P. F., 1961, The Champlain Sea and its sediments, in Legget, R. F., ed., *Soils in Canada: Geological, pedological, and engineering studies*: Royal Soc. Canada Spec. Pub. 3, p. 97-108.
- McDonald, B. C., 1968, Deglaciation and differential postglacial rebound in the Appalachian region of southeastern Quebec: *Jour. Geology*, v. 76, no. 6, p. 664-677.
- Mott, R. J., 1968, A radiocarbon-dated marine algal bed of the Champlain Sea episode near Ottawa, Ontario: *Canadian Jour. Earth Sci.*, v. 5, no. 2, p. 319-324.
- Prest, V. K., 1970, Quaternary geology of Canada, in Douglas, R. J. W., ed., *Geology and economic minerals of Canada*: Canada Geol. Survey Econ. Geol. Rept. 1, 5th ed., p. 676-764.
- Stephens, N., and Synge, F. M., [1966], Pleistocene shorelines, in Dury, G. H., ed., *Essays in geomorphology*: New York, American Elsevier Pub. Co., p. 1-52.
- Stewart, D. P., and MacClintock, Paul, 1969, The surficial geology and Pleistocene history of Vermont: *Vermont Geol. Survey Bull.* 31, 251 p.
- Strauch, Friedrich, 1968, Determination of Cenozoic sea-temperatures using *Hiatella arctica* (Linne'): *Palaeogeography, Palaeoclimatology, Palaeoecology*, v. 5, no. 2, p. 213-233.
- Woodworth, J. B., 1905a, Pleistocene geology of the Mooers quadrangle [N.Y.]: *New York State Mus. Bull.* 83, p. 3-60.
- 1905b, Ancient water levels of the Champlain and Hudson Valleys: *New York State Mus. Bull.* 84, 265 p.



HIGH-PURITY VEINS OF SODA-NITER, NaNO_3 , AND ASSOCIATED SALINE MINERALS IN THE CHILEAN NITRATE DEPOSITS

By GEORGE E. ERICKSEN and MARY E. MROSE,
Washington, D.C.

Abstract.—White veins of soda-niter, NaNO_3 , and other water-soluble saline minerals are abundant and widespread in the Chilean nitrate deposits. They occur as secondary veins in the typical nitrate caliche, which is a saline-cemented regolith, and as primary near-surface veins in bedrock. Soda-niter and halite, NaCl , are the principal saline components. Veins commonly contain more than 50 percent NaNO_3 . Also present, generally in minor amounts, are a wide variety of other saline minerals, some of which are unique to these deposits. Among the most abundant of these minor minerals are niter, KNO_3 ; darapskite, $\text{Na}_3(\text{NO}_3)(\text{SO}_4)\cdot\text{H}_2\text{O}$; glauberite, $\text{Na}_2\text{Ca}(\text{SO}_4)_2$; and bloedite, $\text{Na}_2\text{Mg}(\text{SO}_4)_2\cdot 4\text{H}_2\text{O}$. The veins are well exposed in old underground workings where they were mined during the 19th century and early part of the 20th century.

The unique nitrate deposits of northern Chile are part of the saline complex of the Atacama Desert, which is probably one of the most arid deserts of the world. Similar deposits are not known to exist elsewhere. They are caliche deposits consisting of saline-cemented regolith, which locally contains veins of high-purity soda-niter, NaNO_3 , and of bedrock impregnated with saline materials or laced with veins of soda-niter and other saline minerals. These veins, commonly containing 50 percent or more NaNO_3 , constitute the richest ore of the nitrate fields and were the chief source of nitrate during the early days of the nitrate industry. They are now of interest to the mineral collector but of little value to the nitrate industry, which concentrates on exploitation of large quantities of low-grade nitrate ore.

The deposits that have been exploited are in the northern provinces of Tarapacá and Antofagasta. They are in the area extending from near the latitude of Pisagua in the north to Taltal in the south, a distance of nearly 700 km (fig. 1). Most of the deposits are along the eastern side of the coastal range but deposits are also found in or near depressions within the coastal range, near or around hills in the central valley, and along the lower slopes of the Andes. Although deposits are found throughout this region, most are grouped into five districts, which from north to south are: Tarapacá, Tocopilla, Baquedano, Aguas Blancas, and Taltal (fig. 1). Known deposits that have not been

worked extend at least 50 km north and south of those shown in figure 1. Other deposits that have not been exploited are found in the coastal desert of southern Peru, near Arequipa, about 300 km north of the border with Chile.

The Chilean nitrate deposits furnished most of the world's nitrate for fertilizers, explosives, and other chemicals from the early 19th century until World War I, when synthetic nitrate was first produced on a large scale. They also have been a major source of iodine since the mid-19th century. Total nitrate production recorded from 1830 through 1970 was about 135 million metric tons of NaNO_3 . Early in the 20th century more than 100 nitrate plants (called oficinas) were in operation simultaneously in northern Chile, and annual production was 2 to 3 million metric tons of NaNO_3 . After World War I, synthetic nitrate took an ever-increasing share of the market and by 1970 only four Chilean plants were in operation, and annual production had dropped to less than a million metric tons of NaNO_3 . In 1970, this represented less than two-thirds of a percent of the world demand for fixed nitrogen. On the other hand, byproduct iodine from these four plants supplied more than 50 percent of the world's needs in 1970.

During the early days (early 1800's) of the nitrate industry and until the early 1900's, the high-purity soda-niter veins were mined underground by shafts and tunnels. Figure 2 shows a typical mine area. Starting in the mid 19th century and continuing until the present, lower grade ore was mined in surface openings such as those shown in figure 3.

Because of their unusual nature, the Chilean nitrate deposits have attracted the attention of scientists for more than 100 years. The mode of formation of the deposits has been particularly perplexing, and dozens of published reports describe them and speculate about their origin. To date, however, there is neither a complete and accurate description of the deposits nor an acceptable theory for their origin.

Our information about the high-purity soda-niter veins in the Chilean nitrate deposits is based on field and laboratory studies undertaken during the 1960's. Some of the informa-

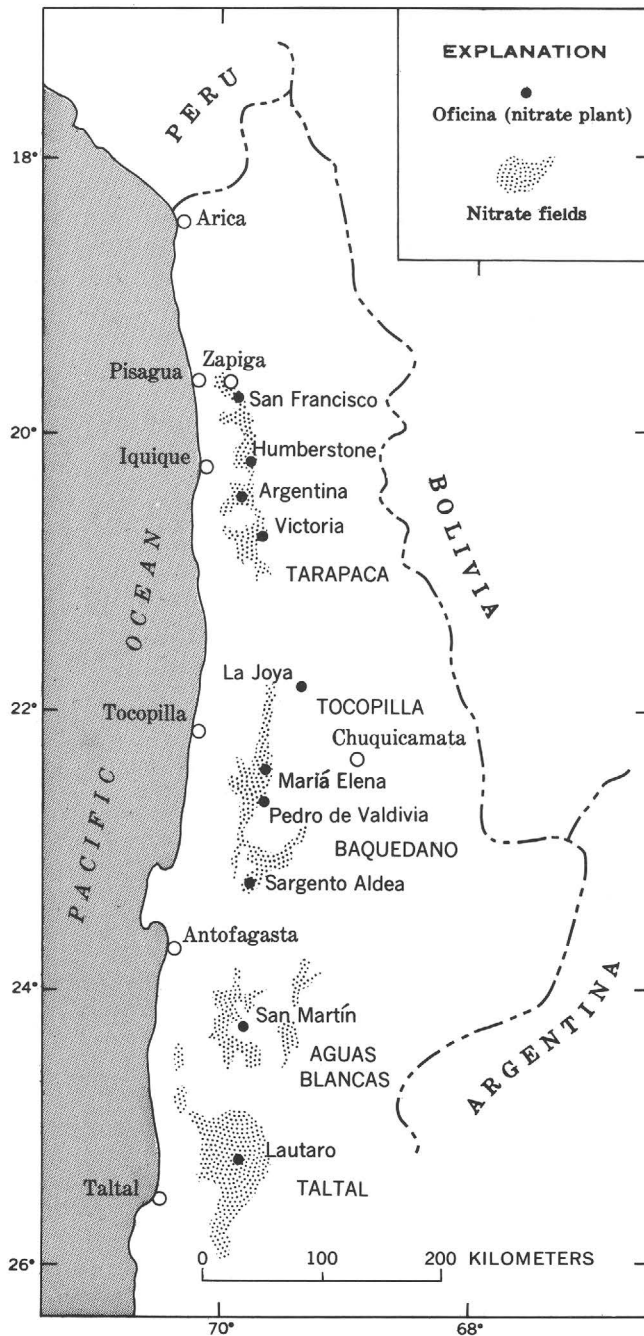


Figure 1.—Index map of northern Chile, showing location of the nitrate fields and of selected nitrate plants.

tion is to be found in reports by Ericksen (1963), Ericksen and Mrose (1970), and Mrose, Fahey, and Ericksen (1970). Among earlier reports that give information about geology and mineralogy of the deposits are those of Brüggén (1938) and Wetzel (1932).

Acknowledgments.—The fieldwork on which this report is based was undertaken under the joint sponsorship of the Instituto de Investigaciones Geológicas of Chile and the United

Nations Special Fund. Identification of minerals in the soda-niter veins is based largely on X-ray powder diffraction studies carried out by the authors in the laboratories of the U.S. Geological Survey.

OCCURRENCE AND DISTRIBUTION OF VEINS

High-purity white soda-niter veins occur in the two major types of nitrate ore, one in which saline minerals cement regolith (unconsolidated clastic sediments) and the other in which they occur as impregnations, veins, and irregular masses in bedrock. The first type generally rests on poorly cemented or uncemented rock debris similar in character to that of the ore layer, or on finer material consisting chiefly of sand- and silt-sized particles. The second type gives way downward to less fractured rock relatively free of saline minerals.

The nitrate deposit consisting of saline-cemented regolith is considered to be made up of several layers: the *chuca* and *costra* (overburden with little or no NaNO_3), *caliche* or the nitrate ore (generally averaging 8–15 percent NaNO_3), and *coba* and *conjelo* (material below the *caliche*, also containing little or no NaNO_3). These layers are shown diagrammatically in figure 4. Exploitable *caliche* is generally 1–3 m thick.

The veins in saline-cemented regolith are secondary in origin, having formed in fractures that opened in the preexisting lower grade nitrate ore, and therefore are younger than this ore. The fractures formed in many ways, including desiccation of the newly formed *caliche* layer, later fracturing of the dry brittle *caliche* layer owing to fault movement and accompanying earthquake shock, and fracturing due to thermal expansion and contraction of the layer. Some of these fractures contain a simple filling of saline minerals; others were first filled and then widened by force of the crystallizing salines. Figure 5 shows typical fracture-filling veinlets of white soda-niter and halite in a *caliche* consisting largely of saline-cemented silt and sand.

Near-horizontal layers of high-purity salines are found locally at the base of the *caliche* consisting of saline-cemented regolith, as is shown in figure 4. More rarely they occur within this type of *caliche*. The layer at the base of the *caliche* is generally at the contact between the firmly cemented *caliche* and the underlying poorly cemented or uncemented *coba* (fig. 4). This basal layer is highly irregular in thickness, ranging from a few centimeters to about 50 cm, and is discontinuous. In a few nitrate fields such layers are widespread, but in most they are relatively sparse. These layers may be of primary origin, having been formed as part of the original nitrate complex, rather than being secondary veins, which were deposited after the enclosing *caliche* had become dry and hard. Therefore, the layers may represent concentrations of salines at the maximum depth that capillary evaporation of soil moisture (or saline ground water) took place. Capillary evaporation is the probable process by which the salines were deposited to form *caliche*.



Figure 2.—Area of extensive underground nitrate workings (cuevas) near Oficina Compañía, Tarapacá district. Near-horizontal discontinuous layers of high-grade soda-niter occur in limestone and interbedded shale, 3–6 m below the surface. Opencut in foreground exploited shallow veins; tunnels from face connect shafts marked by isolated waste piles.

Nitrate-bearing bedrock shows a zoning similar to the layering in the saline-cemented regolith. The surface generally has a layer of uncemented slope debris or windblown sand and dust, commonly ranging from a few centimeters to about 30 cm in thickness, corresponding to *chuca*. Nitrate-bearing veins and impregnations in the underlying bedrock generally show evidence of leaching to depths of 3–6 m. The leached parts of the veins, corresponding to the above-mentioned *costra*, now consist chiefly of powdery to compact calcium sulfate and saline-cemented sand and rock fragments. The underlying caliche zone containing layers, veins, and impregnations of soda-niter and other salines is as much as 2 m thick.

Veins and layers of high-purity salines, typical of the bedrock-type caliche, were formed by crystallization of salines along fractures and bedding planes which, as a consequence, were gradually forced open. Such veins are well shown in figure 6. Lenticular, discontinuous, nearly horizontal layers are extensive in bedrock in certain areas, particularly in Tarapacá.

They range from a few centimeters to about 50 cm in thickness (rarely as much as a meter thick). Generally only one massive layer is found in the caliche zone, but one or more thinner layers may be present, and the fractured rock above and below the main layer may be impregnated by and contain many veinlets of salines through a thickness of several tens of centimeters. In any one nitrate field this type of caliche generally is found at a more or less uniform depth, most commonly 3–6 m below the surface. In hilly or hummocky areas it tends to be parallel or subparallel to the land surface.

High-purity veins are widespread in the nitrate fields as a whole, but are relatively sparse in some fields and very abundant in others. They can best be observed in the underground workings where they were mined during the last century and early part of the present century (fig. 2). Many shafts and tunnels are still open, in spite of being at least 70 years old, and afford an excellent opportunity for studying the veins and collecting samples. Veins can also be found in

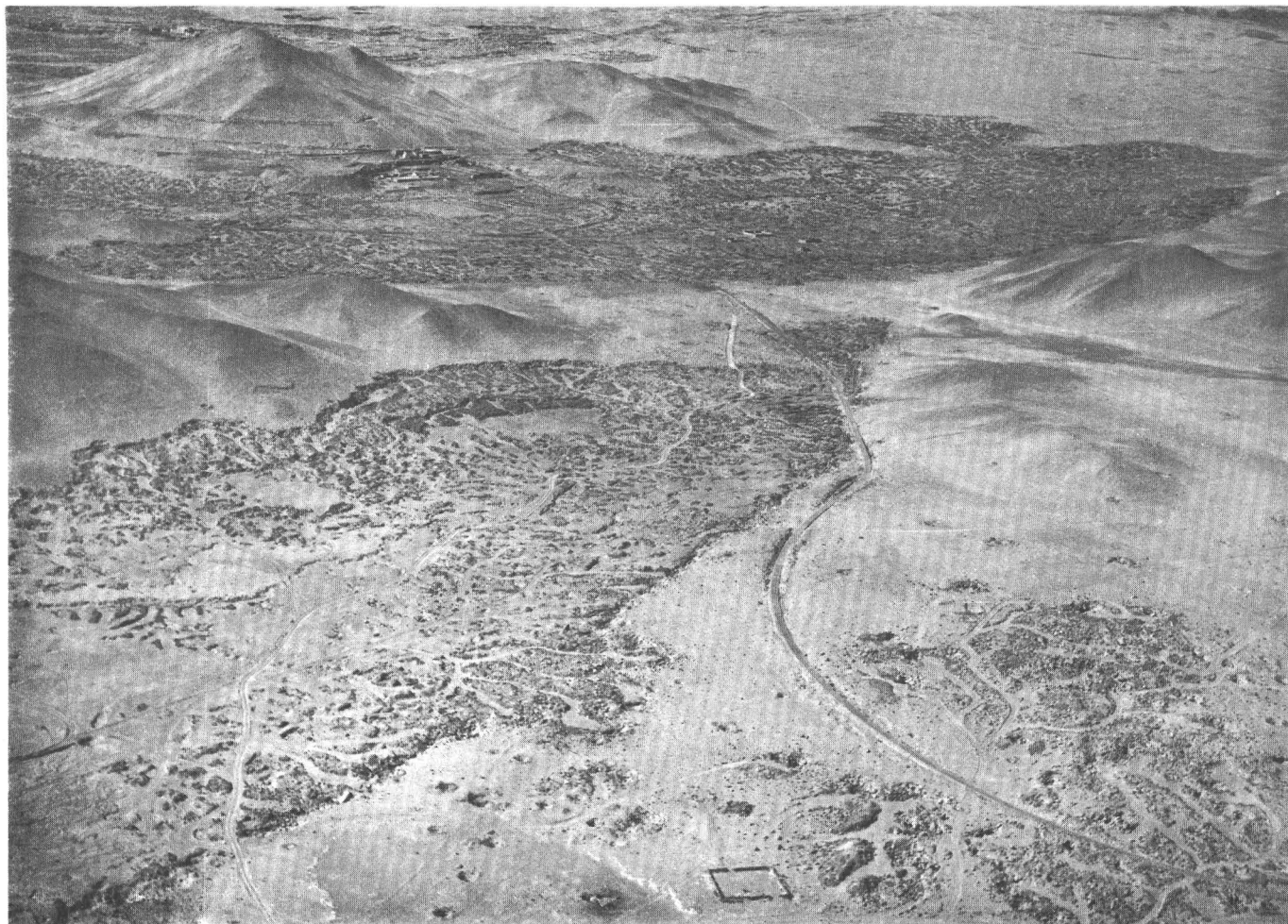


Figure 3.—Aerial view of opencut nitrate workings in the southern part of the Tarapacá district; ore from these workings was processed at Oficina Lagunas Norte, the ruins of which appear in the distance. Caliche here is largely saline-cemented regolith; caliche on lower hillslopes consists of veins and impregnations in fractured andesite. Workings are 2–4 m deep; waste piles give a distinctive pattern to old workings of this type.

surface cuts of recent mining operations, or old cuts where overhanging ledges have protected them from weathering processes.

Veins in bedrock are most numerous in the northernmost nitrate fields of the Tarapacá district (fig. 1), and are particularly well exposed in the extensive underground workings in the vicinity of the former settlement of Zapiga (fig. 1), where the very earliest nitrate plants were constructed in the first decade of the 1800's. A low hill of limestone in a salar (saltpan), about 0.5 km east of Oficina San Francisco (fig. 1), is covered with workings in which are exposed many veins and layers as much as a meter thick. Near-horizontal layers of high-purity soda-niter at the base of saline-cemented regolith are particularly well displayed in underground workings in nitrate fields in the coastal range in the region near Oficina Argentina.

In other regions, veins are not as well exposed and seemingly not as abundant as they are in Tarapacá. Nevertheless, a careful search in almost any of the nitrate fields will disclose

high-purity veins. Some of the best places to observe veins are near the following nitrate plants: Oficina Sargento Aldea in the Baquedano district, Oficina San Martín in the Aguas Blancas district, and Oficina Lautaro in the Taltal district.

CHEMICAL COMPOSITION AND MINERALOGY OF VEINS

The Chilean nitrate deposits, in addition to containing an unusual concentration of soda-niter, have a unique suite of saline minerals as shown in table 1. Of these minerals, humberstonite, lautarite, brüggenite (Mrose and others, 1971), dietzeite, and lopezite are not known to occur elsewhere. Our X-ray studies have shown several other saline minerals to be present locally in very small quantities. These may be either new minerals or minerals for which the published X-ray data are incorrect. Many of the minerals listed in table 1 are found in crystalline form or in exceptional concentrations in the high-purity veins.

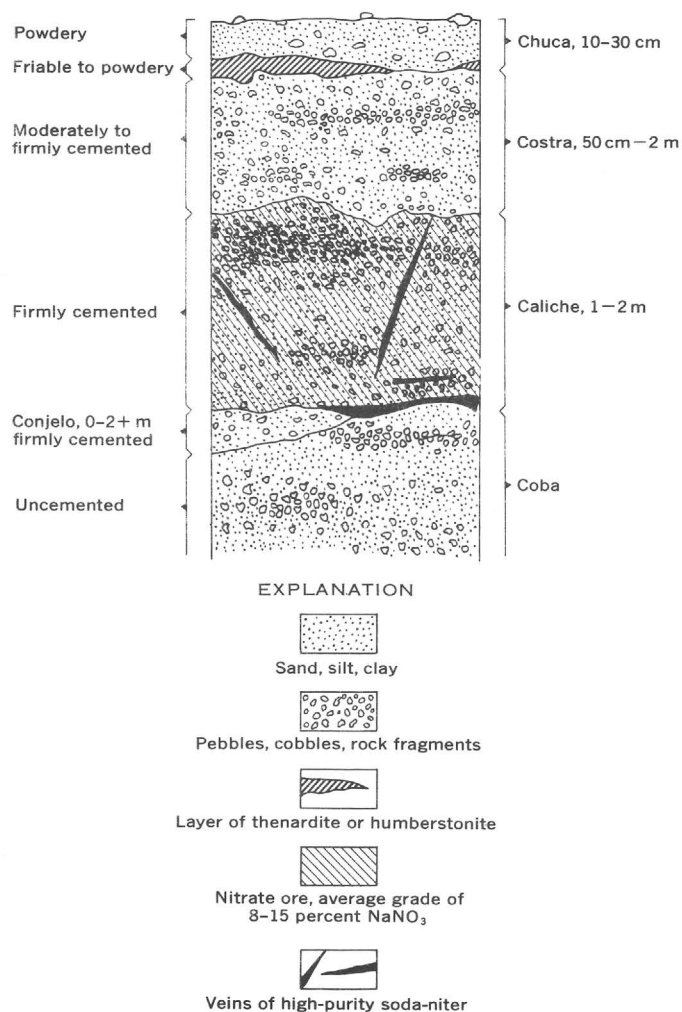


Figure 4.—Diagrammatic section showing typical layering of saline-cemented regolith in a nitrate deposit.

The nitrate deposits, including the high-purity veins, also are unique in having a high concentration of iodine, occurring as the iodate ion (IO_3^-), and of the perchlorate ion (ClO_4^-), which occur widely in amounts indicated in table 2. Iodine occurs only as trace amounts in other saline deposits, and the perchlorate ion has not been found elsewhere in nature.

The typical vein in the Chilean nitrate fields is a mixture of soluble saline minerals, chiefly soda-niter and halite, with

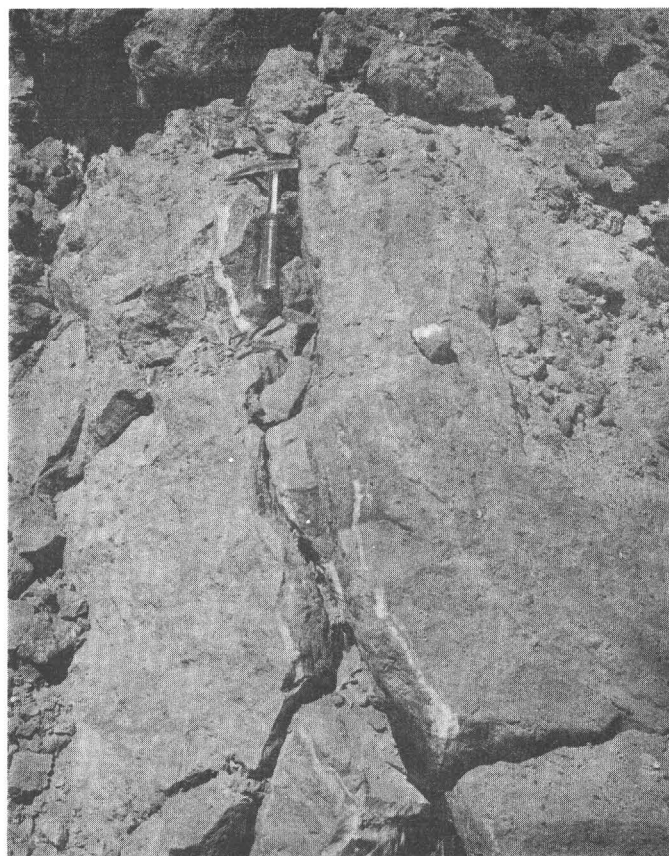


Figure 5.—Veinlets of white high-grade soda-niter in a fresh open cut in workings near Oficina Humberstone; host material is light-brown saline-cemented sand and silt containing about 15 percent NaNO_3 . The vein contains more than 50 percent NaNO_3 .

soda-niter generally being predominant. The veins also contain varying amounts of sulfate minerals of which darapskite and bloedite evidently are the most abundant. Locally, the veins may consist essentially of only one saline mineral. The purest soda-niter veins found in our study are those in the vicinity of Pampa Pique III, about a kilometer north of Oficina Lautaro (fig. 1). A chemical analysis of typical fibrous vein material (fig. 6) shows it to be 99.8 percent NaNO_3 (table 2). Pure halite veins are widespread and abundant in the nitrate fields near Oficina La Joya (fig. 1). We found glauberite veins in the eastern part of the Taltal district (near Oficina Bascunán, not shown in fig. 1). Veins of pure bloedite were found in

Table 1.—Saline minerals in the Chilean nitrate deposits

Halite	NaCl	Glauberite	$\text{Na}_2\text{Ca}(\text{SO}_4)_2$	Ginorite	$\text{Ca}_2\text{B}_{14}\text{O}_{23}\cdot 8\text{H}_2\text{O}$
Soda-niter	NaNO_3	Kieserite	$\text{MgSO}_4\cdot\text{H}_2\text{O}$	Kaliborite	$\text{HKMg}_2\text{B}_{12}\text{O}_{16}(\text{OH})_{10}\cdot 4\text{H}_2\text{O}$
Niter	KNO_3	Epsomite	$\text{MgSO}_4\cdot 7\text{H}_2\text{O}$	Lautarite	$\text{Ca}(\text{IO}_3)_2$
Darapskite	$\text{Na}_3(\text{NO}_3)(\text{SO}_4)\cdot\text{H}_2\text{O}$	Bloedite	$\text{Na}_2\text{Mg}(\text{SO}_4)_2\cdot 4\text{H}_2\text{O}$	Dietzeite	$\text{Ca}_2(\text{IO}_3)_2(\text{CrO}_4)$
Thenardite	Na_2SO_4	Humberstonite	$\text{K}_3\text{Na}_7\text{Mg}_2(\text{SO}_4)_6(\text{NO}_3)_2\cdot 6\text{H}_2\text{O}$	Lopezite	$\text{K}_2(\text{Cr}_2\text{O}_7)$
Anhydrite	CaSO_4	Ulexite	$\text{NaCaB}_5\text{O}_9\cdot 8\text{H}_2\text{O}$	Brüggenite	$\text{Ca}(\text{IO}_3)_2\cdot\text{H}_2\text{O}$
Gypsum	$\text{CaSO}_4\cdot 2\text{H}_2\text{O}$	Probertite	$\text{NaCaB}_5\text{O}_9\cdot 5\text{H}_2\text{O}$		
Bassanite	$2\text{CaSO}_4\cdot\text{H}_2\text{O}$	Hydroboracite	$\text{CaMgB}_6\text{O}_{11}\cdot 6\text{H}_2\text{O}$		

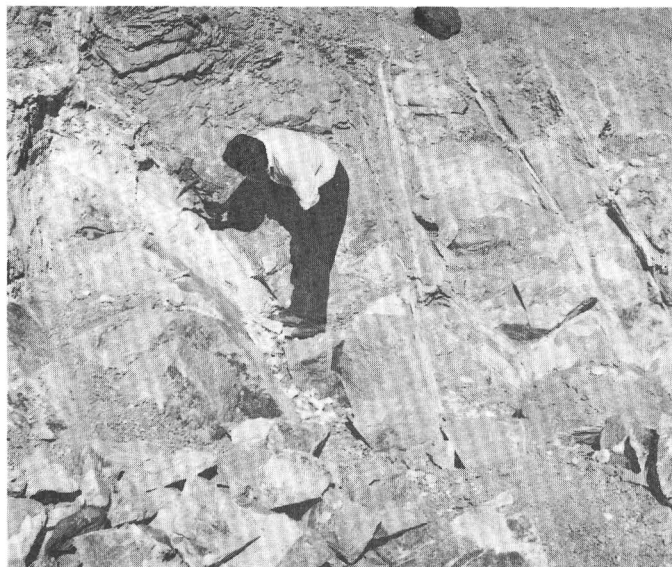


Figure 6.—Veins of fibrous soda-niter in rhyolite tuff, exposed in an open-pit nitrate mine at Pampa Pique III, Oficina Lautaro, Taltal district. Vein material from this locality was found to be of very high purity, one sample (table 2) contains 99.8 percent NaNO_3 and is the purest nitrate-bearing material reported from northern Chile.

association with soda-niter and halite veins at a secondary copper deposit in eastern part of the Baquedano district (several kilometers north of the town of Sierra Gorda).

Some veins particularly at or near contacts with enclosing rock are bright yellow, blue, violet, or pink. The yellow material contains unusual iodate and chromate minerals such as lautarite, dietzeite, and tarapacaite. Blue and violet material has concentrations of blue or violet halite. Pink veins, which



Figure 7.—Nearly horizontal fibrous vein of high-purity soda-niter in fractured rhyolite tuff, Pampa Pique III, Oficina Lautaro.

Table 2.—Chemical composition of selected high-purity soda-niter veins in the nitrate deposits of northern Chile [Composition in weight percent]

	Vein locality			
	1	2	3	4
NO_3	72.15	32.63	44.46	49.65
Cl^-07	21.84	14.97	12.92
SO_4^{-2}10	8.30	2.38	2.72
IO_3^-04	.14	.08
ClO_4^-04	.2556
B0512
K^+32	1.12	6.89
Ca^{+2}05	.32	.36	.14
Mg^{+2}01	.93	.28	.27
H_2O	1.52	3.40	.79
Insoluble residuc ¹82	4.13	6.80	2.07
Equivalent NaNO_3 ²	98.84	44.70	60.91	68.02

1. Oficina Lautaro; analyzed at Oficina Victoria, 1964.
2. Oficina Santa Fe; analyzed at Oficina María Elena, 1966.
3. Oficina Argentina; Semper and Michels (1908, p. 10).
4. Tarapacá district; Penrose (1910, p. 14).

¹ Insoluble in hot water; includes relatively insoluble minerals such as gypsum, $\text{CaSO}_4 \cdot 2\text{H}_2\text{O}$.

² All NO_3^- calculated as NaNO_3 ; Na^+ , the most abundant anion was not determined.

are relatively rare, contain considerable amounts of light-red bloedite.

The soda-niter veins show different textures, which depend largely on the mineralogical composition and mode or depth of emplacement, but which also may be due to other factors not yet understood. The typical vein consists of a dense granular mixture of white saline minerals. Grain size is generally less than 0.5 mm. Other veins, consisting largely or almost entirely of soda-niter, commonly show a fibrous or thin columnar habit wherein individual fibers or columns of soda-niter, generally less than 2 mm in diameter and a few millimeters to several centimeters long, are oriented perpendicular to vein walls (fig. 7). Veins of high-purity halite may show a similar fibrous or columnar habit. Soda-niter and halite in the fibrous veins are not oriented according to one of the principal crystallographic axes, as is readily discernible from direction of cleavage in the fibers. Veins may also consist largely of soda-niter in large clear anhedral crystals 0.5–4 cm long.

Some veins or parts of veins contain considerable amounts of platy darapskite that may show a coarse columnar or platy texture resembling the fibrous texture of soda-niter veins. This texture, however, is due to plates of darapskite oriented perpendicular to vein walls.

An unusual feature of the soda-niter veins is an abundance of microscopic fragments of saline minerals, chiefly soda-niter and halite, that have been incorporated into larger crystals or grains of soda-niter and halite. These fragments indicate a complex history of deposition and fragmentation of the vein as walls were gradually pushed apart by force of crystallization.

REFERENCES

- Brüggen, Juan, 1938, El salitre: Bol. Minero, Santiago de Chile, v. 50, p. 737-754.
- Ericksen, G. E., 1963, Geology of the salt deposits and the salt industry of northern Chile: U.S. Geol. Survey open-file report, 164 p.
- Ericksen, G. E., and Mrose, M. E., 1970, Mineralogical studies of the nitrate deposits of Chile. II. Darapskite, $\text{Na}_3(\text{NO}_3)(\text{SO}_4)\cdot\text{H}_2\text{O}$: Am. Mineralogist, v. 55, p. 1500-1517.
- Mrose, M. E., Ericksen, G. E., and Marinenko, J. W., 1971, Brügggenite, $\text{Ca}(\text{IO}_3)_2\cdot\text{H}_2\text{O}$, a new saline mineral from the Chilean nitrate deposits [abs.]: 20th Clay Minerals Conference, Rapid City, S. Dak., Ann. Mtg., Program, p. 13.
- Mrose, M. E., Fahey, J. J., and Ericksen, G. E., 1970, Mineralogical studies of the nitrate deposits of Chile. III. Humberstonite, $\text{K}_3\text{Na}_7\text{Mg}_2(\text{SO}_4)_6(\text{NO}_3)_2\cdot 6\text{H}_2\text{O}$, a new saline mineral: Am. Mineralogist, v. 55, p. 1518-1533.
- Penrose, R. A. F., Jr., 1910, The nitrate deposits of Chile: Jour. Geology, v. 18, p. 1-32.
- Semper, Dr., and Michels, Dr., 1908, La industria del salitre en Chile; [translated to Spanish and amplified by Javier Gandarillas and Orlando Ghigliotto Salas]: Santiago de Chile, Imprenta Litografía i Encuadernación Barcelona, 418 p.
- Wetzel, Walter, 1932, Nitrat, in Stutzer, Otto, Die wichtigsten Lagerstätten der Nicht-Erze, v. 4: Berlin, Gebrüder Borntraeger, p. 295-374.



THORIUM DISTRIBUTION IN A GRANITE STOCK NEAR BULL CANYON, LEMHI COUNTY, IDAHO

By MORTIMER H. STAATZ, CARL M. BUNKER,
and CHARLES A. BUSH, Denver, Colo.

Abstract.—A granite stock underlying an area of about 4.3 square miles occurs on the west side of the Beaverhead Mountains near Bull Canyon, Idaho. This granite body, which is of probable Silurian age, has intruded both the upper Precambrian Belt Supergroup and the Ordovician Kinnikinic Quartzite. The granite consists principally of perthite and quartz with minor amounts of plagioclase, magnetite, biotite, zircon, apatite, rutile, monazite, and allanite. The average thorium content of 16 representative samples from various parts of the stock is 35 ppm. A radiometric map of the granite stock indicates that the most radioactive area occurs along an arcuate ridge near the east edge of the stock. The most radioactive parts of this area are in widely scattered zones along fractures and in small irregular areas. In these abnormally radioactive areas, which may contain in excess of 100 ppm Th, the principal thorium mineral is thorite, which occurs as tiny crystals along fractures. Late-stage postmagmatic fluids are believed to have altered the original granite and deposited the thorite along favorable zones.

The interest in thorium has been high in Lemhi County, Idaho, since the discovery of the first thorium-bearing vein in the Lemhi Pass district in 1949. This interest led to the discovery of an anomalously radioactive granite on a steep-sided mountain near Bull Canyon during the summer of 1965. The Kay group of claims was located at this time by Carroll Wells, Miley Evans, and George Hammond, and about 7 miles of roads (fig. 1) were cut to expose and furnish access to this granite body. Ownership of these claims passed to the Nuclear Fuels and Golden Pleasures Mining Co., which in 1968 controlled a block of 56 claims in this area. Assay values of several hundred parts per million thorium were obtained from samples of this rock (T. E. Richards, written commun., 1968), and this stock was considered a potential large low-grade source of thorium. The present study was undertaken to determine the size and average grade of this granite body. Fieldwork was carried out during 3 weeks of the summer of 1970 by Staatz aided by Eric C. Grimm.

The granite lies along the west face of the Beaverhead Mountains about 10 miles east-southeast of Leadore. Bull Canyon lies adjacent to the south end of the granite body, and Hawley Creek cuts through its north tip (fig. 2). The granite is exposed along the mountain face for a distance of 4 miles, and

it has a maximum width of 1.7 miles. This rock underlies a total area of 4.3 square miles and is exposed over a vertical distance of 3,500 feet (fig. 1).

GEOLOGY OF AREA

This crudely oval granite body is bounded along most of its northeast side by a thrust fault that separates the granite from the Park City Formation of Permian age (fig. 2). The rest of the northeast side and part of the west side of the granite body are bordered by Kinnikinic Quartzite of Ordovician age. The contact between these two rocks is poorly exposed, and although it is probably a normal contact, it might be a branch of the thrust that separates the granite from the Park City (fig. 1). Kinnikinic Quartzite also lies along the southwest edge of the granite, and it forms a small outcrop on top of the granite body on a ridge near its north edge. The presence of similar quartzite float along other ridges on the west side of the granite indicates that the quartzite once overlay the granite along much of its west side. Along most of the east side and the rest of the southwest side the granite was intruded into a dull-green sericitic siltite and a feldspathic quartzite of the Belt Supergroup of Precambrian age. Outcrops of Belt rocks are poor, but dikes of granite intruding the Belt are exposed along the southeast and southwest sides of the large granite body. Adjacent to these dikes the Belt rocks are commonly partly silicified and are better preserved. Here the contact between the two is commonly gradational because of incorporations and assimilation of Belt rocks in the granite. A small patch of pyroclastic rocks and andesitic flows of Tertiary age overlies the granite-Belt contact on a high saddle along the east side of the granite. Fans and alluvium of Quaternary age also overlie the granite along parts of its southwest side (fig. 1). The geology of this area was discussed in some detail by Lucchitta (1966).

The age of this granite is not precisely known, but it is probably Silurian. Numerous dikes of granite have intruded the Belt quartzites. Contact relations between the Kinnikinic Quartzite and the granite are not clear, but inclusions of Kinnikinic in the granite near the top of the highest peak in

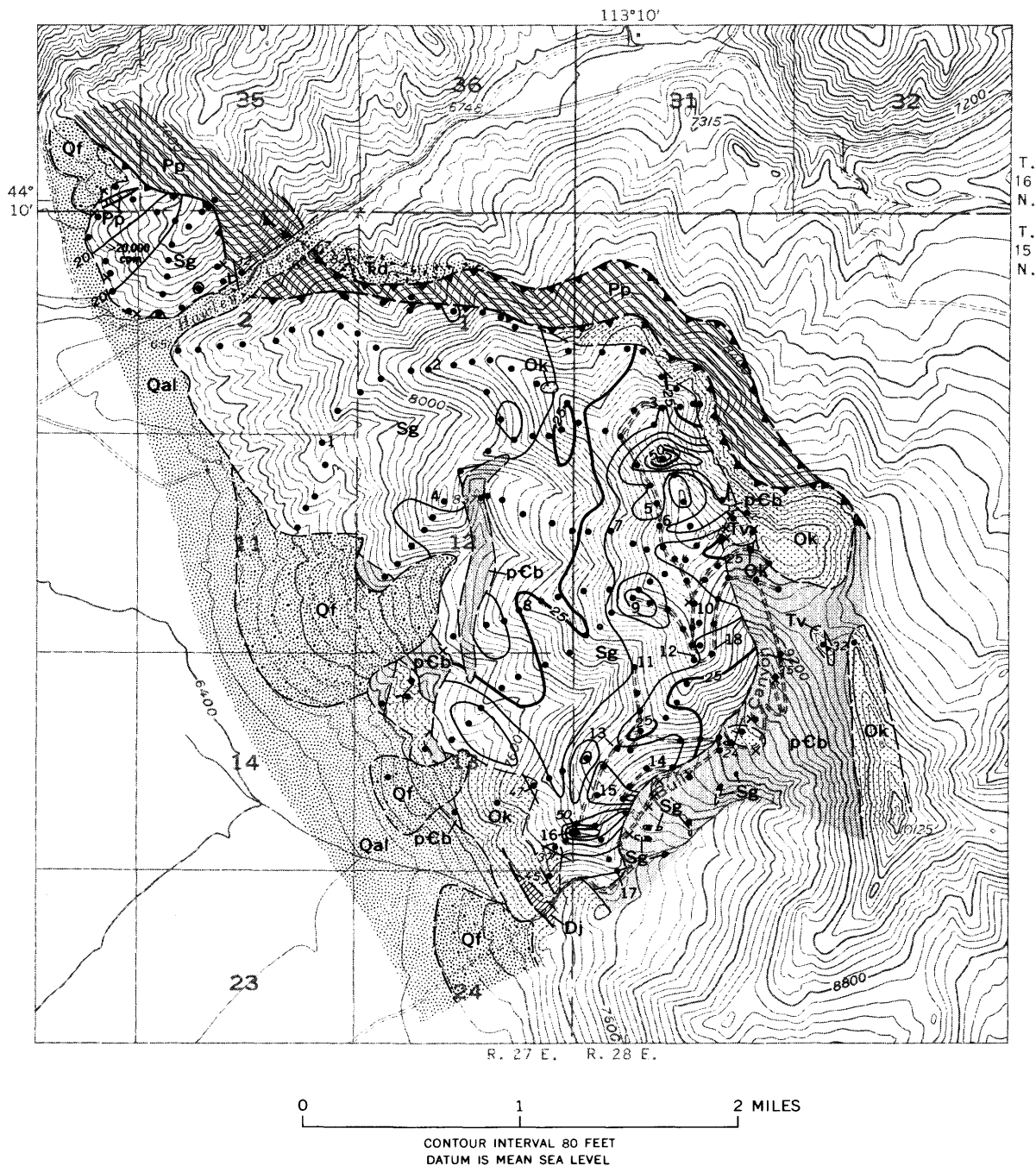


Figure 1.

the area leave little doubt as to the younger age of the granite. Silurian ages were obtained on similar-appearing granites in Railway Canyon, about 7 miles northwest of the granite under discussion, and near Willow Creek, about 10 miles to the south. The age of the granite in Railway Canyon as determined on potassium feldspar by the Rb-Sr method is 410 ± 60 m.y. (million years) (Ruppel, 1968, p. 5); that of the granite near Willow Creek as determined on biotite by the K-Ar method is 441 ± 15 m.y. (Ramsrott and Scholten, 1965, p. 159).

The granite is generally medium grained but ranges from fine to coarse grained. Much of the granite, especially that with a higher radioactivity, is hematitic red or brownish red, but it may be tan, pink, or even white. As the color indicates, the radioactive rocks are partly altered. Altered rocks are most common along the east side of the granite body and least common in the central and northern parts. Unaltered granite consists of 55–75 percent perthite, 0–5 percent plagioclase, 20–45 percent quartz, as much as 2 percent magnetite and

E X P L A N A T I O N

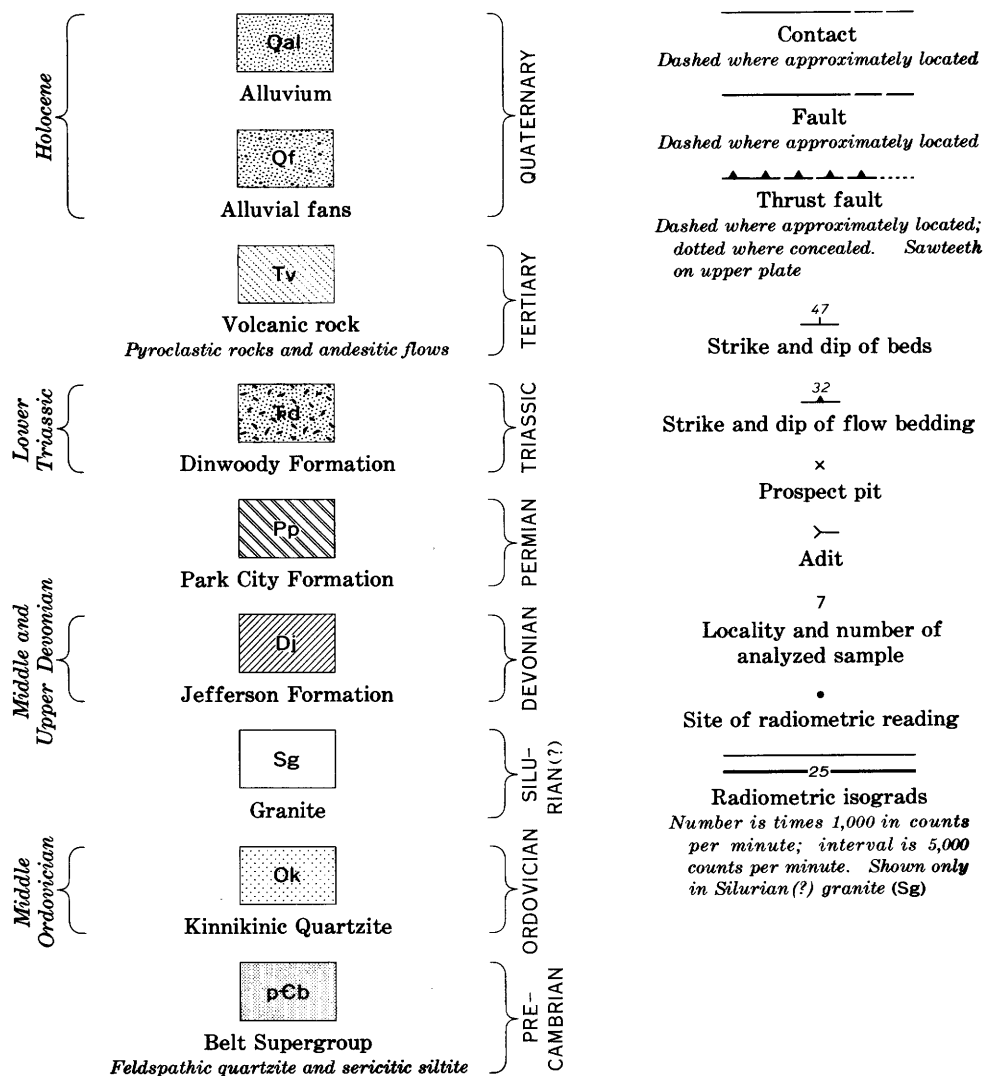


Figure 1.—Radiometric and geologic map of granite stock near Bull Canyon, Idaho. Base from U.S. Geological Survey Morrison Lake quadrangle, 1956.

biotite, and less than 1 percent zircon, apatite, rutile, monazite, and allanite. In the least altered rocks, biotite is commonly partly altered to chlorite. In the more altered rocks most of the chlorite, biotite, apatite, and magnetite are absent; hematite and limonite are present; and some of the perthite is altered to sericite. Although the quartz and feldspar contents of this rock vary somewhat, most if not all of this igneous rock would be classified as a granite. Table 1 gives the chemical analysis and the norm of a hematitic red granite from sample site 18 (fig. 1).

Heavy minerals were separated from the lighter ones in 18 samples by methylene iodide. Heavy minerals made up 0.05–0.85 percent of the samples. Hematite was the most abundant heavy mineral, and zircon was next most abundant.

Hematite occurs in both the red granular and specularite forms. Zircon is present in many different colors and textures, and the following varieties were noted: (1) clove brown, (2) red porcellaneous, (3) purple granular, (4) yellow opaque, (5) glassy orangish yellow, (6) yellowish green opaque, (7) white enameloid, (8) clear yellow, (9) clear pink, and (10) white aggregates. All these different-appearing zircons were identified by their X-ray diffraction patterns. In all but two samples, one to four varieties of zircon were noted in the heavy minerals. Magnetite was found in most samples but was scarce in altered rocks, biotite was found only in relatively unaltered rocks, chlorite was present in little-altered rocks, and limonite occurred in minor amounts in some of the altered rocks. Uncommon minerals include rutile and allanite, each found in

Table 1.—*Chemical analysis and norm of granite from a stock near Bull Canyon Idaho*

[Analyst: E. L. Brandt]

Chemical composition		Norm	
Constituent	Percent	Mineral	Percent
SiO ₂	76.40	Quartz	46.44
Al ₂ O ₃	12.38	Orthoclase	45.59
Fe ₂ O ₃	1.50	Albite	1.57
FeO	.23	Hypersthene	.56
MgO	.18	Magnetite	.23
CaO	.00	Hematite	1.28
Na ₂ O	.24	Ilmenite	.30
K ₂ O	7.62	Corundum	4.08
H ₂ O ⁺	.94	Halite	.12
H ₂ O ⁻	.01	Unalotted	.06
TiO ₂	.17	Total	100.23
P ₂ O ₅	.01		
MnO	.02		
CO ₂	.01		
F	.05		
	99.76		
Less O	.04		
Total	99.72		

two samples, and barite, monazite, thorite, malachite, and chalcopyrite, each found in one sample. Thorite and the two copper minerals were found in sample 6 (table 2, fig. 1).

The amounts of monazite and allanite, which are primary minerals, are too small to account for the amount of thorium found in most of these samples. Zircon is abundant in the heavy minerals and is commonly radioactive. In samples from other areas, zircon may contain at least as much as 2 percent U (Lyons, 1961, p. B70–B71). To see if zircon might also be the source of some of the thorium, grains of zircon were submitted to G. A. Desborough for study on the electron microprobe. Different results were obtained from several different grains of the same sample. Some of the zircon grains consisted of minute intergrowths of at least two phases. One phase of a complex dark-red grain that contained more than 10 percent Th, abundant iron, and relatively little silicon probably was not zircon, but it may have been a mixture of zircon, thorite, and hematite. Thorium content of several zircon grains having only one phase ranged in a single grain from less than 0.05 percent to more than 1 percent across the grain, indicating zoning. Microprobe analyses indicate that the zircon has a high thorium content both within the mineral and as another separate mineral included in the zircon.

RADIOACTIVITY

Abnormal radioactivity of the granite led to prospecting and placing claims in this area. Of 19 samples taken by the U.S. Atomic Energy Commission, 12 contained 0.01 percent ThO₂

Table 2.—*Thorium, uranium, and potassium contents of granite near Bull Canyon measured by gamma-ray spectrometer*

[Analysts: C. M. Bunker and C. A. Bush]

Sample No.	Thorium (ppm)	Uranium (RaeU) (ppm) ¹	Potassium (percent)
1	27.8	2.5	4.2
2	13.5	1.9	5.6
3	37.5	4.5	4.5
4	29.5	2.5	6.2
5	33.8	7.3	4.7
6	236.0	5.9	4.4
7	34.4	6.5	4.5
8	24.3	3.5	6.7
9	36.3	7.5	4.8
10	44.8	6.8	5.1
11	30.9	5.3	5.4
12	29.5	5.5	5.0
13	65.1	1.9	1.6
14	26.0	4.4	5.2
15	28.2	6.1	5.9
16	80.4	17.4	5.0
17	22.3	8.2	4.3

¹The amount of uranium in secular equilibrium that was needed to support the measured amount of Pb²¹⁴.

²Selected sample from small highly radioactive spot.

and one contained 0.15 percent ThO₂ (T. E. Richards, written commun., 1968); a sample collected for the present study contained 0.024 percent Th. A rock sample from this granite stock that was given to the senior author by E. T. Ruppel contained 0.03 percent Th.

The economic potential of the granite stock must be based on a systematic evaluation rather than on isolated samples. Hence, the entire granite body was surveyed radiometrically by use of a portable scintillation counter. Readings were taken at points about 500–700 feet apart along all roads and major ridges. Several measurements were made at each point to obtain an average value for the area. A radiometric map was made by contouring these points, with the contour interval representing 5,000 counts per minute (fig. 1). Counter readings on the granite ranged from 15,000 to 62,000 counts per minute. On the adjacent areas underlain by rocks of the Belt Supergroup the readings ranged from 13,000 to 20,000 counts per minute, and on those areas underlain by the Kinnikinic Quartzite they ranged from 4,500 to 9,000 counts per minute.

The most intense radioactivity in the granite stock occurs on a prominent arcuate ridge along the east edge of the stock. Roads that were built to prospect the granite are confined to this ridge. The northwestern two-thirds of the body has few radiometric measurements that exceed 20,000 counts per minute.

Variations in radiation intensity of the granite were observed at many locations. Generally, the areas of highest radioactivity were altered, were hematitic red, and were related either to a narrow zone along a fracture or to an irregularly shaped area 50 feet or less in diameter. These small areas of high



Figure 2.—Granite (Sg) thrust over dolomite of the Park City Formation (Pp) on the north side of Hawley Creek.

radioactivity are generally along the arcuate ridge, where the overall radioactivity is abnormally high. The abnormally high radioactivity is related to concentrations of radioelements, especially thorium, probably emplaced in some parts of the stock, mostly along fractures, by postmagmatic circulating fluids.

Seventeen samples of the granite were analyzed for thorium, uranium (RaeU), and potassium by Bunker and Bush on a gamma-ray spectrometer (fig. 1, table 2). The accuracy of this method is ± 3 percent for RaeU and Th, and ± 2 percent for K. The uranium (RaeU) analyses are a measure of one of the daughter products (Pb^{214}) of radium and represent the equivalent uranium content of the sample. Thus, the RaeU measurement equals the uranium content of the sample if the uranium is in equilibrium with its radium daughter product. One of the samples of granite (6, table 2) was selected from a small highly radioactive area; the other 16 were selected at random and are fairly representative of the area sampled. The average radioelement concentration of the 16 random samples is 35.2 ppm (parts per million) Th, 5.7 ppm RaeU, and 4.9 percent K. A comparison of the individual analyses indicates that the amount of thorium present is not related to either the amount of radium or the amount of potassium present.

The thorium content of the samples as determined by gamma-ray spectrometer analyses cannot be correlated directly with that obtained by the readings made on the scintillation counter, although samples that have either a very low or very high thorium content as determined by analyses came from

areas that have a low or high counter reading, respectively. Differences in the results occur because: (1) the scintillation counter measures radiation not only from the area directly under the counter but also, to a lesser extent, from the surrounding area, but the gamma-ray spectrometer measures only the pieces sampled; (2) the scintillation counter measures both gamma and high-energy beta rays, but the gamma-ray spectrometer measures only gamma rays; and (3) the scintillation counter measures radiation not only from the thorium but from radium and potassium as well.

The average thorium content of the granite near Bull Canyon is compared, in table 3, with the average thorium content of other granites in the United States and with that of granites in the U.S.S.R. These granites were selected because they had been analyzed for thorium and do not represent a random selection of the granites. In fact, the two granites with the most analyses (Conway Granite and granites of the Tokovskii complex) were analyzed because of their high thorium content. Nevertheless, the average thorium content of the granite near Bull Canyon is somewhat, but not greatly, above the average thorium content of most of the granites in the United States, although it is only about 60 percent of the average of the Conway Granite. Several of the U.S.S.R. granites have a much higher average thorium content.

CONCLUSIONS

The granite stock near Bull Canyon has an average thorium content of about 35 ppm. Most of the thorium occurred originally in zircon, although some is found in allanite and monazite. Late-stage fluids have altered the granite and redistributed the thorium. The most alteration occurs on the high ridge along the east edge of this stock, where the thorium content is abnormally high and the original biotite and most of the magnetite have been changed to hematite and a little limonite. Within this overall abnormally radioactive area local tabular zones along fractures and small irregular areas contain more than 100 ppm Th. Most of the thorium in these small abnormally rich areas occurs as thorite, which is a late mineral present as tiny crystals along fractures in perthite.

This granite stock is not likely to be a source of thorium in the near future. High concentrations of thorium occur in small zones in the granite, but the average thorium content of the rock is moderate.

REFERENCES

- Abramovich, I. I., 1959, Uranium and thorium in the intrusive rocks of central and western Tuva: *Geochemistry*, no. 4, p. 442–450.
- Adams, J. A. S., Kline, M. C., Richardson, K. A., and Rogers, J. J. W., 1962, The Conway granite of New Hampshire as a major low-grade thorium resource: *Natl. Acad. Sci. Proc.*, v. 48, no. 11, p. 1898–1905.
- Filippov, M. S., and Komlev, L. V., 1959, Uranium and thorium in granitoids of the Middle Dnepr region: *Chemistry*, no. 5, p. 535–549.

Table 3.—Average thorium content of granite of Bull Canyon compared with that of various granites from other parts of the United States and from the U.S.S.R.

Area and description	Number of samples	Average thorium content (ppm)	Source of data
United States			
Bull Canyon, Idaho	16	35	Present report.
Sierra Nevada, Calif.	20	18	Rogers (1964, p. 60).
Front Range, Colo.	8	27	Do.
Texas (Enchanted Rock batholith)	81	20	Do.
Oklahoma	9	14	Do.
Minnesota	3	20	Do.
Rhode Island	4	27	Rogers (1964, p. 58).
Massachusetts	8	17	Do.
Southwest Maine	25	26	Do.
New Hampshire (Conway Granite)	312	56	Adams, Kline, Richardson, and Rogers (1962, p. 1901–1902).
U.S.S.R.			
Middle Dnepr region:			
Kirovgrad-Zhitomir complex:			
Porphyritic biotite granite	46	36	Filippov and Komlev (1959, p. 541).
Medium-grained biotite granite	30	23	Do.
Porphyritic muscovite-biotite granite	16	53	Do.
Medium-grained muscovite-biotite granite	8	61	Do.
Tokovoskii complex	101	97	Do.
Central and western Tuva:			
Chingchet complex	12	24	Abramovich (1959, p. 443).
Syutkol complex	21	15	Do.
Yustyd complex	6	36	Do.

Lucchitta, B. K., 1966, Structure of the Hawley Creek area, Idaho-Montana: Pennsylvania State Univ. Ph. D. thesis, 204 p.; Ann Arbor, Mich., University Microfilms, Inc., 235 p.

Lyons, J. B., 1961, Uranium and thorium in the older plutonic rocks of New Hampshire: Art. 32 in U.S. Geol. Survey Prof. Paper 424-B, p. B69–B71.

Ramsport, L. D., and Scholten, Robert, 1965, Early Paleozoic batholith in the Beaverhead Range, Idaho-Montana, in Abstracts for 1964:

Geol. Soc. America Spec. Paper 82, p. 159–160.

Rogers, J. J. W., 1964, Statistical tests of the homogeneity of the radioactive components of granitic rocks, in Adams, J. A. S., and Lowder, W. M., eds., The natural radiation environment, 1964: Chicago Univ. Press, p. 51–62.

Ruppel, E. T., 1968, Geologic map of the Leadore quadrangle, Lemhi County, Idaho: U.S. Geol. Survey Geol. Quad. Map GQ-733, scale 1:62,500, 5 p. text.



WHITE CLAY DEPOSITS OF CENTRE, BLAIR, HUNTINGDON, AND BEDFORD COUNTIES, PENNSYLVANIA

By JOHN W. HOSTERMAN, Beltsville, Md.

Abstract.—The clay deposits of central Pennsylvania contain light-gray to yellowish-gray silty to sandy clays composed of kaolinite and a little illite; gibbsitic kaolinite occurs in at least one deposit. Quartz is the only major nonclay mineral. The largest and most economically important deposits were derived from silty dolomite of the Gatesburg Formation of Cambrian age and were deposited in sinkholes and caverns. They occur as elliptical and lens-shaped bodies surrounded by a clayey, silty sand residuum of the Gatesburg Formation. The smaller clay deposits were formed by the weathering in place of cherty, argillaceous limestone of the Oriskany Group of Devonian age. Formation of these deposits probably began as early as Cretaceous time, but the major period of residual weathering probably occurred during Tertiary time.

The white clay deposits of Pennsylvania occur in three areas. Two of the areas, one near Mount Holly Springs, Cumberland County (fig. 1) (Hosterman, 1969a), and the other near Kunkletown and Saylorburg, Monroe County (Epstein and Hosterman, 1969), have been discussed previously. The present paper deals with the mineralogy, geologic setting, and origin of clay deposits in the third area near the central part of the State in Centre, Huntingdon, Blair, and Bedford Counties. All the clay deposits in central Pennsylvania are in the Gatesburg Formation of Cambrian age and in the Oriskany Group of Devonian age. The three largest and most recently mined claypits in the Gatesburg Formation are Stormstown, Centre County, operated by the Harbison-Walker Refractories Co.; Oreminea 1, Blair County, owned by the Woodbury Clay Co.; and Oreminea 2, Blair County, operated by Gannas Brothers, Inc. Other much smaller and older claypits in the Gatesburg Formation are Baileyville and Kelsey in Centre County; Dungarvin, Pennington, and Shoerberger in Huntingdon County; Martinsburg in Blair County; and Ore Hill and Bakers Summit in Bedford County (fig. 2). The Alexandria Fire Clay Co. is the only company mining clay from the Oriskany Group near Alexandria, Huntingdon County. Other old claypits in the Oriskany Group are near Petersburg and Shirleysburg, Huntingdon County (fig. 2).

The history of clay production in central Pennsylvania is very sketchy. White clay was probably first found in the early part of the 19th century when there was considerable

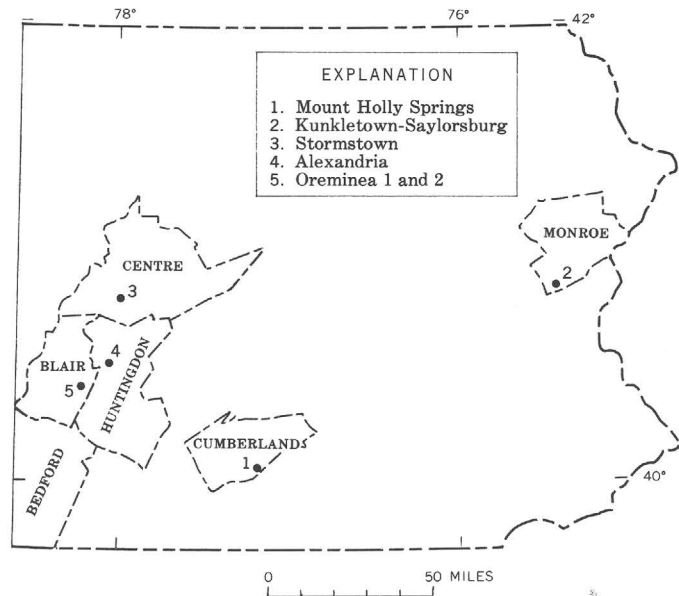


Figure 1.—Index map showing locations of the major white clay deposits in central and eastern Pennsylvania.

prospecting for iron ore. The refractory properties of these white clays were first recognized in 1870 when clay from the Alexandria pit was used to line local iron furnaces. Mining of white clay in central Pennsylvania increased during World War I when the amount of imported white clay from Europe was greatly reduced (Moore, 1922). The clay was used primarily by the steel mills as a mortar in laying refractory brick for coke ovens and open-hearth furnaces. Clay mining decreased after 1935, but World War II caused a renewal in the production of white clay; this production remained fairly steady for about 20 years. Since 1963, the amount of clay produced from central Pennsylvania has decreased steadily; at present only a very small amount is mined each year. It is estimated that about 100,000 tons of clay has been mined from central Pennsylvania. These clays have been tested by paper and china companies, but there are no records indicating that the white clay was used as a filler or in china.

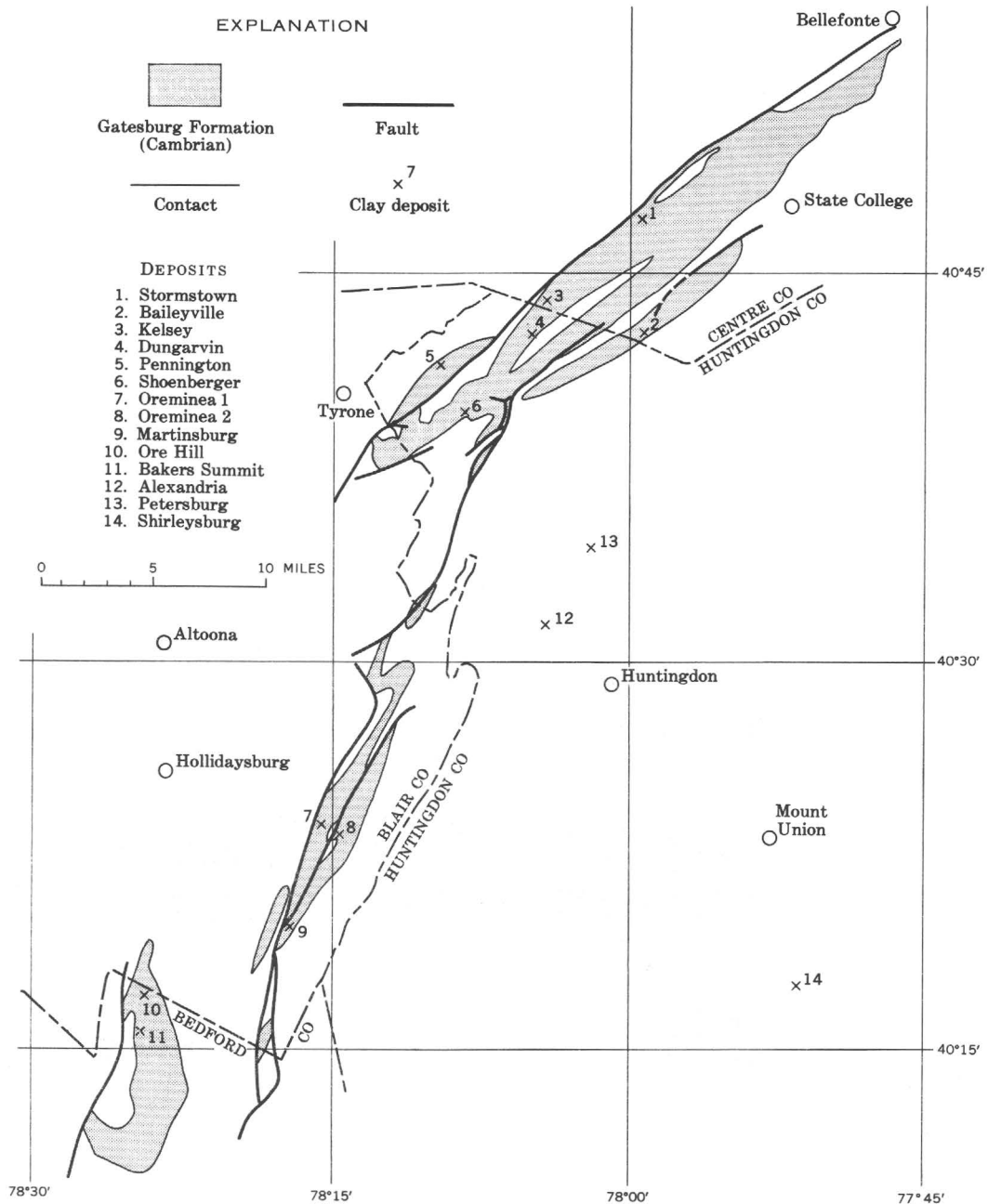


Figure 2.—Map showing clay deposits in the Gatesburg Formation (numbered localities in shaded areas) and claypits in the Oriskany Group in Centre, Blair, Huntingdon, and Bedford Counties, Pa., modified from Gray and others (1960).

METHODS OF INVESTIGATION

Power- and hand-auger drilling equipment was used to sample the clay deposits. Holes were drilled and samples were taken at 2- to 10-foot intervals. When the auger was pulled from the hole after each interval, the sample was taken from between the whorls of the leading auger flights. The sample was disturbed, and any contamination from the walls of the auger hole was easily cut away from the outside of the sample.

The samples were analyzed in the laboratory for mineralogical and chemical composition using X-ray diffraction and X-ray fluorescence methods described earlier (Hosterman, 1969b, p. 6, 7). The whole-rock samples were prepared by grinding to pass through a 170-mesh screen and by pressing each ground sample into a 1¹/₈-inch-diameter disk in an evacuated hydraulic press for a minimum of 30 seconds at a pressure of 30,000 psi. A mixture of boric acid and methyl cellulose was pressed beneath the sample for support. The clay

minerals were concentrated and prepared by allowing a deflocculated suspension of the sample to settle in water for 2 hours and 3 minutes and carefully siphoning off the upper 10 cm which contained the particles less than 4 μm (micrometers) in diameter. An oriented aggregate was obtained by sedimenting the clay onto a 1x2x $\frac{1}{4}$ -inch porous ceramic tile. Water was forced through the tile by vacuum. The ratios of clay, silt, and sand were calculated on the basis of dry-weight percentages using the 230-mesh sieve to remove the sand, and repeated washings (after 2 hours and 3 minutes settling time) to remove the clay from the silt. The description of all the sedimentary samples in this report is based on the system of sediment nomenclature of Hosterman (1969b, fig. 2).

The X-ray diffraction method for mineralogical identification and X-ray fluorescence method for chemical composition are routine. The X-ray diffraction method consisted of $\text{CuK}\alpha_1$ radiation (1.5405 Å) with a diffraction beam monochromator (Hosterman, 1968, p. B117). To distinguish between the various clay minerals, the clay-fraction samples on porous tiles were treated in several ways and examined by X-ray diffraction after each treatment. Samples were treated with ethylene glycol to check for expandable clay (montmorillonite) and were heated to 300°C to check for collapsible clay (vermiculite). Neither montmorillonite nor vermiculite was found in most samples. Several samples were treated with 3N hydrochloric acid to check the presence of chlorite with kaolinite. The clay-mineral ratios are based on peak-height ratios obtained from the X-ray diffraction traces. This method does not give an accurate amount of each clay mineral present, but it does give an approximation of within about 10 percent of the actual amount. The carbonates were dissolved from the dolomite and limy dolomite samples by heating the ground samples in a 20-percent solution of acetic acid.

The X-ray fluorescence method consisted of using a Cr-target X-ray tube for primary radiation with a lithium fluoride analyzing crystal ($2d=4.0267$ Å) for iron and titanium elements and with a pentaerythritol analyzing crystal ($2d=8.78$ Å) for calcium, potassium, silicon, and aluminum elements. All elements are reported as oxides, and total iron oxide is reported as Fe_2O_3 . This method is not as accurate as the wet-chemical method, but it is found to be accurate within 10 percent of the amount of oxide present. Rose and others (1962, 1964) have described more complicated sample-preparation procedures that give more accurate results.

GEOLOGY

The clay deposits in the Gatesburg Formation were formed from and occur within the more or less homogeneous assemblage of Cambrian age silty dolomites. According to Butts and others (1939, p. 10), the Gatesburg Formation is about 1,750 feet thick and is composed predominantly of thick-bedded, coarsely crystalline, medium-gray dolomite with a small amount of thin-bedded, fine-grained, medium-gray

dolomite and a few beds of sandstone generally cemented with dolomite or calcite. The only exposure of unweathered Gatesburg is southeast of Tyrone on the Blair-Huntingdon County line (fig. 2), where Highway 350 along the Little Juniata River is cut through the dolomite half a mile southeast of Birmingham. Six samples of silty dolomite were taken at random from the exposures in this 1,200-foot roadcut. One sample contains a little calcite. The acid-insoluble residue from these rock samples averages approximately 25 percent of the whole rock and ranges from 9 to 40 percent. The grain size of the insoluble material is predominantly clay and silt with a trace of sand; however, half of the insoluble material from one sample is sand. The insoluble material is composed of illite, some chlorite, quartz, feldspar (chiefly microcline), and magnetite.

The outcrop pattern of the Gatesburg Formation (fig. 2) shows a series of fault contacts on the north and northwest sides, and several faults are known to cut the formation. Because exposures are extremely scarce and poor, many more faults and fractures may exist than are indicated on the map. The lack of bedding or sedimentary features in the clay is evident in the recently worked claypits, such as Oreminea 1, Oreminea 2, and Stormstown. Faults and fractures, along with the lack of bedding, may be a major factor in determining the origin of these clay deposits.

The clay deposits in the Gatesburg Formation are lens or oval shaped. The lens-shaped deposits are more than three times as long as they are wide and are probably the result of debris filling a series of coalescing sinkholes that formed along a fault or fracture. The largest lens-shaped deposit, at Stormstown, is 250 feet wide, about 2,000 feet long, and 63 feet deep. This deposit is probably several hundred feet longer, but it becomes narrower to the southwest where the clay has not been mined. The oval- or elliptical-shaped deposits are less than three times as long as they are wide. This type is probably the result of debris filling only one sinkhole. The largest elliptical-shaped deposit is Oreminea 1, which is 1,000 feet long, 500 feet wide, and about 100 feet deep. Oreminea 2 is also elliptical; it is 800 feet long, 300 feet wide, and 30 feet deep. The other clay deposits that could be measured are: Baileyville, 300 by 800 feet; Kelsey, 75 by 400 feet; Dungarvin, 600 by 1,200 feet; Shoenberger, 200 by 1,000 feet; Martinsburg, 200 by 500 feet; and Bakers Summit, about 200 by 200 feet.

In central Pennsylvania, part of the Oriskany Group of Devonian age weathers to a silty clay. The Oriskany Group is divided into an upper zone of thick-bedded coarse-grained sandstone (Ridgeley Sandstone) and a lower zone of cherty argillaceous limestone (Shriver Chert) (Butts and others, 1939, p. 59–62). Both zones are usually cemented by calcite which weathers readily. The clay deposits at Alexandria, Petersburg, and Shirleysburg (fig. 2) are residual material derived from the lower cherty and shaly limestone after the calcite cement has been removed.

MINERALOGY AND CHEMISTRY

At the Stormstown clay deposit, 11 samples were taken from a 63-foot auger hole, and 23 samples were taken at 10-foot intervals across the 250-foot exposed face of the claypit (fig. 3 and table 1). The grain-size composition of the 34 samples averaged 34 percent sand, 10 percent silt, and 56 percent clay, indicating that the average sample is sandy clay. The sand and silt fractions are composed of quartz, and the clay-size fraction is composed of only kaolinite. There is no evidence of any mineralogical or chemical changes with depth (table 1). The samples taken across the face of the pit vary noticeably in chemical composition. The amount of iron at the north and south edges of the pit increases very slightly. In the center, the sandy clay is predominantly white to yellowish white; where the iron content increases (table 1) the color is slightly pink or orange. A visit to the stockpiles near the deposit revealed that some of the clay already removed from the pit is pisolitic. The pisolites are composed of well-crystallized kaolinite and gibbsite. The centers of some pisolites contain poorly crystallized kaolinite with some anatase and rutile. Quartz is not present in the pisolitic or gibbsitic kaolinite clay, which was presumably taken from near the center of the deposit (fig. 3).

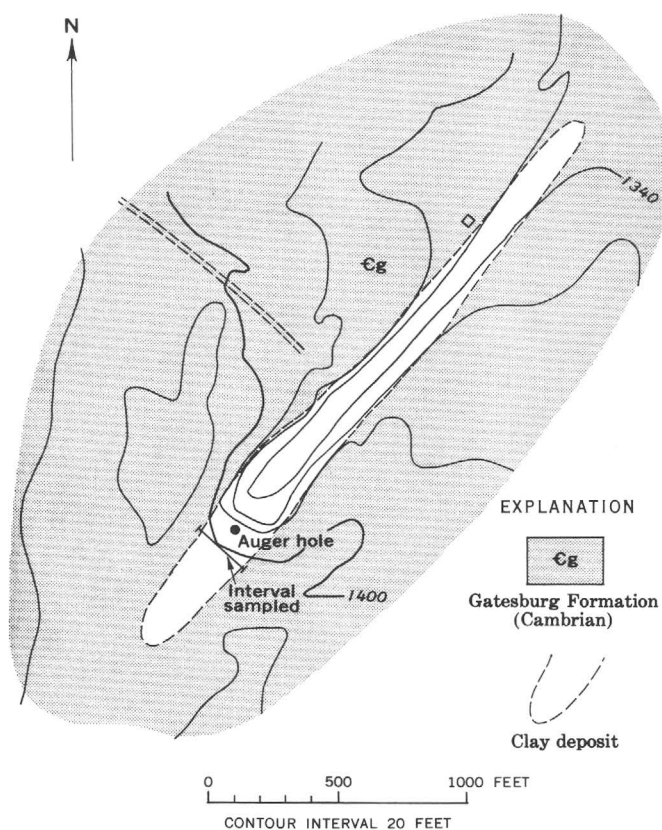


Figure 3.—Map showing outline of the Stormstown claypit and location of auger hole and sampled interval.

The clay at the Oreminea 1 pit has been mined out, and it was not possible to obtain a representative sample of the material produced here. However, Mr. Stevens, the owner of the property, indicated that high-grade white clay, probably mostly kaolinite, was mined here for more than 75 years. Five auger holes were drilled in the vicinity of the claypit (fig. 4 and table 1) in an attempt to find more good white clay. The average grain-size composition of the 38 samples taken from the five holes is 40 percent sand, 33 percent silt, and 27 percent clay, indicating that this material is a clayey silty sand which ranges from clayey sand to sand. There are a few samples of silty clay and clayey silt, but no high-grade clay was found. The sand and silt fractions are composed of quartz; the clay-size fraction is mostly kaolinite and some illite. All these samples are residual material left by the removal of dolomite which was leached during a prolonged and intense weathering period.

One auger hole was drilled at the Oreminea 2 claypit to a depth of 31 feet. The 10 samples taken from this hole (table 1 and fig. 4) have an average grain-size composition of 17 percent sand, 35 percent silt, and 48 percent clay, indicating that the average sample is a silty clay. The sand and silt fractions are composed of quartz, and the clay-size fraction is chiefly kaolinite with very little illite. There is no evidence of mineralogical or chemical changes with depth.

Samples taken from five of the smaller older claypits in the Gatesburg Formation were analyzed for mineralogical composition (table 2). In all samples, the sand and silt fractions are composed of quartz. The clay fraction of a yellowish-gray clayey sandy silt sample from the Baileyville pit contained kaolinite, illite, and montmorillonite in approximately equal amounts. The high amount of illite and montmorillonite makes material from this pit undesirable for refractory products. The Dungarvin claypit contains almost white clayey silt that is composed of kaolinite and a little illite in the clay fraction. A sample from the Pennington pit proved to be a true clay, containing more than 80 percent clay. The clay is very pale orange and is composed of kaolinite and a trace of illite. At the Shoenberger pit, the exposed material is yellowish-gray silty clay composed chiefly of kaolinite and some illite. The pit near Martinsburg contains almost white silty clay composed of about 90 percent kaolinite and 10 percent illite in the clay fraction.

Samples from two pits in the Oriskany Group were analyzed for their mineralogical composition (table 2). A representative sample from the Alexandria pit is a white clayey silt composed of quartz, illite, and kaolinite. At the Shirleysburg pit, the material is a light-gray silty clay composed of quartz, with kaolinite and illite present in equal amounts in the clay-size fraction. Near Frankstown, Blair County, at the General Refractories Co. sand quarry in the Oriskany Group, a 12-inch bed of weak-red (5R 5/2) silty clay is exposed. This clay is composed of quartz, with equal amounts of kaolinite and illite in the clay fraction.

ORIGIN

The clay deposits in the Gatesburg Formation can be interpreted as a product of debris deposited in caverns and sinkholes as a result of leaching. This is similar to the theory proposed by Knechtel (1963) and Dunlap and others (1965, p. L9) for the origin of many bauxite deposits in the southeastern Appalachian region. During a prolonged period of weathering, a residuum of variable depth formed on the dolomite of the Gatesburg Formation. During this same period, faults, fractures, and bedding planes of steeply dipping dolomite beds influenced the course of circulating ground water. The ground water dissolved the carbonate and produced caverns in the dolomite. Subcircular sinkholes formed in the roof of these caverns. Material from the overlying residuum was washed through the sinkholes and into the caverns. Some of these sinkholes and caverns became so jammed with debris, composed largely of clay, that the downward flow of water was restricted, and stagnant ponds formed in the sinkhole depressions at the surface. The clayey material became leached of potassium, iron, and some silicon when water saturated with carbon dioxide (carbonic acid) and humic acid derived from organic matter in the pond slowly percolated downward through the clayey material.

Leaching of the clay continued until little or no carbonate was left. Illite, chlorite, and feldspar altered to kaolinite when soluble alkalis were removed. An increase in the iron content, as indicated by the red, brown, and yellow colors staining some areas adjacent to the clay deposits, appears to have resulted from an outward migration of iron. (Knechtel (1963, p. C153) suggested that such migration may be the result of organic matter reacting with magnetite to reduce iron from ferric to the more soluble ferrous state. The iron is deposited as an oxide or hydroxide when the solutions come in contact with the remaining carbonates outside the clay deposit. This may account for the many secondary iron ore deposits worked during the 19th century and for the large iron ore deposit worked at Scotia, Centre County, by the Carnegie Bros. in the early 1900's.) The quartz remained unaltered in the clay deposit, but the soluble silica, derived from the breakdown of feldspar to form kaolinite and the breakdown of kaolinite to form gibbsite in one deposit, migrated outward to form some of the chert nodules outside the clay deposit.

It is difficult to determine how much the present surface has been lowered, but if 1 foot of clayey silt sand and chert residuum represents about 4 feet of silty dolomite, the topographic lowering may have been considerable. This topographic lowering or collapse may also account for the lack of bedding or other sedimentary features in the residuum surrounding the clay deposits.

Most of the clay deposits occur along the flanks of hills or knolls of more resistant sandy material. The presence of a deposit is commonly indicated by a small depression in the land surface. No bedding or sedimentary features have been observed in any of the pits. The sand-silt-clay ratios (tables 1

and 2) show that the material within the Stormstown and Oreminea 2 clay deposits is finer grained than the material surrounding the deposits (Oreminea 1 auger holes 1-5, table 1).

The origin of the clay deposits in the Oriskany Group of central Pennsylvania is similar to that of the clay deposits near Kunkletown and Saylorsburg, Monroe County (Epstein and Hosterman, 1969, p. D99). These deposits are the product of katamorphic alteration of cherty limy shales. This alteration is the result of intense leaching of downward-percolating ground water through the calcareous sandstone, leaving white clayey silt composed of kaolinite, illite, and quartz as residual debris.

The geologic age of formation of the deposits is problematical. The interpretation by Pierce (1965) indicated that the Great Valley and Valley and Ridge provinces of Pennsylvania have been exposed to subaerial erosion and weathering since Cretaceous time. Griffiths and others (1965) postulated that the most probable date for the beginning of the formation of the clay deposits was the Cretaceous, during which central Pennsylvania was undergoing a period of tropical weathering. This conclusion is supported by the vast accumulation of Cretaceous sediments of the Coastal Plain that were derived from areas to the west and north. However, the major period of weathering, which produced a thick residuum, was probably in Tertiary time. This hypothesis is supported by the residual clay deposits in the Southeastern States (Overstreet, 1964, p. A12), by the residuum in the Shenandoah Valley of Virginia and West Virginia (Hack, 1965, p. 66), by residual kaolinite in Massachusetts (Kaye, 1967, p. C172), and by the residual clay deposits in the Northwestern States (Hosterman and others, 1960, p. 4; Hosterman, 1969b, p. 8). The above evidence of a wide areal distribution of a major weathering period during Tertiary time is strong evidence that it was also a major weathering period in Pennsylvania. In addition, the author thinks that during this major period of weathering the climate was temperate rather than tropical because of the type of vegetation growing during Tertiary time in the Northwestern States (Hosterman, 1969b, p. 8) and because carbonate rocks are more soluble in cold solutions than in warm solutions (Hack, 1965, p. 66).

REFERENCES

- Butts, Charles, 1945, Description of the Hollidaysburg-Huntingdon quadrangles [Pennsylvania]: U.S. Geol. Survey Geol. Atlas Folio 227, 20 p.
- Butts, Charles, Swartz, F. M., and Willard, Bradford, 1939, Tyrone quadrangle [Pennsylvania]: Pennsylvania Geol. Survey, 4th ser., Topog. and Geol. Atlas 96, 118 p. 16 pls., 3 figs.
- Dunlap, J. C., Bergquist, H. R., Craig, L. C., and Overstreet, E. F., 1965, Bauxite deposits of Tennessee: U.S. Geol. Survey Bull. 1199-L, 37 p.
- Epstein, J. B., and Hosterman, J. W., 1969, Residual clay deposits in rocks of Early and Middle Devonian age near Kunkletown, Pennsylvania, in *Geological Survey Research 1969*: U.S. Geol. Survey Prof. Paper 650-D, p. D94-D105.

Table 1.—Chemical and mineralogical composition of material from the Gatesburg Formation at the Stormstown claypit, Centre County, and Oreminea claypits, Blair County, Pa.

[Analysis by X-ray fluorescence methods; results in weight percent except as indicated]

Description ¹	Location or depth (feet)	Moisture content	SiO ₂	Al ₂ O ₃	Fe ₂ O ₃	CaO	K ₂ O	TiO ₂	Loss on ignition (1,000°C)	Sum	Grain-size distribution			Clay minerals (peak-area ratio)	
											Sand	Silt	Clay	Kaolinite	Illite
Stormstown claypit															
Auger hole:															
Sandy clay, yellowish-white (10YR 9/1)	12	8.3	71	22	0.1	0.2	0.1	1.2	5.0	99.6	38	6	56	10	0
Clay, yellowish-gray (10YR 8/1)	15	10.6	57	30	.2	.3	.3	1.7	11.0	100.5	7	18	75	10	0
Sandy clay, light-gray (N8)	20	9.6	61	28	.4	.2	.3	1.8	7.3	99.0	18	12	70	10	0
Sandy clay, yellowish-white (10YR 9/1)	25	10.6	63	26	.2	.0	.1	1.0	9.5	99.8	26	9	65	10	0
Do.	35	8.6	68	24	.1	.3	.1	1.1	5.7	99.3	33	7	60	10	0
Do.	40	10.3	74	19	.2	.2	.1	1.0	5.2	99.7	43	9	48	10	0
Do.	47	9.9	70	22	.2	.2	.1	1.0	5.8	99.3	36	9	55	10	0
Sandy clay, very pale orange (10YR 8/2)	54	15.4	68	23	.1	.3	.5	1.3	7.2	100.4	33	9	58	10	0
Sandy clay, very pale orange (10YR 9/2)	58	13.4	74	19	.5	.2	.1	1.1	5.0	99.9	43	9	48	10	0
Sandy clay, yellowish-white (10YR 9/1)	60	11.4	71	21	.1	.2	.1	1.1	5.8	99.3	41	6	53	10	0
Sandy clay, yellowish-gray (10YR 8/1)	63	9.6	65	26	.2	.0	.6	1.2	6.3	99.4	30	4	66	10	0
Claypit face:															
Silty clay, moderate orange-pink (10R 8/3)		17.0	61	27	.77	.9	9.1	99.4	12	20	68	10	0
Sandy clay, very pale orange (10YR 9/2)		11.0	67	25	.65	1.0	5.9	100.0	28	9	63	10	0
Sandy clay, pale-yellow (2.5Y 9/2)		12.0	72	19	.38	1.0	6.0	99.1	43	10	47	10	0
Clayey sand, white (N9)		9.0	77	17	.25	.8	4.3	99.8	49	8	43	10	0
Do.		9.0	75	18	.26	.7	4.8	99.3	48	8	44	10	0
Clayey sand, pale-yellow (2.5Y 9/2)		9.0	75	18	.37	.7	5.1	99.8	49	6	45	10	0
Sandy clay, white (N9)		8.0	67	24	.36	1.0	6.9	99.8	29	10	61	10	0
Do.		11.0	68	24	.34	.9	6.6	99.2	29	11	60	10	0
Clayey sand, white (N9)		9.0	76	17	.24	.8	4.4	98.8	45	12	43	10	0
Sandy clay, white (N9)		12.0	65	25	.24	1.0	7.5	99.1	25	12	63	10	0
Clay, white (N9)		18.0	50	37	.42	1.2	11.1	99.9	6	4	90	10	0
Sandy clay, white (N9)		14.0	64	26	.24	1.0	8.1	99.7	24	10	66	10	0
Do.		12.0	69	22	.38	1.0	6.6	99.7	33	12	55	10	0
Do.		12.0	68	23	.38	.7	6.7	99.5	34	8	58	10	0
Do.		10.0	67	23	.24	.7	6.1	97.4	34	8	58	10	0
Do.		13.0	66	24	.34	.7	7.3	98.7	30	10	60	10	0
Clayey sand, pale-yellow (2.5Y 9/2)		8.0	67	24	.54	.7	6.2	99.8	32	8	60	10	0
Sand, pale-yellowish-orange (2.5Y 9/4)		9.0	90	7	.35	.2	1.9	99.9	76	6	18	10	0
Sandy clay, white (N9)		9.0	71	22	.24	.4	5.4	99.4	39	6	55	10	0
Do.		9.0	68	23	.13	.5	7.3	99.2	36	6	58	10	0
Do.		10.0	68	24	.13	.6	6.4	99.4	34	6	60	10	0
Sandy clay, weak-yellowish-orange (10YR 8/3)		12.0	65	25	.63	.5	7.2	98.6	30	7	63	10	0
Do.		11.0	69	25	.62	.5	4.6	99.9	33	7	60	10	0
Oreminea 1 claypit															
Auger hole 1:															
Silty clay, yellowish-gray (10YR 7/1)	3	19.2	63	23	0.7	0.3	0.4	1.7	10.3	99.4	9	33	58	9.5	0.5
Silty sand, weak-yellowish-orange (10YR 8/4)	12	12.1	80	14	.7	.2	.5	.5	3.0	98.9	59	22	19	9	1
Clayey silty sand, very pale orange (10YR 8/2)	15	16.6	74	18	.5	.2	.6	.8	5.2	99.3	35	35	30	9	1
Clayey silty sand, very pale orange (10YR 8/3)	19	11.5	79	14	.8	.9	.5	.5	3.3	99.0	50	25	25	9	1
Silty sand, very pale orange (10YR 9/2)	25	11.2	85	10	.7	.3	.4	.2	2.1	98.7	66	19	15	9	1
Sandy silt, yellowish-gray (10YR 8/1)	29	13.8	89	6.9	.2	.3	.6	.2	1.8	99.0	43	45	12	8.5	1.5
Clayey silty sand, very pale orange (10YR 8/3)	39	10.7	82	12	1.1	.2	.7	.6	2.4	99.0	55	24	21	8.5	1.5
Sand, very pale brown (10YR 7/3)	48	13.1	82	11	1.9	.1	1.0	.4	2.0	98.4	75	10	15	8	2

Table 1.—Chemical and mineralogical composition of material from the Gatesburg Formation at the Stormstown claypit, Centre County, and Oreminea claypits, Blair County, Pa.—Continued

[Analysis by X-ray fluorescence methods; results in weight percent except as indicated]

Description ¹	Location or depth (feet)	Moisture content	SiO ₂	Al ₂ O ₃	Fe ₂ O ₃	CaO	K ₂ O	TiO ₂	Loss on ignition (1,000°C)	Sum	Grain-size distribution			Clay minerals (peak-area ratio)	
											Sand	Silt	Clay	Kaolinite	Illite
Oreminea 1 claypit—Continued															
Auger hole 2:															
Clayey sandy silt, light-gray (N8)	5	12.8	77	16	0.2	0.3	0.3	0.7	5.0	99.5	28	37	35	9.5	0.5
Silty sand, light-gray (N8)	10	4.3	91	5.9	.1	.2	.2	.2	1.2	98.8	60	32	8	9.5	.5
Clayey sandy silt, light-gray (N8)	15	13.2	72	20	.1	.3	.4	.9	5.1	98.8	25	41	34	9.5	.5
Clayey silty sand, light-gray (N8)	20	11.0	82	13	.1	.3	.3	.5	3.1	99.3	49	30	21	9	1
Silty sand, yellowish-gray (10YR 8/1)	23	5.0	90	6.6	.2	.3	.3	.2	.8	98.4	74	16	10	9	1
Silty sand, light-gray (N8)	30	4.4	91	5.6	.2	.3	.3	.2	1.1	98.7	70	16	14	8.5	1.5
Clayey silty sand, very pale brown (10YR 7/3)	32	10.0	83	11	1.0	.2	.8	.3	2.4	98.7	54	21	25	8.5	1.5
Sandy silty clay, yellowish-gray (10YR 7/1)	40	15.2	71	19	.6	.3	1.5	.7	5.9	99.0	22	39	39	8	2
Clayey sand, yellowish-gray (10YR 8/1)	44	5.6	88	8.0	.4	.3	.4	.2	1.5	98.8	74	11	15	9	1
Auger hole 3:															
Clayey sandy silt, yellowish-gray (10YR 8/1)	5	13.9	80	14	.4	.2	.4	.6	4.1	99.7	32	42	26	9.5	.5
Clayey silt, yellowish-gray (10YR 8/1)	10	15.5	74	18	.2	.2	.5	1.0	5.5	99.4	11	57	32	9.5	.5
Clayey silt, light-gray (N8)	15	19.1	72.3	17.7	.25	.23	.70	.81	6.1	98.09	11	52	37	9.5	.5
Silty sandy clay, yellowish-gray (10YR 8/1)	18	19.2	82	12	.3	.2	.4	.5	3.8	99.2	27	36	37	9.5	.5
Clayey sandy silt, light-gray (N8)	20	15.2	83	11	.1	.3	.4	.4	4.4	99.6	25	48	27	9.5	.5
Clayey silty sand, light-gray (N8)	25	14.9	82	13	.1	.3	1.0	.4	2.9	99.7	40	33	27	8.5	1.5
Clayey sandy silt, light-gray (N8)	30	17.4	74	18	.2	.2	1.3	.7	4.7	99.1	30	36	34	8.5	1.5
Clayey sand, pale-yellow (2.5Y 9/2)	42	10.8	90	7.3	.2	.2	.6	.2	1.4	99.9	73	13	14	8.5	1.5
Auger hole 4:															
Silty clay, weak yellow (2.5Y 8/2)	3	15.7	70	20	.4	.1	.7	1.1	7.8	99.9	13	42	45	9.5	.5
Clayey silt, yellowish-gray (10YR 8/1)	8	16.2	72.4	19.4	.11	.40	.50	.96	8.0	101.77	20	42	38	9.5	.5
Do.	13	18.0	70	19	.2	.2	.7	1.1	8.1	99.3	6	57	37	9.5	.5
Silty clay, weak-yellow (2.5Y 8/2)	18	18.6	63	25	.3	.4	.6	1.3	8.8	99.4	10	37	53	9.5	.5
Clayey sandy silt, weak-yellow (2.5Y 8/2)	21	14.9	75	17	.4	.3	.5	.8	5.4	99.4	26	39	35	9.5	.5
Clayey silt, yellowish-gray (10YR 8/1)	24	17.8	70	20	.3	.3	.8	1.0	7.8	100.2	17	50	33	9.5	.5
Clayey sandy silt, weak-yellowish-orange (10YR 7/4)	26	14.8	69	18	3.2	.2	.6	.9	7.8	99.7	31	39	30	9.5	.5
Clayey silty sand, weak-orange (7.5YR 7/4)	27	8.9	79	15	.7	.3	.3	.6	3.4	99.3	54	22	24	9.5	.5
Silty sand, pale-orange (7.5YR 8/4)	31	10.2	80	14	.5	.4	.3	.5	3.7	99.4	52	33	15	9.5	.5
Auger hole 5:															
Silty sandy clay, very pale orange (10YR 8/2)	7	12.0	79	14	.4	.4	1.5	.6	4.0	99.9	34	27	39	7	3
Clayey silty sand, yellowish-gray (10YR 8/1)	17	11.1	80	14	.4	.2	.7	.4	3.3	99.0	48	30	22	8.5	1.5
Silty sand, weak-yellow (2.5Y 8/2)	27	11.5	85	10	.6	.2	.6	.4	2.9	99.9	51	33	16	7.5	2.5
Silty sand, yellowish-gray (10YR 7/1)	33	8.6	85	11	.7	.4	.6	.3	1.7	99.7	58	22	20	7.5	2.5
Oreminea 2 claypit															
Auger hole:															
Silty clay, light-gray (N8)	6	11.5	65.1	24.1	0.11	0.0	0.25	1.5	8.9	99.96	4	35	61	10	0
Silty sand, white (N9)	7	1.8	82	14	.2	.2	.2	.4	3.0	100.0	73	8	19	9.5	.5
Silty clay, weak-yellow (2.5Y 7/2)	13	17.9	65	22	.7	.2	.6	1.2	9.6	99.3	5	37	58	9.5	.5
Silty clay, yellowish-gray (10YR 8/1)	17	13.7	67	23	.3	.2	.6	1.2	7.0	99.3	14	35	51	9.5	.5
Do.	20	14.2	66	23	.4	.2	.6	1.2	7.8	99.2	6	46	48	9.5	.5
Do.	22	13.6	67	23	.3	.4	.5	1.3	7.6	100.1	5	45	50	9.5	.5
Clayey silt, yellowish-gray (10YR 8/1)	24	14.8	73.3	16.3	.25	.80	.50	1.2	7.4	99.75	6	53	41	9.5	.5
Silty clay, yellowish-gray (10YR 8/1)	26	14.6	65	24	.3	.3	.6	1.4	7.3	98.9	4	41	55	9.5	.5
Do.	29	15.6	66	23	.2	.1	.6	1.3	7.6	98.8	15	33	52	9.5	.5
Sandy clay, light-gray (N8)	31	13.7	69	22	.1	.1	.5	1.1	6.3	99.1	37	18	45	9.5	.5

HOSTERMAN

B63

¹Color designations from Munsell Color Co. (1954).

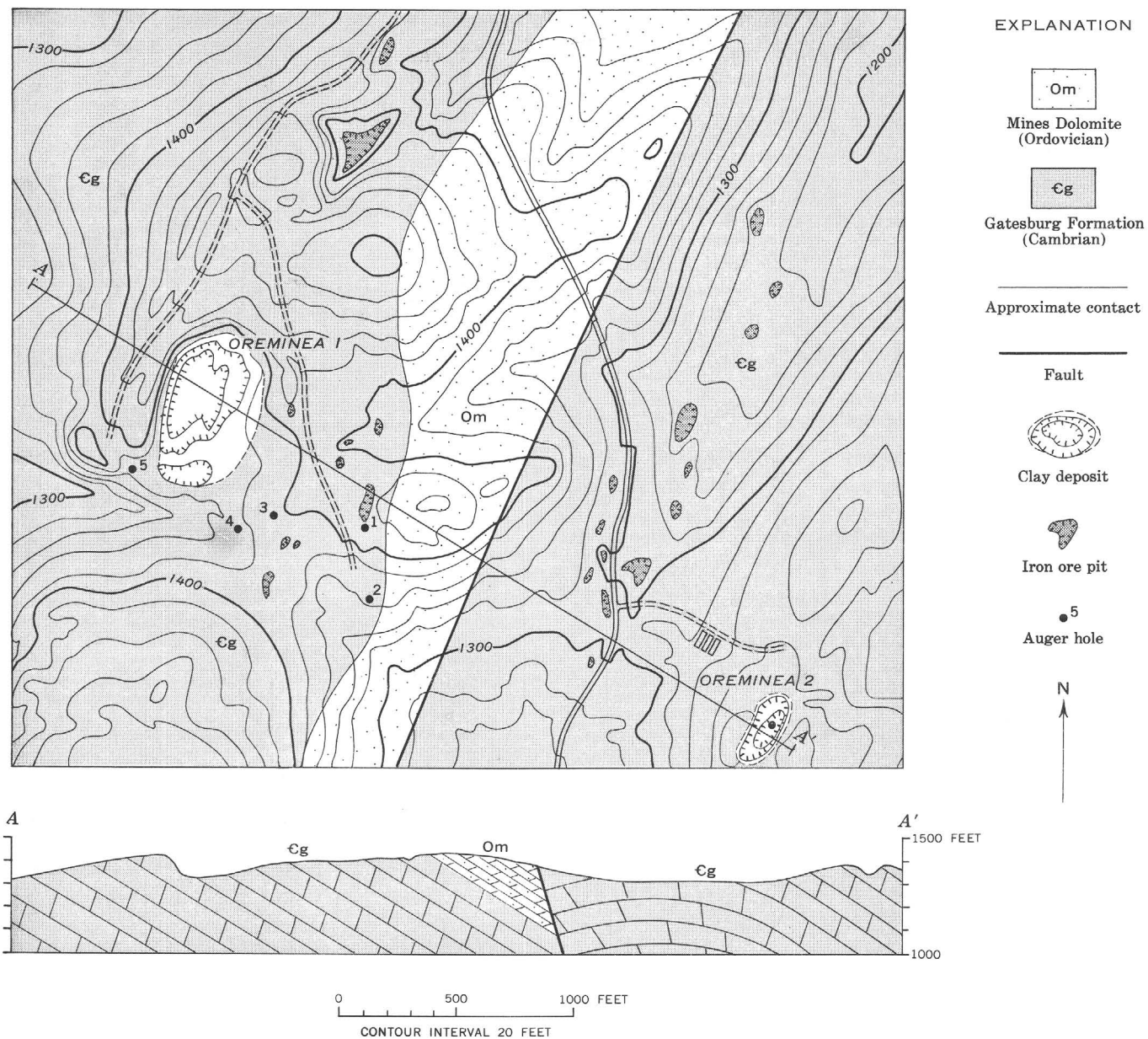


Figure 4.—Map showing the location of auger holes near Oremines 1 and Oremines 2 claypits. Geology modified from Butts (1945).

Table 2.—Mineralogical composition of clay from five small claypits in the Gatesburg Formation and two small pits and one sample in the Oriskany Group

Claypit	Description ¹	Grain-size distribution (weight percent)			Clay minerals (peak-area ratio)		
		Sand	Silt	Clay	Kaolinite	Illite	Montmorillonite
Baileyville	Clayey sandy silt (10YR 8/1)	27	37	36	4	2	4
Dungarvin	Clayey silt (N9)	17	48	35	9	1	...
Pennington	Clay (10YR 8/3)	4	15	81	9.5	.5	...
Shoenberger	Silty clay (10YR 8/1)	3	46	51	9	1	...
Martinsburg	Silty clay (N9)	5	42	53	9	1	...
Alexandria	Clayey silt (N9)	11	49	40	2	8	...
Shirleysburg	Silty clay (N7)	Trace	35	65	5	5	...
Frankstown	Silty clay (5R 5/2)	14	42	44	5	5	...

¹ Color designations from Munsell Color Co. (1954).

- Gray, Carlyle, and others, 1960, Geologic map of Pennsylvania: Harrisburg, Pennsylvania Geol. Survey, 4th ser., scale 1:250,000.
- Griffiths, J. C., Bates, T. F., and Sadle, H. W., 1956, Guide to field trip of Fourth National Clay Conference—Clay minerals in sedimentary rocks, in Swineford, Ada, ed., Clays and clay minerals—Proceedings of the 4th National Conference * * * University Park, Pennsylvania, Oct. 10–13, 1955: Natl. Research Council Pub. 456, p. 1–20.
- Hack, J. T., 1965, Geomorphology of the Shenandoah Valley, Virginia and West Virginia, and origin of the residual ore deposits: U.S. Geol. Survey Prof. Paper 484, 84 p.
- Hosterman, J. W., 1968, Use of the diffracted-beam monochromator in X-ray diffraction of clay minerals, in Geological Survey Research 1968: U.S. Geol. Survey Prof. Paper 600-B, p. B117–B118.
- 1969a, White clay deposits near Mount Holly Springs, Cumberland County, Pennsylvania, in Geological Survey Research 1969: U.S. Geol. Survey Prof. Paper 650-B, p. B66–B72.
- 1969b, Clay deposits of Spokane County, Washington: U.S. Geol. Survey Bull. 1270, 96 p.
- Hosterman, J. W., and others, 1960, Investigations of some clay deposits in Washington and Idaho: U.S. Geol. Survey Bull. 1091, 147 p.
- Kaye, C. A., 1967, Kaolinization of bedrock of the Boston, Massachusetts, area, in Geological Survey Research 1967: U.S. Geol. Survey Prof. Paper 575-C, p. C165–C172.
- Knechtel, M. M., 1963, Bauxitization of terra rossa in the southern Appalachian region: Art. 99 in U.S. Geol. Survey Prof. Paper 475-C, p. C151–C155.
- Moore, E. S., 1922, White clay deposits in central Pennsylvania: Pennsylvania Bur. Topog. and Geol. Survey Bull. 45, 7 p.
- Munsell Color Co., Inc., 1929–1960, Munsell book of color: Baltimore, Md.
- Overstreet, E. F., 1964, Geology of the southeastern bauxite deposits: U.S. Geol. Survey Bull. 1199-A, p. A1–A19.
- Pierce, K. L., 1965, Geomorphic significance of a Cretaceous deposit in the Great Valley of southern Pennsylvania, in Geological Survey Research 1965: U.S. Geol. Survey Prof. Paper 525-C, p. C152–C156.
- Rose, H. J., Jr., Adler, Isidore, and Flanagan, F. J., 1962, Use of La_2O_3 as a heavy absorber in the X-ray fluorescence analysis of silicate rocks: Art. 31 in U.S. Geol. Survey Prof. Paper 450-B, p. B80–B82.
- Rose, H. J., Jr., Cuttitta, Frank, Carron, M. K., and Brown, Robena, 1964, Semimicro X-ray fluorescence analysis of tektites using 50-miligram samples: Art. 157 in U.S. Geol. Survey Prof. Paper 475-D, p. D171–D173.



RECONNAISSANCE GEOLOGY AND MINERAL POTENTIAL OF THOMAS, KEG, AND DESERT CALDERAS, CENTRAL JUAB COUNTY, UTAH

By DANIEL R. SHAWE, Denver, Colo.

Abstract.—Three recently recognized calderas in the Thomas Range, Keg Mountains, and Desert Mountain, central Juab County, Utah, offer exploration possibilities for undiscovered ore deposits. Three major episodes of volcanic activity in the region were (1) early(?) Tertiary eruption of intermediate-composition lavas and agglomerates; (2) middle Tertiary eruption of silicic ash-flow tuffs resulting in collapse of the three calderas; and (3) late Tertiary-Quaternary(?) eruption of basalt and alkali rhyolite. After caldera collapse, magmas invaded parts of the ring-fracture zones or resurgently domed the calderas. Mineralization that formed ore deposits peripheral to the Thomas caldera probably was nearly concurrent with eruption of the late alkali rhyolite. The ore deposits have yielded important amounts of manganese, fluor spar, uranium, and beryllium. Prospecting for deposits of these commodities is warranted where parts of the Thomas caldera rim, as well as of the Keg and Desert caldera rims, are covered by postmineralization surficial deposits. Deep exploration for base and precious metals may be justified beneath the manganese and fluor spar deposits.

Three calderas in the Thomas Range, Keg Mountains¹, and Desert Mountain, central Juab County, Utah, form the source areas for several ash-flow tuff sheets in the region. Ore deposits peripheral to the westernmost Thomas caldera have produced important amounts of fluor spar, uranium, beryllium, and manganese. This paper briefly describes the three calderas and their associated volcanic and intrusive rocks, and suggests a structural relation of the known ore deposits to the periphery of the Thomas caldera. Future prospecting seems warranted where parts of the Thomas, Keg, and Desert caldera rims are covered by postmineralization surficial deposits.

Volcanic rocks in the region were mapped in reconnaissance during a total of about 3 months in the summers of 1963, 1964, and 1966. Stanley Bernold assisted me for about a month in 1963. The volcanic stratigraphy established in the Thomas Range by Staatz and Carr (1964) was extended and volcanic structures mapped to evaluate the potential of the area for beryllium deposits of the type found at Spor

Mountain at the southwest edge of the Thomas Range (see Staatz and Griffiths, 1961; Williams, 1963; Staatz, 1963; Shawe, 1968). A simplified geologic map of the north end of the Drum Mountains, the Thomas Range, the Keg Mountains, and Desert Mountain is given in figure 1.

GEOLOGIC SETTING

The Thomas, Keg, and Desert calderas, named here for the mountains with which they are associated, lie in the eastern part of the Basin and Range structural province. During Precambrian and most of Paleozoic time widespread layers of marine sedimentary rocks—now quartzites, shales, and carbonates—were deposited in the Cordilleran geosyncline that then encompassed the eastern part of the Basin and Range province. Mesozoic marine and continental sedimentary rocks, probably once extensive in this part of Utah, were mostly destroyed during erosion cycles accompanying the Cretaceous Sevier orogeny and late Tertiary development of the Great Basin mountain ranges. The Sevier orogeny (Armstrong, 1968) was characterized by folding and eastward overthrusting in a broad belt extending north-northeastward through eastern Nevada and western Utah.

Tertiary volcanic activity was prevalent in the region during three major episodes: (1) intermediate-composition lavas and agglomerates were erupted widely during an early period, (2) silicic ash-flow tuffs were emplaced, the three calderas described here collapsed, and resurgent magmas invaded parts of the caldera ring-fracture zones or domed the caldera cores, all during a middle period, and (3) a late bimodal association of basalt and alkali rhyolite was erupted during the final episode. The ore deposits peripheral to the Thomas caldera probably formed about concurrently with eruption of the late alkali rhyolite (for example, Staatz and Griffiths, 1961, p. 948–949).

Basin-range block faulting formed the present mountain ranges and intervening alluviated basins in middle to late Tertiary time.

¹The name "Keg Mountains" is a commonly used local term and is shown on earlier U.S. Geological Survey topographic maps, although recent Survey topographic maps use the name "McDowell Mountains."

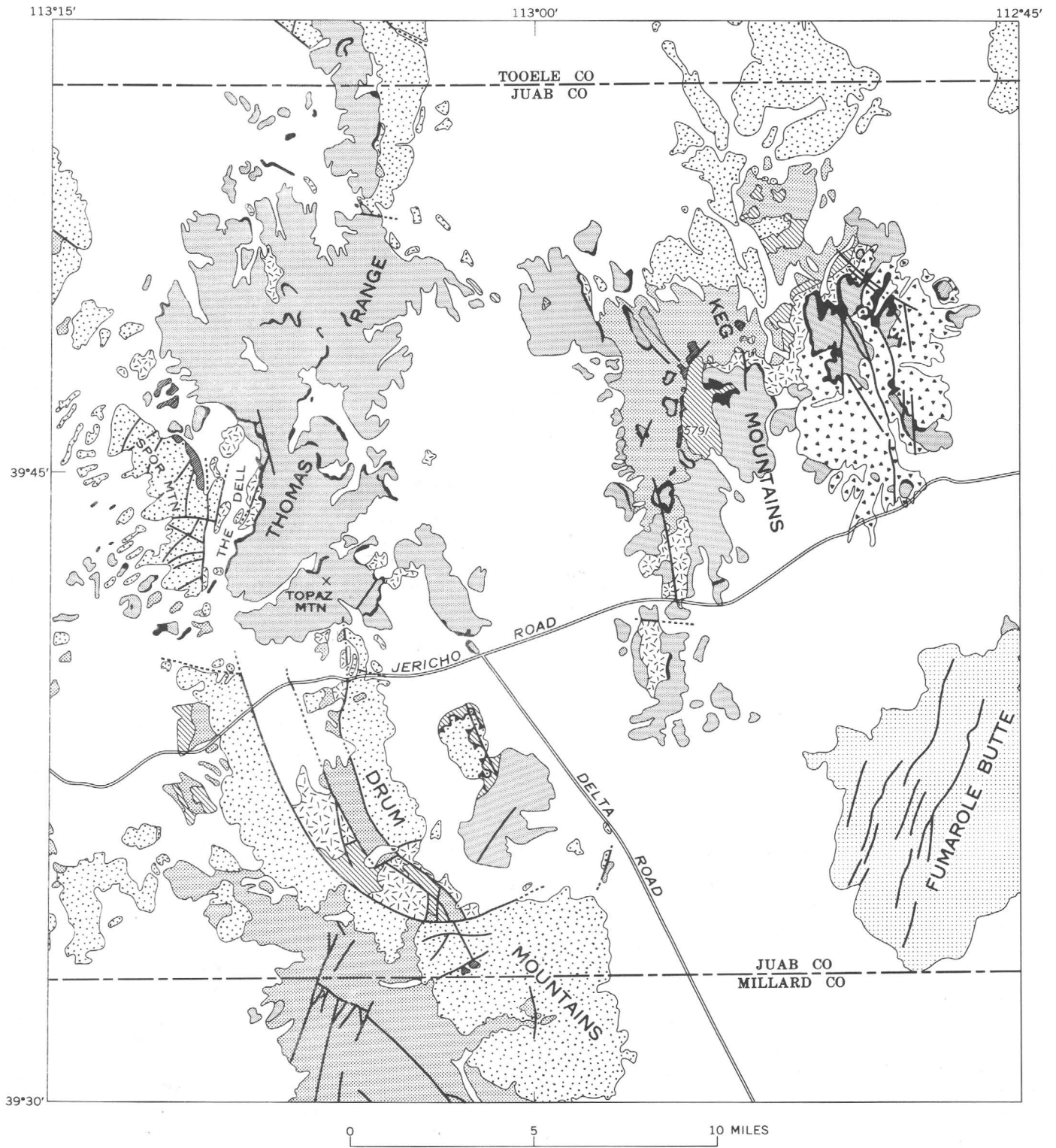


Figure 1.

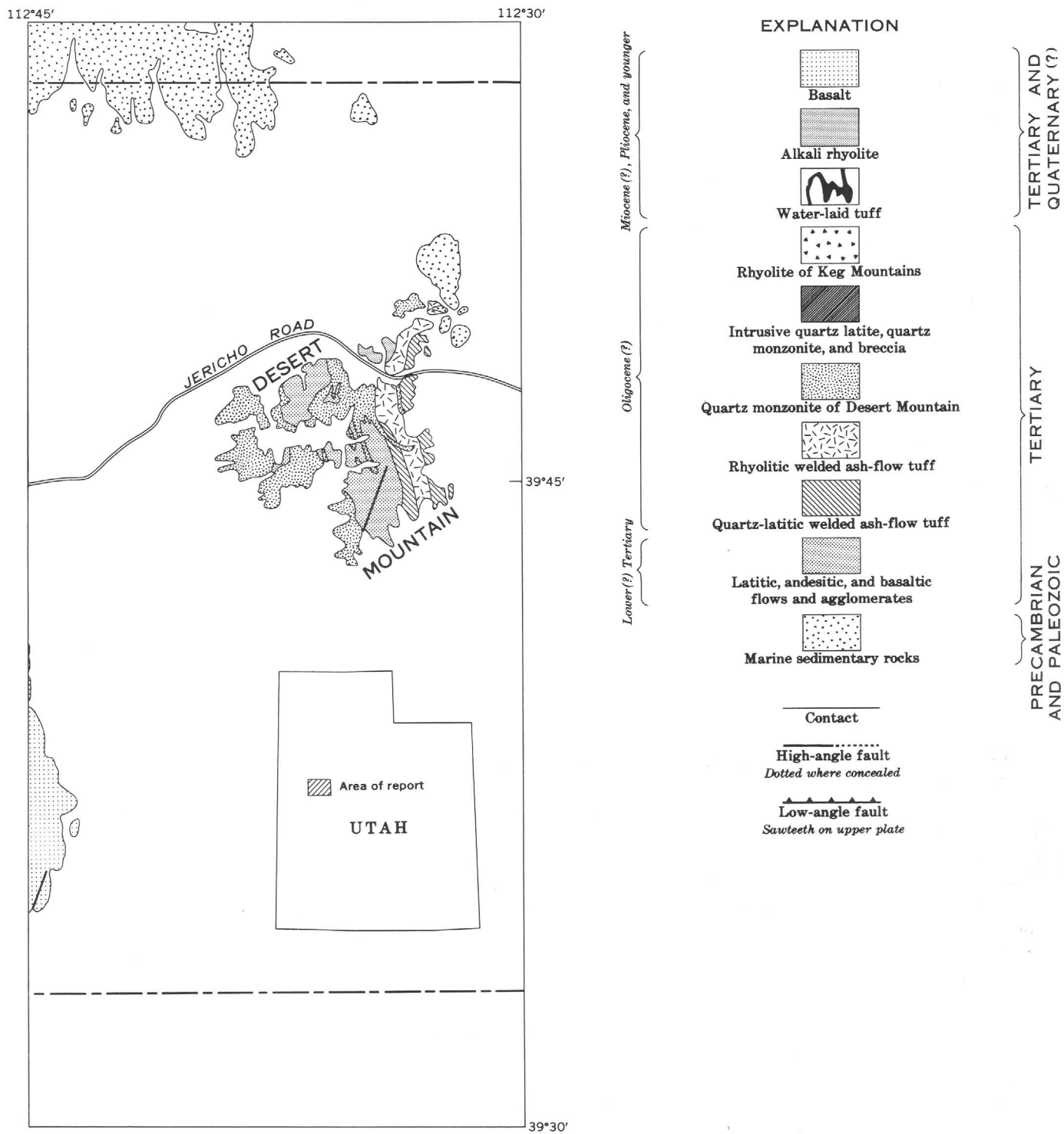


Figure 1.—Simplified geologic map of parts of the Thomas Range and Drum Mountains and of the Keg Mountains and Desert Mountain, Tooele, Juab, and Millard Counties, Utah.

AGES OF THE IGNEOUS ROCKS

Ages of the volcanic and intrusive rocks representing the three major episodes of Tertiary igneous activity in the region are imperfectly known. No ages have been determined on rocks of the oldest period of volcanic activity; by analogy with other regions of similar volcanic history in the Western United States these rocks are likely early to middle Tertiary in age. Quartz monzonite of Desert Mountain, representing resurgent magma intruded late during the middle period of activity, was dated by Armstrong (1970, table 3, p. 216–217) at 28.5 ± 0.6 m.y. (biotite) and 26.5 ± 0.5 m.y. (orthoclase), using the K-Ar method. Other ages, based on the less reliable lead-alpha method, are 36 and 41 m.y. respectively, for “leucogranite” and “hornblende-biotite granite” (inclusion in leucogranite) of Desert Mountain (Odekirk, 1970), and 20 m.y. for rhyolite welded ash-flow tuff of the middle episode of volcanism in the Thomas Range (Staatz and Carr, 1964, p. 116; Jaffe and others, 1959, p. 71). A rhyolite flow of the youngest episode at Topaz Mountain in the Thomas Range was reported by Park (1970) to be 16.2 ± 1.5 m.y., using the K-Ar method on sanidine. However, similar rhyolites from Topaz Mountain and from Smelter Knoll southeast of the Thomas Range (south of the area shown in figure 1) have been dated by Armstrong (1970, table 3, p. 210–211) at 6.0 ± 0.2 and 3.4 ± 0.2 m.y., respectively, by means of the K-Ar method on sanidine.

Older assemblage of rocks

Rocks representing the oldest period of volcanic activity in the region are mostly dark latite, dark rhyodacite, andesite, and andesitic basalt flows and agglomerates. Some intermediate-composition volcanoclastic beds and more silicic tuff layers are interbedded in the flows and agglomerates. Two major episodes of volcanism may be represented by the rocks of the oldest period, inasmuch as some of the oldest rocks are moderately deformed and widely propylitized or more intensely altered, whereas overlying units are only gently tilted and are relatively unaltered.

Dull olive drab to gray andesite and latite flows called the Keg Spring Andesite by Erickson (1963, p. 26) are common among the somewhat altered and deformed older rocks in the Keg Mountains. The andesites contain conspicuous biotite and plagioclase phenocrysts 1–3 mm across, as well as minor augite, hornblende, and sparse quartz phenocrysts, set in an aphanitic groundmass. The lighter colored latites contain abundant plagioclase and sanidine phenocrysts 2–3 mm long, with local biotite and generally sparse quartz phenocrysts. Altered older andesites in the Drum Mountains contain cloudy plagioclase and chlorite- and calcite-rich remnants of augite and hypersthene in a dense propylitized groundmass.

Younger, generally unaltered rocks of the oldest volcanic period are largely flows and agglomerates of pyroxene-rich andesite and andesitic basalt flows containing abundant small phenocrysts of plagioclase, augite, hypersthene, and black

opaque mineral, in a felted groundmass. Locally some of these rocks contain larger but less common phenocrysts of green hornblende, oxyhornblende, and olivine. Some more felsic rocks in the Thomas Range contain similar phenocrysts except for additional sanidine, and have quartz and feldspar in the groundmass (Staatz and Carr, 1964, p. 75–77). The younger dark rocks are altered hydrothermally in local areas adjacent to the ring-fracture zone of the Thomas caldera.

Small andesite and latite intrusive bodies locally cut all units of the oldest volcanic rocks. These rocks have phenocrysts of plagioclase, augite, hypersthene, oxyhornblende, and corroded biotite in a fine-grained feltlike groundmass. In places minor corroded quartz and potassium-feldspar phenocrysts are present. Locally these rocks also are hydrothermally altered.

Middle assemblage of rocks

Rocks representing the middle period of volcanic activity in central Juab County are mostly dacitic, latitic, quartz latitic, and rhyolitic welded ash-flow tuffs. A thick unit of mostly quartz latitic-rhyolitic flows overlies the ash-flow tuffs in the Keg Mountains, all of which were included by Erickson (1963, p. 24–25) in a unit he called Keg Mountain Ignimbrite. Intrusive quartz monzonite in Desert Mountain, quartz latite dikes and plugs at the northwest edge of the Keg caldera, quartz monzonite and quartz diorite plugs at the south edge of the Thomas caldera in the Drum Mountains, and small bodies of intrusive breccia at the west edge of the Thomas caldera in the Thomas Range appear to have been emplaced late in the middle period of igneous activity.

A basal welded ash-flow tuff unit is exposed extensively at the north end of the Drum Mountains in the southern part of the Thomas caldera, and in the northwest part of the Keg caldera. It is a fairly uniform dacite to quartz latite tuff that probably correlates with a plagioclase crystal tuff of Tertiary age described by Staatz and Carr (1964, p. 78–79) in the Thomas Range. The unit is as much as 200 feet thick locally, and the lower part tends to be light gray, the upper part light pinkish gray. Plagioclase phenocrysts (some up to 5 mm long) and biotite, as well as minor oxyhornblende, quartz, a black opaque mineral, sphene, and allanite phenocrysts (1–3 mm in size), occur in an aphanitic groundmass. Phenocrysts are commonly partly resorbed. In places the rock also contains some phenocrysts of sanidine, augite, green hornblende, and zircon. Shard structures are visible in the generally devitrified groundmass.

The next younger important ash-flow tuff unit is a light-pinkish-brown to reddish-brown rhyolitic to quartz latitic crystal-rich welded ash-flow tuff as much as 500 feet thick that is extensively exposed in the Keg Mountains. Thin patches of similar rock are present at the north end of the Drum Mountains, and in the Thomas Range where Staatz and Carr (1964, p. 79–81) described a quartz-sanidine crystal tuff and a sanidine crystal tuff both of Tertiary age. The quartz-sanidine crystal tuff unit was dated by Jaffe, Gottfried, Waring, and

Worthing (1959, p. 71) as 20 m.y. old by the lead-alpha method. Characteristically, abundant sanidine phenocrysts 1–3 mm across and less abundant and smaller phenocrysts of quartz, plagioclase, and biotite, and minor sphene, black opaque mineral, apatite, pyroxene, and green hornblende are set in a vitric to devitrified groundmass. Phenocrysts commonly are broken. Shards and pumice in the groundmass are visible under the microscope. Lithic fragments generally 2–3 cm in size are abundant in the rock; they are chiefly dark-reddish-brown to brownish-gray shale, silty shale, and quartzitic siltstone. The unit may be a single cooling unit made up of several ash flows; no major breaks are evident even where thick sections of the sheet are exposed.

The youngest significant ash-flow tuff unit is a light-brownish-gray rhyolitic to quartz-latic welded tuff that occurs at the north end of the Drum Mountains, where it exceeds 500 feet in thickness, and in small and thin patches in the Thomas Range and Keg Mountains. Staatz and Carr (1964, p. 82–84) described rocks similar to this unit as Tertiary porphyritic rhyolite but identified it, in its outcrops in the Thomas Range, mostly as intrusive plugs and not as a welded ash-flow tuff. This unit is a crystal-rich rock containing abundant commonly broken phenocrysts 1–3 mm across of quartz and sanidine, with lesser amounts of plagioclase, biotite, green hornblende, black opaque mineral, sphene, allanite, and zircon. The subordinate groundmass ranges from vitric to devitrified. Lithic fragments are less abundant than in the underlying rhyolitic welded ash-flow tuff common in the Keg Mountains. In the Thomas caldera in the north part of the Drum Mountains, the ash-flow tuff has abundant flattened black glassy pumice lapilli at the base, and has a major break near its middle, suggesting that there it consists of at least two major cooling units.

Three rhyolitic to quartz-latic welded ash-flow tuff units are exposed at the east edge of Desert Mountain; although somewhat similar to such rocks in the Drum Mountains, Thomas Range, and Keg Mountains, the relative ages are not known. The welded tuffs at Desert Mountain are intruded by quartz monzonite that is 26.5–28.5 m.y. old (Armstrong, 1970, table 3, p. 216–217).

The largest intrusive body formed during the middle period of igneous activity is the quartz monzonite of Desert Mountain. This rock is holocrystalline and equigranular, and consists of abundant 2- to 5-mm crystals of quartz, potassium feldspar, and plagioclase, and minor biotite and hornblende. Intrusive quartz latite in the Keg Mountains forms dikes and small plugs of porphyry along the northwestern periphery of the Keg caldera. These rocks consist of phenocrysts of quartz, plagioclase, sanidine, biotite, black opaque mineral, and allanite in a devitrified groundmass. The feldspar crystals are partly altered to clay minerals and calcite. Fine-grained quartz diorite in the Drum Mountains forms two small stocks just south of the edge of the Thomas caldera. Dikes of quartz monzonite porphyry also present in the area contain phenocrysts of plagioclase,

brown biotite, green hornblende, and minor embayed quartz in a holocrystalline groundmass of quartz and orthoclase (Crittenden and others, 1961, p. 504–505). Intrusive breccia at Spor Mountain and in The Dell in the Thomas Range consists largely of blocks of dolomite, but locally with fragments of porphyritic rhyolite, rhyodacite, limestone, and quartzite, in reddish clayey matrix that contains secondary dolomite and comminuted volcanic material (Staatz and Carr, 1964, p. 86).

Overlying the welded tuff units in the Keg Mountains is a unit as much as 1,000 feet thick of mostly silicic flow rocks, but including some thin, welded tuff members. The silicic flows are commonly light-gray flow-layered rocks that contain lithophysae and geodes concentrated in some layers. The rocks contain crystals as much as 5 mm (less commonly 10 mm) across of quartz, sanidine, plagioclase, oxidized biotite, augite, hornblende, a black opaque mineral, and minor apatite, allanite, and zircon. The matrix is commonly glassy. Associated thin rhyolitic to quartz latitic welded tuff layers are mostly at the base or near the top of the silicic flow unit. Some of these welded tuffs appear to have formed from compaction of air-fall tuff under hot and thick flows, rather than as welded ash-flow tuffs.

Only locally, such as along faults radiating from the periphery of the Keg caldera, are rocks of the middle volcanic period hydrothermally altered.

Younger assemblage of rocks

Rocks making up the youngest sequence of volcanic units in central Juab County are principally basalt and topaz-bearing alkali rhyolite flows; relatively thin but widespread water-laid and ash-fall tuff layers underlie and are locally interlayered with the rhyolite flows.

Water-laid tuff deposited during the youngest volcanic episode was described by Staatz and Carr (1964, p. 90–92) as a Tertiary vitric tuff in the Thomas Range, and designated by Erickson (1963, p. 27–30) as Topaz Mountain Tuff in the Keg Mountains and the Thomas Range. The rock consists of white, tan, green, gray, and pink, compact to friable vitric rhyolitic tuff; some layers contain numerous pebbles of white pumice, other volcanic rocks, and carbonate rocks that typically reflect the lithologies of nearby underlying rocks. The tuff layers exceed 100 feet in thickness only locally. Though dominantly water deposited, the tuffs contain some layers of air-fall material apparently not reworked by water. The tuffs contain abundant broken crystals 1–2 mm in size of quartz and sanidine, and minor to trace amounts of glass, plagioclase, a black opaque mineral, biotite, hornblende, augite, apatite, zircon, topaz, tourmaline, rutile, garnet, and cassiterite. Glass fragments, clay, and zeolite minerals constitute the matrix. Where hydrothermally altered the tuffs contain montmorillonite, calcite, ankerite, opal, chalcedony, adularia, fluorite, and bertrandite (hydrated beryllium silicate).

A sequence of alkali rhyolite flows as much as 1,000 feet thick commonly overlies the water-laid tuff. Locally the rhyolite forms dikes and plugs around the peripheries of the calderas, or makes up large domes localized over ring fractures or other fault zones. These lavas were described by Staatz and Carr (1964, p. 93–99 and pl. 1) as several units within a thick sequence of Tertiary rhyolite flows in the Thomas Range; Erickson (1963, p. 30–34) designated these rocks as Topaz Mountain Rhyolite in the Keg Mountains and the Thomas Range. The rhyolite is a light-gray topaz-rich rock, and individual flows are commonly bounded by layers of black glass. The rock generally consists of phenocrysts of quartz, sanidine, oxidized biotite, plagioclase, hornblende, and a black opaque mineral in devitrified groundmass crowded with minute inclusions. Most of the topaz-bearing rhyolite is flow layered, but in places it is massive and cavernous weathering; locally it contains numerous lithophysae, spherulites, or geodes along flow layers. Where flow layers are conspicuous, gas cavities are commonly lined with topaz, tridymite, chalcedony, or opal. These variants of the topaz-bearing rhyolite are similar in appearance to lithophysal and geode variants of the older rhyolite flows of middle sequence of volcanics in the Keg Mountains previously described, and are difficult to distinguish from them in the field. The Topaz Mountain Rhyolite in the Thomas Range has long been famous for its large (10 mm and larger) water-clear crystals of topaz and smaller crystals of black bixbyite and red beryl (Staatz and Carr, 1964, p. 102–108).

Topaz-bearing alkali rhyolite of the Thomas Range contains 74–77 percent silica and has an unusually high content of several minor elements. The rock contains about 0.03–0.06 percent manganese oxide, 0.14–0.47 percent fluorine, 0.003 percent uranium, 0.0015–0.002 percent beryllium, 0.004–0.007 percent lead, and 0.0005–0.005 percent tin (Staatz and Carr, 1964, tables 15, 17; Shawe, 1966, table 3).

Basalt flows erupted during the youngest period of volcanic activity are present mostly in the vicinity of Fumarole Butte south of the Keg Mountains, where they aggregate probably more than 500 feet in thickness. Erickson (1963, p. 27) designated these rocks as the Fumarole Butte Basalt. Some of these flows may have been erupted quite recently, as a crater is still preserved in basalt just south of Smelter Knoll about 15 miles south of the Keg Mountains. The basalt is commonly vesicular and contains phenocrysts 1–2 mm in length of plagioclase in a very fine grained dark matrix.

The young basalts and alkali rhyolites are hydrothermally altered only locally. For example, near the western periphery of the Keg caldera and at the west edge of the Thomas caldera small areas of topaz-bearing rhyolite are hydrothermally altered.

STRUCTURAL FORM AND EVOLUTION OF THE CALDERAS

Before any of the voluminous ash-flow eruptions that

resulted in the formation of the three described calderas, the region of central Juab County was covered unevenly with the outflow of probably several intermediate-composition central volcanoes. This material had been extensively eroded and only moderate relief existed prior to ash-flow eruption; perhaps some low hills of Paleozoic and Precambrian sedimentary rocks stood amidst the volcanic hills and plains.

The least conspicuous and probably the oldest of the three calderas is the Desert caldera. Its core appears to be more deeply eroded than those of the other calderas. Desert Mountain was at least in part uplifted to its present height by basin-range block faulting, and the relatively deep level of erosion may have resulted in some degree from this uplift.

The ring fractures around the Desert caldera are not exposed; their inferred position, bounding a structure 11–12 miles in diameter, is shown in figure 2. Perhaps the silicic ash-flow tuffs exposed on the east side of Desert Mountain were erupted during the main period of collapse of the caldera. Quartz monzonite of Desert Mountain is interpreted as having formed from resurgent magma that intruded the core of the caldera after collapse and that domed the intermediate flows and silicic ash-flow tuffs, so that the now-exposed volcanics dip steeply to the east. Presumably, volcanic layers underlie alluvium on the north, west, and south sides of Desert Mountain and dip away from the center of the resurgent dome now marked by the quartz monzonite intrusive. The resurgent quartz monzonite magma rose high enough to cut the welded ash-flow tuffs, in the core of the caldera, and possibly reached within a few thousand feet of the surface. Rhyolite at the northeast side of Desert Mountain forms a small plug that may represent the feeder of a ring dome of the caldera. However, the rhyolite is similar to alkali rhyolite of the youngest volcanic episode exposed farther west, and may not be related to the Desert caldera cycle.

The magnetic contours shown in figure 2, obtained from an aeromagnetic survey by the U.S. Geological Survey, suggest the configuration of the Desert caldera. The prominent magnetic high indicated by the 2,500-gamma contour may mark the structurally highest part of an intrusive mass underlying the resurgent dome of the caldera.

The Keg caldera is more completely exposed than the Desert caldera, and its geologic history is better known. The Keg caldera is believed to have formed as a result of eruption of the second widespread ash-flow tuff unit described earlier—the light-reddish-brown rhyolitic ash-flow tuff—because that unit is very thick inside the inferred rim of the caldera in the Keg Mountains just north of the Jericho road, and is much thinner outside the caldera.

The northwest rim of the caldera is exposed in the Keg Mountains and is marked by an arc of faults, dikes, and plugs. A curved fault inferred to be part of the ring-fracture zone was mapped 7 miles north of the Jericho Road (fig. 1). Quartz latite porphyry forms a dike intruded along the southern extension of this ring fault, and forms small plugs along the

fault. A mile northeast of the fault and aligned with it is another small plug of quartz latite porphyry. Projection of the exposed ring-fracture zone indicates a caldera structure 11–12 miles in diameter.

The exposed structural rim of the caldera also formed a topographic rim, as indicated by the fact that the quartz latitic welded ash-flow unit in the Keg Mountains fills a depression whose exposed rim coincides with the structural rim. The tuff unit thickens abruptly to the southeast from the position of the curved fault just described. The overlying light-reddish-brown rhyolitic ash-flow tuff also thickens to the southeast in this part of the caldera.

After eruption of ash-flow tuff in the Keg Mountains and the major collapse of the caldera, rhyolitic to quartz-latitic lava flows in large volume were erupted within the caldera where they puddled to a thickness of about 1,000 feet.

In the Keg Mountains no igneous rock is exposed at the surface that could be interpreted as representing resurgent magma intruded in the core of the caldera. Nevertheless, the magnetic contours in figure 2 suggest that the caldera core was intruded by igneous rock. Furthermore, attitudes of flat silica laminae in geodes in the thick rhyolite flows in the Keg caldera that have been tilted about 5° from horizontal suggest that a post-rhyolite episode of doming occurred in the caldera. The conformity of these attitudes with the magnetic contours relates the doming to intrusion of resurgent magma (fig. 2).

After completion of the Keg caldera cycle, and apparently after a period of erosion, a relatively thin but widespread unit of airfall and water-laid tuffs was deposited in the Keg Mountains. These tuffs spread fairly evenly across rocks of the oldest and middle volcanic episodes, indicating that the earlier units had been nearly leveled by erosion. This fact further indicates that the thick rhyolitic to quartz-latitic flows that erupted late in the Keg caldera cycle filled a depression rather than constituted a constructional dome above the caldera center. The presence in the tuffs of pebbles that were derived from nearby exposures of older rocks shows that some hills of older rocks rose above the level of the stream-laid deposits.

Shortly after deposition of the water-laid tuffs, numerous flows of topaz-bearing alkali rhyolite were poured out. Most of these flows in the Keg Mountains are located near the margins of the Keg caldera and perhaps they were erupted along the ring-fracture zone of the caldera. Near the northwest edge of the caldera small plugs and dikes of alkali rhyolite were intruded in fractures that are generally radial to the caldera.

Faulting that formed the irregular north-striking graben extending through the center of the Keg caldera was probably initiated during resurgent doming. Some of the faults cut younger alkali rhyolite, however, and postdate the doming; these may be related to basin-range tectonics.

The Thomas caldera is the best exposed of the three calderas and it is probably the youngest. It was apparently formed as a result of eruption of the youngest of the widespread ash-flow tuff units—the light-brownish-gray rhyolitic to quartz-latitic

welded tuff—inasmuch as this unit is impressively thick inside the caldera at the north end of the Drum Mountains and is relatively thin elsewhere. A thin layer of this unit overlies the light-reddish-brown rhyolitic to quartz-latitic welded ash-flow tuff believed related to the Keg caldera, indicating that the Thomas caldera probably formed after the Keg caldera.

The ring-fracture zone of the Thomas caldera is only partly exposed, evident as the arcuate fault at the north end of the Drum Mountains (the east segment of which was named Joy fault by Crittenden and others, 1961, p. 506 and pl. 20), faults in The Dell at the south end of the Thomas Range, and a fault at the southwest end of the Keg Mountains. The remainder of the ring-fracture zone is buried beneath alkali rhyolite and alluvium. The entire structure extends 12 miles east to west and 16 miles north to south.

The Thomas caldera does not have exposed in its core igneous rock that represents a resurgent magma intrusion. Even so, like the Keg caldera, its magnetic contours suggest that the core is intruded by igneous rock (fig. 2). The magnetic high in the Thomas caldera is centered above an area where alkali rhyolite directly overlies ash-flow tuffs believed to be older than the rhyolitic ash-flow tuff related to formation of the Thomas caldera. Probably the rhyolitic ash-flow tuff was eroded there, because of doming related to intrusion of a resurgent magma.

Although not dated, the quartz monzonite porphyry plug in the Drum Mountains just south of the Thomas caldera, and the intrusive breccia pipes at the west edge of the caldera, probably were emplaced after development of the ring-fracture system, perhaps at about the same time as resurgent doming occurred.

After the Thomas caldera cycle, the same widespread thin unit of water-laid tuff described for the Keg caldera area was deposited across the Thomas caldera. An anomalous block of Paleozoic sedimentary rocks overlies the water-laid tuff within the caldera. Where exposed, the contact between the Paleozoic rocks and the water-laid tuff is a nearly horizontal fault (Shawe, 1964). Although the Paleozoic rocks may have been emplaced on a regional flat fault, it appears more likely that they moved into place on a gravity slide that broke away from an oversteepened caldera wall composed of Paleozoic rocks and moved out across the water-saturated clay-rich water-laid tuff on the floor of the caldera.

The area of the Thomas caldera was broken by faults after emplacement of the anomalous block of Paleozoic rocks and before subsequent extrusion of alkali rhyolite flows. In the hills 3 miles south of the junction of the Jericho and Delta roads a north-northwesterly fault offsets the flat fault at the base of Paleozoic rocks and is overlapped by a flow of alkali rhyolite. The north-northwesterly fault, and nearby subparallel faults, may represent part of the basin-range faulting that by then was active in the region.

Thick flows of topaz-bearing alkali rhyolite are extensive in the north part of the Thomas caldera. There they appear to

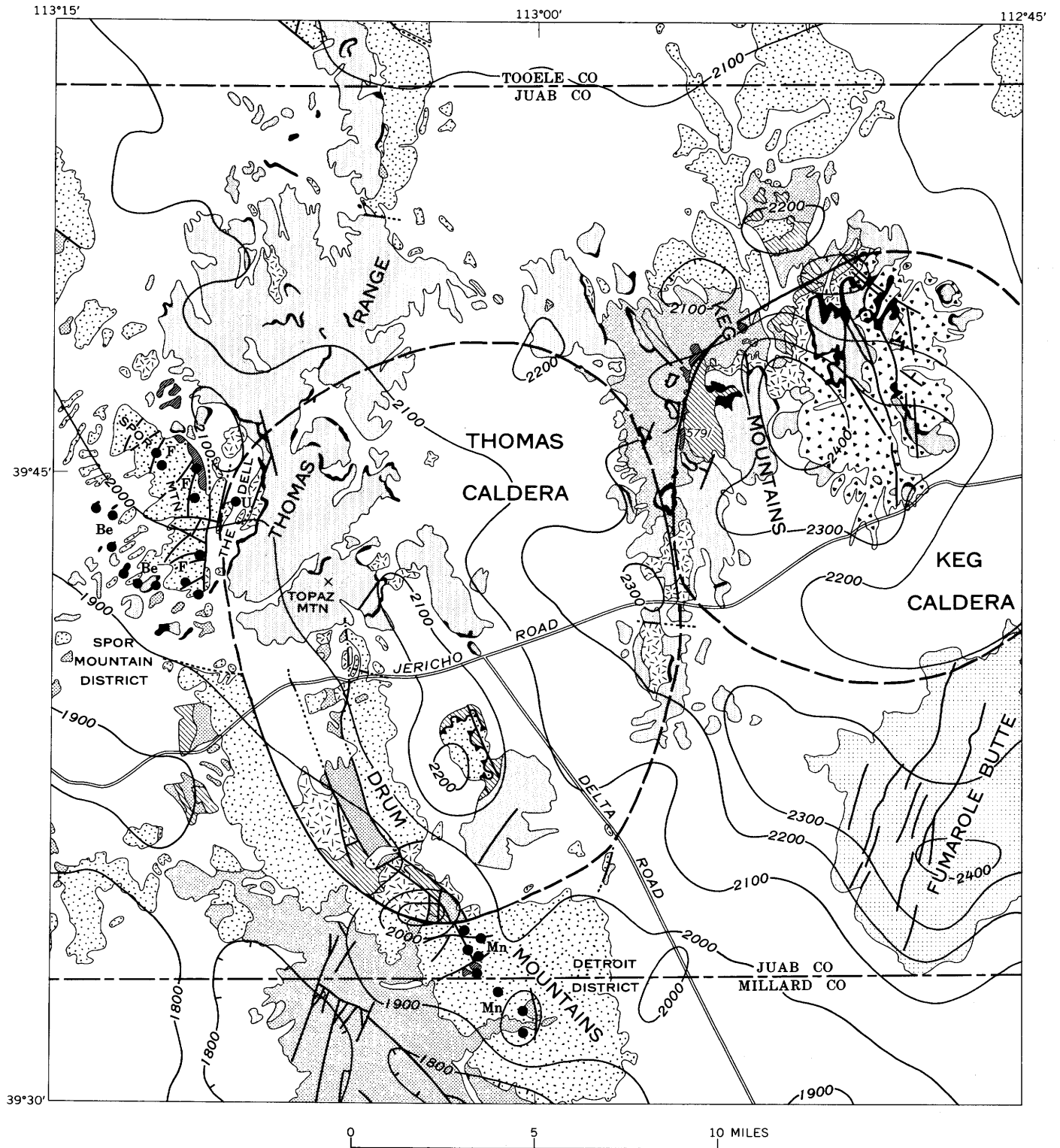


Figure 2.

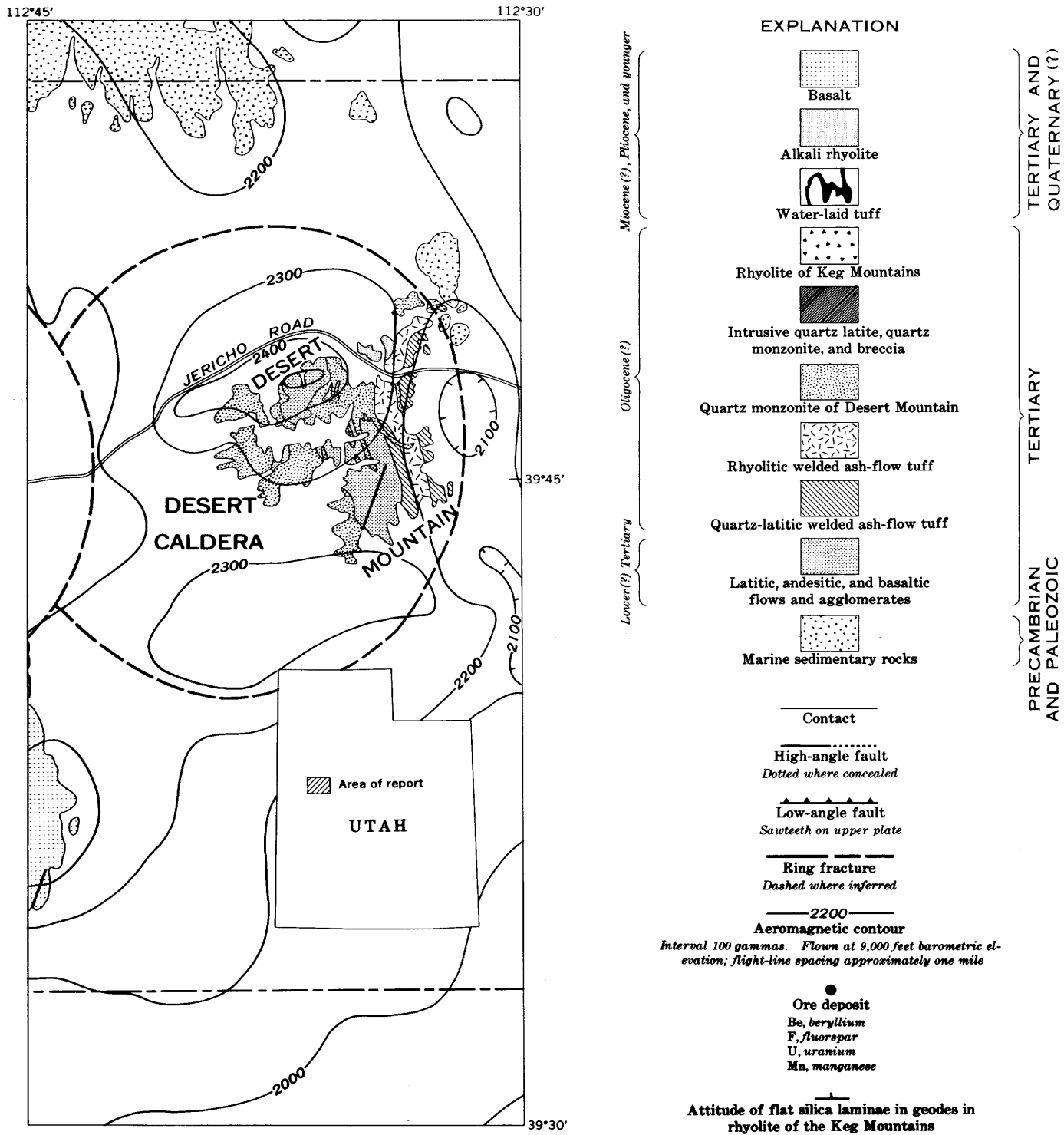


Figure 2.—Map showing inferred outlines of the Thomas, Keg, and Desert calderas, aeromagnetic contours in the region, and locations of ore deposits near the Thomas caldera.

have been extruded from several major centers that form an east-facing arc (Staatz and Carr, 1964, p. 117 and pl. 6). This arc does not coincide with the inferred outline of the Thomas caldera (fig. 2), but perhaps it reflects the ring-fracture zone of another caldera nested closely with the Thomas caldera. Small plugs of alkali rhyolite south of the south boundary of the Thomas caldera appear to be in part related to faults radial to the caldera.

Young flows of basalt, and some flows of alkali rhyolite, appear not to be related to the positions of the calderas. This is noticeably true for flows of rhyolite and basalt at Smelter Knoll 15 miles south of the Keg Mountains, south of the area shown in figure 1. I infer from this that the topaz-bearing alkali rhyolite and the basalt were generated by a mechanism unrelated directly to caldera formation. The caldera structures, however, provided paths of later emplacement of alkali rhyolite and basalt magmas.

ORE DEPOSITS ASSOCIATED WITH THE THOMAS CALDERA

Many ore bodies have been mined around the periphery of the Thomas caldera. Most significant production has been of manganese, fluor spar, uranium, and beryllium during three major periods of activity.

From 1925 to 1953 about 72,500 long tons of manganese ore averaging 25 percent manganese was produced from the Detroit district (Crittenden and others, 1961, p. 493) which lies in the Drum Mountains within about 2 miles south of the south boundary of the Thomas caldera (fig. 2). Manganese oxide ore was produced from weathered replacement bodies of manganese carbonate in two 20-foot beds of Cambrian dolomite. The replacement bodies formed along faults near small intrusives of quartz monzonite porphyry, and the manganese carbonate deposits are younger than the intrusive rocks. The ore bodies formed by weathering to manganese oxides within 100–200 feet of the surface (Crittenden and others, 1961). Minor amounts of copper, gold, bismuth, and silver were produced from the district prior to 1925 (Crittenden and others, 1961, p. 515; Dasch, 1964, p. 140). In recent years mining companies have prospected for disseminated copper in some of the intrusives in the district.

During 1943–52, about 75,000 short tons of fluor spar was produced from what was then called the Thomas Range fluor spar district (Staatz and Osterwald, 1959, p. 1) which lies in Spor Mountain within about 2 miles west of the west boundary of the Thomas caldera (fig. 2). Fluor spar was mined principally from oval to irregular pipes of claylike and pulverulent masses or boxworks consisting of 65–95 percent fluorite in shattered zones in dolomite or volcanics (Staatz and Osterwald, 1959, p. 1–2; 48–50) (fig. 2). Fluor spar deposits formed after most of the volcanic rocks were emplaced. At least 0.05 percent uranium was present in many of the fluor spar pipes, particularly those at the south end of Spor

Mountain, but was not recovered (Staatz and Osterwald, 1959, p. 1). Mining of fluor spar has recently started again in the district.

From 1956 to 1961 the Yellow Chief uranium deposit, purported to contain in the order of 100,000 tons of ore, produced uranium ore averaging about 0.2 percent U_3O_8 (Bowyer, 1963, p. 19). The deposit is in The Dell, virtually on the ring fracture zone at the west boundary of the Thomas caldera (fig. 2). The ore, mined largely in an open cut, consisted of chiefly beta-uranophane in water-laid tuff, volcanoclastic sandstone, and conglomerate made up of fragments of mostly volcanic rocks and some carbonate rocks (Bowyer, 1963, p. 17, 19). The host rock is somewhat similar to the water-laid tuff of the youngest volcanic group in the Thomas Range. The ore was formed after most of the volcanic rocks in the district were deposited.

In 1969 open cut mining of extensive deposits of beryllium ore was started in the Spor Mountain district, which includes the area of earlier fluor spar (Thomas Range district) and uranium mining. The beryllium deposits, probably amounting to about 15 million tons of ore averaging 0.5 percent BeO (Griffitts, 1964, p. 75), lie within about 5 miles west of the west boundary of the Thomas caldera (fig. 2). The deposits are very large (the largest has a strike length of 2.5 miles), tabular, nearly concordant bodies of hydrothermally altered water-laid tuff (vitric tuff—Staatz and Carr, 1965) containing bertrandite, about 5 percent fluorite, 0.7–0.9 percent manganese oxide, about 0.014 percent uranium, and small amounts of lithium, lead, zinc, tin, and tungsten (Shawe, 1968, p. 1153–1155). The deposits are younger than the rhyolite that overlies the mineralized water-laid tuff (Williams, 1963, p. 54).

Although the known ore deposits are distributed around the southern and western periphery of the Thomas caldera and hence possibly are related to igneous rocks of the caldera cycle, the young age of all the deposits suggests instead that they are closely related to the topaz-bearing alkali rhyolites. The common association of manganese, fluorine, uranium, and beryllium, both in the ore deposits and in the topaz-bearing rhyolite, also suggests a common genesis. Staatz and Griffitts (1961, p. 948–949) proposed that the ore deposits formed by escape of mineralizing solutions from buried magma of the type that was extruded as rhyolite. Apparently the caldera provided a favorable structural environment for both intrusion of rhyolite and related mineralization. Only about a third of the periphery of the caldera is now exposed; the remainder, which is covered by late rhyolite flows or Quaternary alluvium, may well contain undiscovered deposits of manganese, fluor spar, uranium, and beryllium. The covered ring-fracture zones of the Keg and Desert calderas offer similar possibilities. Perhaps other structures near alkali rhyolite centers, but not closely related to the calderas, offer potential sites for deposits of manganese, fluor spar, uranium, and beryllium, particularly where favorable host rocks are available.

The ore deposits near the margins of the Thomas caldera are all relatively young and were formed in a near-surface environment. If the interpretation is correct that the mineralizing fluids were derived from underlying alkali rhyolite magma chambers, the fluids must have traversed rocks in deeper zones and may have mineralized them. Staatz and Griffiths (1961, p. 948–949) indicated a plausible depth-zoning relation, with the fluor spar pipes occurring in a central zone of solution flow and beryllium deposits occurring farther outward; the latter formed where solutions no longer carried fluorine sufficient to complex the beryllium. This same reasoning implies that deeper zones may also be worthy of exploring. Metals that may be present at depth are those that occur in minor amounts at the surface, such as copper, gold, silver, lead, and zinc, or those that occur in minor but abnormally high amounts in the alkali rhyolite, such as lead and tin.

The aeromagnetic data presented in figure 2 indicate possible favorable areas for exploration. Beryllium, fluor spar, and uranium mines at the west edge of the Thomas caldera are grouped on the southwest flank of a magnetic high of 2,100 gammas. Manganese deposits at the south edge of the caldera are grouped on the southeast flank of a magnetic high of 2,100 gammas and extend southeastward across a magnetic high of 2,000 gammas. Perhaps the areas of these magnetic highs warrant further exploration, as do magnetic highs of 2,200 gammas at the north edge of the Thomas caldera and of 2,300 gammas at the east edge of the caldera where no mineral deposits are known. Possibly the magnetic highs of 2,200, 2,400, and 2,500 gammas in the cores of the Thomas, Keg, and Desert calderas, respectively, where no mineral deposits are known at the surface, also justify exploration in their vicinities. Magnetic lows of 2,100 gammas each at the northwest edge of the Keg caldera and at the east edge of the Desert caldera may represent areas of sulfide alteration below the surface that are favorable targets for exploration. I emphasize that the magnetic anomalies have only relative significance, and any exploration based on them should be guided also by all available geologic information.

REFERENCES

- Armstrong, R. L., 1968, Sevier orogenic belt in Nevada and Utah: *Geol. Soc. America Bull.*, v. 79, p. 429–458.
- 1970, Geochronology of Tertiary igneous rocks, eastern Basin and Range Province, western Utah, eastern Nevada, and vicinity, U.S.A.: *Geochim. et Cosmochim. Acta*, v. 34, p. 203–232.
- Bowyer, Ben, 1963, Yellow Chief uranium mine, Juab County, Utah, in Sharp, B. J., and Williams, N. C., eds., *Beryllium and uranium mineralization in western Juab County, Utah*: Utah Geol. Soc. Guidebook 17, p. 15–22.
- Crittenden, M. D., Jr., Straczek, J. A., and Roberts, R. J., 1961, Manganese deposits in the Drum Mountains, Juab and Millard Counties, Utah: U.S. Geol. Survey Bull. 1082-H, p. 493–544.
- Dasch, M. D., 1964, Antimony and other minor metals, in *Mineral and water resources of Utah*: U.S. 88th Cong., 2d sess., U.S. Senate Comm. on Interior and Insular Affairs Rept., p. 135–144.
- Erickson, M. P., 1963, Volcanic geology of western Juab County, Utah, in Sharp, B. J., and Williams, N. C., eds., *Beryllium and uranium mineralization in western Juab County, Utah*: Utah Geol. Soc. Guidebook 17, p. 23–25.
- Griffitts, W. R., 1964, Beryllium, in *Mineral and water resources of Utah*: U.S. 88th Cong., 2d sess., U.S. Senate Comm. on Interior and Insular Affairs Rept., p. 71–75.
- Jaffe, H. W., Gottfried, David, Waring, C. L., and Worthing, H. W., 1959, Lead-alpha age determinations of accessory minerals of igneous rocks: U.S. Geol. Survey Bull. 1097-B, 76 p.
- Odekirk, J. R., 1970, Desert Mountain granite, in Whelan, J. A., compiler, *Radioactive and isotopic age determinations of Utah rocks*: Utah Geol. and Mineralog. Survey Bull. 81, p. 33.
- Park, G. M., 1970, Volcanics, Thomas Range, in Whelan, J. A., compiler, *Radioactive and isotopic age determinations of Utah rocks*: Utah Geol. and Mineralog. Survey Bull. 81, p. 23.
- Shawe, D. R., 1964, A late Tertiary low-angle fault in western Juab County, Utah, in *Geological Survey Research 1964*: U.S. Geol. Survey Prof. Paper 501-B, p. B13–B15.
- 1966, Arizona-New Mexico and Nevada-Utah beryllium belts, in *Geological Survey Research 1966*: U.S. Geol. Survey Prof. Paper 550-C, p. C206–C213.
- 1968, Geology of the Spor Mountain beryllium district, Utah, in Ridge, J. D., ed., *Ore deposits of the United States, 1933–1967*: New York, Am. Inst. Mining Metall. Engineers Graton-Sales volume, p. 1148–1161.
- Staatz, M. H., 1963, Geology of the beryllium deposits in the Thomas Range, Juab County, Utah: U.S. Geol. Survey Bull. 1142-M, 36 p.
- Staatz, M. H., and Carr, W. J., 1964, Geology and mineral deposits of the Thomas and Dugway Ranges, Juab and Tooele Counties, Utah: U.S. Geol. Survey Prof. Paper 415, 188 p.
- Staatz, M. H., and Griffiths, W. R., 1961, Beryllium-bearing tuff in the Thomas Range, Juab County, Utah: *Econ. Geology*, v. 56, p. 941–950.
- Staatz, M. H., and Osterwald, F. W., 1959, Geology of the Thomas Range fluor spar district, Juab County, Utah: U.S. Geol. Survey Bull. 1069, 97 p.
- Williams, N. C., 1963, Beryllium deposits, Spor Mountain, Utah, in Sharp, B. J., and Williams, N. C., eds., *Beryllium and uranium mineralization in western Juab County, Utah*: Utah Geol. Soc. Guidebook 17, p. 36–59.



A CLASSIFICATION OF IGNEOUS ROCKS BY THEIR HISTORY OF CRYSTALLIZATION AND EMPLACEMENT

By T. P. THAYER and E. D. JACKSON,
Washington, D.C., Menlo Park, Calif.

Abstract.—Igneous rocks are classified as authigenic, polygenic, and allogenic according to their histories of crystallization and emplacement. Authigenic rocks have crystallized in situ from fluid magma, with or without differentiation; polygenic rocks have crystallized at various times and places during emplacement of magmatic mush containing at least 10 and ordinarily not more than 50 percent crystals; and allogenic rocks crystallized completely at one site and were moved to another by rheid-mush or solid flow at high temperature, with or without reequilibration. The allogenic rocks are characterized for the most part by igneous mineralogy and metamorphic textures and structures. The proposed classification provides for a complete gradational series from authigenic to allogenic rocks. Authigenic and polygenic types occur over the complete composition range of igneous rocks, but allogenic rocks seem to be limited to ultramafic, gabbroic, and possibly anorthositic composition. Stratiform mafic and ultramafic complexes are dominantly authigenic, concentrically zoned ones are dominantly polygenic, and alpine complexes are dominantly allogenic; few large igneous complexes consist of only one class of rocks. The ophiolitic volcanic-plutonic assemblage seems to be unique in consistently including all three classes of rocks.

Several kinds of peridotitic and gabbroic rocks are now recognized, in addition to those characterized as stratiform and alpine by Thayer (1960). Jackson and Thayer (1972) have categorized three great groups of peridotite-gabbro complexes. Wyllie (1967, p. 3–7) proposed 10 ultramafic-ultrabasic plutonic associations, and Naldrett and Gasparri (1972) divided peridotites and related gabbroic rocks into 12 classes and subclasses according to their provenance, size, and other features, including ore deposits. However, no satisfactory scheme has been devised to show how these associations may be related through common igneous and tectonic processes. Lack of such a genetic classification has contributed, for example, to a misconception that all peridotite-gabbro assemblages in orogenic belts belong to or are closely related to the alpine type, *sensu stricto* (Thayer, 1967, p. 222). The genetic classification outlined here has developed from the descriptive classification of Jackson and Thayer (1972), and from consideration of relationships between magmatic ore deposits and the late magmatic history of their host rocks (Thayer, 1972). The classification divides all igneous rocks

into three groups based on their histories of crystallization and emplacement. These two processes may or may not be closely related to the early magmatic history of igneous rocks (Den Tex, 1969; Jackson, 1971). This paper, in conjunction with detailed descriptions elsewhere (Jackson and Thayer, 1972), compares and contrasts features of the three genetic categories of igneous rocks and considers the petrogenic implications involved in this grouping.

Three distinct but intergrading categories of igneous rocks can be defined according to their late magmatic histories: authigenic, polygenic, and allogenic (table 1). Authigenic rocks are defined as those that crystallized subsequent to intrusion from magma that contained very few phenocrysts. Polygenic rocks are those emplaced as mixtures of liquid and crystals (phenocrysts) in which substantial crystallization took place before, during, and after intrusion. Allogenic rocks are those that crystallized at one place and were moved by solid flow or by rheid-mush flow to their present location. Within these major categories, rocks may be subdivided according to composition, differentiation trends, provenance or other distinguishing features. Rocks of two or all three classes may be comagmatic and intimately related in a single intrusive complex or assemblage, and, in fact, few large complexes consist of only one genetic category of rocks.

The close correlation between types of features and timing of crystallization with respect to magmatic transport is brought out in table 1. Cumulates, one of the most important types of authigenic rocks, are formed only in situ, for the most part by fractionation of relatively crystal-free magma. Porphyritic textures and fluidal fabrics reflect crystallization during polygenic movement of crystal mushes that may have ranged from highly fluid to rheid. The amounts and roles of liquid involved in emplacement of allogenic rocks by solid flow are obscure, but must be very important. Four kinds of flowage related to the proportions of crystals to liquid in magma may be distinguished: (1) pure fluidal flow, with less than about 10 percent crystals, (2) fluid-mush flow, with 10 to about 50 percent crystals, (3) rheid- (quasi-solid) mush flow, in magma containing 50 to about 90 percent crystals, and (4)

Table 1.—Comparative features of authigenic, polygenic, and allogenic ultramafic, gabbroic, and basaltic igneous rocks

[XXX, widespread, characteristic or diagnostic; XX, common, characteristic or diagnostic; X, common, not diagnostic; and x not common, not diagnostic]

Features	Authigenic	Polygenic	Allogenic
Number of essential-mineral phases:			
One	x	x	x
Two	X	X	XXX
Three or more	XXX	XXX	XXX
Textures:			
Cumulus	XXX	X	x
Poikilitic	XXX	X	x
Porphyritic	x	XXX	
Ophitic	XXX	XXX	x
Allotriomorphic	X	X	X
Cataclastic		X	XX
Tectonic, granulitic		x	XXX
Liquid-solid reaction	XXX	XXX	x
Solid-solid reequilibration	x	x	XX
Layering:			
Cumulus	XXX	X	x
Chemical-graded (cryptic)	XXX	x	
Fluid flow	X	X	
Solid flow		x	XX
Lamination, cumulus or fluidal:			
Planar	XXX	X	
Lineate	X	XXX	
Foliation, gneissic or schistose			
Lineation, gneissic or schistose		x	XXX
Cyclic units	XXX	x	XXX
Crossbedding and related features	X	X	x
Dikes and pipes:			
Internal	X	XX	X
Into country rocks		XX	
Chilled margins	XXX	XX	x
Contact metamorphism:			
Pyroxene hornfels	XX	X	
Pyroxene granulite		X	x
Amphibolite or lower grade		X	X
<hr/>			
Petrogenetic Processes	Authigenic	Polygenic	Allogenic
Percentage of solids in magma during emplacement			
	<10	10–75	75–100
Mode of emplacement			
	Liquid flow, crystal settling.	Liquid- or rheid-mush flow; remobilization, explosive, or other magmatic type.	Rheid or solid flow.
Primary crystallization	Entirely in situ.	Partly in situ.	Ex situ.
Mode of differentiation, if any, in situ.			
	Crystal settling, marginal chilling, fluid sorting, and convective overturn.	Fluid-mush flow, marginal chilling, and filter pressing (recrystallization, crystal or sulfide liquid settling).	Recrystallization, reequilibration during rheid flow; sub-solidus recrystallization; and local filter pressing.

solid flow in material more than 90 percent crystalline. Pure fluidal flow leaves little mark of transport on the authigenic rocks that ultimately crystallize (Jackson, 1961). Fluid-mush flow aligns phenocrysts and stamps polygenic rocks with lineated shape fabrics (Weiblen, 1965; James, 1971). In magma with about 50 percent liquid, crystals begin to impinge and deform, and polygenic processes give way to allogenic ones as solid flow and syntectonic recrystallization become the dominant processes of transport (Raleigh, 1968; Avé Lallemant and Carter, 1970; Carter and Avé Lallemant, 1970).

The terms "authigenic" and "allogenic" should not be confused with autochthonous and allochthonous. Movement of igneous rocks as integral parts of thrust sheets obviously does not change their late magmatic histories. Cumulus gabbro and peridotite described by Davies (1968; 1969) as part of the Papuan Ultramafic Belt thrust plate still are authigenic, although the plate is allochthonous. Because diapiric masses of serpentinized ultramafic rocks are allochthonous, only internal features might reveal whether the original peridotite was authigenic or allogenic.

Acknowledgments.—C. Ervin Brown, P. W. Guild and J. E. Gair contributed greatly to development of the concepts involved in the proposed classification by patiently discussing problems and possible solutions, and reviewing the manuscript. Suggestions by C. A. Anderson helped greatly in extending the classification to silicic and alkalic rocks.

AUTHIGENIC ROCKS

Authigenic rocks range from homogenous volcanic glass to pegmatites of many kinds and monomineralic cumulates (tables 1, 2). Nonporphyritic chilled border rocks show that most, but not all, ultramafic and gabbroic cumulates of this category crystallized from completely fluid magma. The rate of crystallization and viscosity of fluid magma appear to be the two most important factors in determining the final textural aspects of authigenic rocks. Rapid cooling of small masses of magma and chilling of the borders of large masses prevent differentiation and result in rocks of essentially uniform composition and texture. Slow cooling of large volumes of magma facilitates fractional crystallization that may lead to differentiation by several processes. In flooded chambers, crystals settle to form layered cumulates that display many features of sedimentary rocks. Along steep contacts, such as those described by Taubeneck and Poldervaart (1960) and Moore and Lockwood (1970), diffusion or supercooling produce quite different, but still authigenic, features. In general, efficacy of crystal settling as a differentiation process is related inversely to the viscosity of the magma, and viscosity increases with content of SiO₂ and alkalis. Cumulate features, however, have been described in granites (Emeleus, 1963) and syenites (Ferguson and Pulvertaft, 1963).

POLYGENIC ROCKS

As a group, polygenic rocks are the most varied and probably are the most abundant of the three classes because

most magmas begin to cool and crystallize during ascent from their melting regions. Compositionally, polygenic rocks range from truly ultramafic (Wilson and others, 1969) to granitic (table 2). Porphyritic textures and fluidal fabrics are diagnostic features of these rocks. Planar and lineate lamination shown by oriented undeformed tabular or prismatic crystals commonly are prominent, and these may grade into cataclastic textures. Differentiation within individual intrusive units commonly is limited because crystal settling is impeded by crowding, by flowage itself, and by increase in viscosity of the cooling magma. Cumulus features may be formed locally, however, on a small scale (Irvine, 1967; Wilson and others, 1969). In most polygenic rocks the final crystallization is authigenic because fluidal motion and movement in most magmas cease when crystallization is 50–60 percent complete. At this stage, crystals cannot settle, although immiscible heavy sulfide or oxide liquids might gravitate to some extent (Wilson and others, 1969). In polygenic rocks, crystallization and differentiation may be completely independent and widely separated spatially and temporally.

ALLOGENIC ROCKS

Allogenic rocks are characterized by igneous mineralogy and metamorphic textures and structures (Jackson and Thayer, 1972) that developed during emplacement by solid flow from the site of original crystallization (Rost, 1968; Den Tex, 1969; Thayer, 1969a). Tectonic fabrics imposed during flowage of solid rock may be obscured by syntectonic recrystallization processes that ultimately yield unstrained polygonal mosaics (Raleigh, 1963). Recrystallization of this type not only prevents solid-liquid compositional zoning in minerals, but eliminates any that may have existed previously. Rocks that have reequilibrated isochemically, as from lherzolite to feldspathic lherzolite, garnet pyroxenite to pyroxenite, and pyroxenite to gabbro, during movement from high to lower pressures and temperatures, show characteristic solid-solid reaction features (Green, 1967; Nicolas, 1969; Dickey, 1970).

RELATIONS BETWEEN AUTHIGENIC AND POLYGENIC ROCKS

Authigenic and polygenic rocks intergrade and may be indistinguishable in hand specimens and limited outcrops, but some may be distinguished by careful fabric studies (Jackson, 1961; James, 1971). For example, a plagioclase-olivine cumulate showing good lamination might seem identical in the field to troctolite intruded as a fluid mush. Theoretically, rocks of the two kinds could be formed from one batch of mushy magma, part of which crystallized undisturbed, while the other was moved out of the magma chamber. The first troctolite would be a true cumulate, but the second, in which settling was prevented by fluid flow and chilling, would be a porphyry. This situation is exemplified by Hawaiian extrusive picrites of the ankaramite type, which contain xenoliths of cumulates

and phenocrysts of the same minerals (Beeson and Jackson, 1970). Failure to make an authigenic-polygenic distinction led Wilson and others (1969, p. 297) to use cumulus terminology although they described the Katiniq sill as a porphyry in which olivine had settled only slightly, if at all. Cumulates might be regarded as composed of settled phenocrysts, but there is little evidence to indicate that phenocrysts in polygenic rocks are derived from disaggregated cumulates.

RELATIONS OF ALLOGENIC TO AUTHIGENIC AND POLYGENIC ROCKS

Allogenic rocks, by definition, represent authigenic or polygenic rocks that have been transformed by extensive rheid flow. Chromitite-bearing alpine peridotite and related gabbro are believed to have originated as cumulates in oceanic crust and mantle (Thayer, 1969a), but much of the gabbro may have been polygenic (Davies, 1969). Peridotite bodies of the lherzolite type which have reequilibrated during solid flow are allogenic, but, strictly speaking, the new-formed feldspar (Green, 1964) and gabbro and dunite fractions (Nicolas, 1969; Dickey, 1970) are authigenic, like prehnite in altered graywacke. In these rocks, as in granitic migmatites, igneous and metamorphic processes merge.

Allogenic and polygenic rocks intergrade in the magmatic borderland between mushy and solid flowage. Protoclastic borders of synorogenic intrusions show continuation of polygenic-type magma transport into solid flow, as a subordinate phase. In contrast, generation of gabbro by reequilibration of lherzolite shows local partial fusion as a subordinate aspect of solid flow. Thus, though the percentages of liquid in dominantly polygenic and allogenic processes may overlap at some stages, the processes themselves are quite different.

Secondary pipes and intrusions in the Bushveld (Willemse, 1969, p. 11) and Sudbury (Souch and others, 1969, p. 261) complexes are regarded as polygenic because partial remelting, magmatic liquids, and fluidization mechanisms rather than solid flow appear to have played major roles in the remobilization.

RELATIONS BETWEEN CHEMICAL COMPOSITION OF ROCKS AND LATER MAGMATIC HISTORY

Some fundamental correlations between the chemical composition of rocks and their late magmatic history are brought out by the proposed classification (table 2). Peridotites generally are either authigenic or allogenic, but some highly significant exceptions occur among the concentric complexes (Jackson and Thayer, 1972) and among bodies like the Katiniq and Dundonald sills (Thayer, 1972). Pyroxenites are abundant in authigenic and polygenic complexes, and are minor constituents of allogenic peridotite-gabbro plutons, particularly those of the harzburgite type. Gabbroic rocks are predominantly authigenic or polygenic, although allogenic gabbros are major components of many alpine-type complexes (Thayer,

Table 2.—Composition and relative abundance of authigenic, polygenic, and allogenic igneous rocks

Rock Type	Authigenic	Polygenic	Allogenic
Peridotitic	XX	X	XXX
Pyroxenitic	XX	X	x
Gabbroic-basaltic	XXX	XXX	X
Anorthositic	XXX	XX	x-X?
Dioritic-granitic	XX	XXX	?
Alkalic	XX	XXX	?

1967). Anorthosites appear to be mostly authigenic or polygenic (deWaard, 1968), but alkalic anorthosites of the Roseland type probably are allogenic (Herz, 1968; oral commun., 1971). Dioritic to granitic and all alkalic rocks appear to be authigenic or polygenic.

COMPLEXES AND ASSEMBLAGES

Just as the proposed classification recognizes a complete series of rocks from authigenic to allogenic, it also reveals an analogous broad spectrum of complexes and igneous assemblages. Few large complexes consist of rocks of only one of the three types, and the ophiolite assemblage comprises all three. The Great Dyke (Worst, 1960; Hughes, 1969) seems to consist of conformably layered authigenic cumulates. In the Stillwater and Bushveld Complexes the authigenic cumulates are cut by polygenic dikes and pipes that range from dunite to magnetite (Jones and others, 1960, p. 299; Willemse, 1969, p. 11) which apparently were formed at least partly by remobilization of early formed cumulates (Jackson, 1971). The Muskox intrusion (Irvine and Smith, 1967) may be different. Its feeder dike is polygenic, and the lower part of the layered series as well may be polygenic, if the intrusion mechanism of Bhattacharji and Smith (1964) is the correct one. In the Sudbury Irruptive the ore-bearing (polygenic) breccias clearly cut the main layered (authigenic) sequence (Souch and others, 1969; Naldrett and others, 1970).

Polygenic rocks exceed authigenic rocks volumetrically in many complexes. The Duluth Gabbro Complex consists of several obviously comagmatic but discordant intrusive units. Some units are at least partly cumulate (authigenic) but others are believed to have been intruded as (polygenic) crystal mushes (Taylor, 1964; Weiblen, 1965; Phinney, 1969). The McClure Mountain Complex in Colorado (Shawe and Parker, 1967; Parker and Sharp, 1970) consists mainly of alkalic polygenic rocks that range from pyroxenite to nepheline syenite and carbonatite, but also includes a probable authigenic layered sequence ranging from olivine to plagioclase and magnetite cumulates. The polygenic discordant intrusions appear to make up about three-quarters of the complex.

The ophiolite assemblage appears to be unique in containing rocks of all three categories. As now generally recognized, the ophiolite assemblage is a composite of volcanic and plutonic rocks that are believed to have formed as oceanic crust and

upper mantle (Thayer, 1969b; Moores, 1969; Davies, 1969; Coleman, 1971). Allogenic alpine-type peridotite and gabbro constitute the bulk of the plutonic component in most ophiolitic complexes (Thayer, 1967, p. 222). But in Papua, Davies (1969) has found (authigenic) cumulus peridotites above gneissic peridotites, and these grade up into a cumulus (authigenic) and noncumulus (authigenic and polygenic) gabbro section about 4 km thick. A cover of volcanic rocks (authigenic and polygenic) 4–6 km thick overlies the gabbro. In Cyprus (Gass, 1967) and in Canyon Mountain (Thayer and Himmelberg, 1968), the gabbros are gneissic and allogenic. Structural relations of dioritic and granophyric rocks that make up less than 10 percent of the plutonic component of the ophiolite assemblage (Thayer, 1967) indicate that they intruded the gabbro and volcanic rocks as fluid magmas or mushes, and so are authigenic or polygenic.

SUMMARY

Classification of igneous rocks as authigenic, polygenic, and allogenic according to their history of crystallization and emplacement reveals a continuous series ranging from those that crystallized in place from largely fluid magma to those that were emplaced by solid flow after primary crystallization. A broad spectrum of ultramafic and gabbroic complexes from stratiform to alpine also becomes evident, even within the ophiolitic volcanic-plutonic assemblage. The allogenic class comprises ultramafic to gabbroic or anorthositic rocks only, and ultramafic rocks in general are mostly authigenic or allogenic. Because magmatic ore deposits are formed during the late magmatic stages when the principal structures and textures of their hosts are also formed (Thayer, 1972), the classification may be useful to economic geologists.

REFERENCES

- Avé Lallemand, H. G., and Carter, N. L., 1970, Syntectonic recrystallization of olivine and modes of flow in the upper mantle: *Geol. Soc. America Bull.*, v. 81, p. 2203–2220.
- Beeson, M. H., and Jackson, E. D., 1970, Origin of the garnet pyroxenite xenoliths at Salt Lake Crater, Oahu: *Mineralog. Soc. America, Spec. Paper* 3, p. 95–112.
- Bhattacharji, S., and Smith, C. H., 1964, Flowage differentiation: *Science*, v. 145, p. 150–153.
- Carter, N. L., and Avé Lallemand, H. G., 1970, High temperature flow of dunite and peridotite: *Geol. Soc. America Bull.*, v. 81, p. 2181–2202.
- Coleman, R. G., 1971, Plate tectonic emplacement of upper mantle peridotites along continental edges: *Jour. Geophys. Research*, v. 76, p. 1212–1222.
- Davies, H. L., 1968, Papuan ultramafic belt: *Internat. Geol. Congress*, 23d, Prague, 1968, Rept., Sec. 1, p. 209–220.
- 1969, Peridotite-gabbro-basalt complex in eastern Papua—An overthrust plate of oceanic mantle and crust: *Stanford Univ. unpub. Ph. D. thesis*, 88 p.
- Den Tex, E., 1969, Origin of ultramafic rocks, their tectonic setting and history—A contribution to the discussion of the paper "The origin of ultramafic and ultrabasic rocks" by P. J. Wyllie: *Tectonophysics*, v. 7, p. 457–488.

- deWaard, Dirk, 1968, Annotated bibliography of anorthosite petrogenesis, in Isachsen, Y. W., ed., Origin of anorthosite and related rocks: New York State Mus. and Sci. Service, Mem. 18, p. 1-11 [1969].
- Dickey, J. S., Jr., 1970, Partial fusion products in alpine-type peridotites—Serrania de la Ronda and other examples: Mineralog. Soc. America Spec. Paper 3, p. 33-49.
- Emeleus, C. H., 1963, Structural and petrographic observations on layered granites from southern Greenland: Mineralog. Soc. America Spec. Paper 1, p. 22-29.
- Ferguson, J., and Pulvertaft, T. C. R., 1963, Contrasted styles of igneous layering in the Gardar province in south Greenland: Mineralog. Soc. America Spec. Paper 1, p. 10-21.
- Gass, I. G., 1967, The ultrabasic volcanic assemblage of the Troodos massif, Cyprus, in Wyllie, P. J., ed., Ultramafic and related rocks: New York, John Wiley & Sons, p. 121-134.
- Green, D. H., 1964, The petrogenesis of the high-temperature peridotite intrusion in the Lizard area, Cornwall: Jour. Petrology, v. 5, p. 134-188.
- 1967, High-temperature peridotite intrusions, in Wyllie, P. J., ed., Ultramafic and related rocks: New York, John Wiley & Sons, p. 212-222.
- Herz, Norman, 1968, The Roseland alkalic anorthosite massif, Virginia, in Isachsen, Y. W., ed., Origin of anorthosite and related rocks: New York State Mus. and Sci. Service Mem. 18, p. 357-368 [1969].
- Hughes, C. J., 1969, Major rhythmic layering in ultramafic rocks of the Great Dyke of Rhodesia, with particular reference to the Sebakwe area, in Visser, D. J. L., and Von Gruenewaldt, G., eds., Symposium on the Bushveld Igneous Complex and other layered intrusions: Geol. Soc. South Africa, Spec. Pub. 1, p. 584-609 [1970].
- Irvine, T. N., 1967, The Duke Island Ultramafic Complex, southeastern Alaska, in Wyllie, P. J., ed., Ultramafic and related rocks: New York, John Wiley & Sons, p. 84-97.
- Irvine, T. N., and Smith, C. H., 1967, The ultramafic rocks of the Muskox intrusion, Northwest Territories, Canada, in Wyllie, P. J., ed., Ultramafic and related rocks: New York, John Wiley & Sons, p. 38-49.
- Jackson, E. D., 1961, Primary textures and mineral associations in the ultramafic zone of the Stillwater Complex, Montana: U.S. Geol. Survey Prof. Paper 358, 106 p.
- 1971, The origin of ultramafic rocks by cumulus processes: Fortschr. Mineralogie, v. 48, p. 128-174.
- Jackson, E. D., and Thayer, T. P., 1972, Some criteria for distinguishing between stratiform, concentric, and alpine peridotite-gabbro complexes: Internat. Geol. Congress, 24th, Montreal, 1972. [In press].
- James, O. B., 1971, Origin and emplacement of the ultramafic rocks of the Emigrant Gap area, California: Jour. Petrology, v. 12, p. 523-560.
- Jones, W. R., Peoples, J. W., and Howland, A. L., 1960, Igneous and tectonic structures of the Stillwater Complex, Montana: U.S. Geol. Survey Bull. 1071-H, p. 281-340.
- Moore, J. G., and Lockwood, J. P., 1970, Geometry and genesis of Willow Lake-type banded rocks in the central Sierra Nevada, California [abs.]: Geol. Soc. America Abs. with Programs, v. 2, no. 2, p. 120-121.
- Moore, E. M., 1969, Petrology and structure of the Vourinos ophiolitic complex of northern Greece: Geol. Soc. America Spec. Paper 118, 74 p.
- Naldrett, A. J., Bray, J. G., Gasparrini, E. L., Podolsky, T., and Rucklidge, J. C., 1970, Cryptic variation and the petrology of the Sudbury Nickel Irruptive: Econ. Geology, v. 65, p. 122-155.
- Naldrett, A. J. and Gasparrini, E. L., 1972, Archean nickel sulfide deposits in Canada—Their classification, geological setting, and genesis with some suggestions as to exploration: Geol. Soc. Australia Special Pub. 3. [In press].
- Nicolas, A., 1969, Une vue unitaire concernant l'origine des massifs ultrabasiques des Alpes occidentales internes: Acad. Sci. Paris Comptes Rendus, v. 269, p. 1831-1834.
- Parker, R. L., and Sharp, W. N., 1970, Mafic-ultramafic igneous rocks and associated carbonatites of the Gem Park Complex, Custer and Fremont Counties, Colorado: U.S. Geol. Survey Prof. Paper 649, 24 p.
- Phinney, W. C., 1969, The Duluth complex in the Gabbro Lake quadrangle, Minnesota: Minnesota Geol. Survey Rept. Inv. 9, 20 p.
- Raleigh, C. B., 1963, Fabrics of naturally and experimentally deformed olivine: California Univ., Los Angeles, unpub. Ph. D. thesis, 215 p.
- 1968, Mechanisms of plastic deformation of olivine: Jour. Geophys. Research, v. 73, p. 5391-5406.
- Rost, F., 1968, Über die Fazieseinstufung orogentypischer Peridotite und ihre Beziehungen zur Peridotitischeale des Erdmantels: Internat. Geol. Congress, 23d, Prague, 1968, Rept., Sec. 1, p. 187-196.
- Shawe, D. R., and Parker, R. L., 1967, Mafic-ultramafic layered intrusion at Iron Mountain, Fremont County, Colorado: U.S. Geol. Survey Bull. 1251-A p. 1-29.
- Such, B. E., Podolsky, T., and geological staff of the International Nickel Co. of Canada, Ltd., 1969, The sulfide ores of Sudbury—Their particular relationship to a distinctive inclusion-bearing facies of the Nickel Irruptive, in Wilson, H. D. B., ed., Magmatic ore deposits: Econ. Geology Mon. 4, p. 252-261.
- Taubeneck, W. H., and Poldervaart, Arie, 1960, Geology of the Elkhorn Mountains, northeastern Oregon—Pt. 2, Willow Lake intrusion: Geol. Soc. America Bull., v. 71, p. 1295-1321.
- Taylor, R. B., 1964, Geology of the Duluth Gabbro Complex near Duluth, Minnesota: Minnesota Geol. Survey Bull. 44, 63 p.
- Thayer, T. P., 1960, Some critical differences between alpine-type and stratiform peridotite-gabbro complexes: Internat. Geol. Cong., 21st, Copenhagen, 1960, Rept., pt. 13, p. 247-259.
- 1967, Chemical and structural relations of ultramafic and feldspathic rocks in alpine intrusive complexes, in Wyllie, P. J., ed., Ultramafic and related rocks: New York, John Wiley & Sons, p. 222-239.
- 1969a, Gravity differentiation and magmatic re-emplacment of podiform chromite deposits, in Wilson, H. D. B., ed., Magmatic ore deposits: Econ. Geology Mon. 4, p. 132-146.
- 1969b, Peridotite-gabbro complexes as keys to petrology of mid-oceanic ridges: Geol. Soc. America Bull., v. 80, p. 1515-1522.
- 1972, Authigenic, polygenic, and allogenic ultramafic and gabbroic rocks as hosts for magmatic ore deposits: Geol. Soc. Australia Spec. Pub. 3. [In press].
- Thayer, T. P., and Himmelberg, G. R., 1968, Rock succession in the alpine-type mafic complex at Canyon Mountain, Oregon: Internat. Geol. Cong., 23d, Prague, 1968, Rept., Sec. 1, 175-186.
- Weiblen, P. W., 1965, A funnel-shaped, gabbro-troctolite intrusion in the Duluth complex, Lake County, Minnesota: Minnesota Univ. unpub. Ph. D. thesis, 161 p.
- Willemse, J., 1969, The geology of the Bushveld igneous complex, the largest repository of magmatic ore deposits in the world, in Wilson, H. D. B., ed., Magmatic ore deposits: Econ. Geology Mon. 4, p. 1-22.
- Wilson, H. D. B., Kilburn, L. C., Graham, A. R., and Ramlal, K., 1969, Geochemistry of some Canadian nickeliferous ultrabasic intrusions, in Wilson, H. D. B., ed., Magmatic ore deposits: Econ. Geology Mon. 4, p. 294-309.
- Worst, B. G., 1960, The Great Dyke of Southern Rhodesia: Southern Rhodesia Geol. Survey Bull., no. 47, 239 p.
- Wyllie, P. J., 1967, Petrography and petrology, in Wyllie, P. J., ed., Ultramafic and related rocks: New York, John Wiley & Sons, p. 1-7.

TERTIARY BASALTS IN THE FEATHER RIVER AREA, CALIFORNIA

By ANNA HIETANEN, Menlo Park, Calif.

Abstract.—Two petrologically different stratigraphic units of Tertiary basalt near the Feather River and its tributaries are correlative with the Miocene Lovejoy Basalt and the Pliocene olivine basalt of the Blairsden quadrangle to the east. Two-pyroxene andesites in the area were derived from the olivine basalt magma through crystallization differentiation during which mainly olivine was precipitated and the magma was enriched in silicon, aluminum, and alkalis, and depleted in magnesium, iron, and calcium. This trend is typical of fractionation of tholeiitic basalt at low pressures. Comparison of the chemistry of the Pliocene olivine basalt with that of the older Lovejoy Basalt shows lower contents of Fe, K, Na, Ti, P, Ba, and Zr, and higher contents of Mg, Ca, Ni, Co, Cr, and Co in the olivine basalt, suggesting that it originated at a different level and had a different history of ascent through the earth's crust.

Tertiary volcanic rocks cover much of the higher altitudes on ridges between the South Fork and the Middle Fork of the Feather River and their tributaries in the southwestern part of Plumas County (fig. 1). The best continuous exposures are in the northern part of the American House quadrangle, where the South Fork of the Feather River and the Fall River have cut deep gorges through horizontally lying Tertiary rocks and into several hundred feet of tightly folded pre-Tertiary metamorphic rocks underneath (Hietanen, 1971, fig. 1). Isolated occurrences of similar volcanic rocks in other parts of the Feather River area indicate a widespread Tertiary volcanic activity. Rocks in these isolated occurrences have features that allow correlation with rocks in the American House quadrangle, which were correlated with the Tertiary volcanic rocks in the Blairsden quadrangle and in areas farther northeast.

STRATIGRAPHY AND CORRELATION

Three petrologically different volcanic formations occur in a stratigraphic sequence in various parts of the Feather River area. The oldest of these is a black andesitic plagioclase-pyroxene basalt, the Lovejoy Formation of Durrell (1959a) or the Lovejoy Basalt of Durrell (1959b), which rests on either metamorphic rocks of Paleozoic age, Cretaceous plutonic rocks, or Eocene gravel. In the northeastern part of the American House quadrangle and the southeastern part of the Bucks Lake quadrangle (Hietanen, 1972), it is overlain by pyroclastic andesite, probably the Penman Formation of

Durrell (1959a). In a few localities, gray basalt rich in olivine either lies on the pyroclastic andesite (at Camel Peak) or forms pluglike bodies that have brecciated contacts with the metamorphic bedrocks. In the southern part of the Bucks Lake quadrangle, two-pyroxene basaltic andesite at Mount Ararat and hypersthene andesite at Table Mountain, both rocks with closely spaced horizontal jointing, occupy the same stratigraphic position as the olivine basalt at Camel Peak in the American House quadrangle. The basaltic andesite of Mount Ararat, as well as the olivine basalt at Camel Peak, was shown on the geologic map of the Bidwell Bar quadrangle by Turner (1898) as "late basalt." The age of all these stratigraphic units is still uncertain.

The age of the Lovejoy Basalt is disputed. According to Durrell (1959b), the geologic relations and fossil evidence at La Porte indicate a late Eocene to early Oligocene age. Durrell (1959b, p. 216) described clasts of Lovejoy Basalt in strata underlying a tuff at La Porte, which, according to Potbury (1935), contains late Eocene to early Oligocene flora. The potassium-argon age given by Dalrymple (1964) is younger: the maximum age of 23.8 m.y. obtained for plagioclase in the vitric tuff underlying the Lovejoy Basalt at Oroville South Table Mountain and the minimum age 22.2 m.y. for the overlying rhyolite suggest an early Miocene age for the Lovejoy.

No conclusive evidence to support either age was found during this work, but a black basalt older than the Lovejoy was found at one locality (loc. 1194, fig. 1) and pebbles presumably of this older basalt at two others (loc. 1369 and 1 mile to the south, fig. 1). Correlation and dating of this basalt would help set the maximum age for the Lovejoy in this area.

The "late basalt" of Turner (1898) in the Feather River area is the youngest volcanic unit resting on Durrell's (1959a) Penman Formation of Pliocene age. Similar olivine-rich "late basalt" of Turner in the Blairsden quadrangle to the east was correlated by Durrell (1959a) with the Warner Basalt of Russell (1928) in northeastern California. Durrell (1959a), also described an olivine-free phase of the basalt that he believed to be the Warner in the Blairsden quadrangle and suggested that the pyroxene andesite mapped by Turner (1898) is this phase of the Warner. In the Feather River area the olivine basalt was extruded from isolated local vents, which makes the correla-

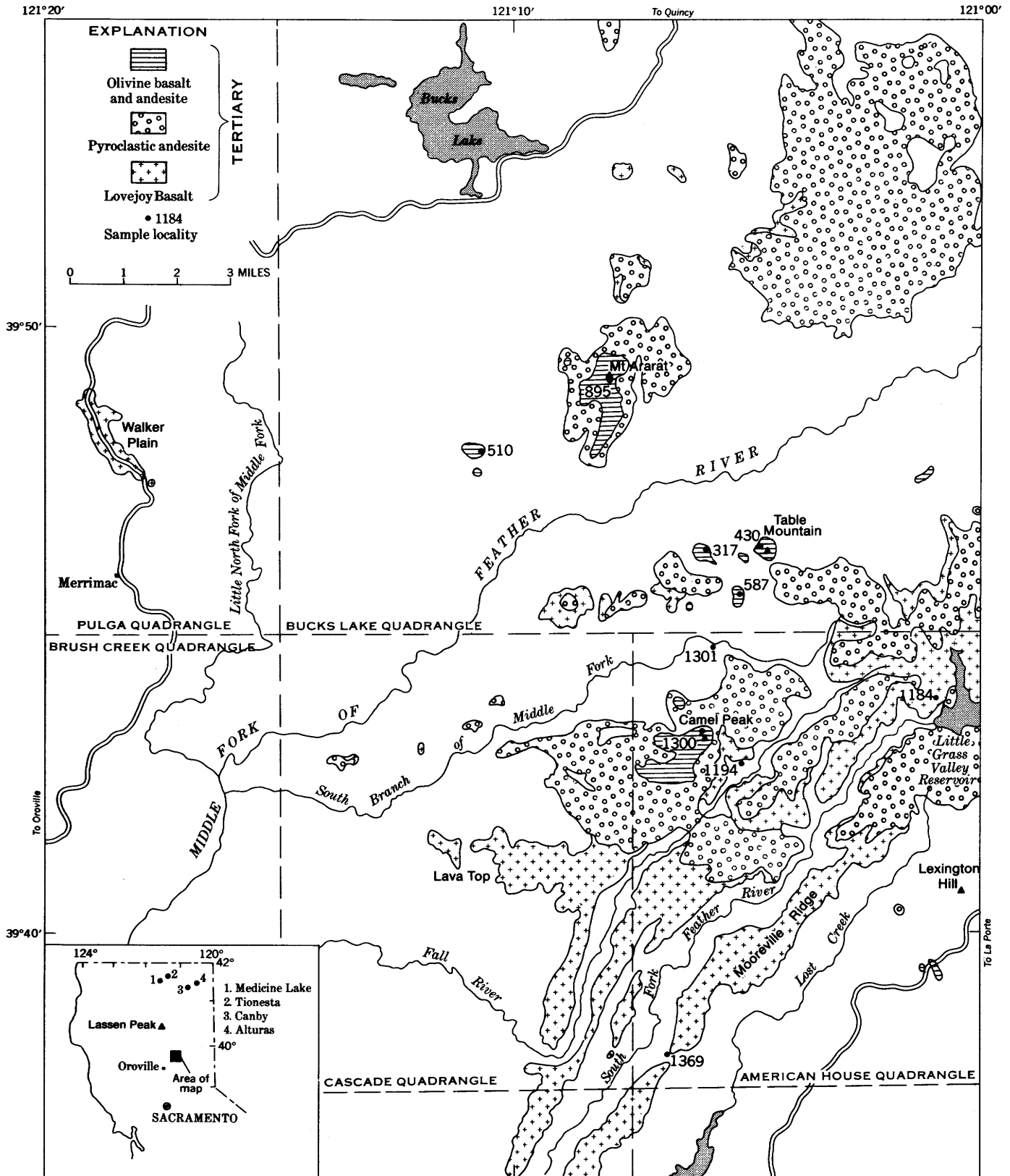


Figure 1.—Sketch map showing distribution of Tertiary volcanic rocks in the Feather River area. Index map of northern California shows the study area and localities referred to in text.

tion uncertain. Similarity in general appearance and texture and grossly similar age may indicate a common origin.

The age of the Warner Basalt of Russell (1928) is not accurately determined. Anderson (1941) suggested a Pliocene age in the Medicine Lake Highland, recognizing that it is younger than early Pliocene and may be as young as early Pleistocene. A late Pliocene age for the Warner Basalt was suggested by Durrell (1959a, 1966) on the basis of its relation to the upper Pliocene Tuscan Formation (Anderson, 1933). Macdonald (1966) has pointed out that the Warner Basalt in northeastern California includes flows that range from Miocene to Pleistocene in age and that may differ also in their chemistry.

VOLCANIC ROCKS OLDER THAN THE LOVEJOY BASALT

A small outcrop of black basalt is exposed in a roadcut about 1 mile southeast of Camel Peak (loc. 1194). It is bordered by metadiorite on either side, and the Lovejoy Basalt is exposed at higher altitude in the north. This basalt resembles the overlying Lovejoy in its black color, fine grain size, and blocky weathering. The texture and mineralogy of the two basalts, however, are different. The basalt at locality 1194 contains numerous euhedral labradorite and augite phenocrysts, 1–2 mm long, and a few small olivine phenocrysts in a fine-grained groundmass consisting of small grains of augite, plagioclase, magnetite, and interstitial glass. Some of the pyroxene phenocrysts are altered in part to light brown or green mica that has bright interference colors. Clay minerals occur along the cracks. Similar basalt in a highly weathered state occurs in a conglomerate (fig. 2) that is exposed under the Lovejoy Basalt on Mooreville Ridge (loc. 1369 and 1 mile to the south) in the southwestern corner of the American House quadrangle and the northwestern corner of the Strawberry Valley quadrangle. The pebbles are 4–12 cm long, round or ellipsoidal, and consist of basalt that contains numerous large, stubby phenocrysts of plagioclase and some phenocrysts of olivine and pyroxene in a groundmass of glass and small crystals of magnetite. Most of the phenocrysts and glass are altered to clay minerals.

LOVEJOY BASALT

The Lovejoy Basalt caps long narrow ridges in the American House quadrangle and extends from there to the western part of the Cascade quadrangle and to the southern part of the Bucks Lake quadrangle (fig. 1). The number of flows and total thickness of the formation change regularly. Six flows are exposed along the South Fork of the Feather River southwest of the Little Grass Valley reservoir, where the total thickness is 580 feet. The number of flows and the total thickness decrease toward the southwest and the north. In the southwest corner of the American House quadrangle, only three flows, each about 100 feet thick, are exposed on Mooreville Ridge



Figure 2.—Conglomerate containing pebbles of porphyritic basalt, exposed under the Lovejoy Basalt on Mooreville Ridge 0.4 mile west of Boehme Ranch (loc. 1369).

between the South Fork of the Feather River and Lost Creek. On Lava Top, in the central part of the Cascade quadrangle, where basalt rests on the Cascade pluton, the total thickness is about 200 feet. Only one flow, about 100 feet thick, is exposed on the canyon walls in the southeastern part of the Bucks Lake quadrangle, where basalt rests on pre-Tertiary rocks and is covered by pyroclastic andesite.

Aerial photographs of the outcrops along the South Fork of the Feather River below the Little Grass Valley reservoir show that the thinning of the Lovejoy Basalt toward the southwest is not due to erosion alone, for some of the flows extend only a short distance below the dam. One of the lower flows, presumably the second, extends only 1 mile southwest of the dam, and the fifth thins out half a mile farther southwest. Erosion removed the sixth flow about 1 mile farther southwest, where the total thickness on Mooreville Ridge is about 300 feet. The source must therefore have been in the east, as Durrell (1959b) has suggested.

Another significant feature is the regular change in the altitude of the lower contact. In the southeastern part of the Bucks Lake quadrangle, the lower contact is at about the 5,200-foot contour line; near Little Grass Valley, it is at the 5,100 foot contour; and it occurs at progressively lower altitudes toward the southwest. In the southeastern corner of the Cascade quadrangle, about 10 miles from the Little Grass Valley, the lower contact of the Lovejoy Basalt is at 4,100 feet, 1,000 feet lower than at the dam of the Little Grass Valley reservoir. This difference in altitudes indicates a slope of about one degree for the lower contact along the South Fork of the Feather River. A slope such as this must have existed at the

time of the eruption in order to account for the westward flowage of the basalt over long distances.

The individual flows form steep slopes or cliffs and either have columnar joints or break into irregular blocks 10–15 cm in diameter. Talus at the foot of the cliffs covers the lower contact. The tops of flows form terraces along the canyons. These terraces, as well as the flat tops of the uppermost flows, are covered by talus that supports only a meager vegetation that contrasts with the densely timbered and brush-covered slopes elsewhere.

The basalt in all flows seems homogeneous and much alike; it is black and fine grained and has a few small scattered or clustered olivine phenocrysts. Small widely spaced vesicles are common; a few outcrops have many large (1–2 cm) vesicles. Thin sections show that the black color is imparted by magnetite that occurs as small euhedral to subhedral crystals in the holocrystalline parts of the flows, but is disseminated or dendritic in the groundmass of the fine-grained rock.

The holocrystalline basalt consists of plagioclase (An_{50}), augite, magnetite, and some olivine. Plagioclase laths are 0.2–0.5 mm long, oriented at random or subparallel to the flow structure. Augite is in subhedral crystals 0.1–0.5 mm long or in equant interstitial grains. Olivine crystals are 0.1–0.5 mm long and subhedral. Magnetite crystals (0.05–0.5 in size) are scattered evenly through the rock. In some thin sections, grain size is larger; plagioclase laths are up to 1 mm long, augite is in interstitial equant grains, 0.3–0.6 mm in diameter; magnetite crystals are clustered.

In the very fine grained basalt, most of the groundmass and interstitial glass is black from disseminated magnetite. Where crystallization has proceeded further and where the groundmass is devitrified, magnetite forms dendritic crystals. There is every gradation from the opaque black groundmass, through glass with dendritic magnetite and small grains of augite, to holocrystalline groundmass with crystals of magnetite and subhedral augite. The habit of the magnetite is closely associated with the grain size and degree of crystallization of the groundmass, as both reflect the rate of cooling of the lava. Slow cooling, which is common in most of the thick flows and in flows that came in rapid succession, allows complete crystallization, whereas rapid cooling, which is characteristic of the top parts of the flows, produces a glassy groundmass with disseminated magnetite. Celadonite occurs in some thin sections and amygdules of calcite or hematite and goethite in others. Apatite in slender prisms is included in interstitial augite and glass.

Chemical analysis of the common fine-grained basalt that has a black groundmass and contains sparse small olivine crystals is shown in table 1 (under specimen 1184). Silica content is higher than is common in basalts with normative olivine and magnesium content lower. Catanorm shows about 3 percent quartz, 11 percent orthoclase, 50 percent plagioclase (An_{40}), 10 percent augite, and 16 percent hypersthene, making the Lovejoy Basalt an andesitic pyroxene basalt rather

Table 1.—*Chemical analyses of Tertiary basalts, Feather River area, California*

[Chemical analyses of specimens 1184, 510, 1300, and 895 by G. O. Riddle; specimen 430 by V. C. Smith. Spectrographic analyses of specimens 118, 510, 1300, and 895 by J. C. Hamilton; specimen 430 by Harriet Neiman]

Rock name	Lovejoy Basalt	Olivine basalt	Basaltic andesite	Hypersthene andesite	
Location	0.5 mile northwest of Little Grass Reservoir	North Branch of Catrell Creek	Camel Peak	Mount Ararat	Table Mountain
Specimen No.	1184	510	1300	895	430
Composition (weight percent)					
SiO ₂	50.42	48.17	50.28	57.21	61.16
Al ₂ O ₃	13.98	14.83	14.63	18.15	18.53
Fe ₂ O ₃	3.39	2.66	5.05	2.11	2.59
FeO	9.16	6.82	4.32	4.64	2.89
MnO24	.18	.22	.15	.13
MgO	4.18	12.83	9.56	4.05	1.91
CaO	7.68	10.47	11.02	7.14	6.34
Na ₂ O	3.18	2.26	2.13	3.46	3.82
K ₂ O	1.84	.60	.83	1.35	1.30
TiO ₂	2.53	.76	.63	.57	.44
P ₂ O ₅	1.14	.14	.16	.26	.32
CO ₂01	0	.0103
Cl01
F03
H ₂ O+	1.23	.15	.69	.39	.11
H ₂ O-40	.17	.38	.42	.22
Total	99.38	100.04	99.91	99.90	99.83
Less O01
					99.82
Composition (cation percent)					
SiO ₂	48.87	43.92	47.00	53.49	57.25
AlO _{3/2}	15.97	15.93	16.12	20.00	20.44
FeO _{3/2}	2.47	1.82	3.55	1.48	1.82
FeO	7.43	5.20	3.38	3.63	2.26
MnO20	.14	.17	.12	.10
MgO	6.04	17.44	13.32	5.64	2.67
CaO	7.98	10.23	11.04	7.15	6.36
NaO _{1/2}	5.98	3.99	3.86	6.27	6.93
KO _{1/2}	2.28	.70	.99	1.61	1.55
TiO ₂	1.84	.52	.44	.40	.31
PO _{5/2}94	.11	.13	.21	.25
CO ₂010104
Cl	(.02)
F	(.09)
OH	(7.95)	(.91)	(4.30)	(2.43)	(.69)
Total	100.01	100.00	100.01	100.00	99.98
Anions	161.21	151.59	157.20	162.20	165.32
Catanorm (molecular percent)					
Q	3.27	1.35	8.73	16.24
Or	11.38	3.49	4.95	8.05	7.76
Ab	29.88	19.97	19.30	31.36	34.59
An	19.30	28.11	28.17	30.29	29.48

Table 1.—*Chemical analyses of Tertiary basalts, Feather River area, California—Continued*

[Chemical analyses of specimens 1184, 510, 1300, and 895 by G. O. Riddle; specimen 430 by V. C. Smith. Spectrographic analyses of specimens 118, 510, 1300, and 895 by J. C. Hamilton; specimen 430 by Harriet Neiman]

Rock name	Lovejoy Basalt	Olivine basalt	Basaltic andesite	Hypersthene andesite	
Location	0.5 mile northwest of Little Grass Reservoir	North Branch of Catrell Creek	Camel Peak	Mount Ararat	Table Mountain
Specimen No.	1184	510	1300	895	430
Catanorm (molecular percent)—Continued					
Co18
Wo	5.09	8.85	10.36	1.50
En	12.08	11.44	26.64	11.29	5.33
Fs	9.08	2.56	2.66	5.21	2.29
Fo	17.57
Fa	3.94
Mt	3.71	2.74	5.33	2.23	2.74
Il	3.69	1.04	.89	.80	.62
Ap	2.49	.29	.34	.55	.68
Cc	.030308
Hi03
Fl01
Total	100.00	100.00	100.00	100.00	100.02
Spectrographic analysis (parts per million)					
Ba	2,100	260	390	600	780
Co	22	41	42	22	10
Cr	12	1,100	840	85	10
Cu	31	61	75	64	16
Ga	25	14	22	24	21
Ni	9	220	140	32	6
Sc	43	42	54	28	12
Sr	370	350	1,100	520	690
V	290	250	410	190	100
Y	50	30	70	20	20
Yb	5	2	5	3	3
Zr	140	50	70	120	150



Figure 3.—Concentric columnar jointing in a small cone in the olivine basalt a mile west of Table Mountain, Bucks Lake quadrangle (loc. 317)

cone-shaped occurrence at the headwaters of Dejonah Creek (loc. 317). The basalt at Camel Peak has a well-developed horizontal flow structure that is paralleled by closely spaced joints. The thickness of the olivine basalt at Camel Peak, where a cone-shaped hill rises above the surrounding level area, is more than 400 feet. On the level area, it is 250 feet.

The plugs are clearly local vents. They have vertical contacts, and a powdery microbreccia, 10 m thick, separates them from the surrounding metamorphic rock. Horizontal flow structure that is conspicuous at Camel Peak is absent in the plugs. The basalt of the plugs has a medium- to light-gray groundmass that is studded with fresh light-olive-green to light-yellowish-brown euhedral olivine phenocrysts, about 2 mm long. In contrast, the phenocrysts in the flows at Camel Peak are brown olivine and green augite, in equal amounts.

Thin sections show that the outer layer of the olivine phenocrysts at Camel Peak is altered to reddish-brown iddingsite, whereas the olivine in the plugs is unaltered. In a small plug at Catrell Creek, its indices of refraction are $\alpha=1.690\pm 0.001$, $\beta=1.770\pm 0.001$, and $\gamma=1.725\pm 0.001$, indicating a composition of $Fe_{0.7}Fa_{2.7}$. The groundmass is fine grained and consists of augite, plagioclase (An_{58-60}), and magnetite in slightly varying amounts. Augite is in small subhedral to anhedral grains among the plagioclase laths, which in places are subparallel to the flow structure. Magnetite is in small euhedral to round corroded crystals. Interstitial glass dusted with microlites is common. Texture is at places diktytaxitic.

Chemical analyses show that the basalt in the plugs at Catrell Creek (table 1, specimen 510) is similar to that at Camel Peak (specimen 1300) except for a lower percentage of SiO_2 and higher percentage of MgO in the plugs resulting in normative olivine. No olivine appears in the norm of the rock from Camel Peak, partly because of the high degree of oxidation of iron, resulting in high percentage of normative magnetite. The percentage of Al_2O_3 is lower than 15; this, together with a

than olivine basalt. In Kuno's (1960, p. 137) diagrams, it plots on the borderline between the tholeiite and alkali basalt fields.

OLIVINE BASALT

The largest exposure of gray olivine basalt in the study area is at Camel Peak and its vicinity in the northwestern part of the American House quadrangle. Small pluglike bodies occur to the north in the southern part of the Bucks Lake quadrangle. All occurrences consist of gray basalt that contains numerous euhedral phenocrysts of light-olive-green to light-brown or reddish-brown olivine and green augite. The basalt is cut by joints that bound thick columns, vertical at Camel Peak and in most of the plugs, but concentric (fig. 3) in a small

low alkali content, indicates that these basalts are tholeiitic in composition. Both analyses fall within the tholeiite field in Kuno's (1960, p. 137) diagrams. The olivine basalt at the headwaters of Dejonah Creek (loc. 317) has more plagioclase and less pyroxene than these two analyzed samples, being richer in Al_2O_3 and alkalis. Conversely, basalt in a small occurrence south of Table Mountain (loc. 587) has less plagioclase and more mafic constituents than in any other occurrence.

Two dikes of olivine basalt, 6 and 15 feet thick, cut the metavolcanic rocks in the streambed of the South Branch of the Middle Fork of the Feather River 2 miles north of Camel Peak (loc. 1301). Basalt in these dikes has features characteristic of the olivine basalt at Camel Peak: It is light gray and has a columnar jointing and a platy fracture perpendicular to the columns. The platy fracture is parallel to the walls of the dikes. The columns are perpendicular to the walls and thus perpendicular to the flowage and the cooling surface, as is common in the flows.

Comparison of the olivine basalt in the Feather River area with the Warner Basalt of Russell (1928) in the northeastern California shows many similarities in general appearance, texture, and mineralogy between these two Pliocene basalts. Certain differences, however, are apparent in the chemical composition, suggesting differences in the history of fractionation. The Warner Basalt in the Medicine Lake Highland, northeastern California, is described by Anderson (1941) as a light-gray rock that contains yellowish-green crystals of olivine ($Fe_{0.8}Fe_{1.8}$) in a network of plagioclase (An_{65-70}) laths. A specimen from a locality half a mile north of the Tionesta railroad station, kindly provided by K. J. Murata, has small round olivine crystals euhedral against the plagioclase laths, which are 0.5–1 mm long and are oriented at random. Pyroxenes fill the interstices between the plagioclase laths. A small amount of interstitial iron ore is common. Chemical analyses of specimens collected from this locality and from near Little Sand Butte, Medicine Lake Highland given by Yoder and Tilley (1962, table 2, analyses 16 and 17) show more than 18 percent Al_2O_3 , typical of the composition of high-alumina basalts, whereas the basalt in the Feather River area has less than 15 percent Al_2O_3 .

TWO-PYROXENE ANDESITES

Two small areas in the southern part of the Bucks Lake quadrangle are capped by light-gray equigranular volcanic rocks composed mainly of plagioclase, hypersthene, augite, and some magnetite. These rocks contain little if any olivine and have more plagioclase than the olivine basalt. They are andesitic in composition and probably represent silicic differentiates of the olivine basalt. At Table Mountain more than 300 feet of this rock rests on metavolcanic rocks. A photograph of the closely spaced horizontal parting in this light-gray hypersthene andesite is shown by Turner (1898, fig. 5). At Mount Ararat a thickness of about 400 feet of basaltic

pyroxene andesite overlies the andesite mudflow breccia of Durrell's (1959a) Penman Formation, thus occupying the same stratigraphic position as the olivine basalt at Camel Peak. Moreover, the gray color and some of the structural features, such as columnar jointing and closely spaced horizontal jointing, make this basaltic andesite appear much like the olivine basalt. Their mineralogy and texture, however, are different: the basaltic andesite at Mount Ararat consists of plagioclase (An_{50}), orthopyroxene, clinopyroxene, magnetite, and a few small grains of olivine. The texture is aphyric. The chemical analysis (table 1, specimen 895) shows a much higher percentage of silicon, aluminum, and alkalis, and lower percentage of iron, magnesium, and calcium than the olivine basalt. The cation norm shows 8.7 percent quartz and 70 percent plagioclase. The hypersthene andesite at Table Mountain is even more silicic, having 16 percent normative quartz (table 1, specimen 430). This rock consists mainly of laths of plagioclase (An_{46}), prisms of orthopyroxene and clinopyroxene, and some grains of magnetite.

CHEMICAL COMPOSITION

Comparison of the chemical analyses of the Lovejoy Basalt (table 1, specimen 1184) with those of the olivine basalt and its postulated differentiates (specimens 510, 1300, and 895) shows that the Lovejoy Basalt is richer in iron, titanium, potassium, and phosphorus, and is considerably poorer in magnesium. The hypersthene andesite on Table Mountain (specimen 430) shows features similar to those of olivine basalt and basaltic andesite except that it has more quartz and alkalis. These chemical relations can be best illustrated by various ternary diagrams (figs. 4 and 5).

The normative amounts of quartz, albite, and orthoclase in ionic percentages are shown in figure 4. The points for the olivine basalt (specimens 510 and 1300), basaltic andesite (specimen 895), and hypersthene andesite (specimen 430) lie along a smooth curve, the hypersthene andesite representing the silicic end member of the differentiation series in which the olivine-rich basalt in the plug at Catrell Creek is the mafic end member. The point for the Lovejoy Basalt lies toward the Or corner from this differentiation curve, indicating a higher potassium content in the Lovejoy. Plotted in the same diagram for comparison are analyses of Warner Basalt from near Little Sand Butte and from near Tionesta railroad station in the Timber Mountain quadrangle, northeastern California (Yoder and Tilley, 1962, table 2, analyses 15, 16, and 17) and the analyses given by Kuno (1965, table 3, analyses 6A–6D, and table 5, analyses 7A and 7B) for Warner Basalt 6 km (3.7 miles) northeast of Alturas and for olivine andesite 45 km (28 miles) southwest of Canby. The analysis point for the olivine basalt from Catrell Creek (specimen 510) is close to the points for Warner Basalt from near Tionesta and from near Alturas, indicating that the quartz-feldspar ratios in the basalts from these three localities are similar. The analyses of the two-pyroxene andesites in the Bucks Lake quadrangle (specimens

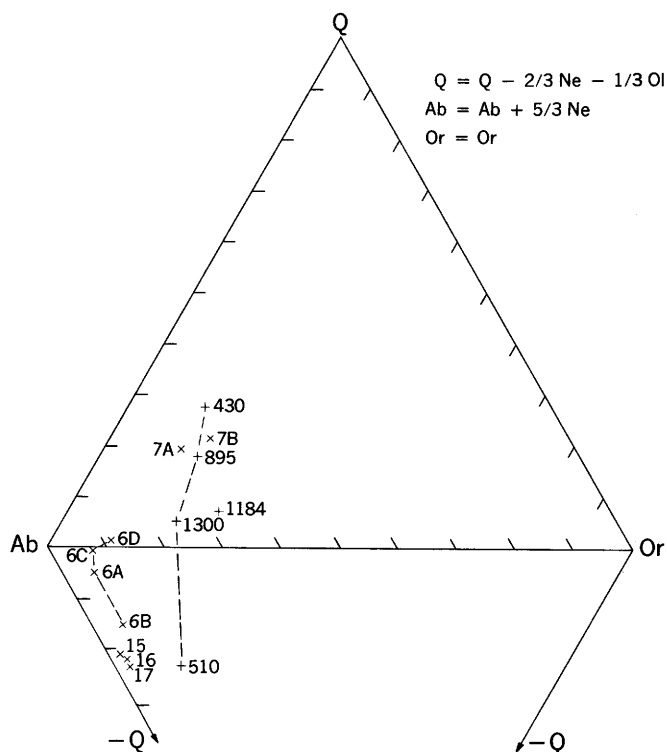


Figure 4.—Q-Ab-Or diagram showing normative amounts of quartz, albite, and orthoclase in molecular percentages in the olivine basalt and its differentiates. Analyses for points 510, 1300, 895, and 430 are in table 1. Analysis points for the Lovejoy Basalt (specimen 1184) and those for Anderson's (1941) Warner Basalt were added for comparison. Of the Warner Basalt, analyses points 15, 16, and 17 are from Yoder and Tilley (1962, table 2), and analyses points 6A, 6B, 6C, 6D, 7A and 7B are from Kuno (1965, tables 3 and 5).

895 and 430) show quartz-feldspar ratios similar to those of the olivine andesite near Canby that according to Kuno (1965) was probably derived from the same source as the high-alumina basalt magma.

The Ab-Or-An diagram (fig. 5A) shows that the olivine basalt (specimens 510 and 1300) has a higher normative anorthite content than the basaltic andesite (specimen 895) and the hypersthene andesite (specimen 430). The normative feldspar in the Lovejoy Basalt contains less anorthite and more albite and orthoclase than even the hypersthene andesite (specimen 430). The analyses of the Warner Basalt from the localities in northeastern California plot near the basalt from Catrell Creek. The olivine andesite near Canby plots near the two-pyroxene andesites in the Feather River area, whereas the segregation vein in the Warner Basalt (analyses 6C and 6D) is richer in normative albite.

In the QFM diagram (fig. 5B) all analyses plot close to the F-M line, indicating that the normative quartz is low in all samples from the Feather River area as well as those from northeastern California. The differentiation of the olivine basalt in the Feather River area is indicated by the increasing amount of feldspars and decreasing amount of mafic constitu-

ents from specimen 510, through specimens 1300 and 895, to specimen 430. In this diagram, the point for the Lovejoy Basalt (specimen 1184) is in the central part of the curve drawn for the olivine basalt. All points for the Warner Basalt from northeastern California are clustered toward the F-M side from the curve and toward the F corner from points for specimens 510 and 1300, indicating a slightly higher feldspar content. The olivine andesite from near Canby has QFM ratios similar to the basaltic andesite (specimen 895) from Mount Ararat.

Differentiation of the olivine basalt is well demonstrated by atomic ratios of the major elements, as shown in Figures 5C through 5F. In each of these ternary diagrams, a smooth curve can be drawn from the mafic end member (specimen 510) through intermediate members (specimens 1300 and 895) to the silicic end member (specimen 430). Specimens 510 and 1300 contain considerably more total iron, magnesium, and calcium, and less aluminum and alkalis than do the silicic differentiates specimens 895 and 430 (fig. 5C). Although a notable decrease in the magnesium content is shown by the Alk-Fe-Mg and Ca-Fe-Mg diagrams (figs. 5D and 5E), the amount of iron in relation to magnesium and alkalis (fig. 5D) stays remarkably uniform. Only a small increase in potassium in relation to sodium and calcium is indicated by the Na-K-Ca diagram (fig. 5F). The major changes during the differentiation of the olivine basalt were an increase in the silicon and sodium content and decrease in the magnesium and calcium content.

In each ternary diagram (figs. 5C-5F) the Lovejoy Basalt plots outside the curve for the olivine basalt-andesite series, indicating differing chemical characteristics. In figures 5D and 5E, it plots toward the Fe corner from the central part of the curve for the olivine basalt-andesite series, indicating a higher iron content. The Na-K-Ca diagram (fig. 5F) indicates a higher potassium content. If compared with the olivine basalt specimen 1300, which has a similar Si content, these differences are accentuated and the higher sodium content of the Lovejoy Basalt becomes noticeable (fig. 5F).

The degree of oxidation of the iron in the basalt flow at Camel Peak is much higher ($\text{Fe}^{+3}/\text{Fe}^{+2} + \text{Fe}^{+3} = 0.512$) than it is in the basalt from the pluglike occurrence on Catrell Creek, where $\text{Fe}^{+3}/\text{Fe}^{+2} + \text{Fe}^{+3} = 0.259$. The same iron ratio in specimen 895 is 0.290, that in specimen 430, 0.446. The Lovejoy Basalt has a lower degree of oxidation of iron (0.249) than any of the specimens of the olivine basalt or andesites.

The analyses points (15, 16, 17, 6A, and 6B) for the Warner Basalt from northeastern California are clustered near the point for the olivine basalt at Camel Peak (figs. 5C-5F), and the olivine andesite from southwest of Canby plots near the two-pyroxene andesite (specimen 895) from Mount Ararat, indicating similarity in the trends of magmatic differentiation. The points for the segregation veins in the Warner Basalt, especially for its central part (analysis point 6D), fall outside the curve, indicating a different trend of differentiation. This is especially noticeable in the Alk-Fe-Mg and Ca-Fe-Mg

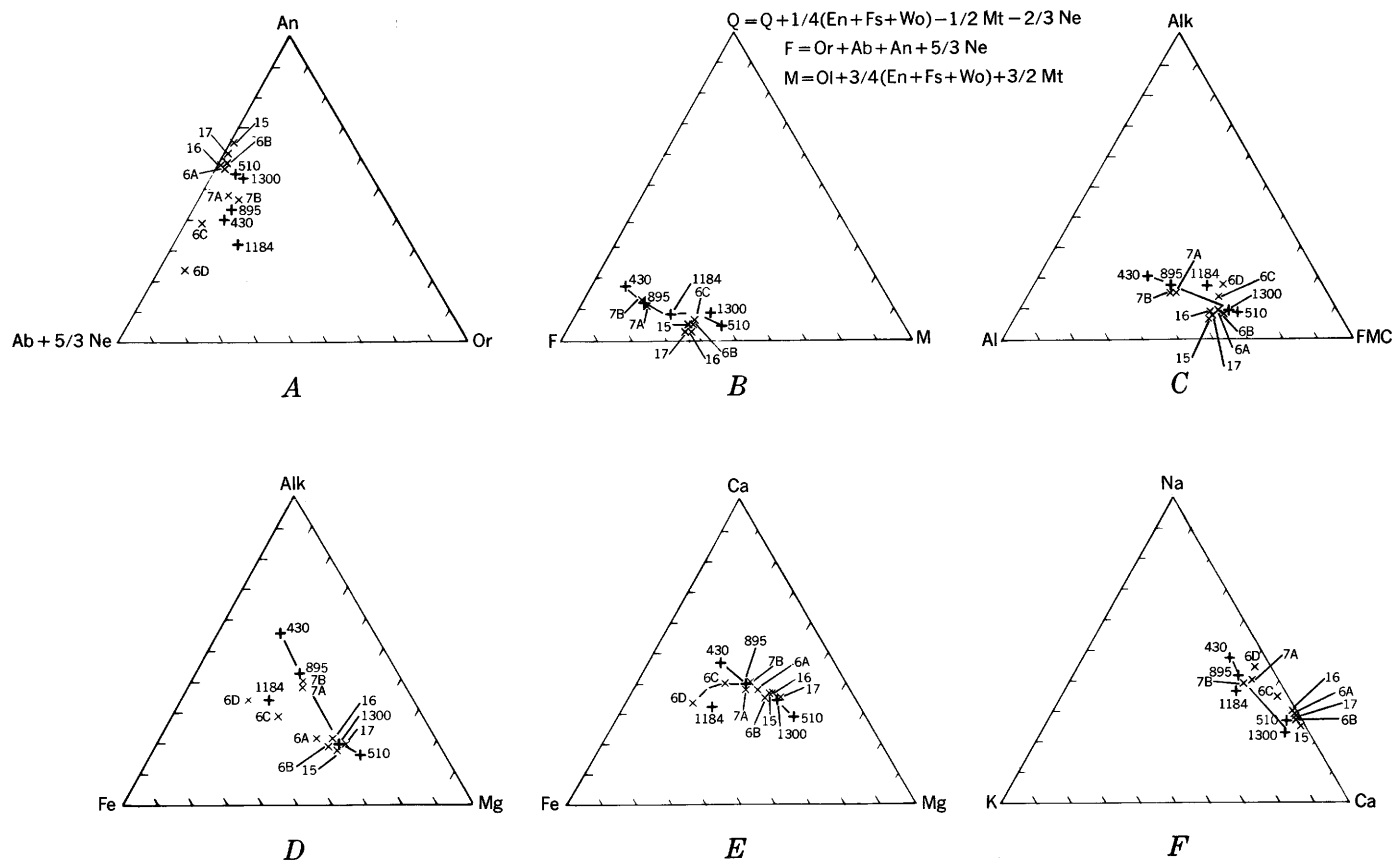


Figure 5.—Ternary diagrams showing variation in composition of the olivine basalt and its differentiates in ionic percentages. For key to specimen and analysis numbers see caption of figure 4.

- A. Normative orthoclase (Or), albite plus nepheline ($Ab + 5/3 Ne$), and anorthite (An).
- B. Normative quartz (Q), feldspar (F), and mafic minerals as nesosilicates (M).
- C. Sodium plus potassium (Alk), aluminum (Al), and combined total iron, manganese, magnesium, and calcium (FMC).
- D. Sodium plus potassium (Alk), total iron plus manganese (Fe), and magnesium (Mg).
- E. Calcium (Ca), total iron plus manganese (Fe), and magnesium (Mg).
- F. Sodium (Na), potassium (K), and calcium (Ca).

diagrams (figs. 5D–5E), where the trend line for the vein deviates considerably from that drawn for the magmatic differentiation. The segregation veins are enriched in normative albite rather than in quartz and orthoclase (figs. 4 and 5A), and they are enriched in iron rather than in alkalis and calcium (figs. 5D and 5E).

TRACE ELEMENTS

Results of quantitative spectrographic analyses are given in table 1 and shown graphically against the SiO_2 content in figure 6. In this figure, the points for the olivine basalt and its differentiates are connected by lines. The regularity in the change of the concentration of the trace elements with the increasing silica content is well demonstrated by the regularity of the curves. Concentration of Ni and Cr is highest in the olivine basalt and decreases rapidly toward the basaltic andesite and andesite. Trend lines for Zr and Ba are opposite to this pattern, showing increasingly higher concentrations

toward the silicic members. V, Cu, Co, Sc, and Y show the highest concentration in the basalt at Camel Peak (specimen 1300) and increasingly lower concentrations toward the silicic members and toward the mafic end member (specimen 510). Sr shows the highest concentration in specimen 1300, which has the highest Ca content (table 1). A specimen of high-alumina basalt from near Tionesta (T in fig. 6) has about the same or only a little lower contents of Cu, Ni, Zr, Sc, Ga, and Y as the olivine basalt in the Feather River area. The contents of Cr, Sr, and Ba are, however, much lower.

The trace-element content of the Lovejoy Basalt differs considerably from the trends for the olivine basalt. The concentration of Ni, Co, Cr, and Cu is much lower than in the intermediate and basic members of the olivine basalt-andesite series, and the concentration of Zr and especially of Ba is much higher. These deviating patterns for the concentration of trace elements confirm the chemical dissimilarity of the Miocene Lovejoy Basalt and the Pliocene olivine basalt.

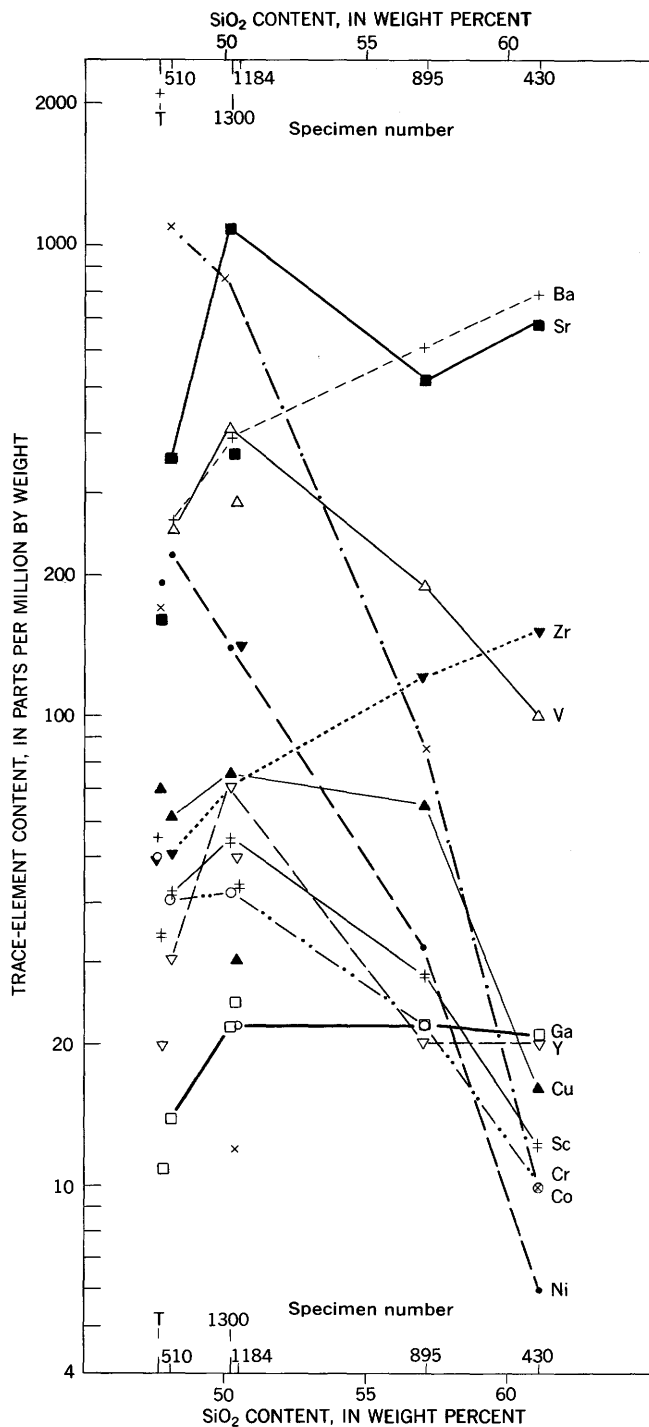


Figure 6.—Trace elements in the olivine basalt and its differentiates and in the Lovejoy Basalt. Specimen numbers refer to table 1. T is a specimen from near Tionesta.

CONCLUSIONS

Similarity of structure, texture, chemical composition, and trace-element content indicates that the Pliocene olivine basalt at Camel Peak and in plugs in the southern part of the Bucks

Lake quadrangle, the basaltic andesite at Mount Ararat, and the hypersthene andesite at Table Mountain are differentiates of the same magma, a tholeiitic basalt. Comparison of the chemical composition of this basalt with that of the Warner Basalt in northeastern California (Yoder and Tilley, 1962; Kuno, 1965) shows that the olivine basalt in the Feather River area contains less aluminum than does the high-alumina phase of the Warner Basalt and therefore cannot be directly correlated with it. In the Feather River area the more silicic derivatives—the basaltic andesite and the hypersthene andesite—were formed through a normal crystallization differentiation of the olivine basalt magma. This is mineralogically demonstrated by gradual decrease in the number of olivine crystals, increase in the percentage and change in the composition of plagioclase, and chemically shown by the decrease in magnesium, calcium, and iron, and the increase in silicon, sodium, and aluminum toward the silicic end member, the hypersthene andesite. The regular change of the trace-element concentrations with the silica content supports the hypothesis of the crystallization differentiation. This type of fractionation is, according to Green, Green, and Ringwood (1967), typical of tholeiitic magma at low pressures; or it may occur during its uninterrupted ascent to the surface (O'Hara, 1965).

The olivine andesite south of Canby (Kuno, 1965, p. 308–309) is chemically and mineralogically similar to the two-pyroxene andesite at Mount Ararat in the Bucks Lake quadrangle, suggesting a similar history of fractionation. Kuno has suggested that this olivine andesite was derived from the same parent magma as the high-alumina Warner Basalt. All these rocks, including the olivine basalt in the Feather River area, may have originated in the same parent magma, the differences in the chemical composition resulting from differences in the history of ascent of the magma to the surface. According to the model of O'Hara (1965) and the experimental work of Green, Green, and Ringwood (1967) and Green and Ringwood (1967), silica-saturated tholeiitic composition is a result of an uninterrupted ascent or of fractionation of magma at low pressures, whereas the high-alumina basalt magma is formed through interruption in ascent and fractionation at intermediate pressures.

The Lovejoy Basalt differs chemically and mineralogically from the derivatives of the olivine basalt and has a different trace-element content. This older basalt must have originated in a different magma chamber, perhaps at a different (higher) level in the earth's crust. The major differences are higher content of iron, potassium, sodium, titanium, phosphorus, barium, and zirconium and noticeably lower content of magnesium, calcium, nickel, cobalt, chromium, and copper in the Lovejoy.

The crystallization differentiation in the surface flows after eruption, as indicated by the composition of segregation veins (Kuno, 1965, table 3), differs considerably from the magmatic differentiation as demonstrated in the Feather River area. In the magmatic differentiation, the enrichment of

magma in silicon and aluminum and depletion in iron and calcium are notable, whereas in the segregation veins iron is enriched and aluminum depleted. In both types of differentiation, magma is depleted in magnesium and enriched in alkalis.

REFERENCES

- Anderson, C. A., 1933, Tuscan formation of northern California: California Univ. Dept. Geol. Sci. Bull., v. 23, p. 215–276.
- 1941, Volcanoes of the Medicine Lake Highland, California: California Univ. Dept. Geol. Sci. Bull., v. 25, p. 347–422.
- Dalrymple, G. B., 1964, Cenozoic chronology of the Sierra Nevada, California: California Univ. Pubs. Geol. Sci., v. 47, p. 1–41.
- Durrell, Cordell, 1959a, Tertiary stratigraphy of the Blairsden quadrangle, Plumas County, California: California Univ. Pubs. Geol. Sci., v. 34, p. 161–192.
- 1959b, The Lovejoy Formation of northern California: California Univ. Pubs. Geol. Sci., v. 34, p. 193–220.
- 1966, Tertiary and Quaternary geology of the northern Sierra Nevada, in Bailey, E. H., ed., Geology of northern California: California Div. Mines and Geology Bull. 190, p. 185–197.
- Green, D. H., and Ringwood, A. E., 1967, The genesis of basaltic magmas: Contr. Mineralogy and Petrology, v. 15, p. 103–190.
- Green, T. H., Green, D. H., and Ringwood, A. E., 1967, The origin of high-alumina basalts and their relationships to quartz tholeiites and alkali basalts: Earth and Planetary Sci. Letters, v. 2, p. 41–51.
- Hietanen, Anna, 1971, Distribution of elements in biotite-hornblende pairs and in an orthopyroxene-clinopyroxene pair from zoned plutons, northern Sierra Nevada, California: Contr. Mineralogy and Petrology, v. 30 p. 161–176.
- 1972, Geology of the Pulga and Bucks Lake quadrangles, Butte and Plumas Counties, California: U.S. Geol. Survey Prof. Paper 731. [In press]
- Kuno, Hisashi, 1960, High-alumina basalt: Jour. Petrology, v. 1, p. 121–165.
- 1965, Fractionation trends of basalt magmas in lava flows: Jour. Petrology, v. 6, p. 302–321.
- Macdonald, G. A., 1966, Geology of the Cascade Range and Modoc Plateau, in Bailey, E. H., ed., Geology of northern California: California Div. Mines and Geology Bull. 190, p. 65–96.
- O'Hara, M. J., 1965, Primary magmas and the origin of basalts: Scottish Jour. Geology, v. 1, p. 19–40.
- Potbury, S. S., 1935, The LaPorte flora of Plumas County, California: Carnegie Inst. Washington Pub. 465, p. 29–81.
- Russell, R. J., 1928, Basin Range structure and stratigraphy of the Warner Range, northeastern California: California Univ. Dept. Geol. Sci. Bull., v. 17, p. 387–496.
- Turner, H. W., 1898, Bidwell Bar: U.S. Geol. Survey Geol. Atlas, Folio 43.
- Yoder, H. S., Jr., and Tilley, C. E., 1962, Origin of basalt magmas. An experimental study of natural and synthetic rock systems: Jour. Petrology, v. 3, p. 342–532.



MAFIC AND ULTRAMAFIC INCLUSIONS, CRATER 160, SAN FRANCISCO VOLCANIC FIELD, ARIZONA

By DAVID CUMMINGS¹, Los Angeles, Calif.

Work done on behalf of the National Aeronautics and Space Administration

Abstract.—Crater 160, in north-central Arizona, is a cinder cone composed mainly of bedded welded olivine basalt cinders with a thin overlying palagonite tuff that contains mafic inclusions. Chemically, the cinders are tholeiites. The mafic xenoliths are dunite, websterite, gabbro, and norite. Textures range from xenomorphic granular to hypidiomorphic granular. The norites, gabbros, and some websterites also have an orthocumulate texture. Minerals identified in these inclusions are enstatite, bronzite and hypersthene, diopside and augite, olivine, andesine-labradorite, hornblende, biotite, green spinel, magnetite, ilmenite, and chromite. The orthopyroxenes and clinopyroxenes both contain exsolution lamellae, and they poikilitically enclose olivine, spinel, pyroxene, and rarely plagioclase. Plagioclase also poikilitically encloses spinel and pyroxene. The xenoliths are chemically similar to the cinders, and they have a cumulate texture and mineralogy. Thus, they are probably cognate material, rather than samples of the Precambrian basement or the mantle. Comparison of the mineral assemblage in the xenoliths with published mineral stability fields suggests that they may have formed at about 10 kb, equivalent to 35 km depth. In northern Arizona, this depth is above the crust-mantle boundary.

The San Francisco volcanic field (Robinson, 1913) covers about 8,000 sq km in north-central Arizona, in the southern part of the Colorado Plateau. The cinder cones and lava flows represent the last phases of volcanic activity and range in age from Tertiary to Quaternary (Colton, 1937).

Crater 160, one of the largest cinder cones in the area, is about 40 km north of Flagstaff (fig. 1). The cinder cone is 2 km in diameter at the base and has a summit diameter of 1.2 km. The rim of the crater slopes northward at about 175 m in 1 km; the surrounding area also slopes northward, but at about 10 m in 1 km. The crater floor is 60 m lower than the area outside the cone. A secondary cinder cone, about 6 m high, occurs on the floor.

The 75 m of exposed section consists mostly of welded olivine basalt cinder beds. One lenticular olivine basalt flow, 7.5 m thick at its center, occurs about 40 m from the top of the wall. Overlying the cinder beds is a palagonite tuff, 15 m

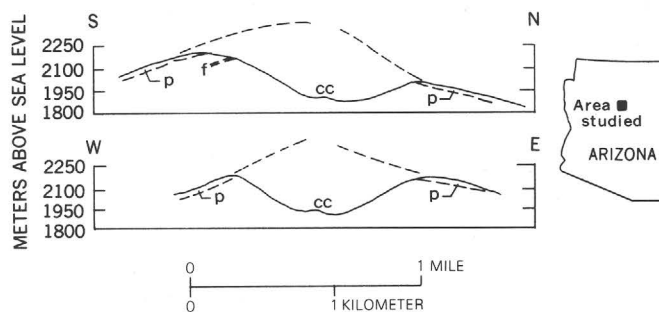


Figure 1.—Vertical aerial photograph, location map, and generalized geologic sections of Crater 160. p = palagonite tuff; f = lava flow; cc = cinder cone. Dashed lines extrapolating present topography indicate hypothetical shape and height of original cone.

¹Occidental College.

thick. An olivine basalt dike, emplaced before the deposition of the palagonite tuff, cuts the cinder beds on the north. The small cinder cone on the floor of the crater marks the last event in the development of Crater 160. On the east rim, the palagonite tuff is overlain by olivine basalt cinders and bombs petrographically similar to the cinders of the secondary cinder cone.

The palagonite tuff contains fragments of rock similar to that in the crater wall but also inclusions of sedimentary rock from the underlying Kaibab Limestone (Permian) and Coconino Sandstone. Inclusions from the Toroweap Formation, which occurs between the Kaibab and Coconino, were not seen. Of special note is the occurrence of mafic inclusions in the palagonite tuff. This tuff represents the explosive phase that enlarged the original vent and formed a crater with the dimensions of a maar.

CINDER BEDS

Individual cinder beds are lens shaped and range in thickness from 0 to 6 m, although few exceed 3 m. They are characteristically reddish brown (hematite stained) on weathered surfaces and dark gray on fresh surfaces. Most cinders are rounded and show some evidence of aerodynamic shaping. The cinders and cinder beds are generally welded, so they were probably partly molten when deposited. The bombs overlying the palagonite tuff on the east side range in size from about 0.3 to 1.5 m. Many are almond shaped, and some of the larger bombs are broken. The latter apparently broke upon impact. The cinders and the lava flow were sampled at about 7.5-m intervals from the exposed section in the south wall.

Petrography

The cinders are aphanitic to porphyritic vesicular olivine basalt (table 1). Phenocrysts of hypersthene and olivine, a few millimeters in size, are surrounded by a trachytic groundmass of andesine, augite, and opaque minerals. Lamellae, parallel to (100) in the hypersthene, pinch out toward the grain boundaries and appear to be a clinopyroxene exsolution product. Olivine phenocrysts are euhedral and show no

alteration. Minor amounts of euhedral olivine are also present in the groundmass. Groundmass augite occurs as short prismatic crystals; twins (100) are common. Andesine occurs as elongate prisms; albite twins are common. Opaque minerals include chromite, magnetite, and ilmenite. A few cinders contain prismatic enstatite phenocrysts, optically similar to those in the mafic inclusions. Hematite, an alteration product, surrounds grains of magnetite, ilmenite, and augite.

The An percentage of the plagioclase and Fo percentage of the olivine in the cinders were examined for trends (fig. 2). An was calculated from the norms in table 2, and Fo was determined optically using the β index (Wahlstrom, 1955, p. 204). A calculated best-fit line through the point scatter of An shows a slight decrease of An from oldest to youngest rocks. A lower Fo content in the younger rocks is suggested.

Petrochemistry

Chemical analyses for major elements, spectrographic analyses for minor elements, and CIPW norms for the cinders and the mafic inclusions are given in table 2.

On the basis of normative composition, the dominant rock type is olivine tholeiite, although alkali basalt is also present (Yoder and Tilley, 1962). Because the cinders at Crater 160 are oxidized, the calculated normative composition may not reflect the true normative composition of the fresh basalt. In order to resolve the difficulty presented by the oxidation, $(\text{FeO} + \text{Fe}_2\text{O}_3)/(\text{FeO} + \text{Fe}_2\text{O}_3 + \text{MgO})$ was plotted against SiO_2 (fig. 3). The calculated best-fit curve more closely approximates the differentiation trend for the tholeiite series than for the alkali basalt series.

The percentage of oxides was plotted against position in the crater wall (fig. 5) to determine if any trends exist. The percentages of Al_2O_3 and Na_2O increase in the younger rocks, whereas those of MgO and TiO_2 decrease. These trends suggest that the younger rocks have a more felsic composition, supporting the An and Fo trends cited previously. The ratios Cr/V and Ni/Co are also plotted against position in crater wall (fig. 5). Both ratios decrease in the younger rocks, also supporting the more felsic trend.

Median contents of selected trace elements from Crater 160 are compared with those for tholeiites and basalt (Prinz, 1967) in table 3. (Fleischer and Chao, 1960, and Prinz, 1967, recommend using median values for comparison, rather than arithmetic means.) Crater 160 has abnormally high concentrations of Ba, Sr, Rb, Ni, and Cr; high concentrations of Cu, Zr, and V; and low concentrations of Y, compared with the median concentrations of tholeiites and basalts. High concentrations of Ni, Cr, V, and Cu are characteristic of mafic rocks; high concentrations of Ba, Sr, Rb, and Zr, felsic rocks.

The high concentrations of Ba, Sr, Rb, and Zr may indicate contamination from basement granites and other felsic rocks. If the magma incorporated basement materials, then assimilation must have been considerable in order to approach (or even exceed, as for Ba and Sr) the element abundances in

Table 1.—Modal analyses of typical basalt samples from Crater 160

[In volume percent, based on 1,500 point counts for each sample]

Sample No	1	4	8	Cinders from secondary cone
Description	cinders	cinders	flow	
Orthopyroxene . . .	5.7	5.2	4.0	6.0
Clinopyroxene . . .	19.2	20.8	18.6	19.2
Opaque minerals . .	1.8	1.3	2.1	2.8
Plagioclase	65.3	69.0	67.2	66.1
Olivine	8.0	4.9	6.9	5.9

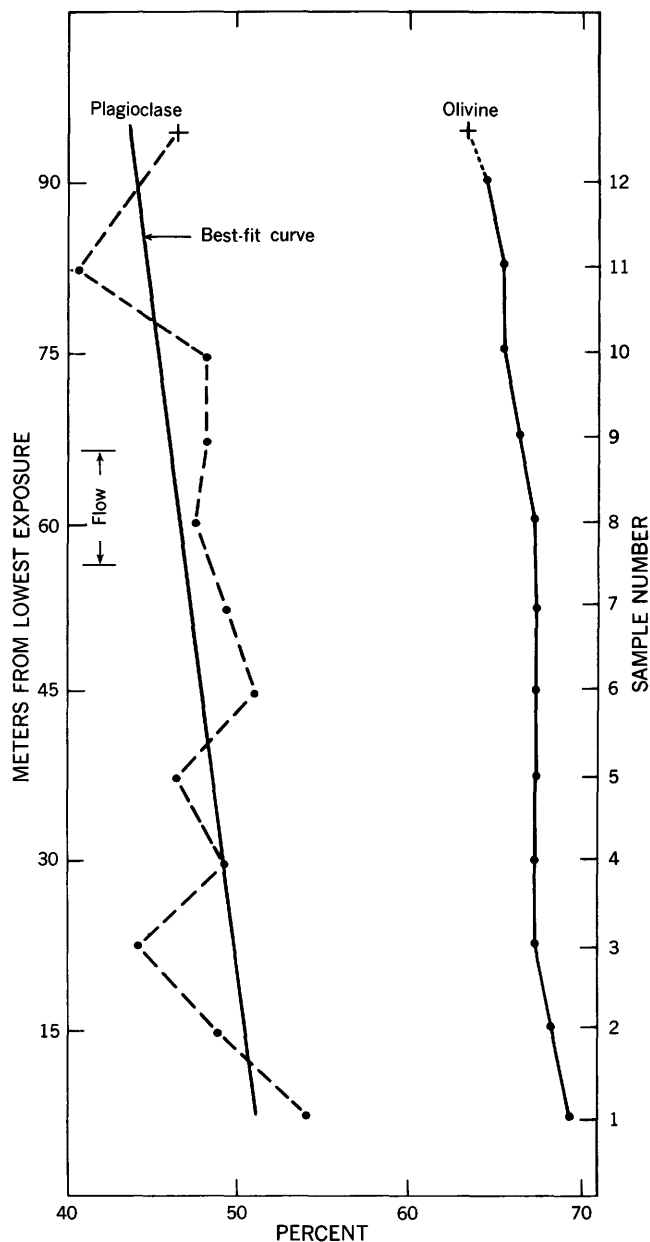


Figure 2.—Percentage of An in plagioclase, based on norms (table 2), and percentage of Fo in olivine, based on β index of refraction, plotted against position in crater wall. Values for An of plagioclase and Fo of olivine for cinder cone shown by plus sign (+).

granites. Ulrich (1968) described granite and pegmatite inclusions in a maar about 13 km northeast of Crater 160, but no granitic inclusions were seen at Crater 160. Smouse (1970) has identified granite gneiss xenoliths in Crater 160. One possible explanation for the anomalously high concentrations of Ba, Sr, Rb, and Zr is that they may have been concentrated at the head of a gas column in the magma, and consequently were incorporated in the vesicular basaltic cinders as they were erupted.

MAFIC XENOLITHS

Mafic inclusions are scattered throughout the palagonite tuff but are extremely rare in the welded cinder layers, the interbedded flow, the dike, and the secondary cinder cone. Twenty-eight were collected and studied. They characteristically have a thin basaltic envelope, are irregularly shaped or subrounded, and range from about 5 to 25 cm in diameter. The varieties found are norite, gabbro, websterite, dunite, and fragments (up to 6 cm long) of olivine crystals.

According to Sabels (1960), a peridotite-dunite (50 percent forsteritic olivine and 50 percent chrome diopside) xenolith was collected from Crater 160 by C. A. Hodges, and Brady and Webb (1943) described fragments of xenoliths and cored bombs from the Sunset Crater (National Monument) area, just east of Crater 160, and the Red Hill area, near Williams, which they suggest are fragments representing the basement complex.

Petrography

The mafic xenoliths are composed of varying proportions of olivine, orthopyroxene, clinopyroxene, and plagioclase as major constituents. Minor constituents include green spinel; magnetite, ilmenite, and chromite; amphibole; and biotite. Textures, in general, are similar to the orthocumulate textures described by Wager (1968).

Chemical analyses of major and minor elements for five samples are given in table 2. Modal analyses of all 28 inclusions are given in table 4 and plotted on figure 6. Petrographic descriptions for the rock types follow. The number of samples collected appears in parentheses after the rock type.

Websterite (14 samples).—Megascopically, the websterite xenoliths are dark green, with a phaneritic texture. Foliation is not apparent. The texture is xenomorphic granular; grains are 0.2 to 0.5 cm long. Orthopyroxene ranges from enstatite ($2V=81^\circ \pm 2^\circ$) to bronzite ($2V=74^\circ \pm 2^\circ$); both contain parallel inclusions (Schiller structure) and are pale green, and neither is pleochroic. Clinopyroxene (diopside, $2V=60^\circ \pm 2^\circ$) is pale green. Several diopside grains have polysynthetic (100) and (001) twins. Exsolution lamellae are common in both ortho- and clinopyroxenes. Minor amounts of euhedral to subhedral green spinel, magnetite, and chromite are present as individual grains and in clusters. Alteration products were not observed.

Dunite (3 samples) and fragments of olivine.—The dunites are yellow green and uniformly hypidiomorphic granular, with euhedral to subhedral olivine grains about 1 cm in diameter. The olivine is rarely zoned and is Fo_{86-87} , on the basis of β index of refraction. Orthopyroxenes (enstatite, $2V=78^\circ \pm 2^\circ$) have poikilitic inclusions of olivine. Isolated crystals of euhedral green spinel are 1 cm in diameter. Neither alteration nor preferred orientation was observed.

Large (up to 6 cm) fragments of olivine scattered in the tuff appear to be pieces of larger crystals. They are dark green, not zoned, and their composition is Fo_{76-77} . Neither alteration

Table 2.—Chemical analyses and norms of cinders and mafic inclusions from Crater 160

[Chemical analyses by M. K. Carron and C. S. Annell. Asterisk (*), average of two readings; N.d., not detected]

Type of material	Cinders													Mafic xenoliths ¹					
	Sample No.	1	2	3	4	5	6	7	8	9	10	11	12	Cinder cone	4	9	16	23	27
Chemical analyses, major element (weight percent)																			
SiO ₂	49.90	47.40	46.49	46.70	46.10	46.40	47.40	48.30	46.20	46.80	45.80	52.70	49.10	43.80	50.30	49.30	52.00	52.60	
Al ₂ O ₃	12.69	13.29	12.27	12.46	12.03	12.25	13.08	13.62	12.72	12.24	12.96	16.27	18.36	15.20	5.88	8.90	15.60	14.70	
Fe ₂ O ₃	9.93	10.08	9.57	9.89	9.13	9.60	10.45	10.85	5.78	9.90	10.13	8.39	10.08	6.73	2.36	3.43	3.77	2.80	
FeO.....	.60	.65	.73	.61	1.15	1.36	.38	N.d.	4.86	N.d.	.15	1.00	.43	4.72	4.57	4.86	6.61	7.23	
MgO.....	9.50	8.61	9.74	9.56	10.77	9.58	8.26	7.93	9.61	9.34	7.94	5.35	5.52	11.20	16.20	15.30	6.61	6.74	
CaO.....	11.52	11.28	12.04	12.77	12.59	12.13	11.28	10.82	12.24	11.83	12.04	8.20	8.58	14.60	18.77	15.40	8.64	9.43	
Na ₂ O....	2.40	2.83	2.31	2.54	2.22	2.35	2.60	2.70	2.70	2.82	2.96	3.74	3.26	1.48	.67	.82	3.90	3.72	
K ₂ O.....	1.46	1.50	1.37	1.31	1.22	1.17	1.49	1.30	0.98	1.47	1.58	1.35	1.00	.18	N.d.	.11	.87	.72	
TiO ₂	2.00	2.13	2.12	2.21	2.12	2.24	2.18	2.21	2.52	2.12	2.08	1.73	1.58	1.54	.91	.91	.79	.81	
MnO.....	.24	.18	.21	.18	.22	.24	.22	.17	.20	.19	.18	.17	.19	.09	.14	.25	.14	.19	
P ₂ O ₅74	.79	1.11	.71	.94	1.03	.87	.68	.75	.86	1.60	.61	.52	.17	.14	.16	.54	.68	
H ₂ O±....	1.73	1.42	1.68	.95	1.53	1.57	1.98	1.87	1.08	2.39	2.79	.82	1.46	.26	.55	.83	.47	.22	
Total..	99.70	100.15	99.64	99.88	99.91	99.91	100.18	100.44	99.63	99.95	100.20	100.33	100.07	99.96	100.48	100.26	99.93	99.83	
Quantitative spectrographic analyses (parts per million)																			
Pb.....	9.7*	17	18	8	12	12	33	12	22	9	7.5	12	25	6.8*	13.5*	4.8*	35	34	
Ag.....	<0.2	<0.2	<0.2	<0.2	<0.2	<0.2	<0.2	<0.2	<0.2	<0.2	<0.2	<0.2	<0.2	<0.2	0.65*	<0.2	0.35	0.28	
Cu.....	133*	133*	170*	142*	122*	120*	149*	158*	164*	82*	113	73	66*	102	310*	47*	373*	433	
Ga.....	20*	21.5*	20.5*	19.5*	18	19*	21*	20*	20.5*	20.5*	20*	24*	22.5	25.5*	8.8*	13*	19*	18.5*	
Mn.....	1,038*	640*	1,000	595	1,260	1,080	750	600	900	615	680	630	690	1,150	695	755	620*	1,110	
Cr.....	855*	860*	910	1,250	1,060	800	835	595	710	715	650	215	60.5*	150	835	1,200	158*	228*	
B.....	N.d.	N.d.	N.d.	N.d.	N.d.	N.d.	N.d.	N.d.	N.d.	19.5*	21.5*	N.d.	N.d.	N.d.	N.d.	N.d.	N.d.	N.d.	
Co.....	54*	45*	56*	47.5*	50	46.5*	46	35.5*	39	40	43.5	23.5*	27.5*	46	42	38.5*	23*	29.5*	
Ni.....	186*	152*	182*	168*	251*	160*	146*	126*	143	128	151*	64.5*	43.5*	122	320	260	63*	69*	
Ba.....	1,290	1,270	1,240	1,035	1,230	1,160	1,220	1,250	1,155	1,170	1,030	1,240	900	151	87	181	665	805*	
Sr.....	695	1,180	1,200	1,000	870	830	1,070	870	955	875	935	980	940	480	265	270	1,280	1,505*	
V.....	231	272	250	275	245	249	245	248	224	249	251	172	166	250	179	232	152	154	
Nb.....	15	21	24	13	23	19	16	23	17	32	30	19	11	<10	<10	<10	<10	<10	
Sc.....	33*	33*	37.5*	35*	36	30*	31.5*	30	36	29*	30*	20*	21.5*	51*	70	60*	19*	26*	
La.....	56	60	60*	54*	<50	54.5*	59	50	54	52*	55*	52*	55*	N.d.	N.d.	N.d.	50*	69*	
Y.....	19*	20*	19*	18*	19.5*	18.5*	19*	20.5*	19*	20*	20*	20*	21.5*	14.5*	12*	15	16.5*	14*	
Zr.....	112*	143*	108*	114*	98*	115*	124*	120*	125	126*	121*	128*	101*	26.5*	27*	33*	30*	66	
Li.....	8.5	7.4*	6.5	5.1	5.1	4.9	9.1	10	4.6	7.8	9.1	12	11	<1	1	1.4	9.5	7	
Rb.....	31*	32*	26*	21*	21*	23.5*	33.5*	38.5*	24*	27.5*	19*	21	24.5	<1	<1	1	11	3.5*	
Cs.....	<1	<1	<1	<1	<1	<1	<1	1.5*	<1	1.1	<1	<1	<1	<1	<1	<1	N.d.	N.d.	
Zn.....	85*	81	83	88	88	90	97	100	81	78	82	88	97	134*	39*	51*	122	150	

Standard CIPW norms (weight percent)

Q	2.6	N.d.	8.7	8.8	N.d.	7.7	N.d.	8.8	N.d.	7.6	8.7	N.d.	8.8	N.d.	1.1	N.d.	0.6	N.d.	4.3	N.d.
Or	5.9	8.7	8.8	8.8	6.6	6.9	8.8	8.8	5.8	8.7	8.7	8.8	8.8	8.8	10.7	N.d.	5.6	6.9	31.5	4.3
Ab	27.6	20.4	23.9	19.6	18.8	19.9	22.0	22.7	21.4	23.9	23.9	23.9	29.8	29.8	34.3	13.0	20.2	22.5	21.3	31.5
An	32.5	19.6	19.1	19.1	19.6	19.4	20.0	21.1	19.8	16.4	16.4	16.4	26.1	26.1	1.0	N.d.	N.d.	N.d.	N.d.	21.3
Ne	N.d.	2.8	2.8	15.5	32.9	22.9	7.0	N.d.	N.d.											
Wo	1.5	12.2	11.5	12.4	14.5	13.5	10.6	8.7	15.1	12.5	12.5	5.4	5.4	5.4	13.1	31.5	33.0	14.4	8.8	8.8
En	13.7	15.9	12.3	17.1	15.0	18.0	17.8	19.7	12.9	10.8	10.8	4.6	4.6	4.6	.3	4.1	4.4	7.0	16.5	16.5
Fs	N.d.	9.8	9.8																	
Pf	N.d.	.8	.8	.8	N.d.	N.d.	N.d.	N.d.	N.d.	N.d.										
Mt	N.d.	9.8	3.4	5.0	5.5	4.0	4.0													
Hm	10.1	10.1	10.1	9.6	9.1	9.6	10.4	10.8	9.9	9.9	9.9	9.3	9.3	9.3	N.d.	N.d.	N.d.	N.d.	N.d.	N.d.
Il	1.3	1.8	1.8	2.0	2.9	3.4	1.2	.4	4.8	.4	.4	2.8	2.8	2.8	2.9	1.7	1.7	1.5	1.5	1.5
Tn	2.2	2.6	10.0	2.6	1.5	1.1	3.7	4.9	N.d.	3.3	3.3	N.d.								
Ap	1.2	1.8	1.9	2.6	2.2	2.4	2.1	1.6	1.8	2.0	2.0	1.6	1.6	1.6	.4	.3	.4	1.3	1.6	1.6
Dt	2.8	22.7	21.4	23.2	27.0	25.3	19.7	16.3	28.3	23.4	23.4	10.0	10.0	10.0	28.9	62.1	43.3	13.6	17.2	17.2
Hy	12.5	5.4	2.4	6.4	2.5	6.3	8.6	12.1	N.d.	6.4	17.0	14.8	18.0	18.0						
OI	N.d.	N.d.	6.4	5.0	8.3	4.1	1.9	8.7	7.9	8.7	8.7	7.1	7.1	7.1	10.7	6.9	4.0	2.2	.3	.3

¹4, olivine-plagioclase websterite; 9 and 16, websterites; 23, gabbro; 27, norite.

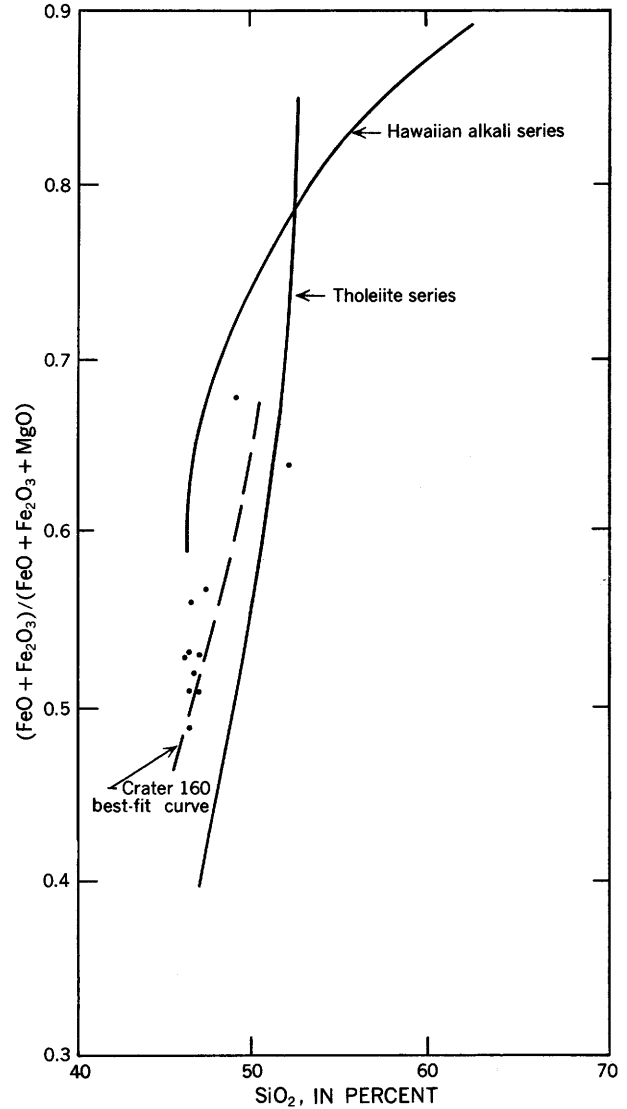


Figure 3.—Plot of SiO₂ against (FeO + Fe₂O₃) / (FeO + Fe₂O₃ + MgO) for cinders of Crater 160 compared with curves for Hawaiian alkali series and tholeiite series (Yoder and Tilley, 1962, p. 423).

nor inclusions were observed. Megascopic fractures are parallel to (010) cleavage.

Olivine-plagioclase websterite (5 samples).—The websterite xenoliths are dark green, with a uniform phaneritic texture and a very weak banding, defined by pyroxene concentration. They have a xenomorphic- to hypidiomorphic-granular orthocumulate texture; grains are 0.2 to 0.5 cm long and 0.1 to 0.2 cm wide (fig. 7C). Orthopyroxene (enstatite, $2V=78^\circ \pm 2^\circ$) is light green with no discernible pleochroism. Parallel inclusions (Schiller structure) are present but too small to be identified optically. Clinopyroxene (diopside, var. diallage, $2V=59^\circ \pm 2^\circ$) is pale green. Both pyroxenes are slightly embayed by plagioclase. The plagioclase is mostly labradorite with minor andesine, and is rarely zoned. Olivine, Fo₈₄, is present in

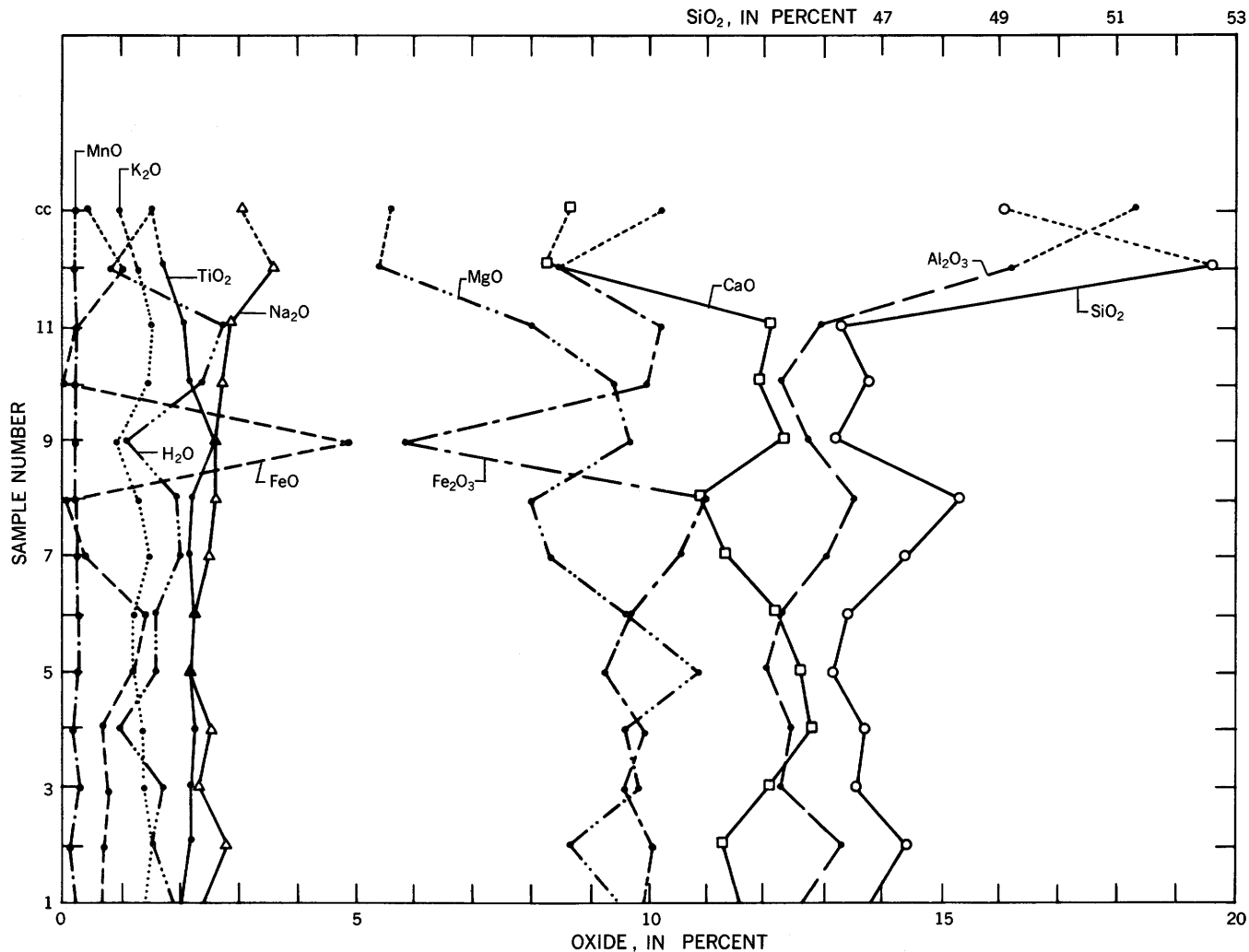


Figure 4.—Percentage of oxides plotted against position of sampling points in crater wall. Sample cc is from cinder cone.

minor amounts. Green spinel, magnetite, ilmenite, and chromite appear as isolated crystals and in clusters. Hornblende is present as a primary mineral.

Pyroxenes are the most common hosts for poikilitic inclusions of olivine, spinel, pyroxene, and rarely, plagioclase. Plagioclase is host for poikilitic inclusions of spinel and pyroxene. Exsolution lamellae occur in both pyroxenes. Olivine has weakly developed (100) deformation bands. The lamellae and deformation bands are described in greater detail later.

Hypersthene gabbro (4 samples).—The gabbro xenoliths are distinctly banded (fig. 7A); mafic minerals are segregated into streaks in a groundmass of plagioclase. The texture is phaneritic, hypidiomorphic granular, and orthocumulate, with large (> 0.5 cm) grains. The orthopyroxene is hypersthene ($2V=60^\circ \pm 2^\circ$), and several crystals contain parallel inclusions (Schiller structure). The clinopyroxene is augite ($2V=70^\circ \pm 2^\circ$). Both pyroxenes commonly display exsolution lamellae and are slightly embayed by plagioclase. The plagioclase is mostly

andesine with some labradorite; zoning is rare. Poikilitic inclusions of spinel and pyroxene occur in plagioclase and both pyroxenes. Euhedral to subhedral magnetite, ilmenite, and green spinel occur as isolated grains and in clusters. Some magnetite appears to be an alteration of augite. Kelyphitic structure is present where the pyroxenes are in contact with the plagioclase, but the radiating crystals in the kelyphitic rim are too small to be identified by ordinary optical methods.

Aegirine-augite norite (2 samples).—The norite xenoliths are also distinctly banded (fig. 7B), but the mafic minerals are clustered in lenses, not segregated into streaks. The banding even shows in thin section (fig. 7D). The texture is phaneritic, hypidiomorphic granular, and orthocumulate; few grains are larger than 0.5 cm. Orthopyroxene (hypersthene, $2V=57^\circ \pm 2^\circ$) does not show Schiller structure. The clinopyroxene, aegirine-augite ($2V=80^\circ \pm 2^\circ$), contains exsolution lamellae, as does the orthopyroxene. Plagioclase, mostly andesine with some labradorite, is rarely zoned. Poikilitic inclusions in pyroxene and plagioclase are common. Kelyphitic structure is present where

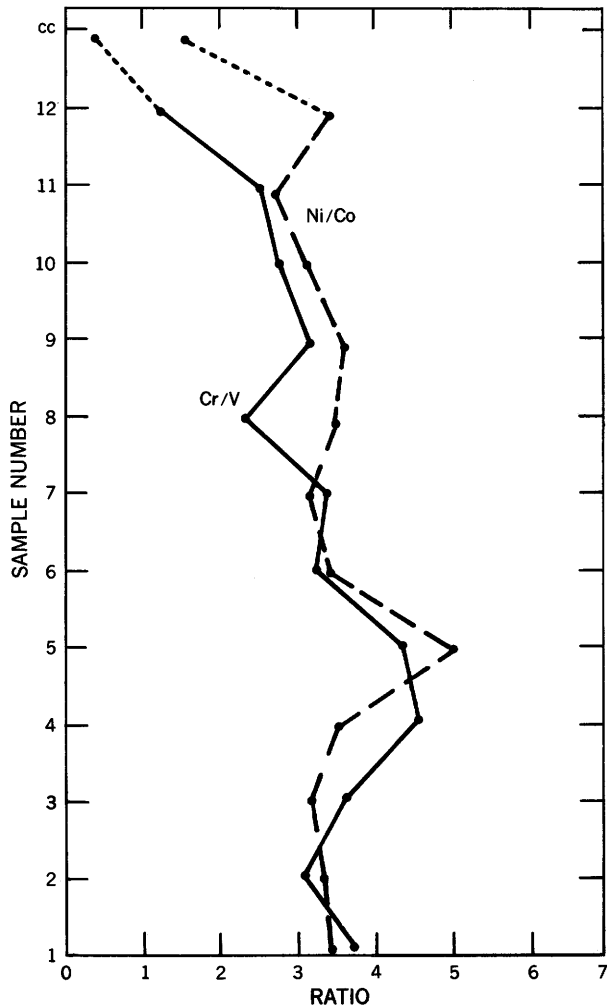


Figure 5.—Ratios Cr/V and Ni/Co plotted against position of sampling points in crater wall. Sample cc is from cinder cone.

the pyroxenes are in contact with the plagioclase. Biotite occurs as a primary mineral, green spinel as isolated crystals. Magnetite and ilmenite occur as isolated crystals and as alteration of aegirine-augite. Hematite and limonite are alteration products surrounding magnetite, aegirine-augite, and biotite.

Oriented intergrowths in pyroxenes.—Exsolution lamellae are narrow (0.002 mm wide) and regularly spaced (0.007–0.016 mm apart). In orthopyroxene, they consist of clinopyroxene and are oriented parallel to (100). Exsolution on (001), indicating exsolution of pigeonite, was not observed. These lamellae wedge out near the edges of the host crystal and resemble some described by Jackson (1961), who suggested (p. 18) that the wedging-out characteristic indicates that the host mineral crystallized below its inversion temperature as primary orthopyroxene, cooled slowly, and later exsolved clinopyroxene.

In clinopyroxene, orthopyroxene lamellae are oriented parallel to (100). These lamellae also pinch out at the edge of

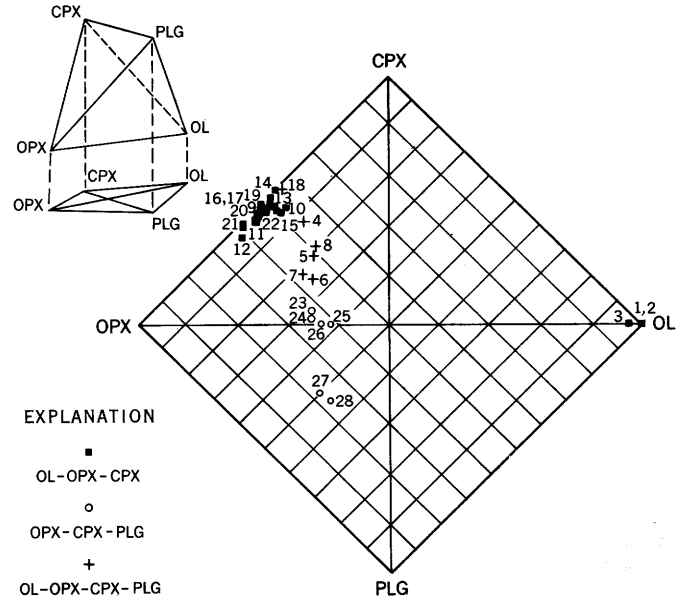


Figure 6.—Projection of 111 tetrahedron OL-OPX-CPX-PLG, showing modal analyses of 28 mafic xenoliths from Crater 160. Four major components (OL = olivine, OPX = orthopyroxene, CPX = clinopyroxene, PLG = plagioclase) in xenoliths recalculated to 100 percent. OL-CPX-PLG and OL-OPX-PLG not represented in xenoliths at Crater 160.

Table 3.—Median contents of selected trace elements, in parts per million, in Crater 160, compared with those for tholeiite and basalt

	Tholeiites		Basalt	Crater 160
	Quartz ¹ norm	Olivine ¹ norm	Olivine ¹ norm	Fused cinders, flow, and cinder cone
Cu	125	75	85	133
Ga	20	19	20	20.5
Cr	125	185	170	800
Co	35	44	40	45
Ni	70	110	80	151
Ba	200	175	200	1,200
Sr	400	300	400	940
V	250	175	210	249
Sc	30	30	30	33
Y	25	24	29	19.5
Zr	100	85	90	120
Li	10	5	5	7.8
Rb	5	2	2	24.5

¹Data from Prinz (1967).

the host crystal. As for the clinopyroxene lamellae in the orthopyroxene, the clinopyroxene may have crystallized below its inversion temperature as primary clinopyroxene, cooled slowly, and later exsolved orthopyroxene.

Deformation bands in olivine.—The mafic xenoliths are remarkably free from cataclasis and other deformation features. The pyroxenes and plagioclase show no evidence of intragranular strain. The only exception is undulatory extinction bands parallel to (100) in olivine in the dunite and olivine-plagioclase websterites, which may indicate intragranular deformation after solidification (Turner, 1942). This

Table 4.—*Modal analyses of mafic xenoliths in Crater 160*
 [Based on 1,500 point counts. Plagioclase composition based on albite twin; minor amounts shown in parentheses.
 Fo content based on β index of refraction. N.d., not detected; Tr., trace]

Rock type	Websterite													
Sample No.	9 ¹	10	11	12	13	14	15	16 ¹	17	18	19	20	21	22
Orthopyroxene	52.3	51.7	55.6	62.1	48.6	53.1	47.1	54.6	52.3	44.9	49.2	52.4	58.7	47.1
	← Enstatite →							← Bronzite →						
Clinopyroxene	47.7	45.6	42.1	35.5	46.1	45.5	43.9	43.6	43.5	51.9	49.1	47.6	40.2	52.9
	← Diopside →													
Plagioclase	N.d.	N.d.	Tr.	N.d.	N.d.	N.d.	N.d.	N.d.	N.d.	.4	Tr.	N.d.	N.d.	N.d.
Olivine	Tr.	1.4	.8	2.4	4.5	Tr.	5.8	N.d.	Tr.	.7	N.d.	N.d.	N.d.	N.d.
	← Fo ₈₄ →													
Opaque minerals	Tr.	1.3	.4	Tr.	.8	Tr.	2.3	Tr.	4.2	3.1	1.7	Tr.	1.1	Tr.
Spinel	Tr.	Tr.	1.1	Tr.	Tr.	2.4	.9	1.8	Tr.	Tr.	Tr.	Tr.	Tr.	Tr.
Amphibole	N.d.	N.d.	N.d.	N.d.	N.d.	N.d.	N.d.	N.d.	N.d.	N.d.	N.d.	N.d.	N.d.	N.d.
Biotite	N.d.	N.d.	N.d.	N.d.	N.d.	N.d.	N.d.	N.d.	N.d.	N.d.	N.d.	N.d.	N.d.	N.d.

Rock type	Dunite			Olivine-plagioclase websterite					Hypersthene gabbro				Aegirine-augite norite	
Sample No.	1	2	3	4 ¹	5	6	7	8	23 ¹	24	25	26	27 ¹	28
Orthopyroxene	N.d.	N.d.	2.3	36.3	30.0	34.3	31.4	31.8	27.9	29.1	21.2	26.7	23.7	21.9
	← Enstatite →			← Enstatite →					← Hypersthene →				← Hypersthene →	
Clinopyroxene	N.d.	N.d.	N.d.	35.6	33.6	31.2	34.0	32.8	34.1	33.4	38.6	35.2	21.0	19.9
	← Diopside →			← Diopside →					← Augite →				← Augite →	
Plagioclase	N.d.	N.d.	N.d.	2.8	12.6	16.9	19.1	15.2	30.0	31.6	38.9	35.4	48.7	50.1
	← Labradorite (andesine) →			← Labradorite (andesine) →					← Andesine (labradorite) →				← Andesine (labradorite) →	
Olivine	95.2	92.9	89.1	8.3	5.0	6.7	2.3	6.1	N.d.	N.d.	N.d.	N.d.	N.d.	N.d.
	← Fo ₈₆₋₈₇ →			← Fo ₈₄ →					← Fo ₈₂ →					
Opaque minerals	Tr.	1.8	3.4	Tr.	1.7	Tr.	4.6	2.1	1.7	2.5	1.3	2.7	1.8	N.d.
Spinel	4.6	5.3	5.2	8.3	10.9	7.8	8.6	12.0	6.3	3.4	Tr.	Tr.	4.2	4.6
Amphibole	N.d.	N.d.	N.d.	6.7	6.2	3.1	N.d.	N.d.	N.d.	N.d.	N.d.	N.d.	N.d.	N.d.
	← Hornblende →			← Hornblende →										
Biotite	N.d.	N.d.	N.d.	N.d.	N.d.	N.d.	N.d.	N.d.	N.d.	N.d.	N.d.	N.d.	.6	1.3

¹Chemically analyzed (table 2).

deformation is rare—less than 2 percent of the olivine in the dunite, less than 1 percent in the olivine-plagioclase websterites. Similarly deformed olivine occurs in the Stillwater Complex (Jackson, 1961).

Petrochemistry of xenoliths

The percentages of the major elements in the mafic xenoliths (table 2) are similar to those in the cinders. The main difference is that the xenoliths have slightly less K₂O, TiO₂, and H₂O. The xenoliths are also similar to the cinders in minor-element composition, except that they have less Ba, Zr, Rb, and perhaps Nb and Sr, and perhaps slightly more Cu and Sc. Percentages of the other elements in the cinders and xenoliths overlap.

Normative percentages (CIPW) of cinders and xenoliths are markedly similar; however, the cinders are oxidized, so the

comparison may not be completely valid. The relatively low percentage of normative orthoclase in the xenoliths reflects the low K₂O content in those rocks. Normative hematite in the cinders reflects the oxidation, whereas normative magnetite is present in the xenoliths. Percentages of other elements overlap in the two groups, with normative diopside and enstatite perhaps a little higher in the xenoliths.

Origin of xenoliths

The xenoliths may represent either (1) basement material, (2) mantle material, or (3) cognate material from the magma that formed Crater 160.

Xenoliths of Precambrian granites and other rocks have been reported in the San Francisco volcanic field (Smouse, 1970; Ulrich, 1968; Brady and Webb, 1943). However, it is unlikely that the mafic inclusions at Crater 160 are also basement

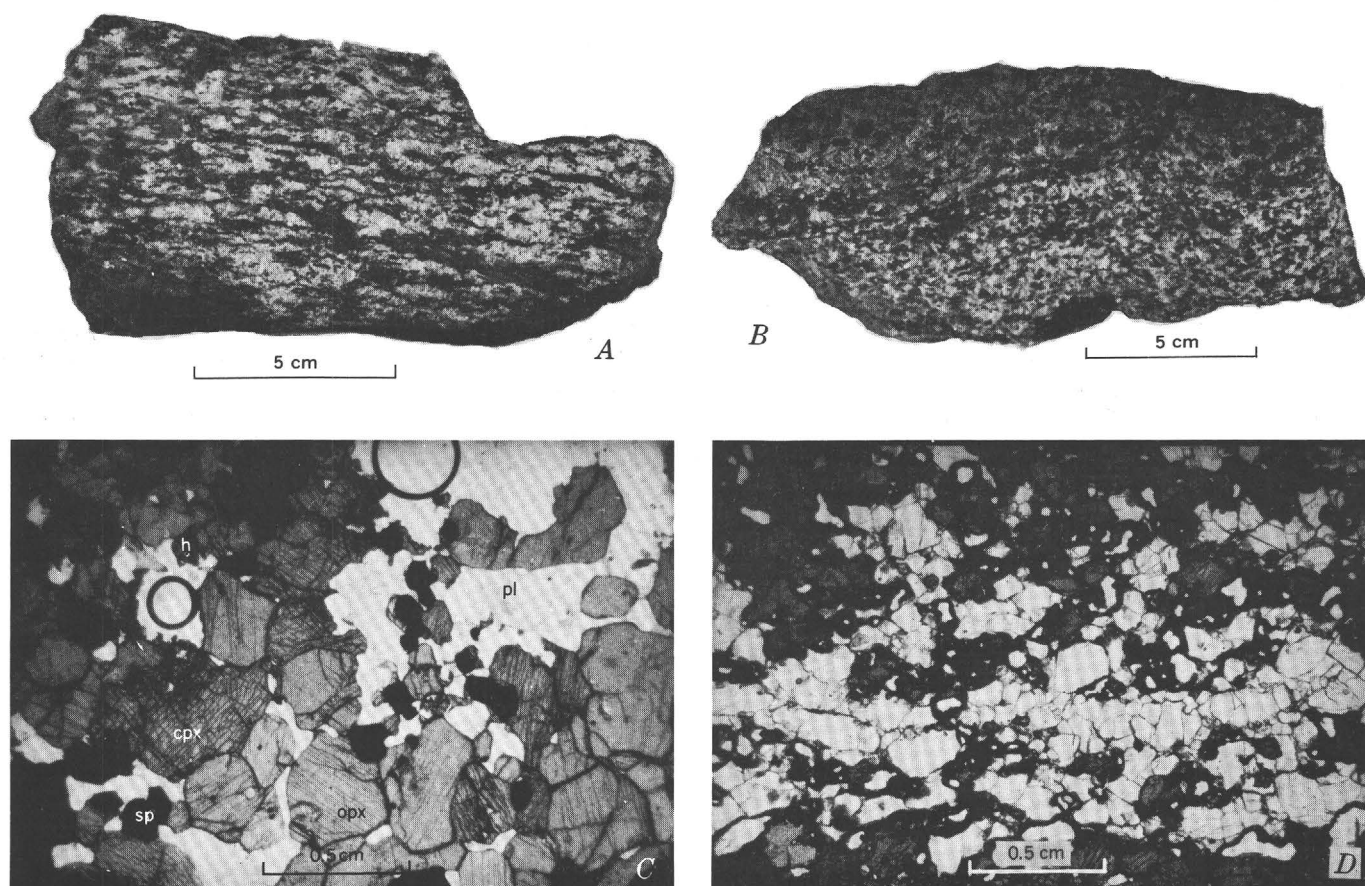


Figure 7.—Photographs and photomicrographs of samples from Crater 160.

- A. Hand sample of gabbro (sample 23); light-gray minerals are plagioclase; dark-gray minerals are pyroxene. Banded structure is interpreted as due to rhythmic (cumulate) layering.
- B. Hand sample of norite (sample 27); light-gray minerals are plagioclase; dark-gray minerals are pyroxene. Banded structure is interpreted as due to rhythmic (cumulate) layering.
- C. Thin section, plane-polarized light, of olivine-plagioclase-websterite (sample 9). pl = plagioclase; cpx = clinopyroxene; opx = orthopyroxene; sp = spinel; h = hornblende.
- D. Thin section, plane-polarized light, of norite (sample 27). Cumulate texture shown in thin section as light-gray band (plagioclase).

materials. The Precambrian rocks in Arizona show evidence of considerable deformation, but the Crater 160 inclusions show no such evidence. Except for minor deformation banding in olivine, they are completely free of cataclasis.

The problem as to whether mafic inclusions, in general, are derived from the mantle or formed by crystal fractionation as cumulates from the magma of the basalts in which they are found has been summarized by Wilshire and Binns (1961) and White (1966). The general hypidiomorphic-granular and cumulate textures of the xenoliths at Crater 160 are common features of rocks formed by differentiation, as distinct from the textures of rocks derived from the mantle. The general absence of plastic deformation in the xenoliths also argues against a mantle origin. The chemical similarities between the xenoliths and the cinders suggest that the xenoliths may be

cognate materials which crystallized early and were erupted during the formation of Crater 160.

As an approximation to the determination of the depth of formation of the mafic and ultramafic xenoliths, recourse is made to laboratory experiments of mineral assemblages. The presence of plagioclase in these xenoliths can be used to estimate their depth of crystallization. Laboratory experiments by Ringwood and Green (for example, Ringwood and Green, 1969) have defined stability fields of mineral assemblages at different temperatures and pressures (fig. 8) that may be applicable to the Crater 160 xenoliths.

The area represented by olivine + orthopyroxene + clinopyroxene + plagioclase (plagioclase pyrolyte) in figure 8 mineralogically approximates the olivine-plagioclase websterites and, with the exception of olivine, the gabbros and

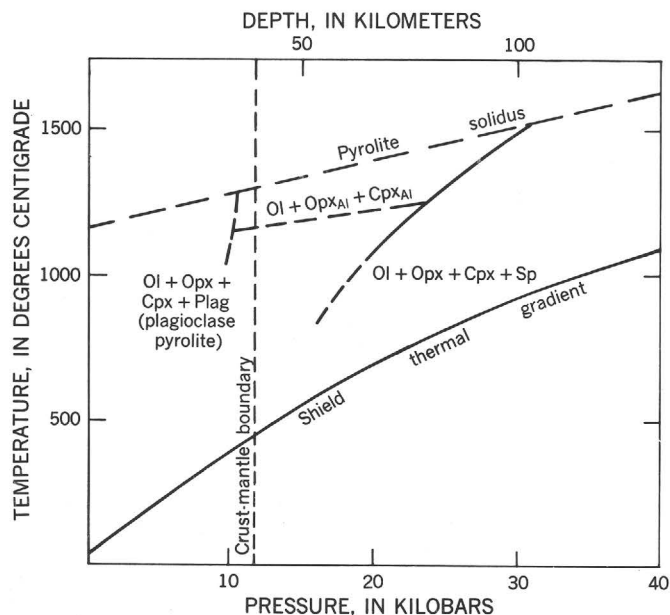


Figure 8.—Mineral-assembly stability fields (from Ringwood and Green, 1969). Depth of crust-mantle boundary in northern Arizona (Winslow, 100 km east of Flagstaff) from Healy and Warren (1969).

norites. The upper temperature and pressure limits for this mineral assemblage are about 1,300°C and 10 kb. This pressure is approximately equivalent to a depth of 35 km, which is close to the crust-mantle boundary (40 km) in this part of Arizona. If water were present in the melt, as the presence of primary hornblende and biotite suggests, then the temperature-pressure stability field for the plagioclase pyrolite would be lower and, consequently, the region of crystallization would be higher in the crust.

Ringwood and Green (1969, p. 644) suggest that in local areas of high heat flow and of relatively thin crust and low partial pressure of water, the plagioclase-pyrolite assemblage may be stable, and they point out that these conditions exist in the Western United States. The mafic inclusions at Crater 160 might be viewed as evidence in support of this idea.

REFERENCES

- Brady, L. F., and Webb, R. L., 1943, Cored bombs from Arizona and California volcanic cones: *Jour. Geology*, v. 51, p. 398–410.
- Colton, H. S., 1937, The basaltic cinder cones and lava flows of the San Francisco Mountain volcanic field, Arizona: *Mus. Northern Ariz. Bull.* 10, 50 p.
- Fleischer, Michael, and Chao, E. C. T., 1960, Some problems in the estimation of abundances of elements in the earth's crust: *Internat. Geol. Cong.*, 21st, Copenhagen 1960, Rept., pt. 1, p. 141–148.
- Healy, J. H., and Warren, D. H., 1969, Explosion seismic studies in North America, in *The earth's crust and upper mantle*: *Am. Geophys. Union Mon.* 13, p. 208–220.
- Jackson, E. D., 1961, Primary textures and mineral associations in the ultramafic zone of the Stillwater complex, Montana: *U.S. Geol. Survey Prof. Paper* 358, 106 p.
- Prinz, Martin, 1967, Geochemistry of basaltic rocks: Trace elements, in H. H. Hess and A. Poldervaart, eds. *Basalts*: New York, Interscience Publishers, p. 271–323.
- Ringwood, A. E., and Green, D. H., 1969, Phase transitions, in *The Earth's crust and upper mantle*: *Am. Geophys. Union Mon.* 13, p. 637–649.
- Robinson, H. H., 1913, The San Francisco volcanic field, Arizona: *U.S. Geol. Survey Prof. Paper* 76, 213 p.
- Sabels, B. E., 1960, Late Cenozoic volcanism in the San Francisco volcanic field and adjacent areas in north-central Arizona: *Univ. Arizona, Tucson, Ph. D. thesis*.
- Smouse, DeForrest, 1970, Inclusions within the lavas of Crater 160, San Francisco volcanic field, Arizona [abs.]: *Geol. Soc. America Rocky Mtn. Sec., 23rd Ann. Mtg., Proc.*, p. 349.
- Turner, F. J., 1942, Preferred orientation of olivine crystals in peridotites, with special reference to New Zealand examples: *Royal Soc. New Zealand Proc. and Trans.*, v. 72, p. 280–300.
- Ulrich, G. E., 1968, Maar deposits in the San Francisco volcanic field, Arizona [abs.]: *Geol. Soc. America Spec. Paper* 121, p. 575.
- Wager, L. R., 1968, Rhythmic and cryptic layering in mafic and ultramafic plutons, in H. H. Hess and A. Poldervaart, eds., *Basalts*: New York, Interscience Publishers, p. 573–622.
- Wahlstrom, E. E., 1955, *Petrographic mineralogy*: New York, John Wiley & Sons, 408 p.
- White, R. W., 1966, Ultramafic inclusions in basaltic rocks from Hawaii: *Contr. Mineralogy and Petrology*, v. 12, p. 245–314.
- Wilshire, H. G., and Binns, R. A., 1961, Basic and ultrabasic xenoliths from volcanic rocks of New South Wales: *Jour. Petrology*, v. 2, p. 185–208.
- Yoder, H. S., Jr., and Tilley, C. E., 1962, Origin of basalt magmas: An experimental study of natural and synthetic rock systems: *Jour. Petrology*, v. 3, p. 342–532.



SOME GENETIC IMPLICATIONS OF THE PHASE COMPOSITION OF A SIMPLE NEW ENGLAND PEGMATITE

By R. O. CASTLE and T. G. THEODORE, Menlo Park, Calif.

Abstract.—The pegmatitic granite facies of the Andover Granite crops out over 80–90 sq km of northeastern Massachusetts. Modal analysis of a relatively fine grained specimen from this facies shows that the selected specimen is composed almost exclusively of quartz, microcline, albitic plagioclase, and white mica; chemical analysis indicates that it is a peraluminous rock free of normative An. Bulk compositions of the essential and varietal phases are:

quartz—

SiO₂

potassium feldspar—

(heated, triclinic) Or₇₆Ab(+An)₂₄

(heated, monoclinic) Or_{79.6}Ab(+An)_{20.4}

(heated, monoclinic) Or_{77.6}Ab(+An)_{22.4}

(heated) Or_{92.2}Ab(+An)_{7.8}

(unheated) Or_{90.0}Ab(+An)_{10.0}

(X-ray diffraction determinations)

(electron microprobe determinations)

plagioclase feldspar—

Ab₉₆An₄ (optical determination)

Ab_{92.8}Or_{1.0}An_{6.2} (electron microprobe determination)

white mica—

Pa_{8.5}Mu_{91.5} (X-ray diffraction determination)

Pa_{10.6}Mu_{89.4} (electron microprobe determination)

The selected specimen probably crystallized from the pegmatitic fluid(s) at about 650°C under a confining pressure of about 5 kb. Minimum temperatures of crystallization deduced from the bulk composition(s) of the potassium feldspar suggest general reequilibration of the alkali feldspar system at subsolidus temperatures (545°–550°C or, less likely, 405°–410°C).

expected in any plutonic rock; hence this natural assemblage is especially well suited for comparisons with experimentally studied systems. (2) The composition and occurrence of this pegmatite, coupled with metamorphic assemblages found in the surrounding host rocks, permit close estimates of the maximum and minimum probable pressures at which this rock initially crystallized from the pegmatitic fluid(s); the maximum permissible difference between these two pressures is thought to be relatively small. This specimen, accordingly, provides a basis for estimating the approximate *P–T* conditions at which this typical, apparently syntectonic pegmatite crystallized.

Acknowledgments.—The generous assistance of several colleagues is gratefully acknowledged. J. H. Carman and O. F. Tuttle of Stanford University permitted use of a high-temperature furnace used to homogenize the cryptoperthitic potassium feldspar. Electron microprobe analyses were made by G. K. Czamanske and W. J. Nokleberg. Plagioclase was hand separated from potassium feldspar by K. C. Crowther, and precise oil immersion measurements of the refractive indices of the plagioclase were made by F. K. Miller. We are particularly indebted to W. C. Luth for assistance in the analysis and interpretation of the feldspar data. Early drafts of the manuscript were read by J. H. Carman and W. G. Ernst of the University of California, Los Angeles.

THE ANDOVER GRANITE

The Andover Granite of eastern Massachusetts is characterized by immense volumes of pegmatite exposed over many square kilometers (Emerson, 1917; Hansen, 1956; Castle, 1964; 1965a). The gross composition of the pegmatite, judged by visual inspection and modal analyses of relatively fine grained facies, ranges from adamellite to granodiorite. The variability of the essential mineral composition is such, however, that individual specimens and even small outcrops may be nearly devoid of either potassium feldspar or plagioclase.

Although we have made no attempt to measure the average modal composition of the pegmatite, compositions of the essential and varietal phases of a selected specimen have been determined with some care for two reasons: (1) The composition of the selected sample is about as simple as could be

The demonstrably igneous Andover Granite crops out over 240–250 sq km and forms a major part of the subalkaline intrusive series of northeastern Massachusetts (Castle, 1965a). The entire series probably is syntectonic for it is broadly conformable with the deformed metasedimentary and meta-volcanic rocks that it intrudes. The Andover Granite itself intrudes metamorphic rocks that are probably no younger than Cambrian and may be as old as late Precambrian (Castle, 1965b, p. C84–C85). Two Rb-Sr whole-rock ages have been reported for this pluton: Handford (1965, p. 14) has dated the Andover at 460±23 m.y., and R. E. Zartman (U.S. Geological Survey, 1967, p. A166–A167) places it at 415±15 m.y. Hence

we infer that the Andover Granite is no older than very late Precambrian or younger than Silurian.

General Characteristics of the Pegmatitic Granite Facies

The pegmatitic granite facies of the Andover Granite crops out over 80–90 sq km, chiefly within the area shown on figure 1. Much of this facies, moreover, is devoid of rock types other than pegmatite. The pegmatitic granite, like much of the Andover Granite, is characterized by a wide variety of fabrics within a relatively narrow compositional range. The finer grained rocks of this facies are characteristically medium to coarse grained and almost uniformly allotriomorphic, whereas the coarser grained typical pegmatites are generally seriate and allotriomorphic but locally hypidiomorphic. Graphic textures are relatively uncommon among the pegmatites, but imperfect examples occur locally. The rocks of the pegmatitic granite facies consist chiefly of quartz, microcline, and plagioclase. Varietal minerals are muscovite and, less commonly, biotite

altered in part to chlorite. Garnet, apatite, epidote, zircon, rutile, and unidentified opaque minerals occur in accessory amounts.

The outcrop from which the selected specimen was chosen (fig. 1) is typically pegmatitic and generally coarser grained than the analyzed specimen. The analyzed rock is somewhat seriate, medium to coarse grained and generally allotriomorphic (fig. 2). It is apparently identical in mineral composition with the mass of the outcrop and consists mainly of quartz, microcline, and albitic plagioclase. The feldspars occur as discrete grains with little visible perthitic or antiperthitic intergrowth, and the rock clearly falls within the subsolvus granite class of Tuttle and Bowen (1958, p. 129). The pegmatitic aspect of both the rock and the outcrop indicates that its general fabric is almost certainly the product of primary crystallization from the pegmatitic fluid(s); it is improbable, in other words, that the fabric can be attributed to subsolvus recrystallization of an initially hypersolvus granite or granite pegmatite.

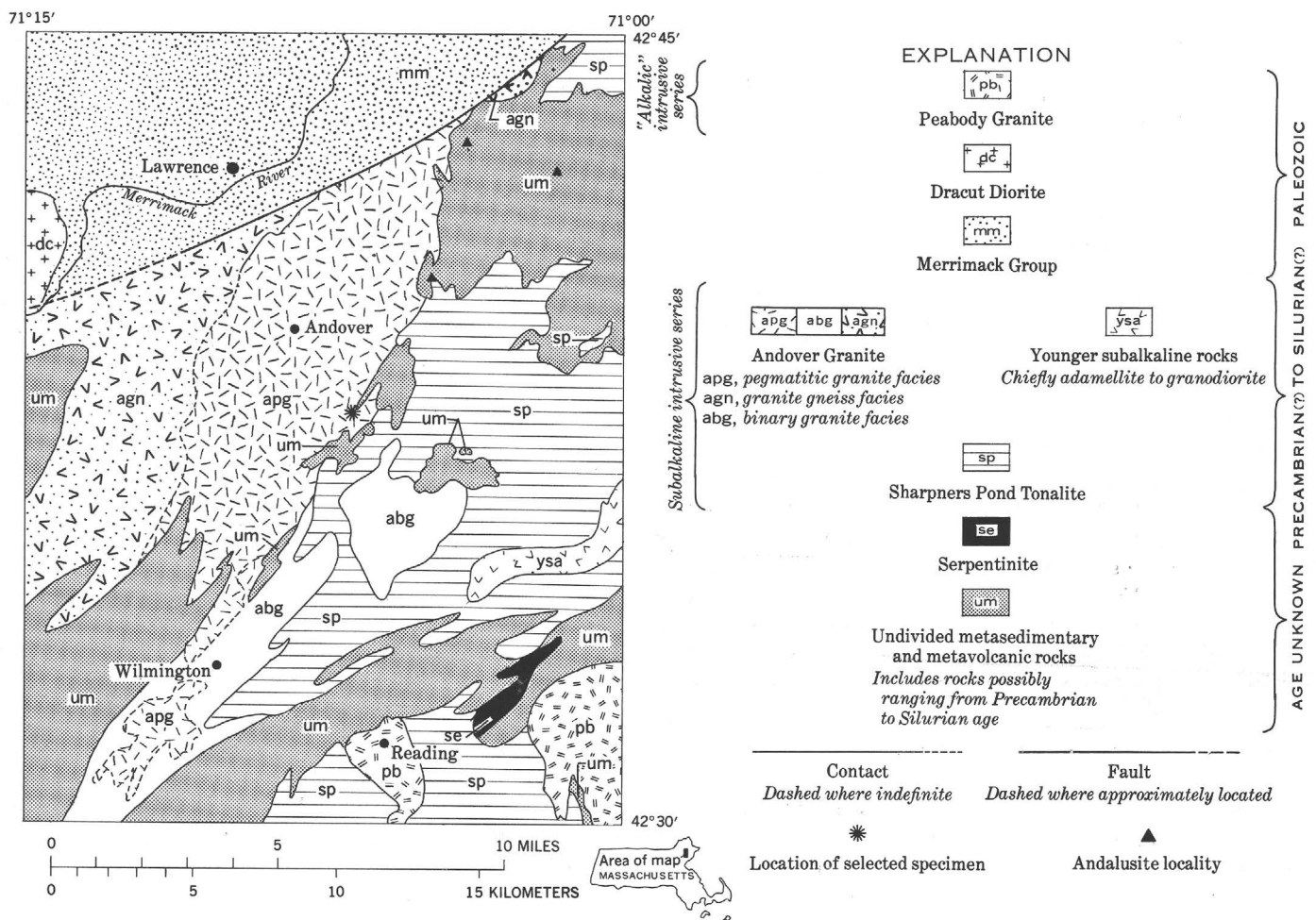


Figure 1.—Generalized geologic map showing distribution of major rock units over part of northeastern Massachusetts. Modified after Castle (1964, pl. 1; 1965a, p. C76).

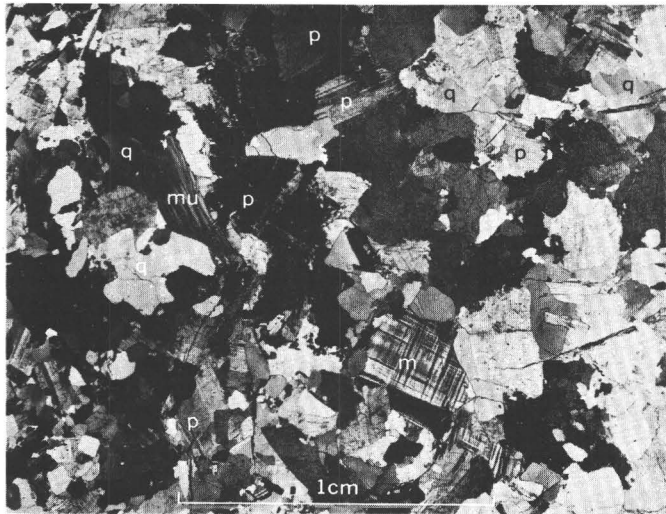


Figure 2.—Photomicrograph of selected specimen from the pegmatitic granite facies of the Andover Granite. q, quartz; m, microcline; p, plagioclase; mu, muscovite. Crossed nicols.

Whole-rock Composition of the Selected Specimen

Modal, chemical, and normative compositions of the selected specimen are given in table 1.

The modal composition is based on point counting over a standard-sized thin section and probably grossly approximates the mineral composition of the specimen from which the section was cut. Similarly, the rapid rock analysis and resultant norm, which clearly identify this specimen as peraluminous ($Al_2O_3 > Na_2O + K_2O + CaO$), are probably equally representative of the gross composition of the selected specimen. Neither of these analyses, however, is representative of the average composition of the pegmatitic granite facies or even of the outcrop from which the specimen was taken. Indeed, the majority of modal analyses of leucocratic granite from this same facies show that the proportion of quartz is somewhat less, and the ratio of microcline to plagioclase is almost invariably greater than it is in this specimen. The value of these analyses lies chiefly in the limits they place on the compositions of the individual mineral phases.

COMPOSITIONS OF THE INDIVIDUAL PHASES

Quartz

The modal quartz is believed to be nearly pure SiO_2 . Nevertheless the examined quartz grains typically include abundant secondary fluid inclusions distributed along microfractures that consist generally of two liquids (water plus liquid CO_2) plus a vapor phase. It is likely that the CO_2 reported in the chemical analysis (table 1) is contained largely within the observed inclusions.

Table 1.—Approximate mode, chemical analysis, and norm of selected specimen from the pegmatitic granite facies of the Andover Granite, Massachusetts
[Chemical analysis by the U.S. Geological Survey rapid rock-analysis laboratory]

Modal analysis (1,000 points counted) (volume percent)			
Quartz	29.2	Biotite	0.2
Microcline	17.0	Chlorite	.6
Plagioclase	48.8	Apatite	.1
White mica	4.1	Garnet	Trace
Chemical analysis (weight percent)			
SiO_2	74.7	K_2O	3.2
Al_2O_3	15.1	TiO_2	.03
Fe_2O_3	.4	P_2O_5	.26
FeO	.6	MnO	.13
MgO	.12	H_2O	.64
CaO	.39	CO_2	.14
Na_2O	4.3	Sum	100
Normative minerals (weight percent)			
Quartz	36.96	Magnetite	0.58
Corundum	4.56	Ilmenite	.06
Orthoclase	18.91	Apatite	.62
Albite	36.38	Calcite	.09
Anorthite	----	Magnesite	.20
Enstatite	.65	Sum	99.97
Ferrosilite	.96		

Microcline

The composition of the cryptoperthitic microcline has been determined both as it presently exists and as it existed in its initially unexsolved state. Its mixed composition may be measured by X-ray methods only after heating and homogenizing the presently perthitic material.

Analytical procedure

The selected hand specimen was partly crushed, and the microcline was stained with sodium cobaltinitrite. Sufficient microcline was then separated by hand under a binocular microscope and washed with dilute hydrochloric acid. Many of the grains retained a slight yellow color, but the volume of stain product must have been very small compared to the volume of uncontaminated feldspar. The separated microcline was then crushed to 100–150 mesh size Tyler sieves and packed in platinum-foil packets.

The packaged samples were heated in a vertical quench furnace for periods of as much as 600 hours. The temperature was maintained by a voltage stabilizing Variac and was measured periodically by means of a platinum-rhodium

thermocouple calibrated against the melting point of gold. The temperature was kept at a maximum of about 1,040°C; except for those very brief intervals during which samples were extracted from the furnace, it seldom fell below 1,035°C.

Compositions of both the perthitic phases of the unheated microcline and the homogenized potassium feldspar have been determined by the 20 $\bar{1}$ X-ray method described by Orville (1963, p. 206–207; 1967, p. 74–76). Each feldspar run, with KBrO₃ (2 θ_{101} = 20.217; CuK α radiation) as an internal standard, was oscillated four times through the range 19.5°–22.0°C. Hence the recorded 2 θ represents an average of eight individual readings based on the distance between the weighted midpoints of the respective peaks ($\Delta 2\theta = 2\theta$ alkali feldspar (20 $\bar{1}$)–2 θ KBrO₃(101)).

Because the time required for homogenization could not be predetermined, a rate study was performed in which the 2 θ position for the 20 $\bar{1}$ reflection was compared with heating time (table 2) (see Ernst, 1960, p. 292–296). The appearance of an asymptotic relation between 2 θ and the time axis suggests complete homogenization (see fig. 3). A check on the degree of mixing is provided by the configuration of the 20 $\bar{1}$ plagioclase peak (Ab); its disappearance is consistent with homogenization (see fig. 4).

The compositions of the triclinic phases may be read directly from a determinative curve which plots 2 θ against molecular percent Or (Orville, 1967, p. 75). The composition of the sanidinized phase is based on a polynomial expression developed by Luth and Querol-Suñé (1970, p. 38). Because a determination based on a curve properly applied to the alternate structural state may introduce errors of up to 3 percent Or (Orville, 1967, p. 76), the structural state for those samples heated beyond four hours was confirmed by the positions and configurations of the 131 and 1 $\bar{3}1$ peaks (fig. 4).

A preliminary set of 2 θ values (for the 20 $\bar{1}$ reflection) measured against heating time was obtained from runs in

Table 2.—Average 20 $\bar{1}$ diffraction angles (CuK α radiation) after various heating times for microcline and plagioclase separates taken from the selected pegmatitic granite specimen

Microcline			
Duration of heating (hours)	Structural state	Or	Perthitic Ab
		Average 2 θ (20 $\bar{1}$)	Average 2 θ (20 $\bar{1}$)
0	Microcline	21.016	22.067
.17	Transitional	21.074	...
.50	...do...	21.095	...
3.58	...do...	21.137	...
17.50	...do...	21.139	...
91.0	...do...	21.190	...
205.8	Sanidine	21.167	...
309.5	...do...	21.165	...
398.0	...do...	21.179	...
597.5	...do...	21.158	...

Plagioclase		
Duration of heating (hours)	Ab+An	Antiperthitic(?) Or
	Average 2 θ (20 $\bar{1}$)	Average 2 θ (20 $\bar{1}$)
0	22.052	20.863
1.25	22.059	...
24.0	22.060	20.866

which the potassium and plagioclase feldspars were unstained and unseparated from each other. These values are represented by the triangles in figure 3. The analytical procedure differed further from that described above in that the feldspar grains were not ground prior to heating (such that differences measured on successive runs are conceivably attributable to initial differences in sample composition) and heating was carried out in a large furnace under poorly controlled temperature conditions. The furnace temperature sought was 900°C; the actual temperature probably was within $\pm 100^\circ\text{C}$ of this figure. Nonetheless, heating over short periods (up to 10 hours) produced consistent and apparently reliable results. Longer heating led to aberrations in the position of the 20 $\bar{1}$

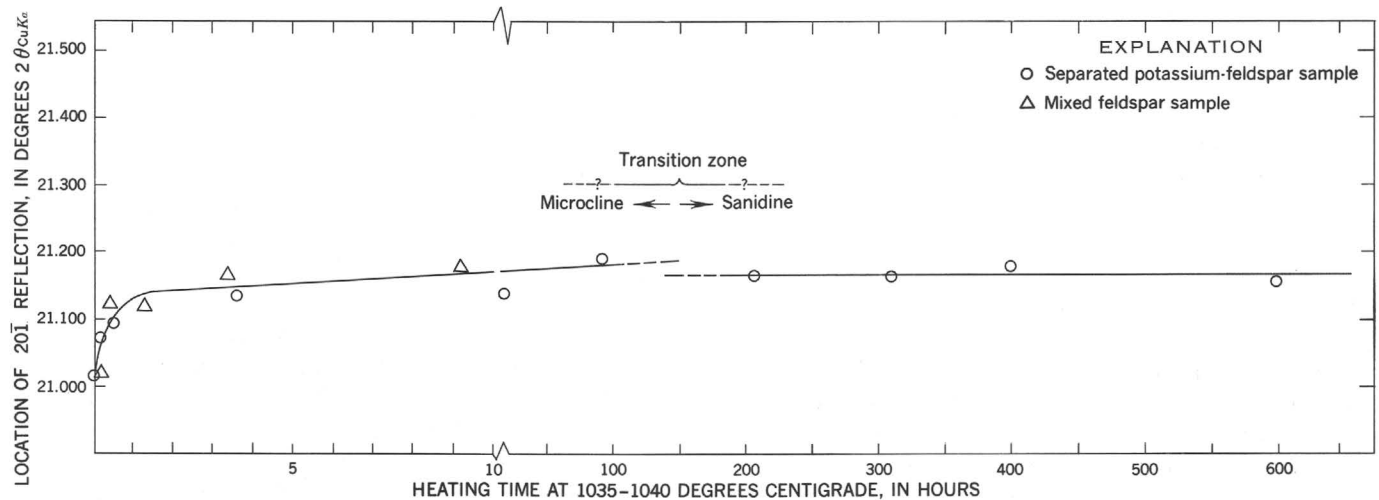


Figure 3.—Rate curve showing 2 θ (20 $\bar{1}$) versus heating time for potassium feldspar from selected specimen of the pegmatitic granite facies. Note change in time scale after 10 hours.

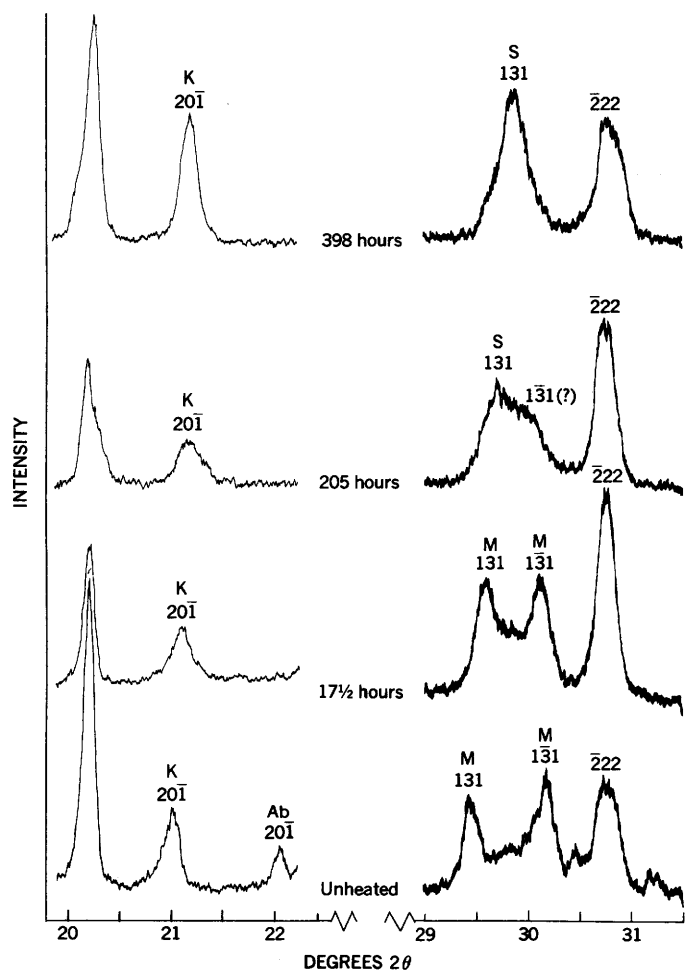


Figure 4.—X-ray diffraction patterns of potassium feldspar from the selected specimen after successive periods of dry heating at 1,035°–1,040°C. K, potassium-rich alkali feldspar; Ab, albitic plagioclase; S, sanidine; M, microcline.

reflection that we are unable to explain. These less rigorous determinations provide, nevertheless, an independent check on the feldspar compositions deduced from the procedure outlined in the preceding paragraphs.

Discussion

Values of 2θ versus heating time (table 2) are plotted in figure 3. Changes in structural state associated with progressively longer periods of heating are deduced from the 131 and $\bar{1}\bar{3}\bar{1}$ reflections (fig. 4). The essential triclinicity was preserved through at least 91 hours of heating; heating beyond 91 hours led to a loss of the triclinic 131 and $\bar{1}\bar{3}\bar{1}$ peaks and the emergence of a 131 monoclinic peak. This control on the inversion of the feldspar from an essentially triclinic structure to a monoclinic form permits a comparison among the homogenized compositions determined for each structural state.

The curve presented in figure 3 has been visually estimated and incorporates the results of the mixed feldspar study. Most of the points lie close to the constructed curve. The left side of the curve (that is, the part of the curve based on 2θ values for triclinic structural states only) shows a gradual rise beyond about 2 hours. This rise would appear even more gradual and the curve more nearly asymptotic, if the time axis had not been compressed beyond the 10-hour point; the single aberrant value that occurs at 17½ hours would appear less so, if the time axis were on a uniform scale. The triclinic potassium feldspar is assumed to have become fully homogenized after 91 hours of heating, by which time the 2θ -time curve had become nearly flat and 2θ had approached a value of 21.190. All four points identified with a saniditized structural state plot along a nearly horizontal line with an average 2θ value of 21.167. Application of Orville's (1967, p. 75) microcline–low-albite determinative curve and Luth and Querol-Suñé's (1970, p. 38) sanidine–high-albite (potassium feldspar) determinative expression ($\text{CuK}\alpha$, radiation) produces the following molecular percent compositional values:

- (1) unheated microcline, host potassium feldspar, $\text{Or}_{96}\text{Ab}_4$;
- (2) unheated microcline, perthitic plagioclase, $\text{Ab}_{100.5}$;
- (3) homogenized triclinic potassium feldspar $\text{Or}_{76}\text{Ab}_{24}$; and
- (4) homogenized monoclinic potassium feldspar,¹ $\text{Or}_{79.6}\text{Ab}_{20.4}$ (experimental data of Orville)
 $\text{Or}_{77.6}\text{Ab}_{22.4}$ (experimental data of Luth and Querol-Suñé).

The “super” albite composition of the perthitic plagioclase although puzzling, may not be unique. Ernst (1960, p. 295–296) has described cryptoperthitic plagioclase characterized by an average 2θ ($20\bar{1}$) of 22.138 ($\text{CuK}\alpha$ radiation). This value suggests a composition as albitic as Ab_{107} , if the feldspar is triclinic, and an even more albitic composition, if it

¹The polynomial expressions developed by Luth and Querol-Suñé (1970, p. 38) for the determination of potassium feldspar (sanidine) compositions from unit-cell edge (a) and unit-cell volume (V) measurements, respectively, may also be used to determine the compositions of the saniditized potassium feldspar samples. Thus, for the 597.5-hour run $a=8.5311$ Å and $V=717.29$ Å³; application of these data to the appropriate expressions produces the following compositions:

- (a) $\text{Or}_{82.4}\text{Ab}_{17.6}$ (experimental data of Orville)
- $\text{Or}_{81.3}\text{Ab}_{18.6}$ (experimental data of Luth and Querol-Suñé)
- (V) $\text{Or}_{85.5}\text{Ab}_{14.5}$ (experimental data of Orville)
- $\text{Or}_{82.6}\text{Ab}_{17.4}$ (experimental data of Luth and Querol-Suñé).

Because the 597.5-hour run is characterized by the lowest 2θ and, hence, the seemingly most potassic composition ($\text{Or}_{80.0}\text{Ab}_{20.0}$ —experimental 2θ data of Orville; $\text{Or}_{78.0}\text{Ab}_{22.0}$ —experimental 2θ data of Luth and Querol-Suñé) of any of the four saniditized samples (table 2), these compositions are reasonably compatible with those deduced from the average 2θ .

is monoclinic. These impossibly enriched values cannot be attributed to structural overprint of the host potassium feldspar; such an overprint would reduce 2θ to values below those attributable to pure Ab+An.

Plagioclase

The composition of the plagioclase has been determined both as it exists in its presently antiperthitic(?) state and as it is inferred to have existed in its initially homogenized form. These compositions differ only slightly if at all.

Analytical procedure

The analyzed plagioclase was separated by hand under a binocular microscope from unstained crushed material; selection of grains was based solely on the recognition of albite twins. Packaged samples were then heated and homogenized in a muffle furnace for periods of 1¼ and 24 hours. The furnace temperature was set for 850°C and almost certainly remained within $\pm 100^\circ\text{C}$ of this figure.

The An content of the unheated plagioclase was determined optically by F. K. Miller. Oil-immersion index measurements under sodium light yielded the following results:

$$n_y = 1.535 \pm 0.001$$

$$n_z = 1.540 \pm 0.001.$$

Determinations of the Or content of both unheated and heated plagioclase phases have been based on the same X-ray diffraction procedure utilized in the analyses of the coexisting triclinic potassium feldspar.

Discussion

Both the refractive indices and the positions of the $20\bar{1}$ diffraction peaks for the unheated material indicate that the plagioclase is a typically plutonic, low-temperature variety. Thus the indices of refraction indicate a composition of $\text{Ab}_{95.5}\text{An}_{4.5}$ (n_y) and $\text{Ab}_{96.7}\text{An}_{3.3}$ (n_z)—or an average of about An_4 —for the unheated material (Deer and others, 1963, p. 131). Application of the $20\bar{1}$ plagioclase 2θ values given in table 2 to Orville's (1967, p. 75) low albite-microcline determinative curve yields the following feldspar compositions in molecular percent:

- (1) unheated plagioclase, host plagioclase phase,
Ab+An_{99.5}Or_{0.5};
- (2) unheated plagioclase, antiperthitic(?) potassium
feldspar phase,
Or_{112.5};
- (3) heated plagioclase, host plagioclase phase,
Ab+An_{100.5}; and
- (4) heated plagioclase, antiperthitic(?) potassium
feldspar phase,
Or₁₁₂.

The An content of the plagioclase, although somewhat greater than expected, is reasonably consistent with that deduced from the bulk chemical composition (table 1).

The deduced composition of the heated plagioclase suggests that the Ab-rich limb of the alkali feldspar solvus may be nearly vertical up to pegmatitic melt temperatures, and even more highly skewed toward the Ab end than generally recognized. Alternatively, this particular specimen simply failed to homogenize after only 1 day of heating at room pressure. This possibility is supported by the apparent persistence of an ill-defined, but recognizable, $20\bar{1}$ Or peak through the 24-hour heating period. (This Or peak may belong to an extraperthitic potassium feldspar phase, but its composition indicates that this is unlikely.) The obviously aberrant compositions assigned to the presumably antiperthitic lamellae provoke skepticism. Structural distortion of the lamellae by the enclosed host no more explains this phenomenon than it does the "super" albite lamellae contained in the unheated microcline. We can, in fact, offer no explanation for the indicated compositions of the antiperthitic lamellae that does not challenge the validity of either the $20\bar{1}$ X-ray diffraction method or the utilized determinative curve.

Electron Microprobe Analyses of the Feldspar Pair

Unresolved questions surrounding the homogenized composition of the potassium feldspar and the anorthite content of the plagioclase indicated that the optically and X-ray determined feldspar compositions should be checked by electron microprobe techniques.

Microprobe analyses were made by G. K. Czamanske and W. J. Nokleberg on polished thin sections and grain mounts, using an Applied Research Laboratories electron microprobe, model EMX-SM. Light-element volatilization was minimized by using a 5μ -diameter electron beam, a low sample current of 0.02–0.03 μa , and an acceleration potential of either 10 or 15 kv. Well-analyzed orthoclase and plagioclase standards were used as controls, and either 10- or 20-second counts were taken on both standards and unknowns. A theoretical computer program, designed by Beeson (1967), corrected all counts for absorption, fluorescence, and atomic number effects and reduced the data. Preliminary analyses for Na_2O , K_2O , and CaO were made on three grains each of heated and unheated potassium feldspar and seven grains of unheated plagioclase; three to six randomly selected spots were analyzed within each grain. Complete major oxide analyses were made on two grains each of unheated potassium feldspar, heated potassium feldspar, and plagioclase; each of these grains was analyzed at 10 to 20 spots.

Oxide analyses, molecular compositions, and structural formulas (for those grains analyzed for all major oxides), as deduced from the microprobe study, are listed in table 3. Average molecular compositions obtained from this study are:

- (1) unheated potassium feldspar, $\text{Or}_{92.2}\text{Ab}+\text{An}_{7.8}$;
- (2) heated potassium feldspar, $\text{Or}_{90.0}\text{Ab}+\text{An}_{10.0}$; and
- (3) unheated plagioclase, $\text{Ab}_{92.8}\text{Or}_{1.0}\text{An}_{6.2}$.

The plagioclase composition, although slightly more anorthitic, is reasonably consistent with that deduced from the whole-rock chemical analysis and optical examination. Both potassium feldspar compositions, however, differ significantly from those determined through X-ray diffraction measurements of the homogenized material.

Although we can suggest two procedural explanations for the disparate potassium feldspar compositions derived from the electron microprobe and X-ray diffraction studies, neither, in our judgment, is particularly satisfactory.

1. Microprobe analyses were generally made on relatively large, mounted grain fragments. The thermally homogenized grains were heated for a maximum period of about 1 hour, and none were ground before heating. Thus the heated grains may have been incompletely homogenized. However, because the K_2O and Na_2O values reported for both heated and unheated microcline are characterized by small and nearly identical standard deviations (table 3), use of a relatively large diameter electron beam has seemingly produced representative bulk compositions. It is improbable, in other words, that the contribution of the albite lamellae could have been excluded from the bulk composition, even in the unheated material. (This argument has some obvious limitations. Were it rigorously true, there should be no difference between analyses of unheated and heated material, whereas, in fact, the average analysis of the heated microcline is clearly richer in Na_2O than that of the unheated microcline.)

2. It could be argued that the low soda content indicated by the microprobe analyses resulted from the inadvertent concentration of analysis points within relatively potassic microcline cores. This possibility, however, was effectively ruled out by careful microprobe analyses in one thin section in which no zoning could be detected to within 20μ of the grain boundaries.

Flame Photometric Analyses of the Potassium Feldspar

Because the potassium feldspar compositions deduced from the $20\bar{1}$ X-ray diffraction and electron microprobe analyses are internally consistent for each method yet differ from each other by at least 10 mol. percent, four potassium feldspar separates were analyzed for alkali content by flame photometric methods. The results of these analyses are listed in table 4.

Owing chiefly to the inevitable problems associated with the separation of pure mineral samples, the determinations listed in table 4 are less than unequivocal. The apparent stoichiometry suggests, nonetheless, that the analyses themselves are generally very accurate. The care exercised in sample preparation and the calculated stoichiometry indicate that the

analyses reported for sample 1 are probably the most accurate of those listed in table 4. The relatively low Or content is almost certainly attributable to the inadvertent inclusion of small amounts of extraperthitic plagioclase with the analyzed specimen. The significantly higher Or content reported for sample 2 may derive from potassium contamination associated with residual stain products. The relatively low Na_2O value reported for sample 4 (and the resultant substoichiometric composition), as contrasted with sample 3, may result from the selective volatilization of Na_2O during heating.

The alkali values listed for samples 3 and 4 are certainly the most meaningful of those reported in table 4. Samples 3 and 4 are the only samples for which we have an independent check on the extraperthitic plagioclase content. Because the $20\bar{1}$ albite peak that characterizes the unheated material disappears completely after only 10 minutes of heating (see table 2 and fig. 4), and because the 002 albite peak disappears after no more and probably much less than 60 hours of heating, the amount of extraperthitic plagioclase contained in the analyzed samples must be less than the resolution of the X-ray diffraction method—probably less than 2 or 3 percent (W. C. Luth, oral comm., 1971). Allowance for as much as 5 percent plagioclase would shift the reported compositions of samples 3 and 4 from $\text{Or}_{73.3}\text{Ab}_{26.7}$ and $\text{Or}_{75.4}\text{Ab}_{24.6}$ to about $\text{Or}_{78}\text{Ab}_{22}$ and $\text{Or}_{80}\text{Ab}_{20}$, respectively.

The problems of mineral separation are such that the flame photometric analyses cannot be considered definitive. These analyses, nevertheless, support the rate-study determinations.

White Mica

White mica occurs in two general habits. Medium- to coarse-grained discrete books (fig. 2) account for fully 90 percent of this material. The remainder occurs as very fine grained fibrolite-appearing needles or needle swarms that commonly show a sheathlike distribution. We have analyzed only the coarse-grained phase.

The white mica has been analyzed by both X-ray diffractometer and electron microprobe methods.

The muscovite-paragonite ratio is easily determined by a basal separation-composition comparison that relates the $(002)_{2M}d$ -spacing to the muscovite-paragonite molar composition (Zen and Albee, 1964, p. 914–917); this method requires only that the 002 diffraction angle (or a suitable repeat) be accurately measured. The prepared sample was oscillated twice through a diffractometer range of 43.5° – 46.5° at a scan speed of $1/8^\circ/\text{min}$; this permitted determination of the 0010 mica peak through comparison with the 111 diamond peak characterized by a known $\text{CuK}\alpha$ diffraction angle of 43.925° . An average of four determinations showed that

$$2\theta_{0010} \text{ mica} = 45.369^\circ$$

and, by the Bragg equation,

$$d_{(0010)} = 1.9989 \text{ \AA}, \text{ and } d_{(002)} = 9.995 \text{ \AA}.$$

Table 3.—*Electron microprobe analyses of feldspars and micas from a selected specimen of the pegmatitic granite facies of the Andover Granite, Massachusetts*

[Abbreviation: N.d.; not detected]

Mineral	Potassium feldspar									
	Heated					Unheated				
Grain No.	1	2	3	4	5	6	7	8	9	10
Major oxides ¹ (weight percent)										
SiO ₂	63.8±0.5	63.6±1.2	62.8±1.0	62.8±0.5
Al ₂ O ₃	18.5±.2	18.4±.4	18.3±.2	18.3±.3
FeO ²	N.d.	.03±.00202±.001	.02±.003
MgO01±.001	.01±.00104±.005	.02±.002
CaO09±.008	.2±.03	N.d.	N.d.	N.d.	.08±.008	.07±.005	0.05	0.05	N.d.
Na ₂ O98±.2	.74±.3	0.6	1.0	0.9	1.3±.2	1.4±.3	1.	1.3	1.1
K ₂ O	15.3±.3	15.5±.6	16.3	15.6	15.8	14.9±.3	14.8±.3	15.8	15.1	15.4
TiO ₂	N.d.	N.d.01±.002	.01
MnO	N.d.	.02±.002	N.d.	N.d.
Total	98.8±1.2	98.5±2.5	97.4±1.7	97.5±1.4
Structural formulas ³										
Si } Z	11.93	11.92	11.89	11.90
Al ^{iv} }	4.07	4.08	4.09	4.09
Al ^{vi} }	.01	N.d.	N.d.	N.d.
Fe } Y	N.d.	.01	N.d.	N.d.
Ti }	N.d.	N.d.	N.d.	N.d.
Mg }	N.d.	N.d.01	.01
Mn }	N.d.	N.d.	N.d.	N.d.
Ca }	.02	.0402	.01
Na } X	.36	.2747	.51
K }	3.65	3.70	3.60	3.58
Molecular percent ⁴										
Or	90.7	92.3	94.8	90.9	92.2	88.1	87.3	91.3	88.0	90.1
Ab	8.8	6.7	5.1	8.9	7.7	11.5	12.4	8.5	11.8	9.7
An5	1.0	.1	.2	.1	.4	.3	.1	.2	.2
Pa
Mu

¹ Analysts: G. K. Czamanske (grains 1, 2, 6, 7, 11, 12, 20–22) and W. J. Nokleberg (grains 3–5, 8–10, 13–19).² Total iron expressed as FeO.³ Calculated on basis of 32 O per formula unit for feldspars, and 22 O per formula unit for micas, using the computer program described by Jackson, Stevens, and Bowen (1967).⁴ Stoichiometry assumed.

Utilization of Zen and Albee's (1964, p. 917) regression curve between (002)_{2M} spacings and analyzed muscovite-paragonite samples indicates that the molar composition of the white mica is Pa_{8.5}Mu_{91.5}.

Electron microprobe analyses of two muscovite grains contained in a single polished thin section were made by G. K. Czamanske (table 3). These analyses used the same instrument and procedures as those used in the total major-oxide analyses of the associated feldspars; they differ only in that a well-analyzed biotite has been used as a standard. The

calculated structural formulas fit almost perfectly with those of the ideal white mica (muscovite-paragonite), and the average composition (Pa_{10.6}Mu_{89.4}) closely accords with that deduced from X-ray diffractometer measurements.

Accessory Phases

We have analyzed only one accessory mineral, biotite. The approximate compositions of the remaining accessories may be deduced from their occurrence and from the chemical composition of the rock (table 1).

Table 1.—Continued

Plagioclase									Muscovite		Biotite
11	12	13	14	15	16	17	18	19	20	21	22
Major oxides ¹ (weight percent)											
66.7±0.3	66.0±0.7	45.8±0.6	45.4±0.7	35.2±1.6
19.8±.1	20.2±.4	35.9±.1	35.7±.4	24.6±3.5
N.d.	N.d.	1.5±0.09	1.6±0.05	23.8±2.7
N.d.	.01±0.00152±0.04	.56±0.03	4.3±.3
.45±0.06	.86±.2	1.2	1.4	1.5	1.3	1.4	1.4	1.4	.02±0.003	N.d.	.12±0.01
11.4±.2	11.7±.1	11.1	11.0	10.8	11.2	11.1	10.9	11.0	1.1±.2	.60±0.07	.25±0.02
.11±.01	.11±.01	.3	.2	.2	.1	.2	.2	.1	10.7±.2	11.4±.1	8.3±.3
N.d.	.02±0.00206±0.01	.15±0.03	.79±.3
N.d.	.01±0.00102±0.002	N.d.	.56±0.05
98.3±.7	98.9±1.4								95.6±1.2	95.3±1.2	97.8±8.7
Structural formulas ³											
...	6.11	6.08	5.25
									1.89	1.92	2.75
									3.74	3.73	1.58
									.17	.18	2.96
...01	.02	.09
									.10	.11	.95
									N.d.	N.d.	.07
									N.d.	N.d.	.02
...29	.16	.07
									1.82	1.94	1.57
Molecular percent ⁴											
...	13.7	7.6	
...	86.3	92.4	

Biotite

Table 3 lists a single microprobe analysis by G. K. Czaman-ske of a somewhat altered biotite grain contained within one of the polished thin sections. The procedures, standards, and instrument used in this analysis are identical with those used in the microprobe analysis of the associated white mica. Because nearly all the biotite has been highly chloritized, replicate analyses were not attempted.

The magnesium-to-iron ionic ratio (Mg/Fe) of the analyzed grain is about 0.32. However, since the probe cannot distinguish

between Fe⁺² and Fe⁺³, total iron is expressed arbitrarily as FeO. Hence, we may say only that the analyzed specimen, while somewhat phlogopitic, lies toward the annite-siderophyllite sideline (Deer and others, 1962b, p. 57).

Apatite

All the phosphate reported in the rock analysis (table 1) is logically assigned to apatite. Furthermore, because other appropriate cations are either unreported or more reasonably associated with other phases, the apatite is assumed to be a nearly pure calcium variety.

Table 4.—*Flame photometric alkali determinations and calculated compositions of potassium feldspar separated from selected specimen of the pegmatitic granite facies of the Andover Granite, Massachusetts*

[In calculating the feldspar compositions, the analyzed samples were assumed to consist exclusively of pure alkali feldspar; the stoichiometry index, which shows the extent to which the reported K_2O and Na_2O satisfy the alkali feldspar structure, is a measure of the validity of this assumption. Analyst, L. B. Schlocker]

Sample	Flame photometric alkali determination (weight percent)		Calculated feldspar composition (mol. percent)	Stoichiometry index (weight percent)
	K_2O	Na_2O		
1	11.94	3.47	Or _{69.4} Ab _{30.6}	100.1
2	13.76	2.12	Or _{80.9} Ab _{19.1}	99.3
3	12.72	3.05	Or _{73.3} Ab _{26.7}	101.0
4	12.73	2.73	Or _{75.4} Ab _{24.6}	98.4

1. Less than 10 mg; fused in Pt. Prepared especially for flame photometric analysis. Each grain was examined and physically cleansed of possible contaminants.
2. Less than 10 mg; fused in Pt. Residual potassium feldspar grains from initial separation.
3. Less than 10 mg; fused in Pt. Unheated split from material utilized in rate study.
4. Fused in graphite. Heated split from material utilized in rate study.

Garnet

The pink to medium-red color of the garnet, together with its occurrence, suggests that it is principally almandine (Deer and others, 1962a, p. 89). Because the spessartite molecule commonly is present in granitic and rhyolitic garnets (Deer and others, 1962a, p. 101), a large part of the MnO reported in the rock analysis (table 1) probably should be assigned to this phase. Hence we conclude that the garnet is probably a spessartitic almandine.

PHYSICAL CONDITIONS OF CRYSTALLIZATION

Determination of the minimum probable pressure at which pegmatitic crystallization took place is based on the following assumptions: (1) the potassium feldspar crystallized initially as a monoclinic phase, (2) the bulk compositions of the presently coexisting feldspars are identical with those crystallized from the pegmatitic fluid(s) and cannot be attributed simply to subsolidus exsolution, (3) the pegmatitic melt remained H_2O saturated during crystallization (that is, $P_{fluid} = P_{total}$), (4) the An content of the feldspar system is sufficiently small that it may be disregarded, and (5) primary crystallization was completed at pressures above the intersection of the minimum melting-of-granite and paragonitic muscovite + quartz breakdown curves.

The first assumption cannot be directly affirmed; it is indirectly supported, however, by the inversion of microcline to orthoclase within metamorphic aureoles surrounding certain granitic intrusions (Steiger and Hart, 1967; Tilling, 1968). The

second and third assumptions are supported by the generally hypidiomorphic and commonly extremely coarse grained fabric. Hence this assemblage must have crystallized within the two-feldspar field and thus above 3.5 kb (Tuttle and Bowen, 1958, p. 71–72). Allowance for any anorthite in the system would reduce this theoretical minimum. In any case, since the white mica is almost certainly a primary magmatic phase, and since the minimum melting-of-granite curve intersects the paragonitic muscovite breakdown curve at about 4.5 kb, it is doubtful that primary crystallization could have occurred below 4.5 kb.

The maximum crystallization pressure is readily inferred from the presence of andalusite in the surrounding country rock (see fig. 1) and from the absence of kyanite for at least 65 km in any direction (Thompson and Norton, 1968, p. 320, 324). According to Richardson, Gilbert, and Bell (1969, p. 266), the aluminum silicate triple point occurs at about 5.46 kb. Although the experimentally established uncertainty field allows for the occurrence of andalusite at pressures as great as 6.75 kb, its occurrence over a wide range of metamorphic facies within the specified 65-km radius suggests that the confining pressure must have been well below the triple-point pressure. For example, at 1 kb below the triple point, andalusite is stable over a temperature range of only about 130°C. Hence, it is extremely unlikely that the maximum confining pressure could have exceeded 5.8 kb. The most likely position of the triple point, as given by Richardson, Gilbert, and Bell (1969, p. 266), indicates that pegmatitic crystallization probably took place at pressures no greater than about 5 kb. Thus the available evidence suggests that the primary crystallization pressure was almost certainly within the 3.5- to 5.5-kb range and probably within the 4.5- to 5.0-kb range.

The P - T field within which primary crystallization of the selected specimen took place is defined by the following: (1) an isobaric line at 5.5 kb, (2) an isobaric line at 3.5 kb, (3) the minimum melting-of-granite curve, and (4) the paragonitic muscovite + quartz univariant breakdown curve. This P - T field is represented in figure 5 by the stippled pattern. The minimum melting-of-granite curve, as determined from experimental investigations in the system Ab-Or-SiO₂-H₂O (Luth and others, 1964, p. 760), is shown as curve A in figure 5. According to W. C. Luth (oral comm., 1970) this curve could (within a peraluminous, persilicic system of the sort under consideration here) be displaced no more than 20°C to the left of curve A. Hence the “minimum” minimum melting-of-granite curve for this system may be represented by curve C. The system muscovite + quartz + H₂O has been studied by Evans (1965). The breakdown curve for pure muscovite in the persilicic, supercritical aqueous environment is shown in figure 5 as curve B. The white mica contained in the selected specimen, however, is impure and composed of Pa_{8.5}Mu_{9.5} (or Pa_{10.6}Mu_{8.4}). Because Evans and Guidotti (1966, p. 59) have suggested that “muscovite of composition Ms_{9.4}Pg₆ can

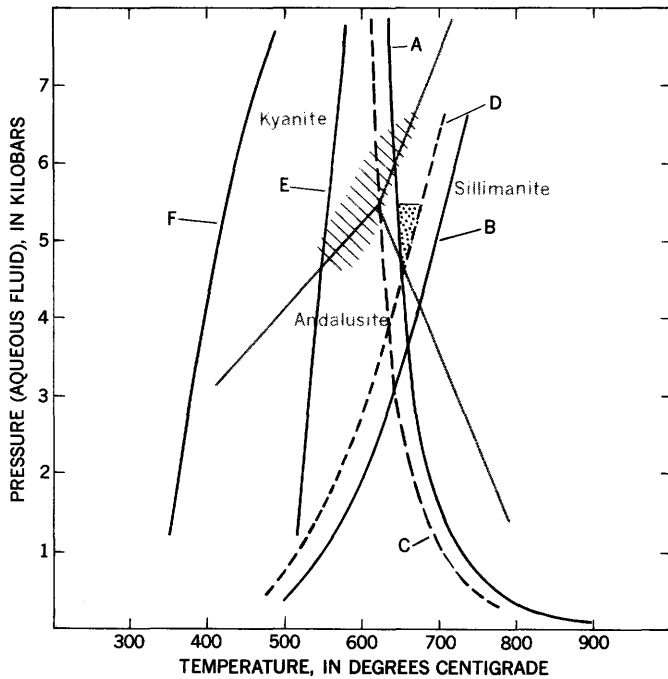


Figure 5.—Experimentally investigated phase relations pertinent to the crystallization of the pegmatitic granite facies. A. Minimum melting-of-granite curve (Luth and others, 1964, p. 760). B. Muscovite + quartz \rightleftharpoons potassium feldspar + sillimanite + quartz + H₂O (Evans, 1965, p. 660). C. Approximate position of “minimum” minimum melting-of-granite curve; see text. D. Approximate position of $\text{Mu}_{91.5}\text{Pa}_{8.5}$ + quartz \rightleftharpoons albitic potassium feldspar + sillimanite + quartz + H₂O; see text for discussion. E. Isocompositional stability trajectory for a monoclinic potassium feldspar of composition $\text{Or}_{80}\text{Ab}_{20}$. F. Isocompositional stability trajectory for a monoclinic potassium feldspar of composition $\text{Or}_{90}\text{Ab}_{10}$. Phase equilibrium relations in the aluminum silicate system shown as screened base (gray); uncertainty in the location of the triple point shown by crosshatch pattern (after Richardson and others 1969, p. 266).

be expected to react with quartz some 20° to 30° below equilibrium [for the pure muscovite system],” we have drawn the breakdown curve for paragonitic muscovite (curve D of fig. 5) 30° to the left of curve B.²

Determination of the minimum temperature of crystallization is most reasonably based on the intersection of the minimum melting-of-granite curve with the isobar corresponding to the maximum likely pressure of crystallization (fig. 5). This intersection suggests that the minimum probable temperature of primary crystallization was about 640°C (curve A) or, less likely, 620°C (curve C).

Alternatively, the minimum temperature of crystallization may be deduced from the bulk composition of the potassium

²Partial chemical analysis of separated muscovite shows that this phase contains 0.0 percent Cl and 0.18 percent F. Analyst Marcelyn Cremer. Hence it is assumed that the position of the paragonitic-muscovite stability curve was unaffected by the halogen concentration in the coexisting fluid(s) from which the mica crystallized.

feldspar. Luth, Fenn, and Martin (1970) have constructed a series of alkali feldspar solvi based on experimental investigations over the pressure range 1.25–10 kb (fig. 6).³ These solvi form a basis for estimating the minimum temperature of primary crystallization. Recognition, however, of the low sanidine-orthoclase(?) discontinuity along the Or limb (fig. 6) suggests that potassium feldspars may, in fact, prove to be insensitive geothermometers; that is, feldspars within the composition range $\text{Or}_{75}\text{Ab}_{25}$ – $\text{Or}_{90}\text{Ab}_{10}$ may, under isobaric conditions, tend to crystallize at about the same temperature.

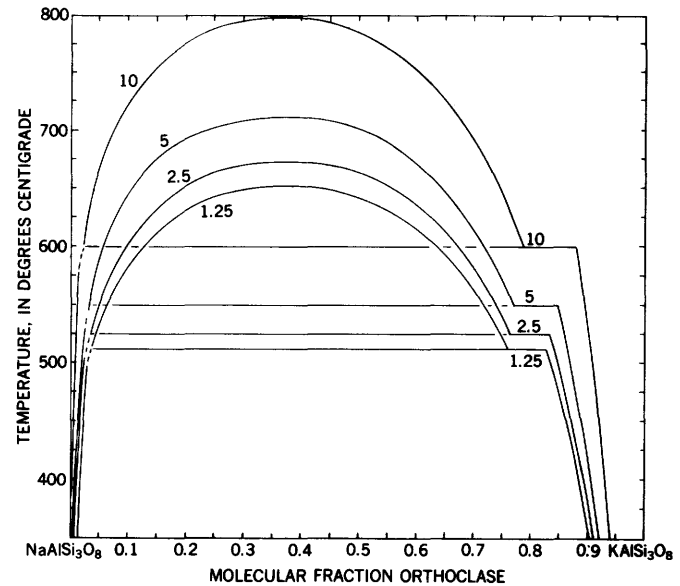


Figure 6.—Alkali feldspar solvi for various confining pressures, in kilobars. After Luth, Fenn, and Martin (1970). Illustration courtesy of W. C. Luth.

Analyses of the potassium feldspar permit the construction of isocompositional stability trajectories within the P – T field represented by figure 5. Thus the stability trajectory of the X-ray-determined average potassium feldspar composition of $\text{Or}_{80}\text{Ab}_{20}$ is defined by curve E; the stability trajectory of the microprobe-determined composition of $\text{Or}_{90}\text{Ab}_{10}$ is defined by curve F. These curves represent the minimum likely temperatures of crystallization at progressively higher pressures. Allowance for any anorthite in the system would displace both curves to the right.

We have only the most limited bases for selecting between curves E and F. However, because the solvi of Luth, Fenn, and Martin (1970), on which we base the construction of these curves, are themselves based on 20 $\bar{1}$ X-ray diffraction analyses

³Although Luth and Tuttle (1966) had previously indicated that the positions of otherwise comparable peralkaline and peraluminous solvi are significantly separated, later work supported by abundant experimental data has shown that (under isobaric conditions) these solvi are virtually coincident (W. C. Luth, oral comm., 1970).

of synthetic materials, the crystallization temperatures defined by curve E should be applicable, regardless of the absolute composition of the analyzed potassium feldspar. Furthermore, since the flame photometric determinations (table 4) indicate that the potassium feldspar is much less potassic than suggested by the electron microprobe study, curve E is accepted provisionally as more representative of the analyzed feldspar. Hence, we infer from the measured composition(s) of the potassium feldspar contained in the selected specimen that the minimum temperature of primary crystallization was about 545° – 550° C (curve E) or, much less likely, 405° – 410° C (curve F). Because both temperatures fall within the solidus field defined by the minimum melting-of-granite (curves A or C), both are almost certainly less than the actual temperature of primary crystallization.

The maximum likely temperature of crystallization for the bulk of the rock is most reliably defined by the intersection of the 5.5-kb isobar with the paragonitic muscovite breakdown curve (fig. 5). This intersection occurs at about 680° C.

CONCLUSIONS

The stability field defined by the stippled pattern shown in figure 5 suggests that the selected specimen, and thus much or most of the pegmatitic granite facies, crystallized initially at a pressure of about 5 kb and a temperature of about 650° C. Because the percentage of anorthite in the rock is sufficiently small that it disappears in the norm, the feldspars may be treated as members of a pure, albeit peraluminous, alkali feldspar system; hence the composition(s) of the potassium feldspar indicate that this rock crystallized at a minimum temperature of 545° – 550° C or 405° – 410° C. The improbably low temperatures suggested by the potassium feldspar composition are conceivably attributable to either: (1) an almost incredible sensitivity to anorthite in the alkali feldspar system, or (2) reequilibration of the alkali feldspars at subsolidus-solvus temperatures. W. C. Luth (oral comm., 1970) suggests, in fact, that alkali ion mobility in the presence of an aqueous fluid phase at elevated subsolidus temperatures is such that reequilibration may occur without in any way affecting the gross fabric of the rock. In other words, our basic assumption regarding the equivalence between the initially crystallized and the presently existing bulk composition of the potassium feldspar may be unworkable.

Thus, we conclude that primary crystallization of much or all of the pegmatitic granite facies probably occurred at a pressure of about 5 kb and a temperature of about 650° C; reequilibration of the alkali feldspars may have continued down to temperatures of about 550° C. The deduced pressure and temperature of primary crystallization correspond to a depth of about 16–18 km and an implied geothermal gradient of about 37° C/km, or roughly 20 percent above the average observed continental gradient of 30° C/km.

REFERENCES

- Beeson, M. H., 1967, A computer program for processing electron microprobe data: U.S. Geol. Survey open-file rept. 40 p.
- Castle R. O., 1964, Geology of the Andover Granite and surrounding rocks, Massachusetts: U.S. Geol. Survey open-file rept., 550 p., 50 pl., 30 figs., 28 tables.
- 1965a, A proposed revision of the subalkaline intrusive series of northeastern Massachusetts, in Geological Survey Research 1965: U.S. Geol. Survey Prof. Paper 525-C, p. C74–C80.
- 1965b, Gneissic rocks in the South Groveland quadrangle, Essex County, Massachusetts, in Geological Survey Research 1965: U.S. Geol. Survey Prof. Paper 525-C, p. C81–C86.
- Deer, W. A., Howie, R. A., and Zussman, J., 1962a, Rock-forming minerals, v. 1, Ortho- and ring silicates: London, Longmans, Green and Co. Ltd., 333 p.
- 1962b, Rock-forming minerals, v. 3, Sheet silicates: London, Longmans, Green and Co. Ltd., 270 p.
- 1963, Rock-forming minerals, v. 4, Framework silicates: London, Longmans, Green and Co., Ltd., 435 p.
- Emerson, B. K., 1917, Geology of Massachusetts and Rhode Island: U.S. Geol. Survey Bull. 597, 289 p.
- Ernst, W. G., 1960, Diabase-granophyre relations in the Endion sill, Duluth, Minnesota: Jour. Petrology, v. 1, p. 286–303.
- Evans, B. W., 1965, Application of a reaction-rate method to the breakdown equilibria of muscovite and muscovite plus quartz: Am. Jour. Sci., v. 263, p. 647–667.
- Evans, B. W., and Guidotti, C. V., 1966, The sillimanite-potash feldspar isograd in western Maine, U.S.A.: Contr. Mineralogy and Petrology, v. 12 p. 25–62.
- Handford, L. S., 1965, Rb-Sr whole rock age study of the Andover and Chelmsford Granites, Massachusetts, in Variations in isotopic abundances of strontium, calcium, and argon and related topics: Massachusetts Inst. Technology, 13th Ann. Prog. Rept. for 1965, U.S. Atomic Energy Comm. contract AT(30-1)-1381, MIT-1381-13, p. 11–14.
- Hansen, W. R., 1956, Geology and mineral resources of the Hudson and Maynard quadrangles, Massachusetts: U.S. Geol. Survey Bull. 1038, 104 p.
- Jackson, E. D., Stevens, R. E., and Bowen, R. W., 1967, A computer-based procedure for deriving mineral formulas from mineral analyses, in Geological Survey Research, 1967: U.S. Geol. Survey Prof. Paper 575-C, p. C23–C31.
- Luth, W. C., Fenn, P. M., and Martin, R. F., 1970, Thermodynamic excess functions, relative activities, and solvus relations for synthetic alkali feldspar: Geol. Soc. America Abs. with Programs, v. 2, no. 7, p. 611–612.
- Luth, W. C., Jahns, R. H., and Tuttle, O. F., 1964, The granite system at pressures of 4 to 10 kilobars: Jour. Geophys. Research, v. 69, p. 759–773.
- Luth, W. C., and Querol-Suñé, 1970, An alkali feldspar series: Contr. Mineralogy and Petrology, v. 25 p. 25–40.
- Luth, W. C., and Tuttle, O. F., 1966, The alkali feldspar solvus in the system $\text{Na}_2\text{O}-\text{K}_2\text{O}-\text{Al}_2\text{O}_3-\text{SiO}_2-\text{H}_2\text{O}$: Am. Mineralogist, v. 51, p. 1359–1373.
- Orville, P. M., 1963, Alkali ion exchange between vapor and feldspar phases: Am. Jour. Sci., v. 261, p. 201–237.
- 1967, Unit-cell parameters of the microcline–low albite and the sanidine–high albite solid solution series: Am. Mineralogist, v. 52, p. 55–86.
- Richardson, S. W., Gilbert, M. C., and Bell, P. M., 1969, Experimental determination of kyanite-andalusite and andalusite-sillimanite equilibria; the aluminum silicate triple point: Am. Jour. Sci., v. 266, p. 259–272.

- Steiger, R. H., and Hart, S. R., 1967, The microcline-orthoclase transition within a contact aureole: *Am. Mineralogist*, v. 52, p. 87–116.
- Thompson, J. B., Jr., and Norton, S. A., 1968, Paleozoic regional metamorphism in New England and adjacent areas, in Zen, E-an and others, eds., *Studies of Appalachian geology*: New York, Interscience Publishers, p. 319–327.
- Tilling, R. I., 1968, Zonal distribution of variations in structural state of alkali feldspar within the Rader Creek pluton, Bolder batholith, Montana: *Jour. Petrology*, v. 9, p. 331–357.
- Tuttle, O. F., and Bowen, N. L., 1958, Origin of granite in the light of experimental studies in the system $\text{NaAlSi}_3\text{O}_8\text{-KAlSi}_3\text{O}_8\text{-SiO}_2\text{-H}_2\text{O}$: *Geol. Soc. America Mem.* 74, 153 p.
- U.S. Geological Survey, 1967, *Geological Survey Research 1967*, Chapter A: U.S. Geol. Survey Prof. Paper 575-A, 377 p.
- Zen, E-an, and Albee, A. L., 1964, Coexistent muscovite and paragonite in pelitic schists: *Am. Mineralogist*, v. 49, p. 904–925.



NEW X-RAY DATA ON NATURAL ATACAMITE

By ARDEN L. LARSON and RICHARD B. TRIPP, Denver, Colo.

Abstract.—New X-ray data for natural atacamite show resolution of two strong doublets and add numerous low-intensity reflections.

Waldo (1935) made the original diffraction pattern for atacamite, $\text{Cu}_2(\text{OH})_3\text{Cl}$, in 1935 with a powder camera. This pattern, still retained as XRDF card 2-0164, did not resolve two doublets of moderate intensity, and many weak lines were not detected.

A recent paper by Sharkey and Lewin (1971) establishes the presence of five additional lines in the diffraction pattern of synthetic atacamite, including the resolution of the doublets unresolved by Waldo. In the present paper these lines are shown for natural atacamite.

We thank Edwin E. Larson and James L. Munoz for their assistance in the use of the University of Colorado computer facilities.

X-RAY DATA

Our data were obtained using a diffractometer and chart-recording system. Single crystals of natural atacamite were powdered in a mortar and mounted on collodion, using a technique described by Gude and Hathaway (1961).

The major reflections at 2.779 Å and 2.278 Å are members of the closely spaced doublets. These doublets would appear as broad single lines in the method used by Waldo. Refinement of technique and instrumentation since 1935 has allowed these doublets to be resolved.

The new diffraction data were indexed and processed to derive cell constants by means of the computer program of Evans, Appleman, and Handwerker (1963). Table 1 is a comparison between measured and calculated d -spacings obtained with the above program. Comparison of intensities derived from the charts and those of diffraction patterns made with a powder camera showed only minor discrepancies.

The crystal system of atacamite is orthorhombic, space group $Pnam$ (Wells, 1949). The following tabulation shows cell dimensions, in angstroms, determined in earlier work and those obtained during this investigation. The cell volume that we obtained is $377.8 \pm 1 \text{ \AA}^3$.

	Brasseur and Toussaint (in Wells, 1949)	XRDF card 2-0146	This paper
<i>a</i>	6.01	6.02	6.030±2
<i>b</i>	9.13	9.15	9.122±2
<i>c</i>	6.84	6.85	6.868±2

The excellent sample used in this study (U.S. Geol. Survey Denver depository mineral sample 6) was collected in 1970 by W. D. Coleman, of the U.S. Geological Survey, from Mina Inca de Oro, Copiapo, Atacama Province, Chile. It consists of bright-green, adamantine prismatic crystals associated with chrysocolla. No inclusions were observed under a magnification of $\times 344$.

Our study adds new X-ray data to the literature on atacamite and, we hope, will aid in the interpretation of the mineralogy of oxidized copper deposits in arid environments.

REFERENCES

- Evans, H. T., Jr., Appleman, D. E., and Handwerker, D. S., 1963, The least squares refinement of crystal unit cells with powder diffraction data by an automatic computer indexing method [abs.]: Am. Cryst. Assoc. Ann. Mtg., Cambridge, Mass., 1963, Program and Abs., no. E-10, p. 42.
- Gude, A. J., 3d, and Hathaway, J. C., 1961, A diffractometer mount for small samples: Am. Mineralogist, v. 46, nos. 7–8, p. 993–998.
- Sharkey, J. B., and Lewin, S. Z., 1971, Conditions governing the formation of atacamite and paratacamite: Am. Mineralogist, v. 56, nos. 1–2, p. 179–192.
- Waldo, A. W., 1935, Identification of the copper ore minerals by means of X-ray powder diffraction patterns: Am. Mineralogist, v. 20, no. 8, p. 575–597.
- Wells, A. F., 1949, The crystal structure of atacamite and the crystal chemistry of cupric compounds: Acta Cryst., v. 2, no. 1, p. 175–180.

Table 1.—X-ray data on atacamite

[All observed (obs) and calculated (calc) values in angstroms. Ni-filtered Cu radiation, fine-focus tube, 1° divergence slit, 0.010-inch receiving slit, scanning speed of $\frac{1}{2}^\circ 2\theta$ per minute. Calculated using refined cell data of $a=6.030\pm 2$ A, $b=9.122\pm 2$ A, $c=6.868\pm 2$ A, and $\text{CuK}\alpha_1=1.5405$ A]

<i>hkl</i>	<i>d</i> (obs)	<i>d</i> (calc)	<i>I/I</i> ₀	<i>hkl</i>	<i>d</i> (obs)	<i>d</i> (calc)	<i>I/I</i> ₀
011	5.48	5.49	100	314	1.2928	1.2924	7
110	5.03	5.03	70	253	1.2895	1.2897	5
020	4.56	4.56	4	125	1.2850	1.2851	3
111	4.05	4.06	12	071	1.2805	1.2803	4
002	3.43	3.43	1	343	1.2591	1.2593	2
121	3.22	3.22	7	403	1.2584	1.2591	8
030	3.04	¹ 3.04	5	440	1.2572	1.2576	7
200	3.01	3.02	8	352	1.2570	1.2571	2
112	2.836	2.836	51	432	1.2550	1.2552	4
031	2.779	2.780	51	324	1.2523	1.2524	2
201	2.759	2.761	55	171	1.2500	1.2501	2
022	2.742	2.743	27	205	1.2395	1.2395	1
130	2.711	2.715	20	163	1.2385	1.2387	4
211	2.641	2.642	14	215	1.2370	1.2371	3
131	2.525	2.525	14	441	1.2248	1.2245	3
220	2.515	2.515	40	154	1.1997	1.1996	1
040	2.278	2.280	69	334	1.1965	1.1963	5
202	2.265	2.265	47	270	1.1809	1.1808	2
013	2.220	2.221	1	442	1.1784	1.1784	1
212	2.198	2.199	17	271	1.1660	1.1659	1
230	2.141	2.141	11	520	1.1550	1.1549	1
132	2.130	2.130	24	254	1.1447	1.1447	1
231	2.043	2.044	17	145	1.1403	1.1402	3
222	2.029	2.029	5	064	1.1382	1.1383	1
310	1.9636	1.9630	12	344	1.1331	1.1330	1
033	1.8287	1.8290	11	272	1.1296	1.1296	7
203	1.8243	1.8234	33	315	1.1254	1.1255	1
232	1.8171	1.8168	27	116	1.1162	1.1162	2
142	² 1.8118	1.8120	9	522	1.1041	1.1041	1
213	1.7882	1.7880	10	443	1.1022	1.1022	1
321	1.7769	1.7767	2	452	1.1008	1.1008	1
241	1.7577	1.7582	10	055	1.0974	1.0974	1
150	1.7465	1.7462	13	245	1.0962	1.0961	1
004	1.7169	1.7171	20	370	1.0934	1.0934	1
312	1.7057	1.7042	10	371	1.0799	1.0798	2
223	1.6930	1.6931	1	363	1.0715	1.0715	2
330	1.6771	1.6768	6	460	1.0705	1.0705	2
114	1.6248	1.6250	3	280	1.0665	1.0665	3
024	1.6060	1.6070	57	182	1.0651	1.0651	2
233	1.5634	1.5638	13	216	1.0629	1.0629	3
250	² 1.5609	1.5609	9	335	1.0626	1.0626	1
143	1.5606	1.5607	9	434	1.0610	1.0614	8
152	1.5564	1.5566	23	513	1.0599	1.0598	5
251	1.5217	1.5221	5	461	² 1.0577	1.0577	3
400	1.5074	1.5075	7	372	1.0418	1.0419	1
313	1.4900	1.4902	1	226	1.0231	1.0231	1
410	1.4875	1.4874	13	046	1.0185	1.0185	1
160	1.4740	1.4742	2	345	1.0154	1.0154	1
341	1.4731	1.4728	11	405	1.0154	1.0154	1
401	1.4723	1.4725	11	190	² .9989	.9989	2
134	1.4513	1.4512	5	601	.9944	.9944	1
243	1.4240	1.4241	5	380	.9918	.9918	11
224	1.4182	1.4181	9	425	.9911	.9911	1
421	1.4013	1.4013	5	191	² .9891	.9891	6
062	1.3897	1.3902	23	316	.9888	.9888	3
342	1.3814	1.3807	7	611	.9816	.9816	1
044	1.3718	1.3717	13	381	.9697	.9696	5
015	1.3582	1.3584	14	274			
162	² 1.3546	1.3547	6	463			
350	1.3515	1.3509	13				
234	1.3397	1.3395	14				
144	² 1.3375	1.3376	4				
261	1.3316	1.3317	2				
422	1.3219	1.3212	5				

¹Does not fit space group *Pnam*.

²Coincides with the position of calculated $K\alpha_2$ reflections of other planes.



ZONAL DISTRIBUTION OF MONTMORILLONITE AND ZEOLITES IN THE LANEY SHALE MEMBER OF THE GREEN RIVER FORMATION IN THE WASHAKIE BASIN, WYOMING

By HENRY W. ROEHLER, Denver, Colo.

Abstract.—Clay minerals and zeolites of diagenetic origin are abundant in lacustrine rocks composing the Laney Shale Member of the Eocene Green River Formation in the Washakie Basin, Wyo., but X-ray diffractometer analyses of the surface samples indicate that (1) montmorillonite, (2) clinoptilolite and mordenite, (3) clinoptilolite, mordenite, and analcime, and (4) analcime are distributed in partly concentric overlapping mineral facies across the basin. These mineral facies probably reflect the paleogeography and paleosalinity of Lake Gosiute during the deposition of the Laney Shale Member.

Zeolites in Eocene rocks from the Washakie Basin, Wyo., were reported in 1914 by Johannsen (p. 214–219), who studied the petrology of samples collected from the Washakie Formation of his terminology (undivided Bridger and Uinta Formations) at the east end of Haystack Mountain in the northern part of the basin. Later, Bradley (1928) identified zeolites in the Green River Formation in Colorado, Wyoming, and Utah, and in a columnar section he (1945) showed several beds containing analcime in the Laney Shale Member in the Washakie Basin.

The distribution and genesis of clay minerals, zeolites, and other authigenic silicate minerals in the Green River Formation in the Green River Basin, Wyo., were studied by Hay (1966, p. 44–52), Goodwin and Surdam (1967), and Iijima and Hay (1968). The zonal order of clay minerals and zeolites in the Laney Shale Member in the Washakie Basin is similar to the zonal order of these minerals in the Tipton Shale Member of the Green River Formation in the Green River Basin (Goodwin, and others, 1969).

Investigations by the U.S. Geological Survey and the U.S. Bureau of Mines now indicate that clinoptilolite, mordenite, and analcime are widely present in the Washakie Basin in a 6,000-foot-thick sequence of lacustrine and fluvial rocks of middle and late Eocene age. This sequence consists of the Wilkins Peak Member and Laney Shale Member of the Green River Formation, the Cathedral Bluffs Tongue of the Wasatch Formation, and the undivided Bridger and Uinta Formations.

METHODS AND ACKNOWLEDGMENTS

Nearly 350 rock samples were collected from small pits dug in beds of the Laney Shale Member. These beds, which are less than 1 foot to slightly more than 15 feet thick, crop out in four stratigraphic sections located as follows (fig. 1):

Sand Butte	Western Washakie Basin. West face of Sand Butte, sec. 21, T. 16 N., R. 100 W.
East Pioneer Field	Southwestern Washakie Basin. On Kinney Rim in center of west part of sec. 23, T. 13 N., R. 99 W.
LaCleda Station	Northern Washakie Basin. On Laney Rim 1½ miles northeast of ruins of LaCleda Stage Station, E½ sec. 15, SW¼ sec. 14 and NW¼ sec. 23, T. 17 N., R. 98 W.
Northwest Flat Top Mountain	Eastern Washakie Basin. Along a fork of Barrel Springs Draw 3½ miles northwest of Flat Top Mountain, E½ and SW¼ sec. 20, NW¼ sec. 29, and E½ sec. 30, T. 15 N., R. 93 W.

The whole-rock samples were powdered, pelletized, and X-rayed by nickel-filtered $\text{CuK}\alpha$ radiation. The clay minerals and zeolites were identified by comparison with standard X-ray diffractometer patterns. Pellets of samples from the LaCleda Station, East Pioneer Field, and Northwest Flat Top Mountain sections were prepared by P. C. Beck. The X-ray diffractograms were prepared by P. L. Hauff. Clay minerals and zeolites in the Sand Butte section were identified, from samples submitted for routine oil-shale assay, by W. A. Robb at the U.S. Bureau of Mines Laramie Energy Center in Laramie, Wyo.

STRATIGRAPHY AND LITHOLOGY

The Laney Shale Member in the Washakie Basin is divided into three informal lithologic units—a dominantly oil-shale unit, a dominantly sandstone unit, and a dominantly mudstone unit. The lowermost unit, called here the “beds near

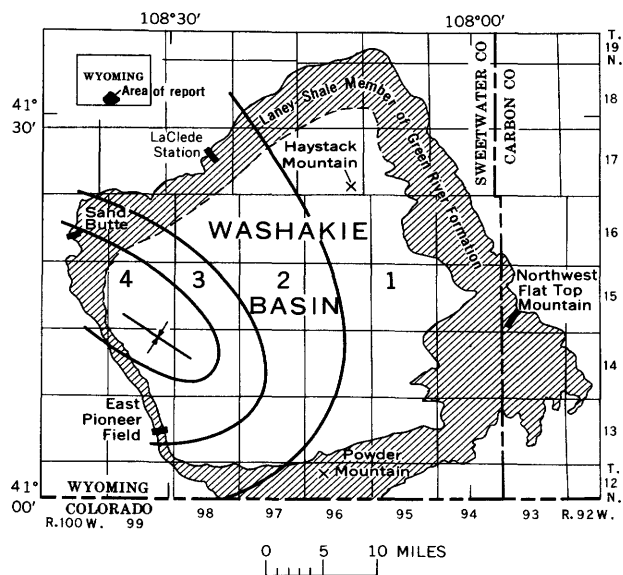


Figure 1.—Map showing sequence and approximate boundaries of authigenic silicate mineral facies in the buff marker bed: 1, montmorillonite, with no zeolites; 2, clinoptilolite and mordenite; 3, clinoptilolite, mordenite, and analcime; and 4, analcime. The stratigraphic position of the buff marker bed is shown in figure 2. Outcrops of the Laney Shale Member are shown by shading; localities of stratigraphic sections are indicated by bars; the inferred deposition center of the buff marker bed is shown by opposed arrows and line.

LaCleda Station," ranges in thickness from 125 to 450 feet; it is mostly oil shale, and it intertongues in the lower part with the Cathedral Bluffs Tongue of the Wasatch Formation (fig. 2). The buff marker bed and the *Cyraulius* marker bed are key strata within the beds near LaCleda Station. The buff marker consists of nearly 60 feet of tuffaceous sandstone and siltstone along the west edge of the basin, but it thins eastward to less than 5 feet before grading indistinguishably into the Cathedral Bluffs Tongue of the Wasatch Formation along the east edge of the basin (fig. 2). The *Cyraulius* marker is a 0.3- to 1.5-foot-thick gray limy siltstone that contains the small gastropod *Cyraulius militaris*. In the western part of the Washakie Basin the beds near LaCleda Station are unconformably overlain by more than 300 feet of mainly tuffaceous sandstone and siltstone that compose the "beds near Sand Butte." Eastward the beds near Sand Butte intertongue with and are in part overlain by 600–650 feet of interbedded mudstone, arkosic sandstone, tuffaceous siltstone, limestone, shale, and oil shale that compose the "beds near Hartt Cabin." Only the lower parts of the beds near Sand Butte and the beds near Hartt Cabin are included in figure 2.

The Laney Shale Member is overlain by the undivided Bridger and Uinta Formations and is underlain by the Cathedral Bluffs Tongue of the Wasatch Formation, all of

fluvial origin. The beds near LaCleda Station and the beds near Sand Butte in the Laney Shale Member are of lacustrine origin, whereas the beds near Hartt Cabin are of lacustrine and fluvial origins. During the deposition of the Laney Shale Member, Lake Gosiute occupied a large part of what is now southwestern Wyoming and smaller adjacent areas of Utah and Colorado. The deepest part of the lake was located in the southwestern part of the Washakie Basin (Roehler, 1969, p. 204, fig. 4). Part of its eastern shoreline was near the eastern margin of the basin as evidenced there by the intertonguing of fluvial and lacustrine rocks (fig. 2), by coarse beach sandstone, and by shallow-water and nearshore deposits including algal limestone. Sediments deposited in the lower part of the Laney Shale Member are chiefly detrital; those deposited in the upper part are chiefly air-laid tuff reworked by streams and lake currents (Roehler, 1970).

MINERALOGY

The principal minerals in the Laney Shale Member, in order of decreasing abundance, are quartz, calcite, dolomite, clay minerals, feldspars, and zeolites. Small amounts of pyrite and aragonite are locally common in the member. Gypsum, a product of weathering, is present in many samples. Illite is everywhere abundant. Kaolinite is less abundant, but locally occurs with montmorillonite. Montmorillonite is abundant in the eastern part of the basin and locally occurs with clinoptilolite and mordenite in the central part. Sparse montmorillonite occurs with analcime in the western part of the basin. Heavy minerals, which consist of hornblende, garnet, epidote, zircon, rutile, tourmaline, and biotite, compose as much as 3 percent of siltstone and sandstone beds.

The zeolites, except for analcime, occur as disseminated microscopic crystals in rocks of nearly all types and colors. Macroscopic analcime commonly occurs in altered tuffs within oil-shale sections, in laminae or thin beds, as clear or gray trapezohedrons that resemble coarse sand grains. Clay minerals and zeolites compose 90 percent or more of some thin altered tuffs.

MINERAL FACIES AND THEIR ORIGIN

The sampling roughly defines four mineral facies across the Washakie Basin, characterized by (1) montmorillonite and no zeolites, (2) clinoptilolite and mordenite, (3) clinoptilolite, mordenite, and analcime, and (4) analcime (fig. 1). The boundaries of the mineral facies are not sharply defined, but they are marked by intertonguing as indicated in figure 2. Diagenetic potassium feldspar probably forms a fifth mineral facies, but sodium and potassium feldspars are ubiquitous, and those of diagenetic origin are not easily differentiated by X-ray diffraction of whole-rock samples from those of volcanic and of plutonic origins.

According to Hay (1966), Goodwin and Surdam (1967), and

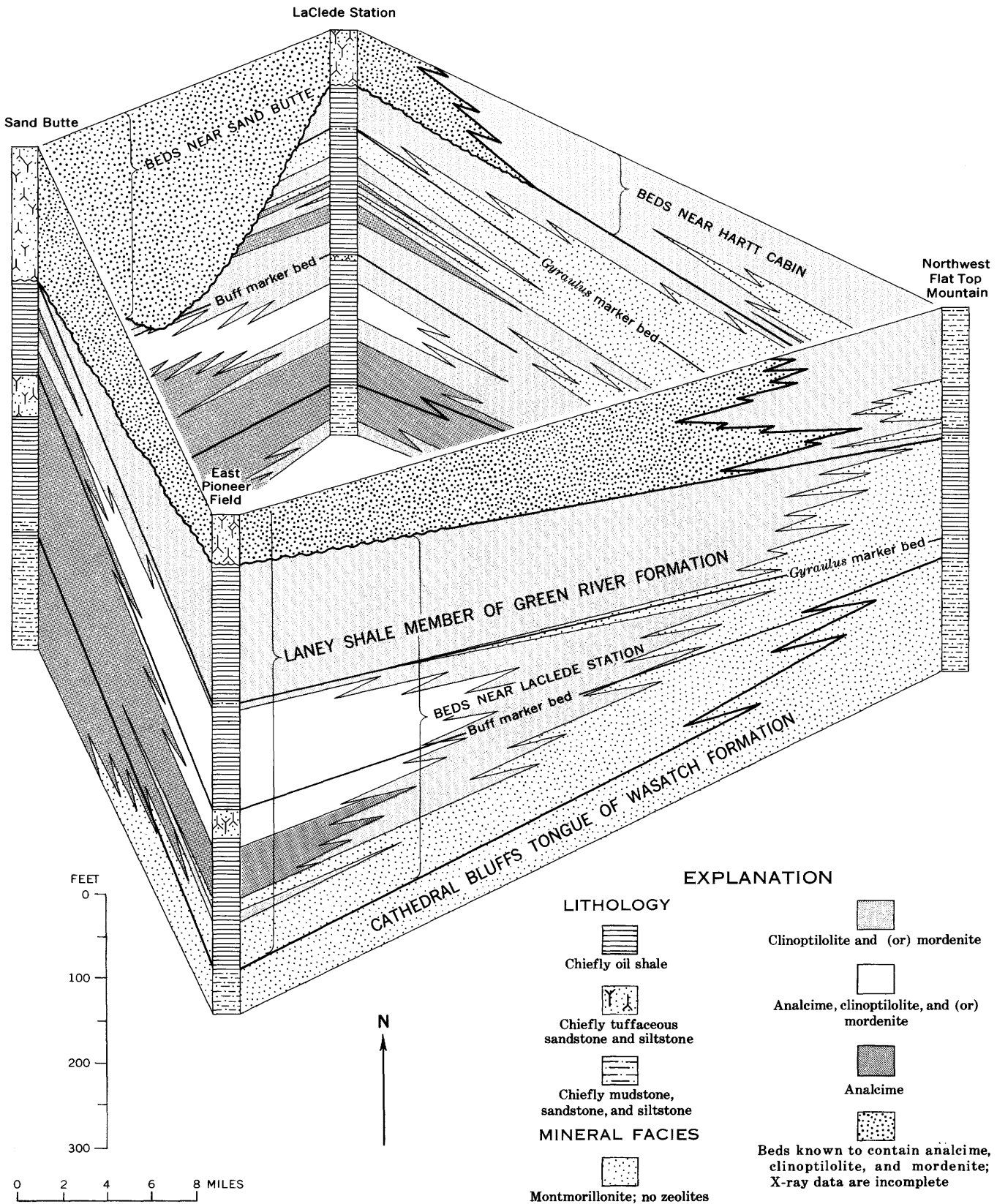


Figure 2.—Fence diagram showing generalized lithologies and the distribution of mineral facies in the Laney Shale Member of the Green River Formation in the Washakie Basin, Wyo. Locations of stratigraphic sections are shown on figure 1.

Sheppard and Gude (1968), among others, clay minerals and zeolites commonly form by the diagenetic alteration of vitric tuffs by saline, alkaline waters. Time and depth of burial are important factors in the alteration process, but the degree of alteration is specifically related to pH, salinity, and cation content of overlying and interstitial waters. High salinity is equated to increased reaction rate and decreased activity of water, which in turn are correlated with water depth in chemically stratified lakes. Lake Gosiute was chemically stratified. The alteration of andesitic vitric tuff in lake water high in sodium carbonate content, such as Lake Gosiute during the deposition of the Laney Shale Member, is typically montmorillonite→clinoptilolite and mordenite→analcime→potassium feldspar. Hence, tuffaceous rocks were diagenetically altered to montmorillonite in fresh-water, nearshore parts of the lake, to clinoptilolite and mordenite in moderately saline, shallow-water parts of the lake, and to analcime in saline, deep-water parts of the lake. Unaltered tuffs have not been recognized in the Laney Shale Member in the Washakie Basin.

The diagenetic origin of most clay minerals and zeolites in the Laney Shale Member is confirmed by changes in the lateral distribution of authigenic silicate minerals in the buff marker bed. The buff marker bed is uniformly tuffaceous sandstone and siltstone over most of the basin, but the authigenic silicate minerals within the bed are like those in the adjacent parts of the Laney Shale Member.

REFERENCES

- Bradley, W. H., 1928, Zeolite beds in the Green River formation: *Science*, v. 67, p. 73-74.
- 1945, *Geology of the Washakie Basin, Sweetwater and Carbon Counties, Wyoming, and Moffat County, Colorado*: U.S. Geol. Survey Oil and Gas Inv. Prelim. Map 32.
- Goodwin, J. H., and Surdam, R. C., 1967, Zeolitization of tuffaceous rocks of the Green River Formation, Wyoming: *Science*, v. 157, no. 3786, p. 307-308.
- Goodwin, J. H., Parker, R. B., and Surdam, R. C., 1969, Authigenic silicates in the Tipton Member of the Green River Formation, Wyoming: *Geol. Soc. America*, 82d Ann. Mtg., Abs. with Programs for 1969, p. 81-82, Atlantic City, N.J.
- Hay, R. L., 1966, Zeolites and zeolitic reactions in sedimentary rocks: *Geol. Soc. America Spec. Paper* 85, 130 p.
- Iijima, Azuma, and Hay, R. L., 1968, Analcime composition in tuffs of the Green River Formation of Wyoming: *Am. Mineralogist*, v. 53, p. 184-200.
- Johannsen, Albert, 1914, Petrographic analysis of the Bridger, Washakie, and other Eocene formations of the Rocky Mountains: *Am. Mus. Nat. History Bull.*, v. 33, p. 209-220.
- Roehler, H. W., 1969, Stratigraphy and oil-shale deposits of Eocene rocks in the Washakie basin, Wyoming, in *Wyoming Geol. Assoc. Guidebook 21st Ann. Field Conf., Tertiary rocks of Wyoming*: p. 197-206.
- 1970, Nonopaque heavy minerals from sandstone of Eocene age in the Washakie Basin, Wyoming, in *Geological Survey Research 1970*: U.S. Geol. Survey Prof. Paper 700-D, p. D181-D187.
- Sheppard, R. A., and Gude, A. J., 3d, 1968, Distribution and genesis of authigenic silicate minerals in tuffs of Pleistocene Lake Tecopa, Inyo County, California: U.S. Geol. Survey Prof. Paper 597, 38 p.



GEOCHEMICAL FACTOR ANALYSIS OF INTRUSION BRECCIA AND RECONSTITUTED ROCKS OF MULE EAR DIATREME, SAN JUAN COUNTY, UTAH

By R. A. CADIGAN and DESIREE E. STUART-ALEXANDER,
Denver, Colo., Menlo Park, Calif.

Abstract.—Factor analysis (R-mode) of the covariance of elements in the core rocks of the Mule Ear diatreme, Utah, leads to the conclusion that alteration is the dominant geologic factor controlling the present intercorrelation of element abundances. Other geologic factors in order of their decreasing effects on the present covariance of 28 elements are interpreted to be: mineral components from assimilated sedimentary rocks, composition of the reconstituted sedimentary dike rocks, mineral components of the deeply originating ultrabasic rock breccia, assimilated interstitial sulfate minerals, traces of hydrothermal activity, and assimilated mica components. Factor analysis (Q-mode) indicates that the three types of rocks selected for study in the diatreme are significantly different in terms of element distribution and covariance. Green and gray intrusion breccias occupying the diatreme pipes are generally higher in metal content than “average” Colorado Plateau sedimentary rocks and are higher by an order of magnitude in magnesium, cobalt, chromium, and nickel. Significant hydrothermal effects, absent at the surface, may increase with depth.

Mule Ear diatreme is one of several diatremes in or adjacent to Comb Ridge monocline (fig. 1) on the east edge of Monument upwarp in the Four Corners area of southeastern Utah and northeastern Arizona. (See Shoemaker, 1956.) The location of these diatremes and their similar age (Stuart-Alexander and others, 1972) suggest that the faulting at depth that produced the monocline also triggered events that produced the diatremes. The first studies of the detailed structures of diatremes were made by Hack (1942) in the Hopi Buttes area of northeastern Arizona. Later, Shoemaker (1956) investigated the diatremes in the Navajo and Hopi Indian Reservations in Utah, Arizona, and New Mexico, as part of a distribution of elements study; he classified them into two groups—those with uranium mineralization and those without uranium mineralization. He classified the Mule Ear as an unmineralized diatreme.

Mule Ear diatreme was produced by gases and particulate rock breccia that rose from unknown depths and pierced an

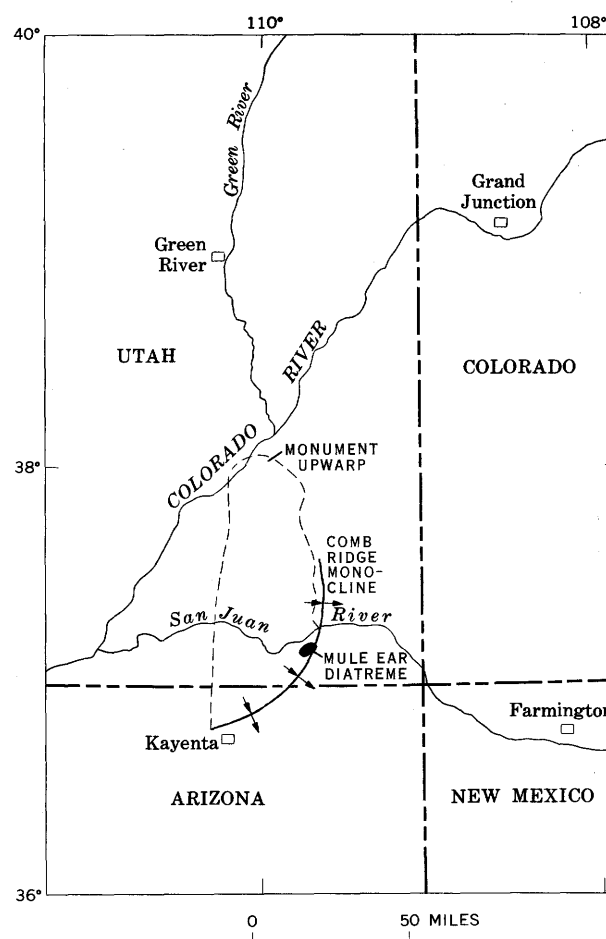


Figure 1.—Location of Mule Ear diatreme in the Four Corners area, southwestern United States.

estimated 5- to 10-km-thick sequence of igneous, metamorphic, and sedimentary rocks. The event occurred about middle Tertiary time, 30 ± 2 m.y. (million years) ago (Naeser and Stuart-Alexander, 1969; Ziony, 1966). Mule Ear is one of the

best exposed diatremes in the Colorado Plateau region. The exposed rocks of the diatreme form a low hill on the western erosional scarp of Comb Ridge, a persistent regional hogback that is the topographic expression of the breached eastward-dipping Comb Ridge monocline. The low collapse-block-strewn hill, the surface expression of the diatreme, represents a ½-km-wide easily accessible cross section of the diatreme rocks that pierced the surrounding rocks of Triassic and Permian age.

In plan view (see map by Stuart-Alexander and others, 1972), Mule Ear diatreme may be roughly divided into two concentric, highly irregularly shaped zones surrounding a core. The thick outer zone consists dominantly of blocks of sedimentary rocks ranging in age from the Permian (Cutler Formation) to and including the Cretaceous (Mancos Shale); the blocks of the Mancos are displaced downward 5,500 feet. This outer zone has a narrow, disordered outermost rind of similarly displaced rocks. Many blocks in the outer zone are imbedded in a matrix of smaller breccia fragments that locally grade into an intrusion breccia; the breccia is similar in character to the intrusion breccia of the core rock. The irregular concentric inner zone is formed by resistant, well-consolidated dikelike bodies of reconstituted clastic sedimentary materials and a minor amount of admixed clastic debris from igneous and metamorphic rocks. These reconstituted rocks grade from sandstone into breccia, are either light ocher or light maroon, and are cemented by magnesite-calcite or by silica. The core of the diatreme is composed of a soft, siltlike matrix of pulverized altered pale-green or gray clayey heterogeneous rock and is designated an intrusion breccia. The core, in plan view, seems to be a section through a series of separate parallel volcanic pipes, although probably these are anastomosing below the present surface and were similarly connected above. The rock in each pipe has a grayish peripheral zone which is cemented by magnesite, and the peripheral zone grades inward to a highly friable (at the surface) clayey green rock that contains little magnesite; the green rock is the typical intrusion breccia.

Forty-two samples collected from the core intrusion breccia and the reconstituted rocks of Mule Ear diatreme (fig. 2) were analyzed for 66 elements. Twenty-eight elements, mostly metallic, were detected in a number of samples sufficient for a statistical study of their covariance. Factor analysis indicates the presence of seven significantly covarying element groups and also indicates significant geochemical differences among the rock types used for the study.

The purpose of the present investigation is fourfold: (1) to obtain an estimate of the abundance and distribution of elements in the matrix and the reconstituted rocks of the diatreme; (2) to determine the major geologic events effecting distribution of the elements; (3) to obtain evidence of the sources of the elements; and (4) to determine if important hydrothermal effects are present. The study is supplemental to a study of the diatreme completed earlier (Stuart-Alexander and others, 1972).

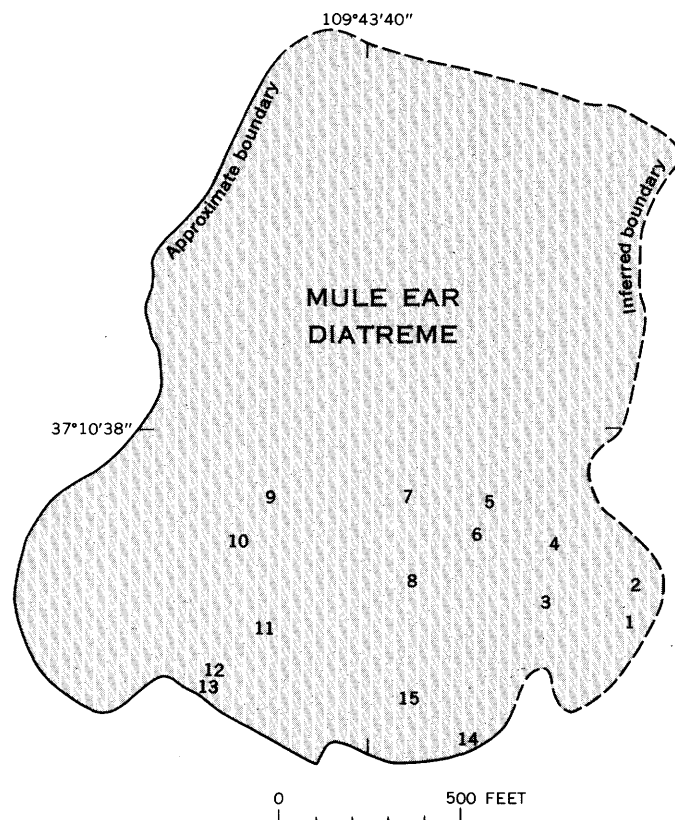


Figure 2.—Map showing sample localities in the Mule Ear diatreme, Utah. The outline of the area is based on unpublished reconnaissance mapping by E. M. Shoemaker. All samples of intrusion breccia were collected from diatreme pipes.

1. CD5262A—D, green intrusion breccia.
2. CD5263A—D, green intrusion breccia.
3. CD5264A, B, sandstone dike; C, D, calcareous sandstone dike.
4. CD5265A, B, sandstone dike; C, D, silicified sandstone dike.
5. CD5266A—D, gray intrusion breccia.
6. CD5267A—D, green intrusion breccia.
7. CD5268A, B, gray intrusion breccia.
8. CD5269A, B, gray intrusion breccia.
9. CD5270A, B, green intrusion breccia.
10. CD5271A, B, green intrusion breccia.
11. CD5272A, B, gray intrusion breccia.
12. CD5273A, B, gray intrusion breccia.
13. CD5274A—D, brown reconstituted sandstone dike.
14. CD5275A, B, green intrusion breccia.
15. CD5276A, B, sand derived by a streamlet from a green breccia pipe.

GEOCHEMICAL STUDIES

Analytical values

Cadigan collected discrete samples of both green and gray intrusion breccias from pipes in the better exposed southern half of the diatreme and samples of brown ocher to maroon reconstituted rock from several points along dikes that crop out persistently in the eastern and southern

parts of the diatreme. Semiquantitative six-step spectrographic analyses were made for 65 elements, and atomic-absorption analyses were done for gold, silver, copper, and mercury. Twenty-eight elements were used in the study, including both spectrographic copper (Cu) and atomic-absorption copper, (Cu_A). The amounts of the 28 elements in the 42 rock samples used in the study are listed in table 1. The elements beryllium, molybdenum, and lithium are present in amounts below the level of detection in most of the samples. These elements were retained in the statistical analysis because their valid values are not distributed randomly, but rather tend to be concentrated in particular rock types. This kind of variation is, of course, critical in both statistical and nonstatistical classification or in grouping procedures applied to rock analyses. Where values are below the limits of detection, an arbitrary estimate is used and is shown in brackets in table 1. This is done to avoid using zero values, which would probably be more incorrect than the estimated values and which could not be used in certain statistical tests. Values for magnesium and calcium that exceed 10 percent, the upper reporting limit, are arbitrarily shown as 20 percent, twice the detection limit, and are marked with an asterisk in table 1. Silica was omitted from the study because all values except two exceeded 10 percent; thus, 40 of the samples would have estimated values of 20 percent silica and would have no statistical variance and would yield no information in a study of covariance. The division of samples by rock type is based on field classification.

Rare elements looked for but not detected in enough rock samples to use for statistical purposes are Au_A, As, Cd, La, Nb, Pd, Pt, Sb, Sn, Te, U, W, Zn, P, Ce, Ge, Hf, In, Re, Ta, Th, Tl, Pr, Nd, Sm, Eu, Gd, Tb, Dy, Ho, Er, Tm, Lu, Ir, Os, Rh, and Ru. Of these, Ge (≥ 10 ppm) was detected in five samples. A heavy-mineral concentrate obtained from a sand derived from one of the diatreme pipes (sample CD5276A, fig. 2) contains, of the rare elements, 70 ppm La, 10 ppm Nb, 500 ppm Ce, 50 ppm Ga, and 150 ppm Nd.

The values in table 1 were converted to logarithms to "normalize" the distributions and were treated statistically by factor analysis utilizing the U.S. Geological Survey's IBM 360/65 computer and available programs. Both the R-mode utilizing a 28 \times 28-element correlation matrix and the Q-mode utilizing a 42 \times 42-sample correlation (cosine theta) matrix were calculated. The purpose of the factor analyses was to determine the presence of groups of chemical metallic elements with significant positive covariance (R-mode), and to determine the presence of groups of rock samples with similarly varying proportions of elements (Q-mode). This grouping of elements and samples, where present, is the effect of geologic factors and may be interpreted in terms of geologic causes. For example: in a suite of sedimentary rock samples some unknown geologic cause produces close positive inter-correlation (covariance) of the occurrence of the metals iron, manganese, titanium, and zirconium. Experience and a knowl-

edge of geochemical associations suggest that such covariance (the effect) might be attributed to the varying proportions of heavy minerals in the samples (the cause). In this example, R-mode factor analysis shows the existence of this particular grouping, but the assignment of the grouping to the geologic cause, or factor, of heavy-mineral variation is an interpretation. Similarly, Q-mode factor analysis may reveal a grouping of certain samples with close similarities in terms of element content, and it may then become the task of the investigator to interpret the grouping in terms of a geologic cause or factor by seeking an answer to the question "Why are these samples similar?". Not all factor groupings of elements (variables) in R-mode analysis or of samples in Q-mode analysis are of the same significance or weight. Only the numbers of factor groupings considered to be the most significant are reported in the order of their significance. Conventionally, only factors with eigenvalues of 1.0 or higher are used.

For a complete discussion of factor analysis, the reader is referred to the authoritative text by Harman (1967) and to a brief, excellent introduction to the subject by Imbrie (1963).

R-mode analysis

The R-mode analysis of the logs of the diatreme sample data (28 variables, 42 samples) yielded seven eigenvalues greater than 1.0, with a cumulative proportion of total variance accounted for of 0.84823 (approximately 85 percent). This suggests that most (85 percent) of the variance in the 28 \times 28 correlation matrix can be attributed to seven causes or factors. The results of the R-mode analysis in terms of seven factors are seven element groupings as shown in table 2. The groupings taken from the reordered oblique vector matrix are listed in columns under the factor numbers. The element at the top of each column coincides with the vector axis around which the other elements are grouped; elements in the columns are listed in order of increasing distance from their respective group axes.

Elements listed in parentheses are those weakly associated with that group. Most of these are also strongly associated with another group and are listed in that group without parentheses.

The numbered factors are interpreted as geologic events, or processes. They are arranged in order of their degree of influence or rank. Factor I had the strongest effect on present element covariance within the samples. Factor VII had the weakest effect.

Interpretation of the factors is subjective and, in a geochemical study like this, dependent for the most part on conventional interpretations of element groupings or known geochemical behavior as described by Rankama and Sahama (1950). An indication of the significance of each factor is the percentage of the total variance attributed to it (shown in parentheses) as given in the tentative interpretations listed below.

Table 1.—Values of metallic elements present in 42 samples of intrusion breccia

[Brackets ([]) indicate arbitrary values assigned where content is below lower reporting limit.
Analyses are semiquantitative six-step spectrographic except for those elements

Sample No.	Fe	Mg	Ca (percent)	Ti	Mn	B	Ba	Be (parts per million)	Co	Cr	Cu	Mo	Ni
Green intrusion breccia													
CD5262A.....	5	*20	1.5	0.1	1,000	[10]	200	[0.05]	70	1,500	20	3.0	1,000
B.....	5	*20	1.5	.15	700	[10]	300	[0.05]	50	1,000	20	3.0	700
C.....	2	10	10.0	.15	700	[10]	300	[0.05]	20	70	10	3.0	300
D.....	7	5	7.0	.5	1,000	[10]	300	[0.05]	50	50	50	3.0	100
CD5263A.....	5	*20	1.5	.2	1,000	[10]	500	[0.05]	70	1,000	50	[1.5]	700
B.....	5	*20	2.0	.15	1,000	[10]	300	[0.05]	70	1,000	50	[1.5]	1,000
C.....	7	5	*20.0	.3	1,000	[10]	300	[0.05]	20	100	50	[1.5]	100
D.....	7	5	3.0	.5	1,500	[10]	300	[0.05]	50	500	100	3.0	200
CD5267A.....	3	10	2.0	.15	500	[10]	700	[0.05]	50	700	20	[1.5]	700
B.....	2	10	2.0	.15	500	20	700	[0.05]	50	700	15	[1.5]	700
C.....	10	1	0.5	.2	200	20	700	[0.05]	20	70	20	5.0	50
D.....	7	2	1.5	.2	1,500	20	700	[0.05]	20	70	10	3.0	50
CD5275A.....	3	*20	1.5	.1	500	20	300	[0.05]	50	500	20	[1.5]	700
B.....	3	*20	2.0	.15	1,000	20	500	[0.05]	50	700	15	[1.5]	700
Brown reconstituted rocks													
CD5264A.....	1.5	2	7.0	0.1	500	20	300	1.0	5	100	7	[1.5]	70
B.....	1.5	3	7.0	.1	500	20	300	1.0	5	100	10	[1.5]	70
C.....	2	3	10.0	.1	700	50	300	3.0	7	50	5	3.0	50
D.....	2	5	10.0	.15	700	50	300	3.0	10	50	5	3.0	100
CD5265A.....	1.5	2	7.0	.07	500	20	300	1.0	5	100	10	[1.5]	100
B.....	1	2	7.0	.07	200	20	300	1.0	5	50	10	[1.5]	50
C.....	1.5	1.5	2.0	.1	200	20	500	1.0	10	200	3	[1.5]	100
D.....	1	2	3.0	.15	200	20	500	2.0	20	200	5	[1.5]	150
CD5274A ¹	3	5	10.0	.1	500	10	300	1.0	30	1,000	10	[1.5]	500
B.....	3	5	10.0	.07	500	10	300	2.0	20	700	7	[1.5]	300
C.....	1.5	1	1.5	.1	100	20	500	2.0	15	200	5	[1.5]	200
D.....	1	1	2.0	.1	200	20	500	1.0	10	500	5	[1.5]	150
Gray intrusion breccia													
CD5266A.....	2	7	1.5	0.07	500	[10]	700	[0.05]	20	700	15	[1.5]	500
B ²	1.5	7	1.0	.07	500	[10]	500	[0.05]	30	300	15	[1.5]	300
C.....	2	5	1.0	.05	300	[10]	500	[0.05]	30	500	70	[1.5]	500
D.....	2	7	1.0	.07	300	[10]	700	[0.05]	30	500	15	[1.5]	300
CD5268A.....	2	7	2.0	.1	500	20	700	[0.05]	30	700	50	[1.5]	500
B.....	3	7	2.0	.1	300	20	1,000	[0.05]	30	700	15	[1.5]	500
CD5269A.....	2	7	1.5	.07	500	[10]	1,000	[0.05]	30	700	10	[1.5]	700
B.....	2	7	1.0	.07	300	20	1,500	[0.05]	20	700	15	[1.5]	500
CD5270A.....	3	10	1.5	.15	500	[10]	700	[0.05]	50	500	15	[1.5]	500
B.....	2	10	1.5	.1	500	20	700	[0.05]	50	700	10	[1.5]	500
CD5271A.....	3	10	1.5	.1	500	20	700	[0.05]	50	700	15	[1.5]	700
B.....	3	*20	1.5	.1	500	20	700	[0.05]	50	700	20	[1.5]	700
CD5272A.....	3	10	1.5	.1	500	[10]	1,000	[0.05]	50	700	20	[1.5]	700
B.....	3	10	1.5	.1	500	[10]	1,000	[0.05]	50	700	10	[1.5]	500
CD5273A.....	2	7	1.5	.07	300	20	700	[0.05]	30	700	15	[1.5]	500
B.....	2	10	1.5	.1	500	20	700	[0.05]	20	500	10	[1.5]	500

¹ Contains 7 percent Si. All others except one contain > 10 percent Si.

² Contains 10 percent Si.

and reconstituted rock from Mule Ear diatreme, San Juan County, Utah

Asterisk (*) indicates arbitrary values assigned where content is above upper reporting limit.
carrying subscript (A), which were done by atomic-absorption procedures]

Pb	Sc	Sr (parts per million)	V	Y	Zr	Al	Na (percent)	K	Ga	Li	Yb (parts per million)	Hg(A)	Cu(A)	Ag(A)
Green intrusion breccia														
10	10	300	70	[5]	[5]	2.0	0.5	[0.35]	5	[25]	0.1	0.02	16	0.6
[5]	15	300	70	20	100	5.0	1.0	1.5	10	50	2.0	.02	21	.6
10	7	300	50	10	100	2.0	1.0	2.0	10	[25]	1.0	.04	11	.6
[5]	30	200	500	30	50	10.0	3.0	2.0	20	[25]	2.0	.02	25	1.2
10	15	200	100	20	100	5.0	.5	1.5	20	50	2.0	.05	36	.8
10	15	200	100	10	50	5.0	1.0	1.5	10	[25]	1.0	.02	35	.6
[5]	30	300	200	30	100	7.0	2.0	1.5	20	[25]	5.0	.02	34	.6
[5]	50	200	200	20	50	10.0	3.0	[0.35]	20	[25]	3.0	.02	55	1.0
10	7	500	50	10	150	3.0	.7	3.0	10	[25]	1.0	.04	13	.6
10	10	300	50	15	150	3.0	.7	2.0	10	50	2.0	.06	12	.6
10	20	200	100	20	100	10.0	2.0	[0.35]	20	[25]	2.0	.02	19	.4
10	20	200	100	30	100	7.0	2.0	1.5	20	[25]	5.0	.09	10	.6
10	10	1,500	50	10	50	2.0	.07	1.5	10	100	1.0	.02	17	.6
10	5	200	50	15	100	3.0	.07	1.0	10	50	2.0	.05	18	.6
Brown reconstituted rocks														
10	5	300	50	20	50	3.0	0.3	7.0	20	[25]	2.0	0.05	[5]	0.2
10	10	300	50	20	100	3.0	.3	7.0	10	[25]	2.0	.06	[5]	.2
10	7	300	70	20	100	5.0	.5	7.0	20	[25]	2.0	.04	[5]	.2
10	10	300	70	50	100	5.0	.3	7.0	20	[25]	3.0	.02	[5]	.2
10	5	200	70	20	30	3.0	.5	7.0	20	[25]	2.0	.05	10	.2
10	5	200	50	10	30	2.0	.3	5.0	10	[25]	1.0	.02	[5]	.2
10	7	200	50	15	50	5.0	.3	7.0	20	[25]	2.0	.04	[5]	.2
10	7	200	50	10	50	5.0	.5	7.0	10	[25]	1.0	.02	[5]	.2
10	10	200	50	10	50	2.0	.7	5.0	10	[25]	1.0	.02	[5]	.6
10	10	200	50	10	70	2.0	.7	5.0	10	[25]	1.0	.06	[5]	.2
10	10	150	30	10	70	3.0	.5	5.0	10	[25]	1.0	.02	[5]	.2
10	10	150	30	10	100	5.0	.7	5.0	10	[25]	1.0	.06	[5]	.2
Gray intrusion breccia														
10	5	200	50	10	70	2.0	0.7	2.0	10	100	1.0	0.04	11	0.4
10	5	150	30	10	50	1.5	1.0	3.0	10	[25]	1.0	.02	12	.4
10	5	700	30	10	50	1.5	.7	3.0	10	[25]	1.0	.05	10	.4
10	7	300	50	[5]	50	2.0	1.0	3.0	10	[25]	1.0	.05	11	.2
20	5	300	50	10	70	3.0	2.0	5.0	10	100	1.0	.04	12	.4
10	10	300	50	15	50	3.0	1.0	3.0	10	100	2.0	.02	11	.6
10	5	700	50	[5]	30	2.0	2.0	3.0	10	100	1.0	.04	10	.4
10	5	700	50	10	50	2.0	1.0	3.0	10	100	1.0	.04	10	.6
10	10	300	50	10	100	3.0	.7	2.0	10	100	1.0	.02	12	.4
10	7	200	50	10	70	2.0	.7	2.0	10	100	1.5	.02	13	.6
10	7	200	50	10	50	2.0	.7	1.5	10	100	1.0	.09	13	.6
15	7	200	50	10	70	2.0	.7	1.5	15	100	1.0	.06	16	.6
10	10	700	50	10	50	2.0	1.0	3.0	10	[25]	1.0	.06	13	.4
5	7	700	50	10	50	2.0	1.0	2.0	10	100	1.0	.02	12	.4
10	5	300	50	10	30	2.0	.7	2.0	10	100	1.0	.02	13	.6
15	10	300	50	15	50	3.0	1.0	3.0	10	100	2.0	.05	10	.4

Table 2.—Results of R-mode analysis in terms of factor groups I–VII

I	II	III	IV	V	VI	VII
Mo	Yb	Ca	Mg	Sr	Hg(A)	B
Mn	Zr	Be	Ag(A)	Ba	Pb(A)	Pb
Fe	Sc	K	Ni			(Li)
V	Ti		Co			(K)
(Cu)	Y		Cu(A)			
(Ti)	Al		Cu			
(Sc)	Ga		Cr			
(Al)	Na		Li			
(Na)	(V)		(Mn)			
(Ga)	(Cu(A))		(Fe)			
	(Fe)					
	(Ba)					

Factor I, the effect of weathering-type alteration and oxidation of igneous rocks, characterized by the close covariance of a group of mobile metals commonly derived from weathered and altered igneous rocks. (Weight: 32 percent.)

Factor II, the effect of the contribution of sedimentary rock minerals, a group of metals associated with detrital light- and heavy-mineral components in sediments. (27 percent.)

Factor III, the effect of the formation of the calcareous, feldspathic brown reconstituted rocks. (8 percent.)

Factor IV, effects of the ultrabasic igneous rock contribution of elements to the diatreme rocks, a suite of elements related to the deeply buried ultrabasic igneous rocks in which the diatreme originated. (5 percent.)

Factor V, effects of common solution-borne elements in sedimentary rocks, elements which occur as sulfates in detrital sedimentary rocks, particularly strontium in mudstones and barium in sandstones. (5 percent.)

Factor VI, effects of weak hydrothermal activity, based on the relation of mercury to hydrothermal effects on rocks. (4 percent.)

Factor VII, effects of the mica fraction derived from silicic igneous and mica-rich sedimentary rocks, based on the occurrence of these elements together in micas. (4 percent.)

In summary, if the meanings of the element groups are correctly interpreted, then the effects of weathering-type alteration and oxidation dominate the element covariance in the exposed diatreme rocks. The effect of the presence of detrital sedimentary rock components is the next most important factor; the effect on element covariance of the formation of reconstituted (brown) rocks is the third most important factor. The next four minor factors are effects of the ultrabasic igneous mineral contributions, sedimentary sulfate minerals, hydrothermal activity, and the presence of micas. Most remaining residual effects, 14 of the remaining 15 percent, are distributed among 12 possible factors, and the remaining 1 percent is distributed among nine possible factors. The absence of a recognizable "mineralization" factor confirms Shoemaker's conclusion (1956) that Mule Ear is unmineralized. The very weak hydrothermal effect (factor VI) all but eliminates the possibility of hydrothermal mineralization in the rocks from which the samples were taken. Movement and

concentrations of elements are, therefore, dominantly the effect of epithermal mechanisms on the altered source material.

Table 3 shows the elements, their communality, and the proportion of positive covariance in percentage of each element with each of the seven factors. The communality indicates the total proportion of variance in the correlation matrix accounted for by the seven factors. The minus signs (–) under the factor headings indicate negative covariance of the respective elements. The zeros indicate zero covariance. If we take iron as an example, we find that it has a communality of 0.86, which means that 86 percent of its variance with the other elements is accounted for by seven factors. The 45 for iron under factor I means that 45 percent of the positive covariance of iron is related to factor I. The remaining positive covariance is related to factor II (28 percent) and factor IV (27 percent). If we read the measures in terms of the factor interpretations, we find that 45 percent of iron covariance is related to alteration of diatreme rocks, 28 percent is related to the incorporated sedimentary rocks, and 27 percent is related to the original basic igneous rocks. This procedure is a simplification of the mathematical relationships involved, but it puts them into a form usable for geologic interpretations.

Increasing or decreasing the number of factors increases or decreases the communalities of the elements and also changes the proportions of covariance.

With reference to the previously listed factor groups, each element is listed in the group in which it has the highest proportion of covariance. The axis element, such as molybdenum, in factor I, is selected mathematically as the central element of the group and becomes the axis element with 100 percent of its positive covariance related to factor I. The 45 percent for iron is a function of the covariance between iron and molybdenum as measured by the appropriate coefficient in the previously mentioned 28×28 element correlation matrix. Note that lead covariance is equally high for both factors VI and VII, indicating equal covariance with the two axis elements mercury and boron.

The 100-percent positive covariance among magnesium, chromium, and nickel is strong evidence of a common origin for these elements and for interpretation of factor IV as the effect of the contribution of ultrabasic igneous rocks from which the first and most of the later intrusion breccias were probably derived.

Q-mode analysis

The Q-mode analysis of the 42×42 cosine theta matrix indicates that five major factors or sample groupings account for 89 percent of the variance among samples. These five factor sample groupings from the reordered oblique vector matrix are listed in table 4.

Inspection of the five sample groups reveals that 1 and 5 are almost exclusively from the selected gray-rock class, 2 includes all samples from the brown-reconstituted-rock class, and 3 and

Table 3—Proportion, in percent, of positive covariance of each metallic element with each factor

[Communalities indicate proportion of total variance of each element in the correlation matrix accounted for by all seven factors. The minus (-) indicates that the covariance is negative between the particular element and factor identified by the space in which it is used]

Element	Communality	Alteration	Sedimentary rocks	Reconstituted rocks	Igneous rocks	Interstitial sulfates	Hydrothermal elements	Micas
		Factor I	Factor II	Factor III	Factor IV	Factor V	Factor VI	Factor VII
Fe	.86	45	28	(-)	27	(-)	(-)	(-)
Mg	.93	0	0	0	100	(-)	(-)	0
Ca	.86	0	(-)	100	(-)	(-)	0	0
Ti	.87	31	52	1	16	(-)	(-)	(-)
Mn	.88	43	14	3	27	(-)	13	(-)
B	.88	0	(-)	0	0	0	0	100
Ba	.93	(-)	37	(-)	(-)	46	(-)	17
Be	.90	(-)	(-)	66	(-)	(-)	2	32
Co	.89	6	25	(-)	69	(-)	(-)	(-)
Cr	.83	(-)	(-)	(-)	100	(-)	(-)	(-)
Cu	.70	30	28	(-)	40	(-)	2	(-)
Mo	.81	100	(-)	0	0	0	0	0
Ni	.94	(-)	(-)	(-)	100	(-)	(-)	(-)
Pb	.76	(-)	(-)	(-)	8	(-)	46	46
Sc	.85	39	54	(-)	7	(-)	(-)	(-)
Sr	.83	(-)	0	0	(-)	100	(-)	(-)
V	.85	36	33	15	16	(-)	(-)	(-)
Y	.89	19	45	18	9	(-)	(-)	9
Zr	.71	(-)	73	(-)	6	(-)	21	(-)
Al	.86	39	61	(-)	(-)	(-)	(-)	(-)
Na	.75	35	44	(-)	4	17	(-)	(-)
K	.88	(-)	(-)	42	(-)	19	6	33
Ga	.77	28	53	12	(-)	(-)	6	1
Li	.85	(-)	14	(-)	34	19	(-)	33
Yb	.90	0	100	(-)	(-)	0	0	0
Hg(A)	.84	(-)	(-)	0	(-)	(-)	100	(-)
Cu(A)	.88	28	32	(-)	40	(-)	(-)	(-)
Ag(A)	.84	22	30	(-)	48	(-)	(-)	(-)

4 are almost exclusively of the green-rock class. This coincidence of rock classes with factor groups is confirmation of the validity of the field identification and classification of rock types, and it is an indication that the criteria used for classification are geochemically significant.

The samples rated by factor analysis as most typical of the five factor groups and which constitute the group vector axes are: (1) CD5273A, (2) CD5265B, (3) 5263D, (4) CD5262A, and (5) CD5266C. Figure 3 was constructed to compare the element content of the five axis samples with each other and with the geometric means of the 42 samples of diatrene rock used in the study.

The factor 1 sample, CD5273A, contains elements in proportions that correlate more closely with those of more samples than any other single sample. It is interpreted to be the axis sample of the gray-rock class and probably is representative of the rock type with the most consistent composition in the sample collection. The factor 5 sample, CD5266C, is also a gray-rock sample. The samples grouped

below sample CD5266C appear to be only slightly different from those grouped below CD5273A. Sample CD5266C is interpreted to be the axis sample of a subclass within the gray-rock class which is characterized by much less consistent composition—higher proportions of copper, potassium, mercury, and strontium, and lower proportions of lithium than in most of the gray rocks.

The factor 2 axis sample, CD5265B, has grouped around it all the brown-rock samples and one green-rock sample, and as shown graphically in figure 2 is significantly lower in total metal content than the 42-sample average. It contains, however, outstandingly higher values of beryllium, potassium, and calcium. The relative values of metal content in the axis sample are end products of metal-value trends in the group as a whole. Sample CD5265B is, thus, not the average brown-rock sample, but is rather the most characteristic or most typical brown-rock sample.

The factor 3 axis sample, CD5263D, and factor 4 axis sample, CD5262A, are the typical samples of the two groups,

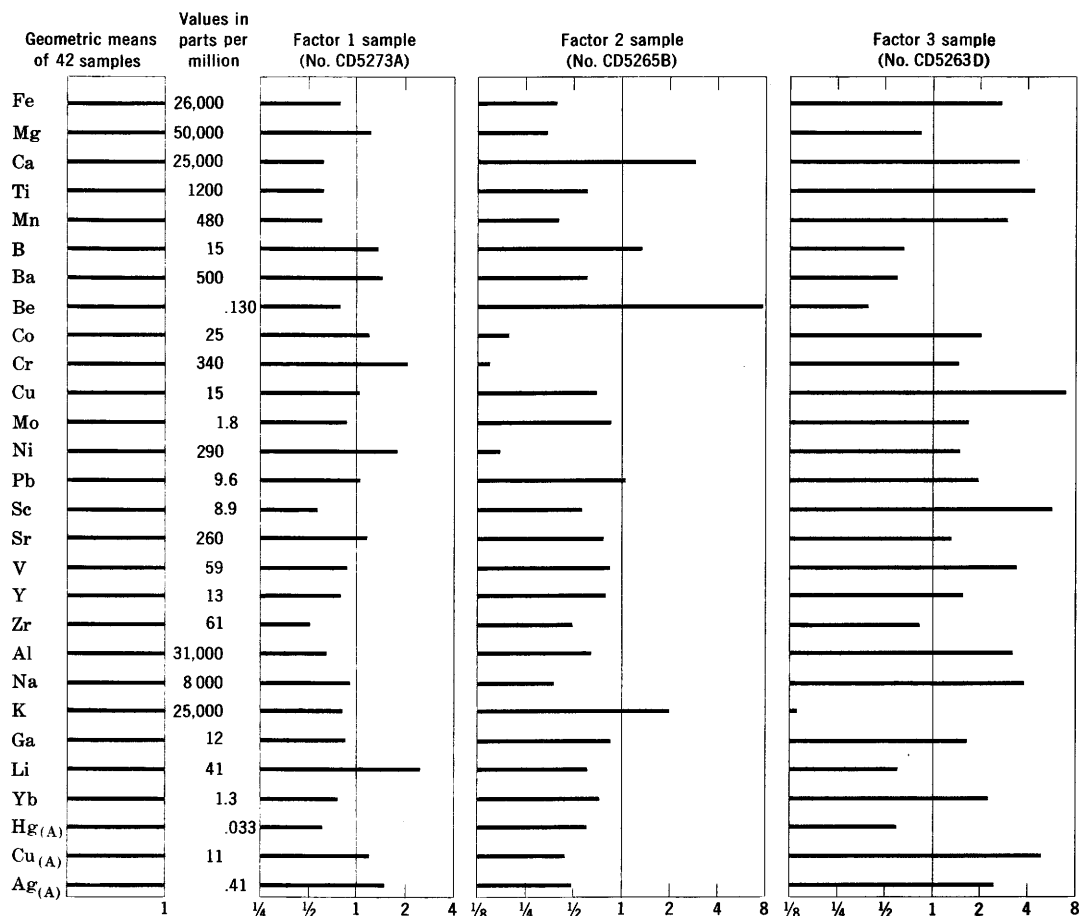


Figure 3.

Table 4.—Results of Q-mode analysis in terms of factor groups 1–5

1	2	3	4	5
CD5273A	CD5265B	CD5263D	CD5262A	CD5266C
5266A	5274C	5267C	5263B	5272A
5268B	5265D	5263C	5275B	5266D
5270B	5264C	5267D	5262B	5267A
5273B	5264D	5262C	5263A	
5269B	5265A		5266B	
5270A	5265C		5267B	
5269A	5264A			
5272B	5264B			
5275A	5274B			
5268A	5274D			
5271A	5274A			
5271B	5262D			

Sample descriptions:

1. All are gray-rock samples except CD5275A, which is green rock.
2. All are brown-rock samples except CD5262D, which is green rock.
3. All are green-rock samples.
4. All are green-rock samples except CD5266B, which is gray rock.
5. All are gray-rock samples except CD5267A, which is green rock.

which together include nearly all of the green-rock samples. The 4 group (compared with the 3 group) trends toward much higher magnesium, chromium, cobalt, and nickel of the ultrabasic igneous-rock element group, and lower cadmium, titanium, yttrium, zirconium, aluminum, sodium, gallium,

scandium, and ytterbium of the sedimentary-rock element group. This two-axis grouping suggests that the green rocks divide into a higher igneous component subclass and a higher sedimentary component subclass, with the sedimentary component subclass, factor 3, as the subgroup with the more uniform composition. The dispersion of green-rock samples (one each) among the factor 1, 2, and 5 groups suggests that the composition of the green-rock class as a whole is more varied than that of the gray- and brown-rock classes. On the basis of the proportion of higher to lower metal values and chi-square, the general metal content of the factor 3 axis sample is significantly higher than that of either the 42-sample average or the factor 2 axis sample, but it is not significantly higher than that of the 1 and 5 axis samples.

A heavy-mineral concentrate from a sand sample collected in the bed of a streamlet draining a green-rock-filled pipe (fig. 2, loc. 15) yielded the relative element values shown graphically in figure 3. Compared with the element value graphs of factors 3 and 4, typical green-rock samples, the heavy-mineral graphs suggest that gravity concentration increased the content of iron, titanium, chromium, molybdenum, scandium, vanadium, zirconium, gallium, and mercury (atomic-absorption); chromium and titanium each attain concentrations of 20,000 ppm,

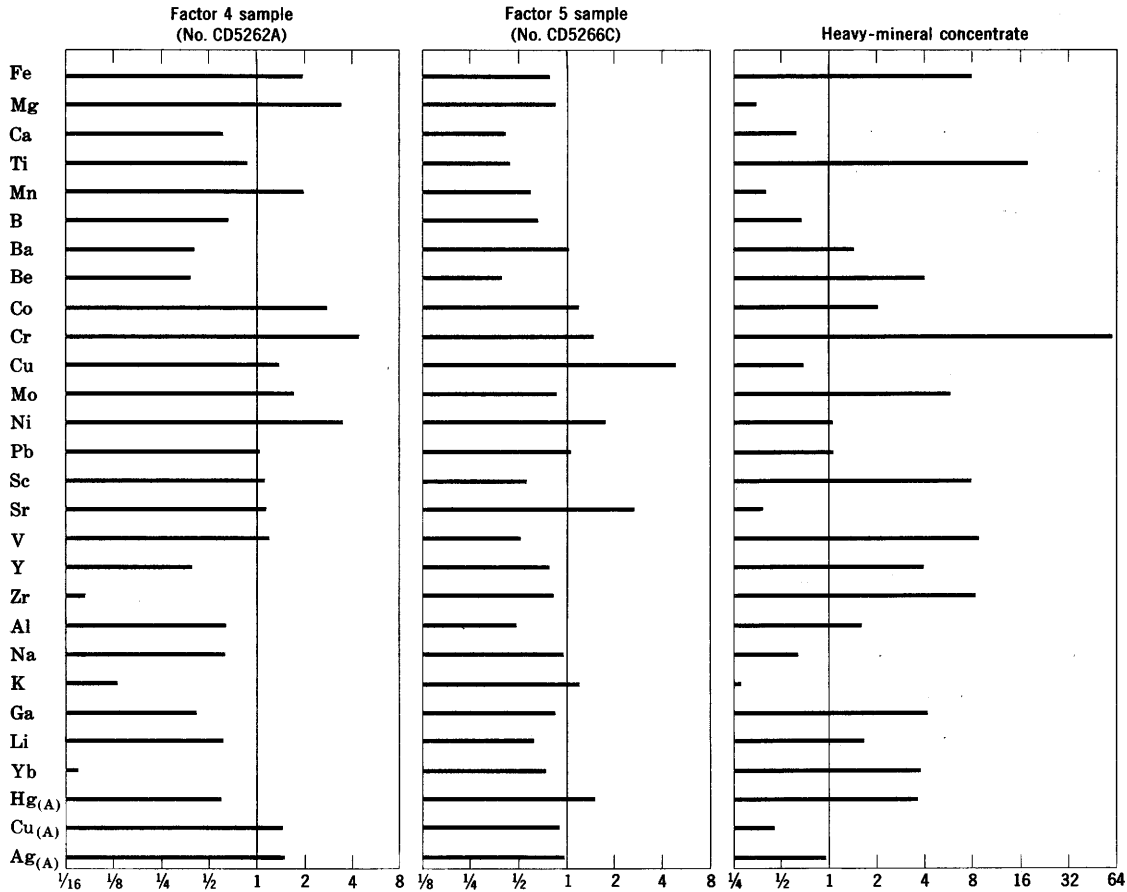


Figure 3.—Comparative values for 28 elements with the geometric mean values of 42 core breccia and reconstituted-rock samples used as a standard, and bar graphs of element values constructed over geometric bases for each of the five Q-mode vector-axis samples and one heavy-mineral concentrate sample. Numbers on the basal scales represent multiples of parts-per-million values given for the 42-sample standard. The scales are graduated geometrically.

or 2 percent, and iron content is approximately 20 percent of the heavy-mineral sample. Heavy minerals constitute about half of the sand sample by weight.

Interpretation

Figure 4 is a graphic comparison of the values of the geometric means of 18 metals determined for 323 samples of the Triassic Moenkopi Formation rocks (Cadigan, 1971) with the 42-sample geometric means in figure 3. The purpose is to offer some comparison between the metal content of the sampled diatreme rocks and that of some regionally indigenous sedimentary rocks. In terms of the 18 metals for which data are available, the Moenkopi rocks, as compared with the diatreme rocks, are significantly deficient in metallic elements. The diatreme rocks have order-of-magnitude excesses (greater than four times) of magnesium, cobalt, chromium, and nickel, the closely covarying metals common in ultrabasic igneous rocks. The metals calcium, titanium, barium, copper (spectrographic), lead, yttrium, zirconium, copper (atomic-

absorption), and silver (atomic-absorption) of probable sedimentary-rock origin are present in amounts similar to those in Moenkopi Formation rocks.

Moenkopi Formation geometric means were used because (1) the analyses on which they were based were done by the same methods as the diatreme sample analyses; (2) the Moenkopi Formation crops out adjacent to the diatreme and was pierced by the diatreme; and (3) these geometric means are available and represent a variety of continental and marine rocks which make up the Moenkopi Formation of the Colorado Plateau region.

Considerable overlapping in range of metal element content exists among the diatreme rocks of different types as suggested, for example, by the factor grouping of green-rock sample CD5262D with the brown reconstituted samples (factor group 2). Such overlapping suggests that metallic elements are distributed less heterogeneously than might be expected in the breccias and reconstituted rocks derived from a wide variety of sedimentary, metamorphic, and igneous rocks. Part of the intermixing of the elements is the result of

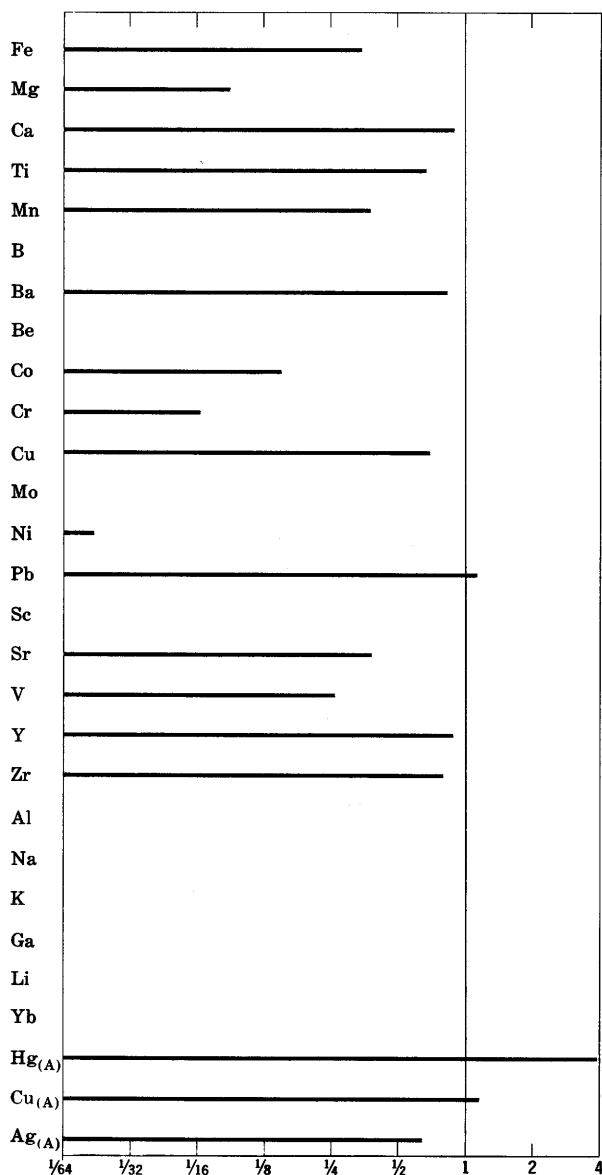


Figure 4.—Average values of 18 metals for 323 samples from the Moenkopi Formation compared graphically with the 42-sample averages for 28 metals of figure 3. Numbers on the basal scale represent multiples of parts-per-million values given for the 42-sample geometric means in figure 3. No bar, data not available.

physical movement of rock blocks and breccia within the diatreme as previously described (Stuart-Alexander and others, 1972), and part is the result of element mobility in a more or less closed system (the diatreme) during the period of diatreme formation and during the period of diagenetic alteration, part of which was probably contemporaneous with diatreme formation.

The active period of the diatreme was characterized by 300°C to no more than 550°C temperatures (Naeser and Stuart-Alexander, 1969), rising volcanic gases, and the foun-

dering of rock blocks and upward churning of breccia from the ultrabasic rocks at the point of origin and from penetrated rock layers. Movement of diatreme core rock toward the surface was characterized by stoping action dependent on pressure, fracturing, and spalling rather than on melting. The diatreme may have broken through to the surface during its active period and manifested itself as a maar.

The brecciated ultrabasic igneous, metamorphic, and sedimentary rock in the diatreme pipe was permeable enough to permit phreatic water from the penetrated formations to circulate within the diatreme. This water, which was charged with oxygen and carbon dioxide, began the weathering and diagenesis which rapidly hydrolyzed the fine-rock breccia to clayey alteration products and dominated the distribution of elements within the diatreme. The intercorrelation of the elements of the factor I group suggests water saturation of the column of debris and precipitation of these mobile metals as a group in all the diatreme rocks represented by the suite of samples. As the labile minerals in the porous detritus occupying the diatreme pipes were altered to clay, the permeability of the diatreme rocks decreased and the rate of circulation slowed. As circulation decreased, rate of alteration at depth also decreased and the rocks of the diatreme reached a state of relative equilibrium.

SUMMARY

The results of the investigation of element distribution indicate that the fine-grained clayey pale-green and pale-gray intrusion breccias of the diatreme pipes, compared with average Colorado Plateau sedimentary rocks, are higher by an order of magnitude in their content of a suite of elements related to their ultrabasic igneous origin; they also contain a second suite of elements of probable sedimentary-metamorphic rock origin which occur in the same order of magnitude as in the "average" sedimentary rocks. The abundance of elements within the brown reconstituted sedimentary dike rocks compared with that of the "average" sedimentary rocks is of generally the same order of magnitude.

The major geologic events or processes that occurred during the history of the core rocks of the diatreme, in order of their effects on covariance of the elements, are: (1) weathering-type alteration or diagenesis which probably occurred during and after the later stages of diatreme formation, (2) homogenization and assimilation of brecciated sedimentary rocks into the diatreme core rocks, (3) formation of dikelike rocks reconstituted from brecciated sedimentary rocks, (4) formation of the diatreme pipes at depth and their filling with brecciated ultrabasic igneous rocks, (5) assimilation of sulfate minerals common to sedimentary rocks into the core rocks, (6) hydrothermal activity, and (7) effects of assimilation of mica-bearing rocks into the core rocks.

These events, listed in order of their effects on element covariance, can be reordered and consolidated to fit into the

history of the diatreme. The suggested historical sequence would be: (1) penetration of the overlying sedimentary and metamorphic rocks by a column of brecciated ultrabasic igneous rocks (factor IV), (2) penecontemporaneous hydrothermal activity at depth (factor VI), (3) assimilation of brecciated sedimentary and metamorphic rocks into the intrusion breccia (factors II, V, and VII), (4) formation of dikelike bodies consisting mostly of brecciated sedimentary rocks (factor III), and (5) epigenetic weathering-type alteration and diagenesis of the intrusion breccia and other fine brecciated core rocks (factor I).

The interpreted minor evidence of hydrothermal effects at the present level of the diatreme does not eliminate the possibility of stronger effects with accompanying significant mineralization at depth.

Field classification of samples into green intrusion breccia, gray intrusion breccia, and brown reconstituted rocks was confirmed by Q-mode factor analysis, which indicated that these classes reflect significant geochemical differences.

REFERENCES

- Cadigan, R. A., 1971, Geochemical distribution of some metals in the Moenkopi Formation and related strata, Colorado Plateau region: U.S. Geol. Survey Bull. 1344, 56 p.
- Hack, J. T., 1942, Sedimentation and volcanism in the Hopi Buttes, Arizona: Geol. Soc. America Bull., v. 53, no. 2, p. 335-372.
- Harman, H. H., 1967, Modern factor analysis: Chicago Univ. Press, 474 p.
- Imbrie, John, 1963, Factor and vector analysis programs for analyzing geologic data: U.S. Office Naval Research Tech. Rept. 6 of ONR Task No. 389-135, Contract Nonr 1228(26), 65 p.
- Naeser, C. W., and Stuart-Alexander, D. E., 1969, The age and temperature of the Mule Ear diatreme, southeastern Utah: Geol. Soc. America Abs. with Programs, pt. 7, p. 155-156.
- Rankama, Kalervo, and Sahama, T. G., 1950, Geochemistry: Chicago Univ. Press, 912 p.
- Shoemaker, E. M., 1956, Occurrence of uranium in diatremes on the Navajo and Hopi reservations, Arizona, New Mexico, and Utah, in Contributions to the geology of uranium and thorium by the United States Geological Survey and Atomic Energy Commission for the United Nations International Conference on peaceful uses of atomic energy, Geneva, Switzerland, 1955: U.S. Geol. Survey Prof. Paper 300, p. 179-185.
- Stuart-Alexander, D. E., Shoemaker, E. M., and Moore, H. J., 1972, Geology of the Mule Ear diatreme, San Juan County, Utah: U.S. Geol. Survey Misc. Geol. Inv. Map I-674, with text.
- Ziony, J. L., 1966, Analysis of systematic jointing in part of the Monument Upwarp, southeastern Utah: California Univ. (Los Angeles) Ph. D. thesis, 152 p.



AN AUTOMATED SPECTROPHOTOMETER

By LEONARD SHAPIRO and C. J. MASSONI,
Washington, D.C.

Abstract.—Equipment is described which sequentially transfers 72 sample solutions into a spectrophotometer cell, measures absorbance, converts to percentage of constituent in the sample, and prints the results. The sample changer is fitted with a switch to disconnect its power after the last solution has been measured. The entire cycle requires 14 minutes. The components are readily available commercially except for the sample changer, the construction of which is described in detail.

In the past few years automated spectrophotometry has become widely available, finding its greatest application in the biological sciences. Hospital laboratories, for example, now make millions of automatic spectrophotometric determinations annually on very small volumes of samples. These systems fill an urgent need arising from the gap between the high demand for analysis and the shortage of skilled technicians. Electronic advances have led to the production of units which can convert any spectrophotometer so that it can read and print directly in terms of percentage of constituent. Sample changers which can be used to obtain fully automated spectrophotometry are available commercially.

A printing spectrophotometer based on the mechanical conversion of photocurrent to a linear function has been previously described by Shapiro and Curtis (1963), but modern electronic converters are faster and more accurate and are therefore used in the present arrangement. An automatic sample changer designed for atomic absorption spectrophotometry (Shapiro and Massoni, 1968) has been modified to increase its capacity and to decrease its size. Commercially available changers handle fewer beakers or are designed for small liquid volumes and require that solutions be transferred to suitable containers. The system described here is more convenient because it accepts 100- and 150-ml beakers, enabling the colored systems to be developed and measured in the same beakers. It measures the absorbance of the solutions from 72 beakers, converts to concentration of constituent, and prints the results in 14 minutes as compared to about 1 hour for reading and calculating manually. The automated spectrophotometer is advantageous, not only for the gain in speed, but also for the elimination of errors in reading meters and dials and in calculating.

DESCRIPTION OF COMPONENTS

The units which make up the entire assembly are the spectrophotometer equipped with a flow-through cell, a digital converter, a printer, a pipetter, and a sample changer. Figure 1 shows the apparatus.

Spectrophotometer, digital converter, and printer

It is possible to combine any good quality spectrophotometer, one of several digital converters available from chemical supply house catalogs, and any printer suitable to the internal code of the digital converter output, but a number of problems are bypassed if the three units are designed by the manufacturer to be used together. Several companies make combinations which can be used in place of the arrangement described below.

The spectrophotometer must be stable with no significant drift over a 15-minute period and must provide an accessible output of its photocurrent so that a digital converter can be connected to it.

We selected the Beckman Model DB-G spectrophotometer¹ and the associated Digital Concentration Converter and Printer. This spectrophotometer is a dual-path instrument, which has the advantage that when a spectrophotometric procedure is used involving a highly absorbing blank solution the absorbance can easily be adjusted to read zero with this same blank solution in both light paths. Such a setting is sometimes impossible with single-path spectrophotometers. The standard 1-cm sample cell is replaced by a 1-cm flow-through cell fitted with small glass inlet and outlet tubes at the top, to which plastic tubing is attached. The volume of the inlet side of the cell must be kept low to allow adequate flushing of one sample by the next one. Therefore, 3-mm ID tubing not more than 12 inches long is attached to the inlet glass tube, while broader gage tubing of any convenient size is attached to the outlet side.

Digital converters designed for spectrophotometers all perform the same functions. The photocurrent generated in a

¹Beckman Instruments, Inc., 2500 Harbor Blvd., Fullerton, Calif.

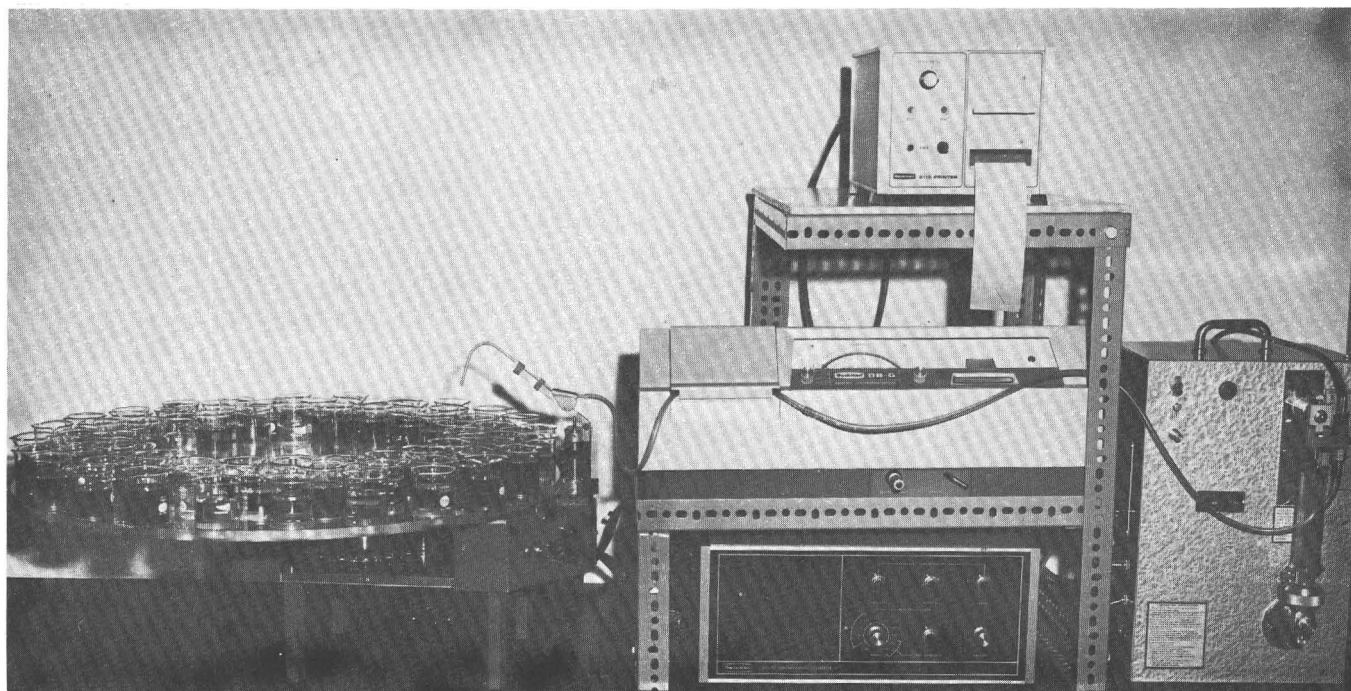


Figure 1.—U.S. Geological Survey modified automated spectrophotometer.

spectrophotometer is a logarithmic function of the concentration of a colored compound in a solution. The converter electronically changes this logarithmic relationship to a linear one and in addition provides an amplifier so that the resultant voltage can be adjusted. It then performs an analog-to-digital conversion which can be read out and (or) fed to a printer. With this device the reading for a blank solution can be set to zero, after which the device can be set to read the numerical value for a standard solution. If the colored system being measured follows Beer's law, as is the general case, subsequent solutions will then read and be printed directly in concentration. The Beckman Digital Concentration Converter used in our laboratory allows percentage transmission and absorbance to be printed as well as concentration.

The printer used prints numbers from 1 to 99 in sequence so that samples can be identified readily. Many other printers are usable but do not provide this convenience. If another printer is used it must be able to be activated by an external switch.

Pipetter

The pipetter provides the suction by which liquid is drawn from the sample beaker, through the flow-through tube and out to waste. Pipettors are available from several companies at reasonable cost. They generally consist of a motor-driven syringe with steel ball valves arranged so that during the downstroke of the syringe piston liquid can flow into the syringe. Then on the upstroke, or discharge stroke, the steel ball valves prevent liquid from entering the inlet side but allow

it to leave the exhaust side. We used the Filamatic Model AB² instrument. The pipetter is modified by adding two cam-activated microswitches. The normally closed switch is in series with the pipetter motor and is positioned to stop the pipetter on the completion of one cycle. The normally open switch activates the printer and is positioned to close just prior to the completion of the pipetting cycle. The pipetter in turn is activated by a switch on the sample changer as the dipper arm approaches its lowest position. The rate of pipetting is 5 seconds per cycle, and the volume is 25 ml.

Sample changer

The sample changer is the only component completely designed and constructed by us. The changer described is a modification of our previous one (Shapiro and Massoni, 1968), using the same Geneva movement to drive and position the placement of each beaker. The motor output speed is 4 rpm, and the gear ratio is selected to allow 12 seconds per sample.

The main design changes resulted from our wish to accommodate more and larger beakers, at the same time reducing the diameter of the carrier plate, a 1/2-inch-thick Plexiglas disk, to 28-inches so the changer could be placed on a standard tabletop. Three concentric circles of twenty-four 2-inch-diameter holes spaced uniformly around the circles are cut so that the centers of the inner and outer holes are on the same radii and the centers of the middle set of holes are

²National Instrument Co., Baltimore, Md.

displaced exactly halfway between each pair of radii. These holes are drilled 7/16-inch deep into the carrier plate and are intended for 100-ml beakers. Holes 2¼-inches in diameter and 7/32-inch deep are drilled at the same centers to accommodate 150-ml beakers. A switching arrangement is constructed for the dipper arm so that it can be automatically shifted from one row of holes to the next at the appropriate time. After the last beaker a final shift is used to activate a latching switch to turn the changer off (fig. 2).

The dipper arm, as seen in figure 2, carries a glass aspirator tube connected by a plastic tube to the inlet of the flow-through tube in the spectrophotometer. The arm pivots at one end, where it is mounted on a rotatable shaft. Also mounted on this shaft, at the lower end, are three collars, each having a projecting peg and a slot 90° away from the peg. The three collars are positioned so that their pegs are offset from each other sufficiently so that a projecting metal shifter plate attached to the sample carrier plate will press against the upper peg as it passes, but will miss the second peg, rotating the movable shaft and thereby shifting the dipper arm so that the glass aspirator tube is over the second row of beakers. A spring detent pressing into one of the collar slots assures that the

dipper arm movement is reproducible. After another full rotation of the carrier plate the metal shifter plate now presses against the second peg and causes the dipper arm to shift so that the glass aspirator tube is over the third row of beakers. At the conclusion of the next full rotation the shifter plate presses against the bottom peg, causing a cam attached to the rotating shaft to press against a latching microswitch which disconnects the drive motor and concludes the operation of the changer. The latching switch must be manually reset before the next cycle can be started. A pilot light connected across this switch serves as a reminder to push the reset button.

The dipper arm is raised and lowered by a cam lifter (pusher rod, fig. 2) as in the earlier sample changer, but in addition a second cam on the same shaft is used to close a microswitch to activate the pipetter when the dipper arm is at its lowest point.

The sample changer has its own on-off switch.

OPERATION

The solutions to be measured are prepared in 100- or 150-ml beakers. The spectrophotometer is turned on to warm up, and

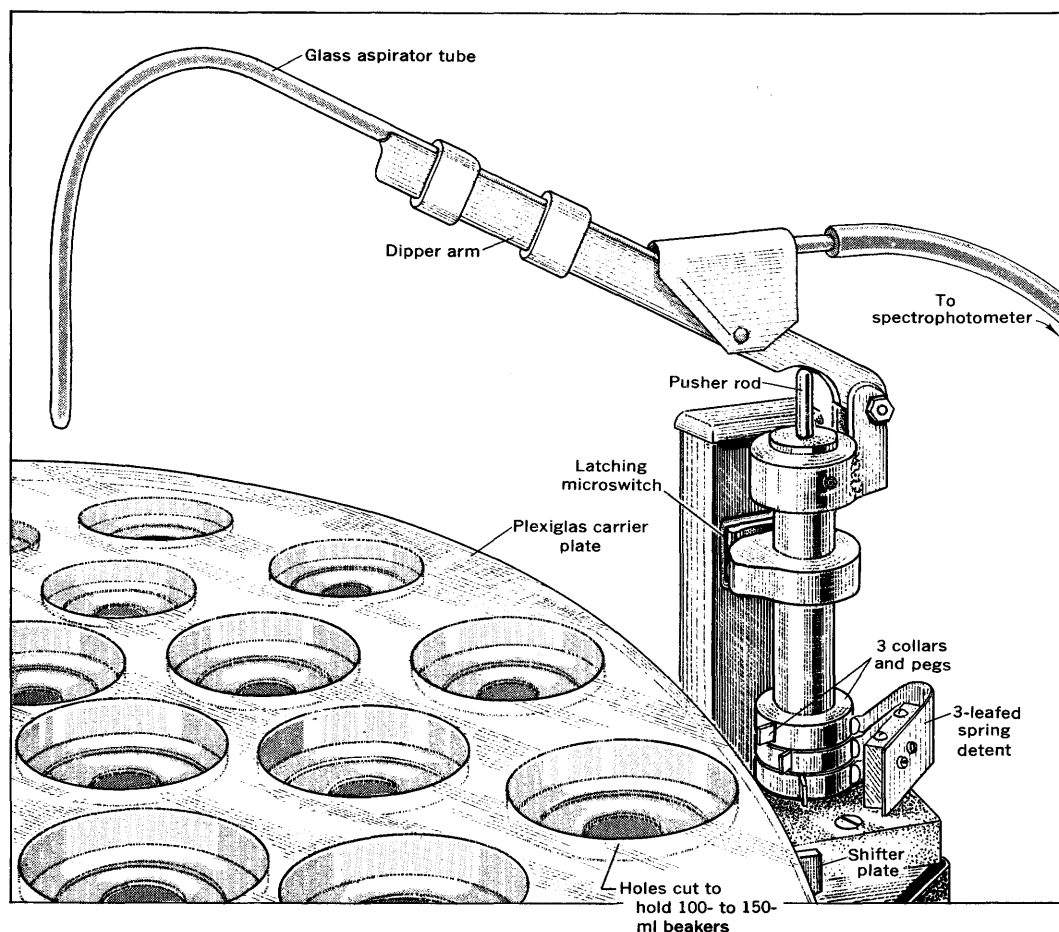


Figure 2.—Schematic drawing of the dipper arm and shifter mechanism of the sample changer.

some of the blank solution is transferred to the reference cell, which is a standard 1-cm cell. If fewer than 72 solutions are available they are placed on the carrier plate with the last one in the last hole so that after the solutions are recorded the changer will be turned off automatically. The first beaker in line contains a blank solution and the second one a known standard. After all the beakers are on the carrier plate it is rotated by hand to place the first beaker under the dipper arm, which must be in the raised position during rotation. The switches for the spectrophotometer, the converter, and the pipetter must all be on and the spectrophotometer set to the proper wavelength; the printer is off. The reset button on the changer is pressed if the changer had cut itself off when used last. The toggle switch for the changer is switched on, causing the arm to lower and in so doing to turn on the pipetter, which then transfers 25 ml of the blank solution through the flow-through tube. When the dipper arm is in the raised position the toggle is put to the "off" position. The spectrophotometer is now adjusted manually to read 100 percent transmittance, the digital converter is set to read concentration, and the zero adjustment is set so that the displayed number is 000. The toggle is now flipped to "on", the table rotates, and the sequence is repeated, transferring the known standard solution. When the dipper arm is up, the toggle is turned to "off" and the concentration adjustment knob is turned manually until the displayed number corres-

ponds to the value of the known standard. The printer is turned on, the toggle switch of the changer is switched to "on", and all the subsequent solutions are measured and the concentrations printed automatically. A few beakers of water are run through to rinse the pipetter after removing the standard beakers from the changer. The entire procedure requires approximately 15 minutes if the changer is loaded to capacity.

SUMMARY

The automated spectrophotometer described differs from commercially available equipment in the use of a pipetter as the transferring mechanism and in the design of the sample changer, which allows a higher capacity container. It has been in daily use in our laboratory for about 6 months with a significant saving in time and reduction in errors.

REFERENCES

- Shapiro, Leonard, and Curtis, E. L., 1963, Percent-constituent printing accessory and flow-through cell for a spectrophotometer: Art. 103 in U.S. Geol. Survey Prof. Paper 475-C, p. C171-C174.
- Shapiro, Leonard, and Massoni, C. J., 1968, Automatic sample changer for atomic absorption spectrophotometry, in Geological Survey Research 1968: U.S. Geol. Survey Prof. Paper 600-B, p. B126-B129.



ELECTROLYTIC CELLS FOR CLEANING CRYSTALS BEFORE FLUID INCLUSION ANALYSIS

By DARRELL M. PINCKNEY, Denver, Colo.

Abstract.—A set of electrolytic cells has been designed and built for cleaning the crystal surfaces as part of the sample preparation for the chemical analysis of fluid inclusions. The parts are readily obtainable and inexpensive, and can be assembled in the laboratory. Cleaning is accomplished by immersing the specimens in water and passing a direct current through the water. The cells are specially constructed U-tubes designed for thorough flushing of both crystals and tubes. The amount of current flowing through each cell can be determined by switching the current from each cell through a meter. Details of the electrical circuit and operation of the cells are described. The cells may be useful also for other purposes such as removing mineral coatings from the surfaces of sand grains.

Chemical analyses of fluid inclusions provide valuable information about the hydrothermal fluids that are responsible for many ore deposits. Extracting the fluid of the inclusions from crystals by the crushing and leaching technique (Roedder and others, 1963) requires that the crystals be free of any unwanted materials. Leaching may introduce contamination by partly dissolving solid inclusions from within the crystal, as well as materials adhering to the surface. Solid inclusions can be eliminated by careful microscopic examination and rejection of crystals containing unwanted inclusions; still, materials adhering to the surface of the crystal and lodged in surface cracks must be removed. Cleaning by washing in solvents and vibrating in an ultrasonic cleaner is helpful, but does not remove all impurities from the crystals. Roedder (1958) applied the concept of electrolytic cleaning to crystals; this process removes all soluble material from the surfaces, cracks, and cleavages of the crystals and also dissolves some material from the crystals. The electrolytic cleaning cell illustrated by Roedder (1958) was found to be difficult to use because of the way in which the cleaning water was removed from the cell; also there was no easy way to monitor the cleaning process. The improved equipment described herein is designed to overcome these deficiencies. The necessary parts are inexpensive, and they can be assembled easily in the laboratory using common tools.

The equipment consists of a source of direct current, one or more large U-tubes, platinum electrodes, a meter to measure the flow of current through the U-tubes, resistors, connectors,

and, if more than one U-tube is used, a selector switch. The assembled equipment is shown in figure 1.

ELECTRICAL CIRCUIT

The electrical circuit for the cells (fig. 2) allows the current flowing through each cell to be measured independently of the other cells. In order to measure the current flowing through each cell (R_1), a resistor (R_2) is placed in series with each cell, and a meter is placed in parallel with resistor R_2 . When the selector switch is open, all the current flows through R_1 and

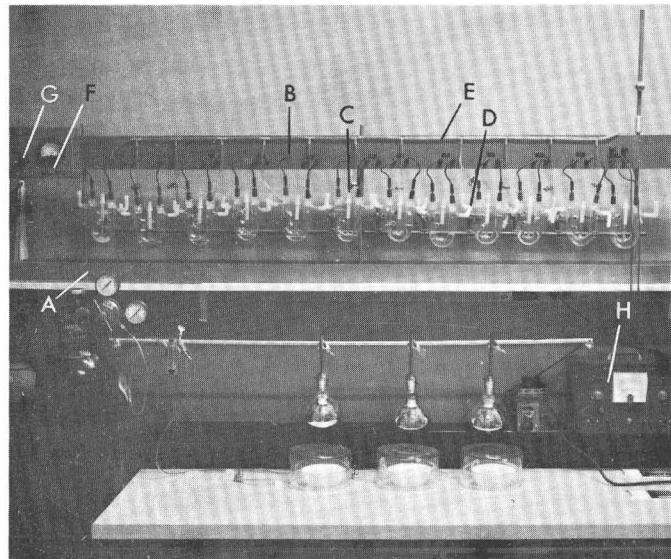


Figure 1.—Electrolytic cleaning cells. The unit is mounted in a shallow wooden trough (A) which serves both as mounting board and as collector of water that overflows from the U-shaped cells. In operation the whole unit is tilted slightly toward one end where a drain tube is located. Resistors and wires are mounted on back of wooden board (B). Clamps hold the cells and allow them to be tilted so that they overflow evenly from both ends at the same time. Hollow polyethylene stoppers (C) keep dust out of the filling tubes. Overflow tubes (D) and tubing for continuous flushing (E) are no longer used. Meter shunt switch (F). Selector switch (G). Variable-voltage d-c power source (H). Drying equipment is on table in foreground.

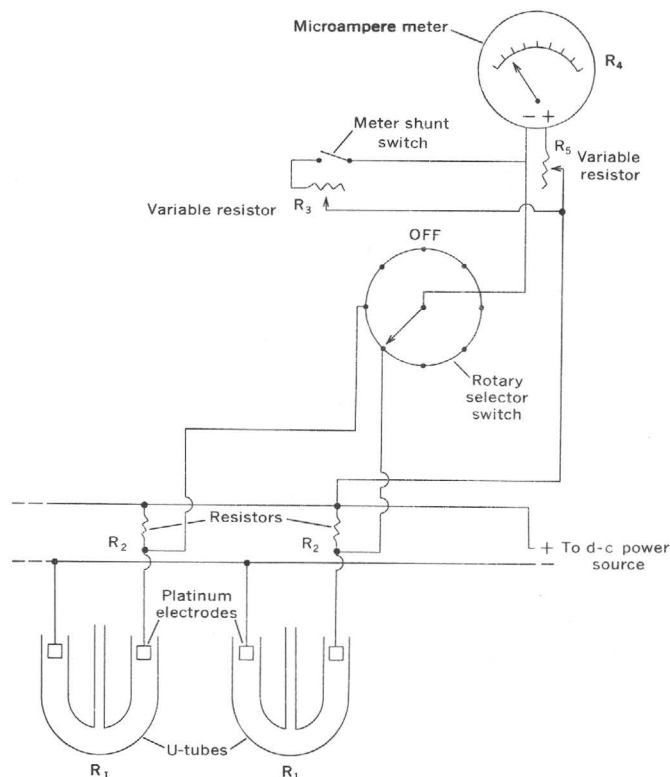


Figure 2.—Wiring diagram for electrolytic cleaning cells.

R_2 . When the selector switch is closed, part of the current flowing through the cell is shunted around R_2 and through the meter. The current flowing through any cell can be easily measured by merely turning the selector switch.

The current flowing through a cell is inversely proportional to $R_1 + R_2$. When the cell is filled with deionized water, R_1 is very large (several million ohms), depending on the purity of the water and size of the cell. R_2 is, relatively, very small (1,000 ohms or less), compared to R_1 ; therefore, the amount of current flowing through a cell is almost entirely controlled by the resistance of the cell, R_1 . Shunting part of the current around R_2 has little effect on the current flowing through the cell, and the meter then provides an accurate measure of the current through the cell.

The resistance of the cells and the voltage used determine the type of meter necessary to measure the current. The resistance, R_4 , of the meter determines the size of resistor R_2 . The cells used by the author have a resistance, when filled with deionized water, of about 12×10^6 ohms. With a potential of 50 volts the current is about 4×10^{-6} amperes. The resistor R_2 that was used is approximately equal to the resistance of the meter, R_4 . Therefore, about half the current flows through R_2 ; the other half flows through the meter and is measured. Consequently a microampere meter was required.

The resistance of the meter being known, a value for R_2 can be selected such that the current flow through R_2 is any

desired multiple of the meter reading. The relation is as follows:

$$I_4 R_4 = I_2 R_2,$$

where I_2 and I_4 are the currents, in amperes, flowing through each resistance, R_2 and R_4 , in ohms. The current through the cell is equal to $I_2 + I_4$.

Because selection of the resistance of R_2 is dependent on the resistance, R_4 , of the meter, the meter should be selected first and R_2 selected to fit the desired R_2/R_4 ratio. If R_2 resistors of the proper size are not readily available, a slightly larger resistor can be used. It will be necessary to increase R_4 accordingly to make the desired R_2/R_4 ratio. R_4 can be increased easily by adding a variable resistor, R_5 , in series with R_4 . The resulting desired ratio will be $R_2/(R_4 + R_5)$.

During operation of the cells the water becomes charged with ions. Because the current, I_4 , may increase beyond the capacity of the meter and damage the meter, a shunt that can be switched into the meter circuit is needed. In the circuit shown in figure 2 a variable resistor, R_3 , allows the shunt circuit to be adjusted so that the meter, with the shunt switch closed, will show any selected fraction of the current in the meter circuit.

VOLTAGE

Direct current used for the cells is provided by a variable-voltage d-c power source. The voltage should be sufficient to produce a measurable flow of current through the cells. Roedder (1958) achieved good results with cells operating at 90 volts. The author has found that at 100 volts some minerals develop a black coating before cleaning is complete. However, at 50 volts many crystals have been cleaned within a few days; yet crystals cleaned for as long as 10 days show no undesirable effects. In the cells built by the author the distance between the electrodes is about 25 cm, and so the average voltage drop at 50 volts is about 2 volts per centimeter.

CELLS

The cells (fig. 3) built by the author are Pyrex glass U-tubes about 25 cm in length and 2 cm in diameter. A small tube attached at the bottom of the U-tube facilitates filling and flushing the U-tube. Clean water added through the small tube passes over the crystals, the electrodes, and the electrode holder before overflowing from the ends of the U-tube. Thereby the crystals, as well as the interior parts of the cell, are thoroughly flushed, and the U-tube is kept filled. Flushing is done with the current on so that ions do not move from near the electrodes back onto the crystals. Electrolysis sometimes produces a gel around the electrodes. If the cell is taken down and the water poured out, some of this material precipitates on the crystals. If the cell is not kept filled and the ends are not thoroughly flushed, this material collects on the walls of the cell above the electrodes.

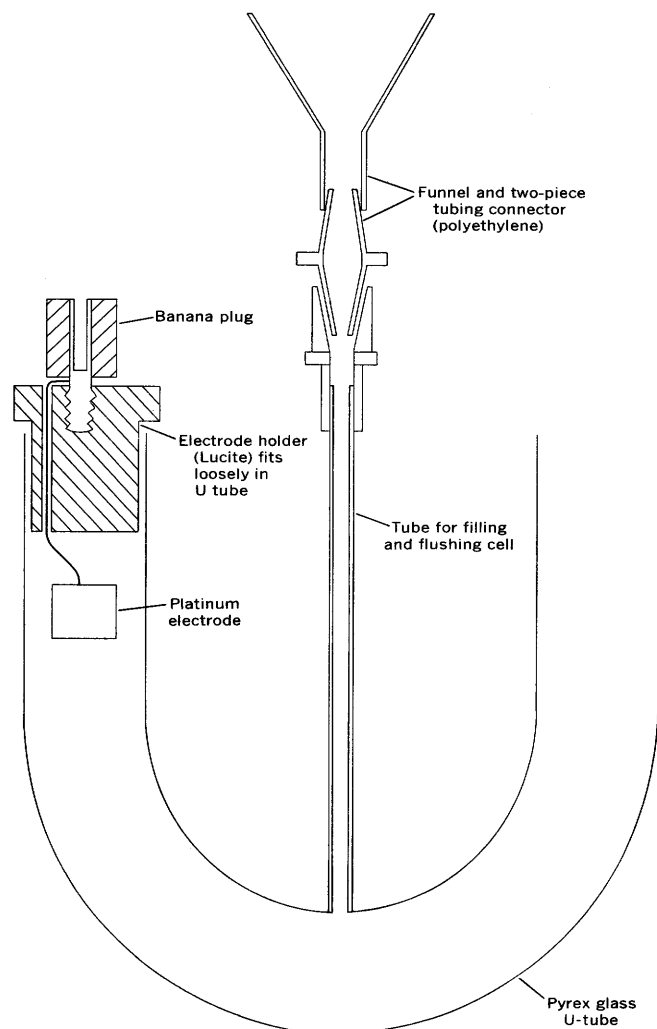


Figure 3.—Construction details of cleaning cells.

The U-tubes shown in figure 1 were made with overflow tubes near the electrodes. The overflow tubes were unsatisfactory because they prevented the end of the U-tubes, above the overflow tube, from being thoroughly flushed, and because dissolved material collected in them. The tube shown in figure 3 is an improved design.

The electrodes for the cells are platinum sheets welded to platinum wire held in loose-fitting Lucite plugs (fig. 3). Banana plugs connect the electrodes to the rest of the circuit.

OPERATION

In operation, crystals are placed in the U-tubes which are then filled with deionized water; the electrodes are inserted into the water, and direct current is applied across the electrodes just as in any electrolytic process. With continued flow of current, material continues to go into solution and is attracted toward the electrodes. This lowers the resistance of the water, which can be noted by an increased flow of current

through the meter. The water needs to be changed every few hours in the early stages of cleaning and at less frequent intervals later on.

After the crystals are clean, the cells are taken down, the electrodes are removed, and the water is poured out. The crystals then can be "poured" from the cells into clean, covered dishes and dried under heat lamps, shown in figure 1, where the covered dishes are ventilated with nitrogen or air from tanks. Afterward the crystals can be "poured" into the crushing equipment or stored in clean plastic bags. This procedure avoids handling the crystals with tongs or forceps after the crystals have been placed in the cleaning cells.

To flush the cells, water is poured rapidly into the funnel, to which is attached one half of a quick-disconnect type of tubing connector (fig. 3). The other half is attached to the glass flushing tube. After approximately 500 to 750 ml of water is poured through the cell, the current flow drops to that obtained from deionized water, indicating complete removal of the old cell water.

The current continually increases as impurities are dissolved and ions are stripped from the surfaces of the crystals. This can be seen readily by means of a graph of current versus time for any water change. Comparison of graphs for each of several changes of water usually shows that at any specified time after the water was changed the current flowing through a cell was less than it was after the same interval of time during the previous water change (fig. 4). Ideally, this value continues to

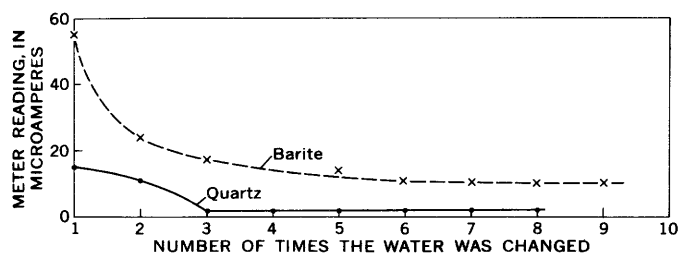


Figure 4.—Variation, with time, of current flowing through cleaning cells. Meter readings made 3 hours after each change of water.

drop with each change of water until a nearly constant value for that particular time is reached. Thereafter the same value should be attained in about the same interval of time no matter how many times the water is changed. This value may be thought of as representing the conductivity of the water attributable to the rate of solution of the mineral under the special conditions of the electrical field. When such a condition is reached, all foreign ions and soluble impurities have been stripped from the surfaces of the crystals, and the water contains only ions dissolved from the crystals.

If two or more cells containing the same mineral are operated at the same time any tendency for the current in one cell to be higher than in the others is easily noted. Such higher

current flow is due to one of two causes: (1) A more soluble mineral impurity is present on the surface of a crystal in the cell having high conductivity; when the impurity is removed the current flow drops to that of other cells containing the same mineral. (2) The deviant cell contains a mineral, such as milky calcite or fluorite, that has very abundant small fluid inclusions. Presumably, slow dissolution of the mineral releases small amounts of saline inclusion water into the cell water, allowing a larger flow of current.

When current-versus-time curves are plotted for each water change, one curve may appear to be slightly erratic, usually after the third to fifth water changes. The erratic curves show a more rapid rate of increase in current followed by a lesser rate of increase. These erratic curves may represent an influx of ions diffusing out of cracks and cleavages in the crystal, or possibly, ions released from broken fluid inclusions.

The behavior of the cells—and consequently the successive graphs of current versus time for each change of water—is different for each mineral that was run, probably reflecting difference in solubility of various minerals. Quartz crystals are usually clean after three or four changes of water (compare samples 6 and 5, table 1). Several days in the same water are required thereafter to produce a small increase in the current. Fluorite and barite, after cleaning, produce a noticeable increase in the current flow within a few hours after each change of water. Calcite produces an increase even sooner.

ANALYSES

Samples of water from the cells were analyzed by atomic absorption to see if graphs of current versus number of washings such as figure 4 accurately indicate when the crystals are clean. The analyses for seven metals in waters surrounding glass blanks, fluorite, and quartz are given in table 1. Analyses of the water used in the cells (sample 7) and of ultrapure water (sample 8) are given for comparison. The water that was used

to bathe a sample of quartz (sample 6) contained only a very small amount of sodium after just three changes of water and 64 hours of cleaning; longer cleaning (sample 5) removed even that small amount of sodium. The waters bathing the glass blanks were free of all elements looked for after 115 hours of electrolysis. Waters bathing fluorite contained calcium (from the fluorite) and some sodium, even after many changes of water. The sodium may have come from the numerous tiny fluid inclusions, many of which were near the surface of the crystals. If the fluorite continually dissolved, brine from inclusions would be released to the cell water.

CONCLUSIONS

Electrolytic cleaning is an effective method for stripping foreign material from crystals being prepared for chemical analysis of fluid inclusions. The equipment which is described here provides an easy method of monitoring the effectiveness of the cleaning process. Graphing the amount of current flowing through a cell for each change of water shows when a steady state has been reached. A steady state is a fairly good indication that any material that is soluble in water has been removed from the crystals. This can be confirmed, if necessary, by analyzing the water in the cell.

The equipment and methods described here were used with good results to clean crystals for fluid inclusion analyses (Rye and Haffty, 1969; Pinckney and Haffty, 1970). W. H. Raymond has suggested that the equipment might be useful also to clean coatings from sand grains or to clean mineral grains and similar materials.

ACKNOWLEDGMENTS

The cells were built by the author in the U.S. Geological Survey laboratory operated by Irving Friedman, whose suggestions were helpful. David Lee suggested using a shunt circuit as a means of measuring current.

Table 1.—Atomic absorption analyses of cell water from blanks and crystals and of laboratory water

[Analyses by Joseph Haffty, using a Perkin-Elmer Model 303 spectrophotometer.
F, found but in amounts too small to be measured]

Sample	Water analyzed	Number of water changes	Time in last water (hours)	Total cleaning time (hours)	Metals (parts per million)						
					Na	Ca	K	Mg	Zn	Fe	Cu
Cell water after washing of:											
1	Glass blanks (3 samples)	5	24	115	0.0	0.0	0.0	0.0	0.0	0.0	0.0
2	Fluorite	10	46	260	F	3.1	.0	.0	.0	.0	.0
3	...do.	10	46	260	F	3.7	.0	.0	.0	.0	.0
4	...do.	10	46	260	F	4.5	.0	.0	.0	.0	.0
5	Quartz	10	46	260	.0	.0	.0	.0	.0	.0	.0
6	...do.	3	16	64	F	.0	.0	.0	.0	.0	.0
Original laboratory water											
before use:											
7	Deionized water used in cells0	.0	.0	.0	.0	.0	.0
8	Distilled, deionized, and redistilled water0	.0	.0	.0	.0	.0	.0

REFERENCES

- Pinckney, D. M., and Haffty, Joseph, 1970, Content of zinc and copper in some fluid inclusions from the Cave-in-Rock district, southern Illinois: *Econ. Geology*, v. 65, p. 451–458.
- Roedder, Edwin, 1958, Technique for the extraction and partial chemical analysis of fluid-filled inclusions from minerals: *Econ. Geology*, v. 53, p. 235–269.
- Roedder, Edwin, Ingram, Blanche, and Hall, W. E., 1963, Studies of fluid inclusions III—Extraction and quantitative analysis of inclusions in the milligram range: *Econ. Geology*, v. 58, p. 353–374.
- Rye, R. O., and Haffty, Joseph, 1969, Chemical composition of the hydrothermal fluids responsible for the lead-zinc deposits at Providencia, Zacatecas, Mexico: *Econ. Geology*, v. 64, p. 629–643.



X-RAY FLUORESCENCE DETERMINATION OF ARSENIC, ANTIMONY, NICKEL, RUBIDIUM, SCANDIUM, VANADIUM, AND ZINC IN ROCK STANDARDS AND OTHER ROCK SAMPLES

By BRENT P. FABBI and LAUREANO F. ESPOS,
Menlo Park, Calif.

Abstract.—Arsenic, antimony, nickel, rubidium, scandium, vanadium, and zinc were determined in 18 rock standards and eight rock samples, making corrections for matrix and interelement effects where necessary. Detection limits for these elements are 3 to 70 ppm. X-ray fluorescence values obtained are in good agreement with the preferred or chemical values.

The determination of many trace elements in the eight U.S. Geological Survey standard rocks by X-ray fluorescence (XRF) methods has been reported by Kaye (1965), Ball (1966), Carmichael, Hampel, and Jack (1968), Parker (1969), and other investigators. Values for nickel, rubidium, scandium, vanadium, and zinc are herein reported for: the U.S. Geological Survey standards granite (G-1), diabase (W-1), granite (G-2), granodiorite (GSP-1), andesite (AGV-1), peridotite (PCC-1), dunite (DTS-1), and basalt (BCR-1); Canadian Association of Applied Spectroscopy standards syenite (S-1) and sulfide ore (S.O.-1); Centre de Recherche Petrographique et Geochimiques standards granite (GR), granite (GA), granite (GH), basalt (BR), diorite (DR-N), and serpentine (UB-N); Leningrad State University standard nepheline syenite (Len-X); and Geological Survey of Tanzania standard tonalite (T-1). Arsenic values were determined for the Canadian Association of Applied Spectroscopy standard sulfide ore (S.O.-1), a mixture of an arsenic mineral (ardennite) and granite (G-2), and three shale samples. Antimony values were determined for

four silicified carbonaceous carbonate samples. Arsenic and antimony values are not reported in the other standard samples because the amount present is below the limit of detection by this XRF method.

X-ray fluorescence has been used successfully by Volborth, Fabbi, and Vincent (1968) to determine many trace elements in the Canadian Association of Applied Spectroscopy standard syenite S-1, using a direct pelletizing technique. Samples prepared by pressing undiluted rock powders do give high X-ray intensities for all elements, and consequently detection limits are low. But the sample surfaces of the undiluted pellets deteriorate and become uneven after prolonged use. The use of a cellulose binder in the direct-dilution pellet preparation method described by Fabbi and Moore (1970) extends pellet life and acts as a diluent to reduce matrix effects. Because the pellets are durable, multielement determinations are possible over long periods of time without repetitive preparation of standards. Matrix and interelement effects of calcium, iron, and titanium must be considered in the determination of the above seven elements.

APPARATUS

A single-channel spectrograph (General Electric XRD-6) with a dual target tube (Cr-W), 5-mil collimator, and flow-proportional counter is used in this work. Instrument parameters are given in table 1.

Table 1.—Instrument parameters for General Electric XRD-6 single-channel spectrograph

Element	As	Sb	Ni	Rb	Sc	V	Zn
Target	W	Cr	W	W	W	W	Cr
Kv	50	50	50	50	50	50	50
Ma	60	45	50	60	50	50	50
Crystal	LiF-2.85 Å	LiF-4.08 Å	LiF-2.85 Å	LiF-2.85 Å	LiF-4.08 Å	LiF-2.85 Å	LiF-2.85 Å
2θ	48.83	106.46	71.26	37.99	97.71	123.16	60.58
Line	Kα ₁	Lβ ₁	Kα ₁				
Counter	Flow						
Counter voltage	1,350 v	1,450 v	1,350 v	1,300 v	1,360 v	1,350 v	1,320 v
Baseline voltage	1.25 v	2.25 v	1.60 v	1.75 v	1.25 v	1.00 v	1.00 v
Window voltage	3.25 v	2.25 v	1.30 v	2.00 v	0.75 v	1.00 v	2.00 v
Path	Air	Air	Air	Air	Vacuum	Air	Air

PROCEDURE

The following procedure is used in pellet preparation and irradiation: transfer 0.5 g of rock powder to a vial and grind in a mixer mill for 10 minutes; pour the ground powder into a mortar and add 0.5 g of chromatographic cellulose; hand grind until well mixed; return the mixture to the vial and regrind for 5 minutes. Press the mixture into a pellet at 30,000 pounds per square inch (Fabbi, 1970).

Irradiate samples for 200 seconds; count both peak intensity and background intensity; subtract background from the peak intensity. Relate the net intensity of each element for all samples and standards to appropriate calibration curves. Make corrections for matrix effects where necessary.

Calibration for each element varies with the procedure used in handling the data:

Scandium—use GSP-1 and Len-X (Nepheline syenite) to calculate $y = mx + b$ equation, W-1 to determine CaO correction; vanadium—W-1 and AGV-1 to calculate $y = mx + b$ equation, GSP-1 to determine TiO₂ correction; nickel—GR and GSP-1 to calculate $y = mx + b$ equation, W-1 to calculate Fe₂O₃ correction; zinc—GA and G-1 to calculate $y = mx + b$ equation, W-1 to calculate Fe₂O₃ correction, or prepare standards of 5.0 to 0.005 percent Zn concentration with Specpure ZnO using G-2 as a base material; arsenic and antimony—prepare standards of 5.0 to 0.005 percent concentration with Specpure oxides of arsenic and antimony using G-2 and National Bureau of Standards sample 1a as base materials; rubidium—use strontium as an internal standard, use the ratio of the intensity of strontium to that of rubidium to determine rubidium, and use W-1 to calculate Fe₂O₃ correction.

DISCUSSION AND RESULTS

Spectral-line interferences, absorption, and enhancement effects on the elements of interest are corrected in the manner described by Fabbi (1971) for barium and strontium. Arsenic, nickel, rubidium, and zinc are corrected for iron absorption; antimony for calcium enhancement; vanadium for titanium spectral interference (Rayburn, 1968); and scandium for calcium spectral interference. Arsenic, nickel, rubidium, and vanadium are corrected for calcium absorption in samples containing greater than 20 percent CaO. Nickel is corrected for low magnesium absorption in mafic rocks containing high MgO. Total iron as Fe₂O₃, MgO, CaO, and TiO₂ are determined in all samples by XRF in order to obtain data for making corrections.

The antimony $L\beta_1$ line is used instead of the $L\alpha_1$ line because both potassium and calcium interfere. An air rather than vacuum path is used in the antimony determination because of calcium spectral interference under vacuum conditions. A chromium target is preferred to a tungsten target in the antimony determination because of its greater efficiency of excitation. The chromium target is preferred in the zinc

determination, as tungsten $L\alpha_1$ interference is less than when using a tungsten target. A tungsten target is preferred to a chromium target in the scandium determination because calcium spectral interference is so much greater using chromium, even though chromium is more efficient in exciting scandium. Although a scintillation counter would be better for rubidium determination than a flow counter, an unusually noisy scintillation counter in the spectrograph made necessary the use of a flow counter in this work. An air rather than vacuum path is used in the vanadium determination because of an increase in titanium interference under vacuum conditions.

Three calibration techniques are used in this work: (1) external standard based on chemical analyses for nickel, scandium, vanadium, and zinc; (2) external standard based on the addition of reagents to make synthetic standards for arsenic, antimony, and zinc; and (3) use of strontium as internal standard for rubidium, as these two elements are ideally suited to this technique. XRF values for these elements using the three calibration techniques are given in tables 2 and 3. There is good agreement between XRF values and the preferred or chemical values. There is also good agreement

Table 2.—X-ray fluorescence determination, in parts per million, of arsenic and antimony in selected samples

Sample	Arsenic		Sample	Antimony		
	XRF	Chemical		XRF	Colorimetric	
Shale	32	¹ 38	Silicified carbonaceous limestone.	90	² 100	
Do	~10	¹ 13		Do	135	² 150
Do	40	¹ 44		Do	250	² 250
Ardennite + G-2 (granite).	3,500	³ 3,400	Do	300	² 250	
S.O.-1 (sulfide ore).	400	⁴ 418				

¹Colorimetric method, Rader and Grimaldi (1961).

²Colorimetric method, E. P. Welsch, analyst (written commun., 1971).

³Ardennite mineral diluted with G-2, C. O. Ingamells, analyst (oral commun., 1970).

⁴Preferred value, Sinc, Taylor, Webber, and Lewis (1969).

between the two calibration methods for zinc, which serves as a check on the applicability of the method used for determining arsenic and antimony. The detection limit at the 2 σ confidence level by this method for As, Sb, Ni, Rb, Sc, V, and Zn is 10, 70, 3, 10, 4, 10, and 7 ppm, respectively. XRF values were obtained on a single pellet. Sampling errors are additive to all other errors normally associated with XRF analysis such as placement, counting, and pellet homogeneity.

REFERENCES

- Ball, T. K., 1966, The geochemistry of the Radesund banded gneisses: *Norsk. Geol. Tidsskr.*, v. 46, p. 379–400.
- Carmichael, I. S. E., Hampel, J., and Jack, R. N., 1968, Analytical data on the U.S.G.S. standard rocks: *Chem. Geology*, v. 3, p. 59–64.
- Fabbi, B. P., 1970, A die for pelletizing samples for X-ray fluorescence analysis, in *Geological Survey Research 1970: U.S. Geol. Survey Prof. Paper 700-B*, p. B187–B189.

Table 3.—X-ray fluorescence determination, in parts per million, of nickel, rubidium, scandium, vanadium, and zinc in standard rocks

Sample		Nickel		Rubidium		Scandium		Vanadium		Zinc			Reference
		XRF	Preferred	XRF	Preferred	XRF	Preferred	XRF	Preferred	XRF			
External standard (chemical)	External standard (synthetic)									Preferred			
Granite	G-1	<3	2	220	220	~4	3	13	16	45	49	45	Fleischer (1969).
Diabase	W-1	83	78	22	22	34	34	240	240	82	82	82	Do.
Granite	G-2	7	6	174	234	7	4	41	37	89	87	75	Flanagan (1969).
Granodiorite	GSP-1	10	11	245	343	9	9	56	52	107	103	143	Do.
Andesite	AGV-1	18	18	67	89	16	13	121	121	89	88	112	Do.
Peridotite	PCC-1	2,480	2,430	<10	.5	13	9	32	31	46	43	53	Do.
Dunite	DTS-1	2,360	2,330	<10	3	7	4	20	19	43	41	61	Do.
Basalt	BCR-1	15	15	49	73	32	36	403	384	124	119	132	Do.
Syenite	S-1	40	42	167	195	6	14	54	89	238	219	219	Sine and others (1969).
Sulfide ore	S.O.-1	14,600	15,100	16	...	22	22	182	189	240	223	294	Do.
Granite	GR	53	55	165	175	8	7	61	65	63	63	60	Roubault and others (1968).
Do.	GA	10	7	161	175	12	7	32	36	85	86	85	Do.
Do.	GH	12	5	¹ 400	390	<4	4	<10	5	78	78	80	Do.
Basalt	BR	275	270	46	46	32	26	246	240	129	124	160	Do.
Diorite	DR-N	16	16	80	75	32	31	205	225	155	158	150	de La Roche and Govindaraju (1969).
Serpentine	UB-N	2,180	2,000	<10	...	16	15	82	100	97	95	87	Do.
Nepheline syenite	Len-X	9	45	212	215	~4	3	64	52	138	139	63	Kukharensko and others (1968).
Tonalite	T-1	21	13	25	<50	15	~10	85	96	137	129	160	Geol. Survey of Tanzania (1963).

¹Rubidium determined by comparing intensity with granitic standards, as strontium intensity is too low for accurate internal standard method.

- Fabbi, B. P., 1971, X-ray fluorescence determination of barium and strontium in geologic samples: *Appl. Spectroscopy*, v. 25, p. 316-318.
- Fabbi, B. P., and Moore, W. J., 1970, Rapid X-ray fluorescence determination of sulfur in mineralized rocks from the Bingham mining district, Utah: *Appl. Spectroscopy*, v. 24, p. 426-428.
- Flanagan, F. J., 1969, U.S. Geological Survey standards—[Pt.] II, First compilation of data for the new USGS rocks: *Geochim. et Cosmochim. Acta*, v. 33, p. 81-119.
- Fleischer, Michael, 1969, U.S. Geological Survey standards—[Pt.] I, Additional data on rocks G-1 and W-1, 1965-1967: *Geochim. et Cosmochim. Acta*, v. 33, p. 65-79.
- Geological Survey of Tanzania, 1963, Standard geochemical sample T-1, msusule tonalite: *Dar Es Salaam, Supp. 1*, p. 1-6.
- Kaye, M. J., 1965, X-ray fluorescent determinations of several trace elements in some standard geochemical samples: *Geochim. et Cosmochim. Acta*, v. 29, p. 139-143.
- Kukhareenko, A. A., Il'inskii, G. A., Ivanova, T. N., Galakhov, A. V., Kozyreva, L. V., Gel'man, Ye. M., Borneman-Starynkevich, I. D., Stolyarova, I. N., Skrizhinskaya, V. I., Ryzhova, R. I., and Melent'ev, B. N., 1968, Klarki Khibinskogo shchelochного massiva: *Vses. Mineralog. Obshchest. Zapiski*, v. 97, p. 133-149.
- de La Roche, H., and Govindaraju, K., 1969, Rapport sur deux roches, diorite DR-N et serpentine UB-N, proposes comme etalons analytiques par un group de laboratoires Francais: *Assoc. Nationale de la Recherche Technique*, p. 1-29.
- Parker, A., 1969, Some trace element determinations on the new U.S.G.S. silicate rock standards: *Chem. Geology*, v. 4, p. 445-449.
- Rader, L. F., and Grimaldi, F. S., 1961, Chemical analyses for selected minor elements in Pierre Shale: *U.S. Geol. Survey Prof. Paper 391-A*, p. A23-A25.
- Rayburn, K. A., 1968, Elemental analysis of cracking catalysts by X-ray fluorescence: *Appl. Spectroscopy*, v. 22, p. 726-729.
- Roubault, M., de La Roche, H., and Govindaraju, K., 1968, Report (1966-1968) on geochemical standards: granites GR, GA, GH; basalt BR; ferriferous biotite mica-Fe; phlogopite mica-Mg: *Sci. Terre*, v. 13, p. 379-404.
- Sine, N. M., Taylor, W. O., Webber, G. R., and Lewis, C. R., 1969, Third report of analytical data for CAAS sulfide ore and syenite rock standards: *Geochim. et Cosmochim. Acta*, v. 33, p. 121-131.
- Volborth, A. V., Fabbi, B. P., and Vincent, H. A., 1968, Total nondestructive analysis of CAAS syenite: *Advances X-ray Analysis*, v. 11, p. 158-163.



DETERMINATION OF MERCURY IN GEOLOGIC MATERIALS BY FLAMELESS ATOMIC ABSORPTION SPECTROMETRY

By JOHN MARINENKO, IRVING MAY, and JOSEPH I. DINNIN,
Washington, D.C.

Abstract.—A flameless atomic absorption method is described for determining submicrogram amounts of mercury. Powdered samples are heated with a calcium oxide–cupric oxide flux in a quartz combustion tube packed with lime and elemental copper. Evolved mercury vapor is swept through a packing of gilded silica where it is amalgamated. The amalgam is rapidly heated and the released mercury vapor is swept through an absorption cell and determined by atomic absorption spectrometry. Two nanograms of mercury absorb 1 percent of the incident signal (I_0).

Flameless atomic absorption methods for determining traces of mercury in a variety of materials are numerous and are summarized in a review by Manning (1970). When sample pyrolysis or combustion techniques are used for the evolution of mercury, it has been a general practice to collect it first on a solid such as gold or silver by amalgamation or on paper impregnated with elemental selenium. Other combustion products formed in the process are vented out with a carrier gas. The mercury collectors used with sample pyrolysis or combustion are numerous. A collector composed of elemental gold squares was used by Vaughn and McCarthy (1964), elemental gold wool by Azzaria (1966), and elemental gold grains by Lidums and Ulfvarson (1968). These authors utilized flameless atomic absorption for the mercury detection. Kosta and Byrne (1969) collected neutron-activated mercury on selenium paper and determined it by gamma spectrometry. Dall'Aglio (1968) released mercury from solution by aeration in the presence of stannous chloride. He collected mercury on granulated quartz covered with auric chloride and elemental gold and determined it spectrographically.

The method described here is applicable to the determination of parts per billion and higher levels of total mercury in geologic materials with good accuracy, precision, and with reasonable speed (approximately 12 samples per man-day). This method appears to be sufficiently sensitive and specific to determine background levels (30–100 ppb) of mercury in commonly occurring geologic materials (Fleischer, 1970). The flux used for the sample decomposition and the packing of the sample combustion tube allows for the decomposition of rocks and minerals with the evolution of mercury, while retaining

other volatile constituents that may be present such as sulfur, selenium, and halogens (Bouton and Duschak 1920; Hillebrand and others, 1953, p. 211). At the same time organic matter is oxidized to carbon dioxide and water. Gilded silica is used for the amalgamation of mercury. Its particle size permits good packing in a collection tube, and its large surface area makes it an efficient mercury collector at room temperatures. The mercury is readily and quantitatively released at elevated temperatures.

REAGENTS

Mercury standard: Dissolve 135.4 mg of mercuric chloride in 1N sulfuric acid and dilute to 100 ml. This solution contains 1,000 $\mu\text{g}/\text{ml}$ of mercury and is further diluted to obtain working standards. The dilute mercury solutions are prepared fresh each day.

Sodium sulfide, reagent grade crystals.

Zinc acetate, reagent grade crystals.

Asbestos fiber, acid-washed medium fiber, ignited to 800°C.

Zinc sulfide-impregnated asbestos fiber: Prepared according to the directions given by Ballard and Thornton (1941), except for the substitution of zinc sulfide for cadmium sulfide. Place 10 g of asbestos fiber into a beaker containing 200 ml of 15-percent zinc acetate, stir and filter through a coarse sintered glass funnel. Transfer the asbestos pad into a beaker containing 200 ml of 5-percent sodium sulfide and stir for 5 minutes. Filter as above and transfer the asbestos pad into a beaker containing 200 ml of 5-percent zinc acetate and stir. Filter, transfer the pad into a beaker containing 500 ml of distilled water. Stir, and filter as above. Wash the zinc sulfide-impregnated asbestos several times with 25-ml portions of distilled water and ignite to 500°C in a porcelain dish. Cool, break up the ignited pad with the sharp end of a porcelain spatula until fluffy, and store in a tightly stoppered bottle.

Copper, light turnings.

Calcium oxide, reagent powder (used for packing the combustion tube).

Magnesium perchlorate, anhydrous.

Calcium carbonate (99.0-percent assay).

Cupric oxide, ACS reagent grade black powder.

Silica, granular, fine (80–120 mesh), washed with hot concentrated hydrochloric acid and rinsed with distilled water.

Lavender oil.

Elemental gold.

Gilded silica (2 percent gold): Dissolve 1 g of gold in 40 ml of aqua regia in a 200-ml porcelain dish. Add 50 g of silica and mix well. Evaporate the acid on a steam bath overnight. Transfer the semidried

silica onto a large sheet of paper and break up any lumps. Mix thoroughly, transfer back into the porcelain dish, and dry in an oven at 110°C for ½ hour. Cool, add 10 ml of lavender oil, and stir the mixture thoroughly. Heat gently on an air bath until fumes cease, stirring the mixture periodically. Ignite to 800°C and maintain the temperature at 800° for 2 hours. The lavender oil reduces the gold, which then forms an adherent coating on the silica. Cool, mix thoroughly, and store in a tightly stoppered bottle.

Calcium oxide–cupric oxide flux: Ignite calcium carbonate powder in a porcelain dish to 1,100°C and cool. Mix two parts by weight of cupric oxide to one part of calcium oxide. Ignite to 1,000°C, cool, and store in a tightly stoppered bottle.

APPARATUS

Although commercially available atomic absorption instruments are satisfactory, the atomic absorption instrument used for this work was assembled from components available in our laboratory. These are:

Grating monochromator: American Instrument Co. Model 4-8400.

Photomultiplier microphotometer: American Instrument Co. Model 10-213.

Recorder: Sargent SRL variable range.

Hollow cathode power supply: Varian-Techtron Pty. Ltd. Model PT35.

Mercury hollow cathode lamp: Perkin-Elmer Instrument Co.

A schematic diagram of the apparatus used for sample decomposition and mercury collection is shown in figure 1. The well furnace is maintained at 500°C, and the combustion

tube furnace at 700°C. The Pyrex tube is filled with 5 g of gilded silica. All the gas connections are made with Tygon tubing. A diagram of the apparatus used for mercury detection is shown in figure 2. A mercury hollow cathode tube is maintained at 10 milliamperes with a multiple-hollow cathode lamp power supply. The absorption cell was constructed from Pyrex tubing with quartz windows cemented at each end with epoxy. The volume of the absorption cell is 19 ml. The absorption cell is alined in the optical path of the instrument by placing a card with a circle cut out in the center over each end of the cell. The diameter of the circle should be no larger than the outer diameter of the cell. Vertical and horizontal adjustments are then made to give a maximum incident signal (I_0).

The heater consists of about 10 turns of No. 14 Nichrome wire wound around a thin-walled (1.5 mm) quartz tube. To keep the wire in place, moist asbestos rope is wound between the coils. The heater is then wrapped with moist asbestos cloth. Heating is accomplished by passing a 13-volt alternating current from a 10-ampere autotransformer through the coil. The coil is heated for several 4-minute heating periods to dry the asbestos.

The mercury resonance line (2,537 Å) is isolated with the grating monochromator. The mounted grating (3,000 Å blaze, 600 grooves/mm) is selected for the ultraviolet wavelength range. The entrance and the exit slit widths are adjusted to 0.38 mm. An ultraviolet-sensitive photomultiplier tube in

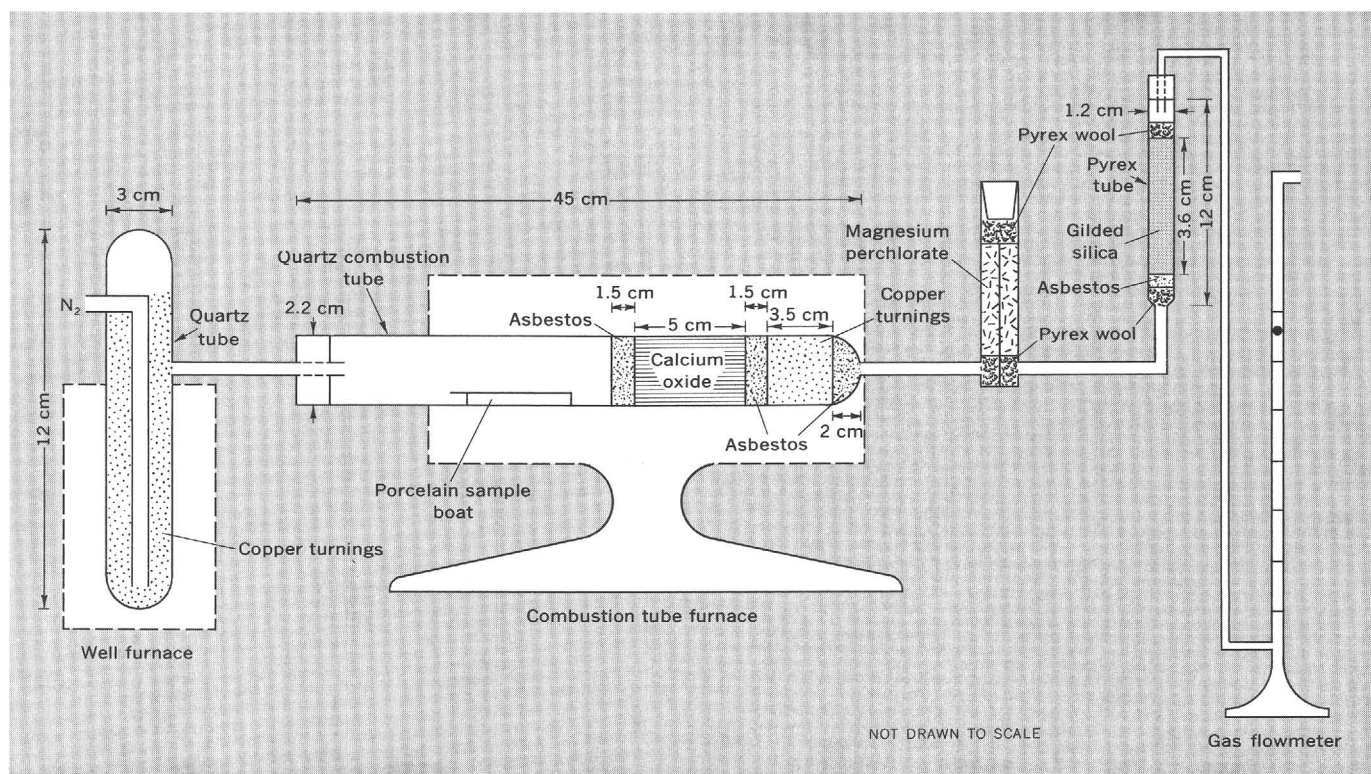


Figure 1.—Schematic diagram of apparatus used for sample decomposition and mercury collection.

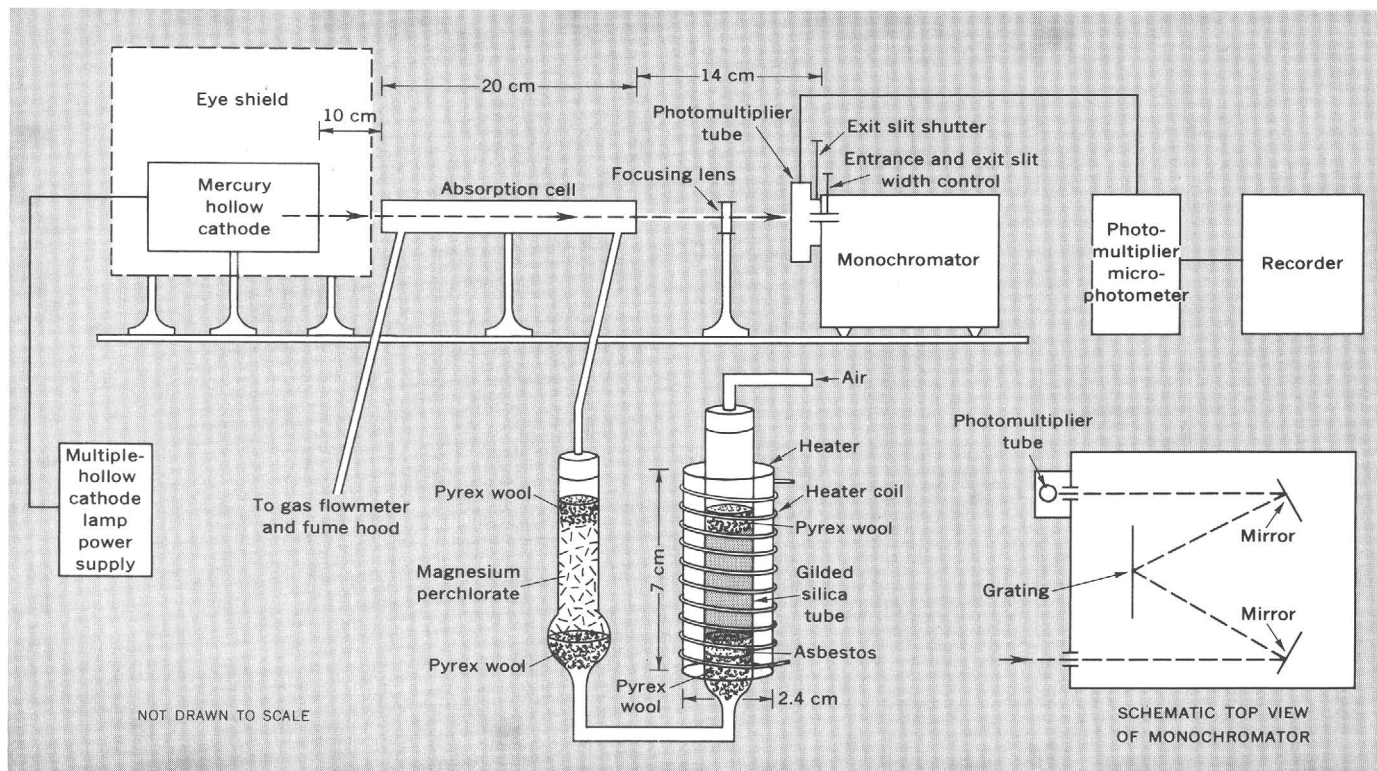


Figure 2.—Schematic diagram of apparatus used for the detection of mercury which has been collected on gilded silica. Heater covered by asbestos cloth (not shown).

conjunction with a photomultiplier microphotometer are used for the signal detection. A variable-range recorder, set in a linear mode, records mercury vapor absorption as a function of time. Chart speed is set at 1/2 inch per minute.

PROCEDURE

Standardization

Weigh into a Coors No. 4 porcelain boat 0.3 g of zinc sulfide-impregnated asbestos. Press the asbestos down firmly with a porcelain spatula. Deliver standard mercury solution on top of the asbestos, dry on a steam bath or overnight at room temperature. A blank and three standards are ordinarily prepared with the highest standard containing not more than 0.2 μg of mercury. Before use, preheat the combustion tube and gilded silica in the following manner to ensure expulsion of any significant amounts of mercury:

Turn the well and the combustion tube furnaces on and deliver nitrogen carrier gas at a flow rate of 38 ml/minute. Place the gilded silica tube into the heater as shown in figure 2. Deliver air carrier gas through the gilded silica at a flow rate of 90 ml/minute. Turn the autotransformer (preset to 13 volts) on and heat the gilded silica for 5 minutes. Turn the power off. Remove the gilded silica tube from the heater and set aside to cool to room temperature. Take the quartz combus-

tion tube out of the furnace when the furnace temperature has reached the operating temperature (about 20 minutes) to cool the tube to room temperature.

For the collection of mercury connect the gilded silica tube as shown in figure 1. Place the boat containing a mercury standard into the cooled quartz combustion tube and heat in the combustion tube furnace for 20 minutes. Maintain the nitrogen flow rate at 38 ml/minute. Transfer the gilded silica tube to the heater, and adjust the air flow to 90 ml/minute. Open the shutter to the photomultiplier tube and set the instrument to 100-percent transmission. Turn the recorder chart and the heater on, and after 5 minutes turn the heater off. The instrument reading should come back to 100-percent transmission after about 6 minutes from start. Turn the recorder chart off and close the shutter to the photomultiplier tube.

Treatment of samples

Weigh 1–2 g of sample rock powder into a 10-ml beaker and mix thoroughly, using a glass stirring rod, with an equal weight of calcium oxide–cupric oxide flux. Transfer the sample and flux into a porcelain boat and repeat the above procedure for the evolution, collection, and detection of mercury. Convert the peak heights of the transmission curves to peak absorbance and compare with the peak absorbances of standards. Repeat

the determination of mercury in samples containing more than $0.2 \mu\text{g}$ of mercury by decreasing the sample weight. For soil samples, increase the ratio of flux to sample tenfold; increase the ratio tenfold to twentyfold for shale samples or for samples with 20–50 percent organic matter.

RESULTS AND DISCUSSION

A typical mercury absorption signal as a function of time of heating and temperature of the gilded silica is shown in figure 3. Under the conditions given above, the peak mercury absorbance is obtained after 3 minutes of heating. This corresponds to about 300°C in the center of the gilded silica packing. Because the method utilizes a single-pass system for mercury detection, it is necessary to hold constant the air carrier gas flow and the heating rate of the gilded silica.

Tracer studies with Hg^{203} indicated 97-percent recovery of

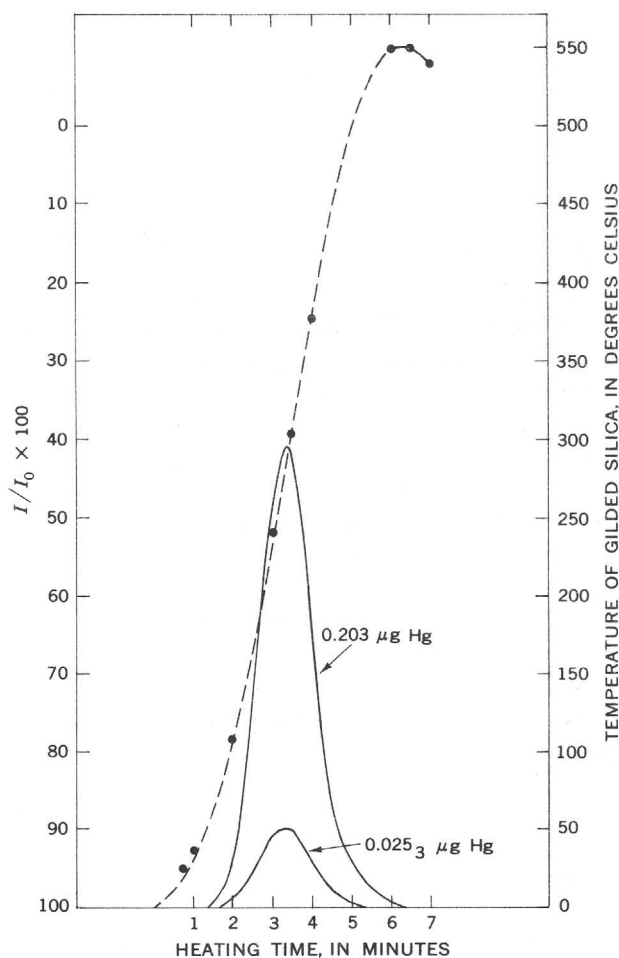


Figure 3.—Absorption signals of mercury (solid lines) released from 5 g of gilded silica (2 percent gold) as a function of time and temperature. Dashed curve represents temperature of gilded silica. Carrier gas flow, 90 ml/minute; chart speed, $\frac{1}{2}$ inch per minute; absorption cell length, 20 cm; absorption cell volume, 19 ml; power to the heater was cut off at 5 minutes.

mercury at submicrogram levels during the sintering and amalgamation step. The release of submicrogram levels of mercury from the gilded silica for its detection by atomic absorption is better than 99 percent complete. Analysis of a synthetic mixture of cinnabar and sphalerite indicates that the procedure can readily handle mercury present as the sulfide.

Ignition of the reagents before use minimizes the mercury blank. A blank run (0.3 g of zinc sulfide-impregnated asbestos plus 1 ml of distilled water) gives an average absorbance of 0.0022, corresponding to about 1 ng (nanogram) of mercury. The average flux blank was determined using 4 g of flux and corresponds to about 0.2 ng of mercury per gram. This may be an advantage over the solution methods where trace mercury content of the reagents may present a problem.

A freshly packed quartz combustion tube should be pre-ignited before any mercury determinations are made. Any condensate on the part of the quartz combustion tube which is outside the furnace should be volatilized by heating with a Meker burner and swept out with the nitrogen carrier gas.

Evaporation of standard mercury solutions on a steam bath or overnight at room temperature in the presence of zinc sulfide-impregnated asbestos eliminates mercury loss by volatilization. The expected precision of standards in the preparation of a calibration curve (0–0.2 μg of mercury) is 0.005. This is the standard error of estimate ($S_{y,x}$) of Y on X, which is a measure of the scatter of standard points about the regression line. The method described above has been applied to the determination of mercury in eight U.S. Geological Survey standard rocks, six analyzed soil samples, and six analyzed shale samples. Four mercury determinations were performed at different times on each standard rock. The average mercury value and its precision for each rock is given in table 1. The results are in good agreement with those described in the literature. The soil and shale samples were selected for mercury analysis primarily to note the degree of interference from organic carbon. The results given in table 2 indicate that carbonaceous materials can be readily analyzed.

REFERENCES

- Azzaria, L. M., 1966, A method of determining traces of mercury in geologic materials: Canada Geol. Survey Paper 66-54, p. 13–26.
- Ballard, A. E., and Thornton, C. D. W., 1941, Photometric method for estimation of minute amounts of mercury: *Indus. Eng. Chemistry, Anal. Ed.*, v. 13, no. 12, p. 893–897.
- Bouton, C. M., and Duschak, L. H., 1920, The determination of mercury: U.S. Bur. Mines Tech. Paper 227, 44 p.
- Dall'Aglio, M., 1968, The abundance of mercury in 300 natural water samples from Tuscany and Latium (Central Italy), in Ahrens, L. H., ed., *Origin and distribution of the elements*: New York, Pergamon Press, p. 1065–1081.
- Ehmann, W. D., and Lovering, J. F., 1967, The abundance of mercury in meteorites and rocks by neutron activation analysis: *Geochim. et Cosmochim. Acta*, v. 31, p. 357–376.
- Flanagan, F. J., 1969, U.S. Geological Survey standards—II. First compilation of data for the new U.S.G.S. rocks: *Geochim. et Cosmochim. Acta*, v. 33, p. 81–120.

Table 1.—Mercury content, in parts per million, of U.S. Geological Survey standard rocks determined by combined combustion-amalgamation-flameless atomic absorption and by other methods

Sample	Approximate sample weight (grams)	Proposed method		Other methods ¹		
		Mercury	Standard deviation	Mercury		
				A	B	C
Granodiorite, GSP-1	2	0.014 ₅	0.0012	0.021	0.015	
Granite, G-2	2	.039 ₈	.0063	.039	.050	
Andesite, AGV-1	2	.009 ₄	.0016	.004	.015	
Basalt, BCR-1	2	.017 ₅	.0017	.007	.005	
Peridotite, PCC-1	2	.019 ₇	.0015	.004	.010	
Dunite, DTS-1	2	.006 ₆	.0008	.004	.008	
Granite, G-1	1	.087 ₃	.0063	0.11, .08
Diabase, W-1	.5	.17 ₅	.01918, .18

¹A, neutron activation (Ehmann and Lovering, 1967); B, atomic absorption (J. H. McCarthy, in Flanagan, 1969); C, flameless atomic absorption following acid digestion (Hatch and Ott, 1968).

Table 2.—Mercury content, in parts per million, of six soil and six shale samples determined by combined combustion-amalgamation-flameless atomic absorption and by other methods

Sample	Approximate sample weight (grams)	Organic carbon (percent)	Mercury			
			Proposed method	Other methods ¹		
				A	B	
Standard soil: ²						
Hg-1	0.1	0.92, 1.07	1.29, 1.20		
Hg-2	.532, .30	.26, .31		
Hg-3	.01	14.2, 14.2	13.8, 13.8		
Hg-4	.03	³ 5.17	5.5, 5.3		
Soil from Missouri:						
D145126	.3	4	.080, .089	.08, .09	0.11	
D145160	1	4	.094	.07, .08	.094	
Shale from Alaska:						
D120656	.2	37	.53, .52	.50		
D120658	.25	25	.51, .48	.47		
D120667	.07	23	2.92, 2.85	3.1		
D120753	.3	24	.18, .20	.22		
D120756	.4	4	.33	.31		
D120764	.2	11	.76	.61		

¹A, flameless atomic absorption following acid digestion, analyst Claude Huffman, Jr., U.S. Geological Survey; B, neutron activation, analyst P. J. Aruscavage, U.S. Geological Survey.

²Samples supplied by Prof. Kenneth Edwards, Colorado School of Mines.

³Mean of four determinations with a standard deviation of 0.30.

Fleischer, Michael, 1970, Summary of the literature on the inorganic geochemistry of mercury, in *Mercury in the environment*: U.S. Geol. Survey Prof. Paper 713, p. 6–13.

Hatch, W. R., and Ott, W. L., 1968, Determination of submicrogram quantities of mercury by atomic absorption spectrophotometry: *Anal. Chemistry*, v. 40, p. 2085–2087.

Hillebrand, W. F., Lundell, G. E. F., Bright, H. A., and Hoffman, J. I., 1953, *Applied inorganic analysis*, 2d ed.: New York, John Wiley & Sons, 1034 p.

Kosta, L., and Byrne, A. R., 1969, Activation analysis for mercury in biological samples at nanogram level: *Talanta*, v. 16, p. 1297–1303.

Lidums, V., and Ulfvarson, U., 1968, Mercury analysis in biological material by direct combustion in oxygen and photometric determination of the mercury vapour: *Acta Chemica Scandinavica*, v. 22, p. 2150–2156.

Manning, D. C., 1970, Non flame methods for mercury determination by atomic absorption, a review: *Atomic Absorption Newsletter*, v. 9, no. 5, p. 97–99.

Vaughn, W. W., and McCarthy, J. H., Jr., 1964, An instrumental technique for the determination of submicrogram concentrations of mercury in soils, rocks, and gas, in *Geological Survey Research 1964*: U.S. Geol. Survey Prof. Paper 501-D, p. D123–D127.



CHEMICAL ANALYSIS OF RUTILE—DIRECT SPECTROPHOTOMETRIC DETERMINATION OF TITANIUM, TOTAL IRON, NIOBIUM, PHOSPHORUS, AND VANADIUM

By ROBERT MEYROWITZ, Washington, D.C.

Abstract.—Titanium, total iron, niobium, phosphorus, and vanadium are directly determined in rutile using hydrogen peroxide, 1,10-phenanthroline, 4-(2-pyridylazo)-resorcinol[PAR], heteropoly blue, and phosphotungstovanadate procedures, respectively. One part of each sample is decomposed by potassium pyrosulfate fusion in a transparent quartz crucible, and a sulfuric acid solution of the melt is used for the determination of titanium, iron, niobium, and phosphorus. A second part is decomposed by sodium carbonate fusion in a platinum crucible, and a sulfuric acid solution of the melt is used for the determination of vanadium. The elements commonly present in rutile do not interfere in the determination of titanium, iron, and phosphorus. Titanium and iron interference in the determination of niobium is eliminated by adding the titanium and iron contents of the sample to the standard niobium solutions used for the standard niobium curve. Similarly, iron interference in the determination of vanadium is overcome by adding the iron content of the sample to the standard vanadium solutions used for the standard vanadium curve.

Relatively few complete analyses of rutile, brookite, and anatase have been published. These minerals are crystalline forms of titanium dioxide and may also contain silicon, iron, aluminum, vanadium, chromium, niobium, tantalum, zirconium, tin, and phosphorus. Published procedures for the analysis of titanium dioxide are for industrial materials and require large samples (Schoeller and Powell, 1955, p 130–133; Codell, 1959, chapters 24 and 25).

This paper describing microprocedures and semimicroprocedures is the first in a series which on completion will provide the schematics for the complete analysis of small samples of rutile, brookite, and anatase. The procedures will provide, in most instances, for the determination of those constituents whose concentrations are 0.1 percent or more. A semiquantitative spectrographic analysis of the sample is needed to select the constituents to be determined, the size of sample to be dissolved, and the size of aliquots of solutions to be taken for analysis. The procedures described herein are based on methods in use at the U.S. Geological Survey for the analysis of small samples of minerals.

PREPARATION OF SAMPLE SOLUTION, 2.4N SULFURIC ACID, FOR THE DETERMINATION OF TITANIUM, TOTAL IRON, NIOBIUM, AND PHOSPHORUS

Reagents and apparatus

Potassium pyrosulfate, $K_2S_2O_7$, powdered.
Sulfuric acid, 18*N*.
Crucibles and covers, quartz, transparent, 5-ml capacity, $1\frac{5}{16}$ -in. height, 1-in. top diameter, and $\frac{1}{2}$ -in. bottom diameter.
Beaker, platinum, 100-ml capacity, $2\frac{1}{2}$ -in. height, and 2-in. diameter.
Furnace, electric, temperature controlled.
Quartz plate for bottom of furnace.
Tweezers, with long platinum tips whose ends have been bent at right angles.
Stirring rod, Teflon, $4\frac{1}{2}$ -in. \times $\frac{1}{8}$ -in.
Dish, petri, $2\frac{3}{8}$ -in. \times $\frac{1}{2}$ -in.
Hotplate, thermostatically controlled.
Surface temperature thermometer, 0° – 540° C.

Procedure

1. Weigh duplicate 80- to 100-mg (± 0.1 mg) < 200-mesh samples in 5-ml quartz crucibles reserving two crucibles for the preparation of procedural blanks.
2. Add 2.0 g $K_2S_2O_7$ and tap to settle contents of the crucibles.
3. Place crucibles with covers on a quartz plate in the electric furnace at room temperature and set the controller at 650° C. When the temperature reaches 500° C occasionally remove the crucible from furnace and twirl to mix contents of the crucible. Heat at 650° C for 30 minutes. Twirl at 5-minute intervals until the molten mass is clear.
4. Remove from the furnace, place on a copper cooling block, and allow to cool to room temperature. Place crucible and cover in a 100-ml platinum beaker containing a Teflon stirring rod and add 13.3 ml of 18*N* H_2SO_4 .

- Place beaker in hot-air bath and warm until melt dissolves completely. Stir frequently to aid solution of the melt. Add small amounts of water dropwise with mixing to replace water lost by evaporation. Rinse down inside of beaker with water, and mix. Use the platinum-tipped tweezers with right-angle tips to lift the crucible cover and then the crucible out of the solution. Rinse cover, crucible, and tweezers with a fine stream of water from a plastic wash bottle. Rinse down the inside surface of the beaker and mix. Stir frequently during this operation to prevent precipitation of the titanium.
- Place beaker in an open petri dish on a hotplate, surface temperature 270°C, and evaporate to fumes of H₂SO₄ to dehydrate the SiO₂ that may be present.
- Cool. Add 2 ml of water dropwise while mixing. Rinse down inside surface of the beaker, dilute to approximately 25 ml and mix.
- Filter through a 7-cm fast filter paper into a 100-ml volumetric flask. Wash precipitate with water. Mix filtrate occasionally to prevent precipitation of TiO₂.
- Cool to room temperature, dilute to volume and mix. Discard precipitate.

Discussion

Duplicate samples should differ in weight by 10–20 percent. This provides a built-in quality control for the reliability of the analysis. The quartz crucibles and covers must be free of the burned-in surface markings which are of iron oxide and which may be removed by grinding. Crucibles without markings are available commercially.

The 2.4*N* H₂SO₄ solution of the rutile can be used for the determination of aluminum, chromium, tantalum, zirconium, and tin.

SPECTROPHOTOMETRIC DETERMINATION OF TiO₂, USING HYDROGEN PEROXIDE

Reagents and apparatus

Sulfuric acid, 10*N*.

Titanium solution, 1,000 ppm TiO₂, 1.8*N* H₂SO₄, 1.0-percent K₂S₂O₇. Prepare a stock solution using U.S. National Bureau of Standards standard titanium oxide, No. 154a. Weigh by difference 500.0 mg of TiO₂ in a 15-ml transparent quartz crucible. Add 5.0 g of K₂S₂O₇. Tap to settle contents of the crucible and place on cover. Using a Bunsen burner, heat gently at first because effervescence is initially very rapid. When effervescence is slow, increase the size of the flame slowly to keep spattering to a minimum. Heat strongly until melt is clear and the solution of the TiO₂ is complete. Invert burner and heat crucible cover to melt the spattered material on the underside of the crucible cover. Cool to room temperature and place crucible and cover in a 150-ml borosilicate beaker. Add 50 ml of 18*N* H₂SO₄ and heat to dissolve the melt, stirring frequently to aid solution of the melt. Use platinum-tipped tweezers with right-angle tips to lift the crucible cover and then the crucible out of the solution. Rinse cover,

crucible, and tweezers with a fine stream of water from a plastic wash bottle. Rinse down the inside surface of the beaker and mix. Stir frequently during this operation to prevent precipitation of the titanium. Transfer the solution to a 500-ml volumetric flask. Dilute to approximately 450 ml. Mix frequently the contents of the flask during the transfer of the solution and during the dilution to prevent the precipitation of the titanium. Cool to room temperature and dilute to volume.

Titanium solution, 250 ppm TiO₂, 0.45*N* H₂SO₄.

Hydrogen peroxide, 3-percent (v/v). Prepare fresh daily from 30-percent H₂O₂.

Crucible and cover, quartz, transparent, high form, 15-ml capacity, 1⁵/₁₆-in. height, and 1¹/₄-in. top diameter.

Spectrophotometer.

Cells, absorption, 1-cm light path.

Preparation of solution for the determination of TiO₂

- Transfer 10.00 ml of the 2.4*N* H₂SO₄ solutions of the procedural blanks and the samples to 25-ml volumetric flasks.
- Rinse down the necks of the flasks and add 0.6 ml of 10*N* H₂SO₄. Rinse again. Mix well and dilute to volume. The resulting acid concentration is 1.2*N*.

Procedure

- Transfer duplicate 5.00-ml aliquots from each of the 1.2*N* H₂SO₄ solutions of the diluted procedural blanks and samples to 50-ml volumetric flasks. Rinse down the necks of the flasks and add 9.4 ml of 10*N* H₂SO₄.
- Transfer 0.00-, 7.00-, 8.00-, 9.00-, and 10.00-ml aliquots of 250-ppm TiO₂ solution to 50-ml volumetric flasks. Add 10.0 ml of 10*N* H₂SO₄ to the first flask, and 9.7, 9.6, 9.6, and 9.5 ml to the others in succession.
- Rinse down the necks of all the flasks, dilute to approximately 40 ml and mix. Add 3.0 ml of 3-percent H₂O₂. Mix and dilute to volume.
- Determine the absorbances at 410 nm (nanometers), in 1-cm cells, using distilled water as the reference.
- Subtract the absorbances of the appropriate procedural blanks from the absorbances of the standard and the unknown solutions to obtain the net values.
- Plot a standard curve, and determine the TiO₂ content of the unknowns.

Discussion

This procedure is practically the same as that described by the author for the determination of TiO₂ in sphene (Meyrowitz, 1971, p. B166). The weight of sample in the final hydrogen peroxide solution is approximately 2.5 and 2.0 mg for the sphene and rutile, respectively. Using the data given in the sphene paper (TiO₂ procedure, discussion, p. B166), one calculates that 12.5 percent Fe₂O₃ (total iron) and 5 percent each of V₂O₅, Cr₂O₃(Cr³⁺), Nb₂O₅, and Nb₂O₅ plus Fe₂O₃ (Fe³⁺) do not interfere in the hydrogen peroxide procedure

for the determination of TiO_2 in rutile. The concentrations of these elements usually found in rutile are less than those tested. All the flasks contain approximately 100 meq (milliequivalents) of H^+ before the addition of the hydrogen peroxide.

SPECTROPHOTOMETRIC DETERMINATION OF TOTAL IRON, USING 1,10-PHENANTHROLINE

Reagents and apparatus

Sulfuric acid, 6*N*.

Iron solution, 1,000-ppm Fe_2O_3 , 0.12*N* H_2SO_4 . Dissolve 4.9112 g ferrous ammonium sulfate hexahydrate, $\text{Fe}(\text{NH}_4)_2(\text{SO}_4)_2 \cdot 6\text{H}_2\text{O}$, in distilled water, add 20.0 ml of 6*N* H_2SO_4 and dilute to 1 liter.

Iron solutions containing 5.00, 10.00, and 20.00 ppm Fe_2O_3 in 1.2*N* H_2SO_4 . Prepare, using the stock solution.

Hydroxylamine hydrochloride, $\text{NH}_2\text{OH} \cdot \text{HCl}$, 10-percent (w/v). Prepare 250 ml. Filter through a fast paper.

1,10-phenanthroline, 0.25-percent (w/v). Prepare 250 ml of solution in the cold, using a magnetic stirrer to dissolve the reagent. Filter through a fast paper.

Sodium acetate, $\text{NaC}_2\text{H}_3\text{O}_2 \cdot 3\text{H}_2\text{O}$, 25-percent (w/v). Prepare 500 ml of solution. Filter through a fast paper.

Cells, absorption, 1-cm, 2-cm, and 5-cm light path.

Procedure

- Transfer duplicate 5.00-ml aliquots of the 2.4*N* H_2SO_4 solutions of the procedural blanks and samples to 25-ml volumetric flasks. Rinse down the necks of the flasks with a small portion of water.
- For the range 0.0–0.5 percent Fe_2O_3 transfer 0.00, 3.00, 4.00, 5.00, 6.00, and 7.00 ml of the 5.00-ppm Fe_2O_3 solution (in 1.2*N* H_2SO_4) to 25-ml volumetric flasks. Rinse down the necks of the flasks with a small portion of water. Add in turn 2.0, 1.4, 1.2, 1.0, 0.8, and 0.6 ml of 6*N* H_2SO_4 and mix. For the range 0.5–1.0 percent Fe_2O_3 use the 10.00-ppm Fe_2O_3 solution. For the range 1.0–3.0 percent Fe_2O_3 transfer 0.00, 4.00, 5.00, 6.00, 7.00, and 8.00 ml of 20.00-ppm solution and add in turn 2.0, 1.2, 1.0, 0.8, 0.6, and 0.4 ml of 6*N* H_2SO_4 .
- Add 2.0 ml of hydroxylamine hydrochloride, 2.0 ml of 1,10-phenanthroline, and 10.0 ml of sodium acetate solutions. Rinse down the necks of the flasks, dilute to mark, mix and let stand for 30 minutes.
- Determine the absorbances at 510 nm in 5-cm cells for the range 0.0–0.5 percent Fe_2O_3 , in 2-cm cells for the range 0.5–1.0 percent Fe_2O_3 , and in 1-cm cells for the range 1.0–3.0 percent Fe_2O_3 , using water as the reference solution.
- Subtract the absorbances of the appropriate procedural blanks from the absorbances of the standard and the unknown solutions to obtain the net values.
- Plot a standard curve and determine the total iron content of the unknowns. Report as FeO. The factor for converting Fe_2O_3 to FeO is 0.89981.

Discussion

Norwitz and Codell (1954, p. 350) found it necessary to add ammonium tartrate to prevent the precipitation of titanium at pH 4.55. Hibbits, Davis, and Menke (1961, p. 163) and Meyrowitz (1971, p. B166–B167) added citric acid to prevent the formation of a precipitate at pH 4.0 and 4.0–4.3, respectively. However, Budanová, Nenasheva, and Matrosova (1956, p. 1421) claimed that neither tartrate nor citrate is necessary at pH 3–4. The claim was confirmed by this author, who found, using this procedure, that the net absorbances of a solution containing 5 μg (micrograms) of Fe_2O_3 alone and a solution containing 5 μg of Fe_2O_3 and 4,165 μg of TiO_2 were 0.141 and 0.142, respectively. Similarly, the net absorbances of a solution containing 0.5 μg of Fe_2O_3 alone and 0.5 μg of Fe_2O_3 and 8,330 μg of TiO_2 were 0.014 and 0.017, respectively.

To further establish the reliability of the above procedure, U.S. National Bureau of Standards titanium base alloys 173a (6A1-4V), 174(4A1-4Mn), and 176(5A1-2.5 Sn) were analyzed. The standards were dissolved by boiling in 22 ml of 9*N* H_2SO_4 , then adding 2.0 ml of 30-percent hydrogen peroxide and boiling to destroy the excess hydrogen peroxide. The cooled solutions were filtered through a slow filter into a 100-ml volumetric flask and diluted to mark resulting in an acid concentration of 1.8*N*. A blank solution was prepared using 20 ml of 9*N* H_2SO_4 . The final titanium solutions were colored. Five milliliters of the solutions were analyzed by the above procedure except that for 173a and 174 the solutions were allowed to stand for 45 minutes before the addition of the 1,10-phenanthroline reagent to allow the solution to decolorize. For 176, after the 45-minute waiting period, the solution was still colored. The flask was heated to boiling over a small flame. The solution rapidly decolorized. The flask and contents were then cooled in an ice-water bath until they were at room temperature, and the usual procedure was then followed. The results obtained are given in table 1.

The amount of acid in the solution must be 12 meq of H^+ before the addition of the hydroxylamine hydrochloride reagent. The pH of the final solution should range between 4.0 and 4.3. However, according to Schilt (1969, p. 56), the pH is not critical, for "the orange-red ferrous chelate forms quantitatively over the pH range 2–9." The concentrations of

Table 1.—1,10-Phenanthroline spectrophotometric determination of total iron in U.S. National Bureau of Standards titanium base alloys

Sample No.	Weight of sample decomposed (milligrams)	Fe values (weight percent)	
		Determined	Certificate of analysis
173a.....	254.2	0.145	0.15
173a.....	291.1	.147	
174.....	253.1	.182	.175
174.....	278.7	.183	
176.....	279.8	.073	.070
176.....	255.9	.073	

vanadium, chromium, niobium, zirconium, and tantalum normally present in rutile do not interfere in the 1, 10-phenanthroline procedure as described above.

The diluted sample solution (1.2N H₂SO₄) prepared for the determination of TiO₂ can be used for the total iron determination.

SPECTROPHOTOMETRIC DETERMINATION OF Nb₂O₅, USING 4-(2-PYRIDYLAZO)-RESORCINOL [PAR]

Reagents and apparatus

Sodium hydroxide, 0.5N. Prepare 500 ml, using plastic apparatus and store in a plastic bottle.

Potassium pyrosulfate, 2-percent (w/v). Place 10.0 g of powdered K₂S₂O₇ in a 15-ml transparent quartz crucible and tap to settle contents of the crucible. Cover with crucible cover. Place crucible with cover in the electric furnace at room temperature and set the controller at 650°C. Heat at 650°C for 30 minutes. Remove from the furnace, place on a copper cooling block and allow to cool to room temperature. Place crucible and cover in a 150-ml beaker, add sufficient water to cover crucible, warm to dissolve the melt. Remove and rinse off crucible cover and crucible. Transfer solution to a 500-ml volumetric flask; dilute to volume, and mix well. Store in a glass bottle.

d-Tartaric acid, [CHOHCOOH]₂, 2-percent (w/v). Filter through a fast paper.

Sodium tartrate, Na₂C₄H₄O₆·2H₂O, 15-percent (w/v) with disodium (ethylenedinitrilo) tetraacetate, Na₂C₁₀H₁₄O₈N₂·2H₂O, of 0.75-percent (w/v). Dissolve 150 g of sodium tartrate and 7.5 g of disodium EDTA in 1 liter of water. Filter through a fast filter. Store in a glass bottle with plastic stopper.

Hydrofluoric acid, concentrated.

4-(2-pyridylazo)-resorcinol [PAR], 0.04-percent (w/v). Dissolve 80 mg of 4-(2-pyridylazo) resorcinol disodium salt, [(CHCH)₂CN₃C₆H₃(ONa)₂·2H₂O] in a small amount of water in a 50-ml beaker. Filter through a slow filter paper into a 250-ml glass stoppered bottle. Dilute to 200 ml and mix well. Prepare just prior to using.

Sodium acetate, NaC₂H₃O₂·3H₂O, crystal, 50-percent (w/v). Dissolve 500 g of NaC₂H₃O₂·3H₂O in 1 liter of water. Filter through a fast paper and store in a glass bottle with a plastic stopper.

Niobium stock solution, 200 ppm Nb₂O₅, 1.0N H₂SO₄, 2.0-percent d-tartaric acid (w/v). Weigh 100 mg of Nb₂O₅ in a 30-ml platinum beaker reserving another beaker for the preparation of a blank. Add 7.7 ml of 18N H₂SO₄, 5.0 ml of concentrated HF, and mix. Place the beakers on a petri dish, 2³/₈-in.×½-in., and evaporate on a hotplate until most of the water is gone. Place in an inverted petri dish on a hotplate whose surface temperature is 300°–310°C, evaporate to fumes of H₂SO₄ and cool. Add water dropwise with constant mixing and rinse down inside of beaker with water. Dilute to approximately 7 ml, cool, add 5.0 ml concentrated HF and mix. Evaporate most of the water and then heat to fumes of H₂SO₄ and cool. Add water dropwise with constant mixing and rinse down inside of beaker with water. Evaporate most of the water and then fume as described above and cool. Repeat addition of water, rinsing, evaporation, fuming, and cooling a second and third time. Add 4.0 ml of water dropwise with constant mixing. Cool, add 10.0 ml of 18N H₂SO₄ and mix. Transfer solution to a 500-ml volumetric flask containing approximately 75 ml of solution containing 180 meq of H₂SO₄ and approximately 50 ml of filtered solution equivalent to 10.0 g of d-tartaric acid. Mix well and cool. Dilute to approximately 450 ml and cool to room temperature. Dilute to volume and mix

well. Filter the solution through a slow filter paper into a glass-stoppered bottle. Standardize the solution as described in detail in the next section of this paper. Discard after 30 days.

Niobium solutions containing 1.00, 3.00, 5.00, 8.00, 10.00, 20.00, and 30.00 ppm Nb₂O₅ in 1.0N H₂SO₄ and 2.0 percent d-tartaric acid.

The d-tartaric acid is dissolved in water and filtered through a fast filter before using.

Titanium solution, 1,000 ppm TiO₂, approximately 1.8N H₂SO₄; 2.0 percent K₂S₂O₇.

Ferric-iron solution, 1,000 ppm Fe₂O₃, 1.0N H₂SO₄. Dissolve 3.0 g ferric ammonium sulfate, FeNH₄(SO₄)₂·12 H₂O in 500 ml of 1.0N H₂SO₄. Filter through a slow paper. Standardize spectrophotometrically, using 1,10-phenanthroline.

Ferric-iron solutions, containing, 10.00 and 20.00 ppm Fe₂O₃ in 0.1N H₂SO₄, prepared by appropriate dilutions.

Beaker, platinum, 30 ml.

Procedure

1. Transfer duplicate 5.00-ml aliquots from the 2.4N H₂SO₄ solution of the sample to 100-ml volumetric flasks. Rinse down the necks of the flasks with water. Add 5.00 ml of 2.0-percent d-tartaric acid, rinse down the neck of the flask and mix.
2. For the range 0.0–1.0 percent Nb₂O₅ transfer 5.00-ml aliquots of 1.00-, 3.00-, 5.00-, 8.00-, and 10.00-ppm Nb₂O₅ solutions (1.0N H₂SO₄, 2.0-percent d-tartaric acid) to 100-ml volumetric flasks. Rinse down the necks of the flasks and mix. For the range 1.0–3.0 percent Nb₂O₅ transfer 5.00 ml of 10.00-ppm Nb₂O₅, 4.00-ml and 5.00-ml aliquots of 20.00-ppm Nb₂O₅, and 4.00-ml and 5.00-ml aliquots of 30.00-ppm Nb₂O₅ to the flasks. For the range 2.0–4.0 percent Nb₂O₅ transfer 5.00 ml of 20.00-ppm Nb₂O₅, and 4.00 ml and 5.00 ml of 40.00-ppm Nb₂O₅ to the flasks.
3. Add 1.0 ml of 2.0-percent tartaric acid to the flasks which contain 4.00-ml aliquots of the standard niobium solutions.
4. Add the amounts of titanium and iron solutions to the standard niobium solutions to match the sample. Add sufficient 2.0-percent K₂S₂O₇ so that the total amount of K₂S₂O₇ present will be equivalent to 5.0 ml of 2.0-percent K₂S₂O₇. Rinse down necks of the flasks and mix.
5. Add 10.0 ml of sodium tartrate-disodium EDTA solution. Rinse down the necks of the flasks and mix.
6. Add 10.00 ml of PAR solution with a transfer pipet. Rinse down the necks of the flasks and mix.
7. Add 10.0 ml of sodium acetate solution and rinse down the neck of the flask and mix.
8. Using a 10-ml measuring (Mohr) pipet add, while swirling the flask, the necessary amounts of 0.5N NaOH to all the flasks. Do not use a graduated cylinder. Rinse down the necks of the flasks and mix. The number of milliliters of 0.5N NaOH to be added to each flask is equal to 1+[2(No. of meq of H₂SO₄ present in the flask)]. The H₂SO₄ in the initial 5.00 ml of solution,

in the titanium solution, and in the iron solution make up this total amount of H_2SO_4 . Disregard the residual H_2SO_4 due to the fused $K_2S_2O_7$. All the flasks contain the same amount of fused $K_2S_2O_7$ and of d-tartaric acid.

9. Dilute to mark, mix, and let stand for 60 minutes.
10. Determine the absorbance at 550 nm, using water as the reference solution. Use 5-cm cells for the range 0.0–1.0 percent Nb_2O_5 , 2-cm cells for the range 1.0–3.0 percent Nb_2O_5 , and 1-cm cells for the range 2.0–4.0 percent Nb_2O_5 .
11. Measure the pH of all final solutions.
12. Plot a standard curve and determine the Nb_2O_5 content of the unknowns.

Discussion

This method is based on the work of Belcher, Ramakrishna, and West (1963) and Wood and Jones (1968). The color is developed in an acetate-tartrate-(ethylenedinitrilo) tetraacetate [EDTA] medium. Belcher and others (1963, p. 1014–1015) report that “the colour system is independent of pH over the range 5.8–6.4” and that they prefer “to work at pH 6.0” (1963, p. 1021). Wood and Jones report that “absorbance was shown to be independent over the range 6.0–6.4” (1968, p. 133). The pH of the final solution of the author’s method is usually 6.0 but may range between 5.8 and 6.2. Although there is a slight but measurable change in absorbance between a pH of 5.8 and 6.2, the procedure is reliable if the samples and standards within a set do not differ by more than 0.2 pH unit. If these limits are not obtained, check the solutions used and repeat the determination. Belcher and others (1963, p. 1021) used pH paper while Wood and Jones (1968, p. 132) used a “direct-reading pH meter.” The author’s method as described above does not require the use of either pH paper or pH meter to obtain the selected pH of 6.0.

Belcher and others were not concerned with very high concentrations of titanium. Wood and Jones (1968, p. 137–138) found it necessary to make an extractive separation of the niobium in order to determine low concentrations of niobium in titanium and in iron. To overcome the interference of titanium and iron, the author adds the same amounts of titanium and iron present in the portion of 1.2N H_2SO_4 solution of the mineral taken for analysis to the standard niobium solutions used to prepare the standard niobium curve. One microgram of Nb_2O_5 is equivalent to approximately 1,000 and 100 micrograms of TiO_2 and Fe_2O_3 (ferric iron), respectively. At pH 6.0, it was established that 2.5 ppm Al_2O_3 , ZrO_2 , and V_2O_4 , 1.0 ppm V_2O_5 , 0.4 ppm Cr_2O_3 , 0.25 ppm Ta_2O_5 , and 0.5 ppm F do not interfere. The limiting tolerance of measured absorbance of test solution versus blank was ± 0.003 absorbance unit (≈ 0.003 ppm Nb_2O_5). If the aliquot of solution analyzed for Nb_2O_5 is equivalent to 5.0 mg of sample, then 0.02 percent Nb_2O_5 can

be determined in the presence of 5.0 percent Al_2O_3 , ZrO_2 , and V_2O_4 , 2.0 percent V_2O_5 , 0.8 percent Cr_2O_3 , and 0.2 percent Ta_2O_5 . The concentrations of these elements usually found in rutile are less than those tested.

There is a linear relationship between absorbance and concentration of niobium for (a) a 5-cm cell path in the range 0.05 to 0.50 ppm Nb_2O_5 , (b) a 2-cm cell path in the range 0.25 to 1.00 ppm Nb_2O_5 , and (c) a 1-cm cell path in the range 0.50 to 2.00 ppm Nb_2O_5 . The absorbances of reagent blank, 0.05 ppm and 0.10 ppm Nb_2O_5 , remain constant (± 0.003 absorbance units) for 2 hours after the initial 1-hour waiting period.

GRAVIMETRIC STANDARDIZATION OF THE 200-PPM Nb_2O_5 SOLUTION

Reagents and apparatus

N-phenylbenzohydroxamic acid, $C_6H_5CON(OH)C_6H_5$, NPBHA, 1.0-percent (w/v). Dissolve 0.5 g of NPBHA in 25 ml ethanol or reagent alcohol. Add water dropwise while mixing until volume is 50 ml. Filter through a medium filter into a glass-stoppered glass bottle. Prepare just before using.

Wash solution saturated with NPBHA. Add 0.5 g NPBHA to 500 ml of water, heat until solution is complete, and let stand at room temperature overnight. Filter through a fast filter into a glass-stoppered glass bottle. Prepare the day before using.

Barium chloride, $BaCl_2 \cdot H_2O$, 10-percent (w/v). Prepare 100 ml and filter through a fast filter.

Hot-air bath, approximately $60^\circ C$.

Crucibles, with cover, platinum, 15-ml capacity.

Procedure

1. Transfer duplicate 50.00-ml aliquots of the approximately 200-ppm Nb_2O_5 (1.0N H_2SO_4 ; 2.0-percent d-tartaric acid) solution to 100-ml beakers. Heat to approximately $60^\circ C$.
2. Add 10.0 ml of 1.0-percent NPBHA dropwise with constant stirring to precipitate the niobium. Place in a $60^\circ C$ hot-air bath for 90 minutes and stir occasionally.
3. Filter hot through a 7-cm medium filter paper.
4. Replace beaker containing the filtrate with another 100-ml beaker. To the filtrate add 2.0 ml 1.0-percent NPBHA and place beaker in the hot-air bath for 60 minutes to test for complete precipitation.
5. Use hot wash solution (approximately 40–50 ml) to transfer the precipitate to the filter paper. Then wash with successive 3-ml portions of hot wash solution until only a faint test for sulfate in the wash solution is obtained (that is, most of the sulfuric acid has been removed).
6. Place filter paper in a platinum crucible and dry in a hot-air bath at $110^\circ C$. Use a platinum crucible and cover that has been ignited previously to constant weight (± 0.02 mg) at $900^\circ C$.

7. Place covered crucible in an electric furnace at room temperature and set controller at 900°C. Heat to this temperature, remove from furnace, cool slightly on a copper cooling block and place in a desiccator for 30 minutes and weigh.
8. Ignite at 900°C for 15-minute intervals with 30-minute cooling periods to constant weight (± 0.02 mg).
9. Calculate the concentration of the niobium solution.

Discussion

N-phenylbenzohydroxamic acid (N-benzoyl-N-phenylhydroxylamine), $C_6H_5CON(OH)C_6H_5$, has been used to standardize niobium solutions (Majumdar and Pal, 1962, p. 357; 1963, p. 169; Belcher and others, 1963, p. 1021). The above procedure is based on Langmyhr and Hongso's paper (1960) on the separation and gravimetric determination of niobium, tantalum, and titanium by precipitation with N-phenylbenzohydroxamic acid. In this work the niobium is precipitated in 1N H_2SO_4 in the presence of tartaric acid at a temperature of 60°C (Langmyhr and Hongso, 1960, p. 302–303). In the author's procedure the mixture is filtered hot rather than cold and washed with hot wash solution as recommended by Majumdar and Mukherjee (1958, p. 24). The concentration of the precipitating reagent is one percent instead of 10 percent because the amount of Nb_2O_5 precipitated is small (10 mg). The reagent is made up in 50-percent rather than 100-percent ethanol to lower the concentration of solvent in the solution during precipitation, thereby reducing the solubility of the precipitate.

SPECTROPHOTOMETRIC DETERMINATION OF P_2O_5 , USING THE HETEROPOLY BLUE METHOD

Procedure

The heteropoly blue procedure described by the author for the determination of phosphorus in sphene (Meyrowitz, 1971, p. B167–B168) can be used for the determination of phosphorus in rutile by changing step 1 of the procedure to read as follows:

Transfer duplicate 1.00-ml aliquots from each of the 2.4N H_2SO_4 solutions of the procedural blanks and the unknown samples to 50-ml flasks. Rinse down the necks of the flasks. Add 8.0 ml of 1.2N H_2SO_4 .

Discussion

In the earlier paper by the author (Meyrowitz, 1971, p. B167) it was reported that 2 ppm each of V_2O_5 , ZrO_2 , Nb_2O_5 , and Cr_2O_3 does not interfere. In the procedure above, the aliquot of solution analyzed is equivalent to approximately 1 mg of sample. In the above procedure, 10 percent each of these oxides does not interfere. One microgram of P_2O_5 is equivalent to approximately 1,000 μg V_2O_5 or 500 μg Nb_2O_5 .

PREPARATION OF SAMPLE SOLUTION FOR THE DETERMINATION OF VANADIUM

Reagents and apparatus

Sodium carbonate, anhydrous, granular.

Sodium nitrate, crystal.

Vanadium solution, 1,000-ppm V_2O_5 , 0.12N H_2SO_4 . Dissolve 643 mg of ammonium metavanadate, NH_4VO_3 , in 40 ml of water containing 60 meq of sulfuric acid. Transfer to a 500-ml volumetric flask and dilute to volume.

Vanadium solution, 4.00-ppm V_2O_5 , 0.12N H_2SO_4 .

Crucibles and covers, platinum, 1.3-ml capacity, 14-mm height, 12-mm top diameter, and 9-mm bottom diameter.

Beakers, borosilicate glass, 20-ml.

Watchglasses, diameter 40 mm.

Triangles, Nichrome, covered with glazed, opaque silica tubes. Length of tubes, 12 mm. Diameter of tubes, 6 mm.

Procedure

1. Weigh duplicate 5- to 6-mg (± 0.01 mg) < 200-mesh samples in a 1.3-ml platinum crucible, reserving two crucibles for the preparation of procedural blanks.
2. Weigh 150 ± 2 mg anhydrous sodium carbonate, transfer to the platinum crucible and tap to settle mixture. Add a few crystals of sodium nitrate and cover the crucible with a platinum crucible cover.
3. Support crucible on a Nichrome triangle covered with glazed opaque silica. Ignite with a Meker burner for 5 minutes, heating gently at first.
4. Mix by swirling, keeping the crucible within the flame. Place crucible on the triangle and ignite for another 5 minutes. Remove from flame, place on a copper cooling block, and allow to cool to room temperature.
5. Transfer crucible and cover to a 20-ml borosilicate beaker, and add 5 ml of water. Warm to disintegrate the melt.
6. Cover breaker with a watchglass. Add slowly 4.5 ml of 6N sulfuric acid through the lip of the beaker. Mix by swirling. Warm in a hot-air bath until effervescence ceases and the solution is clear. Rinse the watchglass into the beaker. Use platinum-tipped tweezers with right-angle tips to lift crucible cover and then the crucible out of solution. Rinse crucible cover and tweezers with small portions of a fine stream of water from a plastic wash bottle. Rinse down inside surface of the beaker, place in a hot-air bath and evaporate to approximately 10 ml.
7. Transfer the blank solutions to 50-ml volumetric flasks.
8. Transfer the sample solutions to 50-ml volumetric flasks containing 5.00 ml of 4.00-ppm V_2O_5 (0.12N H_2SO_4).

SPECTROPHOTOMETRIC DETERMINATION OF VANADIUM, USING THE PHOSPHOTUNGSTOVANADATE METHOD

Reagents and apparatus

Vanadium solutions containing 0.00, 4.00, 8.00, 12.00, 16.00, 20.00

ppm V_2O_5 in 0.12N H_2SO_4 prepared by appropriate dilutions using the 1,000-ppm V_2O_5 solution.

Nitric acid, 4N.

Phosphoric acid, 15N.

Sodium tungstate, $Na_2WO_4 \cdot 2H_2O$, 0.25N. Dissolve 41.3 g of sodium tungstate in approximately 100 ml of water. Filter through a slow paper and dilute to 1 liter.

Iron solution, 1,000-ppm Fe_2O_3 , approximately 0.2N HNO_3 . Dissolve 349.7 mg of vanadium-free iron sponge using 50-ml of 4N HNO_3 . Warm to dissolve. Boil to expel oxides of nitrogen. Cool to room temperature. Dilute to 500 ml and mix.

Iron solution, 100-ppm Fe_2O_3 , 0.02N HNO_3 , 0.10N H_2SO_4 .

Iron solution, 20-ppm Fe_2O_3 , 0.12N H_2SO_4 , 0.004N HNO_3 .

Iron solution, 10-ppm Fe_2O_3 , 0.12N H_2SO_4 , 0.002N HNO_3 .

Hot-water bath. This is made of a borosilicate crystallizing dish, 190×100 mm, with six small water-bath thermometer clamps attached (overall length, 3½ in.). The rim of the dish is covered with a small piece of slit rubber tubing before the clamps are attached. The dish is supported on an iron tripod and heated by a Meker-type gas burner.

Procedure

1. Transfer 5.00-ml aliquots of 0.00-, 4.00-, 8.00-, 12.00-, 16.00-, and 20.00-ppm V_2O_5 solutions (0.12N H_2SO_4 solutions) to 50-ml volumetric flasks. Rinse down the necks of the flasks with water.
2. Add the amounts of iron to the standard vanadium solutions to match the sample. Add sufficient 6N H_2SO_4 so that the total number of milliequivalents of H^+ present is 24. Prepare a separate set of standard vanadium solutions plus iron for each sample solution of rutile.
3. To each of the flasks (procedural blanks, standard solutions, and samples) add 5.0 ml of 15N phosphoric acid while swirling the flasks. Rinse down the necks of the flasks.
4. Dilute to approximately 30 ml, mix and add 10.0 ml of 0.25N sodium tungstate while swirling the flask. Rinse down the necks of the flasks, mix, dilute with water to approximately 45 ml and mix. There should be a void below the necks of the flask to allow space for expansion of the solution.
5. Place the flasks in a boiling hot-water bath for 15 minutes. Cool rapidly in a cold-water bath containing ice until the flask is at room temperature.
6. Dilute to volume and mix well.
7. Determine the absorbance at 410 nm in 5-cm cells, using water as the reference.
8. Subtract the absorbance of the appropriate procedural blanks from the absorbance of the standard and the unknown solutions to obtain the net absorbance.
9. Plot a standard V_2O_5 curve from the data for the standard solutions.
10. Calculate the total V_2O_5 content (V_2O_5 present in sample plus 20.00 μg V_2O_5 added) from the standard curve. Calculate V_2O_5 present in sample.

11. Calculate the vanadium content of the samples as V_2O_3 . The factor for converting V_2O_5 to V_2O_3 is 0.8241.

Discussion

This method is based upon the work of Cooper and Winter (1949) and Wright and Mellon (1937). Although according to Sandell (1959, p. 926) "the acidity of the solution may vary over a fairly wide range," the above procedure is based on the presence of 24 meq of H^+ in the solution before the addition of the phosphoric acid reagent.

Of the elements likely to be found in rutile, only iron is present in concentrations that might interfere. The iron interference is overcome by adding as ferric iron the total iron content of the sample to the standard vanadium solutions used for the preparation of the standard vanadium curve. One microgram of V_2O_5 is approximately equal to 20 μg Fe_2O_3 . A final concentration of 180 ppm of TiO_2 does not form a precipitate. In a 5-mg sample, 10 percent of Nb_2O_5 and 1 percent of ZrO_2 (the highest concentrations tested) do not interfere. One percent of Cr_2O_3 (as Cr^{3+}) and 0.4 percent of Cr_2O_3 (as Cr^{6+}) do not interfere.

The system conforms to Beer's law over the range 0.4–3.6 ppm V_2O_5 , using a 5-cm cell path for pure vanadium solutions and for vanadium solutions containing 100 ppm TiO_2 and 15 ppm Fe_2O_3 . The sensitivity by Sandell's definition (1959, p. 83) is 0.031 μg V/cm^2 at 410 nm. Because a 5-mg sample of rutile will frequently contain less than 20 μg of V_2O_5 (< 0.4 percent V_2O_5) and the system does not conform to Beer's law below 0.4 ppm V_2O_5 , it is best to add to each rutile sample solution at least 20 μg of V_2O_5 .

ANALYSIS OF COMMERCIAL RUTILE CONCENTRATES

Table 2 gives the results obtained using the recommended procedures for the analysis of a commercial rutile and a rutile substitute made available to the author by John W. Stamper, U.S. Bureau of Mines, Arlington, Va. To reduce the sampling error large sample sizes were used. For the determination of 0.1 percent or more of V_2O_3 , a sample size of 3 mg is sufficient. Similarly, a sample size of 25–50 mg can be used with no or slight change in the recommended procedures for the determination of titanium, total iron, niobium, and phosphorus. Typical changes would be (a) the omission of the dilution of the 2.4N H_2SO_4 sample solution for the determination of titanium together with the change in the volume of 10N H_2SO_4 added in step 1 of the procedure for the determination of titanium, (b) the use of less concentrated standard solutions for the preparation of the standard curves, for example, the determination of titanium, and (c) the use of longer cell paths for the determination of the absorbance. Even smaller sizes of sample can be used for the $K_2S_2O_7$ decomposition by changing the technique of the decomposi-

Table 2.—TiO₂, total iron, Nb₂O₅, P₂O₅, and V₂O₃ content of a rutile substitute and a rutile concentrate

Constituent	Weight of sample (milligrams)		Contents (weight percent)	Mean
	Fused	Used		
U.S. Bureau of Mines rutile substitute, No. 1-250-F				
TiO ₂	85.45 107.47	1.72 2.15	92.5 93.1	92.8
FeO	85.45 107.47	4.27 5.37	1.75 1.83	1.79
Nb ₂ O ₅	85.45 107.47	4.27 5.37	2.09 2.12	2.11
P ₂ O ₅	85.45 107.47	.86 1.07	.08 .09	.09
V ₂ O ₃	5.56 6.04	5.56 6.04	.19 .19	.19
Total				97.0
N.S.W. Rutile Mining Co., PTY, Ltd., rutile concentrate, Rm-84				
TiO ₂	86.26 102.55	1.73 2.05	95.6 95.8	95.7
FeO	86.26 102.55	4.31 5.13	.58 .59	.59
Nb ₂ O ₅	86.26 102.55	4.31 5.13	.34 .36	.35
P ₂ O ₅	86.26 102.55	.86 1.03	<.02 <.02	<.02
V ₂ O ₃	6.01 5.33	6.01 5.33	.53 .56	.55
Total				97.2

tion. Using a 3-ml transparent quartz crucible and cover and 100 mg of flux, a sample solution of identical acid and salt concentration can be prepared by dilution of the sample solution to 50 ml instead of 100 ml. The volume of 18N H₂SO₄ added in step 4 of the "sample solution preparation" procedure is changed from 13.3 ml to 6.7 ml. A 30-ml platinum beaker is used in place of the 100-ml beaker.

REFERENCES

- Belcher, R., Ramakrishna, T. V., and West, T. S., 1963, Absorptiometric determination of niobium with 4-(2-pyridylazo)-resorcinol as reagent: *Talanta*, v. 10, p. 1013-1022.
- Budanova, L. M., Nenashva, L. A., and Matrosova, T. V., 1956, Determination of magnesium and iron in titanium and its alloys: *Zavodskaya Lab.*, v. 22, p. 1419-1421. [In Russian]
- Codell, Maurice, 1959, Analytical chemistry of titanium metals and compounds: New York, Interscience Publishers, Inc., 378 p.
- Cooper, M. D., and Winter, P. K., 1949, Vanadium as phosphotungstovanadate: *Anal. Chemistry*, v. 21, p. 605-609.
- Hibbits, J. O., Davis, W. F., and Menke, M. R., 1961, The determination of iron with 1,10-phenanthroline: *Talanta*, v. 8, p. 163-164.
- Langmyhr, F. J., and Hongslo, T., 1960, Separation and gravimetric determination of niobium, tantalum and titanium by precipitation with N-benzoyl-N-phenylhydroxylamine: *Anal. Chim. Acta*, v. 22, p. 301-305.
- Majumdar, A. K., and Mukherjee, A. K., 1958, Separation of niobium and tantalum with N-benzoyl-N-phenylhydroxylamine: *Anal. Chim. Acta*, v. 19, p. 23-26.
- Majumdar, A. K., and Pal, B. K., 1962, Separation of niobium and tantalum with benzo- and phenylacetylhydroxamic acids: *Anal. Chim. Acta*, v. 27, p. 356-358.
- 1963, Gravimetric separation of titanium and zirconium from niobium with phenylacetylhydroxamic acid: *Anal. Chim. Acta*, v. 29, p. 168-171.
- Meyrowitz, Robert, 1971, Chemical analysis of sphene—Spectrophotometric determination of silicon, aluminum, titanium, total iron, and phosphorus, in *Geological Survey Research 1971*: U.S. Geol. Survey Prof. Paper 750-B, p. B165-B170.
- Norwitz, George, and Codell, Maurice, 1954, Colorimetric determination of iron in titanium alloys: *Anal. Chim. Acta*, v. 11, p. 350-358.
- Sandell, E. B., 1959, Colorimetric determination of traces of metals, 3d ed.: New York, Interscience Publishers, Inc., 1,032 p.
- Schilt, A. A., 1969, Analytical applications of 1,10-phenanthroline and related compounds, 1st ed.: Oxford, England, Pergamon Press, 193 p.
- Schoeller, W. R., and Powell, A. R., 1955, The analysis of minerals and ores of the rarer elements, 3d ed.: New York, Hafner Publishing Co., 408 p.
- Wood, D. F., and Jones, J. T., 1968, Spectrophotometric determination of niobium in zirconium, titanium and other metals with 4-(2-pyridylazo)resorcinol: *Analyst (London)*, v. 93, p. 131-141.
- Wright, E. R., and Mellon, M. G., 1937, The phosphotungstate method for vanadium: *Indus. Eng. Chemistry, Anal. Ed.*, v. 9, p. 251-254.



BOULDER TRACKS ON THE MOON AND EARTH

By H. J. MOORE, W. A. VISCHER¹, and G. L. MARTIN²,
Menlo Park, Calif., Corvallis, Oreg., Bozeman, Mont.

Work done on behalf of the National Aeronautics and Space Administration

Abstract.—Tracks produced by bouncing, skidding, and rolling boulders are common on both the Earth and Moon. Most boulders are triaxial and prismatic, some are spheroidal. The tracks are curvilinear arrays of pits, or continuous depressions with locally deep parts. Both these types are indicative of bouncing motion. Bearing capacities of the surface materials are estimated from boulders at the end of tracks shown on vertical photographs. The results are generally reasonable, although individual estimates may be significantly in error. Such errors probably arise from measurement errors and assumptions.

Lunar Orbiter photographs of the Moon reveal numerous tracks produced by boulders that bounced, skidded, or rolled downslope or along nearly level surfaces. Data from these tracks and boulders can be used to estimate the mechanical properties of lunar surface materials, if suitable measurements can be made. A study of terrestrial and lunar boulder tracks was undertaken to explore some problems inherent in this approach. Five tracks and boulders found in the Hebgen Lake area near West Yellowstone, Mont., were investigated during the summer of 1969. The boulders were set in motion during the Hebgen Lake earthquake on August 17, 1959 (U.S. Geological Survey, 1964). Despite their age, the tracks are well preserved. Except at Cabin Creek, where construction has partly destroyed the track, there is no evidence for extensive erosion and infilling. Fresh fragments shed from the boulders are found on the floor of the tracks and are not covered with soil. Rims and aprons seen on vertical photographs taken in 1959 are still visible.

HEBGEN LAKE BOULDER TRACKS

Procedures

Five boulder tracks were investigated in the Hebgen Lake area (fig. 1): two on Kirkwood Ridge, one at Cabin Creek campground, one in Beaver Creek, and one on the Madison Slide. Topographic maps of areas around each boulder were prepared at scales between 1:60 and 1:180 by standard

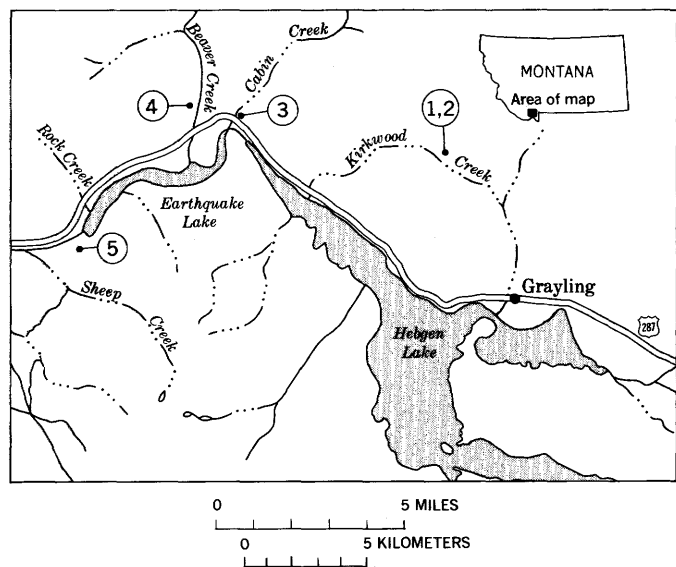


Figure 1.—Index map showing location of boulder tracks in Hebgen Lake area, southwestern Montana. 1, 2, Kirkwood Ridge; 3, Cabin Creek; 4, Beaver Creek; and 5, Madison Slide.

surveying techniques. Soil density was measured in place near the boulders on Kirkwood Ridge. The densities of the boulders were measured from samples of the boulders. Cone penetrometer and shear-vane measurements were made at Cabin Creek. The cone had a diameter of 7.6 cm and an altitude of 14 cm. The shear vane had four blades tapered at each end. Each blade extended 2.54 cm from the axis of a 1.9-cm-diameter rod. The vane lengths were 15.2 cm along the rod and 9.5 cm along their distal edges because of the taper. Grain sizes of samples from Kirkwood Ridge and Cabin Creek were obtained by sieve analyses. Grain sizes were visually estimated at Beaver Creek because of the large amount of coarse material. Fragment counts and measurements along a stretched tape were used for the material of the Madison Slide. Moisture contents of samples collected near the tracks were determined by comparing weights before and after heating.

¹U.S. Forest Service.

²Montana State University.

Lunar boulder tracks were measured on X 7 and X 36 enlargements of Lunar Orbiter photographs (U.S. Natl. Aeronautics and Space Administration, 1969), using data on Lunar Orbiter V (Moyers, 1969) and procedures discussed by Moore (1970).

Description

Although the materials at these five sites have significantly different grain sizes, the tracks are fundamentally the same. Some are curvilinear arrays of discontinuous pits; others, continuous depressions with deeper and wider parts at intervals. Aprons of displaced materials are found on the downslope side of those boulders that rest on slopes. Rims commonly form along the track. Typically, the boulders are irregular in shape. Most are roughly tabular, prismatic, and triaxial, and others are ellipsoidal. Boulder densities are all near 2.7 to 2.9 g/cm³. Large fresh fragments found near the boulder and in pits upslope are evidence that the boulders lost some of their mass while in motion.

Underlying materials—easily deformed colluvium, alluvium, landslide debris, and talus—vary markedly in grain size. The alluvium is a well-graded silty sand with minor amounts of angular fragments ranging from coarse sand to cobble sizes. The colluvium has more fragments than the alluvium. In contrast, talus is composed chiefly of gravel- and cobble-size angular fragments. Table 1 summarizes the data on the Hebgen Lake boulder tracks.

Kirkwood Ridge (1)

One of the tracks on Kirkwood Ridge (fig. 2A) was produced by an ellipsoidal boulder of dense cherty limestone. The track is in colluvium composed chiefly of angular gravel-size fragments set in a matrix of sand and silt. Axes of the boulder, measured with a tape, are 5.2 by 3.3 by 2.1 m. The boulder rests on its side, the long axis pointing downhill and the short axis normal to the slope. The surface of contact is difficult to measure, but it is no more than 8.8 m². Using a density of 2.7 g/cm³ measured on small fragments of the block (a triaxial ellipsoidal boulder) and the estimated contact area, the mass per unit area is calculated as 580 g/cm² and the bearing pressure 0.57×10⁶ dynes/cm² (≈8.4 pounds per square inch).

The colluvium near the track is well-graded gravel. Sieve analyses indicate that 54 percent is composed of angular to subangular fragments with diameters between 2.54 and 0.95 cm, 14 percent has diameters between 0.95 and 0.07 cm, and 32 percent is less than 0.074 cm. Materials finer than 0.42 cm have a plastic index near 4. In-place measurements with a Soiltest Volumeasure indicate a density of 1.2 g/cm³ (75 pounds per cubic foot). The vegetation—small flowers, woody plants, and scattered trees—is rather sparse, but the colluvium contains some root fibers.

The boulder probably originated from outcrops of the Mississippian Madison Limestone at elevations near 2,900 to

Table 1.—Data on Hebgen Lake, Mont., boulder tracks

[N.d., not determined]

Designation and location	Boulder				Soil			Type of material	Type of track	Motion
	Density (g/cm ³)	Estimated volume (10 ⁶ cm ³)	Estimated bearing area (10 ⁴ cm ²)	Load-bearing pressure (10 ⁶ dynes/cm ²)	Density (g/cm ³)	Moisture (percent)	Classification ¹			
1. Kirkwood Ridge, NW¼ sec. 22, T. 11 S., R. 4 E., Tepee Creek quadrangle.	2.7	19	8.8	0.57	1.2	11.5	Gravel, sand, silt (GM).	Colluvium.	Down-slope.	Walked.
2. Do.	2.7	4.0–2.0	2.5	.42–.21	1.2	11.5	do	do	Cross-slope. Partly flat.	Bounced.
3. Cabin Creek, SE¼ sec. 15, T. 11 S., R. 3 E., Hebgen Dam quadrangle.	2.75	8.6–4.5	4.8	.49–.26	1.2	11.5	Silty sand (ML).	Alluvium.	Partly flat.	Do.
4. Beaver Creek, SW¼ sec. 16, T. 11 S., R. 3 E., Hebgen Dam quadrangle.	2.7	13	3.0	1.2	N.d.	N.d.	Gravel, sand, silt (GM).	Talus.	Down-slope.	Do.
5. Madison Slide, NE¼ sec. 1, T. 12 S., R. 2 E., Hebgen Dam quadrangle.	2.72	4.4	2.2	.53	≈1.9	Dry	Well-graded gravel (GW).	Landslide debris.	do	Bounced and rolled.

¹ Letters in parentheses are soil designations from The Unified Soil Classification System (U.S. Army, 1953, table 1).

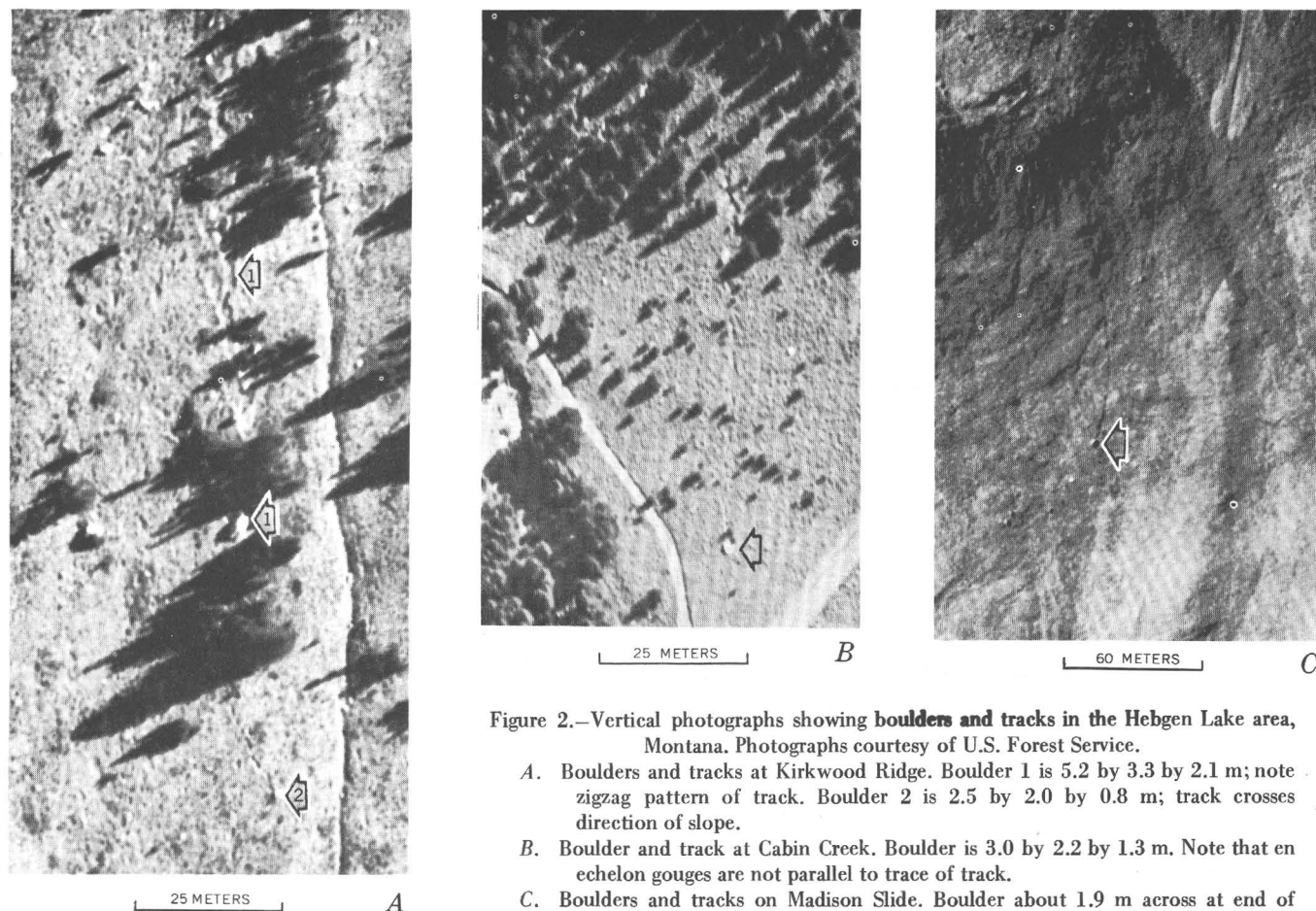


Figure 2.—Vertical photographs showing **boulders and tracks in the Hebgen Lake area, Montana**. Photographs courtesy of U.S. Forest Service.

- A. Boulders and tracks at Kirkwood Ridge. Boulder 1 is 5.2 by 3.3 by 2.1 m; note zigzag pattern of track. Boulder 2 is 2.5 by 2.0 by 0.8 m; track crosses direction of slope.
- B. Boulder and track at Cabin Creek. Boulder is 3.0 by 2.2 by 1.3 m. Note that echelon gouges are not parallel to trace of track.
- C. Boulders and tracks on Madison Slide. Boulder about 1.9 m across at end of 75-m track is indicated with an arrow. This is the track mentioned in the text. A second track can be seen from the U.S. Forest Service viewing station near Earthquake Lake.

3,000 m. It traveled down a uniform slope of 26° to 27° and came to rest at an elevation near 2,650 m. The track indicates that the motion was complicated. About 61 m of the track nearest the boulder was mapped in detail. In the uppermost 30 m, the deepest parts alternate from side to side, forming a zigzag track; in the lower 30 m, the deep parts are aligned along the center of the track. The boulder thus appears to have “walked” and bounced downslope. It now rests in a depression about 0.3 to 0.6 m deep, 8.5 m long, and 3.7 m wide. An apron of displaced colluvium on the downslope side of the depression extends about 4 m horizontally, or 4.5 m measured along the slope from the base of the boulder, and is about 6 m across. Lateral displacement along the track is also indicated by rims along the sides of the track (see figure 2A).

Track depressions upslope from the boulder contain very angular unweathered fragments of limestone 0.3 m and more in diameter. These fragments differ from those in the colluvium because of their sharp edges and unweathered appearance. Additionally, a large piece of limestone is found next to the main boulder and had separated from it. Thus, the

boulder is clearly smaller than when it started to move downslope.

Kirkwood Ridge (2)

The other track on Kirkwood Ridge (fig. 2A) was produced by a rectangular, tabular boulder of dense cherty limestone. It differs from the first in three ways: (1) the trace of the track indicates that the boulder moved across slope at an angle of 30° to 50° to the direction of maximum slope, (2) the boulder is tabular, and (3) the section of track nearest the boulder is a series of individual depressions as wide as or wider than the minimum dimension of the block.

The boulder rests on its side, the long axis aligned with the direction of slope, the intermediate axis parallel to the contours, and the short axis roughly normal to the surface. The surface of contact of the boulder is estimated to be about 2.5 m². Averages of tape measurements of the three dimensions are 2.5, 2.0, and 0.8 m. If the block were a rectangle, the volume of the boulder would be 4.0 m³, and the bearing pressure calculated from this would be about 0.42×10^6

dynes/cm². If ellipsoidal, the volume would be 2.0 m³, and the bearing pressure 0.21×10⁶ dynes/cm².

The boulder now rests at the lower end of an elongate depression about 4 m long, 1.5 m wide, and 0.2 to 0.5 m deep. The long axis of the depression is 50° to the direction of slope. Again, an apron of displaced colluvium is found on the downslope side of the boulder. The plane of bilateral symmetry of the apron is parallel to the direction of slope, not to the long axis of the depression.

In contrast with the other track, the depressions of this one are individual pits along that part of the track within 30.5 m of the boulder. Some pits are comparable in width and length to the minimum block dimension. The widths of others are comparable to the minimum block dimension, whereas the lengths are comparable to the longer dimension; and some pits are as wide as the maximum block dimensions and are longer. Judging from the track, the boulder bounced and rolled downslope, making contact with its various edges and corners until it came to rest.

Cabin Creek

The Cabin Creek track (fig. 2B) was produced by a boulder of dense cherty limestone partly in colluvium on steep slopes and partly in alluvium on flat ground. The boulder probably originated from outcrops on a ridge to the northeast at elevations between 2,200 and 2,450 m. Well-preserved tracks are found on the slopes, but the track on the flat has been partly destroyed by construction of a parking lot and restroom facilities at Cabin Creek campground.

Part of the boulder is an irregular solid bounded by six more or less planar surfaces. The average dimensions measured with a tape are about 3.0, 2.2, and 1.3 m. The volume of a rectangular solid with these dimensions is 8.6 m³; the volume of an ellipsoid, 4.5 m³. Using the estimated bearing surface of 4.8 m², which was obtained by tape measure, bearing pressures of near 0.49×10⁶ and 0.26×10⁶ dynes/cm² are calculated.

The alluvium is similar to the colluvium but contains less coarse debris, and the fragments are better rounded. Sieve analysis shows that 96 percent of the alluvium is finer than 4.76 cm, 82 percent finer than 0.42 cm, and 43 percent finer than 0.074 cm. Shear vane and penetrometer readings are tabulated below.

<i>Shear vane</i>		<i>Measured values</i>		
Depth	cm ..	18	18	18
Vane shear strength	10 ⁶ dynes/cm ² ..	.48	.57	.85
Do.	pounds per sq inch ..	7.1	8.4	12.5
<i>Penetrometer</i>				
Depth	cm ..	13	28	44
Penetration resistance	10 ⁶ dynes/cm ² ..	2.6	7.9	12.9
Do.	pounds per sq inch ..	38	116	189

Mapping indicates that a boulder bounced and rolled down the steep slopes until it hit a tree and broke. Part of the boulder, measuring 1.8 by 1.4 by 0.76 m, came to rest near the base of the slope; a larger part, measuring 3.0 by 2.2 by 1.3 m, bounced on down the slope and across the flat some 91 m. Aerial photographs of the 91 m of track on the flat, taken shortly after the earthquake, show various patterns. Near the boulder the track is fairly continuous. About one-third of the track is made of seven or eight en echelon gouges. The trace of the whole track across the flat does not coincide with the elongation of the depressions. Thus the track records a complex motion.

In contrast with the other boulder tracks, no evidence was found for an apron of displaced material around the boulder on the flat.

Beaver Creek

One of the numerous boulder tracks in the Beaver Creek area was mapped. The tracks were produced in talus composed chiefly of rock fragments 1.3 to 30 cm in diameter with a matrix of silty soil. Visual estimates indicate 10 to 25 percent of the talus is sand and silt. The fragments are schist, gneiss, and amphibolite. No soil tests were made because of the large amount of very coarse fragments. Slopes at the boulder and for a distance of 76 m uphill are near 1:3 (≈18.5°); they are generally steeper than this at higher elevations.

The rectangular boulder that produced the track measured 3.0 by 2.2 by 2.0 m, its volume was near 13 m³, and the bearing surface was 3 m². Since the density of the boulder was about 2.7 g/cm³, the bearing pressure is near 1.2×10⁶ dynes/cm². About 20 m of the track nearest the boulder was mapped in detail. The track is a series of depressions, so the boulder appears to have bounced most of the way downslope. The last part of the track is an elongate trough 6 m long 2.4 m wide with an irregular bottom. Here, the boulder bounced less and began to roll before it came to rest. An apron of displaced talus occurs on the downslope side of the boulder.

Madison Slide

One track was mapped on the Madison Slide, near the outlet of Earthquake Lake (fig. 2C). This track is in very coarse angular debris composed of schist, amphibolite, and gneiss. No soil tests were made because the material was so coarse grained. Fragment sizes were measured along a stretched tape; all the fragments intersecting the tape were 49 cm and less across, 72 percent were less than 12 cm across, 46 percent less than 5.8 cm, 16 percent less than 2.8 cm, and 0.4 percent were less than 1.4 cm across; fine materials were virtually absent. The material was cohesionless, and maximum local slopes uphill of the track were near 41°, whereas those near the boulder were 33°.

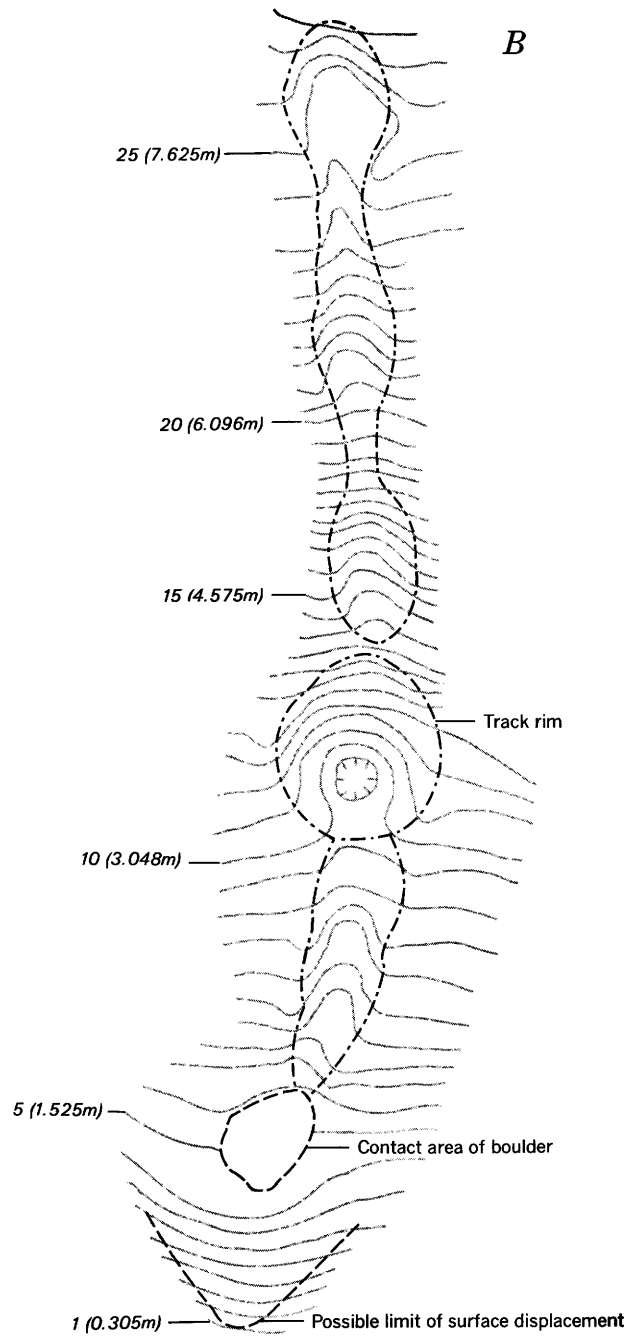
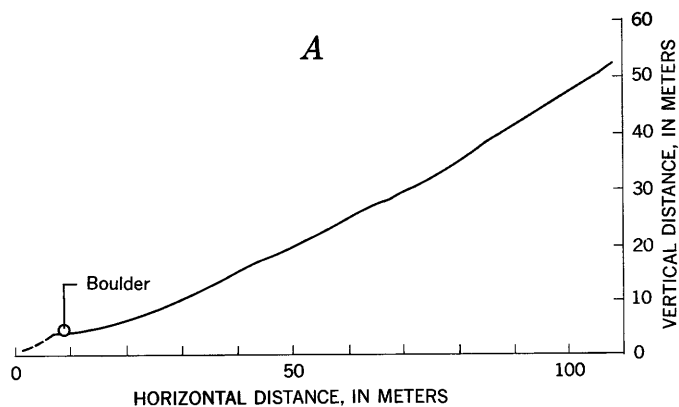


Figure 3.—Diagrams of boulder track on the Madison Slide, Mont.

A. Profile along track of boulder in figure 2C.

B. Contour map showing contact area of boulder in figure 2C, 20 m (66 feet) of track nearest boulder, and displaced debris downslope from boulder. Contour interval is 0.5 foot (≈15 cm).

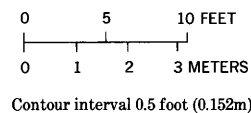
The roughly ellipsoidal boulder that produced this track measured 1.86 by 1.89 by 2.34 m,¹ the volume was near 4.4 m³, and the bearing surface was slightly less than 2.2 m². The indicated bearing pressure is 0.53×10⁶ dynes/cm². Hence, as on other slopes, the boulder came to rest in a rimmed depression made by displacement of material to form an apron on the downslope side of the boulder. This apron, which can be recognized by its morphology, extends about 2.7 to 3.0 m along the downslope direction.

The arcuate track produced by this boulder is clearly recognizable for about 85 to 90 m along the track, and suggestive evidence of a track is found for another 40 m or so. The boulder originated at an elevation at least 80 m higher than its present location. The uppermost slopes along the path of the boulder are near 41°, and average slopes decrease to about 11° just above the boulder and steepen to about 20° just below it (fig. 3A). In detail, however, slopes are variable, and within the track they are locally near 30°. Inspection of aerial photographs taken by the U.S. Forest Service shortly after the earthquake (fig. 2C) and detailed mapping of the track (fig. 3B) clearly indicate that the boulder bounced and probably rolled downslope, producing a rimmed track.

General features of terrestrial tracks

In summary, these studies of terrestrial boulder tracks show that (1) tracks are produced in easily deformed materials, (2) boulders are usually irregular in shape and rarely equidimensional, (3) when boulders come to rest, their smallest dimensions are approximately normal to the ground surface, (4) grain size distribution of the deformed material varies

¹These numbers are more accurate than those reported previously (Moore, 1971).



considerably, (5) boulders bounce, roll, skid, and “walk,” but bouncing is commonest, (6) aprons of displaced material are found on the downslope side of the boulders, and (7) tracks usually have low rims.

LUNAR BOULDER TRACKS

Over 300 boulder tracks have been studied on photographs of the Moon (Grolier and others, 1968). Lunar tracks are strikingly similar to terrestrial tracks. Most of the lunar boulders bounced downhill; others skidded, "walked," or rolled. Interpretations of the tracks suggest that surface materials are easily deformed. The lunar boulders and tracks studied are generally larger than the Montana examples because the resolution of Lunar Orbiter high-resolution photographs is near 2 to 5 m (U.S. Natl. Aeronautics and Space Administration, 1969).

Examples of lunar boulder tracks are shown in figures 4 and 5. Figure 4A shows a very large angular boulder on the wall of a small crater within the crater Petavius. The boulder, which measures 68 by 81 m, is at the downslope end of a rimmed track measuring 50 by 137 m. Shadows in the crater indicate that the slope of the crater wall exceeds 20° . The boulder probably slid or skidded because the track is short and continuous, with fairly straight rims.

Two tracks produced by boulders bouncing down the walls of Schröter's Valley are shown in figure 4B. The boulder to the left bounced downslope and onto a flat. It measures about 16 by 16 m, and its shadow, which is cast on a fairly level surface, indicates that it is 9 m tall. The segment of track nearest the boulder is 7 by 21 m and 0.7 m deep. The pits along the track increase in both width and depth from the block toward the base of the slope, where the pits are as large as 11 by 16 by 1.5 m. Pits further upslope are as large as 16 by 24 m and more than 2 m deep. Individual pits are rimmed, suggesting failure by general shear. Little can be said about the grain size of the deformed material because the resolution of the photograph is 2 m. The presence of large blocks on the walls of Schröter's Valley suggests that the mean grain size could be quite large, however.

Inspection of the boulder's image and track suggests that the boulder is prismatic and resting on an edge. If this is so and the angles between boulder faces are 64° and 116° , its dimensions are near 9.4 by 9.4 by 16 m on an edge, and the volume would be $1,338 \text{ m}^3$. An ellipsoidal boulder 9 by 16 by 16 m has a volume of $1,206 \text{ m}^3$. Thus, the mass of the boulder for the shapes assumed is near $3,600$ to $4,000 \times 10^6 \text{ g}$, if the density is 3.0 g/cm^3 . For a bearing surface of 16 by 7 m and an acceleration of gravity of 163 cm/sec^2 , the bearing pressure is 0.58×10^6 to $0.52 \times 10^6 \text{ dynes/cm}^2$. Such a low value for bearing pressure indicates that the surface is easily deformed. For example, material with a cohesion of 10^6 dynes/cm^2 and a friction angle of 45° would not fail and produce a 7-m wide, 0.66-m deep track if subjected to this bearing pressure.

A track similar to the Kirkwood Ridge (1) track, but larger, is shown in figure 4D. The boulder is about 19 by 35 m, and the track is over 540 m long. The pits of the track alternate from side to side, forming a continuous zigzag line. Such a track suggests that the oblong boulder "walked" downslope.

Some tracks are found on fairly level surfaces and are in no way associated with slopes sufficiently steep to permit the inference that they bounced downslope. Two such tracks, about 100 m long, are shown in figure 4C. The tracks and boulders are about 2.7 km from the rim of Censorinus, a fresh crater about 3.8 km across. Apparently the blocks were ejected from Censorinus, and after impact they bounced and rolled on a fairly level surface, producing tracks with rims and pits. Here, a problem in interpretation arises. Both tracks have large craters at the end of the track farthest from the boulders. One crater appears deep and fresh, the other shallow and subdued. Were they produced by the two boulders? If so, the right-hand crater has been filled in. Alternatively, the left-hand block and crater may have formed after the right-hand ones. Or, the left-hand crater could be a primary impact crater formed after the track. In any event, examination of other such tracks near Censorinus suggests that many of these tracks have been partly filled.

The left-hand boulder of figure 4C measures about 3.2 by 4.7 m and, judging from the shadow, is 5.8 m tall. For an ellipsoidal boulder, with a density of 3.0 g/cm^3 , the mass is about $140 \times 10^6 \text{ g}$. The bearing area is about 12 m^2 , and the bearing pressure $0.26 \times 10^6 \text{ dynes/cm}^2$. Similarly, for the right-hand boulder, which measures about 4.7 by 5.8 m and is 4.8 m tall, and rests on a bearing area less than 22 m^2 , the minimum bearing pressure is about $0.16 \times 10^6 \text{ dynes/cm}^2$. Thus, the surface material is easily deformed.

Large boulders at the end of tracks have been found on the floor of the crater Copernicus, and several such tracks are shown in figure 4E. The angular boulder in the lower part of figure 4E lies on a fairly level surface some 240 m from the base of the slope that it bounced down. It is about 47 by 54 m and 25 m tall. The segment of the track nearest the boulder is about 20 by 52 m and, judging from the shadow in it, about 2 m deep. Although the shape is irregular, the mass is probably near $102,000 \times 10^6 \text{ g}$, and the bearing area near 890 m^2 or less. The bearing pressure is thus $1.9 \times 10^6 \text{ dynes/cm}^2$ or more.

Most boulders seen on Lunar Orbiter photographs are not spheres but are prismatic and triaxial. Figure 4F shows such boulders at the base of a slope in Hyginus Rille. The two largest are clearly regular prisms, about 20 by 22 m and 10 m tall. Close inspection of the 8-m boulders at the end of the tracks shows that they are not spheres, and their shadows indicate heights of less than 5 m. Small boulders about 2 to 4 m across approach the limit of resolution, and their shapes are indeterminate.

Some lunar boulder tracks pose problems in interpretation. For example, a cursory examination of figure 5A suggests that one boulder, 11 by 21 by 11 m, "walked" downslope, producing a track with pits that alternate from side to side. However, closer study shows that most of the pits on the right side of the track are superposed on pits on the left side, and that there are, in fact, two separate tracks. The second boulder is apparently resting on its side, adjacent to the boulder casting the shadow. This second boulder casts no shadow and is

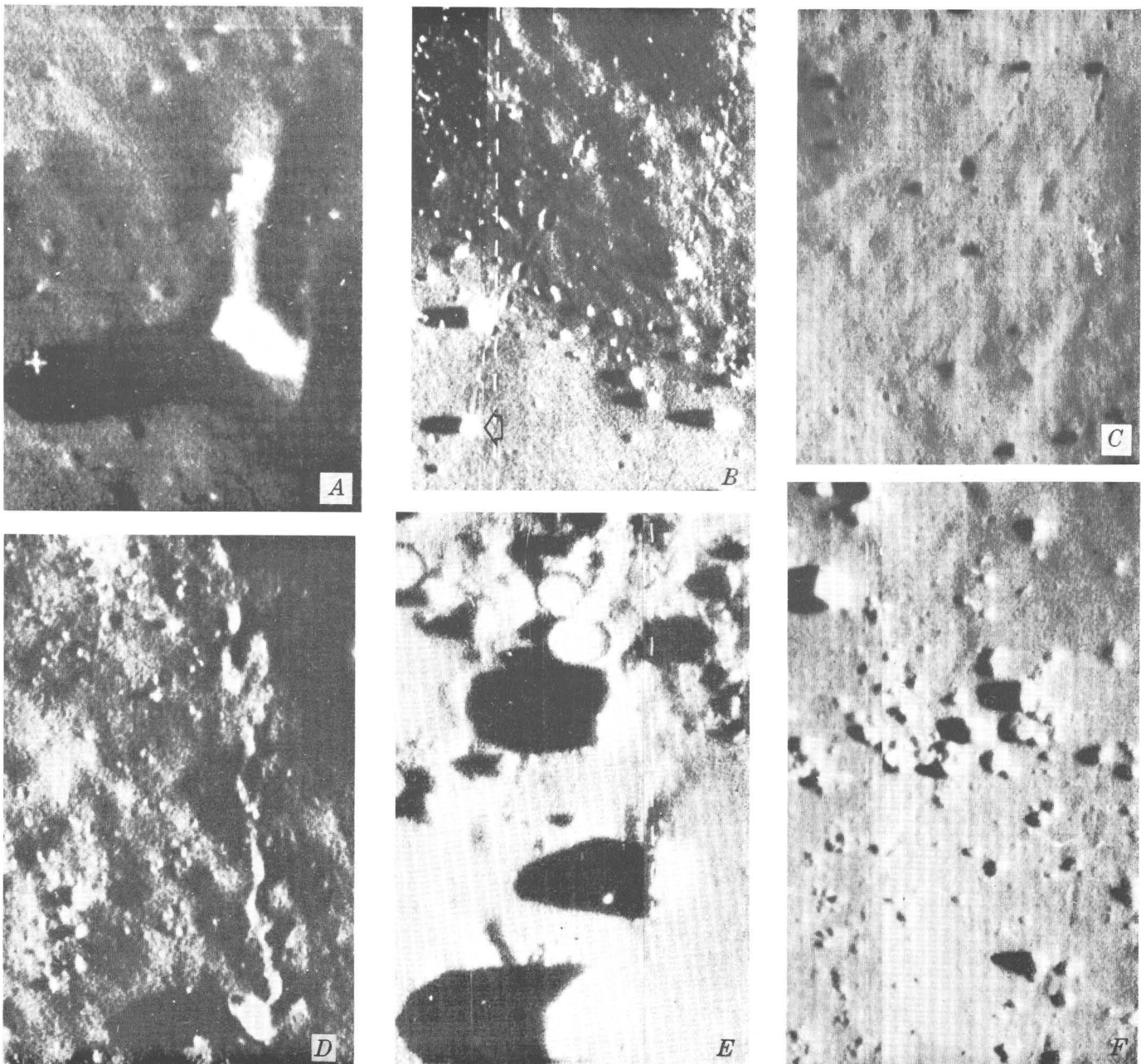


Figure 4.—Lunar Orbiter V photographs of boulder tracks, showing types of tracks. Sun is to right.

- A. Track produced by skidding boulder in the crater Petavius. Boulder is about 68 by 81 m; track is 50 by 137 m. Note angularity of boulder. Frame H-36, framelet 144, 24.8° S., 59.8° E.
- B. Tracks produced by bouncing boulders in Schröter's Valley on slope and flat. Boulder on flat indicated by white arrow is about 16 by 16 m and 9 m tall; track nearest boulder is 7 by 21 m and 0.7 m deep; pits upslope (not shown) are as large as 16 by 24 m and more than 2 m deep; track visible more than 600 m upslope. Boulder is prismatic. Frame H-204, framelets 221–222, 49.8° W., 25.6° N.
- C. Tracks produced by boulders ejected from the crater Censorinus. Larger boulder (right) is 4.7 by 5.8 m and 4.8 m tall; other is 3.2 by 4.7 m and 5.8 m tall; tracks are about 100 m long. Boulders are about 2.7 km from rim of Censorinus. Frame H-63, framelet 738, 0.4° S., 32.8° E.
- D. Track produced by "walking" boulder in Schröter's Valley. Boulder is 19 by 35 m; length of track shown is near 540 m. Note zigzag pattern of track and angularity of boulder. Frame H-204, framelet 223, 49.8° W., 25.6° N.
- E. Tracks produced by large boulders on floor of the crater Copernicus. Largest boulder is 47 by 54 m and 25 m tall; part of track nearest boulder is 20 by 52 m and 2.0 m deep. Note angularity of boulder. Frame H-151, framelet 326, 9.5° S., 19.8° W.
- F. Boulders and tracks in Hyginus Rille. Note shapes of boulders. Largest two boulders near the top are about 20 by 22 m and 10 m tall; they are clearly regular prisms. In contrast, shapes of smallest boulders 2 to 4 m across are indeterminate. Two boulders at end of tracks in lower right are 7.5 and 8.8 m across. Smaller one is angular; larger one is not a sphere since its shadow indicates it is 4.7 m tall. Frame H-97, framelet 181, 5.8° E., 8.3° N.

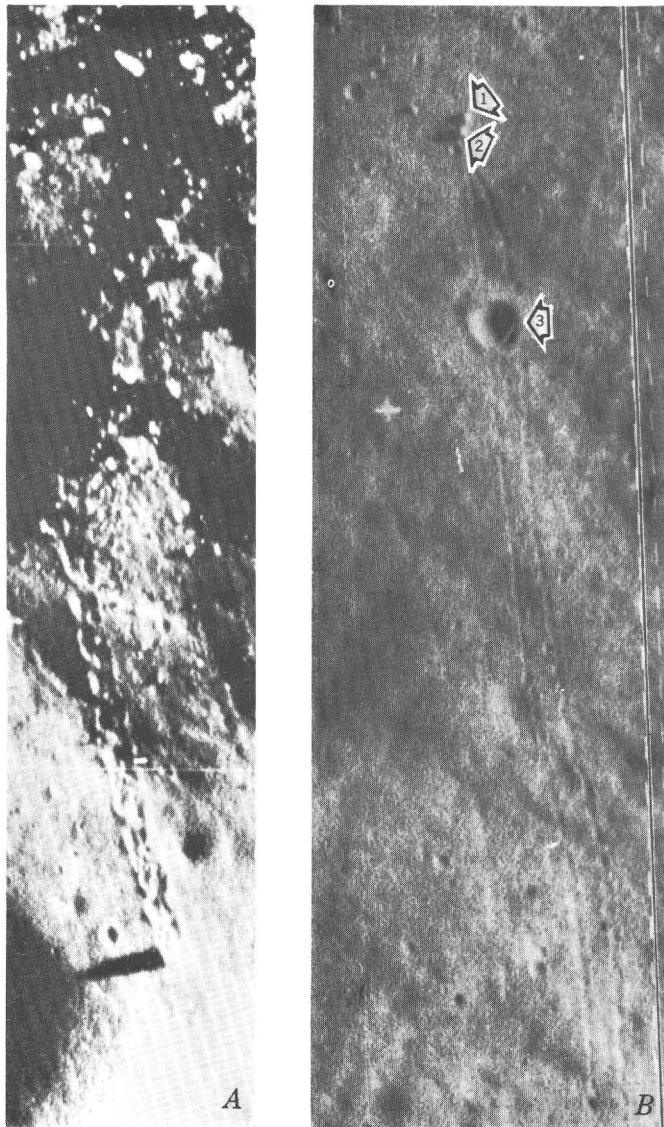


Figure 5.—Lunar Orbiter V photographs of boulder tracks, showing interpretation problem and alteration of tracks with time. Sun is to right.

- A. Tracks produced by two boulders in the crater Vitello. One measures 11 by 21 m and, judging from its shadow, is 11 m tall. Second boulder shows as bright spot to right of first boulder. Frame H-168, framelet 519, 30.4° S., 38.5° W.
- B. Boulder tracks and crater near the crater Gassendi. Boulders are nearly 4.5 m across, crater is nearly 30 m across. One boulder (1) bounced and rolled downslope; then a second boulder (2) bounced and rolled across track of first boulder. Impact crater (3) formed after both tracks and filled them with ejecta. Pits of track to far left of the paired tracks are apparently filled more on upslope part (bottom of photograph) than on downslope part (top of photograph). Erosion and filling by impact may be more subtle than examples here. Photogrammetry (Raymond Jordan, unpub. data) indicates average slope along track is near 20° . Frame H-179, framelet 972, 16.1° S., 39.7° W.

represented by a rectangular bright spot to the right of the first boulder.

The appearance of lunar boulder tracks changes with time, and tracks may be obliterated by meteor bombardment (see, for example, Moore, 1971) and creep. Figure 5B illustrates this. Boulder 1 first bounced downslope. Later, boulder 2 crossed the track of No. 1 and stopped adjacent to it. After both tracks had formed, a crater (3) formed, excavating and filling parts of both tracks. A third large track to the left of the paired tracks becomes progressively subdued upslope (toward bottom of figure 5B), perhaps because of soil creep. Thus, boulder tracks change with time, and their absence does not necessarily indicate a hard undersurface. Additionally, the changes may be much more subtle than in these examples.

Examination of lunar boulders and tracks shows that (1) they are produced in easily deformed material, (2) boulders are usually irregular in shape and rarely equidimensional, (3) smallest dimensions of the boulders are approximately normal to the local surface, (4) grain size distribution of the surface material may vary considerably, (5) boulders bounce, skid, "walk," and roll but in general bounce, (6) most tracks have rims, and (7) tracks change with time.

ESTIMATES OF STATIC BEARING CAPACITY

Earth

The terrestrial boulder tracks illustrate the problem of using static analysis to estimate bearing capacity. For example, the bearing pressure of the boulder on the Madison Slide is estimated as 0.53×10^6 dynes/cm². The static bearing capacity of a soil may be computed using Terzaghi's equation (1948, p. 125):

$$B = 1.3 CN_c + \rho g D_f N_g + 0.6 \rho g R N_\gamma, \quad (1)$$

where

B = bearing capacity

C = cohesion

ρ = soil density

g = acceleration of gravity

D_f = footing depth

R = footing radius

N_c , N_g , N_γ are dimensionless numbers and a function of the angle of internal friction and local slope (Meyerhof, 1951).

If the material of the slide is considered cohesionless, the depth of footing taken as zero, the angle of internal friction 40° , and the local slope 20° , then equation 1 yields 3.3×10^6 dynes/cm². If the angle of internal friction is changed to 30° , equation 1 yields 0.66×10^6 dynes/cm². Thus, the estimated bearing pressure (0.53×10^6 dynes/cm²) is less than the expected bearing capacity. The limit of deformation might also be used to estimate friction angle. For a logarithmic spiral

failure surface, a friction angle of 30° , and computing for the angle $\pi - \frac{\pi}{6} - \frac{\pi}{9}$, the intersection of the failure surface with the slope surface should be 3.4 m, as compared with 2.7–3.0 m measured along the slope. The use of a 40° friction angle yields 6.1 m. Thus, both analyses above are fairly consistent with a friction angle slightly less than 30° and inconsistent with a 40° angle of repose measured high on the slope. Maximum local slopes along the track near the boulder are near 33° , however.

It is entirely possible that the load was larger and that the limit of displacement cannot be accurately determined. Indeed, the change in potential energy of the boulder from the first circular pit upslope to its final position is near 2×10^{12} ergs, and the block velocity at impact may have been as large as 5.0 m/sec. Apparent dynamic strength (Moore, 1970) taken as $\frac{1}{2} \frac{m}{A} \frac{V^2}{P}$ would be near 2×10^6 dynes/cm², where m is the boulder mass, A contact area, V velocity, and P penetration (taken as 30 cm). Thus, static analyses of boulder tracks should be viewed with caution. Additionally, they probably represent lower bound estimates for bearing capacity.

Measurements using the aerial photograph (fig. 2C) yield a boulder diameter near 2.3 m and a track width near the boulder of 1.9 m. For a spherical boulder with a density 2.7 g/cm³ and a circular bearing surface with a radius of 1.45 m the bearing pressure would be 0.62×10^6 dynes/cm². Although this agrees with the estimate on the ground (0.53×10^6 dynes/cm²), one wonders why, because the boulder and the bearing area are, in fact, smaller than measured on the photograph.

Moon

The principal problems in using lunar boulder tracks to estimate bearing capacity are in measuring boulder and bearing-surface dimensions and estimating boulder density. Measurement problems can be illustrated using the boulder track in Sabine D (Filice, 1967; Eggleston and others, 1968; Hovland and Mitchell, 1970; Moore, 1970). The measurements reported for this spheroidal boulder are listed in table 2.

The various observers use different assumptions in calculating the area: Filice uses a semicircular footing, Eggleston a

spherical segment, Mitchell a semicircle, and Moore a circle. Filice's load for a circular area is 2.0×10^6 dynes/cm², Eggleston's for a semicircular area is 1.9×10^6 dynes/cm². Hovland and Mitchell's for a circular footing is 0.47×10^6 dynes/cm², and Moore's for a semicircular footing is 1.3×10^6 dynes/cm². Thus, assumptions and measurements can easily produce bearing-pressure errors of nearly a factor of 5 to 9.

Such measurement and assumption errors could account for variations in estimates of friction angles for lunar soils. For example, Hovland and Mitchell (1970) assume spherical boulders with a density near 2.7 g/cm³, a lunar soil density near 1.6 g/cm³, a lunar soil cohesion of 10^3 dynes/cm², and a rectangular strip footing with an area equal to that of a semicircle which is determined from the geometry of boulder diameter and track width. For 69 lunar tracks, the average friction angle is near 33° to 34° , and the standard deviation is about 6.6° . Their average results compare well with Surveyor data (Choate and others, 1969a, p. 117; 1969b, p. 168; Scott and Roberson, 1969, p. 178). The standard deviation represents a sizable difference in bearing pressure, however. Consider a level circular bearing surface 5 m across with an area of 19.6 m² resting at a depth of 50 cm in a lunar soil with a density of 1.6 g/cm³ and a cohesion of 10^3 dynes/cm². Terzaghi's (1948) bearing capacity equation (using an acceleration of gravity of 163 cm/sec²) yields bearing capacities near 1.8×10^6 , 4.4×10^6 , and 0.57×10^6 dynes/cm² for friction angles of 33° , 39.6° , and 26.4° respectively. Thus, the ratio of bearing capacities for (+) 1σ and (-) 1σ is about 7.7. This is not surprising, in view of possible errors in measurement and assumptions. It should also be noted that most lunar boulders are not spheres. Judging from a sample of 150 blocks shown on Lunar Orbiter photographs, they are, on the average, between 0.5 and 0.6 as tall as they are wide.

Attempts to use secondary impact craters to estimate mechanical properties of the lunar surface also yield figures with sizable scatter (Moore, 1970). For the secondary impact craters, the ratio of coefficients of the Clark-McCarty penetration equation (Clark and McCarty, 1963) computed for the lunar secondary impact craters and their blocks at (+) 1σ and (-) 1σ was near 2.25. A similar conclusion is obtained when considering results from dynamic analyses of lunar boulder tracks (Hovland, 1971). For these dynamic analyses, the average angle of internal friction is near 36.8° , and values near 28.5° and 45.0° are obtained at (-) 1σ and (+) 1σ , respectively.

Table 2.—Measurement data for the boulder track in Sabine D on the Moon

Observer	Block density (g/cm ³)	Block dimension (meters)	Block volume (cubic meters)	Track width (meters)	Area assumed (square meters)	Bearing pressure (10 ⁶ dynes/cm ²)	Slope (degrees)
Felice (1967)	3.0	13 by 13 by 13	1,150	6.0	14.1	4.0	...
Eggleston and others (1968) . . .	3.0	9 by 9 by 9	382	5.0	21.2	.88	13
Hovland and Mitchell (1970)	2.7	8.7 by 8.7 by 8.7	345	6.4	16.1	.95	13
Moore (1970)	2.7	8.5 by 8.5 by 7.7	291	5.0	19.5	.65	² 16–19

¹ Assumed for calculation.

² Unpublished data supplied by Raymond Jordan, U.S. Geol. Survey.

SUMMARY

Tracks produced in easily deformed materials by boulders bouncing down slopes are common on both the Earth and Moon. Boulders generally bounce, but they may also "walk," skid, and roll. Most are triaxial and prismatic, some are ellipsoidal. When they come to rest, the minor axis is normally at a high angle to the local surface.

Bearing pressures estimated from block and track dimensions measured on vertical photographs may be significantly in error. Block dimensions are often difficult to measure accurately, and bearing surfaces are never visible. Additionally, block and soil densities must be estimated and may be in error. Studies of lunar boulder tracks generally yield reasonable values of angles of internal friction for the lunar regolith, but isolated determinations can be significantly in error.

REFERENCES

- Choate, Raoul, Batterson, S. A., Christensen, E. M., Hutton, R. E., Jaffe, L. D., Jones, R. H., Ko, H. Y., Spencer, R. L., and Sperling, F. B., 1969a, Lunar surface mechanical properties, in *Surveyor VII, a preliminary report*: U.S. Natl. Aeronautics and Space Adm. Spec. Pub. SP-173, p. 83-119.
- Choate, Raoul, Batterson, S. A., Christensen, E. M., Hutton, R. E., Jaffe, L. D., Jones, R. H., Ko, H. Y., Scott, R. F., Spencer, R. L., Sperling, F. B., and Sutton, G. H., 1969b, Lunar surface mechanical properties, in *Surveyor program results*: U.S. Natl. Aeronautics and Space Adm. Spec. Pub. SP-184, p. 129-169.
- Clark, L. V., and McCarty, J. L., 1963, The effect of vacuum on the penetration characteristics of projectiles into fine particles: U.S. Natl. Aeronautics and Space Adm. Tech. Note D-1519, 26 p.
- Eggleston, J. M., Patterson, A. W., Throop, J. E., Arant, W. H., and Spooner, D. L., 1968, Lunar "rolling stones": *Photogramm. Eng.*, v. 34, p. 246-255.
- Filice, A. L., 1967, Lunar surface strength estimate from Orbiter II photograph: *Science*, v. 156, no. 3781, p. 1486-1487.
- Grolier, M. J., Moore, H. J., and Martin, G. L., 1968, Lunar block tracks, in *A preliminary geologic evaluation of areas photographed by Lunar Orbiter V including an Apollo landing analysis of one of the areas*: U.S. Natl. Aeronautics and Space Adm., Langley Research Center, Langley Working Paper LWP 506, p. 143-154.
- Hovland, H. J., 1971, *Mechanics of rolling sphere-soil slope interaction*: California Univ., Berkeley, Ph. D. thesis, 230 p. [Available from University Microfilms, Ann Arbor, Mich.]
- Hovland, H. J., and Mitchell, J. K., 1970, Soil property evaluations from boulder tracks on the lunar surface, in *Lunar surface engineering properties experiment definition, final report-v. 2 of Lunar soil properties from photographic records*: California Univ., Space Sci. Lab. Ser. 11, issue 11, p. 1-1-1-64.
- Meyerhof, G. G., 1951, The ultimate bearing capacity of foundations: *Geotechnique*, v. 2, no. 4, p. 301-332.
- Moore, H. J., 1970, Estimates of the mechanical properties of lunar surface using tracks and secondary impact craters produced by blocks and boulders: U.S. Geol. Survey open-file report, 65 p.
- 1971, Geologic interpretation of lunar data: *Earth Sci. Rev.*, v. 7, no. 1, p. 5-33.
- Moyers, W. G., 1969, Lunar Orbiter improved photo support data: Seattle, Wash., Boeing Co., Doc. D2-100815-5, 1,364 p. (NASA CR-66735-5).
- Scott, R. F., and Roberson, F. I., 1969, Soil mechanics surface sampler, in *Surveyor VII, a preliminary report*: U.S. Natl. Aeronautics and Space Adm. Spec. Pub. SP-184, p. 171-179.
- Terzaghi, Karl, 1948, *Theoretical soil mechanics*: New York, John Wiley and Sons, 509 p.
- U.S. Army, 1953, The unified soil classification system: U.S. Army Corps Engineers, Waterways Expt. Sta. Tech. Memo. 3-357, v. 1, 3 p.
- U.S. Geological Survey, 1964, The Hebgen Lake, Montana, earthquake of August 17, 1959: U.S. Geol. Survey Prof. Paper 435, 241 p.
- U.S. National Aeronautics and Space Administration, 1969, Lunar Orbiter photographic data: Greenbelt, Md., Goddard Space Flight Center, U.S. Natl. Space Sci. Data Center Users' Note NSSDC 69-05, 37 p.



LONG-WAVELENGTH RADAR IMAGES OF NORTHERN ARIZONA—A GEOLOGIC EVALUATION

By GERALD G. SCHABER and WALTER E. BROWN, JR.,¹
Flagstaff, Ariz., Pasadena, Calif.

*Work done on behalf of the National Aeronautics and Space Administration
under NASA contracts NAS7-100 and W-12872*

Abstract.—Radar images at 25-cm wavelength (λ) were obtained in 1969 in an area near Flagstaff, in northern Arizona, as part of a feasibility program to evaluate the geologic potential of long-wavelength radar systems for terrestrial applications, as well as for lunar and planetary orbital research. The instrument, operating in a side-looking mode (0° – 45° look angle), provided image data which sharply delineated regions of fine-grained alluvium as areas of very low radar backscatter. The 25-cm data enhance such alluvial materials far more than both 0.86-cm- λ radar data and low-altitude aerial photography of the site. Similar radar sensors with varying wavelengths in the decimeter range may enable discrimination of unconsolidated materials of a significantly greater range in grain size.

Four strips² of 25-cm-wavelength radar images, covering a total area of 2,650 km², were obtained in an area near Flagstaff, in northern Arizona (fig. 1), on May 19, 1969, by personnel from the Jet Propulsion Laboratory, California Institute of Technology, Pasadena. The overflights were requested by the U.S. Geological Survey as part of a feasibility study of a long-wavelength radar sounding system similar to one presently scheduled for use aboard the Apollo 17 Service Module.

The instrument was operated in a side-looking mode (0° – 45° look angle) with a slotted antenna array. Horizontally polarized radiation was transmitted and then recorded on 35-mm film. The images were developed by optical correlation at the Willow Run Laboratory, University of Michigan, Ann Arbor. The radar equipment was flown aboard a National Aeronautics and Space Administration Convair 990 jet aircraft operated by the Airborne Sciences Office, Ames Research Center, Mountain View, Calif. The aircraft maintained an altitude of 29,000 feet and a ground speed of between 450 and 500 miles per hour during all overflights.

The San Francisco volcanic field in northern Arizona was selected as an overflight area because of the relatively dry

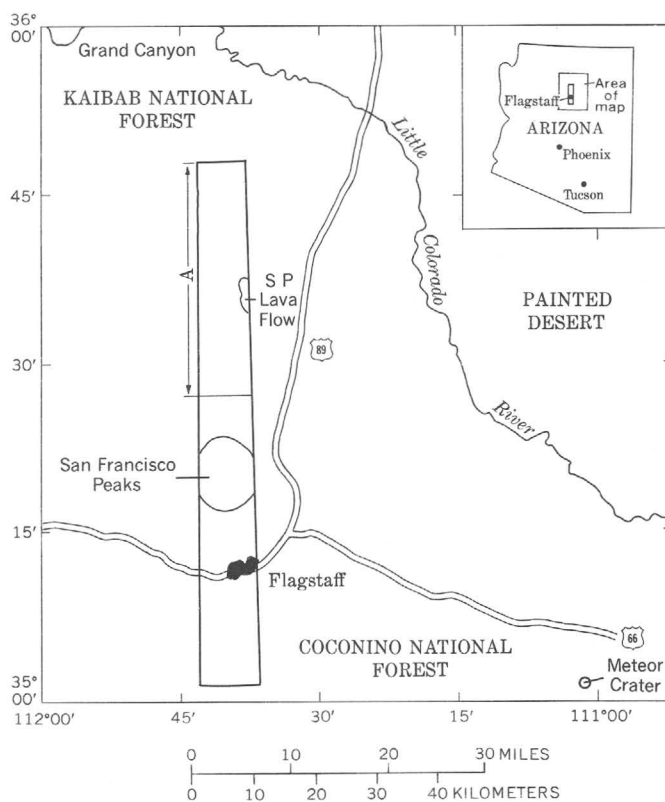


Figure 1.—Location map and footprint of one 25-cm radar flightline strip near Flagstaff, Ariz. Area A is shown in figures 3 and 4 and is discussed in the text. The outlines of the lava flow and mountains are omitted outside the strip.

high-desert conditions, existence of geologic ground-control data, and availability of 0.86-cm (K-band) side-looking radar data and high-resolution aerial photography for purposes of comparison (Schaber, 1967, 1968).

The scale of the original 35-mm radar images is approximately 1:185,000 along track but is an average of 1:300,000

¹Jet Propulsion Laboratory, California Institute of Technology.

²Only one flightline is discussed in this paper.

across track out to an angle of 45° from vertical. The part of the image nearest the flightline is considerably foreshortened owing to inherent characteristics of the image acquisition and processing techniques. Ground resolution in range is approximately 60 to 100 m at the 45° look angle, while azimuthal resolution at any angle is about 20 m.

EVALUATION OF RADAR IMAGES

Images of topographically expressed geologic features such as basaltic flow fronts, cinder cones, normal faults, and graben structures are only moderately to poorly distinct, as are those of most cultural features. However, the quality of these images varies with azimuthal orientation relative to the flightline and distance from it. Compared with conventional, shorter wavelength (1-cm) side-looking airborne radar (SLAR) systems, shadowing effects on the 25-cm radar data are reduced, owing to the shallower look angle of 0° – 45° from vertical and the low signal-to-noise ratio at the maximum look angle. Conventional SLAR systems commonly have effective incident angles of from 10° to 70° . The aforementioned topographically expressed geologic features are clearly seen on shorter wavelength K-band (0.86-cm) SLAR images (Schaber, 1967) (fig. 2).

Evaluation of the radar data for the area south of Crater 160 (figs. 3 and 4A) indicated a rather extensive region of very low radar backscatter, with abrupt boundaries. This region has not as yet been mapped, but field checking and study of low-altitude aerial photographs established that the patch of lowest radar backscatter (unit B, figs. 4A and 5) is a fenced, topographically flat farming plot consisting of very fine grained alluvium with virtually no surface lag-cinder cover, unlike the immediately surrounding areas. The cultivated region is enclosed on the north, west, and east by basaltic

cinder cones which form a catchment basin for sediments derived from erosion of the San Francisco Peaks to the south (figs. 3 and 5). The vegetation cover in the farming plot is very scanty compared with that of adjacent surroundings and the other alluvial deposits described above. It consists of scattered sage and desert grasses. The farm plot did not appear to have been worked in recent years.

Size analysis of soil samples collected in and near the farm plot indicates that the darkest tones (lowest backscatter) on the radar images correlate with the finest grained and deepest alluvial deposits (figs. 4A, 5, and 6). These particular areas also support the densest growth of sage, owing to greater moisture concentrations.

GEOLOGIC IMPLICATIONS

The flightline shown in figure 1 was flown from an area 19 km south of Flagstaff northward for a distance of 85 km. The image covers a total area of 690 km². That part of the flightline extending from 13 km north of the San Francisco Peaks to the north end of the flightline shows the best contrast on the radar image and the greatest amount of geologic data, owing to the general lack of vegetation, low moisture content, and diversity of volcanic and sedimentary materials. This part of the strip (designated "A" on figure 1) ranges in elevation from 5,800 to 7,300 feet and is characterized by abundant juniper and scattered pinyon pine in the higher elevations to the south, but by only very sparse juniper and scattered Upper Sonoran desert grasses at the lower elevations to the north. South of area A, the region ranging in elevation from 7,000 to 12,600 feet (highest point in the San Francisco Peaks) is dominated by a dense stand of ponderosa pine.

Much of area A is composed of basalt flows and basaltic cinders of Tertiary age and carbonate rocks of the Kaibab

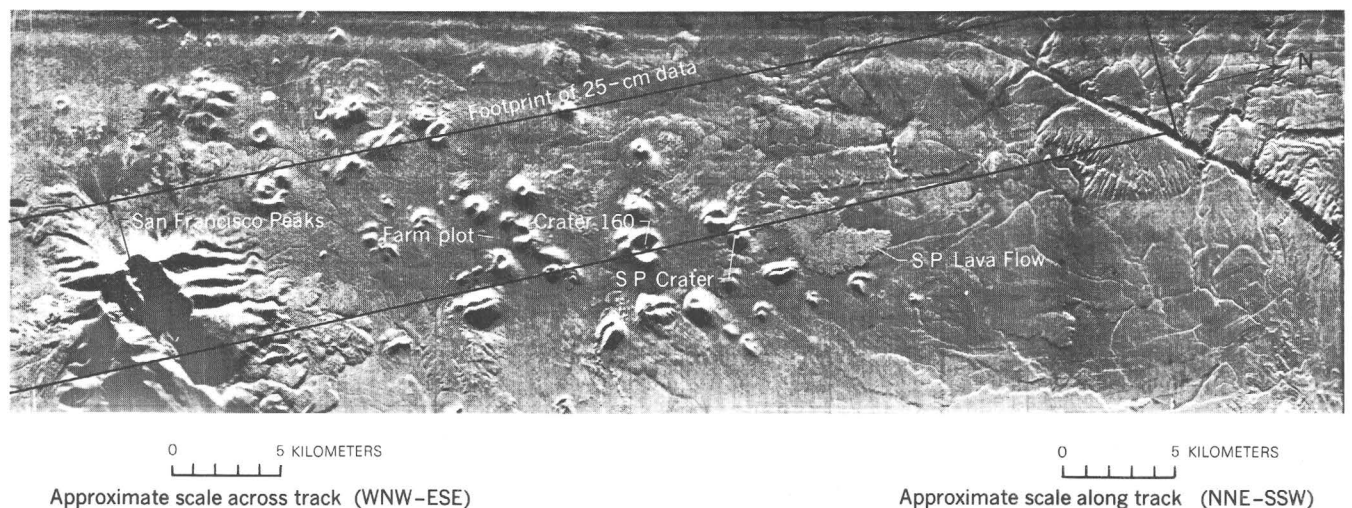


Figure 2.—K-band (0.86-cm) side-looking (10° – 70° look angle) radar image of the region north of Flagstaff, Ariz., showing footprint of 25-cm radar flightline. (See figs. 1, 3, and 4.)



Figure 3.—High-altitude (60,000 feet) photograph of the western half of the San Francisco volcanic field, showing the surface coverage of figures 4A, 4B, and 4C. White areas primarily Kaibab Limestone; dark areas basaltic cinders and flows.

Limestone. The Kaibab, of Permian age, is exposed only in the northern half of this region (fig. 3). The most recent surface materials in area A include Quaternary alluvium and basaltic cinders and lava. A lava flow, known as the S. P. Lava Flow, was first described by Colton (1937) and is associated with the 4,000- to 5,000-year-old S. P. Crater (figs. 1–3, and 4B).

Quaternary alluvial deposits in area A are very well delineated by low backscatter on the 25-cm radar data. We attribute this effect to the level surfaces and the fine-grained texture of the alluvium relative to the cinders and cinder-covered basalt flow materials that occupy much of the rest of the area.

Figures 4B and 4C illustrate the excellent correlation between alluvial deposits mapped on the ground and dark,

low-backscattering areas on the radar images. Some of the areas of low to moderately low backscattering not previously mapped as alluvium were found to be either (1) thinner deposits of alluvium with varying percentages of cinders overlying basalt flows (unit 4, figs. 4B and 4C) or (2) well-developed alluvial materials not mapped on the ground because of their small extent (unit X, figs. 4B and 4C). Virtually all the low-backscattering areas are covered by at least 4 to 5 inches of fine-grained materials.

Radar differentiation between areas of fine-grained alluvium and areas covered by cinders is distinct and of geologic significance. Neither aerial photography (fig. 5) nor shorter wavelength radar (0.86-cm) (fig. 2) data provide so characteristic an alluvium-cinder contact signature. There is, except by

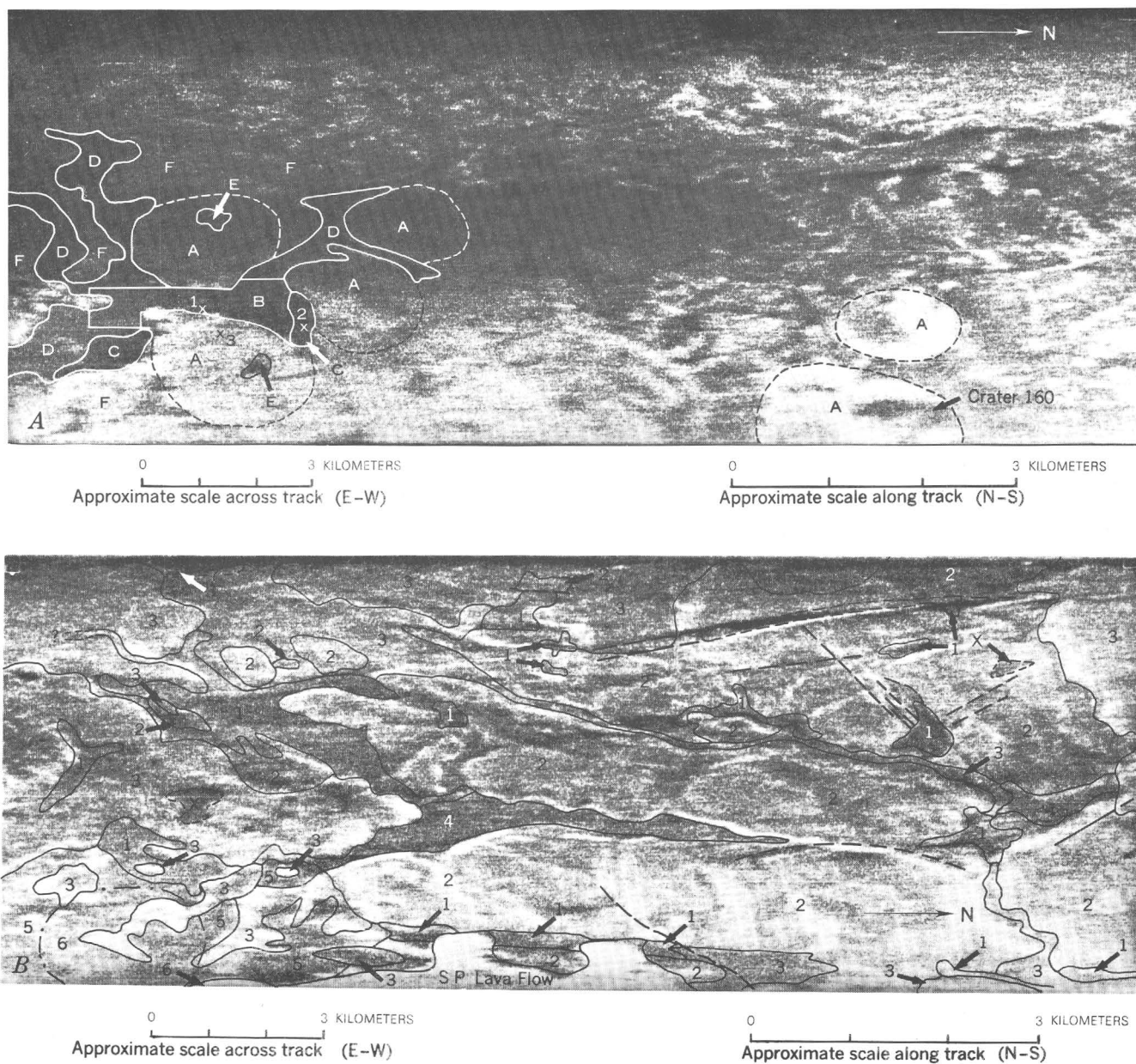


Figure 4.

inference, no information in the aerial photograph or shorter wavelength radar data regarding the textural nature of the material underlying the farming plot. Gray tones similar to those portraying the plot are also seen in many other parts of the photographic and 0.86-cm radar data.

ECHO INTERPRETATION ASPECTS

The radar echo strength for any given resolution element is a function of incidence angle, dielectric constant, and texture of surficial material (radii of curvature of particles). Usually, variation in surface texture is the dominant cause of echo

strength fluctuations for imagery where the angle of incidence is between, for instance, 5° to 30° from vertical. As shown in figure 7, the backscatter cross section area ($\sigma/\pi a^2$) of a sphere varies as the fourth power of the ratio of radii to radar wavelength (a/λ) when a/λ is less than 0.1. To a first approximation, the strength of the backscatter from a planar array of dielectric spheres is not affected when the backscatter angle is off of normal. For this discussion, the backscatter energy corresponds to the energy returned along the line of incidence.

A planar array of particles with radii of curvature equal to or greater than $a/\lambda=0.1$ has a relatively uniform backscatter

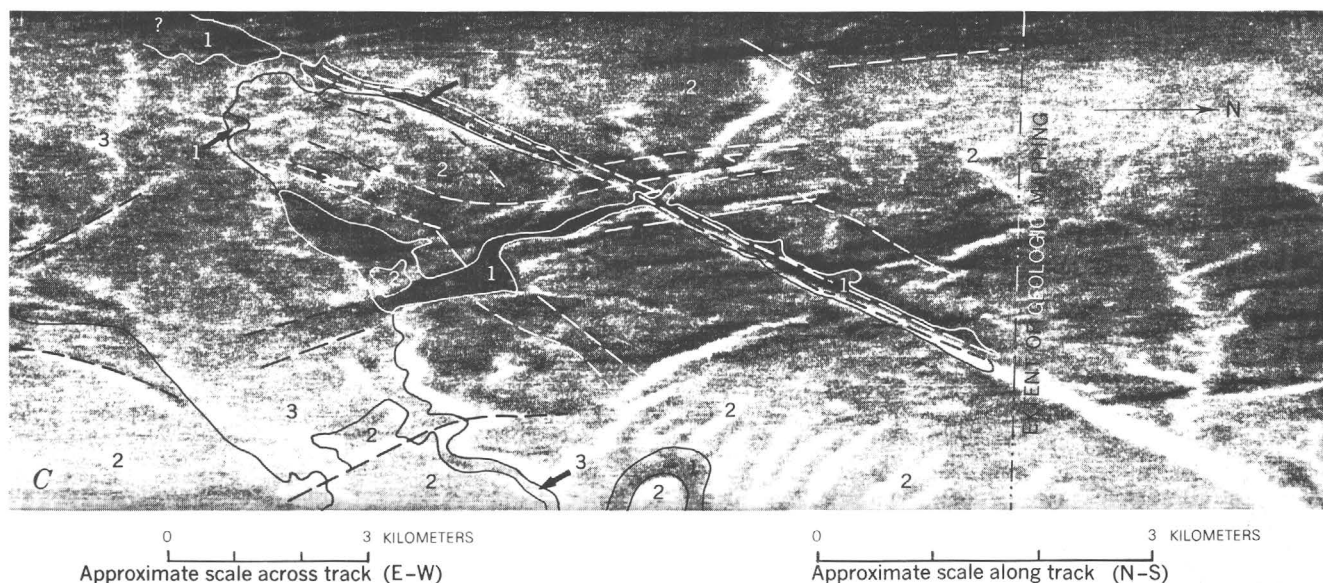


Figure 4.—Radar images of area A in figures 1 and 3.

- A. Southern one-third of the radar image sequence. X's and associated numbers are soil sample localities. A, basaltic cinder cones; coarse lag cinder on surface with abundant juniper; B, farming plot alluvium area having very low radar backscatter and virtually no surface lag cinder or basalt; very sparse cover of desert grasses and scattered sage; C, regions of lowest radar backscatter and finest soil; supports more abundant sage than unit B; D, areas of fine alluvium with scattered lag cinder; E, alluvium inside summit craters of cinder cones; F, areas of coarse lag cinder and isolated basalt outcrop; moderately well covered by juniper and sage.
- B. Middle one-third of the radar image sequence. 1, areas of previously mapped fine Quaternary alluvium giving the lowest radar backscatter in the image; 2, Kaibab Limestone—dolomite, highly jointed and faulted; 3, basalt flows only thinly covered by ash and cinders; 4, basalt flows covered by a moderate thickness of alluvium and containing more abundant lag cinder and basalt than unit 1; 5, areas covered by a thick mantle of Quaternary cinders and ash; 6, basaltic cinder cones with moderate juniper cover; X, low-radar-backscatter areas not previously mapped as alluvium but verified as such from the radar data and subsequent field investigation. Faults shown by heavy dashed lines. Geologic data on image taken from unpublished map of the SP Mountain quadrangle.
- C. Northern one-third of the radar image sequence. See paragraph B above for explanation of units.

function versus angle, and the echo strength is nearly independent of the average slope on which the particles rest.

Generally, unconsolidated surface materials vary irregularly in size. The larger the range of sizes, the smaller the change in backscatter with variation of wavelength. For these reasons, a multiwavelength measurement of backscatter, made simultaneously and with the same geometry (same look angle), could be used to determine the probable frequency distribution of particle sizes in various unconsolidated materials.

The four large cinder cones labeled "A" in figure 5 are not identifiable as topographic features on the radar image (fig. 4A). The maximum size of the coarse irregular cinders on the slopes of these cones is 10 cm, the average 1–2 cm. This is a size that for a wavelength of 25 cm would theoretically approach uniform backscatter, regardless of incidence angle. Variations in the angle of incidence around the cones therefore have little effect on returned signal strength. The angles of incidence around the easternmost cone in figure 5, for example, range from 10° to 52°. The fine-grained alluvium in the summit crater of the easternmost cone, however, is clearly visible as a dark area (less energy returned to the radar receiver) (figs. 4A and 5).

CONCLUSIONS

Preliminary geologic investigation of the 25-cm radar images indicates definite value with regard to the delineation of alluvial materials of sand and silt size. Areas covered by fine-grained soil with an average particle diameter approximately 1/1,000th of the radar wavelength are distinctly portrayed on the radar imagery by their very low backscatter. The lack of extensive lag-cinder material at the surface of the alluvial deposits is an important factor in the character of the resultant image.

An important observation resulting from this study is that a slight increase in soil fineness may result in notably increased darkening of the image tone (more specular to the radar). Regions of finest surface material could possibly be mapped by using such a long-wavelength radar sensor.

Another asset of the 25-cm radar imagery is the apparent lack of influence of surface vegetation, except in regions of heavy forest cover. Scattered sage and desert grasses do not appear to significantly affect the tone of the images. The very poor resolution of cultural features, such as fence lines and roads, does not generally detract from the geologic value of

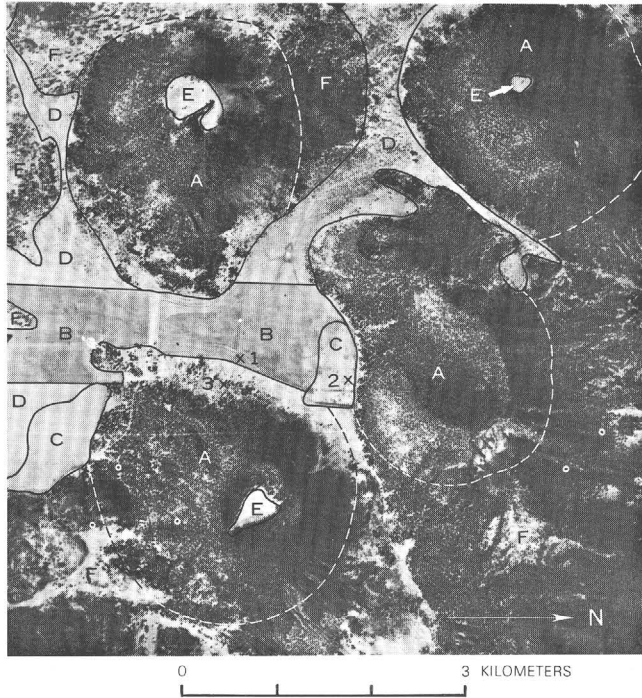


Figure 5.—Aerial photograph showing the farming plot indicated as unit B in figure 4A. Symbols explained in caption of figure 4A.

the data, except to hinder efforts at establishing geographic location and orientation.

The poor topographic portrayal of 25-cm radar imagery facilitates interpretation of texture of surface materials, but it makes this type of imagery nearly useless for structural and morphologic studies. However, these types of data are nicely portrayed on the more conventional, shorter wavelength (1-cm) SLAR images. The combination of two such radar sensors flown simultaneously with aerial photography should therefore provide a maximum of valuable geologic information.

REFERENCES

Colton, H. S., 1937, The basaltic cinder cones and lava flows of the San Francisco Mountain volcanic field, Ariz.: Mus. Northern Arizona Bull. 10, 50 p.
 Kerr, D. E., 1951, Propagation of short radio waves: Massachusetts Inst.

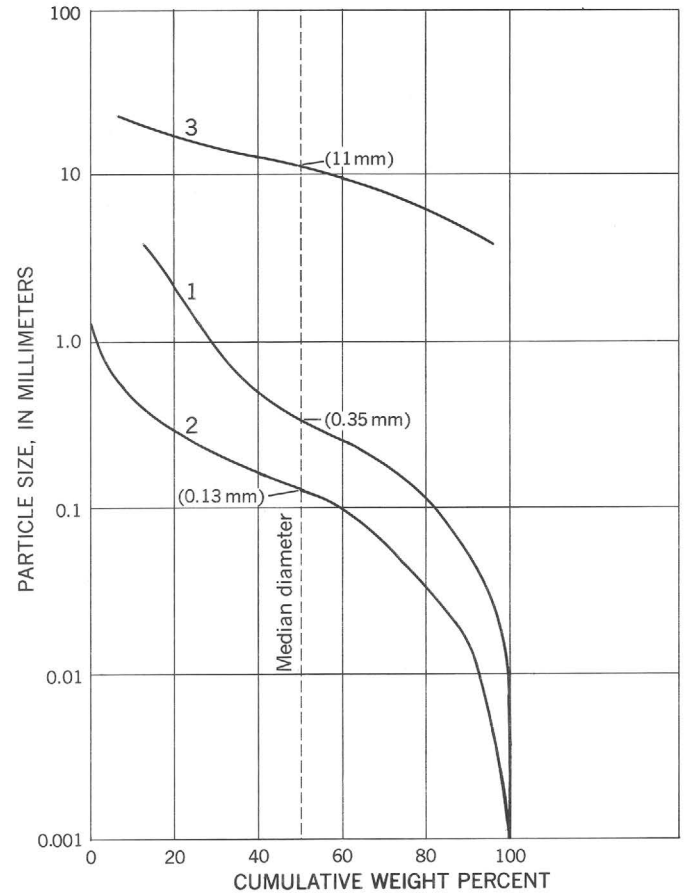


Figure 6.—Semilog plot showing particle size distribution of the three surface samples collected in the vicinity of the farming plot shown in figures 4A and 5. Samples 1 and 2 are fine alluvium with medium grain sizes (by weight) of 0.35 and 0.13 mm, respectively. Sample 3 is lag-cinder material. Soil sample 2, the finest grained material, is from the area of lowest radar backscatter (see figs. 4A and 5).

Technology Radiation Lab. Series 13, Lexington, Mass., Boston Technical Publishers Inc., 728 p.
 Schaber, G. G., 1967, Radar images—San Francisco volcanic field, Arizona—A preliminary evaluation: U.S. Geol. Survey open-file report, 10 p.
 — 1968, Radar and infrared in geological studies of northern Arizona, in Earth resources aircraft program status review, v. 1: Natl. Aeronautics and Space Adm., Manned Spacecraft Center, Houston, Tex.

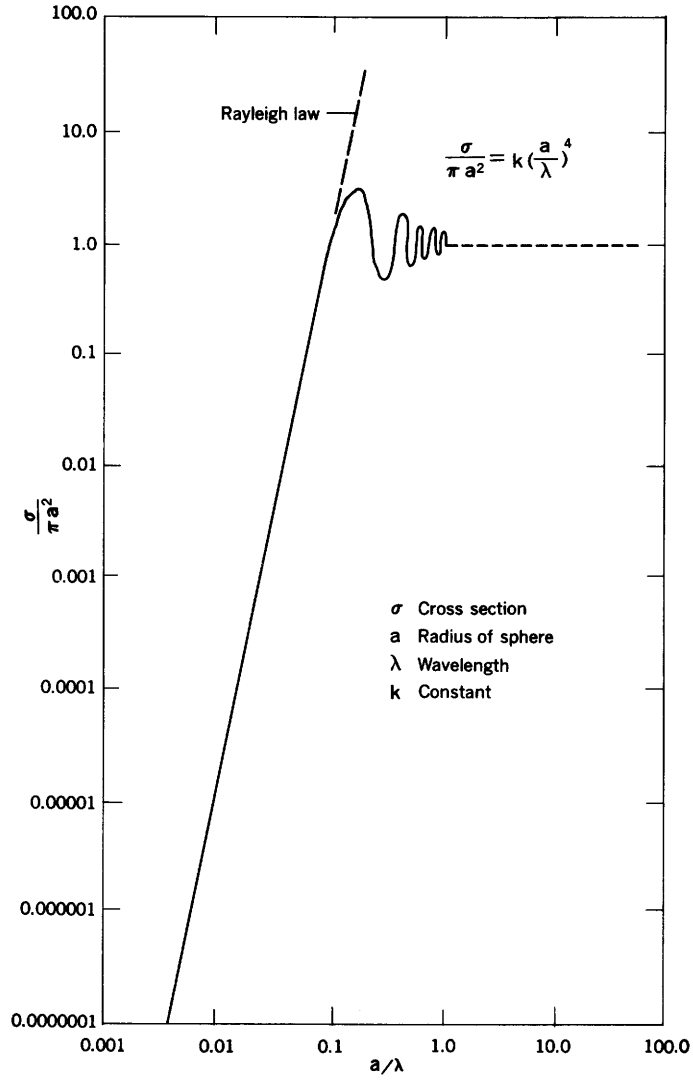


Figure 7.—Log-log plot of the ratio of backscattering radar cross section area to geometric cross section area as a function of the ratio of particle radius to wavelength for a sphere with infinite conductivity (modified from Kerr, 1951, fig. 6.1 (p. 453)). The curve follows the Rayleigh scattering law closely for small a/λ , but above about $a/\lambda = 0.1$ the higher order multipole moments become larger and fluctuate in phase and magnitude in a complicated way, causing marked oscillations in the curve.



GRAVITY STUDY OF THE SAN JUAN MOUNTAINS, COLORADO

By DONALD PLOUFF and L. C. PAKISER,
Menlo Park, Calif.

Abstract.—A regional gravity low in the San Juan Mountains area suggests that a concealed batholith that is genetically related to a near-surface caldera complex underlies much of the area now covered by volcanic rocks. A two-dimensional interpretation of the regional gravity low and a correlated magnetic high indicate the approximate configuration of a postulated igneous complex beneath the San Juan Mountains. The depth to the top of the batholith ranges from less than 2 km to 7 km beneath the surface along the interpreted profile. The bottom of the batholith may extend to a depth greater than 19 km. Local gravity anomalies superimposed on the regional low can be correlated with individual calderas, intrusive centers, Precambrian rock masses, and structures of various ages. One particularly large local gravity low can be interpreted as the effect of a caldera that can be represented by a 16-km-diameter vertical cylinder that extends from the surface to a depth of 4 km.

The location of the present gravity study in the San Juan Mountains, Colo. (fig. 1), coincides with the area described by Larsen and Cross (1956) (fig. 2). A number of other geologists, including Steven and Ratté (1960, 1965), Bromfield (1967), Olson, Hedlund, and Hansen (1968), Luedke and Burbank (1968), Barker (1969), and Lipman, Steven, and Mehnert (1970), later contributed information to the geologic knowledge of the area. T. A. Steven (1968, p. 2–4) has summarized the general geology of the San Juan Mountains:

The Precambrian rocks, although highly varied, for present purposes can be considered as a unit of crystalline metamorphic and igneous rocks underlying most of the sedimentary and volcanic rocks and exposed in the cores of anticlinal uplifts***. These are overlain by sedimentary rocks of Paleozoic, Mesozoic, and early Tertiary age***. The distribution of various sedimentary rocks is controlled for the most part by tectonic features***. The San Juan Mountains are made up principally of igneous rocks, which comprise probable Upper Cretaceous and lower Tertiary laccolithic intrusives along the west side of the region, and a great mass of middle Tertiary volcanic rocks throughout the central part of the region. ***widespread basalt flows in the eastern San Juans***rest unconformably on the intermediate to silicic volcanic rocks that make up the great bulk of the volcanic field***. The San Luis Valley along the east side of the San Juan region is a great alluvium-filled segment of the Rio Grande trough***.

A network of 2,444 gravity stations was established in the San Juan Mountains area between 1961 and 1970. The

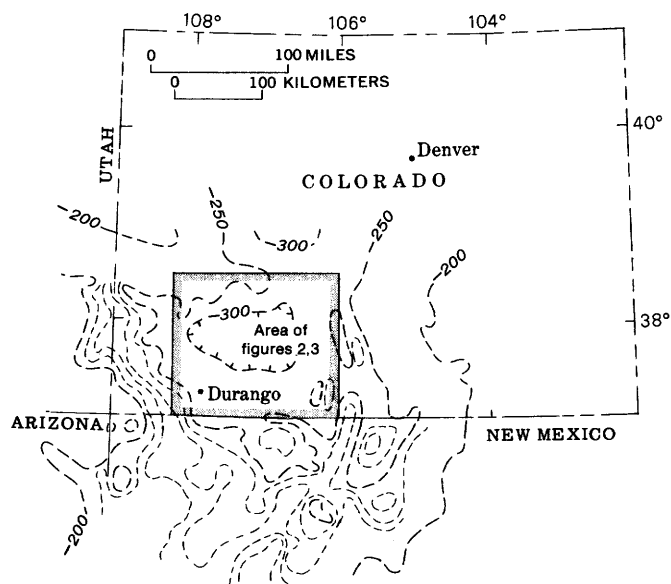


Figure 1.—Index map of Colorado and adjacent States. Dashed lines indicate Bouguer gravity-anomaly contours (Aeronautical Chart and Information Center, 1968). Contours labeled at 50-milligal interval. Selected intermediate contours are at an interval of 10 milligals. Hachures indicate low side of gravity contour.

observed gravity values of a network of base stations were established by making several ties to a gravity station near the Denver Federal Center. The gravity value at the Denver station has been tied to the observed gravity datum of Behrendt and Woollard (1961). A total of 2,200 stations have been corrected for terrain to a distance of 166.7 km. The remaining stations, which are not needed in gravity contouring, were not corrected for terrain inside a circle of radius 2.6 km. A near-surface density of 2.67 g/cm^3 was used in making the terrain corrections. A computer program described by Plouff (1966) was used to make the terrain corrections beyond 2.6 km from the stations. This program uses digitized topography consisting of average elevations within rectangular compartments of 1 by 1 and 3 by 3 minutes of geographic distance and a supplementary compartment size of 30 seconds for distances as near as 0.9 km from the stations. A Bouguer gravity-anomaly map (fig. 3) based on an assumed density of 2.67

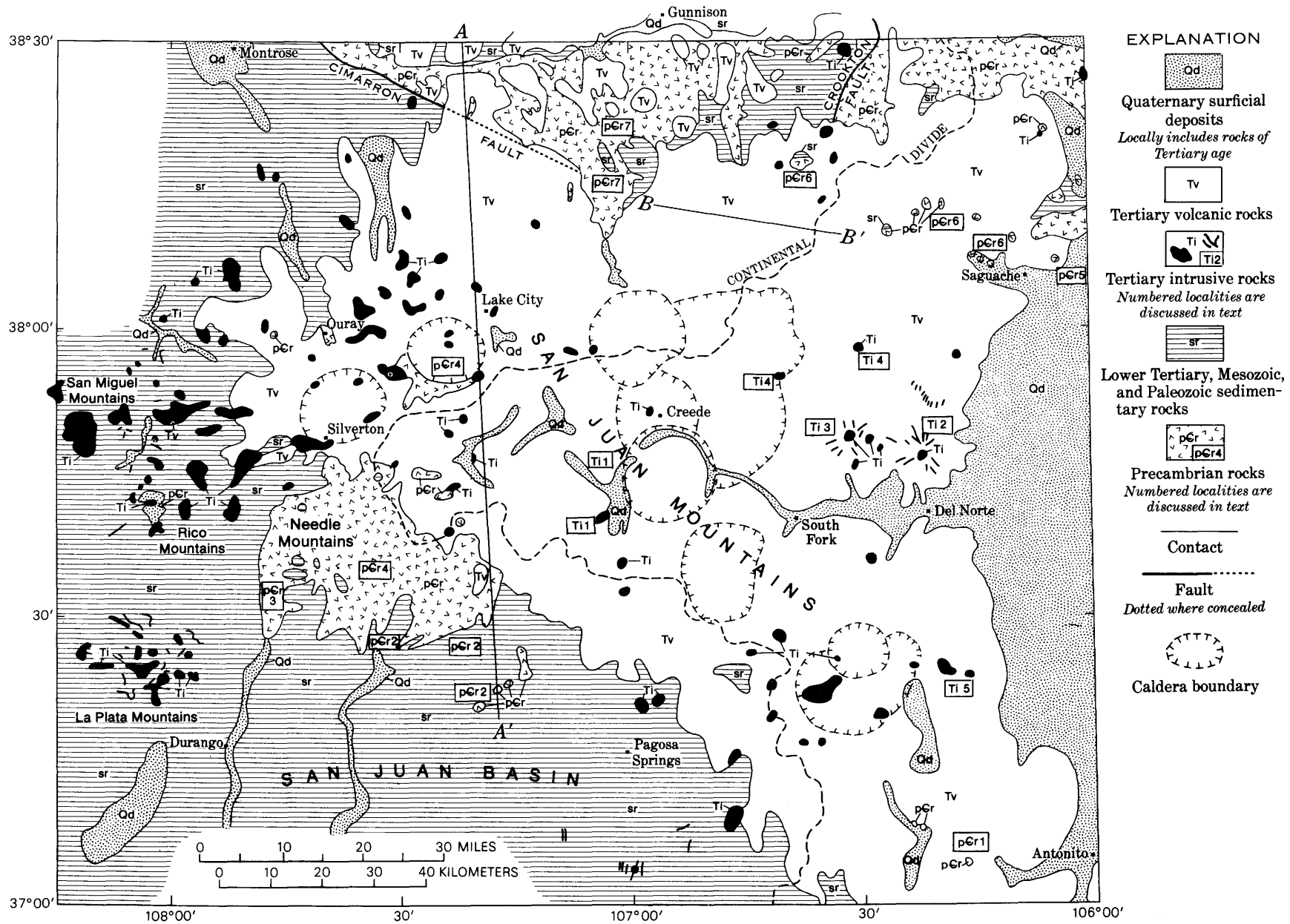


Figure 2.—Geologic map of San Juan Mountains area (generalized from Larsen and Cross, 1956, pl. 1; Bush and Bromfield, 1966; Bush and others, 1959, pl. 4; Bush and others, 1960, pl. 19; Burbank and others, 1935; and Vogel, 1962), showing calderas (Lipman and others, 1970, fig. 1) and locations of profiles A-A' and B-B'.

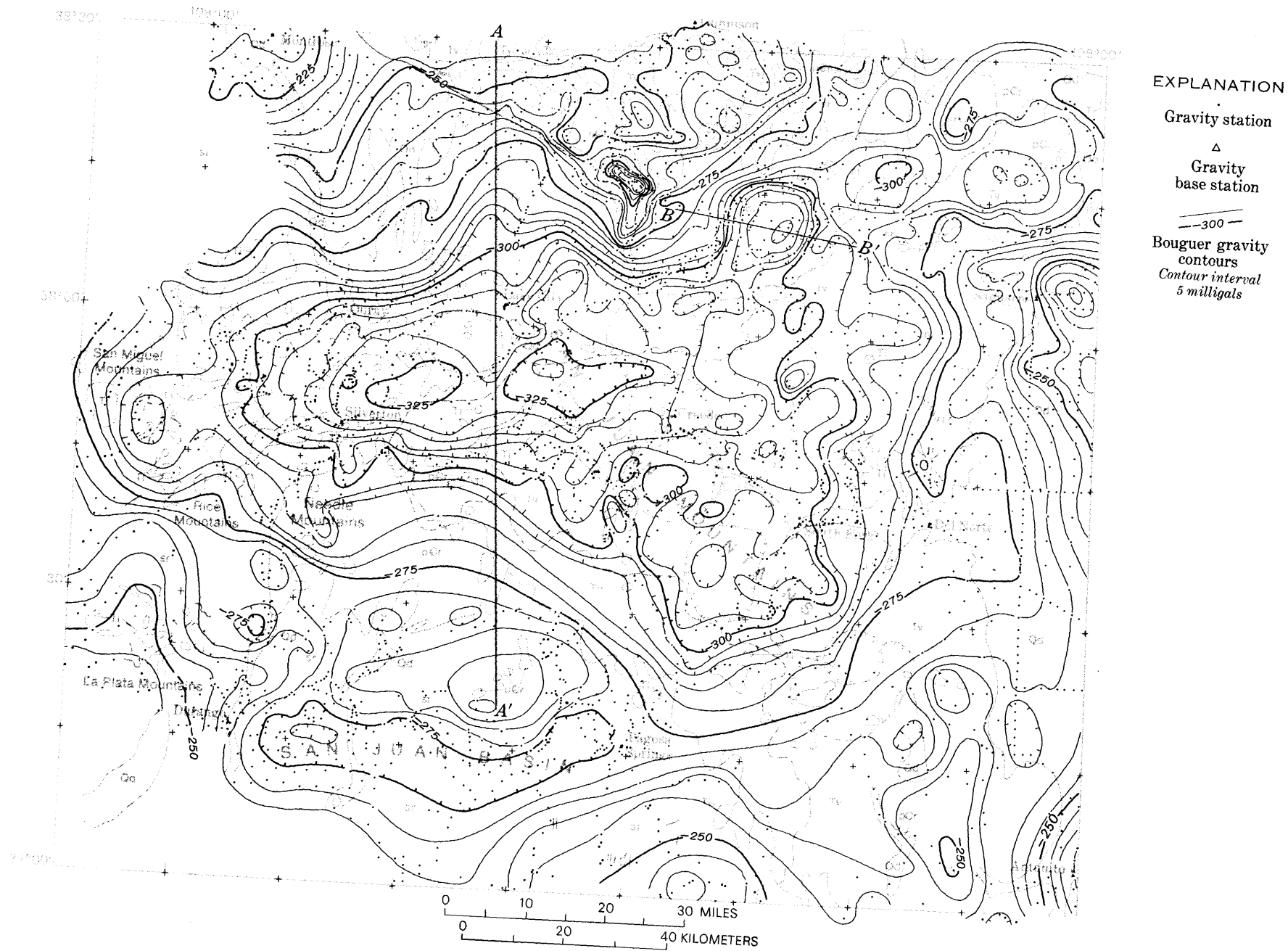


Figure 3.—Bouguer gravity-anomaly map of the San Juan Mountains area, showing locations of profiles A-A' and B-B'.

POUFF AND PAKISER

g/cm^3 for rocks above sea level was prepared by using standard gravity reduction methods. In order to show complete gravity coverage of the eastern part of the area studied, Bouguer gravity values of 239 gravity stations of Gaca and Karig (1965) were incorporated in the map.

The largest expected error from all sources is less than the 5-mgal (milligal) contour interval of the map. There is little change in anomaly pattern when the map contours are based on an average rock density of $2.5 g/cm^3$.

GRAVITY ANOMALY RELATED TO A POSTULATED IGNEOUS COMPLEX

The gravity map (fig. 3) is complex in detail, but it is dominated by a large regional gravity low with dimensions of approximately 100 by 150 km. The area covered by the regional gravity low is nearly coincident with the distribution of volcanic rocks in the San Juan Mountains and must be causally related to them. Erosional remnants of volcanic rock are absent near the west edge of the gravity low, and volcanic rock extends southeast of the southeast edge of the major gravity low. Because of the types and thicknesses of volcanic rock units involved and the small density contrast between the volcanic rocks and the surrounding near-surface rocks, the volcanic rocks alone are probably not sufficient to explain the magnitude and shape of the anomaly. An inverse correlation between the Bouguer gravity anomaly and the altitude above sea level exists in this area, but gradients along the edges of the gravity low are too steep to explain the anomaly entirely in terms of isostatic compensation by a crustal root. Therefore, a low-density igneous complex consisting of numerous coalescing calderas underlain by a concealed batholith is suggested as the primary cause of the anomaly. The calderas filled with volcanic rocks were formed in the subsiding roof of the formerly molten batholith (fig 3). Pakiser (1964) has suggested a similar explanation for a gravity low near Lassen Volcanic National Park, Calif. Case (1967) concluded that a similar gravity low about 150 km northeast of the San Juan Mountains probably is caused by a silicic batholith of Tertiary age.

Batholith

The boundary of the hypothetical batholith that underlies the inferred caldera complex (fig. 2) can be placed approximately midway along and normal to the steepest gradients at the edge of the gravity near the -300-mgal contour (fig. 3). The edge of the concealed batholith probably is not vertical; therefore the suggested boundary presumably represents a generalized average of the position of the batholith's lateral contact with the surrounding rocks. The gravity values continue to increase outward (fig. 1) from the batholith, but uncertainty due to coalescence with the gravity effects along the flanks of other major structural elements, such as the

Uncompahgre uplift to the northwest and the San Juan Basin to the southwest, prevents confident definition of the outer limits of the postulated batholith.

A two-dimensional analysis of the gravity anomaly along a geologic section from Larsen and Cross (1956, pls. 1 and 2) gives a rough estimate of the subsurface configuration of the postulated batholith. The section ($A-A'$, figs. 2 and 3) is nearly normal to the gravity contours. Bott's (1960) iterative method was adapted to determine a possible subsurface mass configuration that fits the observed gravity anomaly (fig. 4). An arbitrary density contrast of $0.1 g/cm^3$ was assumed, and the gravity anomaly was reduced to a residual profile by subtracting a linear regional gravity gradient. A starting depth of 24.2 km beneath the surface (average altitude about 3,200 m above sea level) was found by trial and error, so that the top of the batholith nearly reaches the surface (fig. 4D). This approach that assumes that the gravity effect of the batholith has been isolated has evident disadvantages, especially at the north end of the profile, where it produces an artificial downward-extending spike. Near the north end of the profile, one finds an independent set of contrasting rock types that contributes to the shape of the gravity profile. Near-surface density variations were ignored in the gravity calculations.

A two-dimensional analysis of the magnetic field along section $A-A'$ was also made (fig. 4C and 4D). A total magnetic intensity map (U.S. Geological Survey, unpub.) of part of the San Juan Mountains area was used for the magnetic analysis. The aeromagnetic survey was flown at a constant barometric elevation of 4.4 km, using east-west lines spaced at 1.6 km. A regional magnetic high of 300-gamma intensity occurs along the profile, and its location and horizontal dimensions are compatible with the gravity profile. The existence of the magnetic anomaly might be expected, because some near-surface intrusive and extrusive rocks derived from the original magma body are strongly magnetic. Sample measurements and interpretation of magnetic maps of Popenoe and Steven (1969) and Popenoe and Luedke (1970) in the San Juan Mountains demonstrated that several magnetic anomalies in the San Juan volcanic field are correlated with mapped volcanic units.

Two possible cross sections of the "magnetic batholith" have been determined (fig. 4D) by using a single magnetization contrast of 0.001 electromagnetic unit/ cm^3 and alignment of remanent magnetization, if any, along the earth's present field. The effect of topography is not apparent on the magnetic map; hence this effect and that due to local anomalies are ignored in the interpretation. These assumptions do not preclude the possibility that the superposition of gradual changes in thickness and depth of local volcanic units could cause the broad anomaly. The difference between the two models depends on the interpretation of interfering local anomalies near the north end of the profile. The roof thickness over the magnetic body ranges from 2 to 7 km. The total relief of the body is 19 km, or about half the thickness of the earth's

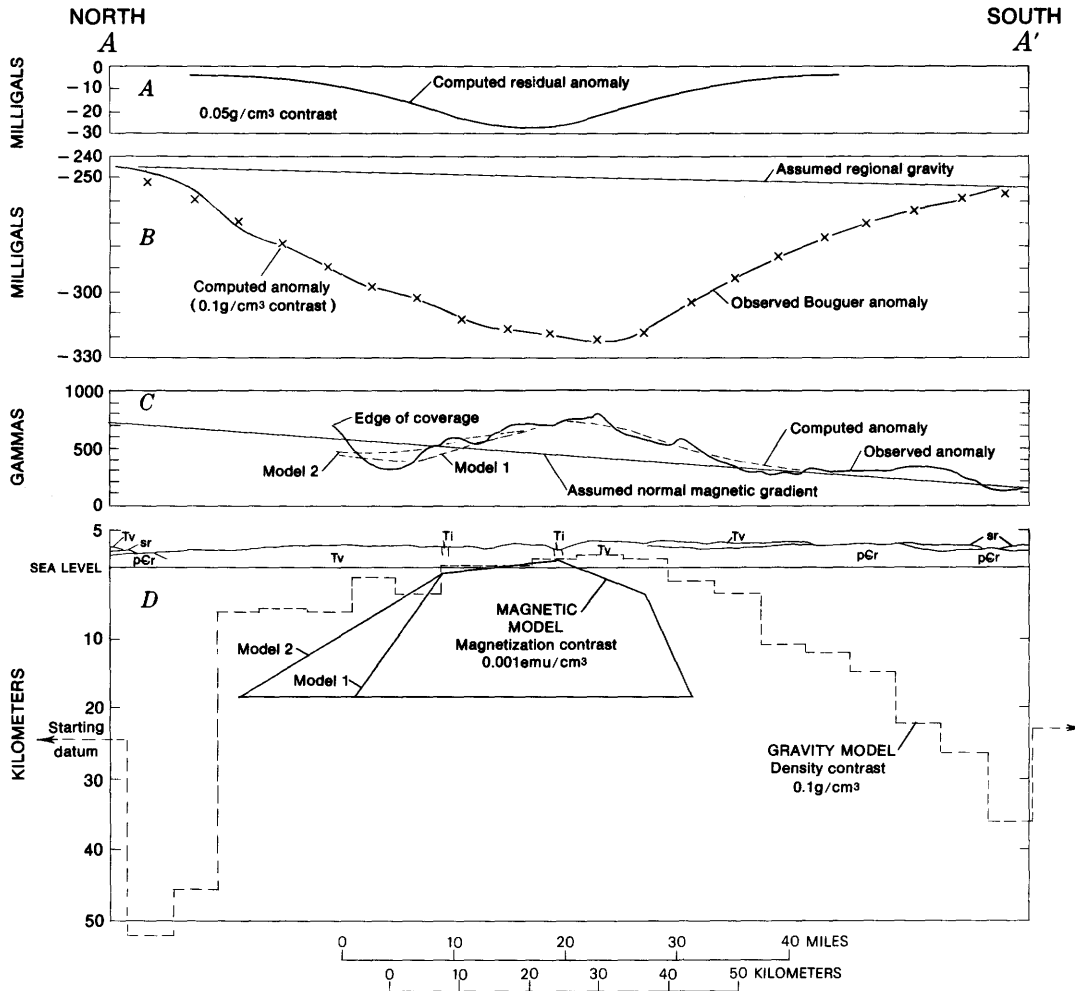


Figure 4.—Interpretation of gravity and magnetic anomalies along profile A—A' (from figs. 2 and 3). Geologic section generalized from Larsen and Cross (1956, pl. 2).

crust in this area. The bottom of the magnetic body may coincide with the Curie geotherm (573°C for magnetite), suggesting a very high geothermal gradient that is compatible with the Cenozoic volcanic history of the San Juan Mountains.

The magnetic model, although somewhat artificial in appearance, was derived independently without consideration of the surface geology. In this model the magnetic body must be closest to the surface beneath the Lake City caldera.

The upper surface of the central part of the magnetic body corresponds well with that of the gravity model. That the magnetic body is narrower than the anomalous body of the gravity model suggests that the central part of the presumed pluton is more magnetic than the outer part. If the density contrast is 0.1 g/cm³, the maximum amplitude of the gravity anomaly that corresponds to the interpreted magnetic body is about 55 mgal; this roughly corresponds to the 70-mgal residual anomaly measured. But the gravity gradients along the edges of the model are steeper than those of the actual anomaly. Therefore, if the magnetic model were to represent

the entire batholith, the assumed density contrast would have to be reduced to about 0.05 g/cm³; consequently the amplitude has been reduced to about 28 mgal (fig. 4A) to yield calculated gravity gradients that do not exceed the observed gradients. A nearly symmetric anomaly of 42 mgal remains to be explained. Recent studies (Lipman and others, 1970, p. 2347) indicate a zonation within the magma chamber that should be considered during further refinement of the model.

Calderas

The San Juan Mountains contain a number of calderas that appear to coalesce into a caldera complex above the postulated batholith (fig. 2), but distinctive gravity anomalies are not obviously associated with the principal calderas near the center of the mountains. This result is to be expected, because in the interior of the San Juan Mountains there is little contrast in density between the downropped volcanic rocks within the

calderas and the volcanic rocks that surround them. The locations of the calderas north of Silverton, southwest of Lake City, and southwest of South Fork, however, seem to be partly expressed by the shape of the boundary of the San Juan Mountains regional gravity low (fig. 3). This correlation may reflect the contrast in density between the surrounding basement rocks and both the batholith and the downdropped volcanic rocks within the igneous complex.

A caldera is apparently expressed by a gravity low centered in the Bonanza quadrangle 24 km north of Saguache, as suggested by Karig (1965). The Precambrian rocks on all except the west side of the gravity low tend to accentuate the anomaly. A similar low 23 km west of the Bonanza anomaly also may indicate a caldera. A pronounced gravity low centered 45 km southeast of Gunnison may be caused by a caldera filled with low-density volcanic rock, by the cupola of an underlying batholith, or by a combination of the two. Steep gravity gradients on all except the south-southwest side, where the thickest volcanic rocks are present, suggest a body with approximately vertical sides near the surface. The observed gravity profile $B-B'$ (figs. 2 and 3) can be closely matched by a model of an underlying block of low-density rocks shaped like a vertical cylinder. A good fit is obtained from a 16-km-diameter cylinder that extends from the surface to a depth of 4 km with a density contrast of 0.25 g/cm^3 (fig. 5). The eastward displacement of the centermost gravity closure agrees with the assumed regional gravity gradient. Like

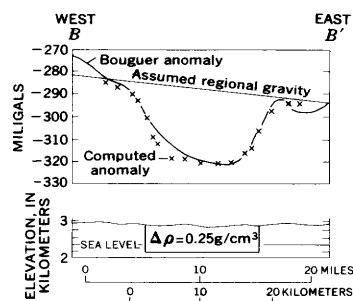


Figure 5.—Gravity anomaly and simplified model of a buried vertical cylinder along profile $B-B'$ (see figs. 2 and 3).

any simplified model, the exact shape of the underlying body and complications of the density variations cannot be truly represented without possible ambiguity. Geologic interpretation, however, must account for a body of this approximate size and shape with a mass deficiency of about $2 \times 10^{17} \text{ g}$.

GRAVITY ANOMALIES RELATED TO INTRUSIVE CENTERS

Several gravity highs or noses as much as 8 km wide are located over mapped intrusive bodies. The anomalies probably

cannot be wholly explained in terms of the density contrast between the intrusive bodies and the surrounding near-surface rocks. The contrast in density between a pluton beneath the intrusive centers and the surrounding near-surface rocks is expected to contribute significantly to the size of the gravity highs.

The following numbered localities are shown in figure 2:

1. A large stock of syenogabbro porphyry described by Larsen and Cross (1956, p. 114) 23 km south-southwest of Creede might extend to the southeast beneath surface rocks in the direction of elongation of an associated gravity high (figs. 2 and 3). A small gravity high 8 km north of the larger stock may have a similar source. T. A. Steven (written commun., 1971) suggests that the former gravity high could result from multiple intrusions rather than from a single stock.

2. Several closely spaced gravity stations were established near Summer Coon volcano, 11 km north of Del Norte. The central stocks that consist of dense gray medium-grained to porphyritic diorite and quartz monzonite porphyry (Lipman, 1968, p. 225) correlate with a local gravity high. Extensions at depth south-southeast and east-northeast of the volcano are suggested by the gravity data. The gravity high is accentuated by the postulated low-density batholith to the west and by a thickened section of alluvium to the east.

3. A zone of minor intrusive bodies extends from the Summer Coon center to the Embargo intrusive center 21 km northwest of Del Norte (Larsen and Cross, 1956, p. 112). Although no gravity closure can be drawn, the westward deflection or nose in the otherwise north-trending gravity contours indicates a local gravity high.

4. The Wanamaker Creek center 24 km east-northeast of Creede "is a granodiorite porphyry much like that of Embargo and Summer Coon" (Larsen and Cross, 1956, p. 113). The strong gravity high over the center may extend eastward 16 km to join the gravity nose over similar rocks of the Royal Park intrusive center, although the gravity coverage in this area is not dense enough to demonstrate this extension.

5. A closed gravity high occurs over a large monzonite body (Larsen and Cross, 1956, p. 110) and two nearby intrusive outcrops centered 30 km south of Del Norte. This high, however, may be related to the larger gravity high that extends southward to the border of the mapped area.

The widespread intrusive rocks in the west part of the area do not generally correlate with gravity highs. These rocks, for the most part, are associated with laccoliths rather than with volcano centers that typify the eastern gravity highs and sills.

GRAVITY ANOMALIES RELATED TO PRECAMBRIAN ROCK

Several gravity highs or noses are located over mapped outcrops of Precambrian rock. These highs are caused by the greater density of Precambrian rock compared with that of the surrounding sedimentary or volcanic rocks or in some places

by the contrast in density between two types of Precambrian rocks.

The following numbered localities are shown in figure 2:

1. An outcrop of Precambrian rock 24 km west of Antonito coincides with a gravity high; two outcrops of Precambrian rock appear on a westward extension of this high (figs. 2 and 3). Larsen and Cross (1956, p. 16) interpret these rocks as outliers of much larger bodies in New Mexico, but the closed form of the anomaly and the gravity lows to the east and west suggest a horstlike structure or a local high in the Precambrian basement surface.

2. A gravity high centered 28 km west-northwest of Pagosa Springs encloses four outcrops of Precambrian rock along the Piedra River. The width of the anomaly—20 to 45 km—and the vertical position of the outcrops, which are at low altitudes, indicate that the contrast with a thin sedimentary rock cover is not sufficient to cause the anomaly. Two gravity highs about 20 km to the north and northwest may be contoured alternatively as a single closed anomaly along the contact between Precambrian and sedimentary rocks.

3. A gravity high 30 km north of Durango probably is caused by the relatively dense Electra Lake Gabbro of Precambrian age (Barker, 1969, p. A27) at this locality.

4. The 25- by 45-km complex of Precambrian rock in the Needle Mountains south of Silverton has no strong gravity expression. This mass of rock may be part of the roof that overlies the south edge of the postulated batholith, forming a relatively thin plate above it. The 3- by 14-km block of Precambrian rock 18 km southwest of Lake City has no expression on the gravity contours and probably is also part of a thin roof over the batholith.

5. The major gravity high centered 8 km east of Saguache was interpreted by Gaca and Karig (1965, p. 15) as the gravity expression of a horst of Precambrian rock buried by basin fill. Additional gravity coverage east of Saguache supports Gaca and Karig's depth estimate of less than 200 m to the top of the Precambrian mass. The amplitude of the anomaly indicates that the body extends to depths of thousands of meters and suggests that the constituent rocks are significantly denser than the granitic and gneissic rocks exposed at the surface northeast of Saguache.

A small-amplitude flat-topped magnetic high (U.S. Geological Survey, 1970) 4 km west of the gravity high indicates that the rocks of the postulated horst are not very magnetic. The combination of a high density and low magnetic susceptibility may, for example, suggest an underlying amphibolite rock similar to that reported by Case (1966) near the west border of Colorado. A magnetic gradient of about 60 gammas/km, with lower magnetic values to the northeast, extends for 50 km northwestward and at least 15 km southeastward from the east flank of the gravity anomaly. This trend follows the southwest fault-bounded edge of San Luis Valley.

6. Several small outcrops of Precambrian rock, extending 48 km northwest of Saguache, are expressed by a gravity nose.

The nose interrupts the westward gravity gradient at the northeast edge of the postulated batholith. This relationship suggests that the roof of older rocks overlying the batholith is thicker here than it is to the northeast and to the southwest.

7. A 20- to 25-mgal elliptical gravity high 33 km south-southwest of Gunnison can be correlated with the Iron Hill complex, a composite stock of alkalic mafic igneous rock, largely pyroxenite (Larsen, 1942). Though its age probably is Cambrian (U.S. Geol. Survey, 1969), the stock is lumped within Precambrian rocks for convenience (figs. 2 and 3). If the density of the pyroxenite stock is 3.2 g/cm^3 and the density of the surrounding granite is 2.65 g/cm^3 , the alkalic stock must extend at least 3,000 m downward to account for the gravity anomaly. A strong magnetic high is associated with the gravity high. An east-trending band of Precambrian greenstone can be correlated with a smaller elongate gravity high 13 km north of the alkalic stock.

STRUCTURAL FEATURES

The alkalic stock noted above forms the south apex of a triangular block of Precambrian rock that extends 35 km into the area studied (fig. 2) and is 80 km wide at the north border. These rocks are part of the Gunnison uplift (Kelley, 1955, p. 23), and they are expressed by a gravity high. The gravity contours (fig. 3) along the southwest edge of the block, except for a minor reentrant, are nearly parallel to the Cimarron fault. A subsurface faultlike boundary along the southeast edge of the block may be present along the linear -275-mgal contour. The north edge of the gravity high strikes east about 13 km north of Gunnison (Aeronautical Chart and Information Center, 1968). The Crookton fault (Stark and Behre, 1936, p. 106) is parallel to the eastern edge of the anomaly 10 km southeast of the -275-mgal contour. The block of Precambrian rock just east of the Crookton fault coincides with a gravity high.

The fold structures within the sedimentary rocks northwest and southeast of Pagosa Springs trend northwestward along the Archuleta anticlinorium (Kelley, 1955, p. 23). A line joining the broad gravity highs 28 km west-northwest and 30 km southeast of Pagosa Springs is consistent with this trend, but the gravity low between Pagosa Springs and Durango interrupts the trend. The trend of the gravity contours south of the gravity low (fig. 1) is parallel to the structural grain, but the gravity values increase to the southwest toward the center of the San Juan Basin, where the thickest section of low-density sedimentary rocks is present. Hence the gravity gradient trends in the opposite direction from what might be expected.

REFERENCES

- Aeronautical Chart and Information Center, 1968, Transcontinental geophysical survey (35° – 39° N) Bouguer gravity map from 100° to 112° W longitude: U.S. Geol. Survey Misc. Geol. Inv. Map I-533-B, scale 1:1,000,000.

- Barker, Fred, 1969, Precambrian geology of the Needle Mountains, southwestern Colorado: U.S. Geol. Survey Prof. Paper 644-A, 35 p.
- Behrendt, J. G., and Woollard, G. P., 1961, An evaluation of the gravity control network in North America: *Geophysics*, v. 26, no. 1, p. 57-76.
- Bott, M. H. P., 1960, The use of rapid digital computer methods for direct gravity interpretation of sedimentary basins: *Royal Astron. Soc. Geophys. Jour.*, v. 3, p. 63-67.
- Bromfield, C. S., 1967, Geology of the Mount Wilson quadrangle, western San Juan Mountains, Colorado: U.S. Geol. Survey Bull. 1227, 100 p.
- Burbank, W. S., Lovering, T. S., Goddard, E. N., Eckel, E. B., compilers, 1935, Geologic map of Colorado: U.S. Geol. Survey, scale 1:500,000. [reprinted 1959]
- Bush, A. L., and Bromfield, C. S., 1966, Geologic map and sections of the Dolores Peak quadrangle, Dolores and San Miguel Counties, Colorado: U.S. Geol. Survey Geol. Quad. Map GQ-536, scale 1:24,000.
- Bush, A. L., Bromfield, C. S., and Pierson, C. T., 1959, Areal geology of the Placerville quadrangle, San Miguel County, Colorado: U.S. Geol. Survey Bull. 1072-E, p. 299-384.
- Bush, A. L., Marsh, O. T., and Taylor, R. B., 1960, Areal geology of the Little Cone quadrangle, Colorado: U.S. Geol. Survey Bull. 1082-G, p. 423-492. [1961]
- Case, J. E., 1966, Geophysical anomalies over Precambrian rocks, northwestern Uncompahgre Plateau, Utah and Colorado: *Am. Assoc. Petroleum Geologists Bull.*, v. 50, no. 7, p. 1423-1443.
- 1967, Geophysical ore guides along the Colorado Mineral Belt: U.S. Geol. Survey open-file report, 16 p.
- Gaca, J. R., and Karig, D. G., 1965, Gravity survey in the San Luis Valley area, Colorado: U.S. Geol. Survey open-file report, 43 p.
- Karig, D. E., 1965, Geophysical evidence of a caldera at Bonanza, Colorado, in *Geological Survey Research 1965*: U.S. Geol. Survey Prof. Paper 525-B, p. B9-B12.
- Kelley, V. C., 1955, Regional tectonics of the Colorado Plateau and relationship to the origin and distribution of uranium: *New Mexico Univ. Pubs. Geology*, no. 5, 120 p.
- Larsen, E. S., 1942, Alkalic rocks of Iron Hill, Gunnison County, Colorado: U.S. Geol. Survey Prof. Paper 197-A, 64 p.
- Larsen, E. S., Jr., and Cross, Whitman, 1956, Geology and petrology of the San Juan region, southwestern Colorado: U.S. Geol. Survey Prof. Paper 258, 303 p.
- Lipman, P. W., 1968, Geology of the Summer Coon volcanic center, eastern San Juan Mountains, Colorado: *Colorado School Mines Quart.*, v. 63, no. 3, p. 211-236.
- Lipman, P. W., Steven, T. A., and Mehnert, H. H., 1970, Volcanic history of the San Juan Mountains, Colorado, as indicated by potassium-argon dating: *Geol. Soc. America Bull.*, v. 81, no. 8, p. 2329-2352.
- Luedke, R. G., and Burbank, W. S., 1968, Volcanism and cauldron development in the western San Juan Mountains, Colorado: *Colorado School Mines Quart.*, v. 63, no. 3, p. 175-208.
- Olson, J. C., Hedlund, D. C., and Hansen, W. R., 1968, Tertiary volcanic stratigraphy in the Powderhorn-Black Canyon region, Gunnison and Montrose Counties, Colorado: U.S. Geol. Survey Bull. 1251-C, 29 p.
- Pakisier, L. C., 1964, Gravity, volcanism, and crustal structure in the southern Cascade Range, California: *Geol. Soc. America Bull.*, v. 75, p. 611-620.
- Plouff, Donald, 1966, Digital terrain corrections based on geographic coordinates [abs.]: *Geophysics*, v. 31, no. 6, p. 1208.
- Popenoe, Peter, and Luedke, R. G., 1970, Interpretation of the aeromagnetic pattern of the Uncompahgre primitive area, San Juan Mountains, Colorado: U.S. Geol. Survey open-file report, 26 p.
- Popenoe, Peter, and Steven, T. A., 1969, Interpretation of the aeromagnetic pattern of the San Juan primitive area, Colorado: U.S. Geol. Survey open-file report, 7 p.
- Stark, J. T., and Behre, C. H., Jr., 1936, Tomichi Dome flow: *Geol. Soc. America Bull.*, v. 47, p. 101-110.
- Steven, T. A., 1968, Critical review of the San Juan peneplain, southwestern Colorado: U.S. Geol. Survey Prof. Paper 594-I, 19 p.
- Steven, T. A., and Ratté, J. C., 1960, Geology and ore deposits of the Summitville district, San Juan Mountains, Colorado: U.S. Geol. Survey Prof. Paper 343, 70 p.
- 1965, Geology and structural control of ore deposition in the Creede district, San Juan Mountains, Colorado: U.S. Geol. Survey Prof. Paper 487, 90 p.
- U.S. Geological Survey, 1969, *Geological Survey Research 1969*, chapter A: U.S. Geol. Survey Prof. Paper 650-A, p. A41.
- 1970, Aeromagnetic map of the Cripple Creek-Saguache area, south-central Colorado: U.S. Geol. Survey open-file map, 3 sheets.
- Vogel, J. D., 1962, Geology of the Cortez 2° quadrangle: U.S. Geol. Survey open-file map.



Rb-Sr AND FISSION-TRACK AGE DETERMINATIONS IN THE PRECAMBRIAN PLUTONIC BASEMENT AROUND THE SUPERSTITION VOLCANIC FIELD, ARIZONA

By J. S. STUCKLESS¹ and C. W. NAESER, Dekalb, Ill., Denver, Colo.

Abstract.—The plutonic rocks of the Precambrian basement around the Superstition volcanic field, Arizona, show the effects of three geologic events. The oldest is the emplacement of quartz diorite, and the second is the emplacement of granite (1,395±45 m.y. by Rb-Sr mineral and whole-rock isochron and 1,390±40 m.y. by fission-track age in sphene). The second event was intense enough to completely reset the fission-track age for sphene in the quartz diorite (1,390±60 m.y.) and to disturb the Rb-Sr whole-rock isochron (1,540±84 m.y.). The third event is related to cooling of the rock below 100°C after Laramide uplift and is indicated by a fission-track age in apatite of 50.1±0.8 m.y.

The Superstition volcanic field is approximately 60 km east of Phoenix, Ariz. and is surrounded by Precambrian plutonic rocks (fig. 1). The plutonic rocks range from quartz diorite to granite but are largely quartz monzonite. They are generally weathered and decomposed. In a few places, prospects with shafts as much as 20 m in depth expose no fresh rock.

Two different plutonic rocks may be distinguished in the Precambrian basement around the Superstition volcanic field. One is a biotite quartz diorite to quartz monzonite which contains more than 10 percent mafic minerals (fig. 1, AP-209, AP-211, AP-231, and 8144). In outcrop, the rock is typically dark and coarsely equigranular, and it may be slightly foliated. Mafic segregates of biotite and hornblende occur locally. This unit somewhat resembles the Madera Diorite (Ransome, 1903) which crops out in the Pinal Mountains east of Superior, Ariz.

The second plutonic unit is a porphyritic granite to quartz monzonite which contains less than 10 percent mafic minerals (fig. 1, AP-202, 8145). In outcrops, this rock is typically light pink and coarse grained, and it contains large (5 cm) phenocrysts of orthoclase. This unit is similar to the Ruin Granite (Ransome, 1903) which crops out east of Superior.

ANALYTICAL PROCEDURES

Fission-track dating

The methods used in separating, mounting, and polishing

¹Department of Geology, Northern Illinois University.

grains used in this study are similar to those described by Naeser (1967). Spontaneous fission tracks were etched in sphene by using 50-molal NaOH at 130°C for 5 minutes. Apatite was etched with 10-percent HNO₃ at 20°C for 25 seconds.

After etching, the mineral mounts were covered with muscovite and irradiated. The neutron flux was monitored by use of a glass standard containing 0.35 ppm U.

After irradiation, the muscovite detectors were etched and mounted, and the glass standard was mounted, polished, and etched. The neutron dose was determined by counting the fission tracks in the glass standard. Fission tracks were counted in the minerals and corresponding areas in the muscovite. In this study, all of the mineral surfaces etched were polished surfaces; therefore, the tracks on these surfaces were produced by radiation from two directions. The induced tracks in the muscovite were caused by radiation from only one direction; therefore, the number of tracks counted in the muscovite must be doubled when applied to the age equation (Fleischer and others, 1965).

The “±” following the age determination on a single grain (table 1) represents one standard deviation and is calculated from the induced, fossil, and standard track densities. The “±” following the mean ages is two times the standard error of the mean. The decay constant used in calculating the ages reported was 6.85×10^{-17} year⁻¹.

Table 1.—Fission-track ages for the granitic basement of the Superstition area, Arizona

Sample No.	Unit	Sphene (million years)	Apatite (million years)
AP-202 ...	Granite ..	1,440±219	49.9±8.8 } 48.9±16 } 50.5±8.7 } 51.0±12 }
		1,340±267	
		1,410±289	
		1,380±295	
		1,390±40	
AP-211	Quartz diorite ..	1,300±145	1,390±60
		1,480±164	
		1,480±157	
		1,410±151	
		1,300±150	
		1,360±154	

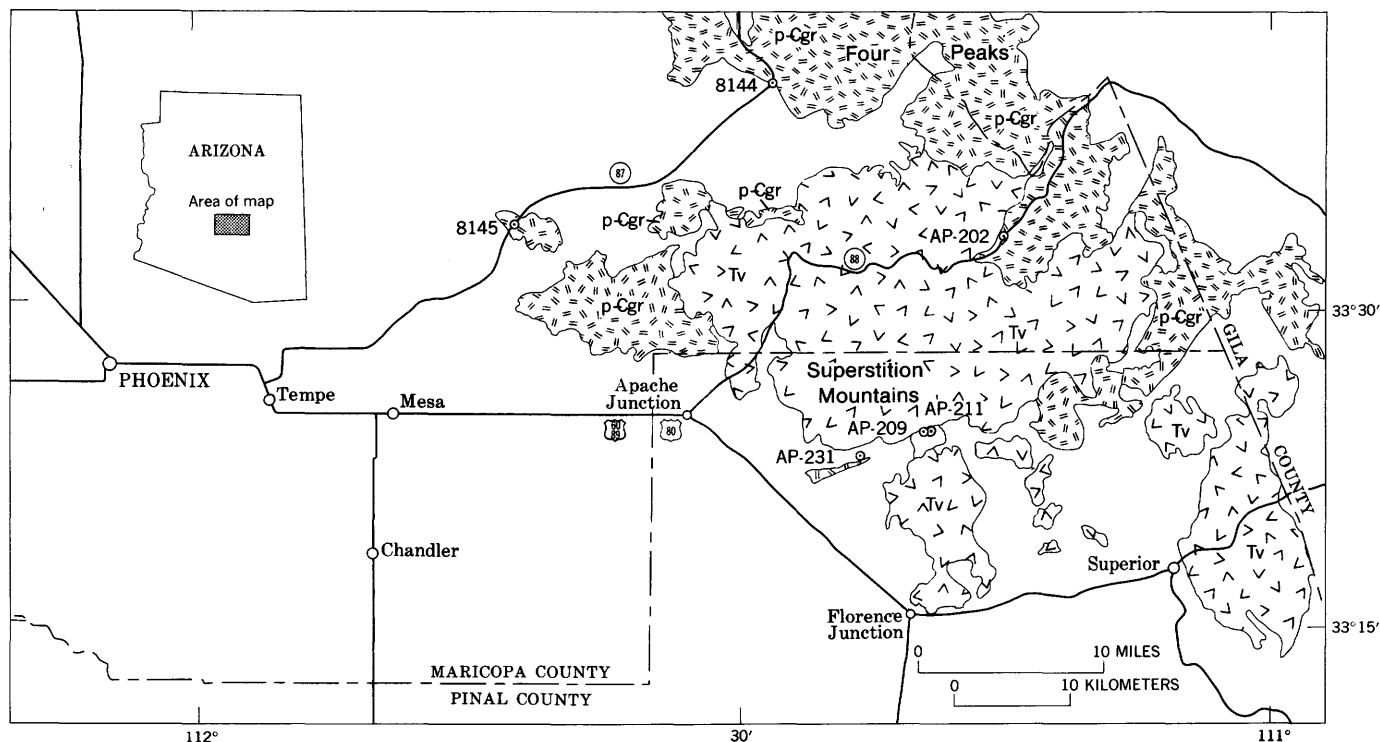


Figure 1.—Index map of Tertiary volcanic rocks (Tv), the surrounding Precambrian granitic rocks (p-Cgr), and sample locations in the Superstition-Superior area, Arizona. Generalized geology from Wilson and others (1969).

Rb-Sr dating

Plagioclase, potassium feldspar, and biotite typically compose 70 to 80 percent of the rocks used in this study and account for almost all the rubidium and strontium. Because these minerals have greatly different Rb/Sr and $\text{Sr}^{87}/\text{Sr}^{86}$ values, large (1–2 kg) whole-rock samples were used and were finely crushed (~100 mesh) before final splitting. It is believed that this procedure made sampling error small relative to other sources of error.

Samples of 1 to 0.5 g were split off and dissolved in analytical grade HF and H_2SO_4 or HClO_4 in Teflon or platinum crucibles. After dissolution the solutions were evaporated to dryness, and the residues were leached with 2.6N HCl. The strontium was then separated from rubidium in an ion-exchange column. Blank measurements for strontium and rubidium show strontium always less than $0.03 \mu\text{g}$ per analysis. Spikes enriched in Sr^{84} and Rb^{87} were added at the start of dissolution.

Mass analyses were made on a 30-cm radius, 90° sector, single-focusing mass spectrometer using a triple-filament ionization mode and a simple Faraday cage as the collector. The purified elements were loaded as chlorides on previously outgassed rhenium filaments. The isotopic composition of strontium were normalized to a $\text{Sr}^{86}/\text{Sr}^{88}$ value of 0.1194. During this study a $\text{Sr}^{87}/\text{Sr}^{86}$ value of 0.7083 ± 0.0001 was determined for the Eimer and Amend SrCO_3 standard.

The $\text{Sr}^{87}/\text{Sr}^{86}$ values were calculated from spiked analyses after correcting for machine discrimination. The precision of the $\text{Sr}^{87}/\text{Sr}^{86}$ measurements is estimated to be ± 0.0004 . The concentrations of rubidium were calculated using raw machine ratios for the spiked samples and common rubidium. The precision of the rubidium concentrations is estimated to be 1.5 percent.

The ages reported in table 2 are calculated according to the two-error regression of McIntyre, Brooks, Compston, and Turek (1966), using a Rb^{87} decay constant of $1.39 \times 10^{-11} \text{ year}^{-1}$. The errors reported for age and initial $\text{Sr}^{87}/\text{Sr}^{86}$ values are given at the 95-percent level of confidence.

RESULTS AND CONCLUSIONS

The Rb-Sr data for the granite fit an isochron indicating an age of $1,395 \pm 45$ m.y. (table 2) within the limits of experimental error (model 1 of McIntyre and others, 1966). This age agrees closely with that determined by fission-track dating of sphene from the granite ($1,390 \pm 40$ m.y., table 1). Together, the two methods suggest that the granite was emplaced approximately 1,390 m.y. ago and has not been subjected to chemical or large thermal disturbances since its emplacement.

Livingston (1960) has dated a rock in Gila County, Ariz., that he identified as the Ruin Granite. He reported K-Ar ages of $1,440 \pm 25$ m.y. for biotite and plagioclase, and a Rb-Sr age of $1,470 \pm 110$ m.y. for mineral and whole-rock samples.

Table 2.—Rb-Sr isotope data and ages for the granitic basement of the Superstition area, Arizona

Sample No. ¹	Sample type	Calculated Sr ⁸⁷ /Sr ⁸⁶ _N	Sr ⁸⁶ × 10 ⁻⁸ moles/gram	Rb ⁸⁷ × 10 ⁻⁸ moles/gram	Rb ⁸⁷ /Sr ⁸⁶
Rocks of the younger pluton (calculated age 1,395 ± 45 m.y.) ²					
AP-202	Whole-rock granite	0.80809	14.85	77.61	5.226
AP-202	Plagioclase	.70714	55.73	7.120	.1277
AP-202	Biotite	7.7679	.9609	347.9	363.1
8145	Whole-rock granite	1.0906	7.209	142.2	19.72
Rocks of the older pluton (calculated age 1,540 ± 84 m.y.) ³					
AP-209	Whole-rock quartz diorite.	0.73607	31.44	42.85	1.363
AP-211	do.	.72309	37.70	26.42	.7010
AP-231	Whole-rock quartz monzonite.	.99187	7.461	97.90	13.12
8144	do.	.76691	22.64	61.99	2.738

¹Sample locations are shown on figure 1. Sr⁸⁷/Sr⁸⁶_N values are normalized to Sr⁸⁷/Sr⁸⁶ = 0.1194. Sr⁸⁷/Sr⁸⁶_i is the calculated initial ratio.

²Sr⁸⁷/Sr⁸⁶_i = 0.7047 ± 0.0017 (by model 1 of McIntyre and others, 1966).

³Sr⁸⁷/Sr⁸⁶_i = 0.7074 ± 0.0026 (by model 3 of McIntyre and others, 1966).

Livingston (1969) also reported a Rb-Sr whole-rock date of 1,370 ± 60 m.y. for a granite body east of Four Peaks (fig. 1). Damon (1968) summarized dates obtained on several Arizona granitoid bodies as being between 1,375 and 1,450 m.y. The ages obtained for the granite during this study are in good agreement with the age of the plutonic episode described above.

The Rb-Sr data for the older quartz diorite do not fit an isochron within the limits of experimental error. The best fit is obtained with model 3 of McIntyre and others (1966), which is applicable for samples having different initial Sr⁸⁷/Sr⁸⁶ values or systems which have not remained completely closed. The calculated age for the isochron is 1,540 ± 84 m.y., with an initial Sr⁸⁷/Sr⁸⁶ value of 0.7074 ± 0.0026 (table 2). The relatively high initial ratio suggests that the system has been disturbed, but the high initial ratio also could be attributed to an earlier high-grade metamorphic origin.

The fission-track age determined for sphene from the older plutonic rock (1,390 ± 60 m.y., table 1) also indicates that the older pluton has not remained a closed system since its formation. The fission-track date indicates that the rock was heated above 400°C at the time the granite was intruded (Naeser and Faul, 1969). This heating could have been accompanied by an incomplete redistribution of rubidium and (or) strontium.

If the rocks of the older pluton have been disturbed, the measured Rb-Sr age probably will be too young. A major plutonic and orogenic episode is well documented in Arizona and adjacent areas between 1,650 and 1,760 m.y. ago (for summaries, see Wasserburg and Lanphere, 1965; Livingston and Damon, 1968). Silver (1966) has obtained a U-Pb age on zircon of 1,660 m.y. at Sunflower (20 km north of Four

Peaks, fig. 1). Livingston (1969) obtained Rb-Sr whole-rock ages of 1,630 ± 90 m.y. (east of Four Peaks) and 1,730 ± 30 m.y. (at Mount Madera in the Pinal Mountains east of Superior).

In comparison with these dates, the older plutonic rocks appear to yield an age which is too young to be an emplacement age. Because the sphene was completely reset at 1,390 m.y., and because the Rb-Sr results do not fit an isochron within the limits of analytical uncertainty, we conclude that the reported age (1,540 ± 84 m.y., table 2) represents an averaging of the age of emplacement and the age of heating by the granite. Further, we conclude that the older plutonic rocks may be part of the older plutonic basement in Arizona.

The youngest age recorded in the Precambrian rocks near the Superstition volcanic field is from the fission-track age in apatite (50.1 ± 0.8 m.y., table 1). This age may be related to the cooling of the rocks to less than 100°C after Laramide uplift and erosion (Naeser and Faul, 1969). In central Arizona, extensive basin-fill arkosic conglomerates provide evidence that this uplift occurred after the early Tertiary (Sell, 1968). Thus, the fission-track date is in accord with this age assignment.

REFERENCES

- Damon, P. E., 1968, Application of the potassium-argon method to the dating of igneous and metamorphic rocks within the Basin Ranges of the southwest: *Arizona Geol. Soc. Southern Arizona Guidebook III*, p. 7-20.
- Fleischer, R. L., Price, P. B., and Walker, R. M., 1965, Effects of temperature, pressure, and ionization on the formation and stability of fission tracks in minerals and glasses: *Jour. Geophys. Research*, v. 70, p. 1497-1502.

- Livingston, D. E., 1969, Geochronology of older Precambrian rocks in Gila County, Arizona: Arizona Univ., Tucson, Ph. D. thesis, 224 p.
- Livingston, D. E., and Damon, P. E., 1968, The ages of stratified Precambrian rock sequences in central Arizona and northern Sonora: Canadian Jour. Earth Sci., v. 5, p. 763-772.
- McIntyre, G. A., Brooks, C., Compston, W., and Turek, A., 1966, A statistical assessment of Rb-Sr isochrons: Jour. Geophys. Research, v. 71, p. 5459-5468.
- Naeser, C. W., 1967, The use of apatite and sphene for fission track age determinations: Geol. Soc. America Bull., v. 78, p. 1523-1526.
- Naeser, C. W., and Faul, H., 1969, Fission track annealing in apatite and sphene: Jour. Geophys. Research, v. 74, p. 705-710.
- Ransome, R. L., 1903, Geology of the Globe Copper district, Arizona: U.S. Geol. Survey Prof. Paper 12, 1968 p.
- Sell, J. D., 1968, Correlation of some post-Laramide Tertiary units, Globe (Gila County) to Gila Bend (Maricopa County), Arizona: Arizona Geol. Soc. Southern Arizona Guidebook III, p. 69-74.
- Silver, L. T., 1966, U-Pb isotope relations in Precambrian zircons from Bagdad, Arizona [abs.]: Geol. Soc. America, Rocky Mountain sec., 19th Ann. Mtg., Program, p. 62.
- Wasserburg, G. J., and Lanphere, M. A., 1965, Age determinations in the Precambrian of Arizona and Nevada: Geol. Soc. America Bull., v. 76, p. 735-758.
- Wilson, E. D., Moore, R. T., and Cooper, J. R., 1969, The geologic map of Arizona: Arizona Bur. Mines and U.S. Geol. Survey, scale 1:500,000.



PERMIAN(?) TO JURASSIC(?) METAVOLCANIC AND RELATED ROCKS THAT MARK A MAJOR STRUCTURAL BREAK IN THE NORTHERN WHITE MOUNTAINS, CALIFORNIA-NEVADA

By D. F. CROWDER¹ and D. C. ROSS, Menlo Park, Calif.

Abstract.—Contorted, faulted, and altered metavolcanic rocks and associated volcanoclastic rocks, probably in the age range of Permian to Jurassic, are exposed in a north-trending belt in the northern White Mountains, Calif. The volcanic belt is abruptly cut off to the south and east by Jurassic and Cretaceous granitic intrusive bodies, which fill a major structural break between the volcanic belt and upper Precambrian and Cambrian metasedimentary rocks. This break is most probably a thrust fault on which the older sedimentary rocks have overridden the volcanic and volcanoclastic section. The section consists dominantly of a volcanic pile—flows, tuffs, and breccias—with a considerable compositional variation from rhyolite to basalt. Overlying and underlying the pile are volcanoclastic and related sedimentary rocks, dominantly siltstone and sandstone with abundant layers and lenses of pebble and cobble conglomerate.

From 1964 to 1969 Dwight F. Crowder made a detailed geologic study of the pre-Tertiary rocks of the White Mountain Peak and Benton quadrangles in the rugged northern White Mountains of California-Nevada. He had completed the geologic mapping, had nearly completed preparing the geologic maps for publication, and was about to begin report writing when he was killed in an automobile accident in April 1970. At this time I (Ross) was assigned the job of completing the maps for publication and preparing such reports as might be suitable. Like most of us, Dwight carried his ideas on the kind of reports he wanted to write in his head. Therefore this report is a synthesis of as much data as I could glean from Dwight's field and thin section notes, combined with further hand specimen and thin section study by me. I made a brief two-week trip to the field area to familiarize myself with the rock units, but anyone who knows the awesome topography of the field area can appreciate the limitations of such a visit. I want to emphasize that the raw material for this report was almost solely Dwight's. By necessity, the words and conclusions of the report are solely mine. I hope I have succeeded in transmitting some of the thoughts that Dwight would have intended to express.

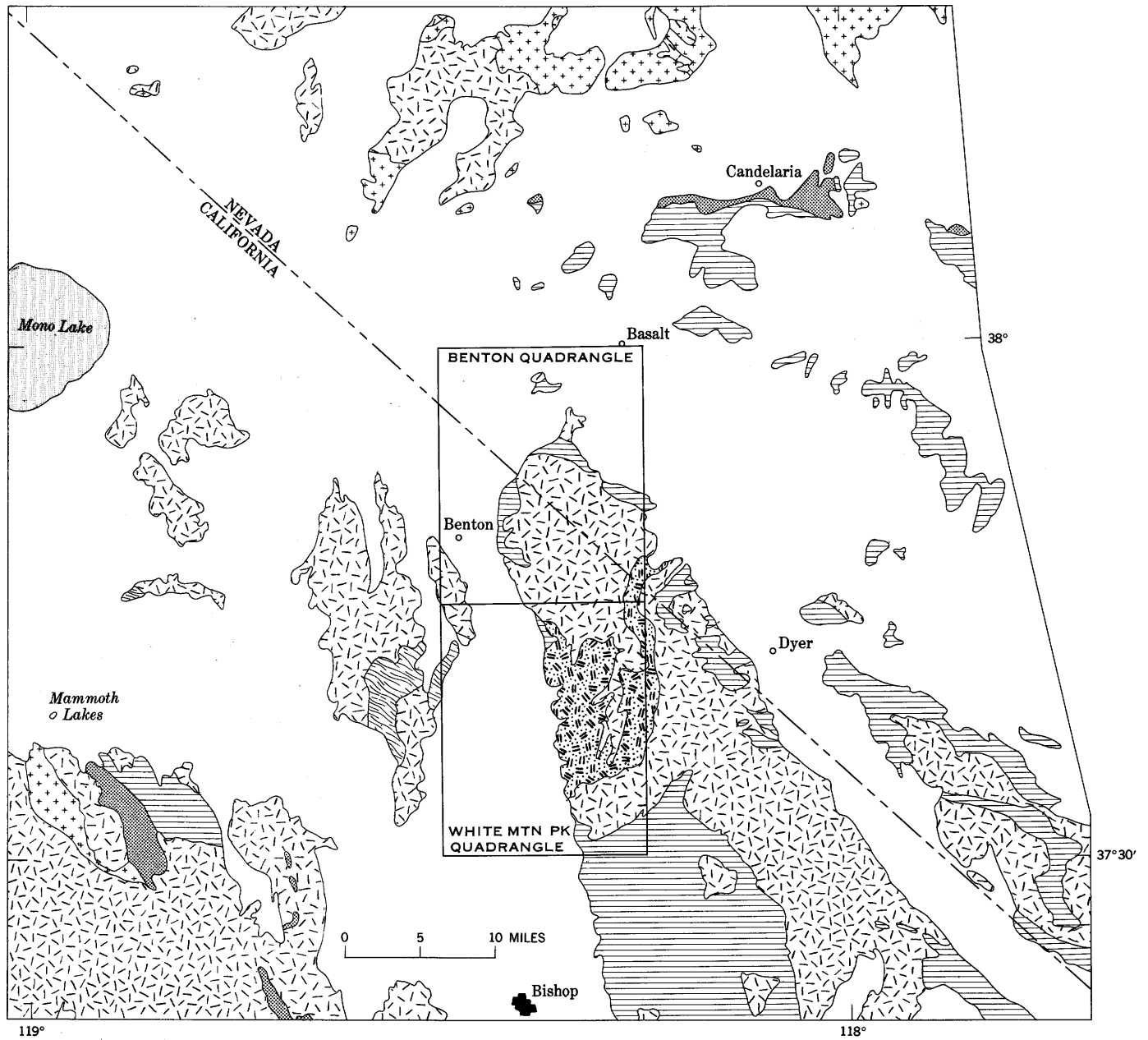
¹Deceased April 8, 1970.

REGIONAL SETTING

The metavolcanic rocks and the associated volcanoclastic metasedimentary rocks of the northern White Mountains (fig. 1) form a grossly north-trending belt that is much contorted and faulted, particularly in its western part (fig. 2). These units have been mapped in the following quadrangles: White Mountain Peak (Crowder and Sheridan, 1972), Benton (Crowder and others, 1972), Mount Barcroft (Krauskopf, 1972), and Davis Mountain (unpub. data, Robinson and Crowder). The paucity of structural symbols in many areas of these quadrangles reflects alteration that has masked original structures and (or) fearsome topography that limited access. Crude reconstruction of the much disturbed metavolcanic and volcanoclastic section (fig. 2) suggests a lower sequence of volcanoclastic metasedimentary rocks, with limestone and conglomerate, that is overlain by a sequence of felsic and mafic flows, breccias, and tuffs. These volcanic rocks appear to be overlain by a higher sedimentary sequence of volcanoclastic character that is very similar to the basal sedimentary sequence. Krauskopf (1972) notes that the upper sedimentary sequence is unconformable on the metavolcanic rocks. This unconformity may be a relatively minor break, such as would be expected in the accumulation of a section of volcanic and volcanoclastic rocks.

The nearest comparable rocks are in Mineral County, Nev., about 30 miles to the north (fig. 3). Large areas there are covered by metamorphosed flows, tuffs, and volcanic breccias ranging in composition from rhyolite to andesite. Associated with these rocks are some limestones as well as fine- to coarse-grained clastic sedimentary rocks, parts of which are rich in volcanic debris. Some of these rocks are Triassic and Jurassic (Muller and Ferguson, 1936), but recent work (Speed, 1971) suggests that upper Paleozoic rocks are also present. Metamorphosed volcanic rocks and volcanoclastic sedimentary rocks with a wide range of composition, and with widespread Triassic and Jurassic fossils, are also common just west of Mineral County (Moore, 1960, 1969).

The Ritter Range pendant (fig. 3), about 40 miles to the



119°

118°

EXPLANATION

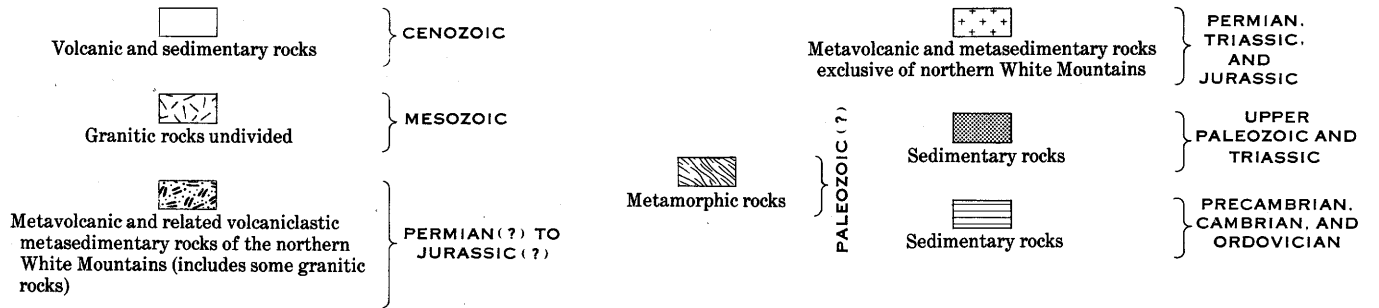


Figure 1.—Geologic setting of metavolcanic and related rocks of the northern White Mountains area, California-Nevada.

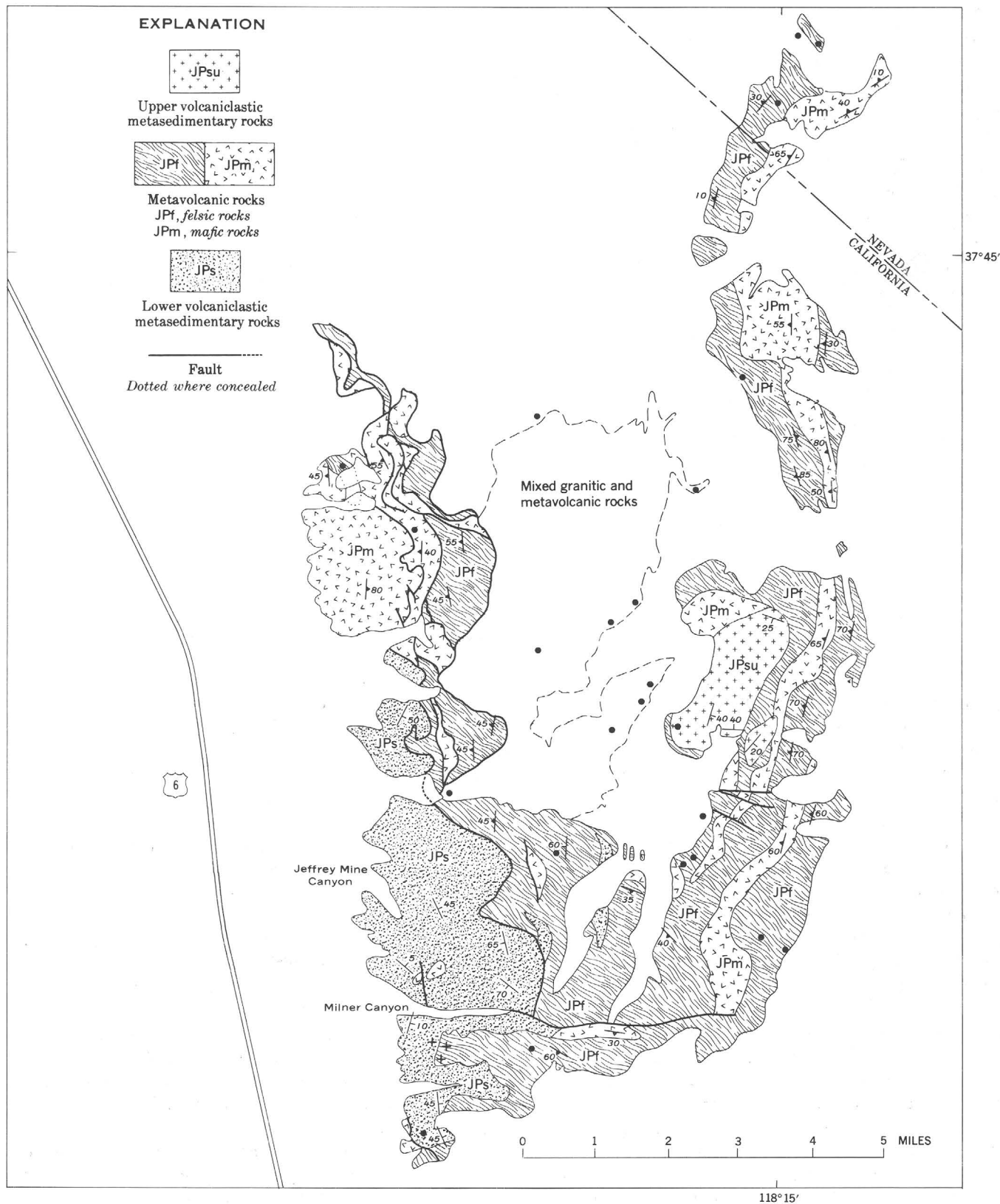


Figure 2.—Index to Permian(?) to Jurassic(?) metavolcanic rocks of the northern White Mountains. Attitudes generalized from larger scale geologic maps. Dots show locations of specimens with porphyritic volcanic texture and intense alteration to chessboard albite and quartz.

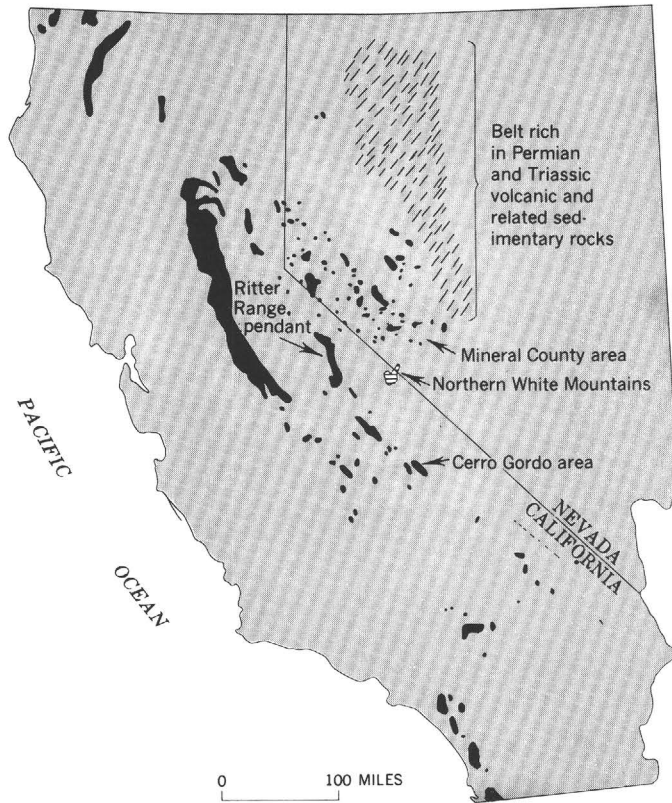


Figure 3.—Distribution of Permian and Mesozoic volcanic and related sedimentary rocks in California and western Nevada.

west, contains a section of some 30,000 feet of dominantly metavolcanic rocks (Huber and Rinehart, 1965). The upper half of the section is dominantly tuff breccia with fragments as large as 1 foot. The lower half is chiefly crystal lithic tuff. Flows and hypabyssal intrusive rocks are less common. Though compositions range from rhyolite to basalt, the average is near rhyodacite or dacite. Scattered through the section are metamorphosed clastic sedimentary layers, in part tuffaceous, ranging from granule conglomerate to mudstone. Carbonate layers are also present. Fossils of Early Jurassic age are present about 8,500 feet above the base; the section is considered Triassic(?) and Jurassic in age.

Another comparable section is located in the Cerro Gordo area, about 70 miles to the south (fig. 3), where there are some 2,200 feet of tuffaceous rocks, shale, sandstone, and conglomerate overlain by and intercalated with a pile of flows, breccias, and tuffs in which both quartz-free and quartz-bearing units have been recognized (Merriam, 1963, p. 29). The volcanic section is considered Middle Triassic(?) in age, though the upper beds could be as young as Jurassic.

These relatively nearby volcanic sections all have some affinities with the northern White Mountains rocks, but specific correlations cannot even be suggested at this time. About all that can be said is that these northern White Mountains rocks are made up of the same general rock types as

the regionally significant pile of upper Paleozoic and Mesozoic volcanic and volcanoclastic rocks. Similar rock types are not known elsewhere in the pre-Tertiary section of this region. Granitic rocks of Jurassic and Cretaceous age intrude the metavolcanic section of the northern White Mountains.

The White Mountains metavolcanic rocks appear to mark the southern end of a broad belt of similar rocks containing volcanic strata of Permian, Triassic, and Jurassic ages (Silberling and Roberts, 1962) that extends southwestward from western Nevada (fig. 3). The metavolcanic units also mark an abrupt break in the distribution of Mesozoic volcanic rocks in this region. The metavolcanic rocks of the White Mountains terminate abruptly against Precambrian and Cambrian sedimentary rocks (Nelson, 1966). Unfortunately, Jurassic and Cretaceous granitic rocks fill the break between the two sequences, so it is not possible to determine if the break is a fault or an unconformity. In southern Mineral County, Permian clastic rocks unconformably overlie Ordovician clastic rocks, so this break could be an unconformity. However, Stewart and others (1966) have noted that to the south and east of this region there is abundant evidence that upper Precambrian, Cambrian, and Ordovician strata are thrust over upper Paleozoic rocks. The abrupt termination of the metavolcanic and related rocks, coupled with the fact that they are virtually surrounded by Precambrian and lower Paleozoic rocks, certainly suggests a thrust relationship.

VOLCANICLASTIC AND OTHER SEDIMENTARY ROCKS

A thick section of volcanoclastic and associated sedimentary rocks is well exposed along the base of the White Mountains, in the Milner Canyon area. The base of this section is not exposed, and the total thickness cannot be measured because of structural complications, but several thousand feet of beds are probably present. South of Milner Canyon these beds are overlain by a thick section of metavolcanic rocks. The nearly horizontal contact is readily visible from U.S. Highway 6 opposite Milner Canyon. The contact north of Milner Canyon is a fault zone, and there is some shearing south of the canyon also at the contact.

The metavolcanic sequence near Milner Canyon is overlain by another section of volcanoclastic rocks, similar to the lower ones. These rocks are thought to rest unconformably on the metavolcanic rocks in the Mount Barcroft quadrangle (Krauskopf, 1972), but there also appears to be some local interlayering between the two sequences. At least several hundred feet of beds are exposed, but the original total thickness cannot be estimated because an unknown thickness has been eroded away.

From a distance the lower volcanoclastic sequence appears to form very distinctive silvery-gray to greenish-gray slopes. In part these rocks are phyllitic to schistose, and the slopes glisten distinctly in the sunlight. Closer observation shows that these slopes are liberally laced with lenses and layers that weather out in relief (fig. 4). These beds are coarser clastic



Figure 4.—Volcaniclastic and clastic sedimentary rocks on the north slope of Milner Canyon. Prominent darker lenses are mostly conglomerate and less commonly limestone.

layers, including conglomerates with clasts as large as 6 inches, and carbonate layers, that tend to weather brownish gray.

The bulk of the lower section is siltstone and fine-grained sandstone with abundant micaceous material (fig. 5). These rocks are commonly metamorphosed to slate, phyllite, and

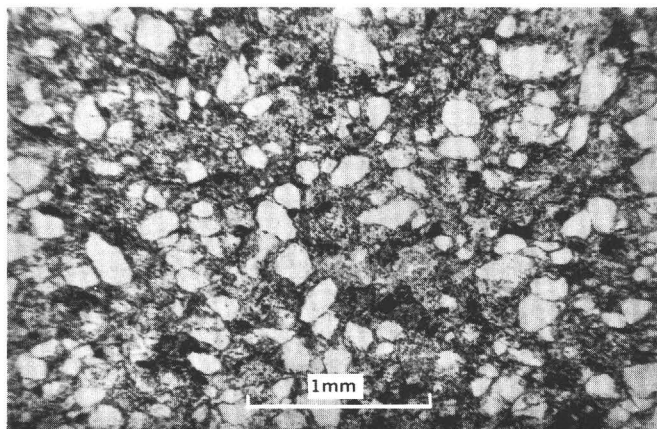


Figure 5.—Rounded to angular quartz grains in sericite and quartz matrix. Plane light.

schist, but the clastic nature of the rock is almost invariably preserved. These rocks grade to coarser green to gray sandstone and up into pebble and cobble conglomerate. Many of the coarser clastic rocks have recognizable volcanic clasts, and some of the finer grained rocks resemble tuffs; also, some sericite-rich schists were probably originally rhyolitic tuffs or tuffaceous sediments. Many of the coarser layers have well-rounded clasts that are dominantly quartzite (fig. 6). The finer grained conglomerates and coarse sandy rocks seem to be richer in volcanic debris and also tend to be more extensively stretched (fig. 7). Most conglomerates have a quartz-rich sandy matrix, but some have a carbonate matrix instead. Most of the sandstone could more specifically be called graywacke, as it is rich in micaceous material and in part has recognizable rock fragments.

In the section of volcaniclastic metasedimentary rocks overlying the metavolcanic rocks the finer grained rocks are dominantly gray to green siltstone and graywacke with some calcareous layers; these rocks contain volcanic clasts. Conglomerate is common in the lower part of the section and may locally form the base of the sequence. Clasts as much as several inches across consist of quartzite and of volcanic rock. The latter are particularly abundant. Some of the volcanic clast-

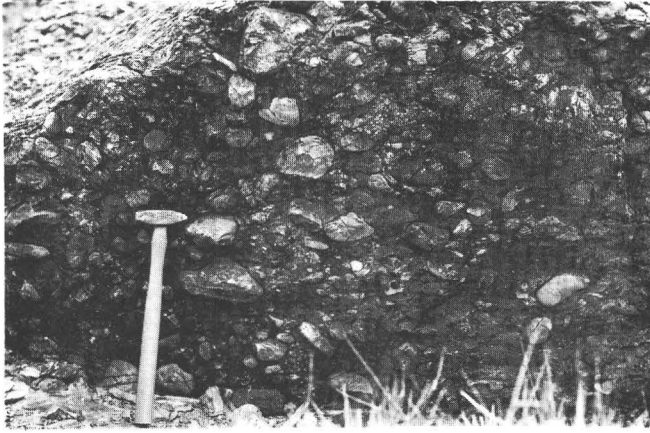


Figure 6.—Conglomerate with well-rounded clasts in lower volcanoclastic and sedimentary sequence. Most coarser fragments are quartzite; lesser metavolcanic and carbonate clasts are present.

rich conglomerate is distinctly purple. These upper volcanoclastic rocks appear to be less phyllitic and schistose than the lower unit near Milner Canyon. Additional volcanoclastic metasedimentary rocks ranging in grain size from siltstone to

conglomerate with clasts several inches across are also present within the metavolcanic section.

METAVOLCANIC ROCKS

In field mapping, the metavolcanic rocks were subdivided on the basis of color into two units—mafic and felsic. This was a very practical field classification, but more detailed study of specimens suggests that the amount of originally mafic volcanic rock (andesite and basalt) was somewhat overemphasized by the field classification. Some of the dark rocks are found to be of intermediate or felsic composition when examined in thin section. On the other hand, albitization and the selective replacement and removal of original ferromagnesian minerals has changed some mafic volcanic rocks into light-colored, felsic-appearing rocks. For example, in all the thin sections examined no pyroxene is preserved, and the only amphibole, probably secondary actinolite, was found in two specimens from the northernmost end of the volcanic rocks. Nonetheless, intermediate and felsic volcanic rocks probably were more abundant than basalt and andesite in the original volcanic pile.

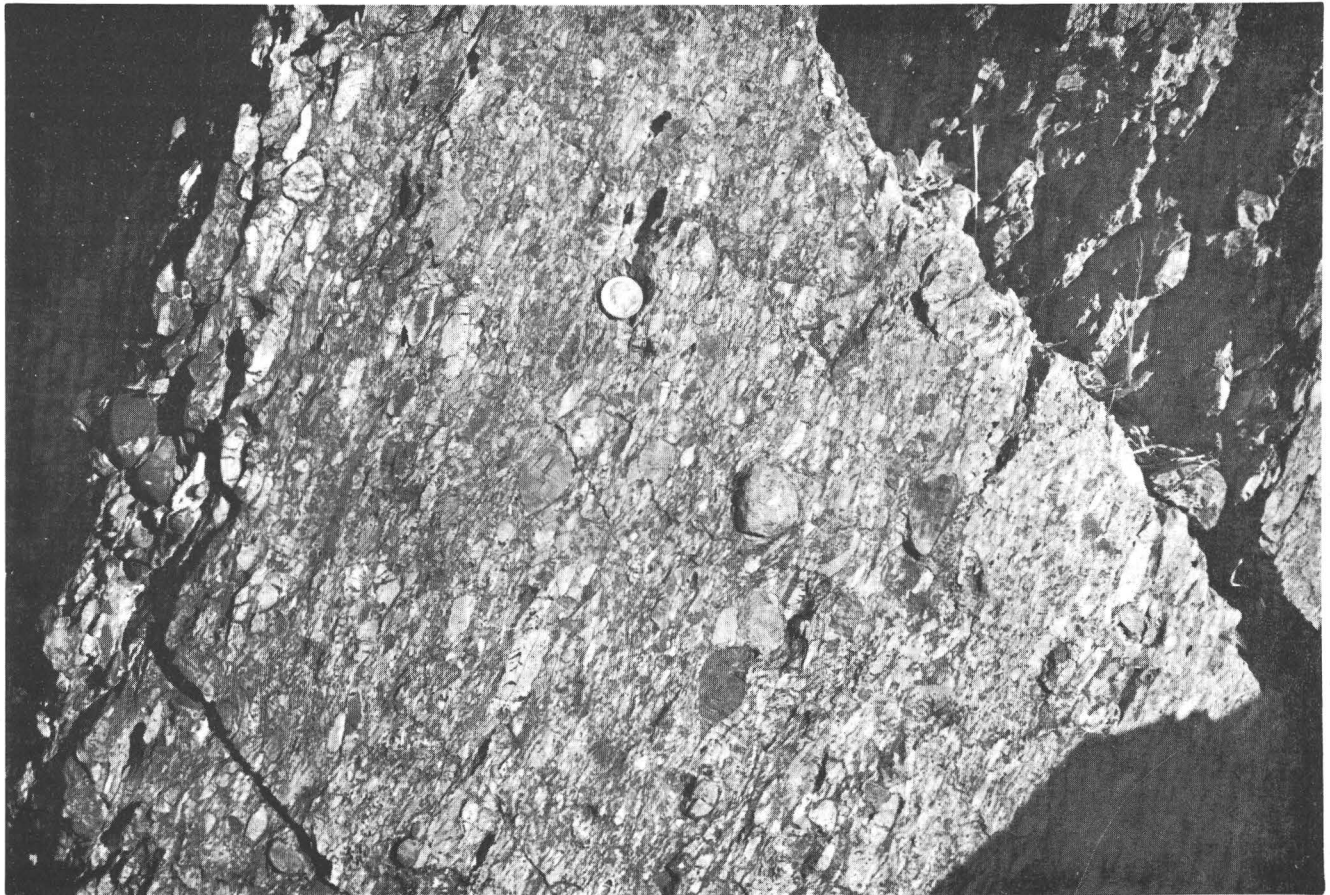


Figure 7.—Somewhat stretched conglomerate with abundant metavolcanic clasts. Quarter dollar shows scale.

Mafic metavolcanic rocks

As already mentioned, primary ferromagnesian minerals have not been preserved in the volcanic rocks. Some of the darker hand specimens are rich in epidote, shreds of light-olive biotite, and opaque minerals. Some of these in clots and clusters suggest pseudomorphs after ferromagnesian minerals. A felty volcanic texture of plagioclase laths is preserved in some rocks, and in part the rocks are porphyritic. All plagioclase has been somewhat altered and now ranges from dirty, saussuritized crystals whose An content cannot be determined, to relatively clear and fresh secondary albite that in part seems to mimic the original volcanic texture.

Those dark specimens now rich in epidote and biotite and low or lacking in quartz are assumed to have been originally andesite or basalt. Preservation of original texture locally indicates that some of these rocks were flows. Others have the appearance of tuff, and some coarser volcanic breccia was seen in the field. Rounded blebs variously filled with quartz, epidote, and sericite are interpreted as amygdules; amygdules are very obvious and abundant in some hand specimens.

One of the most petrologically interesting features of some of these altered mafic metavolcanic rocks is their mineralogic similarity to nearby granitic rocks. Plagioclase is liberally sprinkled with sericite, epidote, and light-olive biotite, and throughout the rest of the rock the only ferromagnesian mineral is biotite sprinkled in shreds and small clusters (fig. 8). Also, metallic opaque minerals are common and in part encrusted with sphene. These are the same features that characterize the nearby granitic terranes. The absence of amphibole and pyroxene in some of the rather dark granitic rocks as well as in the originally mafic volcanic rocks seems particularly noteworthy. In general it seems as though the mafic metavolcanic rocks and the adjoining granitic rocks

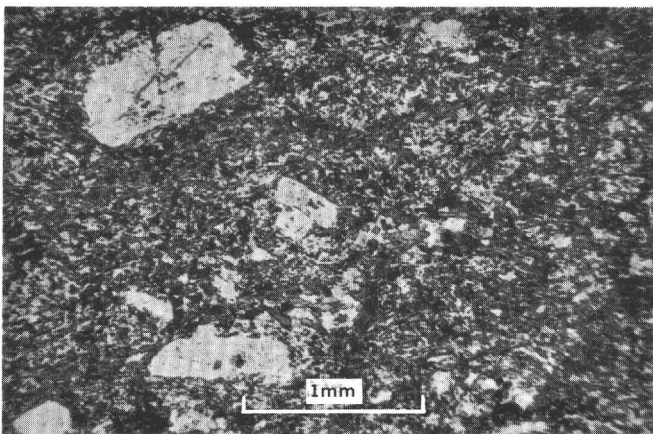


Figure 8.—Intermediate to mafic volcanic rock that preserves somewhat altered plagioclase phenocrysts in a groundmass rich in shreds of biotite—no other ferromagnesian minerals are present.

have both undergone alteration and metamorphism that led to the destruction or recrystallization of the dark minerals. Some of the presumed mafic volcanics that have these characteristics could in fact be parts of dikes or small masses of intrusive granitic material, as they do not have definite volcanic textures, but some do have these same mineralogic features superimposed on a felty, porphyritic volcanic texture and were undoubtedly volcanic rocks.

Felsic metavolcanic rocks

The distinction made here between felsic and mafic metavolcanic rocks is admittedly somewhat arbitrary, as there is a spectrum of types from basalt to rhyolite and there is more interlayering than the generalized map suggests. Nevertheless, there is a preponderance of rather light-colored rocks, many of which superficially resemble quartzite with a somewhat dull sheen. Other rocks in this section closely resemble fine-grained aplite. However, close observation in the field and particularly in thin section clearly shows volcanic textures. These rocks are almost invariably albitized, and some are now composed solely of chessboard albite and quartz, while still retaining a pronounced porphyritic volcanic texture. Some intermediate to mafic metavolcanic rocks have probably been so intensely albitized that they now are felsic in appearance. In fact some strongly albitized specimens have significant sprinkles of biotite, suggesting a transition stage to "felsic" from original mafic rocks. Also, much silica may have been redistributed during the alteration process, for large vein quartz masses are mixed in with altered volcanic rocks in places. Undoubtedly some of the light-colored, altered rocks are transformed mafic metavolcanic rocks, but the bulk of the quartz-rich altered rocks were probably originally felsic metavolcanic rocks.

Many of the less altered rocks consist of various combinations of sodic plagioclase, K-feldspar, and quartz, and lesser amounts of muscovite (or sericite) and biotite. It is surprising, however, that original volcanic texture is well preserved in many specimens, even in some that are totally albitized. Felty mats of plagioclase laths inset with coarser euhedral to subhedral plagioclase and lesser K-feldspar and quartz in crystals as large as 5 mm, but more commonly 2–3 mm across, are particularly striking. Other specimens look like crystal tuff with "phenocrysts," broken fragments and some partly resorbed quartz crystals set in a groundmass rich in sericitic material that seems to mimic flow structure in part. In this terrane it might more commonly reflect shearing. Despite the alteration, some of these specimens display features characteristic of ash flow tuffs. In addition, some schistose rocks rich in sericite may have been ash-rich tuffaceous layers, but this is speculative.

In spite of all the alteration and replacement, it seems safe to suggest that there were abundant rhyolite (and possibly rhyodacite) flows and crystal tuffs (possibly ash flows) in the original volcanic section.

ALTERATION OF THE VOLCANIC SECTION

As already alluded to in the rock descriptions, the whole volcanic section has been to some extent altered (metamorphosed). It has been noted that no primary ferromagnesian minerals are preserved and that albitization is widespread and, in part, intensive. For example, many specimens are now composed almost solely of clean, fresh albite and quartz. X-ray diffractometer runs on selected samples of these rocks showed virtually pure albite of An_{1-3} . Much of the albite has striking chessboard twinning (fig. 9). The complete absence of K-

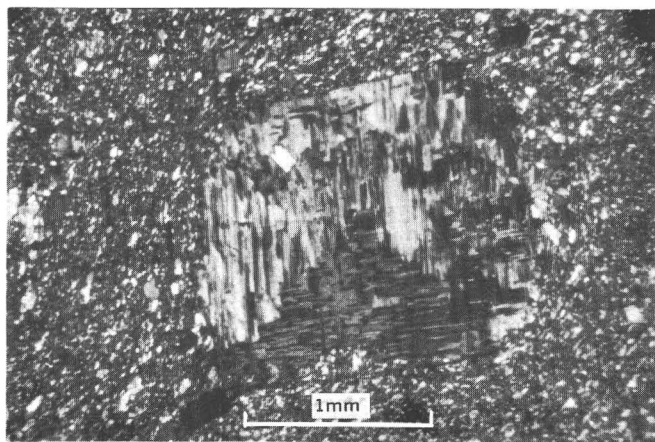


Figure 9.—Plagioclase phenocryst completely altered to chessboard albite. Set in dense groundmass.

feldspar is a hallmark of these rocks. It is even more noteworthy that these specimens preserve a porphyritic volcanic texture. Samples of the most intensely albitized rocks do not appear to be localized by any structures, nor are they concentrated near exposed granitic contacts. Also, these specimens are ones from which thin sections were made; intensive albitization is undoubtedly more widespread, and though it would be very difficult to delineate in mapping, albitization is probably pervasive and present to some extent throughout the volcanic terrane.

Albitization of this sort was described in the granitic rocks of the northern White Mountains by Anderson (1937, p. 55), who noted the same combination of chessboard albite and quartz and interpreted it as the ultimate product of albitization.

Albitization and other alteration give rise to the rather vivid reds, oranges, and yellows of the felsic volcanic rocks, particularly along the White Mountains fault zone. It is particularly evident in Jeffrey Mine Canyon and is strikingly visible from Highway 6. The strongly albitized volcanic rocks in places have a strange "messy" texture (fig. 10), which Anderson (1934) called pseudocataclastic and attributed to replacement. Gilluly (1933) attributed similar looking textures to crushing that provided channels for easy access by albitizing

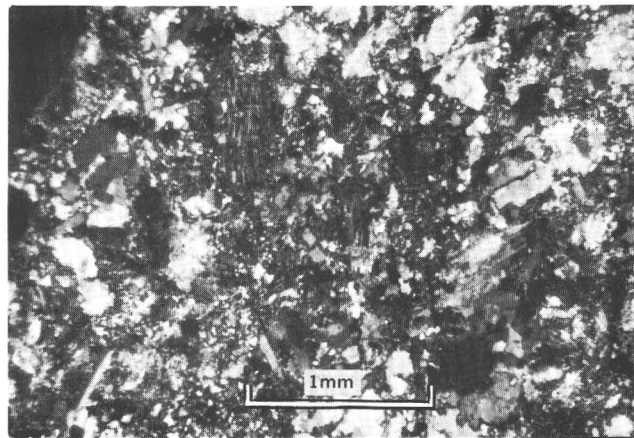


Figure 10.—Pseudocataclastic texture of Anderson (1934) with preserved phenocryst form (block outline). Original volcanic rock is now solely quartz and albite.

solutions. Both processes were probably at work in the White Mountains rocks, but despite the almost complete transformation of the metavolcanic rocks, phenocrysts that point to the original volcanic nature of these rocks are commonly preserved (fig. 10).

The metavolcanic rocks in Jeffrey Mine Canyon (fig. 2) were subjected to intense, but rather localized alteration of another sort. Here andalusite, corundum, diaspore, and pyrophyllite, as well as a number of other minerals, form replacement deposits that have been mined for andalusite. Lemmon (1937) studied this area in detail and considered the deposits to be the result of contact metamorphism. The andalusite deposits are in what Lemmon called metaquartzite—possibly altered metavolcanics. The "metaquartzite" is associated with quartz-sericite schist, sericite schist, and tourmaline schist considered by Lemmon to have been volcanic rocks, and fine-grained metaporphyritic intrusive rocks.

About 1 mile northeast of the Jeffrey Mine Canyon area are prominent turreted outcrops several hundred feet across that consist chiefly of great masses of vein quartz and dull quartzite-like material, parts of which display relict volcanic texture. These rocks also contain rosettes of pyrophyllite. Thus, they seem to bear some relation to the Jeffrey Mine Canyon deposits. This local intense "aluminization" is probably part of the same metasomatic process that destroyed all the primary dark minerals and albitized a vast terrane.

CONCLUSIONS

The metavolcanic and related volcanoclastic metasedimentary rocks of the White Mountains probably belong to the Permian to Jurassic interval, a time of widespread volcanism in this region. They mark the southernmost occurrence of a broad belt that extends through western Nevada, and they are well east of the main northwest-trending metavolcanic belt in the Sierra Nevada.

Little can be concluded about their original composition, as their ferromagnesian minerals and plagioclase have been almost entirely reconstituted, and we know that considerable migration of constituents has taken place. In addition to alteration, structural complications—particularly along the White Mountains front—have confused the original sequence of events.

Probably a range of compositions from basalt to rhyolite was originally present. The section is of unknown thickness, but surely at least several thousand feet thick. Flows, tuffs, and breccias have been recognized, but their relative proportions are not known. The basal part of the section was probably a thick pile of fine- to coarse-grained clastic rocks with some carbonate interlayers. Volcanic debris was common, but coarser beds were also rich in quartzite clasts. These volcanoclastic rocks are overlain by a thick pile of felsic and mafic flows and tuffs in an interlayered sequence that also includes some volcanoclastic beds. Unconformably overlying the volcanic pile are more volcanoclastic deposits much like the lower volcanoclastic rocks.

The fact that these rocks of probable Permian to Jurassic age abruptly abut upper Precambrian and Lower Cambrian strata in the White Mountains indicates a profound break along their east and south sides. Although an unconformity is possible, a fault, probably a thrust, seems much more likely. There is a suggestion that upper Precambrian and Lower Cambrian rocks may form the upper plate of a thrust over Permian(?) to Jurassic(?) rocks, but intrusion of granitic rocks has obliterated any contact evidence.

REFERENCES

- Anderson, G. H., 1934, Pseudo-cataclastic texture of replacement origin in igneous rocks: *Am. Mineralogist*, v. 19, no. 5, p. 185–193.
- 1937, Granitization, albitization, and related phenomena in the northern Inyo Range of California-Nevada: *Geol. Soc. America Bull.*, v. 48, p. 1–74.
- Crowder, D. F., Robinson, P. T., and Harris, D. L., 1972, Geologic map of the Benton quadrangle, California-Nevada: U.S. Geol. Survey Geol. Quad. Map GQ-1013. [In press]
- Crowder, D. F., and Sheridan, M. F., 1972, Geologic map of the White Mountain Peak quadrangle, Mono County, California: U.S. Geol. Survey Geol. Quad. Map GQ-1012. [In press]
- Gilluly, James, 1933, Replacement origin of the albite granite near Sparta, Oregon: U.S. Geol. Survey Prof. Paper 175-C, p. 65–81.
- Huber, N. K., and Rinehart, C. D., 1965, Geologic map of the Devils Postpile quadrangle, Sierra Nevada, California: U.S. Geol. Survey Geol. Quad. Map GQ-437.
- Krauskopf, K. B., 1972, Geologic map of the Mount Barcroft quadrangle, California-Nevada: U.S. Geol. Survey Geol. Quad. Map GQ-960.
- Lemmon, D. M., 1937, Geology of the andalusite deposits in the northern Inyo Range, California: Stanford Univ., Stanford, Calif., Ph. D. thesis, 70 p.
- Merriam, C. W., 1963, Geology of the Cerro Gordo mining district, Inyo County, California: U.S. Geol. Survey Prof. Paper 408, 83 p.
- Moore, J. G., 1960, Mesozoic age of roof pendants in west-central Nevada: Art. 131 in U.S. Geol. Survey Prof. Paper 400-B, p. B285–B289.
- 1969, Geology and mineral deposits of Lyon, Douglas, and Ormsby Counties, Nevada: Nevada Bur. Mines Bull. 75, 45 p.
- Muller, S. W., and Ferguson, H. G., 1936, Triassic and Jurassic formations of west-central Nevada: *Geol. Soc. America Bull.*, v. 47, p. 241–251.
- Nelson, C. A., 1966, Geologic map of the Blanco Mountain quadrangle, Inyo and Mono Counties, California: U.S. Geol. Survey Geol. Quad. Map GQ-529.
- Silberling, N. J., and Roberts, R. J., 1962, Pre-Tertiary stratigraphy and structure of northwestern Nevada: *Geol. Soc. America Spec. Paper* 72, 58 p.
- Speed, R. C., 1971, Golconda thrust, western Nevada: Regional extent: *Geol. Soc. America Abs. with Programs*, v. 3, no. 2, p. 199.
- Stewart, J. H., Ross, D. C., Nelson, C. A., and Burchfiel, B. C., 1966, Last Chance thrust—A major fault in the eastern part of Inyo County, California, in *Geological Survey Research 1966*: U.S. Geol. Survey Prof. Paper 550-D, p. D23–D34.



A CONSPICUOUS FLEXURE IN REGIONAL STRUCTURAL TREND IN THE PUNA OF NORTHWESTERN ARGENTINA

By KENNETH SEGERSTROM and J. C. M. TURNER¹,
Denver, Colo., Buenos Aires, Argentina

Work done in cooperation with the Dirección Nacional de Geología y Minería, under the auspices of the Government of Argentina and the Agency for International Development, U.S. Department of State

Abstract.—Fault-block mountain ranges and valleys of the Puna of northwestern Argentina generally trend north. A major valley or structural trough, occupied by the Salar (saltpan) de Antofalla, exhibits a pronounced dextral bend between lats 25° and 26° S. It is suggested that an east-west lineament between the same latitudes in Chile, which has been observed in satellite photographs, represents an ancient zone of lateral crustal movement along which the preexisting Keile (wedges) and Furchen (furrows) of the Puna were deformed. The deformation, which locally produced flexure rather than faulting of north-south structural features, was Jurassic. Late Cenozoic uplift of the Andes accentuated displacements of the north-striking faults without reactivating the ancient transverse structure.

The Argentine Puna is a high, arid, remote area of interior drainage in northwestern Argentina; the region extends approximately from the Chilean border eastward to long 66° W., and from lat 27° S. northward to the Bolivian border at about 22° S., where it merges with the Bolivian Altiplano (plateau). Reconnaissance mapping of part of the area between 25° and 27° (fig. 1), at 1:500,000 scale, was done by Turner in a single field season (1959–60); the results of his work, together with results of work by others in adjacent areas to the north and east, are summarized by him (Turner, 1970).

In 1965, vertical aerial photographs of the region were taken by Spartan Air Services and were compiled into large mosaics at 1:50,000 and 1:200,000 scale. The photographs give a new insight into regional structure. Through photointerpretation the area of figure 2 was preliminarily mapped at 1:50,000 scale and partially field checked by Segerstrom in October and November 1970 as part of a program of photogeologic mapping and geochemical sampling of Catamarca Province by the Dirección Nacional de Geología y Minería (Plan NOA-1), with headquarters in San Miguel de Tucumán. A parallel

program was undertaken by Fabricaciones Militares for Salta Province, with headquarters in the city of Salta (fig. 1).

REGIONAL SETTING

Location

The area of figure 2 is located in the arid Puna at the extreme northern end of Catamarca Province, about 400 km by road from Salta, Argentina. The road, National Route 53, ends at Antofagasta de la Sierra; a branch leads to the Tincalayu borax mine in the northeast corner of the area. The tiny settlement of Antofalla, in the western part of the area, can be reached with difficulty by jeep. During 1971 a new road, which will give more direct access from San Miguel de Tucumán to Antofagasta de la Sierra, was under construction.

Geology

The puna of northwestern Argentina is characterized by fault-block mountain ranges which rise 5,000–6,000 m above sea level; these ranges are separated by undrained valleys generally covered by salares (salt pans) at 3,500–4,200 m. The regional strike of uplifted and downdropped blocks is approximately north (Turner, 1970, p. 1059). The mountain ranges are composed mainly of Ordovician rocks, which are locally capped by Cenozoic andesite.

Two of the principal downdropped blocks of the area, those of Antofalla and Sijes (fig. 1), can be traced for distances of 235 km and 120 km, respectively; both are very narrow relative to their length, and they are occupied in part by salt pans. The downdropped block that extends southward from the Salar de Antofalla is the locus of Holocene basaltic eruptive centers. The blocks exhibit a pronounced northeast-southwest flexure between the 25th and 26th parallels. The

¹Dirección Nacional de Geología y Minería, Buenos Aires.

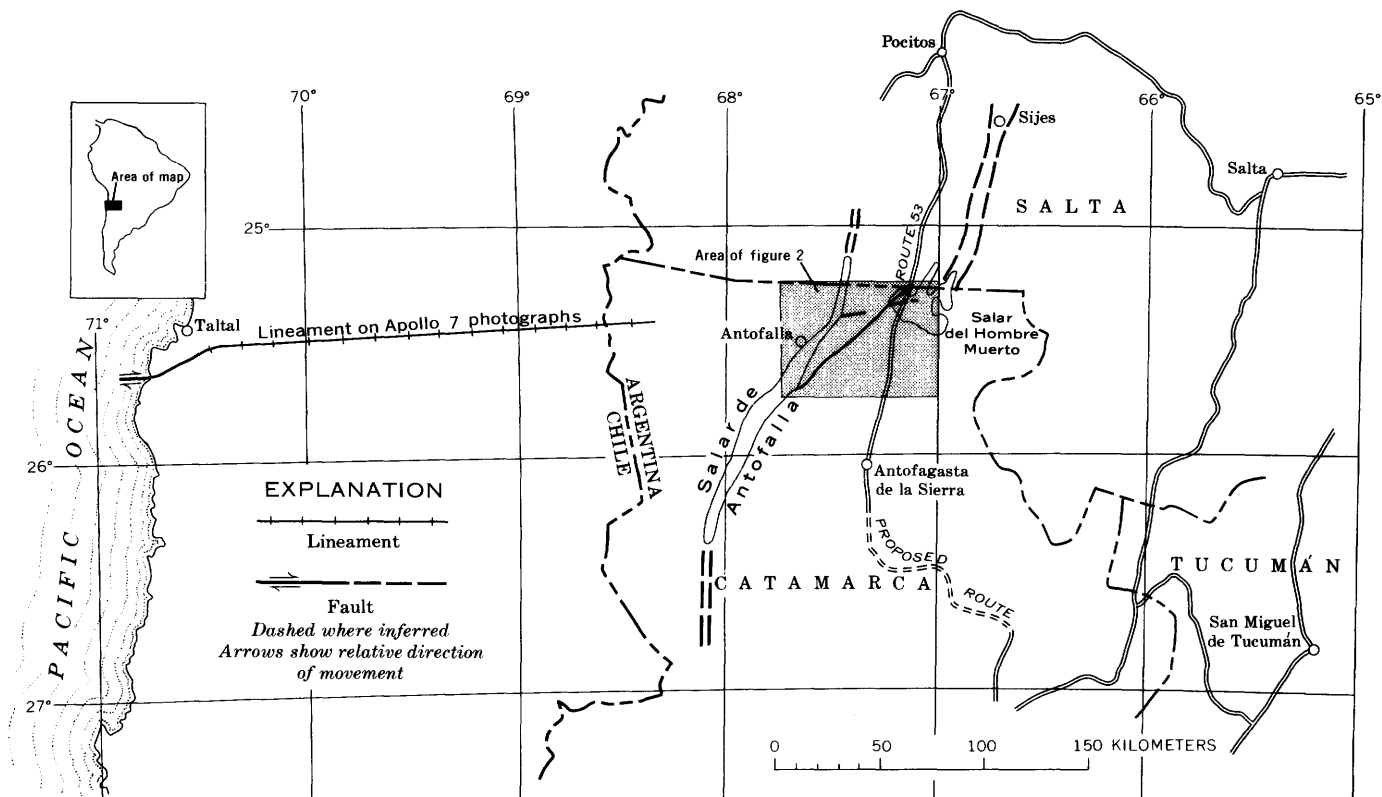


Figure 1.—Index map of part of northwestern Argentina and northern Chile, showing area of figure 2 and the east-west lineament across Chile.

flexure is approximately in line with an east-west lineament across Chile (fig. 1), which was first detected in satellite photographs (Segerstrom, 1970). Branching and sympathetic faults accentuate the transverse structural trend between the Salar de Antofalla and the Salar del Hombre Muerto (fig. 2).

GEOLOGY OF THE ANTOFALLA—HOMBRE MUERTO AREA

Topography

The principal topographic features of the area of figure 2 are the Antofalla and Hombre Muerto salares and two mountains, Cerro Tebenquicho Grande and Cerro de Calalaste, which rise 1,500–2,000 m above the salares. The flat floor of the Salar de Antofalla is overlain at the margins by symmetrical alluvial fans, as much as 8 km across, which debouch from steep tributary gullies on either side. A line of low ridges and knolls rises from the floor of the Salar de Antofalla near its eastern margin.

Rock units

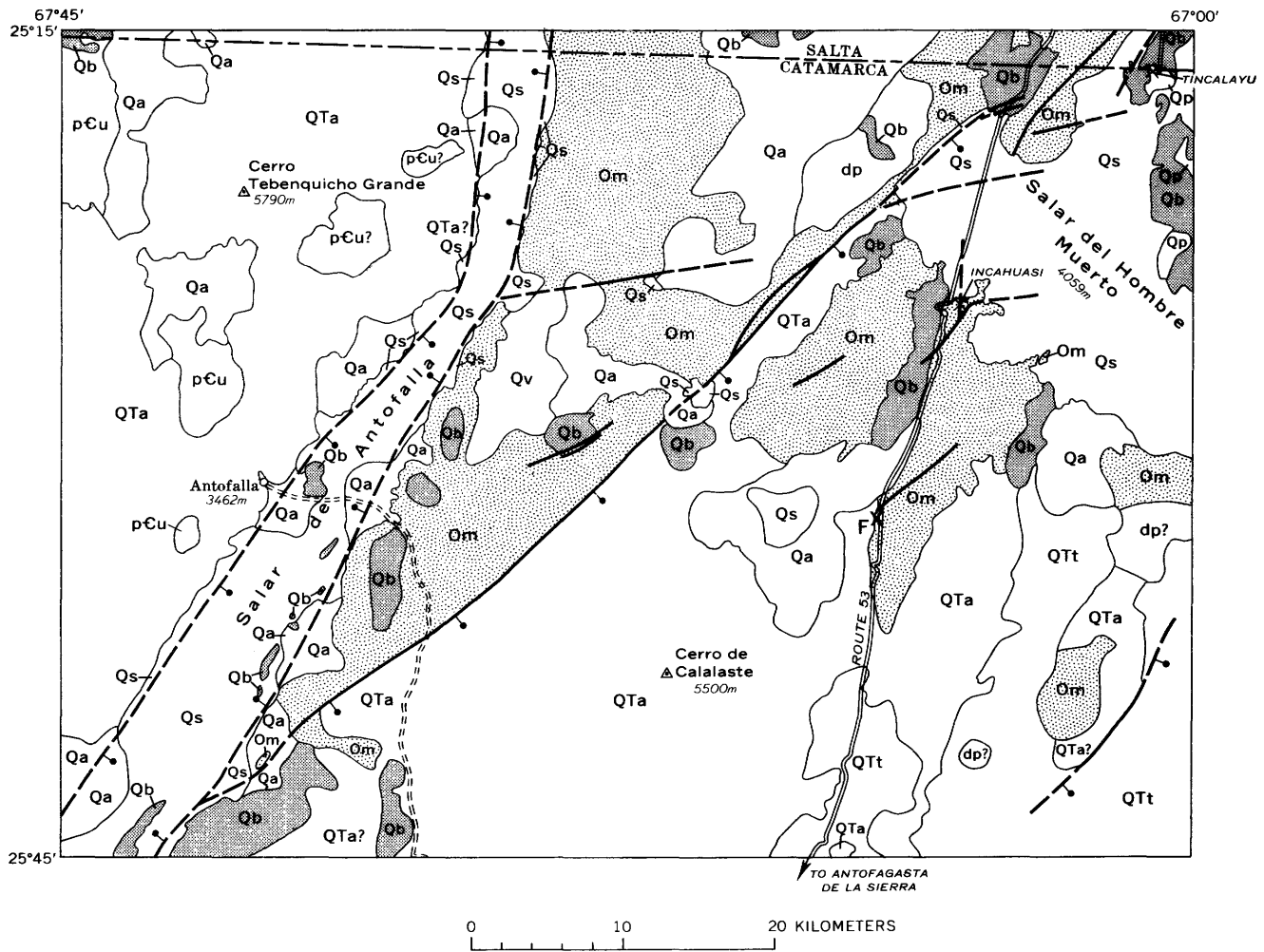
The oldest rocks in the area are metamorphic. Gneissic rocks crop out in the western part; these are believed to be of

Precambrian age. Most of the metamorphic rocks, however, are argillites and metagraywackes; Ordovician graptolites were found in these rocks about 16 km south of the Salar del Hombre Muerto (fig. 2) and near Pocitos and Antofagasta de la Sierra (fig. 1) by paleontologists of the University of Tucumán in 1971.

Dacite porphyry of unknown age intrudes the Ordovician rocks west of the Salar del Hombre Muerto. Unfoliated rocks are exposed in windows eroded through a volcanic cover in several other localities; although these were not visited by the authors, they are thought to be intrusive rocks because on the aerial photographs they appear similar to known outcrops of dacite porphyry.

Cerro Tebenquicho Grande and Cerro de Calalaste are enormous stratovolcanoes made up of gray to brown andesite flows, breccias, and tuffs. Similar volcanic rocks cover areas to the east and south of the two volcanoes. The degree of dissection of the andesite is fairly well advanced, indicating that these volcanics are at least as old as Pleistocene. However, they are probably younger than Pliocene clastic deposits that crop out in nearby areas, because those beds do not contain clasts of volcanic rocks. The andesites are faulted and tilted.

Light-gray tuffs, most of which are dacitic, occur in depressions and overlap the flanks of andesitic mountains. Their age is probably a somewhat younger Pleistocene than that of the andesites.



EXPLANATION

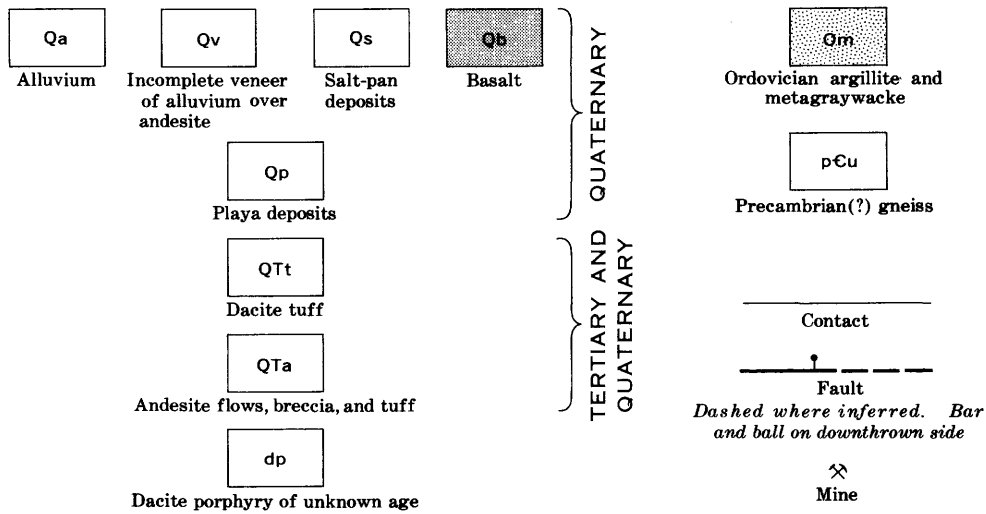


Figure 2.—Reconnaissance geologic map of the area between the Salar de Antofalla and the Salar del Hombre Muerto, Argentina. F, fossil locality.

A deformed sedimentary series of clastic rocks and evaporites crops out on the northeastern side of the Salar del Hombre Muerto. The total thickness of this unit is unknown; however, several hundred meters of clastic rocks, chiefly claystone and siltstone, is exposed. In the unit a deposit of faulted and intensely folded crystalline borax several meters thick is being exploited (Tincalayu mine). Its lithology and relationship to other rock units suggest that the series is equivalent to unit 1 of the Sijes trough (Pratt, 1961, p. 1544–1545), which contains fossil diatoms of Pleistocene age. The beds at Tincalayu were deposited in an ancient playa or salar like that of Hombre Muerto and were subsequently uplifted. Their deformation is exceptionally severe because of incompetence of the beds.

Fairly undeformed basalt flows locally cover ancient and modern salar deposits or directly overlie older rock units of the area. The flows are nearly undissected, and they exhibit primary flow lines and ropy texture. Local eruptions of basalt near the east side of the Salar de Antofalla are represented by a line of outcrops on the map (fig. 2).

The areas mapped as alluvium are bolson and alluvial fan deposits and high-terrace gravels. These deposits both underlie and overlie the basalt flows, and they overlie all the other map units. In many places the alluvium is covered with drifting sand; in a few places dunes occur directly on top of older units. Wind-driven sand (not mapped) has produced a remarkable abundance of ventifacts in an area of basalt float near the southwest corner of the Salar del Hombre Muerto.

STRUCTURE

Regional structure

The fault-block structure of the Argentine Puna, with its northerly trend, has been recognized and described by many authors, as summarized by Pratt (1961, p. 1545–1546). It is tempting and probably justified to relate the dextral flexure in the Antofalla trough to the east-west lineament across Chile. Both features are transverse to a general northerly trend and occur at about the same latitude. The lineament probably represents a structural discontinuity or an ancient zone of weakness (Segerstrom, 1970, p. D12), which may well extend eastward across the northern end of Catamarca Province.

Structure of the Antofalla–Hombre Muerto area

The Ordovician beds are tightly folded along north-northeast-striking axes. Paired synclines and anticlines, plunging and nearly isoclinal, are commonly seen in the airphotographs of Ordovician beds. In most places the strata dip from 70° to vertical. The rocks that overlie these beds are in great angular discordance, presenting gentle dips for the most part. The Pleistocene strata of clastics and evaporites constitute a noteworthy exception, for locally they are intensely deformed. This deformation does not extend into the older volcanics.

In the area of figure 2, the Antofalla trough is flanked on the east by a fault scarp of Ordovician metasedimentary rocks and on the west by volcanics which mostly cover older rocks. In this rift valley are elongate outcrops of Holocene basalt noticeably and significantly parallel to the sides of the downdropped block. The block varies in width from 2 to 7 km, the narrowest part occurring at the point of sharpest flexure (north part of fig. 2).

Two faults branch from the Antofalla trough at points of flexure. A fault that diverges eastward at the sharpest flexure has an inferred length of about 17 km. A major fault that diverges from a point of slight flexure near the southwest corner of the area of figure 2 can be traced northeastward about 60 km to a place where it seems to branch into diverging fractures at the Salar del Hombre Muerto. The faults are breaks in lithology represented as lineaments on the aerial photographs. A deep, narrow valley is eroded along the major fault for a distance of 19 km southwest of the Salar del Hombre Muerto. Lesser faults nearby are parallel to the main fault and its ramifications.

Although none of the planes of mapped faults were observed by the authors, the relatively straight surface traces of most faults indicate that the planes are steeply dipping, rather than low angle. According to our observations, the faults could be either normal or reverse. The opinion of other observers is that reverse faults, rather than normal faults, are the rule regionally (Whiting, 1959, p. 911) and that the depressed blocks widen downward as Furchen (furrows), rather than as typical grabens (Schwab, 1970, p. 1064, 1075–1080). Structure maps of the northwestern part of the Argentine Puna and adjacent areas by Whiting (1959, fig. 2) and Schwab (1970, fig. 6) have a blank space in the Antofalla–Hombre Muerto sector; according to Schwab's map, this sector is bordered to the north, east, and south by Furchen, and Keile (wedges and uplifted blocks narrowing downward) rather than by typical horsts.

Two noteworthy shear zones as much as 30 m wide are exposed in the Ordovician beds, one on the north side of the Salar del Hombre Muerto, the other on the south side. Crushed rock in the zones is stained with iron oxide. The two zones may well represent a single major structure that has been displaced right laterally under the salar. At the Incahuasi gold mine, in the shear zone on the south side of the salar, a 3-m quartz vein strikes north to N. 25° W. Evidence of rock alteration and mineralization was not observed along the margins of the Antofalla trough.

The aligned low hills and ridges of basalt in the Salar de Antofalla clearly resulted from extrusion of lava along one or more fissures that parallel the border faults. Such features in rift valleys have been described for East Africa by Willis (1936, p. 311–312) and by other workers.

SUMMARY AND CONCLUSIONS

The geographic position of the north-northeast-north bend of the Antofalla trough relative to the lineament observed in

satellite photographs suggests that the two structural features may be related. Moreover, the shape of the flexure is that which would be expected from application of a shear couple in a right-lateral (dextral) sense. Displacement of pre-Upper Jurassic rocks along the lineament near the Chilean coast is right-lateral (Segerstrom, 1970, p. D17). These observations lead logically to the following inferences: (1) A single structural discontinuity extends across northwestern Argentina and Chile between the 25th and 26th parallels (fig. 1). (2) The block north of the discontinuity has moved eastward relative to the southern block. (3) This movement either is contemporaneous with development of the Antofalla trough or postdates it.

Although the east-west structural discontinuity can be traced across Chile in satellite photography, it cannot be traced continuously on the ground, and displacement of Upper Jurassic and younger rocks is not apparent along it (Segerstrom, 1970). Inasmuch as this structural feature apparently has been inactive during part of Mesozoic and all of Cenozoic time, the ancestral Antofalla trough or furrow, deformed as it was by movements along the transverse structure, is Late Jurassic or older. (The same may also be true of other fault blocks in the Puna of northwestern Argentina.)

Pliocene and Pleistocene fault movements that accompanied the major uplift of the Andes have accentuated displacements along the main north-striking block faults and have produced the two subsidiary faults which branch from the flexure in the Antofalla trough. Lesser fault movements have probably continued nearly to the present time.

REFERENCES

- Pratt, W. P., 1961, Local evidence of Pleistocene to Recent orogeny in the Argentine Andes: *Geol. Soc. America Bull.*, v. 72, no. 10, p. 1539–1550.
- Schwab, Klaus, 1970, Ein Beitrag zur jungen Bruchtektonik der argentinischen Puna und ihr Verhältnis zu den angrenzenden Andenabschnitten: *Geol. Rundschau*, v. 59, no. 3, p. 1064–1087.
- Segerstrom, Kenneth, 1970, Apollo 7 photography in Antofagasta Province, Chile—An interpretation, in *Geological Survey Research 1970: U.S. Geol. Survey Prof. Paper 700-D*, p. D10–D17 [1971].
- Turner, J. C. M., 1970, The Andes of northwestern Argentina: *Geol. Rundschau*, v. 59, no. 3, p. 1028–1063.
- Whiting, F. B., 1959, Structural belts and mineral deposits of northwestern Argentina: *Econ. Geology*, v. 54, no. 5, p. 903–912.
- Willis, Bailey, 1936, *Studies in comparative seismology; East African plateaus and rift valleys*: Carnegie Inst. Washington Pub. 470, 343 p.



SOUTHEASTERN ALASKA—A DISPLACED CONTINENTAL FRAGMENT?

By DAVID L. JONES, WILLIAM P. IRWIN,
and A. THOMAS OVENSINE, Menlo Park, Calif.

Abstract.—Lower Paleozoic rocks of southeastern Alaska are part of an anomalous continental fragment. Their presence substantiates evidence presented by Monger and Ross in 1971, that a belt of upper Paleozoic rocks along the northern Pacific coast is detached from the main continental mass of North America. Silurian facies trends and other data seem to preclude lateral rifting as the main mode of detachment. Right-lateral transcurrent faulting seems more likely, and California seems to be the only suitable source for the anomalous fragment. Comparison of general lithologies supports the hypothesis that the Klamath Mountains and southeast Alaska are parts of a once-continuous terrane that was dismembered during latest Paleozoic or early Mesozoic time.

Lower Paleozoic sedimentary, volcanic, and plutonic rocks that form the continental crust in southeastern Alaska are anomalous, as similar rocks of comparable age are unknown elsewhere along the northwestern continental margin north of California, and as they appear to be separated from the main continental mass of North America by a belt of younger rocks deposited directly on oceanic crust (fig. 1). These anomalous lower Paleozoic rocks, as well as younger Paleozoic rocks to the south, have been considered by some (Wilson, 1968; Danner, 1970) to be fragments of Asia that were left behind after a collision of Asia and North America. In a recent paper, Monger and Ross (1971) suggest that upper Paleozoic rocks along the coast of British Columbia and southeastern Alaska may be a fragment of the North American Continent that has undergone large-scale movement to attain its present position. Their suggestion is based mainly on the distribution of upper Paleozoic fusulinacean faunas but also takes into account the distribution of lithofacies. Our purpose in this report is to suggest that the anomalous Paleozoic rocks of southeastern Alaska are a displaced fragment of California.

The belt of lower and upper Paleozoic rocks along the coast of southeastern Alaska and British Columbia (Monger and Ross' western belt), is separated from the main continental mass of North America by an extensive parallel belt of upper Paleozoic rocks thought to be deposited directly on oceanic crust (Monger and Ross' central belt). The northwestern part of the western belt consists of a block of old Paleozoic continental crust that constitutes the Alexander Archipelago

and contiguous areas of southeastern Alaska. Its continental nature is indicated by a long record of sedimentation and intermittent volcanism (Brew and others, 1966) beginning at least as early as Ordovician and extending through the Paleozoic into the Mesozoic, and by intrusion of granitic rocks of Ordovician and Silurian ages (Lanphere and others, 1964, 1965). The history of the southeastern Alaskan block is complex, and the record of sedimentation is broken by many unconformities that indicate intermittent uplift and erosion (Ovenshine and others, 1970).

The eastern and southern parts of the western belt consist of upper Paleozoic sedimentary and volcanic rocks discussed by Monger and Ross; these extend south along the coast of British Columbia and terminate against the trans-Idaho discontinuity of Yates (1968). Precambrian and older Paleozoic rocks apparently do not underlie these parts of the western belt. The relation of the older Paleozoic rocks in southeastern Alaska to the upper Paleozoic rocks occurring nearby to the east and southeast is not clearly defined; the contact may occur on Annette and Gravina Islands in southeastern Alaska where a complex zone of major thrusting has been inferred by H. C. Berg (oral commun., 1971).

The oceanic nature of the upper Paleozoic rocks in the central belt to the east is indicated by the presence of abundant ultramafic rock associated with gabbro, pillow basalt, chert, and other sedimentary rocks including fusulinid-bearing limestones (Monger and Ross, 1971).

DISTRIBUTION OF PERMIAN FUSULINACEAN FAUNAS

The existence of distinctly different but coeval Permian fusulinid faunas has long been recognized (for an excellent review, see Ross, 1967). In British Columbia, Monger and Ross (1971) showed that two well-defined fusulinacean assemblages occur in separate belts. One assemblage, dominated by genera of the family Schwagerinidae, forms an eastern belt (Monger and Ross, 1971, fig. 2); the other, dominated by genera of the family Verbeekinidae, forms a central belt. In a belt lying west of the central belt, along the coast of British Columbia and in

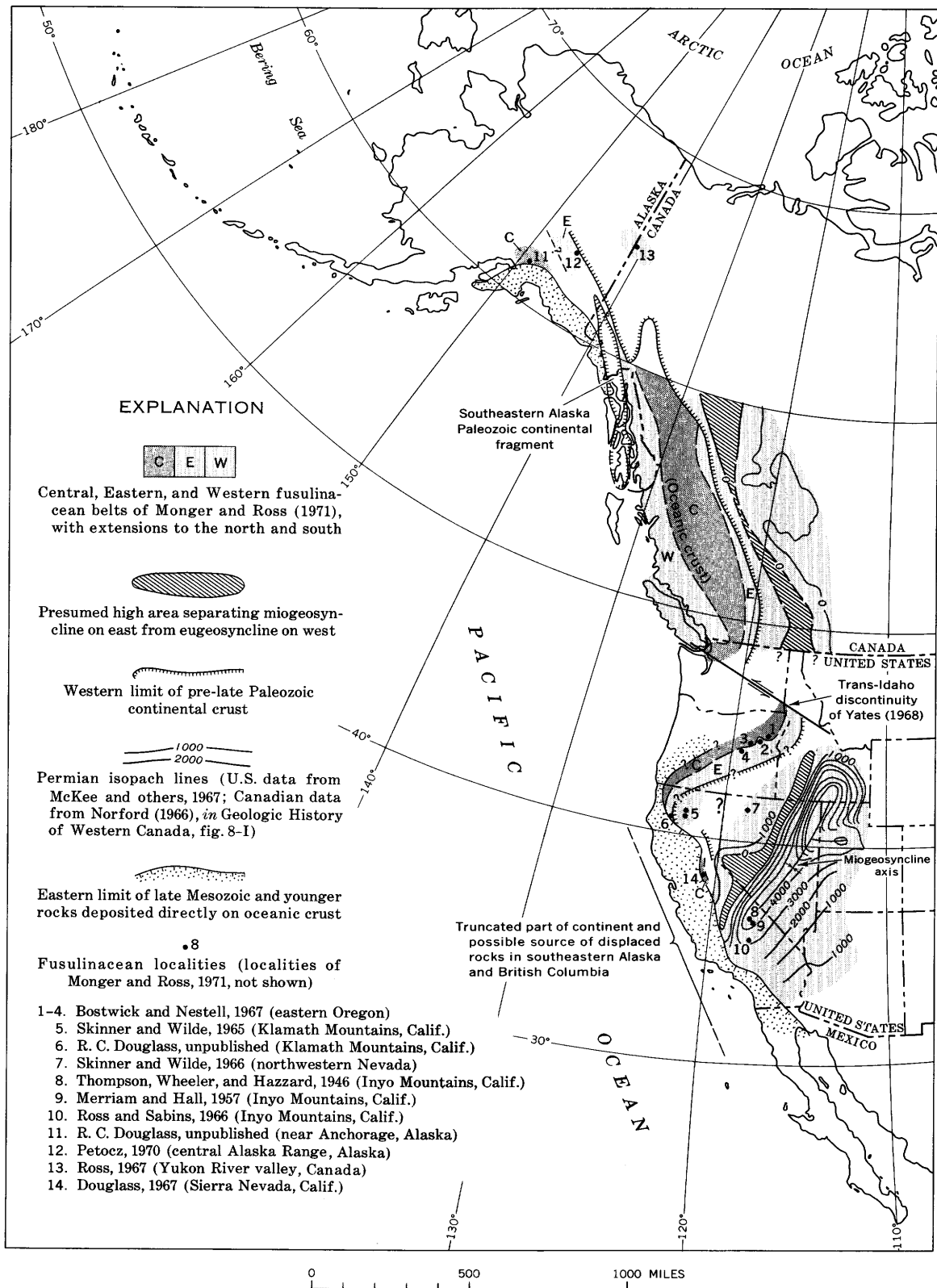


Figure 1.—Map showing distribution of Permian fusulinacean faunas and position of displaced continental fragment in southeastern Alaska.

southeastern Alaska, Permian rocks contain Schwagerinid faunas similar to those of the eastern belt. The Schwagerinid faunas of both the eastern and western belts show close ties to other North American faunas of the same age; the Verbeekinid faunas of the central belt show close ties to faunas from Japan and elsewhere in Asia and are referred to as Tethyan (Ross, 1967; Gobbett, 1967; Bostwick and Nestell, 1967; Douglass, 1967). Hamilton (1969, p. 2412) has suggested that Permian terranes bearing Tethyan fusulinid faunas in western North America may have formed in an island arc in the north-central Pacific and were later swept against the continent. We accept the view of their extracontinental origin, but not necessarily the island arc environment.

Three models are proposed by Monger and Ross (1971) to account for this pattern of faunal belts. The first model is ecological, in which the differing fusulinid faunas result from differences in local environment. The second and third models are tectonic. The second envisages simple splitting and separation parallel to the continental margin, with generation of new oceanic crust within the widening rift zone and concomitant subduction on both sides of the rift. The eastern and western belts would thus be dismembered portions of the same terrane. The central belt, confined to the new oceanic crust, would present different ecological conditions and hence would be characterized by a different fauna. The third model is one in which a continentward Schwagerinid zone and an oceanward Verbeekinid zone are cut by a major right-lateral transcurrent fault, such that some of the eastern zone comes to lie west of part of the central zone.

It is instructive to examine the distribution of Paleozoic rocks and trends of facies along the continental margin of North America to determine whether the source of the dislocated terrane can be located. On figure 1 we have extended the eastern and central belts of Monger and Ross south through Oregon and north into Alaska, based on published information and on unpublished identifications by R. C. Douglass. We have used the same faunal criteria for these extensions as were used by Monger and Ross for British Columbia.

Our basic premise is that the late Paleozoic continental margin of much of western North America is defined approximately by the boundary between the eastern and central fusulinacean belts. Hence, where this boundary is continuous and can be observed, significant post-Paleozoic truncation of the continent has not occurred. In areas near the coast where the central belt is missing, however, truncation may have occurred. Any such truncated area should be evaluated as a possible source terrane for the displaced Paleozoic rocks of southeastern Alaska.

The western fusulinacean belt is restricted to British Columbia and southeastern Alaska as shown by Monger and Ross. To the north, in southern Alaska, the presence of the eastern belt has been established by the work of Ross (1967) in northwest Canada and of Petocz (1970) in the central

Alaska Range (locs. 12 and 13, fig. 1). The presence of the central belt is indicated by Tethyan fusulinids collected near Anchorage (loc. 11) by Sandra Clark and identified by R. C. Douglass. Permian rocks extend farther to the southwest, but, as they have not yielded fusulinids, the distribution of the belts cannot be discerned. South of Alaska the central (oceanic) belt can be traced through central Oregon and may occur in California. South of British Columbia the eastern fusulinacean belt broadens to cover much of the Western United States and continues southward beyond the last trace of the central belt.

The boundary between the eastern and central belts occurs in eastern and central Oregon (loc. 1-4, fig. 1) where both Verbeekinid and Schwagerinid faunas have been described (Bostwick and Nestell, 1967, p. 95). To the southwest, Schwagerinid faunas are well developed in the McCloud Limestone (loc. 5) (Skinner and Wilde, 1965) and elsewhere in the eastern half of the Klamath Mountains (loc. 6).

Rocks similar to those of the central belt are present in the western Klamath Mountains of California, but a Tethyan affinity has not been established on a paleontologic basis. According to N. J. Silberling (oral commun., 1971) a marginal sea with oceanic crust may have existed in late Paleozoic time east of the Klamath Mountains. If this is so, then in northern California and central Oregon the margin defined by the boundary between the central and eastern fusulinacean zones occurs on a microcontinental fragment lying west of the main continental mass.

In the foothills of the Sierra Nevada, Calif., three occurrences are known of Tethyan fusulinids in limestone in the western outcrop belt of the Calaveras Formation (loc. 14, fig. 1) (Douglass, 1967; Clark, 1964, p. 13-14). At least one of these occurrences is a limestone block incorporated in younger rocks (Clark, 1964, p. 13-14). Possibly the other occurrences are displaced tectonically and thus may not accurately represent the extent of the central belt or the position of the Paleozoic continental margin.

FACIES TRENDS AND TRUNCATION OF WESTERN NORTH AMERICA

Distribution of the fusulinacean belts and some other elements of the Paleozoic of western North America is shown on figures 1, 2, and 3. In British Columbia, Permian isopachs and Silurian and Ordovician lithologic belts trend parallel to the coastline, but to the south, after apparent left-lateral offset by the trans-Idaho discontinuity, they trend southwestward at a large angle to the Pacific coastline. In California the trends of older Paleozoic rocks of the main continental mass of western North America clearly are truncated (Hamilton and Myers, 1966, p. 513; Hamilton, 1969, p. 2412), as are the fusulinacean belts. The Mesozoic rocks west of the truncated Paleozoic rocks trend northwestward and lack an older continental basement (Irwin, 1964, p. C4; Hamilton, 1969; Bailey and others, 1970).

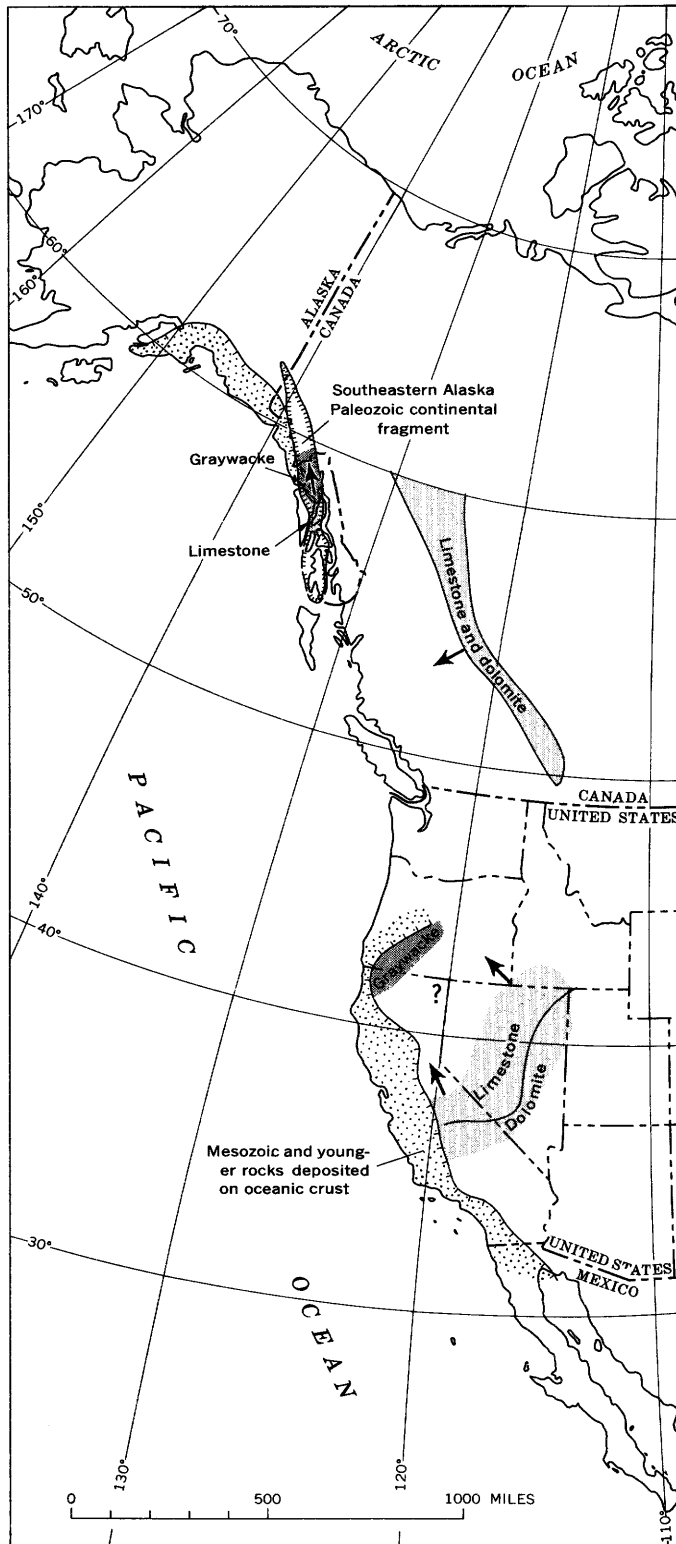


Figure 2.—Distribution of Silurian facies belts, showing truncation of trends in California. Arrows show main direction of change in facies. Data for southwestern United States from Merriam (unpub.); for Alaska from Ovenshine (unpub. palinspastic reconstruction); and for Canada from Norford (1966).

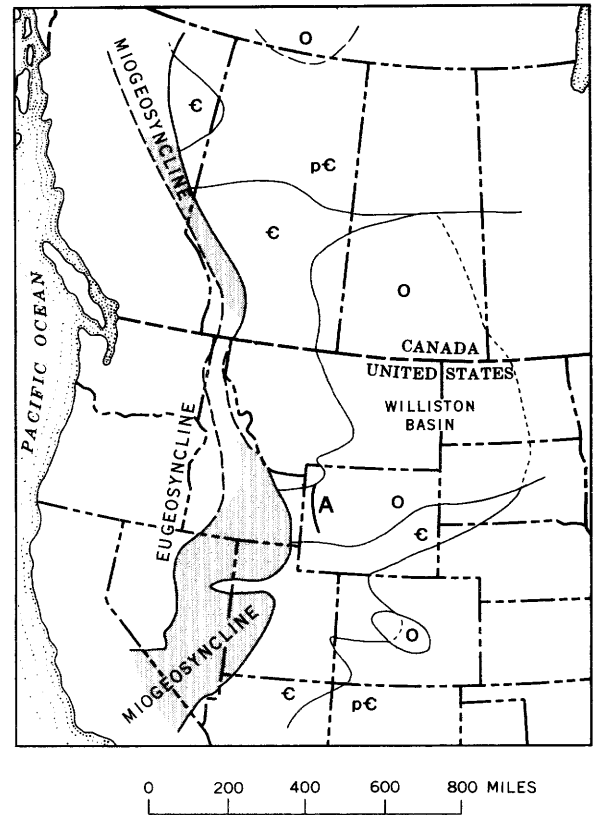


Figure 3.—Western North America, showing extent of Ordovician quartzite (shaded) in the miogeosyncline; and Precambrian (pC), Cambrian (C), and Ordovician (O) terranes east of the geosyncline. A, western limit of Ordovician quartz sand in the Williston basin (from Ketner, 1968, p. 170, fig. 1).

SOURCE OF CONTINENTAL FRAGMENT

The fusulinacean data from the western belt suggest that the displaced rocks along the coast of British Columbia and Alaska have close ties to continental North America, rather than having originated in Asia. Movement of the displaced rocks could have been by rifting with generation of the central oceanic belt in the growing rift zone, by lateral faulting along transform faults, or by some other means such as large-scale thrust faulting. Monger and Ross (1971, p. 276) pointed out that their rifting model is not supported by faunal data. It is also not supported by an analysis of Silurian facies trends.

The generalized distribution of Silurian sedimentary rocks is shown in figure 2, with the direction of dominant change in facies from shallow-water carbonates to deeper water graywacke and flyschlike deposits indicated by arrows. In California and Nevada, the direction of facies change is northwesterly (C. W. Merriam, unpub. data; Berry and Boucot, 1971), and in southeastern Alaska it is similar although slightly more northerly. These directions contrast markedly with the direction of facies change in British Columbia. There the lithologic

belts trend northwesterly (Norford, 1966), and the direction of facies change is southwesterly at nearly right angles to that of southeastern Alaska. This difference strongly suggests that the southeastern Alaska terrane was not detached from the main continental mass nearby in British Columbia unless it was subsequently rotated through a large angle. Rather, the similarity in direction of change of facies in California and southeastern Alaska suggests that the Silurian rocks of these two areas could have been deposited within the same general terrane. This possibility is supported by a close similarity of the Silurian rocks in the two areas.

Middle and Upper Silurian rocks of southeastern Alaska comprise a southern belt of limestone and conglomerate and a northern belt of calcareous graywacke. Clasts of andesite, chert, and diorite are conspicuous in the conglomerate zones, which are locally as much as 2,000 feet thick. Similar conglomerate also occurs locally in the time-equivalent graywacke sequence to the north. In the Klamath Mountains, Middle and Upper Silurian rocks (lower part of the Gazelle Formation) consist of graywacke, mudstone, conglomerate, limestone, and volcanic rocks (Wells and others, 1959). As in southeastern Alaska, some of the conglomerates contain clasts of andesite and diorite (Rohr and Boucot, 1971). Also, Silurian faunas from southeastern Alaska have close affinities with those of the Klamath Mountains (Churkin and Langenheim, 1960).

This similarity of Silurian rocks and faunas in southeastern Alaska and in California permits the speculation that the southeastern Alaskan continental fragment originated in California and was rafted northward following truncation of the continent. This speculation is comparable to Monger and Ross' (1971, p. 275, fig. 5) model involving major transcurrent faulting, although they did not suggest a possible source for the dislocated upper Paleozoic terrane.

A detailed comparison of the geology of the possible source area and the presumed detached fragment will not be attempted in this short report, but a summary of the stratigraphic units in southeastern Alaska, the Klamath Mountains, and the Inyo Mountains of California is given in table 1 (p. B216).

This table shows that whereas the Paleozoic rocks of southeastern Alaska are not like those of the western Great Basin, represented by the miogeosynclinal rocks of the Inyo Mountains, they do resemble the eugeosynclinal rocks of the eastern Klamath Mountains, although stratigraphic details are highly discordant. Rapid and drastic facies changes along strike coupled with structural complexity characterize the Paleozoic rocks in both places, as is shown by the detailed stratigraphic studies of Eberlein and Churkin (1970) in southeastern Alaska, and by the difficulty in correlating the Paleozoic stratigraphy of the eastern Klamath Mountains with that of the nearby Taylorsville area of the northern Sierra Nevada (compare Irwin, 1966, p. 23, with McMath, 1966, p. 176). Hence, it may be unreasonable to expect a closer fit in lithologic details than

the table demonstrates. In any case, it is obvious that if the southeastern Alaskan Paleozoic rocks were derived from California, they could only have come from the northern part of the State, as the rocks in the southern part are wholly dissimilar. The fate of the truncated miogeosynclinal Paleozoic rocks and the Precambrian basement rocks of southern California is unknown.

REFERENCES

- Bailey, E. H., Blake, M. C., Jr., and Jones, D. L., 1970, On-land Mesozoic oceanic crust in California Coast Ranges, in *Geological Survey Research 1970: U.S. Geol. Survey Prof. Paper 700-C*, p. C70-C81.
- Berry, W. B. N., and Boucot, A. J., 1971, Correlation of the North American Silurian rocks: *Geol. Soc. America Spec. Paper 102*, 289 p., 13 figs., 2 pls., 2 tables.
- Bostwick, D. A., and Nestell, M. K., 1967, Permian Tethyan fusulinid faunas of the northwestern United States: *Systematics Assoc. Pub. 7*, p. 93-102.
- Brew, D. A., Loney, R. A., and Muffler, L. J. P., 1966, Tectonic history of southeastern Alaska: *Canadian Inst. Mining and Metallurgy Spec. Volume 8*, p. 149-170.
- Churkin, Michael, Jr., and Langenheim, R. L., Jr., 1960, Silurian strata of the Klamath Mountains, California: *Am. Jour. Sci.*, v. 258, p. 258-273.
- Clark, L. D., 1964, Stratigraphy and structure of part of the western Sierra Nevada metamorphic belt, California: *U.S. Geol. Survey Prof. Paper 410*, 70 p., 11 pls., 16 figs., 6 tables.
- Danner, W. R., 1970, Paleontologic and stratigraphic evidence for and against sea floor spreading and opening and closing oceans in the Pacific Northwest: *Geol. Soc. America Abs. with Programs*, v. 2, no. 2, p. 84-85.
- Douglass, R. C., 1967, Permian Tethyan fusulinids from California: *U.S. Geol. Survey Prof. Paper 593-A*, 13 p.
- Eberlein, G. D., and Churkin, Michael, Jr., 1970, Paleozoic stratigraphy in the northwest coastal area of Prince of Wales Island, southeastern Alaska: *U.S. Geol. Survey Bull. 1284*, 67 p., 2 pls., 31 figs.
- Gobbett, D. J., 1967, Palaeozoogeography of the Verbeekinidae (Permian Foraminifera): *Systematics Assoc. Pub. 7*, p. 77-91.
- Hamilton, Warren, 1969, Mesozoic California and the underflow of Pacific mantle: *Geol. Soc. America Bull.*, v. 80, p. 2409-2430, 5 figs.
- Hamilton, Warren, and Myers, W. B., 1966, Cenozoic tectonics of the Western United States: *Rev. Geophysics*, v. 4, no. 4, p. 509-549.
- Irwin, W. P., 1964, Late Mesozoic orogenies in the ultramafic belts of northwestern California and southwestern Oregon, in *Geological Survey Research 1964: U.S. Geol. Survey Prof. Paper 501-C*, p. C1-C9.
- 1966, *Geology of the Klamath Mountains Province: California Div. Mines and Geology Bull. 190*, p. 19-38.
- Ketner, K. B., 1968, Origin of Ordovician quartzite in the Cordilleran miogeosyncline, in *Geological Survey Research 1968: U.S. Geol. Survey Prof. Paper 600-B*, p. B169-B177.
- Lanphere, M. A., Loney, R. A., and Brew, D. A., 1965, Potassium-argon ages of some plutonic rocks, Tenakee area, Chichagof Island, southeastern Alaska, in *Geological Survey Research 1965: U.S. Geol. Survey Prof. Paper 525-B*, p. B108-B111.
- Lanphere, M. A., MacKevett, E. M., Jr., and Stern, T. W., 1964, Potassium-argon and lead-alpha ages of plutonic rocks, Bokan Mountain area, Alaska: *Science*, v. 145, no. 3633, p. 705-707.
- Latham, E. H., Pomeroy, J. S., Berg, H. C., and Loney, R. A., 1965,

Table 1.—Comparison of stratigraphic sequence in southeastern Alaska with that of the Klamath Mountains and Inyo Mountains, California

Age	Southeastern Alaska (data from Eberlein and Churkin, 1970, and Lathram and others, 1965)	Eastern Klamath Mountains, California (data from Irwin, 1966)	Inyo Mountains, California (data from McKee and Nelson, 1967; Ross, 1966)	
Permian	Pybus Formation Dolomite and chert	Dekkas Andesite—fragmental lava, pyroclastics, and minor sedimentary rocks Nosoni Formation—mudstone and tuff McCloud Limestone—massive limestone and chert	Owens Valley Formation	Limestone and shale
	Cannery Formation—argillite, graywacke, chert, minor volcanic rocks		Keeler Canyon Formation	Limestone and shale
Pennsylvanian	Klawak and Ladrones Formations—sandstone and limestone	Baird Formation, upper part		
Mississippian	Peratrovich Formation Thick-bedded limestone, limestone, and chert Chert, minor limestone	Baird Formation, lower part— pyroclastic rocks, mudstone, keratophyre	Rest Spring Shale	Shale and siltstone
		Bragdon Formation—shale, sandstone, conglomerate, chert, and pyroclastic rocks	Perdido Formation	Shale, siltstone, sandstone, and conglomerate
Devonian	Port Refugio Formation—graywacke, shale, volcanic rocks	Kennett Formation—mudstone and tuff	Sunday Canyon Formation/ Vaughn Gulch Limestone (Silurian and Devonian?)	Argillaceous limestone and mudstone/limestone
	Wadleigh Limestone } St. Joseph Island Volcanics (Devonian?) Coronados Volcanics	Balaklala Rhyolite—quartz keratophyre and tuff		
Silurian	Karheen Formation—sandstone and shale Heceta Limestone—massive limestone, with minor sandstone and conglomerate	Copley Greenstone—keratophyre and spilite		
		Gazelle Formation—graywacke, mudstone, conglomerate. Includes Payton Ranch Limestone Member of Churkin and Langenheim (1960)		
Ordovician	Descon Formation—graywacke, mudstone, siltstone, conglomerate, minor limestone, and volcanic rock	Duzel Formation (Ordovician?)—phyllitic graywacke, chert, and limestone	Ely Springs Dolomite Johnson Spring Formation Barrel Spring Formation Badger Flat Limestone Al Rose Formation	Dolomite and chert Quartzite, dolomite, limestone Shale, limestone, quartzite Limestone, siltstone, quartzite Shale, mudstone, limestone
	(Ultramafic basement)	(Ultramafic basement)		
Cambrian			Tamarack Canyon Dolomite Lead Gulch Formation Bonanza King Dolomite Monola Formation Mule Spring Limestone Saline Valley Formation Harkless Formation Poleta Formation Campito Formation Deep Spring Formation Reed Dolomite Wyman Formation	Dolomite Cherty limestone, shale, dolomite Dolomite and limestone Siltstone and limestone Blue-gray limestone Siltstone and quartzite Shale and quartzite, minor limestone Shale, limestone, and quartzite Siltstone, shale, and sandstone Quartzitic sandstone and limestone Buff to gray dolomite Argillite and quartzite
Precambrian				

- Reconnaissance geology of Admiralty Island, Alaska: U.S. Geol. Survey Bull. 1181-R, 48 p., 2 pls., 2 figs., 2 tables.
- McKee, E. D., and others, 1967, Paleotectonic maps of the Permian System: U.S. Geol. Survey Misc. Geol. Inv. Map I-450.
- McKee, E. H., and Nelson, C. A., 1967, Geologic map of the Soldier Pass quadrangle, California and Nevada: U.S. Geol. Survey Geol. Quad. Map GQ-654, scale 1:62,500.
- McMath, V. E., 1966, Geology of the Taylorsville area, northern Sierra Nevada, California: California Div. Mines and Geology Bull. 190, p. 173-183.
- Merriam, C. W., and Hall, W. E., 1957, Pennsylvanian and Permian rocks of the southern Inyo Mountains, California: U.S. Geol. Survey Bull. 1061-A, 13 p.
- Monger, J. W. H., and Ross, C. A., 1971, Distribution of fusulinaceans in the western Canadian cordillera: Canadian Jour. Earth Sci., v. 8, no. 2, p. 259-278.
- Norford, B. S., 1966, in *Geological history of western Canada*, 2d ed.: Calgary, Alberta, Alberta Soc. Petroleum Geologists, chap. 7, pt. 2, p. 42-48.
- Ovenshine, A. T., Eberlein, G. D., and Churkin, Michael, Jr., 1970, Paleotectonic significance of a Silurian-Devonian clastic wedge, southeastern Alaska: Geol. Soc. America Abs. with Programs for 1969, pt. 3, p. 50.
- Petocz, R. G., 1970, Biostratigraphy and Lower Permian Fusulinidae of the upper Delta River area, east-central Alaska Range: Geol. Soc. America Spec. Paper 130, 94 p., 10 pls.
- Rohr, David, and Boucot, A. J., 1971, Northern California (Klamath Mountains) pre-Late Silurian igneous complex [abs.]: Geol. Soc. America, Abs. with Programs, v. 3, no. 2, p. 186.
- Ross, C. A., 1967, Development of fusulinid (Foraminiferid) faunal realms: Jour. Paleontology, v. 41, no. 6, p. 1341-1354.
- Ross, C. H., and Sabins, F. F., Jr., 1966, Permian fusulinids from El Paso Mountains, California: Jour. Paleontology, v. 40, no. 1, p. 155-161, pls. 19-20.
- Ross, D. C., 1966, Stratigraphy of some Paleozoic formations in the Independence quadrangle, Inyo County, California: U.S. Geol. Survey Prof. Paper 396, 64 p., 5 pls., 19 figs.
- Skinner, J. W., and Wilde, G. L., 1965, Permian biostratigraphy and fusulinid faunas of the Shasta Lake area, northern California: Kansas Univ. Paleont. Contr., art. 6, 98 p., 65 pls., 3 figs.
- 1966, Permian fusulinids from Pacific Northwest and Alaska: Kansas Univ. Paleont. Contr.—Paper 4, 64 p., 49 pls.
- Thompson, M. L., Wheeler, H. E., and Hazzard, J. C., 1946, Permian fusulinids of California: Geol. Soc. America Mem. 17, 77 p., 18 pls.
- Wells, F. G., Walker, G. W., and Merriam, C. W., 1959, Upper Ordovician(?) and Upper Silurian formations of the northern Klamath Mountains, California: Geol. Soc. America Bull., v. 70, p. 645-650.
- Wilson, T. J., 1968, Static or mobile earth: the current scientific revolution: Am. Philos. Soc. Proc., v. 112, no. 5, p. 309-319.
- Yates, R. G., 1968, The trans-Idaho discontinuity: Internat. Geol. Cong., 23d, Prague, 1968, Rept., v. 1, p. 117-123.



POPULATION DENSITY AS AN INDIRECT INDICATOR OF URBAN AND SUBURBAN LAND-SURFACE MODIFICATIONS

By STEPHEN J. STANKOWSKI, Trenton, N.J.

Work done in cooperation with the New Jersey Department of Environmental Protection, Division of Water Resources

Abstract.—A new method is developed for determining a quantitative index of urban and suburban land-use characteristics for application in regional water-resources analyses. Easily obtainable population density is the only independent variable needed to estimate empirically the proportion of impervious area resulting from different degrees of urban and suburban development. This formulation is based on correlations between population density and the proportions of land area in each of six urban and suburban land-use categories. The proportions of land use are, in turn, weighted by the average percentage of impervious area found in each land-use category. The method is illustrated using county land-use and population-density data for New Jersey. The concept and procedure presented, though limited by inherent averaging processes, is an inexpensive and rapid technique for generating quantitative indices of past, present, and future conditions of land-surface development for use in preliminary and general hydrologic studies and projections.

Flood peaks can increase significantly when land is converted from forest or agricultural use to highly developed metropolitan use. Many hydrologic studies have used the percentage of paved or impervious surface of the land as a measure of the degree of urbanization. Imperviousness, as used in this report, refers to the inability of water to penetrate those areas of the land surface occupied by manmade structures.

Percentages of impervious area are generally determined by laborious and expensive sampling from aerial photographs and large-scale maps. For example, Harris and Rantz (1964) determined the magnitude of impervious cover for a project area in Santa Clara County, Calif., by estimating an average impervious area for each of several types of building construction. Using these unit figures as a base, the structures were counted on aerial photographs and the total impervious area computed. Martens (1968) determined the percentage of impervious area of watersheds in metropolitan Charlotte, N.C., by superimposing a transparent grid over detailed topographic maps of the study areas. Percentages of impervious area were

estimated in relation to the proportion of grid intersections overlying manmade impervious surfaces.

The time and expense required to use these detailed sampling techniques and the lack of large-scale photography or topographic maps would hinder or preclude the definition of impervious cover in many basins. Furthermore, it is impossible to apply these techniques to investigate conditions of 40 years ago or more when aerial photography and large-scale topographic maps were nonexistent.

APPROACH TO THE PROBLEM

In an attempt to overcome some of the problems listed above, population density was investigated for its potential usefulness as an indirect indicator of urbanization. From county data for New Jersey, close relations were found between population density and the percentages of land area contained within each of six urban and suburban land-use categories. By weighting the proportions of land use with average percentages of impervious area found in corresponding land-use categories, the total percentage of impervious area created by urban and suburban development can be estimated from easily obtainable population-density data.

On the basis of this technique and the hypothesis that a similar relation existed in the past as at present for intensity of land use and concomitant population density, and on the assumption that these trends will continue into the future, quantitative land-use and impervious-area data that might otherwise be indeterminate can be generated for the past, present, and future. Census data, available since the beginning of the twentieth century for States, counties, cities, townships, boroughs, and wards, may be used to investigate hydrologic relations that existed when the earliest reliable streamflow data were collected. Furthermore, it should be possible to project estimates of changes in the hydrologic regimen into the future because population estimates, which are an element of

every comprehensive planning study, are readily available from various regional, State, and local planning agencies.

A convenient source of population data is the "National Location Code Manual" prepared by the U.S. Bureau of the Census (1962). This manual divides the United States into approximately 43,000 small geographic areas known as standard location areas. The manual includes large-scale maps showing the geographic boundaries of the standard location areas and data listings containing their names, populations, and geographic coordinates. The population within any drainage basin can be determined by superimposing an outline of the basin divide over corresponding standard-location-area maps. Using the percentages of the standard location areas contained within the basin as weighting factors, the total basin population can be determined as the weighted sum of the standard location-area populations listed in the manual. The inherent assumption of a uniform distribution of population within each standard location area is reasonable because each area is designed to achieve uniformity of population characteristics, economic status, and living conditions.

FORMULATION OF A QUANTITATIVE INDEX

Urbanization process

Urbanization begins with the occupancy of rural lands by small concentrated communities with close groupings of homes, schools, churches, and commercial facilities. Further growth is characterized by large residential subdivisions, additional schools, shopping centers, some industrial buildings, and an enlarged network of streets and sidewalks. Central business districts evolve; these contain large stores and offices and often cultural and civic centers. Industrial growth continues along waterways, railroad lines, and major highways. The process continues until homes, apartment complexes, commercial and industrial buildings, streets, parking lots, and sidewalks occupy all or most of the former rural land area. The changes in the characteristics of land use and concomitant surface cover significantly affect the hydrology of the drainage-basin segments that are included in the areas of development (Leopold, 1968).

Most metropolitan areas have had similar patterns of past growth. Before World War II, communities were generally clustered around railroad stations and harbor areas. As the communities expanded, their growth followed rail lines and main roads until the developed parts of the average large city resembled a rimless wheel, with a central area forming the hub and fingerlike developments along the highways and commuter rail lines forming the spokes. The end of World War II triggered a substantial increase in population, a building boom, and a significant change in the pattern of urban development. With the suburbanization of industry and commercial facilities, satellite subcenters developed along the highways and rail lines, resulting in more dispersed urbanization which fills in

the open spaces between the spokes. This familiar pattern of urban sprawl is well established, and future urban and suburban development can be expected to follow this trend.

The multitown and radial-corridor patterns of land development represent typical alternatives to urban sprawl. The multitown pattern of development calls for clusters of communities throughout a region. The town clusters are separated by belts and pockets of open space that break the tendency toward uncontrolled urban sprawl. The radial-corridor pattern limits urban development to corridors along commuter rail lines and main highways. Wedges separating the corridors are reserved for open space and for residential development of very low density. Actually, the radial-corridor growth pattern represents a resurgence of the pattern of concentration of development along commuter rail lines and highways which preceded World War II.

These uneven patterns of urban development are accompanied by uneven distributions of population. Analysis of relations between population density, proportions of land use, and percentages of impervious cover provides a tool for relating the divergent factors of total population, total land area, and total impervious cover. For example, Spieker (1970) reported that relatively little difference would exist in the density of population and the percentages of various land uses in 1990 in the Salt Creek basin of Illinois, regardless of whether urban sprawl were allowed to continue or the multitown pattern of development were followed. Spieker's data also show that the population density of the basin would be substantially greater if the radial-corridor pattern were used; however, supporting graphs and figures indicate that this would be accompanied by a corresponding increase in the percentages of high-density residential, commercial, and industrial land. These results confirm the hypothesis that a similar relation exists between population density and percentages of urban and suburban land use for the various spatial growth patterns that occur in time.

In terms of general lumped-sum parameters, the obvious effects of urbanization are to increase population density and the concentration of residential, industrial, and commercial buildings and facilities, with a resultant increase in the areal proportion of impervious cover as represented by the percentage of roof area, paved streets, driveways, sidewalks, and parking lots. For the purpose of this study, artificial ponds, lakes, and reservoirs, though manmade and impervious, are considered to be included with the areas of natural streams, ponds, and lakes as a category independent of population density.

Land use

A most important phase in any comprehensive planning program is the land-use survey. It provides the foundation for the study of existing problems and the drafting of future land-use plans. The following six categories, for which data are readily available in New Jersey, provide a convenient and

generally applicable land-use classification in relation to regional water-resources investigations:

1. Single-family residential; single-family dwellings predominate.
2. Multiple-family residential; multiple-family units predominate. These units include multiple-family homes, garden apartments, and high-rise apartments.
3. Commercial; wholesale and retail business, personal and business services, and other related business.
4. Industrial; research and development, light and heavy manufacturing, large utility installations, and railroad yards.
5. Public and quasi-public; hospitals, institutions, schools, other public buildings, churches, airports, golf courses, and government installations. For water-resources and especially storm-runoff considerations, the golf courses would fit better under the sixth category, but available data included them in the fifth.
6. Conservational, recreational, and open land; parks and preserves; public and private watersheds; agricultural, forest, and vacant lands.

Table 1 contains information regarding population density, land area, land use, and impervious area for each of the 21 counties in New Jersey. The population-density data were compiled from 1966 population estimates prepared by the Research and Statistics Section, Department of Conservation and Economic Development, State of New Jersey. The percentages of land area in each land-use category were compiled from 1966 data prepared by the Division of State and Regional Planning, Department of Community Affairs, State of New Jersey. The percentages of impervious area were calculated for a range of urban and suburban land-surface

modifications, as described later, representing average conditions found in semirural areas, suburbs and central cities.

Figure 1 shows county population-density data plotted against the percentage of land area contained within each of the six land-use categories. The curves shown fitted to each set of plotted data are second-degree polynomials defined by the logarithmic transforms of the following equations:

$$SFR = 0.000528 D^{2.520} - 0.339 \log D,$$

$$MFR = 0.004446 D^{0.127} + 0.181 \log D,$$

$$C = 0.000427 D^{1.818} - 0.202 \log D,$$

$$IND = 0.00005 D^{2.210} - 0.212 \log D,$$

$$P = 0.02769 D^{1.737} - 0.227 \log D, \text{ and}$$

$$CRO = 25.16 D^{0.555} - 0.135 \log D,$$

where

SFR = single-family residential land, in percent of land area,

D = population density, in persons per square mile,

MFR = multiple-family residential land, in percent of land area,

C = commercial land, in percent of land area,

IND = industrial land, in percent of land area,

P = public and quasi-public land, in percent of land area, and

CRO = conservational, recreational, and open land, in percent of land area.

Table 1.—Population density, land area, land use, and impervious area for counties in New Jersey as of 1966

County	Population density (persons per sq mi)	Land area (sq mi)	Land use (percent of land area)						Impervious area (percent of land area)		
			Single-family residential	Multiple-family residential	Commercial	Industrial	Public and quasi-public	Conservational, recreational, and open	Low	Intermediate	High
Atlantic	317	565.55	4.83	0.11	0.90	0.29	2.93	90.94	2.9	4.0	5.4
Bergen	3,773	235.68	40.18	1.18	5.18	3.76	7.90	41.80	15.1	22.9	31.5
Burlington	362	819.30	5.71	.20	.77	.56	4.81	87.95	4.0	5.5	7.3
Camden	2,044	222.16	21.98	2.00	4.64	4.04	4.16	63.18	11.2	16.4	21.8
Cape May	199	265.34	6.14	.40	.65	.35	2.85	89.61	3.1	4.4	5.9
Cumberland	244	502.40	4.48	.08	.43	1.80	1.54	91.67	2.4	3.8	5.1
Essex	7,488	127.44	42.34	7.85	2.56	8.30	10.79	28.16	20.6	30.7	41.3
Gloucester	486	328.60	11.00	.04	1.06	1.87	1.42	84.61	3.6	5.9	8.2
Hudson	13,795	44.10	9.73	19.48	5.58	27.26	6.28	31.67	31.4	43.9	54.3
Hunterdon	145	437.00	4.19	0	.58	.37	1.27	93.59	1.8	2.6	3.6
Mercer	1,335	226.00	15.95	1.90	1.98	4.78	6.09	69.30	9.6	14.1	18.8
Middlesex	1,781	308.79	19.81	1.26	2.01	6.21	4.46	66.25	9.5	14.7	19.9
Monmouth	902	477.01	14.75	.38	2.22	1.60	9.00	72.05	8.9	12.5	16.6
Morris	715	477.70	13.05	.30	1.40	2.33	6.45	76.47	7.0	10.2	13.8
Ocean	235	641.00	7.02	.16	.76	.81	6.39	84.86	5.1	7.0	9.2
Passaic	2,354	192.20	19.73	1.19	2.80	4.32	4.33	67.63	9.2	13.9	18.8
Salem	190	343.02	5.29	.02	.45	.92	2.78	90.54	2.8	4.1	5.5
Somerset	620	305.10	20.15	.20	.98	2.15	4.51	72.01	6.4	10.3	14.5
Sussex	121	526.30	5.10	0	.28	.08	.85	93.69	1.3	2.1	3.0
Union	5,452	103.39	44.74	4.11	4.56	11.32	9.80	25.47	20.9	32.0	43.3
Warren	197	362.00	5.08	0	.76	.45	3.38	90.33	3.1	4.3	5.7

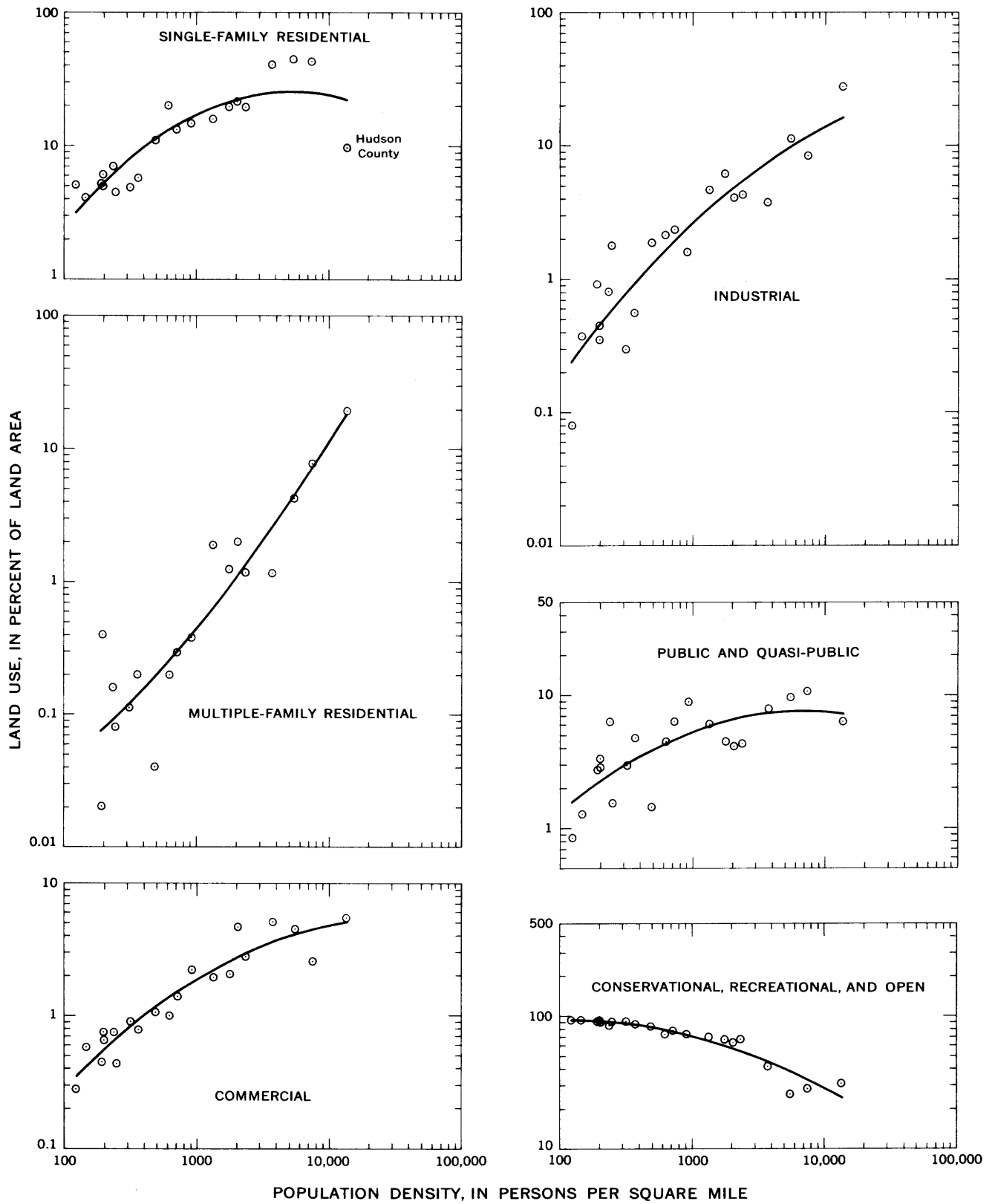


Figure 1.—Relations between land use and population density for counties in New Jersey.

In the single-family residential graph shown in figure 1, variations between the data and the fitted curve in the range of high population-density values indicate that an improved estimating relation for this land-use category might be developed by disregarding the outlying Hudson County data point. However, recognition must be given to the fact that Hudson County, situated across the Hudson River from downtown New York City, is the most densely populated county in the State. Some municipalities in this county have population densities above 40,000 persons per square mile. Also, the surface of the land cannot accommodate population densities above a certain limit in single-family residential housing. As population densities rise above some critical value, land that would ordinarily contain single-family housing units must be converted to multiple-family apartment use. This results in a decrease in the percentage of land devoted to single-family residential use, as illustrated by the reversal of the single-family residential curve in figure 1. Further studies based on larger sets of land-use data covering a wider range of population-density values should yield improved estimating relations compatible with this phenomenon.

In order to avoid difficulties associated with the use of zeros in the regression analysis only the 18 nonzero data points were used in generating the multiple-family residential curve shown in figure 1. An alternative approach in further studies would be to increase all values of percentage of multiple-family residential land by a value of 1.00 percent.

Impervious area

In order to transform the details of land-use patterns to a single numerical index that characterizes the hydrology of an urban area, a range of average percentages of impervious cover representing the effects of typical urban and suburban land-surface modifications found in each land-use category was estimated. These estimates, given in table 2, are based on general field observations and studies by Carter (1961); Felton and Lull (1963); Antoine (1964); and Stall, Terstriep, and Huff (1970).

Table 2.—Impervious land area within land-use categories

Land-use category	Impervious land area (percent)		
	Low	Intermediate	High
Single-family residential	12	25	40
Multiple-family residential	60	70	80
Commercial	80	90	100
Industrial	40	70	90
Public and quasi-public	50	60	75
Conservational, recreational, and open . .	0	0	0

Each land-use category contains a wide variation in proportions of impervious land area. The proportion of impervious land surface is generally maximum within central city neighborhoods, intermediate in suburban neighborhoods, and low-

est in rural areas. The proportion of impervious cover in residential areas decreases markedly as size of lot increases. Carter (1961) found the percentage of impervious surface area in suburban Washington, D.C., to be about 12 percent. Antoine (1964) concluded that 25 percent of the surface area is impervious on lots averaging 15,000 square feet in size, whereas 80 percent of the surface area is impervious on lots averaging 6,000 square feet. The industrial land-use category includes both industrial parks with lawns occupying a large percentage of the land area, and central-city manufacturing complexes where asphalt and concrete completely dominate the landscape. The public and quasi-public land-use category includes some relatively large tracts of rural land where impervious surfaces are almost nonexistent. These variations, which are an inherent part of any generalized land-use classification, were taken into account in arriving at the range of estimates given in table 2. The intermediate values given in table 2 are approximate average estimates for New Jersey.

By use of each set of estimates for percentage of impervious area (table 2) as weighting factors, the impervious area in each county was determined as the sum of the weighted proportions of land area in each land-use category. Table 1 contains the results in percent of total land area for each county.

The data given in table 1 were used to generate curves relating percentages of impervious land area to corresponding population-density values. The curves, which are presented in figure 2 along with county data corresponding to the intermediate impervious-area weighting factors, are second-degree polynomials defined by the logarithmic transforms of the following equations:

$$I_{\text{low}} = 0.170 D^{1.165} - 0.094 \log D,$$

$$I_{\text{intermediate}} = 0.0218 D^{1.206} - 0.100 \log D, \text{ and}$$

$$I_{\text{high}} = 0.0263 D^{1.247} - 0.108 \log D,$$

where

I_{low} , $I_{\text{intermediate}}$, and I_{high} = percentages of impervious land area based on the low, intermediate, and high impervious-area weighting factors, respectively, and

D = population density, in persons per square mile.

CONCLUSIONS

Urban and suburban land-use characteristics in New Jersey are clearly related to population density. This close relation makes possible the use of population density as a valuable tool in the indirect determination of past, present, and future land-surface modifications resulting from urban and suburban development.

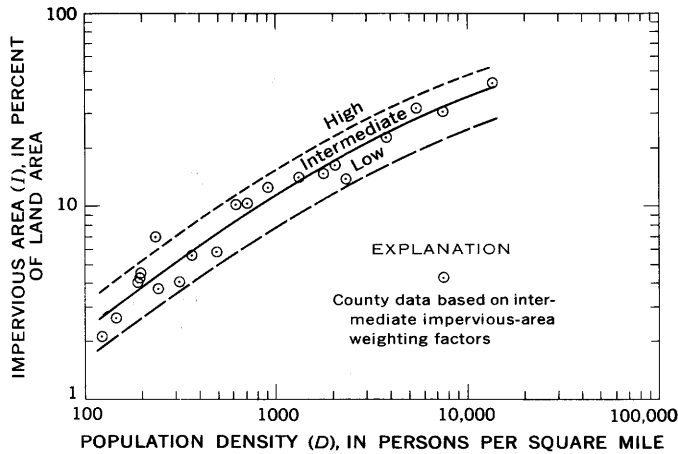


Figure 2.—Relation between impervious land area and population density for counties in New Jersey.

Information of this type is essential to the study of a wide variety of problems in urban hydrology. For example, annual peak discharge data are analyzed and fitted with some probability distribution to determine the recurrence intervals of the peaks. These methods do not incorporate the mechanics necessary for an evaluation of progressive changes in the hydrologic system. The ability to estimate the effects of past urban and suburban development provides a unique opportunity to use these conventional methods for the evaluation of long-term hydrologic data for basins in various stages of urban and suburban development as well as for basins in which urbanization is nearly complete. For example, several 10-year increments of annual peak-discharge data may be used to generate a series of mean annual floods corresponding to various stages of basin development. Progressive changes in the mean annual flood could then be evaluated in relation to an average percentage of impervious area estimated for each time period. Application of this approach to the study of long-term records for basins of different degrees of urbanization, in conjunction with appropriate data from related research by Carter (1961), Martens (1968), and Anderson (1970), could form a basis for improving current estimates of flood magnitude and frequency and for estimating the effects of future urban and suburban development on peak discharge characteristics.

Quantitative relations among population density, land use, and impervious area may also form a basis for solving a major problem in water-resources investigations in urban areas—namely, the utilization of hydrologic data in urban planning. Hydrologic parameters such as flood-peak magnitude and frequency, and lag-time, sediment-yield, and chemical-quality characteristics, are not readily adaptable to planning processes.

These parameters must be interpreted in direct relation to planning problems if effective decisions as related to water resources are to be made by the planner (Schneider, 1969). For example, the hydrologic effects of urbanization on peak streamflow characteristics are generally evaluated for different degrees of urbanization, as measured by the percentage of impervious cover in a basin (Carter, 1961; Anderson, 1970). Interpretation of these data in terms of planning-oriented parameters such as population density and land use is essential if alternatives that affect the hydrologic functioning of basins are to be evaluated. Conversely, the effects of differing degrees of urbanization on hydrologic parameters such as sediment-yield and chemical-quality characteristics are generally evaluated in terms of generalized land-use classifications. Translation of descriptive land-use terms to a single numerical index such as population density is helpful or even necessary if quantitative relations between hydrologic parameters and basin characteristics are to be developed. The rapidly growing need for quantitative indices of urbanization useful to the hydrologist and planner alike makes the indirect population-density technique one that may prove both widely applicable and very useful.

REFERENCES

- Anderson, D. G., 1970, Effects of urban development on floods in northern Virginia: U.S. Geol. Survey Water-Supply Paper 2001-C, 22 p.
- Antoine, L. H., 1964, Drainage and best use of urban land: Public Works (New York), v. 95, p. 88–90.
- Carter, R. W., 1961, Magnitude and frequency of floods in suburban areas: Art. 5 in U.S. Geol. Survey Prof. Paper 424-B, p. B9–B11.
- Felton, P. N., and Lull, H. W., 1963, Suburban hydrology can improve watershed conditions: Public Works (New York), v. 94, p. 93–94.
- Harris, E. E., and Rantz, S. E., 1964, Effect of urban growth on streamflow regimen of Permanente Creek, Santa Clara County, California: U.S. Geol. Survey Water-Supply Paper 1591-B, 18 p.
- Leopold, L. B., 1968, Hydrology for urban land planning—a guidebook on the hydrologic effects of urban land use: U.S. Geol. Survey Circ. 554, 18 p.
- Martens, L. A., 1968, Flood inundation and effects of urbanization in metropolitan Charlotte, North Carolina: U.S. Geol. Survey Water-Supply Paper 1591-C, 60 p.
- Schneider, W. J., 1969, The U.S. Geological Survey urban water program, in Moore, W. L., and Morgan, C. W., eds., Effects of watershed changes on streamflow: Austin, Tex., Univ. Texas Press, p. 165–168.
- Spieker, A. M., 1970, Water in urban planning, Salt Creek basin, Illinois: U.S. Geol. Survey Water-Supply Paper 2002, 147 p.
- Stall, J. B., Terstriep, M. L., and Huff, F. A., 1970, Some effects of urbanization on floods: Am. Soc. Civil Engineers Natl. Water Resources Eng. Mtg. (Memphis, Tenn.) Preprint 1130, 30 p.
- U.S. Bureau of the Census, 1962, National location code manual: Washington, U.S. Govt. Printing Office, 8 v.



PRELIMINARY HYDROGEOLOGIC APPRAISAL OF NITRATE IN GROUND WATER AND STREAMS, SOUTHERN NASSAU COUNTY, LONG ISLAND, NEW YORK

By NATHANIEL M. PERLMUTTER and ELLIS KOCH, Mineola, N.Y.

Work done in cooperation with the Nassau County Department of Public Works

Abstract.—Increase in nitrate content of ground water and streams, mainly due to infiltration of sewage, leachate from chemical fertilizers, and wastes from decayed crops, is a major water-quality problem in a 180-square-mile area studied from 1966 to 1970. This area consists of hydrologically similar adjoining sewered and unsewered parts. Nitrate content of water in the upper glacial aquifer, expressed as nitrate ion, averaged 30 mg/l and in seven places equaled or exceeded 100 mg/l. In comparison, the estimated average natural nitrate content is less than 1 mg/l. Nitrate content of ground-water fed streams averaged 11 and 25 mg/l in the sewered and unsewered areas, respectively. Nitrate-enriched water has also moved down into the underlying Magothy aquifer. For example, the nitrate content of water from 234 public-supply wells screened in the Magothy averaged 10 mg/l, but in 16 wells the nitrate content ranged from 45 to 94 mg/l. Reduction of nitrate to ammonium ion and subsequent ion exchange or sorption of the ammonium ion may retard southward movement of the "nitrate front." Increased pumping, however, could accelerate movement.

Deterioration of the chemical quality of the water resources of Nassau County is a major concern to nearly 1½ million residents and several thousand industrial and commercial users who depend solely on local ground water for supply. Infiltration of dissolved inorganic and some organic chemicals from a variety of sources has caused a marked increase in the hardness and in the contents of nitrate, chloride, sulfate, and other dissolved constituents in ground water and ground-water fed streams. Of the dissolved constituents, nitrate is presently (1971) one of the most serious threats to the public water supply.

Because water quality is a major consideration in long-term plans for developing Nassau County's water resources, the U.S. Geological Survey and the Nassau County Department of Public Works cooperatively studied the quality of water in aquifers and streams in a 180-square-mile area of southern Nassau County (fig. 1) from 1966 to 1970. The major objectives of the overall investigation were to delineate vertical and areal distributions of the principal dissolved chemical constituents in the water and to define the pattern of

movement and trends in concentrations of these constituents. Summary reports have been published on the effects of urbanization on stream quality (Koch, 1970) and on detergent and phosphate contents of the water (Perlmutter and Koch, 1971) in the study area. The present report discusses preliminary findings on nitrate content only. An interpretive report on the overall investigation and a basic-data report also are in preparation.

Nitrate content of ground water in many parts of the study area approaches or exceeds the recommended limit of 45 mg/l (milligrams per liter)¹ for drinking water (U.S. Public Health Service, 1962, p. 7). Ingestion of water whose nitrate content exceeds 45 mg/l may cause cyanosis or blue-baby disease in infants, and high concentrations may also affect adults and animals (U.S. Public Health Service, 1962, p. 48–50). Nitrite may be harmful also, but the nitrite content of the water in the study area was very low, generally less than 0.01 mg/l.

The study area includes hydrologically similar adjoining sewered and unsewered parts (fig. 1). The sewered part (about 75 square miles) consists of Nassau County Sewer District 2, which was completed largely between 1952 and 1964, and the village of Freeport, which has operated its own sewage system since 1927. Sewage from these areas receives secondary treatment; effluent from the two areas is discharged into tidewater south of Bay Park and Freeport, respectively. The present (1971) unsewered area, consisting of 105 square miles in southeastern Nassau County, is referred to as Sewer District 3 (fig. 1). Sewer construction now in progress in Sewer District 3 is scheduled for completion in about 1983. About 175,000 cesspools and septic-tank systems were in use in the unsewered

¹The U.S. Geological Survey presently (1971) reports nitrate content in terms of nitrate ion (NO_3^-). Nitrate content expressed as the nitrate ion can be converted to its equivalent elemental nitrogen (N) content by dividing by 4.428. For example, 45 mg/l nitrate as nitrate ion is equivalent to about 10 mg/l elemental nitrogen. Nitrate content in this report is expressed as nitrate ion unless otherwise indicated.

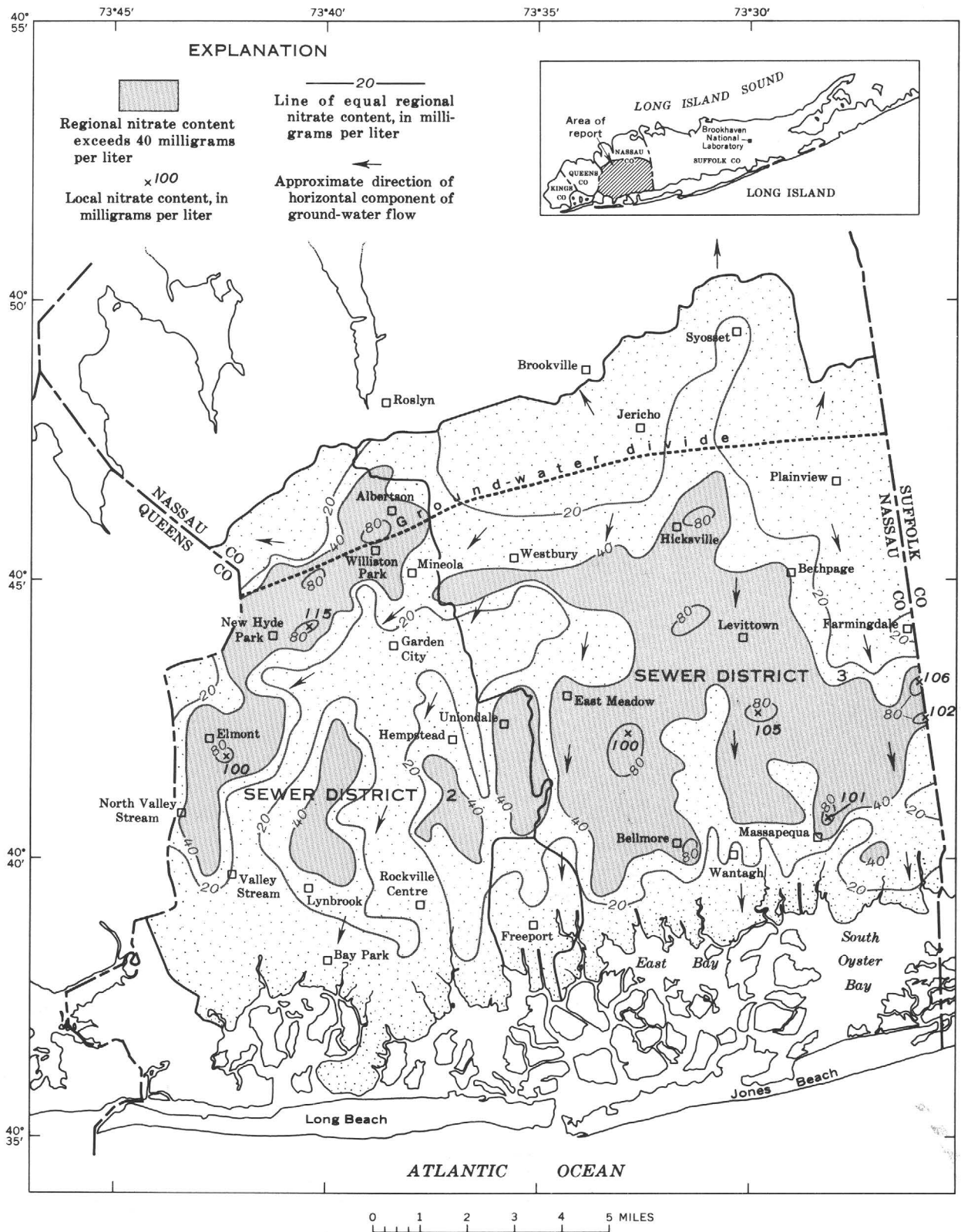


Figure 1.—Regional nitrate content of water in upper glacial aquifer in report area (patterned), southern Nassau County, Long Island, N.Y., 1966–70. Sewer District 3, under construction, 1971.

area in 1971. The number of active cesspools and septic tanks in the sewered area is unknown. However, all remaining sanitary waste-disposal systems in the sewered area were required by law to be connected to public sewers by April 1971 (F. J. Flood, oral commun., 1971). The present study was limited mainly to Sewer Districts 2 and 3 in southern Nassau County to help determine whether the presence or the absence of sewers has materially influenced the water quality in those areas.

Isbister (1966) discussed nitrate content of water from selected wells in northeastern Nassau County, and Smith and Baier (1969) evaluated status of and statistical trends in the nitrate content of water from public-supply wells in Nassau County. The Nassau-Suffolk Research Task Group (1969) investigated the nitrogen content of domestic sewage and of ground water in the vicinity of cesspools and systems consisting of septic-tank seepage beds at six sites in Nassau and Suffolk Counties.

About 3,000 chemical analyses of water from wells generally ranging in depth from 20 to 1,000 feet were examined in the present study. Many of these analyses were part of a long-term surveillance program on water quality started in about 1952 by the Nassau County Department of Health. The analyses were made under the supervision of Maxim Lieber. In addition, about 150 analyses of water samples were made by the U.S. Geological Survey.

Appreciation is expressed to John H. Peters, Commissioner, Nassau County Department of Public Works and to Dr. John H. Kinnaman, former Commissioner, Nassau County Department of Health for their support. Charles Kirsner, of the Nassau County Department of Public Works, supervised construction and sampling of test wells.

DESCRIPTION OF GROUND-WATER RESERVOIR AND FLOW PATTERN

The ground-water reservoir of Nassau County (fig. 2) consists of four major aquifers and two major confining units composed of unconsolidated materials of Pleistocene and Cretaceous ages (Cohen and others, 1968). The upper glacial aquifer, the most permeable aquifer on Long Island, consists chiefly of sand and gravel and contains unconfined water. The Magothy aquifer, beneath the upper glacial aquifer in most of the study area, consists of beds and lenses of fine to medium sand, clay, silt, and gravel, and contains confined water. These two aquifers are closely connected hydraulically in most of the area. Near the south shore, however, Gardiners Clay retards movement of water between the aquifers. The Jameco aquifer underlies the Gardiners Clay in southwestern Nassau County. Because of its small areal extent, the Jameco aquifer is not a significant water-bearing unit in the study area and is not discussed further.

Raritan clay is a major confining unit between the Magothy and the Lloyd aquifers. The Lloyd aquifer, consisting mostly

of sand, gravel, and some clay, contains confined water. Few wells tap the Lloyd aquifer in the study area, and not one of these yields nitrate-enriched water. Largely impermeable crystalline rock forms the bottom of the ground-water reservoir.

All fresh ground water (water other than salty ground water hydraulically connected to the sea) in the study area was originally derived from local precipitation. The average annual precipitation in the study area is about 45 inches. Under natural conditions, about half the average annual precipitation (180 million gallons per day) percolates down to the water table. Except for about 10 percent that runs off into streams, the remainder on the land surface returns to the atmosphere by evaporation and transpiration.

Depth of the water table below the land surface generally ranges from a few inches near the south shore to about 250 feet in the irregular hilly northern region. The highest altitude of the water table on the ground-water divide in east-central Nassau County (fig. 1) was about 80 feet in 1970.

Most of the ground water in the upper glacial aquifer moves southward from the ground-water divide (fig. 1) toward discharge areas in bays and streams at the south shore; some moves northward toward Long Island Sound; and some moves westward toward Queens County. The estimated combined average flow of 15 gaining streams at gaging stations near the south shore was 40 cfs (cubic feet per second) in the 1966-70 water years.

Deep confined aquifers are recharged by downward movement of water from the upper glacial aquifer in central Nassau County (fig. 2). Overall directions of ground-water movement in the deep aquifers (figs. 2 and 3) are generally similar to those in the upper glacial aquifer.

Pumpage for public supply, mainly from the Magothy aquifer, averaged about 140 mgd in 1969. About 60 mgd of the water used for public supply in the sewered area was discharged into nearby salty tidewater after secondary treatment. The remainder of the pumpage, except for small consumptive losses, returned to the upper glacial aquifer, mainly in the unsewered area, by infiltration of effluent from cesspools and septic tanks. Heavy pumping in Nassau and Queens Counties and loss of water by discharge of treated sewage to tidewater has caused a decline of ground-water levels (Franke, 1968) and development of westward and southwestward components of ground-water flow near the border of Queens and Nassau Counties.

WATERBORNE NITRATE

Natural content and sources of enrichment

To provide a basis for comparing past and present nitrate contents and to map the present (1971) extent of nitrate-enriched water, the earliest available records of water analyses in Nassau and Suffolk Counties were examined for indications of the predevelopment, or natural, nitrate content of water.

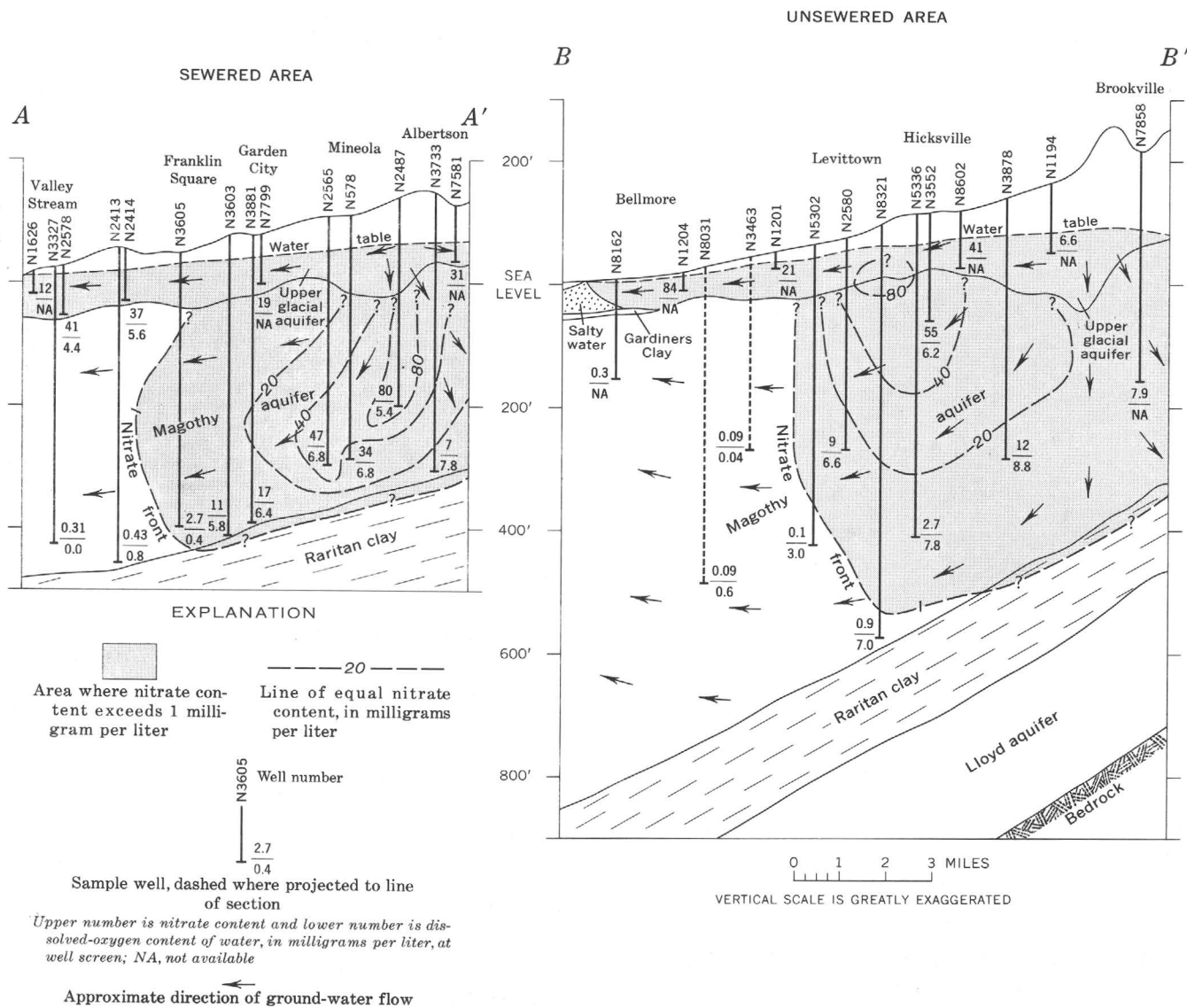


Figure 2.—Vertical distribution of nitrate in water in upper glacial and Magothy aquifers, southern Nassau County, Long Island, N.Y., 1968–70. Lines of sections are shown on figure 3.

According to these records, the nitrate content of water from wells 24–110 feet deep at five well fields in formerly sparsely populated southeastern Nassau County ranged from 0.0 to 2.5 and averaged 0.7 mg/l from 1897 to 1902 (Burr and others, 1904). Moreover, in 84 samples from 10 wells, between 32 and 135 feet deep and mostly in largely undeveloped parts of Brookhaven National Laboratory in central Suffolk County (fig. 1), the nitrate content ranged from 0.0 to 2.8 and averaged about 0.2 mg/l from 1948 to 1953 (deLaguna, 1964, table 6). Those values above 1 mg/l may partly reflect the influence of man's activities. These data and several hundred analyses of water from deep aquifers in Nassau and Suffolk Counties, suggest that the natural nitrate content of most of the water in the study area averaged less than 1 mg/l.

The estimated low natural nitrate content of the ground water probably reflects general absence of nitrogen-bearing minerals in the aquifer materials and minor leaching of nitrogen from natural soils. For discussion in this report, an average nitrate content greater than 1 mg/l was generally assumed to be due to man's activities.

A greater than 1 mg/l nitrate content of water in the study area probably mostly reflects: (1) infiltration of sewage from several hundred thousand active or abandoned cesspools and septic tanks and from seepage beds at several active or abandoned inland sewage-treatment plants, and (2) leaching of fertilizers and possibly of nitrogenous wastes from decayed crops, or a combination of the two. Precipitation is not a major source of nitrate enrichment of water in southern

Nassau County according to the nitrate content of 41 composite monthly samples at Mineola, N.Y., which averaged 1.5 mg/l from 1965 to 1970.

The fact that large volumes of water rich in nitrogen percolate into the upper glacial aquifer from cesspools and septic tanks in Long Island has been well documented by the Nassau-Suffolk Research Task Group (1969). Additional information obtained in the present study showed that the ammonia nitrogen content of partly treated effluent from a small sewage-treatment plant near Uniondale in central Nassau County (fig. 3) was 20 mg/l in May 1970. The ammonia nitrogen content of water from well N8673, screened at a depth of 33 feet in the upper glacial aquifer about 115 feet downgradient from seepage beds at the treatment plant, was 16 mg/l. If the ammonia were completely oxidized, as it is in most of Long Island's water, the nitrate content of the ground water would be about 70 mg/l.

Quantitative determination of input and removal of nitrogen from an agricultural soil-plant-water system is complex because of factors such as cultivation of the soil, type of crops and cropping practices, and type, time, and amount of fertilizer used (Stanford and others, 1970). Such determinations of the nitrogen balance were not available. Indirect evidence, however, suggests that conditions favorable for leaching fertilizer nitrogen from the soil zone has probably existed in the study area for many years. Farming began in colonial time and continued through the early 1950's, especially in the eastern part. However, since the end of World War I, farmland has been gradually sold for residential construction. In 1971 there were probably less than 10 farms in the study area.

Initially, animal manure was the principal fertilizer applied to the soil. But from about 1920 to 1950, millions of pounds of synthetic chemical fertilizers containing nitrogen, mostly in the form of ammonium nitrate, ammonium sulfate, and urea, were spread over thousands of acres of farmland. Availability of abundant natural recharge from precipitation and introduction of irrigation systems doubtless provided further opportunity for downward leaching of nitrate from the soil.

Although data are scanty, a few old water analyses suggest that nitrate contents of 17 mg/l at Hicksville in 1932 and 35 mg/l at Levittown in 1947 largely reflect former agricultural use of the land in those two communities (fig. 1).

Two other examples of probable nitrate enrichment of water from infiltration of fertilizers are average nitrate contents of 40 mg/l for water in the upper glacial aquifer beneath heavily fertilized farmland in sparsely populated eastern Suffolk County (deLaguna, 1964, p. 35) and 45 mg/l for water in the Magothy aquifer in a sparsely populated farmed area in west-central Suffolk County (Julian Soren, written commun., 1970).

Additional sources of nitrate enrichment of water are: (1) fertilizers applied to lawns and gardens, (2) decayed organic material in sanitary landfills, (3) recharge from storm-water

basins, and (4) possibly some local seepage of effluent from leaky sewer lines in parts of Sewer District 2. The specific sources of nitrate in water in some parts of the study area are uncertain because complex pumping and recharge patterns in the past 25 years have probably caused partial mixing of water from multiple sources discussed previously.

Nitrate in the upper glacial aquifer

In sewage and in ground water immediately downgradient from sewage-disposal systems, where the dissolved-oxygen content is low and nitrogen-reducing bacteria are abundant, the ammonium ion is the predominant species of nitrogen (Nassau-Suffolk Research Task Group, 1969). However, in the sewered area and at points remote from cesspools and septic tanks in the unsewered area, the water is generally more highly oxygenated and nitrate is the predominant species of nitrogen.

Approximate regional distribution and concentration of nitrate in water in the upper glacial aquifer for about 200 randomly located wells are shown by contours in figure 1. The wells were generally remote from specific sources of nitrate enrichment. The average nitrate content of the ground water was 28 and 36 mg/l, respectively, in the sewered and unsewered areas, and in seven places the nitrate content equaled or exceeded 100 mg/l. Scarcity of data, scattered marshlands, artificial fill, and salty ground water did not permit detailed mapping of the nitrate content of the water near the south shore.

Darker toned areas on figure 1 indicate places where water with a high nitrate content (generally greater than 40 mg/l) occupies part of the upper glacial aquifer in both sewered and unsewered areas. The high nitrate content of shallow ground water in parts of the study area is due mostly to factors discussed previously in the section on sources of nitrate enrichment.

The low nitrate content (generally about 1 to 20 mg/l) of some of the shallow ground water (see fig. 1) is attributed partly to the beneficial effects of several village-owned sewer systems; for example, the systems of Mineola and Garden City, which were in operation before the construction of Sewer District 2. Water of low nitrate content was also found beneath several parks, golf courses, a cemetery, and undeveloped land where infiltration of sewage is minimal.

Nitrate in the Magothy aquifer

Partly because of the natural flow pattern and partly because of pumping of deep wells, water from the upper glacial aquifer has moved down into the underlying Magothy aquifer, where it has formed a major body of nitrate-enriched water (figs. 2 and 3).

The northern limit of the main body of nitrate-enriched water (nitrate content generally exceeds 1 mg/l) extends beyond the northern limit of Sewer Districts 2 and 3 but was not mapped for this investigation. The approximate southern

limit or "toe" of the nitrate-enriched water body is along an imaginary line extending from about North Valley Stream eastward to Farmingdale (fig. 3). That line has been named the "nitrate front" in this report. South of the nitrate front, the nitrate content of most of the water in the Magothy aquifer is less than 1 mg/l (fig. 2), and ammonium and nitrite contents are generally less than 0.02 mg/l.

Nitrate-enriched water occupies nearly the full thickness of the Magothy aquifer in the northern and the central parts of the study area (fig. 2). The nitrate content generally decreases downward and laterally from as much as 94 mg/l near the center of the nitrate-enriched water body in the sewered area to 1 mg/l at the nitrate front. General hydrologic relations suggest that some nitrate-enriched water may have penetrated the upper part of the Raritan clay (fig. 2).

Hydraulic and geochemical controls on movement of the nitrate front

The position of the nitrate front in the Magothy aquifer (figs 2 and 3) is probably controlled chiefly by regional direction and rate of movement of ground water and possibly to some extent by geochemical processes. Computations involving estimates of the hydraulic coefficients of the Magothy aquifer and of present (1971) hydraulic gradients (by methods described in Ferris and others, 1962, p. 71-73) give a range in the rate of vertical movement of the nitrate-enriched water of 5 to 25 feet per year. If vertical movement in the saturated zone had averaged 10 feet per year, it would have taken about 50 years for the water to move 500 feet from the water table to the top of the Raritan clay.

On the basis of scanty hydraulic data, the estimated average rate of horizontal movement of nitrate-enriched water in the Magothy aquifer is 130 feet per year. Therefore, if hydraulic gradients are unchanged in the future, the nitrate front would reach the shoreline, about 6 miles to the south, in about 250 years. However, locally, where hydraulic gradients are steepened because of heavy pumping and where the hydraulic conductivity of the Magothy aquifer is greater than average, tongues of nitrate-enriched water may move faster than the preceding estimated rate.

Movement of the nitrate front in the Magothy aquifer may also be partly controlled by natural chemical reduction of the nitrate to ammonium ions in the reducing environment of the water near and south of the line of zero dissolved-oxygen content in the southern part of the study area (fig. 3). Sorption or exchange of the ammonium ion on silt or clay fractions in the Magothy aquifer or other significant loss of nitrogen from the water would further retard movement of the nitrate front. The existence of the reducing environment is premised largely on the downgradient loss of dissolved oxygen in the water (figs. 2 and 3). Depletion of oxygen was reported by Padar (1968, p. 421) and by Smith and Baier (1969, p. 27). Pearson and Friedman (1970, p. 1780) suggested that the

oxygen loss was caused mainly by oxidation of lignite (carbonaceous material) in the Magothy aquifer.

Nitrate in streams

Ground water with high-nitrate content discharges naturally from the upper glacial aquifer into stream channels in the southern part of the study area. The average nitrate content and the total daily load of 15 ground-water fed streams were about 11 mg/l and 650 pounds per day, respectively, in the sewered area, and about 25 mg/l and 3,750 pounds per day, respectively, in the unsewered area. The average nitrate content and the average daily load of 12 individual streams sampled during the study are shown in figure 4. The average nitrate content of streams in the sewered area generally was substantially lower than that of the streams in the unsewered area, perhaps because of the beneficial influence of sewerage on the quality of the ground water. The lower discharge of the streams in the sewered area (due to decline of ground-water levels, Franke, 1968) compared with the discharge of streams in the unsewered area also helps account for the smaller average nitrate load of streams in the sewered area.

Estimates of load of nitrate and of phosphate (Perlmutter and Koch, 1971) in streams are important because these constituents are among the primary nutrients necessary for the growth of algae and other aquatic plants in streams, ponds, and bays. However, the interrelation of changes in the overall nutrient balance and in other environmental conditions such as light intensity and temperature that favor development or decay of algal blooms are only partly understood at present (after Stanford and others, 1970).

CHANGES IN NITRATE CONTENT

Upper glacial aquifer

The quality of water in the upper glacial aquifer is influenced by numerous factors, including changes in rates of precipitation, pumpage, and infiltration of nitrate-enriched water. Consequently, short-term records of nitrate content (generally 1-5 years) commonly show wide fluctuations and are not necessarily indicative of long-term trends.

Short-term fluctuations in nitrate content of water in the upper glacial aquifer during this investigation are illustrated by the graphs in figure 5. Graphs of the nitrate content of water from observation wells N1428 and N8149 at Lynbrook, in the sewered area, show net upward trends from 1966 to 1970. In contrast, the graphs of nitrate content of water from observation wells at Uniondale (N8396) and Freeport (N1167 and N8337), also in sewered areas, show no significant net change during the same period.

The nitrate content of water from well N6664 screened in the upper glacial aquifer at Levittown in the unsewered area shows no significant net change from 1966 to 1970; however, it fluctuated nearly 50 mg/l during that period. This large

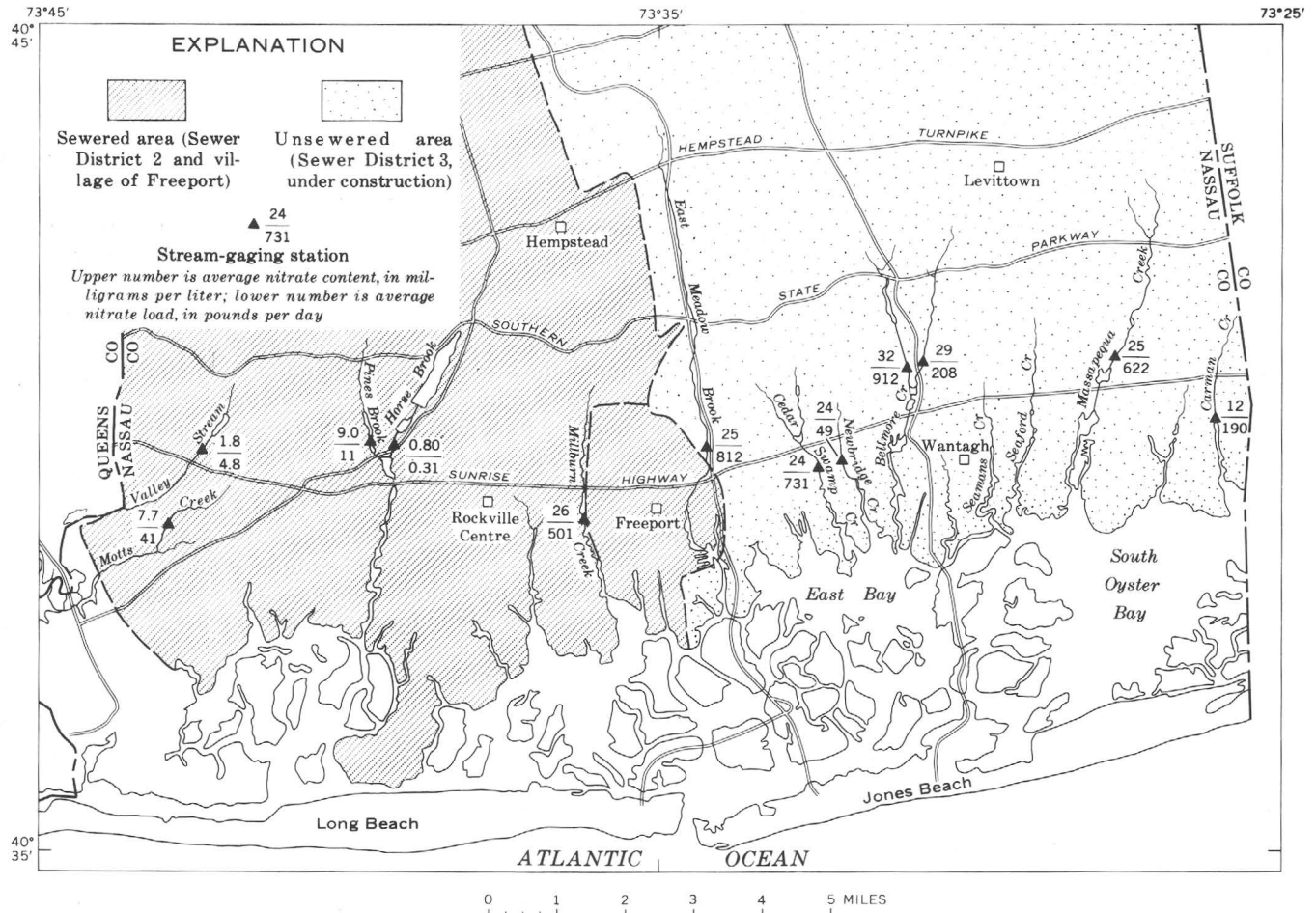


Figure 4.—Average content and daily load of nitrate in water at gaging stations on selected streams in southern Nassau County, Long Island, N.Y., 1966–70.

fluctuation of nitrate content is probably related chiefly to dilution effects of increased recharge from precipitation after the end of a regional drought that lasted from 1962 to 1966 (Cohen and others 1969). The nitrate content of water from well N7950 at Massapequa, also in the unsewered area, shows a sharp net increase of about 75 mg/l from 1966 to 1970. Apparently, infiltration of nitrate-enriched water (most likely from sewage) in this area exceeded the influence of dilution from natural recharge.

Long-term records of analyses are more meaningful indicators of trends in nitrate content of water in the upper glacial aquifer. Data for seven of 10 public-supply wells screened in the upper glacial aquifer in the sewered area show net nitrate declines ranging from 4 to 26 mg/l and averaging 17 mg/l from about 1955 to 1970. For example, the graph (fig. 5) for well N4077 near New Hyde Park (fig. 3) shows a net decline in nitrate content of about 22 mg/l since the area was sewered in about 1955. The nitrate content of water from the other three public-supply wells showed no significant net change during the same period.

Few data on long-term nitrate trends in water in the upper glacial aquifer in the unsewered area are available because most public-supply wells screened in the upper glacial aquifer in that area have been abandoned or are rarely pumped. The graph (fig. 5) for N2403, a former shallow public-supply well in Levittown, shows an increase in nitrate content of 17 mg/l from 1953 to 1965. The well was abandoned in 1965 because of high nitrate. Similarly, the nitrate content of water from two other wells in the unsewered area in southeastern Nassau County increased 28 and 34 mg/l, respectively, from 1952 to 1963 and from 1952 to 1969.

Magothy aquifer

According to data by Smith and Baier (1969), 72 of 234 public-supply wells screened in the Magothy aquifer in the study area yielded water that showed statistically significant upward trends in nitrate content from 1952 to 1969. Although the rate of increase in nitrate content of water from the 72 wells averaged 0.8 mg/l per year, continued upward

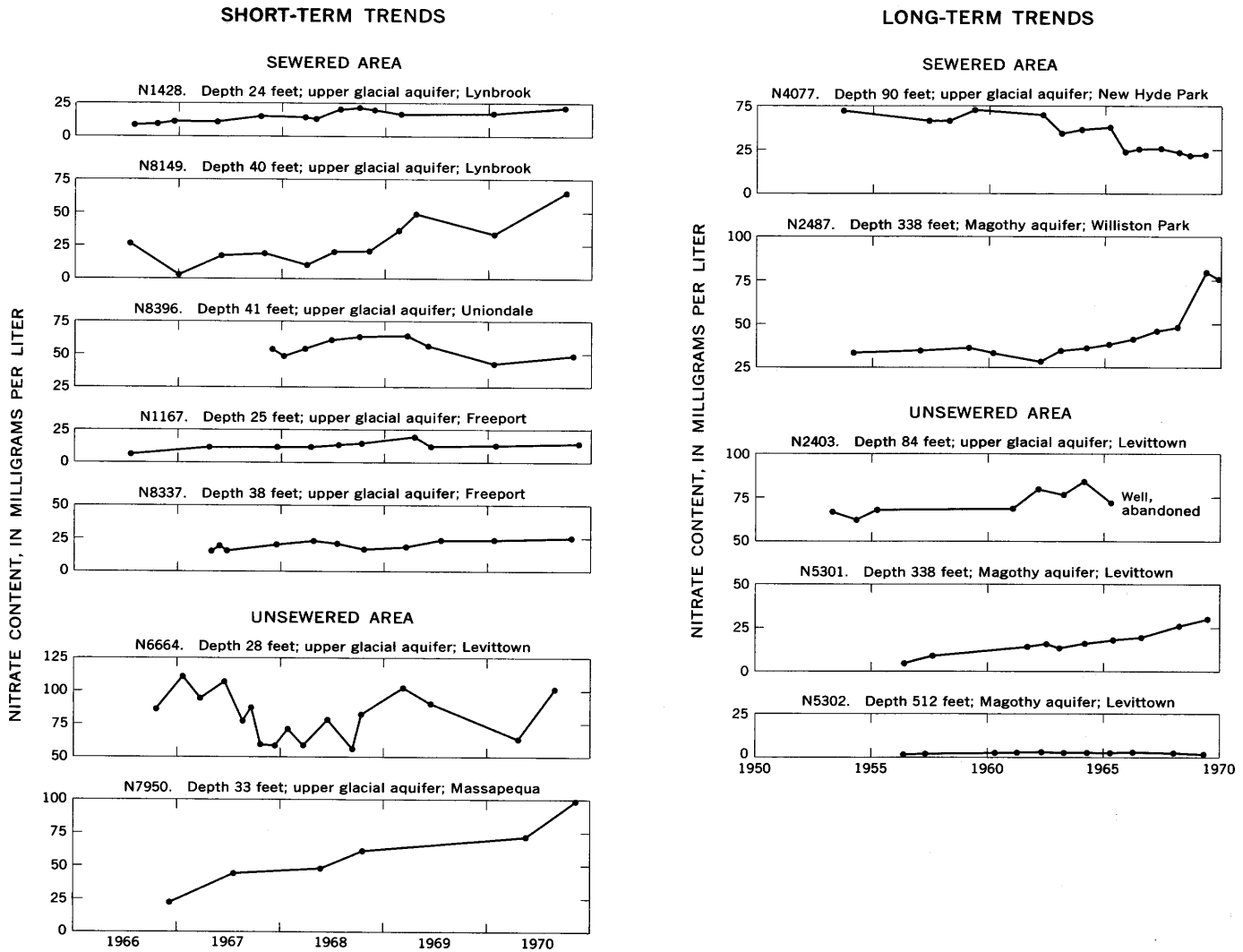


Figure 5.—Trends in nitrate content of water in upper glacial and Magothy aquifers. See figure 3 for location of wells.

trends represent a potential long-term threat to the chemical quality of the water in the Magothy aquifer. On the basis of data listed by Smith and Baier and continuation of present upward trends, within the next 50 years the nitrate content of water from 40 to 50 public-supply wells screened in the Magothy aquifer in the study area may exceed the limit recommended by the U.S. Public Health Service (1962) for drinking water.

Upward trends in nitrate content of water from several deep public-supply wells in the vicinity of the ground-water divide in central Nassau County (fig. 3) are of particular concern. Examples of such trends are shown by the graphs (fig. 5) for wells N2487 (Williston Park) and N5301 (Levittown) in the sewered and unsewered areas, respectively. Downward components of ground-water flow are steepest along the ground-water divide, and the rapid increases in the nitrate content of the water in the Magothy aquifer beneath the ground-water divide largely reflect that fact.

Farther downgradient from the ground-water divide, where the water in the Magothy aquifer is moving nearly horizontally, the nitrate content is apparently increasing more slowly. South of the nitrate front, no upward trends in nitrate content were observed in water from deep wells (for example, see graph for N5302, figs. 2 and 5). Furthermore, nitrate contents greater than 45 mg/l are not anticipated in water south of the nitrate front for many decades. However, some pumping wells, screened in the Magothy aquifer, locally may induce downward movement of nitrate-enriched water from the overlying upper glacial aquifer.

Streams

Discontinuous records of nitrate content of water in streams in the study area show annual fluctuations ranging from 4 to 28 mg/l from 1966 to 1970. However, as shown by graphs (fig. 6) for Millburn Creek in the sewered area and for Massapequa

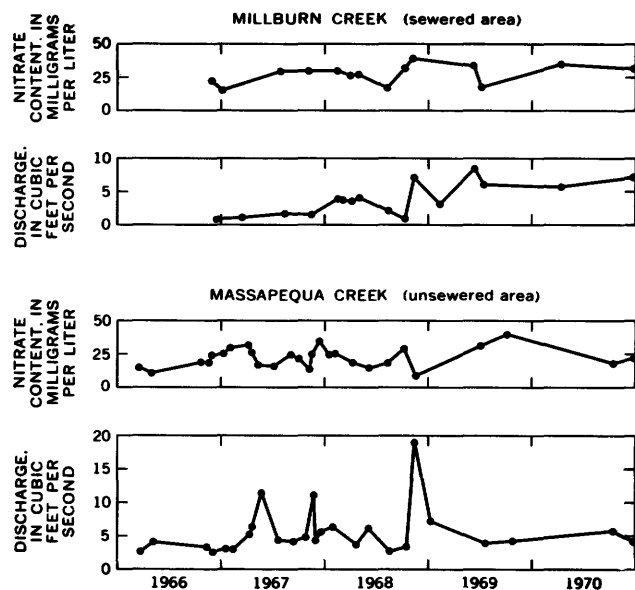


Figure 6.—Trends in nitrate content of water from Millburn and Massapequa Creeks, 1966–70. See figure 4 for location of sampling points.

Creek in the unsewered area, no well-defined trends in nitrate content are apparent from the overall 5-year period of record.

No correlation was observed between the upward trend in the nitrate content of water from observation well N7950 at Massapequa (figs. 3 and 5) from 1966 to 1970 and the relatively flat average trend in nitrate content of water at the gaging station on Massapequa Creek (figs. 4 and 6). Quality of the streamflow apparently more closely reflects the integrated quality of ground water from the contributing area above the gaging station rather than the quality of ground water at the nearby well.

The long-term influence of man's activities on the quality of the streamflow in the unsewered area is indicated by an increase of 13 to 18 times the average nitrate contents of East Meadow Brook, Newbridge Creek, Bellmore Creek, and Massapequa Creek from 1966 to 1970 (fig. 4) compared with the average from 1897 to 1902 (Burr and others, 1904, p. 338–342). Similarly, in the sewered area the average nitrate contents of Millburn Creek and of Pines Brook, respectively, from 1966 to 1970 (fig. 4) were 7 and 2 times those determined for the period 1897 to 1902.

EFFECT OF NITRATE ON USE OF WATER FOR PUBLIC SUPPLY

Largely because of high concentrations of nitrate and other chemical constituents, less than 5 percent of the water used for public supply in the study area is pumped from the upper glacial aquifer. Only 11 wells tapping the upper glacial aquifer, all except one in the sewered area, were pumped for public supply in 1970; and these were pumped intermittently. Nitrate

content of water from the public-supply wells tapping the upper glacial aquifer ranged from 19 to 74 mg/l and exceeded 45 mg/l at three installations. Locally, during peak water demand, shallow ground water whose nitrate content exceeds 45 mg/l is diluted with water of good quality (water with nitrate content generally less than 1 mg/l) from deep aquifers to meet U.S. Public Health Service drinking-water standards.

The nitrate content of water from 234 public-supply wells screened in the Magothy aquifer averaged 10 mg/l in 1970. However, water with a nitrate content of more than 1 mg/l was found in parts of the Magothy aquifer (fig. 3) beneath 26 of 32 public water-supply systems, and the nitrate content of water from about 60 percent of the public-supply wells in the study area exceeded 1 mg/l. The nitrate content of water from 16 public-supply wells screened in the Magothy aquifer ranged from 45 to 94 mg/l. Abandonment, relocation, and deepening of wells, reduction in pumpage, and blending of water from several wells have helped temporarily to alleviate the nitrate problem. Several suppliers are also considering the feasibility of removal or substantial reduction of nitrate content by on-site chemical treatment of nitrate-enriched water.

CONCLUSIONS

1. Substantial quantities of water in the upper glacial aquifer, both in sewered and unsewered areas, have a nitrate content that approaches or exceeds the recommended limit of 45 mg/l for drinking water. The chief sources of the nitrate are infiltrated sewage, mostly from domestic waste-disposal systems, and leachate from chemical fertilizers.

2. Nitrate-enriched water from the upper glacial aquifer has seeped down through the full thickness of the Magothy aquifer in parts of central Nassau County, where it forms a major water body having a nitrate content ranging from 1 to 94 mg/l.

3. At presently (1971) estimated rates of movement, the nitrate front in the Magothy aquifer, defined as the zone of contact between nitrate-enriched water and natural water (nitrate content less than 1 mg/l), may reach the south shore in about 250 years. However, movement of the front may be accelerated if pumpage increases or may be retarded if nitrate is removed from the water by natural reduction to the ammonium ion and the ammonium ion is subsequently removed by sorption or ion exchange.

4. Streams whose discharge is supported largely by ground-water inflow had average nitrate contents of 11 and 25 mg/l in the sewered and unsewered areas, respectively.

5. Nitrate contents for periods of 1–5 years generally were too variable to be useful as trend indicators. However, from 1955 to 1970 the decrease in nitrate content of water from seven of 10 public-supply wells screened in the upper glacial aquifer in the sewered area ranged from 4 to 26 mg/l and averaged 17 mg/l. Water from the other three wells showed no significant net change in nitrate content. The increase in nitrate content of water from 72 wells screened in the

Magothy aquifer in the sewered and unsewered areas generally ranged from 1 to 90 mg/l.

6. Improvement in the quality of chemically deteriorated ground water after construction of sanitary sewers is a slow process that may require several decades for effective natural dilution and discharge of most of the residual nitrate in the ground water. On-site chemical treatment of water for removal or reduction of nitrate content, blending of high-nitrate water (nitrate content generally exceeds 45 mg/l) with water of good quality (nitrate content generally less than 1 mg/l), and pumping fresh water into aquifers containing nitrate-enriched water are possible interim remedies for the nitrate problem.

7. Even after the construction of sanitary sewers, reduction in nitrate content of ground water and streams in sewered areas may be retarded if other potential sources of nitrate enrichment such as leakage of effluent from abandoned cesspools and septic-tank systems, sanitary landfills, inland sewage-treatment plants, industrial and storm-water discharge into ground-water bodies, excessive use of chemical fertilizers on lawns, and scattered leakage from public-sewer systems are not eliminated or controlled.

REFERENCES

- Burr, W. H., Hering, Rudolph, and Freeman, J. R., 1904, Report of the Commission on Additional Water Supply for the City of New York: New York, Martin B. Brown Co., 980 p.
- Cohen, Philip, Franke, O. L., and Foxworthy, B. L., 1968, An atlas of Long Island's water resources: New York Water Resources Comm. Bull. 62, 117 p.
- Cohen, Philip, Franke, O. L., and McClymonds, N. E., 1969, Hydrologic effects of the 1962-66 drought on Long Island, New York: U.S. Geol. Survey Water-Supply Paper 1879-F, 18 p.
- deLaguna, Wallace, 1964, Chemical quality of water, Brookhaven National Laboratory and vicinity, Suffolk County, New York: U.S. Geol. Survey Bull. 1156-D, 73 p.
- Ferris, J. G., Knowles, D. B., Brown, R. H., and Stallman, R. W., 1962, Theory of aquifer tests: U.S. Geol. Survey Water-Supply Paper 1536-E, 174 p.
- Franke, O. L., 1968, Double-mass-curve analysis of the effects of sewerage on ground-water levels in Long Island, New York, in Geological Survey Research 1966: U.S. Geol. Survey Prof. Paper 600-B, p. B205-B209.
- Isbister, John, 1966, Geology and hydrology of northeastern Nassau County, Long Island, New York: U.S. Geol. Survey Water-Supply Paper 1825, 89 p.
- Koch, Ellis, 1970, Man's effect on the quality of selected streams in southern Nassau County, Long Island, New York, in Geological Survey Research 1970: U.S. Geol. Survey Prof. Paper 700-C, p. C189-C192.
- Nassau-Suffolk Research Task Group, 1969, The Long Island water pollution study: New York State Dept. Health, 395 p.
- Padar, F. V., 1968, Health Department surveillance of ground-water quality, in 4th Am. Water Resources Conf. Proc., New York City, Nov. 18-22, 1968: Am. Water Resources Assoc., p. 414-424.
- Pearson, F. J., Jr., and Friedman, Irving, 1970, Sources of dissolved carbonate in an aquifer free of carbonate minerals: Water Resources Research, v. 6, no. 6, p. 1775-1781.
- Perlmutter, N. M., and Koch, Ellis, 1971, Preliminary findings on the detergent and phosphate content of the waters of southern Nassau County, New York, in Geological Survey Research 1971: U.S. Geol. Survey Prof. Paper 750-D, p. D171-D177.
- Smith, S. O., and Baier, J. H., 1969, Report on nitrate pollution of ground water in Nassau County, Long Island: Mineola, N. Y., Nassau County Dept. Health, 49 p.
- Stanford, George, England, C. B., and Taylor, A. W., 1970, Fertilizer use and water quality: U.S. Dept. Agriculture, ARS 41-168, 19 p.
- U.S. Public Health Service, 1962, Drinking water standards: Public Health Service Pub. 956, 61 p.



TRAVEL OF POLLUTION-INDICATOR BACTERIA THROUGH THE MAGOTHY AQUIFER, LONG ISLAND, NEW YORK

By JOHN VECCHIOLI, GARRY G. EHRLICH, and THEODORE A. EHLKE,
Mineola, N.Y., Menlo Park, Calif., Albany, N.Y.

Prepared in cooperation with the Nassau County Department of Public Works

Abstract.—Results of experimental injection of reclaimed water (highly treated but unchlorinated sewage) into the Magothy aquifer at Bay Park, Long Island, N.Y., indicate very restricted travel of pollution-indicator bacteria. Although the injected water had substantial total-coliform, fecal-coliform, and fecal-streptococcal densities, no fecal-coliform or fecal-streptococcal bacteria and only nominal total-coliform bacteria were found in water from an observation well 20 feet away from the point of injection. Restriction of bacterial travel through the Magothy aquifer is due primarily to the high filter efficiency of the fine to medium sand characteristic of the aquifer and to bacterial capture by a filter mat and (or) slime deposits that form around the injection well during injection.

Experimental ground-water recharge using reclaimed water obtained from tertiary-treated sewage is being studied at Bay Park, Long Island, N.Y. (Cohen and Durfor, 1967; Peters and Rose, 1968). Recharge is accomplished by means of an injection well screened from 418 to 480 feet in the Magothy aquifer of Late Cretaceous age. G. G. Ehrlich, T. A. Ehlke, and John Vecchioli (1972) (p. B241–B245, this chapter) discussed the microbiological phenomena that occurred when chlorinated, virtually bacteria-free reclaimed water was injected at Bay Park, April 14 to May 17, 1970.

In December 1970, unchlorinated reclaimed water containing substantial total-coliform, fecal-coliform, and fecal-streptococcal densities was injected for a 10-day period. This experiment afforded an excellent opportunity to evaluate the extent of travel of pollution-indicator bacteria through the Magothy aquifer.

METHODS AND RESULTS

Unchlorinated reclaimed water was injected at a continuous rate of 340 gallons per minute for 10 days. Except for the absence of chlorine in the water, physical and chemical qualities of the injectant were virtually the same as those reported earlier (Vecchioli, 1970; Ehrlich and others, 1972).

Total-coliform, fecal-coliform, and fecal-streptococcal densities were determined by membrane-filter methods described by the American Public Health Association and others (1971). Results of the microbiological tests are given in table 1.

Observation wells located 20 and 100 feet radially from the injection well and screened within the injection zone were monitored for arrival of the injected water by determining the specific conductance of water from the wells. Specific conductance of water in the Magothy aquifer was about 35 $\mu\text{mhos/cm}$ (micromhos per centimeter) at 25°C, whereas the specific conductance of the injected water was about 750 $\mu\text{mhos/cm}$ at 25°C. Results of the monitoring showed that the injected water had almost completely displaced the water in the Magothy aquifer in the 20-foot well after the second day, but it constituted only about 40 percent of the water obtained from the 100-foot well on the 10th day.

Neither fecal-coliform nor fecal-streptococcal bacteria were found in any samples collected from the observation wells during the test. Positive indications of total-coliform bacteria were found in the observation well 20 feet away on the second, sixth, seventh, and eighth days of the test and, also, in a sample obtained from that well 26 days after the end of the test. All counts were low, and those coliform present may have been due to growth of extraneous bacteria such as soil bacteria or of other bacteria inadvertently introduced from the land surface into the observation well.

Shortly after the end of the test, the injection well was pumped briefly to clear the casing and to recover water from short distances beyond the screen. The bacterial count of the repumped water was almost the same as that of the injected water. The injection well was then shut down for 26 days. After 26 days, water was again pumped from the injection well. Total-coliform and fecal-coliform counts of repumped water were much lower than they had been at the end of the test but were still substantial. The fecal-streptococcal count after 26 days downtime was about the same as it was at the end of the test.

Table 1.—Bacterial colony counts of water sampled during and after the injection test of Nov. 30–Dec. 10, 1970

[All results in number per 100 ml; (e), estimated count based on non-ideal colony count]

Date	Injected water	Observation wells		Injection well ¹
		20 feet from injection well	100 feet from injection well	
Total coliform				
12-1-70....	9,700	19
12-2-70....	27,000	<1
12-3-70....	10,000	<1
12-4-70....	47,000	<1
12-5-70....	60,000	1(e)
12-6-70....	61,000	1(e)
12-7-70....	60,000	1(e)	<1	...
12-8-70....	54,000	<1	<1	...
12-9-70....	55,000	<1	<1	...
12-10-70....	83,000
1-5-71....	...	4(e)	<1	3,200
Fecal coliform				
12-1-70....	200	<1
12-2-70....	1,200	<1
12-3-70....	...	<1
12-4-70....	2,000	<1
12-5-70....	1,500	<1
12-6-70....	750(e)	...	<1	...
12-7-70....	1,100	<1	<1	...
12-8-70....	2,200	<1	<1	...
12-9-70....	960	<1	<1	...
12-10-70....	2,800
1-5-71....	...	<1	<1	10(e)
Fecal streptococcus				
12-1-70....	1(e)	<1
12-2-70....	80	<1
12-3-70....	11(e)	<1
12-4-70....	39	<1
12-5-70....	31	<1
12-6-70....	30	<1
12-7-70....	10(e)	<1	<1	...
12-8-70....	15(e)	<1	<1	...
12-9-70....	22	<1	<1	...
12-10-70....	57
1-5-71....	...	<1	<1	32

¹Water repumped from injection well after end of injection on Dec. 10, 1970.²All counts reported as <1 represent no colonies counted in a 100-ml sample.

DISCUSSION

Rate of travel of bacterial cells through an aquifer is probably controlled by complex interactions of many physical, chemical, and biological factors. Nevertheless, in an investigation of the travel of pollutants, the California State Water Pollution Control Board (1954, p. 105) found that, at maximum penetration of coliforms into the aquifer, the logarithm of the coliform density decreased linearly with distance from the injection well. They also observed that the injection rate and, hence, the velocity of water movement in this confined aquifer had little effect on the rate of decrease of the number of organisms with distance from the site of injection. The board concluded that the extent of penetration of the bacteria was

limited primarily by physical factors. The relationship was expressed in the following way:

$$\log N_2 = \log N_1 - F(r_2 - r_1),$$

where

N_1 = most probable number of organisms at any sampling point in the aquifer, r_1 ;

N_2 = most probable number of organisms at any other point, r_2 ;

r_1, r_2 = distance between sampling points and point of injection; and

F = coefficient of filter efficiency of the aquifer (the California State Water Pollution Control Board defined F as "filterability" of the system.).

When the equation is applied to the Bay Park observations and values of 50,000 colonies per 100 ml for the water injected ($r_1 = 0$) and one colony per 100 ml for water from the observation well 20 feet from the injection well ($r_2 = 20$) are used, the calculated coefficient of filter efficiency of the Magothy aquifer is 0.23. The coefficient is conservatively low because the observation well's coliform density used in the calculation (one per 100 ml) was the highest count observed during the test. The high first-day count was not included in the interpretation. The calculated filter efficiency is adequate for comparison purposes.

Fractional reduction in bacterial density per foot of travel may be determined from the following formula (California State Water Pollution Control Board, 1954, p. 106):

$$-F = \log(1-R),$$

where R = fractional reduction of bacteria per foot of travel. With an F value of 0.23, the computed R value is 0.41. This is interpreted as a 41-percent reduction in bacterial count per foot of travel.

In the California study, the coefficient of filter efficiency varied somewhat with direction of water movement from the injection well, but the average R values ranged from 19 to 24 percent (California State Water Pollution Control Board, 1954, p. 107). The aquifer under test in the California study, a stratum of sand and pea gravel, had a hydraulic conductivity of about 250 fpd (feet per day). The injection zone in the Magothy aquifer at Bay Park, a slightly silty fine to medium sand with thin beds of coarse sand, had an average hydraulic conductivity of about 130 fpd (G. D. Bennett, written commun., 1970). On the basis of grain size and hydraulic conductivity, the greater fractional reduction values found for the Magothy aquifer seem reasonable.

The California group noted that coliform counts in water from observation wells reached maximum values and then decreased as injection continued, possibly because of a filter mat that formed in the vicinity of the injection well during injection. Some bacteria in the injectant presumably were captured by the filter mat, which consisted of solids accumu-

lated at the injection well–aquifer interface (California State Water Pollution Control Board, 1954, p. 153). Formation of a filter mat and (or) microbial slime deposits have been noted also in the Bay Park study. Bacterial capture by the filter mat complicates evaluation of the computed aquifer filter efficiency. However, this effect can be minimized by using bacterial-density data for times early in the injection period before much development of the filter mat. The computed coefficient of filter efficiency for the early period would approximate the filtration component related to the effective porosity of the aquifer.

In this study, a significant number of indicator bacteria survived for at least 26 days in the vicinity of the injection well. Virtually undiluted injected water reached the observation well 20 feet from the injection well within 2 days. Only a nominal coliform count was observed in this water. If the bacterial cells had been traveling at a rate comparable with that of the injectant, significant coliform counts should have been observed on about the second day. Large diminution of counts owing to die-off would not be expected in a period of only 2 days because the bacteria could survive for as long as 100 days (Romero, 1970, p. 42). Therefore, filtration phenomena rather than organism die-off probably were the primary reason for the large reduction in numbers. Similar conclusions were reached by the California group (California State Water Pollution Control Board, 1954, p. 113).

Movement of bacteria through porous media has been the subject of many reports reviewed by Romero (1970). The results of our study are consistent with the conclusion reached in other studies that the travel of bacteria in fine-grained materials is limited to short distances. However, pathogens

that are more persistent than the indicator bacteria might travel farther into the aquifer than the indicator bacteria. Absence of fecal coliform and of fecal streptococci does not preclude the possibility that pathogens occur in the Magothy aquifer at some distance from the injection well. Nevertheless, detection of pathogens in the aquifer would be difficult because their density, if they were present, most likely would be very low.

REFERENCES

- American Public Health Association, American Waterworks Association, and Water Pollution Control Federation, 1971, Standard methods for the examination of water and wastewater: New York, Am. Public Health Assoc., 874 p. [13th ed.]
- California State Water Pollution Control Board, 1954, Report on the investigation of travel of pollution: Sacramento, Calif., Pub. 11, 218 p.
- Cohen, Philip, and Durfor, C. N., 1967, Artificial-recharge experiments utilizing renovated sewage-plant effluent—A feasibility study at Bay Park, New York, U.S.A., in Artificial recharge and management of aquifers—Symposium of Haifa, 1967: Internat. Assoc. Sci. Hydrology Pub. 72, p. 193–199.
- Ehrlich, G. G., Ehlke, T. A., and Vecchioli, John, 1972, Microbiological aspects of ground-water recharge—Injection of purified chlorinated sewage effluent, in Geological Survey Research 1972: U.S. Geol. Survey Prof. Paper 800-B, p. B241–B245.
- Peters, J. H., and Rose, J. L., 1968, Water conservation by reclamation and recharge: Am. Soc. Civil Engineers Proc., Jour. Sanitary Eng. Div., v. 94, no. SA4, p. 625–639.
- Romero, J. C., 1970, The movement of bacteria and viruses through porous media: Ground Water, v. 8, no. 2, p. 37–48.
- Vecchioli, John, 1970, A note on bacterial growth around a recharge well at Bay Park, Long Island, New York: Water Resources Research, v. 6., no. 5., p. 1415–1419.



MICROBIOLOGICAL ASPECTS OF GROUND-WATER RECHARGE— INJECTION OF PURIFIED CHLORINATED SEWAGE EFFLUENT

By GARRY G. EHRLICH, THEODORE A. EHLKE, and JOHN VECCHIOLI,
Menlo Park, Calif., Albany, N.Y., Mineola, N.Y.

Work done in cooperation with the Nassau County Department of Public Works

Abstract.—Chlorinated, purified sewage was injected through a well at Bay Park, N.Y., at rates of 350 gpm (gallons per minute) and 200 gpm for 33 days. Observed injection-well head buildup was correlated with the content of mostly inorganic particulate matter in the injectant. Bacterial slimes were not present in repumped water or in a sand probe placed near the injection zone during the test. Several species of aerobic and facultative anaerobic bacteria were found in repumped water samples. Microbial growth occurs in the aquifer after chlorine has been inactivated by the aquifer materials.

Recharge of ground water through injection wells generally results in gradual reduction of aquifer hydraulic conductivity in the immediate vicinity of the well. The observed reduction of hydraulic conductivity is caused by physical, chemical, or biological agents, acting singly or in combination. The biological component has not been studied in detail. Earlier studies have focused on the persistence and mechanisms of transport of coliform and other bacterial indicators of fecal contamination with a major emphasis on the long-range transport of pathogenic organisms through the aquifer. This work has been reviewed by Romero (1970). Completed studies at Bay Park, Long Island, N.Y., (Vecchioli and others, 1972) (p. B237–B239, this chapter) indicate that bacterial travel is restricted to negligible distances in fine-grained materials and that the possibility of public health problems is generally minimal.

Several investigators, including the California State Water Pollution Control Board (1954), Sniegocki (1963), and Rebhun and Schwartz (1968) have suggested that the suspended particulate organic and inorganic matter in the injection water is collected in an organically rich mat near the well. Although extensive biological activity could occur in this mat, the subject has received little attention. Rebhun and Schwartz (1968) and Vecchioli (1970) found high nonfecal coliform counts in repumped water when there was an appreciable pause between injection and redevelopment, even though chlorinated water of drinking quality was used for

injection. These observations were interpreted to mean that bacterial growth occurred after the termination of injection.

Indigenous microorganisms may play important roles in artificial recharge. First, aquifer pores may be blocked by bacterial cells, causing decreased hydraulic conductivity. Second, particulate organic matter may be solubilized by bacteria and released to the aquifer. Third, microbial action could degrade ground-water quality by producing undesirable organic compounds. Virtually no information is available about the bacterial flora inhabiting the organic mat or its potential to produce these effects. This report describes some bacteria isolated from an injection well at the conclusion of a recharge test.

EXPERIMENTAL PROCEDURE

A field recharge test was done at Bay Park, Long Island, N.Y., from April 14 to May 17, 1970. Recharge was through a gravel-packed well consisting of an 18-inch-diameter fiberglass casing above a 16-inch-diameter stainless steel screen set 418 to 480 feet below land surface (Cohen and Durfor, 1966). The well taps the Magothy aquifer of Late Cretaceous age. The injection zone is composed of unconsolidated silty fine to medium sand and thin beds of coarse sand.

Water for the test was supplied by a pilot tertiary sewage treatment plant (Peters, 1968; Peters and Rose, 1968). The ranges of observed physical, chemical, and bacterial properties of the injection water during the test are given in table 1.

Purified sewage was injected into the recharge well under positive head at a rate of 350 gpm (gallons per minute) for the first 19 days and 200 gpm for the last 14 days of the test. Chlorine residual in the injectant was maintained above 2 mg/l (milligrams per liter) in the final days of injection. The total quantity of water injected was approximately 14×10^6 gallons.

A cylindrical container, 2 inches in diameter and 19 inches long, made of stainless steel screen was filled with sand from the aquifer. This sand probe was autoclaved repeatedly until

Table 1.—*Chemical, physical, and bacterial quality of recharge water in the test of April 14 to May 17, 1970, at Bay Park, Long Island, N. Y.*

[Chemical analyses given in milligrams per liter except for aluminum, iron, and manganese, which are in micrograms per liter. Abbreviations: C, Celsius; cm, centimeter; No., number; and ml, milliliter]

Parameter	Maximum observed	Minimum observed	Median
Chemical and physical properties			
Silica (SiO ₂)	18	12	13
Aluminum (Al), total	300	0	0
Iron (Fe), total	2,600	180	790
Manganese (Mn), total	420	30	70
Calcium (Ca)	19	13	15
Magnesium (Mg)	5.4	4.3	4.8
Sodium (Na)	71	57	64
Potassium (K)	12	11	12
Bicarbonate (HCO ₃)	70	39	59
Sulfate (SO ₄)	240	100	140
Chlorine, total residual	4.0	0	2.5
Chloride (Cl)	76	63	68
Fluoride (F)	1.0	0	.1
Organic nitrogen (N)	4.0	.57	.9
Nitrite (NO ₂)	.30	0	0
Ammonia as NH ₄	34	25	32
Nitrate (NO ₃)	2.8	0	.4
Phosphate as PO ₄ , total	2.8	.30	1.2
Dissolved solids, residue at 180°C	372	316	339
Dissolved solids, calculated from determined constituents	467	306	374
Total solids, residue, volatile	42	2	16
Hardness as CaCO ₃ (Ca, Mg)	67	50	58
Noncarbonate hardness	35	0	8
Specific conductance (micromhos/cm at 25°C)	778	677	717
pH	6.9	5.3	6.0
Water temperature (°C)	20	16	18
Dissolved oxygen	6.7	3.8	5.9
Chemical oxygen demand (0.025N K ₂ Cr ₂ O ₇)	18	0	8
Detergents (methylene blue active substance)	.49	0	.05
Total chlorine residual (mg/l)	4.0	0	2.5
Bacterial quality			
Coliforms (No./100 ml)	>100	0	0
Fecal coliforms (No./100 ml)	1,200	0	0
Fecal streptococci (No./100 ml)	1	0	0

the contents were sterile as shown by the absence of growth in tubes of nutrient broth seeded with sand from the probe. Immediately before the start of the test, the sterile sand probe was lowered approximately 450 feet into an observation well in the gravel pack surrounding the recharge well. The sand probe was removed immediately before the well was redeveloped. Sand from the probe was suspended in sterile buffered dilution water that was used to establish a dilution series. Samples were

planted in plate count agar as described by the American Public Health Association and others (1965).

Well redevelopment by pumping was started 48 hours after the injection test ended. The water in the well casing at the time of redevelopment gave a strong positive response when tested for residual chlorine and was considered to be virtually bacteria free. Water was pumped from the aquifer at a rate of 300 gpm. Samples were collected in sterile bottles immediately after a volume of water equal to the volume of the well casing had been pumped from the well and after 30 minutes, 4 hours, and 24 hours of pumping.

Aerobic bacteria were isolated by filtering measured volumes of sample through membrane filters (mean pore size 0.45 microns). The exposed filters were placed on plates of plate count agar with the bacteria-laden side up. Plates were inverted, incubated at 30°C, and examined for colony development after 24 and 48 hours. Material from well-developed colonies was purified by serial picking and streaking on nutrient agar plates. Stock cultures were maintained on nutrient agar slants with biweekly transfers.

Coliform counts were made by the membrane-filter method described by the American Public Health Association and others (1965).

Denitrifying bacteria counts were determined by the method described by Alexander (1965).

Presence of sulfate-reducing bacteria was determined by the method described by the American Petroleum Institute (1959).

Tests for anaerobic bacteria were done by two methods: (1) 0.1 ml of water sample was spread over the surface of a plate of predried Anaerobic Agar (BBL, Division of Bioquest); (2) exposed membrane filters were laid on plates of Anaerobic Agar. Cultures were incubated in Gas Pak Jars (BBL, Division of Bioquest) at room temperature.

Characterization of pure cultures was done according to methods described by the Committee on Bacteriologic Technique (1957) and Skerman (1967).

RESULTS AND DISCUSSION

Specific capacity of the injection well decreased from 24 gpm per foot at the start of the test to 2.5 gpm per foot at the end. Specific capacity as a function of time is shown in figure 1. Turbidity values during the test and a cumulative plot of these values compared to the head buildup in the injection well are shown in figure 2. The rapid rise in head buildup followed closely the increase in turbidity observed from about the 12th to the 22d day. This suggests that the observed loss of well capacity resulted primarily from the introduction of particulate matter from the injectant into the aquifer pores.

The first water recovered from the aquifer was grayish tan, opaque, and very turbid. The volatility of suspended matter was 25 percent, indicating that it was composed primarily of inorganic material. The suspended material had the appearance of an alum floc that could have carried over from the tertiary

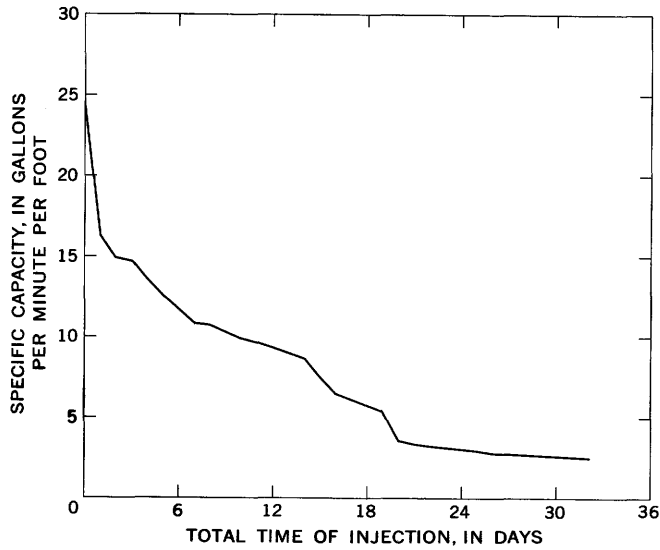


Figure 1.—Decrease of injection-well specific capacity during the test of April 14 to May 17, 1970.

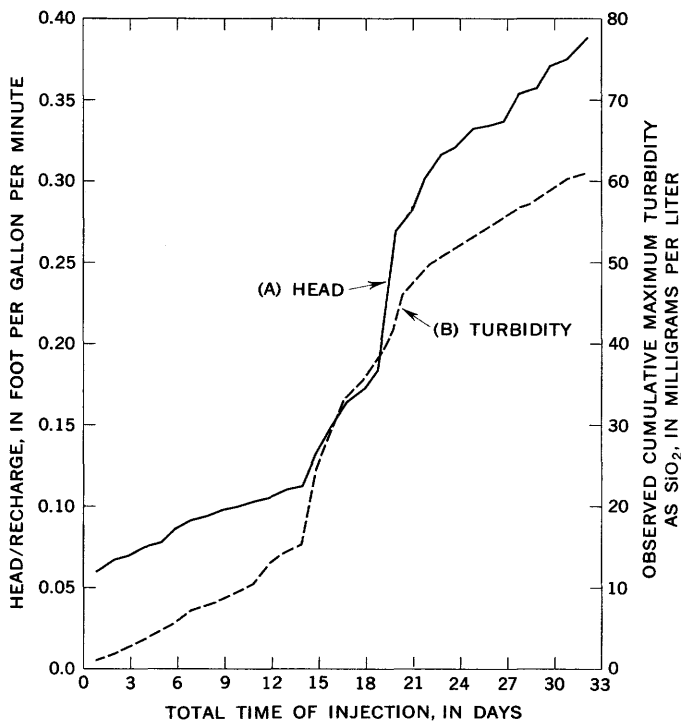


Figure 2.—Comparison of head buildup and turbidity during test of April 14 to May 17, 1970. A, head buildup divided by rate of injection; B, cumulative maximum turbidity.

treatment process. Water clarity gradually improved with the pumping. Visible turbidity disappeared within several hours. No dissolved oxygen in the repumped water was detectable by the Winkler method. Residual chlorine was not detected in the repumped water.

Results of plate counts, coliform determinations, and denitrifying bacteria determinations are given in table 2. Some bacteria were detected in the sand probe, but no attempt was made to determine the bacterial density. No obvious signs of microbial activity, such as slimy growths or noticeable odors, were associated with the sand probe.

The bacterial count of the first water recovered from the aquifer was only about 5,000 colonies per 100 ml. This further suggests that the observed clogging was caused by particulate matter rather than bacterial growth. After 30 minutes of pumping, the count increased to 5×10^6 colonies per 100 ml. Denitrifying bacteria accounted for about 1 percent of the total count. The few colonies (67 per 100 ml) of coliform bacteria were not significant in the total count. Fecal coliforms were not detected. Bacterial densities of water samples taken after 4 hours and 24 hours of pumping were about the same as that of the sample taken after 30 minutes of pumping.

Table 2.—Bacterial counts of water recovered from injection well after injection test of April 14 to May 17, 1970

[Total bacteria and coliform counts given as colonies per 100 ml; denitrifying bacteria given as most probable number per 100 ml]

Pumping time (minutes)	Total bacteria count	Denitrifying bacteria count	Coliform count
0	5×10^3	0
30	5×10^6	5×10^4	67
240	5×10^6	5×10^4	70
1,440	5×10^6	5×10^4	90

No anaerobic bacteria were found. Whether this condition represents the absence of these organisms in the aquifer or the use of improper media and isolation techniques is not known. The seeming absence of anaerobic bacteria is under further study.

After primary plating and picking, 25 isolates from the aerobic plates were selected for further study. Skerman's (1967) generic classification was used with the following exception: certain rod-shaped, nonmotile, gram-negative, oxidase-negative bacteria were assigned to the genus *Acinetobacter* Brisou and Prevot emended by Baumann and others (1968) rather than to the genera *Achromobacter* Bergey and others or *Alcaligenes* Castellani and Chalmers prescribed by Skerman's (1967) key.

The 25 isolates were assigned to eight genera. The identified genera and their frequency of isolation are listed in table 3.

Specific identification was not attempted; therefore, more than one species may be grouped under a single genus listed in table 3. For example, several strains from at least two distinct genera are present among the pseudomonads. Two of these, *Pseudomonas* type 1 and *Pseudomonas* type 2, were isolated only from the sand probe. Type 2 was a vigorous denitrifier,

Table 3.—Genera of bacteria isolated from recharge well 2 days after cessation of extended recharge test

Genus	In sand probe	Frequency of isolation				
		In repumped water samples				
		Pumping time in minutes				
		0	30	240	1,440	
<i>Pseudomonas</i>	type 1..	1	0	0	0	0
	type 2..	1	0	0	0	0
	type 3..	0	0	4	2	0
<i>Micrococcus</i>	0	1	0	0	0	0
<i>Alcaligenes</i>	0	2	1	0	1	1
<i>Flavobacterium</i>	0	1	0	0	0	0
<i>Acinetobacter</i>	0	1	0	0	0	3
<i>Aeromonas</i>	0	0	1	1	0	0
<i>Serratia</i>	0	0	2	0	0	0
<i>Proteus</i>	0	0	0	2	1	1

whereas type 1 lacked this ability. They seem to be different biotypes of *Pseudomonas fluorescens*. Although no specimens of denitrifying bacteria were isolated directly from the plated colonies, there was positive evidence for their presence in the repumped water samples from the denitrifying bacteria count tests. Cultures of bacteria similar to *Pseudomonas* type 2 were readily isolated from positive tests on 30-, 240-, and 1,440-minute samples. Denitrifying bacteria represented only a small fraction of the total count and were overlooked in the initial selection of strains for study. Other species of pseudomonads, found in the 30- and 240-minute samples, are lumped together under the designation *Pseudomonas* type 3. Further characterization of all isolates is now under way.

The generic composition of bacteria in the repumped water resembled that of a typical activated sewage-sludge floc. McKinney (1962) reported that the following genera are typically present in activated sludge: *Alcaligenes*, *Flavobacterium*, and *Bacillus*; if hydrocarbons or carbohydrates are present, *Pseudomonas* is also found. With one exception, *Bacillus*, the same genera were found in the repumped water. *Bacillus* was not found at this time but has been isolated from the injection well at other times. The primary source of the seed bacteria from which this bacterial flora developed is not known. It is probably derived partly from organisms in the injectant and partly from soil bacteria that have worked their way into the injection well.

Absence of dissolved oxygen in the repumped water indicates anaerobic conditions in the aquifer. Only negligible growth of strictly aerobic species of *Alcaligenes*, *Micrococcus*, *Flavobacterium*, and *Acinetobacter* can occur under anaerobic circumstances. A few genera of facultative anaerobes such as *Proteus*, *Aeromonas*, and *Serratia* were found. These bacteria can grow under anaerobic circumstances if fermentable carbohydrates are available. *Pseudomonas* type 2 can grow under anaerobic conditions by using nitrate in place of oxygen. Although nitrate concentration was typically only about 0.4 mg/l, this low concentration would be sufficient to sustain a

small population of denitrifying bacteria. *Pseudomonas* types 1 and 2 can also sustain growth under anaerobic conditions by decomposing arginine, an amino acid. The relative importance of arginine metabolism is unknown because no data on arginine concentrations are available. Obligate anaerobic bacteria were not found in any of the repumped water samples. The contribution of anaerobic processes to the total biological activity in the aquifer is thus uncertain at this time.

Water samples taken from an observation well 20 feet from the injection well 72 hours after the test had a foul odor that resembled hydrogen sulfide. This odor had not been observed before the injection study. Tests for sulfate-reducing bacteria were positive. The injectant evidently contained adequate nutrients to sustain a population of sulfate-reducing bacteria.

Recovery of highly turbid water with a significant concentration of predominantly inorganic particulate matter at the onset of pumping suggests that an efficient filtering action took place in the aquifer very near to the well bore. The low bacterial density (table 2) suggests that bacterial growth in this zone was inhibited by chlorine. The sharp increase in bacterial densities and absence of chlorine in later repumped water samples indicates that this inhibiting action is confined to short distances from the well screen. The fact that only aerobic or facultative anaerobes were found suggests that oxygen persisted in the injectant longer than chlorine. Depletion of dissolved oxygen can occur by reaction with aquifer materials as well as through aerobic metabolism. Isolation of sulfate-reducing bacteria and their characteristic product at a considerable distance from the injection well suggests that some bacterial nutrients persisted in the injectant after its passage through the zone of aerobic metabolism near the well.

Additional injection studies are now in progress, and bacterial isolates are being studied in greater detail. Continued study will improve the understanding of the role of bacteria in artificial recharge. This knowledge should lead to improved methods of artificial ground-water recharge.

REFERENCES

- Alexander, Martin, 1965, Denitrifying bacteria, in *Methods of soil analysis*, Pt. 2, Chemical and microbiological properties: Madison, Wis., Am. Soc. Agronomy, p. 1484-1486.
- American Petroleum Institute, 1959, Recommended practice for biological analysis of water-flood injection waters: Dallas, Tex., Am. Petroleum Inst. Recommended Practice 38, 10 p.
- American Public Health Association, American Waterworks Association, and Water Pollution Control Federation, 1965, Standard methods for the examination of water and wastewater: New York, Am. Public Health Assoc., 769 p.
- Baumann, Paul, Doudoroff, Michael, and Stanier, R. Y., 1968, A study of the Moraxella Group-II, oxidative negative species (Genus *Acinetobacter*): *Jour. Bacteriology*, v. 95, no. 5, p. 1520-1541.
- California State Water Pollution Control Board, 1954, Report on the investigation of travel of pollution: Sacramento, Calif., Pub. 11, 218 p.
- Cohen, Philip, and Durfor, C. N., 1966, Design and construction of a unique injection well on Long Island, New York, in *Geological*

- Survey Research 1966: U.S. Geol. Survey Prof. Paper 550-D, p. D253–D257.
- Committee on Bacteriologic Technique, 1957, Manual of microbiological methods: New York, McGraw-Hill, 315 p.
- McKinney, R. E., 1962, Microbiology for sanitary engineers: New York, McGraw-Hill, 293 p.
- Peters, J. L., 1968, Supplemental water supply by tertiary treatment and recharge, in Proc. 4th Am. Water Resources Conf. series 6: New York, Am. Water Resources Assoc., p. 330–340.
- Peters, J. H., and Rose, J. L., 1968, Water conservation by reclamation and recharge: Am. Soc. Civil Engineers, Jour. Sanitary Eng. Div., v. 94, no. SA4, p. 625–639.
- Rebhun, M., and Schwarz, J., 1968, Clogging and contamination processes in recharge wells: Water Resources Research, v. 4, no. 6, p. 1207–1217.
- Romero, J. C., 1970, The movement of bacteria and viruses through porous media: Ground Water, v. 8, no. 2, p. 37–48.
- Skerman, V. D. B., 1967, Guide to the identification of the genera of bacteria, 2d ed.: Baltimore, Md., Williams and Wilkins, 303 p.
- Sniegocki, R. T., 1963, Problems in artificial recharge through wells in the Grand Prairie Region, Arkansas: U.S. Geol. Survey Water-Supply Paper 1615-F, p. F1–F25.
- Vecchioli, John, 1970, A note on bacterial growth around a recharge well at Bay Park, Long Island, New York: Water Resources Research, v. 6, no. 5, p. 1415–1419.
- Vecchioli, John, Ehrlich, G. G., and Ehlke, T. A., 1972, Travel of pollution-indicator bacteria through the Magothy aquifer, Long Island, New York, in Geological Survey Research 1972: U.S. Geol. Survey Prof. Paper 800-B, p. B237–B239.



CORROSION OF WELL-CASING AND SCREEN METALS IN WATER FROM THE MAGOTHY AQUIFER AND IN INJECTED RECLAIMED WATER, BAY PARK, LONG ISLAND, NEW YORK

By JOHN VECCHIOLI and ANTHONY A. GIAIMO, Mineola, N.Y.

Prepared in cooperation with the Nassau County Department of Public Works

Abstract.—Short-term (1- to 5-month) corrosion rates were determined for mild steel, stainless steel, and copper in contact with both water from the Magothy aquifer and injected reclaimed water. Only mild steel showed significant corrosion. Average corrosion rates for mild steel were 0.003 and 0.007 inch per year penetration for water from the Magothy aquifer and reclaimed water, respectively. The corrosion rates indicate that water from both sources is moderately corrosive to mild steel. Although corrosion rates were somewhat higher in reclaimed water than in Magothy water, electrochemical relationships show that water from the Magothy aquifer is more undersaturated with ferrous iron and, thus, is potentially more corrosive than reclaimed water. Higher rates of corrosion in reclaimed water are attributed to catalytic action of sulfate-reducing bacteria.

The U.S. Geological Survey in cooperation with the Nassau County Department of Public Works is studying the feasibility of injecting reclaimed water (highly treated sewage) into the Magothy aquifer on Long Island, N.Y. Experimental injection is being done at Bay Park in southern Nassau County (Cohen and Durfor, 1967). Reclaimed water is obtained from a demonstration tertiary-treatment plant, which further purifies a small part of the effluent from the Bay Park activated-sludge-type sewage-treatment plant (Peters and Rose, 1968). Studies of metal corrosion were made before and during some of the injection experiments to acquire data needed to assess the suitability of various metals used in well casings and screens. This paper compares the corrosivity of water from the Magothy aquifer with that of the injected water after contact with the aquifer.

METHODS OF INVESTIGATION

Analysis of water samples by conventional laboratory methods (Rainwater and Thatcher, 1960) was supplemented by onsite determinations of unstable properties or constituent concentrations that would be expected to change during transit to the laboratory. Onsite determinations included pH

(negative logarithm of hydrogen-ion concentration), Eh (electrode potential), and ferrous iron and sulfide contents of water in contact with corrosion test probes. Eh was measured by the method described by Back and Barnes (1961). This method uses a platinum-calomel electrode system installed in a special cell through which flows a continuous stream of sample water.

Short-term (maximum of 162 days) corrosion rates were measured with electrical-resistance-type probes of thin-walled tubing. The probes were inserted into either the injection well (N7884) or an observation well (N7886) 20 feet away. Both wells are screened in the same zone of the Magothy aquifer—from about 420 to 480 feet below land surface. Three separate tubular probes consisting of mild steel (alloy 1020), copper, and stainless steel (alloy 304) were used in all tests. The probes were suspended opposite the screens in the wells and thus were exposed to water presumably identical, or nearly so, with that in the surrounding aquifer. The probes were removed periodically from the wells, and changes in their electrical resistance were determined with a portable Kelvin Bridge circuit (corrosometer). Changes in electrical resistance represent loss of metal from the probes; corrosion meter dial readings can be converted to corrosion rates. For the probes used in this study, corrosion rates are obtained from the following formula:

Corrosion rate (inches of penetration per year) =

$$\frac{\Delta \text{ in dial reading}}{\Delta T \text{ (time in days)}} \times 0.00146.$$

This method of determining rates of corrosion is described in detail by Barnes and Clarke (1969). Corrosion rates, expressed in IPY (inches of penetration per year), of 0 to 0.002, 0.002 to 0.02, 0.02 to 0.05, and greater than 0.05 are considered to represent insignificant, moderate, severe, and extreme damage, respectively (Barnes and Clarke, 1969, p. 4).

CORROSION RATES

Corrosion probes were exposed to aquifer water in two test periods. In the first test, the probes were suspended in the screened interval of well N7884 for 75 days (fig. 1). In the second test, the probes were suspended for 162 days in the

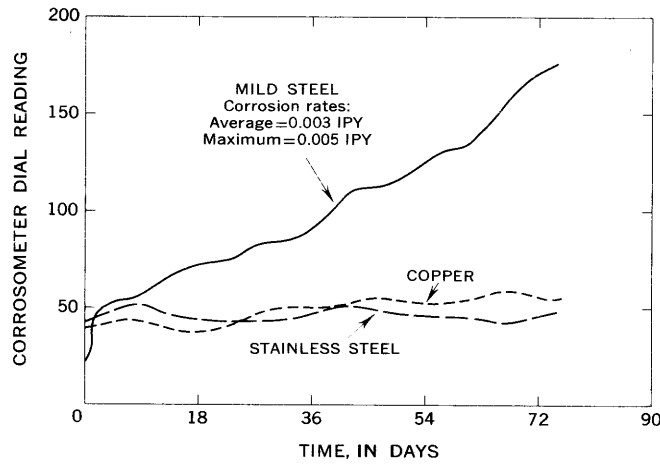


Figure 1.—Corrosion curves for metals in water from the Magothy aquifer, Long Island, N.Y., well N7884. IPY, inches penetration per year.

screened interval of well N7886 (fig. 2). Average corrosion rates for the mild-steel probe of 0.003 IPY were determined from both tests. Maximum corrosion rates were 0.005 and 0.007 IPY for the first and second tests, respectively. These rates fall toward the lower end of the moderate corrosion range. No significant corrosion of either the stainless-steel probe or the copper probe was observed in either test.

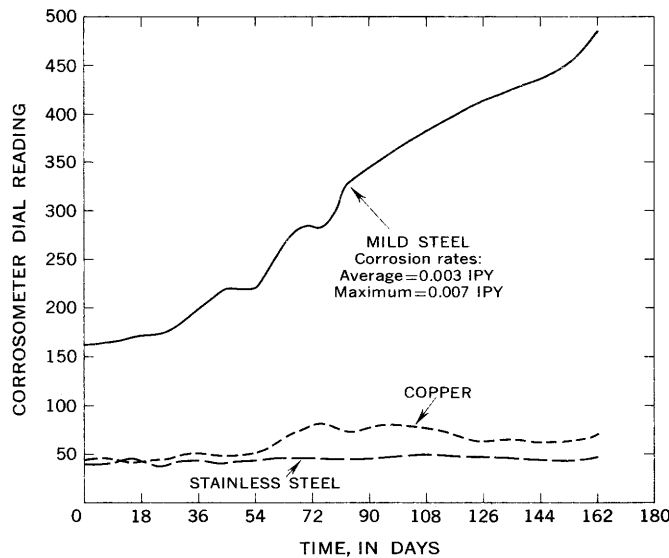


Figure 2.—Corrosion curves for metals in water from the Magothy aquifer, well N7886. IPY, inches penetration per year.

Three similar probes suspended in observation well N7886 were exposed later to the reclaimed water after it had been injected into and had traveled through the Magothy aquifer for 20 feet. For two tests of 36-day (injection test 5) and 30-day (injection test 7) duration, average corrosion rates of mild steel were 0.007 and 0.006 IPY, respectively. (See figs. 3 and 4.) These data indicate moderate corrosion. However, maximum corrosion rates of mild steel in the two tests, 0.029 and 0.019 IPY respectively, were in the upper-moderate to low-severe corrosion range. Copper and stainless-steel probes showed no significant corrosion.

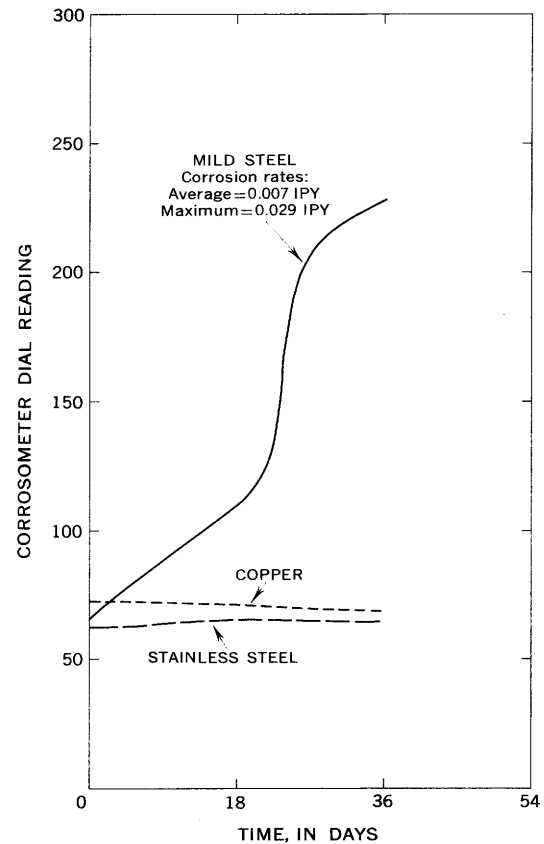


Figure 3.—Corrosion curves for metals in reclaimed water injected in test 5, well N7886. IPY, inches penetration per year.

DISCUSSION

Corrosion in aqueous media is commonly recognized as electrochemical in nature. Hence, the cited corrosion rates can be evaluated in terms of water chemistry and degree of saturation of the water with respect to ferrous ion activity by using the redox reaction



and the Nernst-law relation

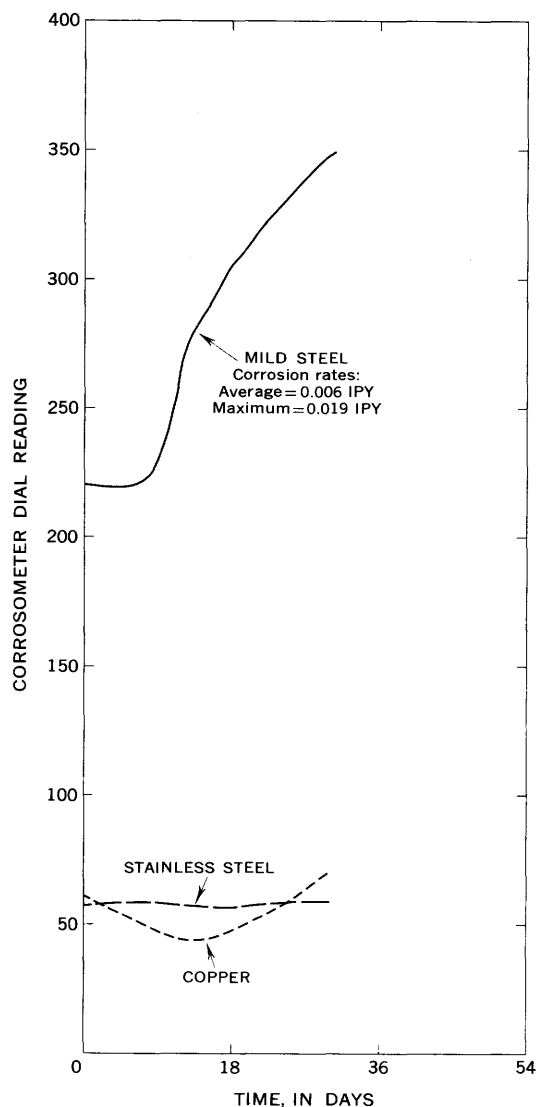


Figure 4.—Corrosion curves for metals in reclaimed water injected in test 7, well N7886. IPY, inches penetration per year.

$$Eh_T = E_T^\circ + \frac{RT}{2F} \ln \alpha Fe^{+2},$$

where

- Eh_T = redox potential at temperature T ,
- E_T° = standard-state electrical potential adjusted for departure from the reference state of 25°C (Celsius),
- R = gas constant,
- T = temperature in degrees Kelvin,
- F = Faraday constant, and
- α = ion activity.

Temperatures of water from the Magothy aquifer and injected reclaimed water were about 15°C; the 10° difference from the reference temperature of 25°C results in an adjust-

ment of only +0.005 volts in the standard-state electrical potential, E° . Moreover, Hem (1970, p. 22) states that temperature departures of ±10° to 15°C from reference temperatures are not large enough to preclude the direct application of standard-state conditions to most natural-water environments. Therefore, standard-state conditions are assumed in the following computations.

The Fe^{+2} (ferrous ion) concentration of the actual state and a calculated concentration for the state of equilibrium at the measured redox potential can be expressed as a ratio, CR . CR is defined as the ratio of cation concentration or activity actually determined to cation concentration or activity at equilibrium (Barnes and Clarke, 1969). According to Barnes and Clarke (1969, p. 28), values of $\log_{10} CR$ greater than zero represent supersaturated conditions leading to possible encrustation and protection against corrosion. Values of $\log_{10} CR$ equal to zero represent equilibrium conditions with uncertain results; values less than zero represent unsaturated conditions leading to corrosion.

Applying the method described by Barnes and Clarke (1969), consider first the water in the Magothy aquifer (table 1). According to F. J. Pearson, Jr. (written commun., 1970), the measured Eh was about -0.100 volts, the molal concentration of Fe^{+2} was 5×10^{-6} , and the ionic strength of the solution was $5 \times 10^{-4} M$ (molar). But, at the measured molal concentration of Fe^{+2} (5×10^{-6}) and ionic strength of the solution ($5 \times 10^{-4} M$), the equilibrium Eh should be -0.597 volts; and at the measured Eh (-0.100 volts), the equilibrium molal concentration of Fe^{+2} should be 3.4×10^{11} .

Considering next the injected reclaimed water recovered from observation well N7886 in tests 5 and 7 (table 1), the

Table 1.—Selected chemical analyses of water from the Magothy aquifer, Long Island, N.Y., and injected reclaimed water sampled from observation well N7886

Constituents and properties	Water from the Magothy aquifer ¹	[Chemical analyses in milligrams per liter]	
		Injected reclaimed water recovered from well N7886	
		Test 5 (range)	Test 7 (range)
Ferrous iron (Fe^{+2})	0.3	0.38–0.51	0.95–2.5
Calcium (Ca)7	8.2–13	9.2–18
Magnesium (Mg)2	4.2–4.4	4.1–5.1
Sodium (Na)	3.8	67–70	56–62
Potassium (K)6	9–11	7.1–11
Ammonium (NH_4)	0	27–32	25–31
Bicarbonate (HCO_3)	5	34–62	9–34
Sulfate (SO_4)	4.2	125–130	110–168
Chloride (Cl)	3.8	73–76	58–70
Fluoride (F)1	.1–.2	.1–.3
Nitrate (NO_3)	0	0–.1	0–.5
Dissolved solids, sum	26	348–372	308–374
pH	5.2–5.7	6.0–6.3	5.3–6.0
Eh (volts)	-.03 to -.12	² -.10 to -.20	² -.10 to -.20

¹F. J. Pearson, Jr. (written commun., 1970).
² Eh values from later tests.

measured Eh was about -0.200 volts, the greatest molal concentration of Fe^{+2} was 6.6×10^{-5} , and the ionic strength of the solution was $8.1 \times 10^{-3} M$. The equilibrium Eh should be -0.574 volts at the measured molal concentration of Fe^{+2} and ionic strength, and the equilibrium molal concentration of Fe^{+2} should be 1.9×10^8 at the measured Eh.

Computed CR's are 1.4×10^{-17} for water from the Magothy aquifer and 2.4×10^{-13} for the injected reclaimed water. Hence, water from both is greatly undersaturated with Fe^{+2} . According to Clarke and Barnes (1969, p. 35):

The degree of undersaturation or supersaturation determined by this analysis is an indication of the driving forces in pertinent chemical processes. Such calculations do not indicate chemical effects on well components in a quantitative way because such effects also are influenced by kinetic and catalytic factors.

Both water from the Magothy aquifer and reclaimed water have the potential to corrode iron metal.

Logarithms of the determined CR's are plotted against the observed corrosion rates in figure 5. Water from the Magothy aquifer is more undersaturated with Fe^{+2} than is the injected reclaimed water. However, of the two, corrosion rates are greater for the reclaimed water. This may be related to increased activity of sulfate-reducing bacteria stimulated by the nutrients in the reclaimed water. "Bacterial sulfate reduction is a common depolarizing process in anaerobic environments," according to Clarke and Barnes (1969, p. 31). Kuznetsov and others (1963, p. 178) stated that the presence of strongly reducing conditions, sulfates, and organic substances creates the most favorable conditions for the activity of sulfate-reducing bacteria. The reclaimed water had an Eh only slightly more negative than water from the Magothy aquifer, but the sulfate and organic contents of the reclaimed water were much higher than those of water from the Magothy aquifer. F. J. Pearson, Jr. (written commun., 1970) noted hydrogen sulfide in water from the Magothy aquifer, but its presence was more noticeable in the reclaimed water that had been in contact with the aquifer. Qualitative tests for sulfate-reducing bacteria have yielded positive results for both water from the Magothy aquifer and reclaimed water. However, these organisms would be more active in the comparatively nutrient-rich reclaimed water than in the nutrient-poor water from the Magothy aquifer. Although sulfate-reducing bacteria do not actually attack the metal, they catalyze the combination of atomic hydrogen with sulfate ions and thereby remove the protective layer of hydrogen from the cathode and allow corrosion to continue (Clarke and Barnes, 1969, p. 32). Hence, the catalytic action is greater and the corrosion rate is higher in reclaimed water than in water from the Magothy aquifer.

No studies have been made to define the corrosivity of the reclaimed water to mild steel under aerobic conditions; that is, corrosivity of the injection water at land surface and in the injection well. On entering the injection well, the reclaimed

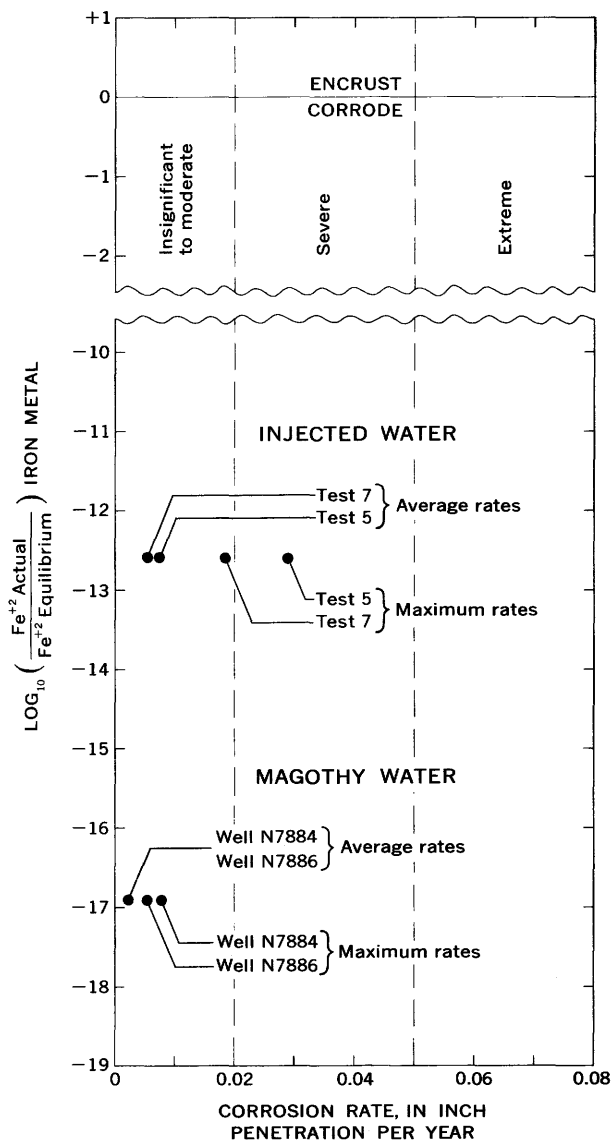


Figure 5.—Average and maximum corrosion rates of mild steel in water from the Magothy aquifer and injected reclaimed water plotted against reaction states for iron metal.

water typically has a dissolved-oxygen content of 3 to 6 mg/l, a residual chlorine (total) content of about 2.5 mg/l, and an Eh of about 0.6 to 0.7 volts. However, soon after the water flows through the well screen into the aquifer, its dissolved-oxygen and chlorine contents decrease to zero; then anaerobic reducing conditions similar to those described for observation well N7886 occur, probably within several feet of the injection well. Concentrations of hydrogen sulfide in water recovered from the injection well after a dormant period of 24 days after injection were as high as 2.9 mg/l. The high hydrogen sulfide content presumably reflects a high degree of activity of sulfate-reducing bacteria supported by a nutrient-rich organic mat, which accumulated in the aquifer around the injection-well screen. Hence, corrosive conditions in and around the

injection well most likely would be as severe as those around the observation well, at least during intermittent periods of inoperation.

CONCLUSIONS

Corrosion studies at Bay Park show that both water from the Magothy aquifer and injected reclaimed water are moderately corrosive to mild steel. Injected reclaimed water is the more corrosive of the two. Because of the corrosion of mild steel, its use for well casings and (or) screens for construction of either injection wells or associated observation wells on Long Island may be impracticable. This is particularly true for installations planned for long-term operation.

REFERENCES

- Back, William, and Barnes, Ivan, 1961, Equipment for field measurement of electrochemical potentials: Art. 280 in U.S. Geol. Survey Prof. Paper 424-C, p. C366-C368.
- Barnes, Ivan, and Clarke, F. E., 1969, Chemical properties of ground water and their corrosion and encrustation effects on wells: U.S. Geol. Survey Prof. Paper 498-D, 58 p.
- Clarke, F. E., and Barnes, Ivan, 1969, Evaluation and control of corrosion and encrustation in tube wells of the Indus Plains, West Pakistan: U.S. Geol. Survey Water-Supply Paper 1608-L, 61 p.
- Cohen, Philip, and Durfor, C. N., 1967, Artificial-recharge experiments utilizing renovated sewage-plant effluent—A feasibility study at Bay Park, New York, U.S.A., in *Artificial recharge and management of aquifers—Symposium of Haifa, 1967*: Internat. Assoc. Sci. Hydrology Pub. 72, p. 193-199.
- Hem, J. D., 1970, Study and interpretation of the chemical characteristics of natural water (2d ed.): U.S. Geol. Survey Water-Supply Paper 1473, 363 p.
- Kuznetsov, S. I., Ivanov, M. V., and Lyalikova, N. N., 1963, Introduction to geological microbiology: New York, McGraw-Hill, Inc., 252 p. [Translated by P. T. Broneer]
- Peters, J. H., and Rose, J. L., 1968, Water conservation by reclamation and recharge: Am. Soc. Civil Engineers Proc., Jour. Sanitary Eng. Div., v. 94, no. SA4, p. 625-639.
- Rainwater, F. H., and Thatcher, L. L., 1960, Methods for collection and analysis of water samples: U.S. Geol. Survey Water-Supply Paper 1454, 301 p.



HURRICANE CAMILLE—EFFECT ON STAGES IN ROSS BARNETT RESERVOIR, MISSISSIPPI

By K. V. WILSON, Jackson, Miss.

Abstract.—Hurricane Camille's winds tilted the surface of Ross Barnett Reservoir, Miss., as the storm center passed over the lake. At 8:00 a.m. on August 18, 1969, winds of 50 mph blowing directly downstream created stages of 298.0 feet at the gatehouse of the dam and 296.4 feet at State Highway 43. Between 8:00 and 9:00 a.m. the winds reversed and a large volume of water moved upstream. The inclination of the lake surface caused by the wind had a time lag in adjusting to changing wind direction.

Hurricane Camille was the most intense hurricane on record to enter the United States mainland. According to the National Weather Service, maximum winds were estimated to be at least 190 mph and minimum observed barometric pressure was 26.61 inches of mercury. Tides along the Mississippi coast reached elevations about 25 feet above mean sea level.

About 8 hours after Camille entered Mississippi, the weakened storm center passed over Ross Barnett Reservoir near Jackson, Miss. This paper documenting the effect of Camille on reservoir stages presents data which should be of value in engineering design.

Ross Barnett Reservoir, a shallow 31,000-acre lake, extends about 17 miles in a northeasterly direction up the Pearl River from a point about 10 miles northeast of Jackson. The reservoir varies from a width of 3½ miles and a depth of about 15 feet at the dam to a width of 2½ miles and a depth of about 5 feet at State Highway 43, 11 miles upstream from the dam.

The eye of Hurricane Camille, traveling almost due north at about 14 mph, passed over Ross Barnett Reservoir on August 18, 1969. The path of Camille across the reservoir as plotted from the U.S. Weather Bureau's "best track" positions is shown on figure 1.

Wind speed and direction were recorded hourly at the gatehouse of the reservoir between 12:00 noon August 17 and 5:00 p.m. August 18, and are shown on figure 1. According to the wind vectors, easterly winds up to 20 mph blew at an angle of about 45 degrees to the dam between 12:00 noon and 11:00 p.m. August 17, tending to pile water against the dam. At midnight the winds shifted to northeasterly, blowing

directly toward the dam. The intensity of the winds increased to at least 50 mph between 7:00 and 8:00 a.m.; the wind then reversed as Camille's center passed just east of the gatehouse (fig. 1).

The National Weather Service, at the Jackson Municipal Airport 6 miles south of the gatehouse, recorded peak wind gusts of 67 mph and a minimum barometric pressure of 28.60 inches of mercury at 7:56 a.m. on August 18. The minimum pressure occurred simultaneously with the peak stage at the gatehouse. A barograph for the storm period is shown on figure 1.

Stage hydrographs recorded at the gatehouse and at State Highway 43 (11 miles northeast of the gatehouse) are also presented on figure 1. The stages at both of these gages at 12:00 noon August 17 were about 297.0 feet. The gatehouse hydrograph rose less than 0.1 foot during the afternoon of August 17 while the east winds were blowing up to 20 mph. After the winds shifted northeasterly at midnight and increased to 50 mph, the water surface at the gatehouse began rising at a rate of about 0.1 foot per hour and crested at 8:00 a.m. as Camille's center passed. The crest of 298.0 feet reflected 1.0 foot of pileup caused by the northeasterly winds. By 9:30 a.m. the reservoir level at the dam had fallen to 296.9 feet. During the next 12 hours it gradually rose to 297.2 feet.

Upstream at State Highway 43, the stage changes were different. By 3:00 a.m. August 18, the 30-mph northeast winds began moving the water from the highway vicinity. Between 3 a.m. and 10:30 a.m. the reservoir level had been reduced from 296.9 feet to 296.2 feet. At 10:30 a.m. the stage at State Highway 43 suddenly began rising and peaked at 297.5 feet at 12:00 noon. The stage then gradually fell during the next 12 hours to 297.1 feet as the water was redistributed after passage of the storm.

Although the wind direction reversed between 8:00 and 9:00 a.m. and a large volume of water began moving upstream, 3 or 4 hours were required for the lake surface to reflect the change at State Highway 43. The peak stage at the gatehouse occurred at 8:00 a.m. as the wind reversed. At the highway the peak stage occurred at 12:00 noon, at which time southerly winds had prevailed for 3 hours and Camille's center was more than 50 miles to the north.

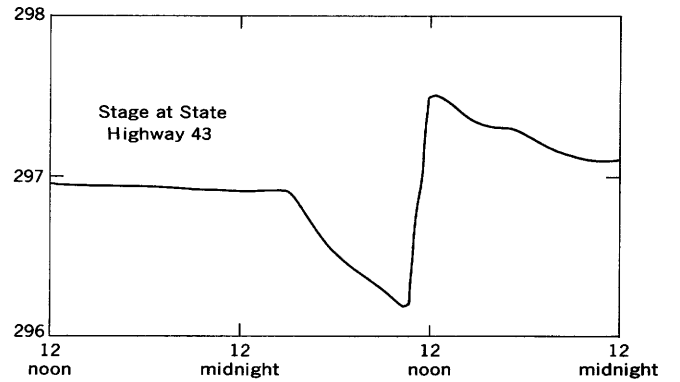
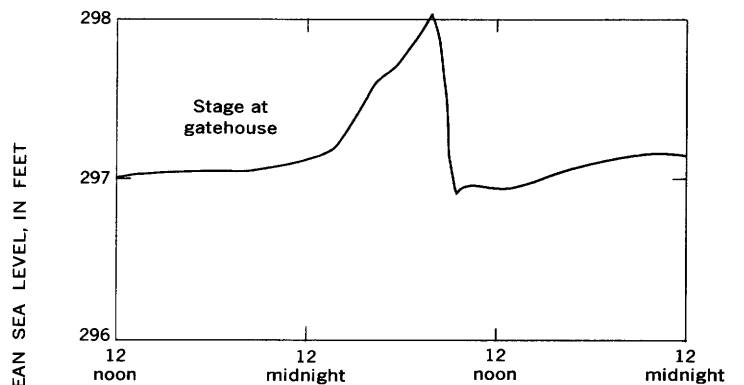
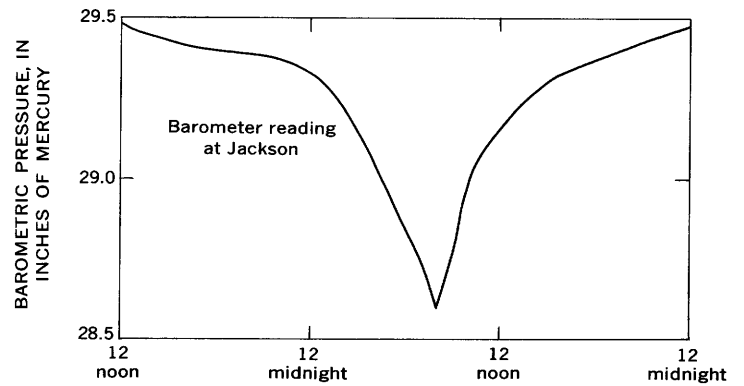
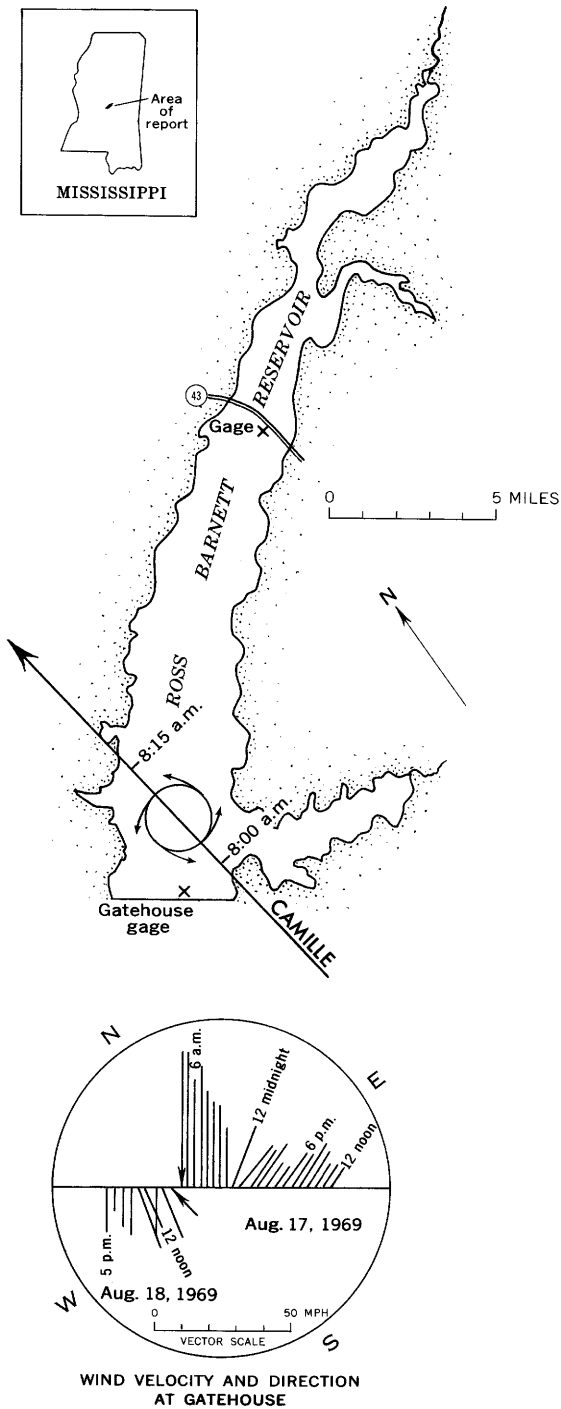


Figure 1.—Hurricane Camille at Ross Barnett Reservoir, Miss.

Few data are available on wave height during the storm. Waves overtopped State Highway 43 (elevation 301 feet), and wave action caused considerable erosion of the highway fill. The highest stage recorded at the highway was 297.5 feet; therefore, waves must have been more than 3½ feet high.

The storm passed too rapidly for steady-state conditions of the lake surface to be achieved. Therefore, the conditions described represent a nonsteady state. If the storm had moved

slower, higher peaks and greater tilt of the lake's surface would probably have developed (Haurwitz, 1951).

REFERENCE

Haurwitz, B., 1951, The slope of lake surface under variable wind stresses: U.S. Army Erosion Board Tech. Memo. 25, 23 p.



UNUSUAL TEMPERATURE VARIATIONS IN TWO SMALL STREAMS IN NORTHERN VIRGINIA

By E. J. PLUHOWSKI, Arlington, Va.

Abstract.—Temporary, unexpected disruptions in the temperature regimen of two small streams in northern Virginia are ascribed to short-term disruptions in the energy balances of the streams. A combination of meteorologic events on February 14–15, 1970, caused unusual water-temperature changes in Nichols Run near Great Falls, Va. Ice floes on Lake Fairfax near Reston, Va., driven past the lake's flat-crested outlet by high winds on February 11, 1970, caused an anomalous drop of 4°C in the receiving waters of Colvin Run.

As part of a study to isolate the effect of man's activities on stream-temperature patterns, two small streams in northern Virginia, Colvin Run and Nichols Run, were selected for intensive thermal analyses. Although the streams are only a few miles apart and are hydrologically similar, their immediate environments are decidedly dissimilar. Nichols Run (fig. 1) drains an area characterized by heavy forest cover, with only a few well-spaced residences situated away from the stream. This stream is virtually in its natural state. Colvin Run (fig. 2), on the other hand, drains much of the new town of Reston—an area which is rapidly becoming urbanized. Both streams are periodically instrumented with recording thermographs at the sites shown in figures 1 and 2. Stream-temperature patterns at sites on Colvin Run are compared with those along the "control" stream (Nichols Run) to assess man-induced thermal anomalies. Shallow water and extensive mixing caused by turbulent flow in both streams assures nearly isothermal conditions in most cross sections.

The principal factor controlling diurnal stream-temperature fluctuations at any particular point on a stream is the amount of solar energy absorbed by the stream above the measurement site. Brown and Krygier (1970) reported a 10°C (Celsius) increase in maximum diurnal stream-temperature fluctuation in a small watershed in Oregon after clearcutting of timber in the basin. This sharp rise in diurnal water-temperature fluctuation was due principally to higher maximum temperatures stemming from increased insolation after clearcutting. Conversely, a reduction in temperature of 5°–6°C in a small stream in Wisconsin during a summer day was effected by routing the stream through a heavily shading stand of willow (Stoeckeler and Voskuil, 1959). In any season, diurnal

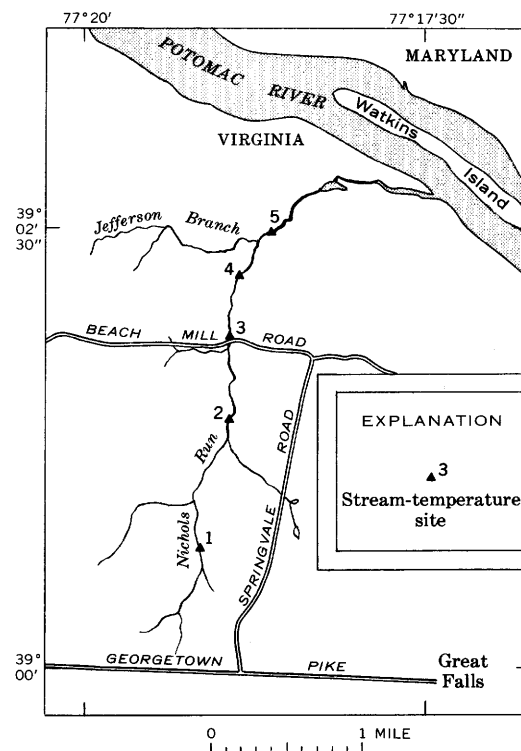


Figure 1.—Map of Nichols Run near Great Falls, Va., showing the location of five stream-temperature sites.

stream-temperature fluctuations are generally larger under sunny skies than on heavily overcast days.

Fairly large short-term temperature fluctuations have been documented even under cloudy conditions. Commonly, such anomalous thermal events occur during periods of heavy storm runoff, especially in urbanized areas where the runoff may be significantly heated or cooled while flowing over paved surfaces (Pluhowski, 1970, p. D44). The purpose of this paper is to report on two rare stream-temperature variations resulting from the interaction of several meteorologic, hydrologic, and environmental factors.

largely a function of the difference in temperature between the precipitation and ambient stream temperature—the greater this difference the greater the change in stream temperature. Because the thermal difference between frozen precipitation and streamflow is greatest along the upper reaches of Nichols Run, water temperatures there respond rapidly to changes in snowfall rates.

COLVIN RUN

A unique thermal pattern (fig. 4) was recorded on February 11, 1970, at site 3 (fig. 2) on Colvin Run. Unlike the weather during the above-described thermal event on Nichols Run, skies were mostly sunny on February 11, with nearly 80 percent of the maximum possible solar radiation reaching fully exposed stream reaches. Temperature site 3 is in a county park below the outlet of Lake Fairfax—the area is used exclusively for recreational purposes. A strong northwest wind, which prevailed throughout the day, reached peak velocities between 1100 and 1500 hours (fig. 4).

Stream temperatures reached minimum levels at dawn and began a gradual rise shortly thereafter. Air temperatures

ranged from a minimum of 1°C at 0700 hours to a maximum of 6.5°C at 1300. The expected stream-temperature pattern under mostly sunny skies is shown by the dashed line. A maximum stream temperature of 5°–5.5°C was anticipated by midafternoon, followed by a gradual recession as the sun began to set. Recorded temperatures began to deviate from expected values around 1000 hours, when an anomalous thermal trend was first established. A steep drop in stream temperature occurred at noon, producing a minimum temperature for the day (0.5°C) at 1230, fully 4°C below expected values. Temperatures began a gradual recovery after 1230, and, except for a short period in the late afternoon, they continued to rise until equilibrium was again reached near midnight.

A reconnaissance of Lake Fairfax near noon on the 11th revealed the presence of several large ice floes, which were forced by strong winds against the face of a manmade dike used to create the lake (fig. 4). The ice floes had an average thickness of only 1–2 cm, so that most were thin enough to be forced over the broad, flat-crested concrete spillway above the recording thermograph. Once beyond the spillway crest, the rapidly fracturing ice masses plunged down a vertical 15-foot embankment into the tailwater reach. Subsequent to this steep plunge, the ice particles were, at most, 4–10 cm² in size. Owing to the sharp increase in wind velocities near midday, the rate at which the ice floes were transported across the spillway and into the tailwater channel was greatest from 1200 to 1300 hours. At this time, streamflow past the recording thermograph at site 3 was a mixture of water and many small pieces of floating ice. This anomalous stream condition caused the sharp drop in water temperature. Temperatures began to rise only after the wind slackened somewhat, thereby curtailing the rate of downstream ice transport. A slight increase in windspeeds near 1600 hours resulted in a secondary trough in stream-temperature patterns at that time.

The effect of the thermal anomaly below Lake Fairfax was quickly dissipated downstream. The temperature at Hunter Mill Road (site 4) was 1.5°C at 1230, or about 3°C below expected values. No disturbance was detectable in the temperature patterns at site 5, just above the confluence with Difficult Run.

CONCLUSIONS

The limited capacity of small streams to store heat energy predisposes them to anomalous temperature patterns. It is, however, difficult to predict the precise effect on stream temperature of a given set of meteorologic factors. Moreover, manmade changes in the immediate vicinity of streams have a profound effect on the energy balance of such streams (Pluhowski, 1970), further complicating their thermal regimen. In general, anomalous stream-temperature patterns are most likely to occur in small urban watercourses, where man's impact on the environment is greatest. The water-temperature

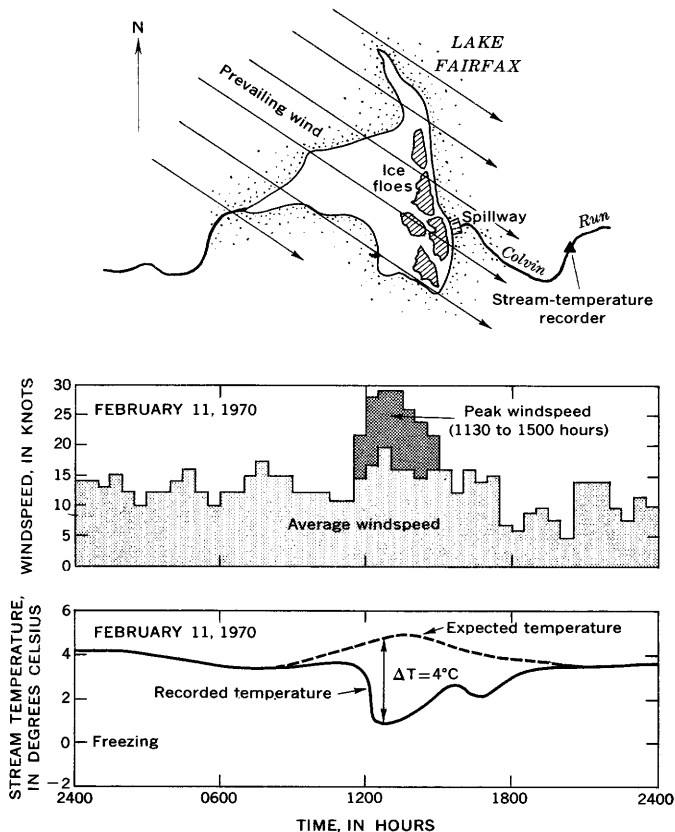


Figure 4.—Map of Lake Fairfax near Reston, Va., showing location of site 3 on Colvin Run (fig. 2). The graphs show the windspeeds recorded by the National Weather Service at Dulles International Airport, about 7 miles to the west, and the stream temperatures recorded at site 3 on February 11, 1970.

anomalies, although occasionally large, are usually of short duration, lasting less than 24 hours.

REFERENCES

Brown, G. W., and Krygier, J. T., 1970, Effects of clear-cutting on

stream temperature: *Water Resources Research*, v. 6, no. 4, p. 1133-1139.

Pluhowski, E. J., 1970, Urbanization and its effect on the temperature of the streams on Long Island, New York: U.S. Geol. Survey Prof. Paper 627-D, 110 p.

Stoekeler, J. H., and Voskuil, G. J., 1959, Water temperature reduction in shortened spring channels of southwestern Wisconsin trout streams: *Am. Fisheries Soc. Trans.*, v. 88, p. 286-288.



TREE RINGS, STREAM RUNOFF, AND PRECIPITATION IN CENTRAL NEW YORK—A REEVALUATION

By RICHARD L. PHIPPS, Arlington, Va.

Abstract.—Correspondence of years of extreme tree growth, as measured from increment cores of conifers in central New York, to years of extreme stream runoff and precipitation indicates that years of large amounts of stream runoff, years of large amounts of precipitation, and years of small amounts of precipitation can be determined from tree rings of certain trees growing in certain habitats.

Water availability can be limiting to virtually every known physiological growth process in trees (Kozłowski, 1964). Indeed, water appears to be the single most important factor limiting tree growth. Since a factor cannot be correlated with growth unless it limits growth, it seems reasonable to assume that of the measurable environmental variables some hydrologic parameter, or parameters, might be most correlative with tree growth. If a significant, reliable correlation can be proven to exist, then it should be possible to utilize growth records (tree rings) to predict or estimate the hydrologic parameter.

BACKGROUND—ORIGINAL STUDY

A study of streamflow changes after coniferous plantings on abandoned farmland in central New York indicated a 23-percent decrease in streamflow of Shackham Brook watershed near Cortland between the early 1930's and late 1950's (Schneider and Ayer, 1961). As a followup study to examine the relationships between tree growth and hydrology on a year-to-year basis, R. S. Sigafos and W. J. Schneider systematically collected tree-ring samples from more than 100 trees in the Shackham Brook watershed.

Abandoned parcels of land in New York had been claimed by the State and planted in trees in the early 1930's. Planting was done only within boundaries of State-owned land, resulting in sort of a patchwork coverage that amounted to less than 60 percent of the Shackham Brook watershed. Patches, or blocks, were planted with one to four tree species. Part or all of each of 24 blocks were included in the watershed. Though other species were planted in the watershed, the Sigafos and Schneider collection was composed entirely of Norway spruce (*Picea abies* (L.) Karst.), European larch (*Larix decidua* Mill.), red pine (*Pinus resinosa* Ait.), and Scotch pine (*Pinus sylvestris*

L.). Increment cores were obtained from five trees of each of one or two species in each of 12 of the 24 blocks. Data concerning block number (presented to allow cross reference with the map of the watershed (fig. 1) and with Schneider and Ayer (1962)), species sampled, and brief descriptions of the sample sites are included in table 1. Locations of sample sites listed in table 1 are shown on the topographic map of the watershed (fig. 1).

Shackham Brook watershed was visited in October 1970 in an attempt to locate sites sampled by Schneider and Sigafos. (Sites not found or those whose locations were questionable are indicated with a question mark (?) in table 1.) For about 2 weeks immediately preceding the visit to the watershed on October 14, rain fell nearly every day. October 14, though, was characterized by unseasonably mild temperatures and partly cloudy skies. These conditions permitted distinction between poorly drained and well-drained sites. Poorly drained sites were characterized by very wet ground litter with many small depressions of a few meters diameter being saturated or actually containing standing water. Well-drained sites were characterized by relatively dry ground litter. No attempt was made to divide soil drainage into categories other than well drained or poorly drained. Also, since these terms only pertain to this study, they are relative only to each other in reference to Shackham Brook.

The analysis of the original tree-ring measurements (Schneider and Conover, 1964) involved graphic use of the sequential probability-ratio test of Wald (1947), which amounted to testing the probability that year-to-year increases or decreases in tree-ring width corresponded to year-to-year increases or decreases in precipitation reception. This type of analysis treats each datum entry with equal weight, so that a mismatch during a year when both tree growth and rainfall changed only slightly from the preceding year received as much weight as when both changed greatly. The results of the analysis, presented in a report by Schneider and Conover (1964), indicated that though tree growth and precipitation were not independent of each other, “*** the results do not justify the use of tree-ring widths as sensitive indicators in the humid continental climate of central New York.” In other

Table 1.—Species and habitat combinations sampled for tree growth in central New York

[Sampled by R. S. Sigafos and W. J. Schneider, October 1961. Site descriptions are from October 1970 revisit except where noted by question mark (?). Species habitat combinations that provided good correspondence between extremes in growth and extremes in streamflow or precipitation marked by asterisk (*)]

Species	Site (letter) and block (No.)	Nature of site	Drainage
Norway spruce	A 2	Flat upland.*	Good
	C 3	Gentle, straight east-facing slope.	Poor
	J 19	Streamside.	Do.
	K, N 11, 18	Gentle west-facing slope.	Do.
	P 21	Straight to concave east-facing slope.	Good
Scotch pine . . .	A 2	Flat upland.*	Do.
	B 2	Gentle southwest-facing convex slope.	Do.
	D 5	Straight west- to southwest-facing slope.	Do.
	M 16	Gentle northwest-facing upland.	Do.
	Red pine	D 5	Straight west- to southwest-facing slope.
E 6		Steep, straight east-facing slope.*	Do.
F 6		Flat upland.*	Do.
G 7		Gentle convex east-facing slope.	Do.
H 7		Straight east-facing slope.	Do.
R? 24		Straight west-facing slope (?).	(?)
European larch		H 7	Straight east-facing slope.
	J 19	Streamside.*	Poor
	L? 11	Flat upland (?).	(?)
	K 11	Gentle west-facing slope.	Poor
	O 20	Convex east-facing slope.	Good
	P 21	Straight to concave east-facing slope.	Do.

¹Originally described by Sigafos and Schneider as having been block 7.

words, the analysis did not reveal relationships between tree growth and precipitation that would allow reliable estimates of precipitation conditions from tree rings.

ANALYSIS OF REMEASURED CORES

The basic data used for analysis were streamflow and precipitation data obtained directly from the Schneider and Ayer report, and tree-ring width (annual growth increment) as determined from the remeasurement of the original Sigafos and Schneider collection.

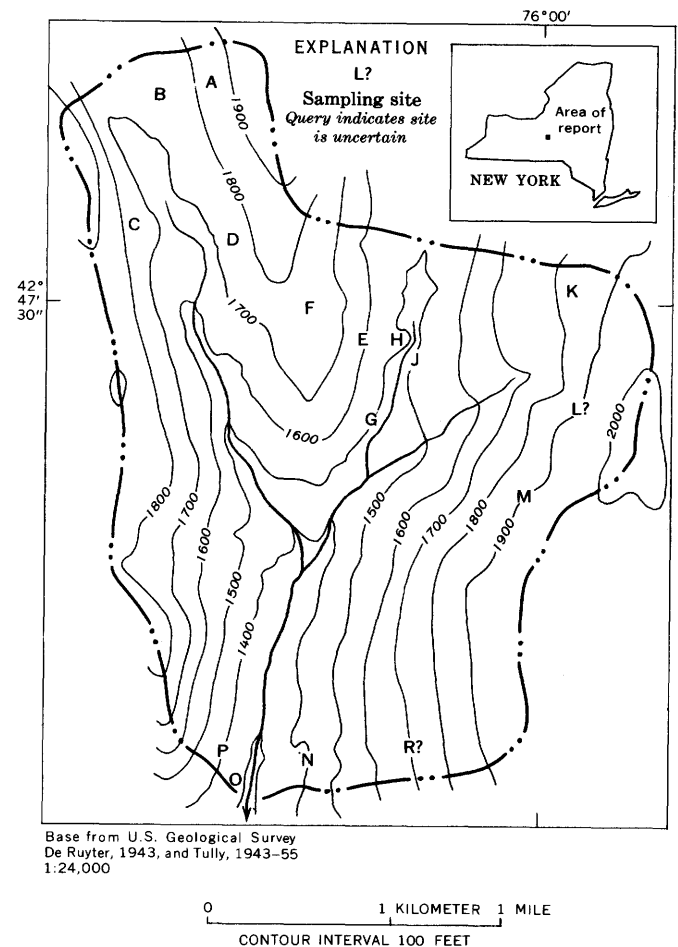


Figure 1.—Topography and location of sampling sites, Shackham Brook watershed, New York.

Cores of the original 1961 Shackham Brook collection were completely resurfaced and remeasured by the U.S. Geological Survey Tree-Ring Laboratory. It was found that at the time of collection cores had been broken into pieces and placed in envelopes, thus requiring that the pieces be replaced in exact original order to insure proper sequence of tree-ring measurements. When the cores were resurfaced by personnel of the Tree-Ring Laboratory, all cores that could not be aligned were discarded. Five cores of those included in this analysis were not measured for this reason. Cores from 111 trees were measured and were found to have an average ring width of 4.18 mm and an average measurement error of ± 0.065 mm, or about 1½ percent error. (Measurement error was calculated as the standard deviation of the differences between measurements obtained by measuring each ring of each sample twice.)

Streamflow and precipitation values used were 6-month totals ending October 31 taken directly from the Schneider and Ayer report. The use of annual values or other monthly combinations was not attempted. Streamflow and precipitation data presented in Schneider and Ayer (1961) were from 1933 through 1957. Some of the increment cores collected by

Sigafoos and Schneider in 1961 did not contain rings dating back prior to the early 1940's. Thus, in order to match the years of tree-ring records with the years of hydrologic records, it was necessary to limit this analysis to a 13-year period from 1945 through 1957.

Two approaches to analysis of the data were attempted: a modified probability-ratio test similar to that used by Schneider and Conover (1964) in the original analysis of the tree-ring samples, and an analysis based on correlation of extremes in tree-ring width to extremes in precipitation and stream runoff.

The analysis reported by Schneider and Conover was designed to determine if an increase (or decrease) in annual tree-growth increment (tree-ring width) corresponded to an increase (or decrease) in annual or growth-season precipitation. A probability of correspondence of 0.70 was selected as the probability value for which to test. Thus the correspondence between tree growth and precipitation was not to be considered as significant unless the probability of correspondence was greater than 0.7. They found the probability of correspondence to be less than 0.7 between yearly or seasonal precipitation and any of the four species as a group. This same type of analysis was repeated with the remeasured samples except that instead of yearly and seasonal values of precipitation, seasonal values of both precipitation and stream runoff were used. As with the original work, the analysis was intended to determine if the probability of successful correspondence was greater or less than 0.7. As was done by Schneider and Conover (1964), a "success" was defined as "a comparison of ring size with precipitation (or runoff) in which both showed an increase over the previous year or half year, or in which both showed a decrease." A zone of indifference was established such that only if the number of successes fell outside the zone was the probability of correspondence definitely greater or less than 0.7. The boundaries of the zone of indifference were defined by the relationship

$$d_v = 0.706v \pm 6.17,$$

based on the number of trials (v) and the number of successes (d_v) as described by Schneider and Conover. Results of this analysis are presented in table 2. When the samples from all sites for a given species were lumped together (see totals for each species, table 2), all four species indicated a probability of correspondence of less than 0.7 to either precipitation or runoff. Thus highly accurate remeasurement of the samples did not change the outcome of the sequential probability-ratio test. Testing each of the 21 species-habitat combinations (table 1) revealed no probabilities greater than 0.7 with either precipitation or runoff. However, eight of the 21 combinations (noted in table 2) fell into the zone of indifference—the probability of correspondence was too close to 0.7 to be definitely declared above or below 0.7.

These results do little more than confirm the conclusions stated previously by Schneider and Conover (1964), that

Table 2.—Number of times (successes) when tree growth and precipitation or runoff both increased or both decreased from the value of the previous year

[When the number of successes is below the range of the zone of indifference, a probability of correspondence of less than 0.7 is suggested]

Species	Site	Number of rings compared	Zone of indifference	Number of successes	
				With precipitation	With runoff
Norway spruce . . .	A	96	62–74	56	49
	C	108	70–82	59	58
	J	60	36–49	¹ 37	31
	K, N	300	206–218	170	164
	P	60	36–49	<u>140</u>	<u>136</u>
Totals		624	434–447	362	338
Scotch pine	A	60	36–49	¹ 37	29
	B	108	70–82	69	57
	D	96	62–74	¹ 65	61
	M	48	28–40	24	27
Totals		312	214–226	195	174
Red pine	D	72	45–57	44	42
	E	60	36–49	145	137
	F	60	36–49	139	31
	G	48	28–40	130	16
	H	60	36–49	35	137
	R	84	53–65	49	41
Totals		384	264–277	242	204
European larch . . .	H	84	53–65	48	34
	J	72	45–57	38	26
	L	60	36–49	34	28
	K	48	28–40	25	18
	O	72	45–57	26	30
	P	60	36–49	<u>33</u>	<u>33</u>
Totals		396	273–286	204	169

¹ A number of successes within the zone of indifference indicates that the probability of correspondence is near 0.7.

though tree growth is obviously not independent of precipitation (and stream runoff) a high year-to-year simple correlation does not exist.

The second type of analysis examined the correspondence between only the extremes in runoff or precipitation and extremes in tree growth. It was felt that since growth is the cumulative result of interacting factors limiting to growth, no single factor, such as precipitation or streamflow, could be expected to show any strong correspondence to growth except during years when that factor was at some extreme level. In other words it can be speculated that, under extreme conditions, a factor may become so limiting to growth as to overshadow or negate the obvious effects of other factors. Neither precipitation nor runoff directly affect tree growth but may reflect a factor directly affecting growth: internal water stress of the tree. Thus, low precipitation may under certain circumstances result in high internal water stresses in the tree (as well as low stream runoff), which in turn would result in lower growth rates. Internal water stress develops in a tree any time that the rate of water loss from the tree (transpiration) exceeds the rate of water uptake through the roots. This situation can result from a variety of soil and

Table 3.—*Precipitation and stream runoff, in inches, at Shackham Brook watershed, New York*

[Data from Schneider and Ayer (1961). Extreme values indicated with superscript (+ = high; - = low)]

Year	6-month period ending October 31	
	Precipitation	Runoff
1957	16.60	4.05
1956	15.17	4.39
1955	27.05 ⁺	3.07 ⁻
1954	13.79 ⁻	3.02 ⁻
1953	15.71	3.07 ⁻
1952	21.63	5.55
1951	16.79	2.50 ⁻
1950	18.70	3.74
1949	22.38	4.89
1948	18.08	5.08
1947	19.86	10.62
1946	27.38 ⁺	10.67
1945	27.84 ⁺	12.07 ⁺

atmospheric conditions not necessarily occurring during or limited to periods of little or no precipitation (Kozlowski, 1964; Phipps, 1970). For these reasons it was felt that a quantitative analysis, such as one involving simple linear regression, would be of little value. Instead it was decided to examine correspondence between extremes in tree growth and extremes in precipitation and runoff. To include extreme values of growth and precipitation or streamflow which occurred in more than one year, a rather arbitrary method of delimiting extreme years from a list of the ranked data was devised. Values in addition to the single largest and smallest (table 3) were selected if they were closer to the largest and smallest values than the average spread between consecutive values in the rank. Years of extremes in May-to-October precipitation and streamflow for the sample period 1945–57 are indicated in table 3. Extremes in tree growth were determined in the same manner as described for precipitation and runoff. Determination of correspondence was then simply a matter of matching years of extreme tree growth with years of extreme precipitation or runoff. The questions for which answers were sought were how reliably and under what circumstances do years of extreme tree growth reflect years of extreme precipitation or extreme runoff?

YEARS OF LOW STREAMFLOW

No obvious correspondence was found between tree growth and low streamflow, but no one or two years of that short sample period 1945–57 really stood out as having been years of extremely small streamflow.

YEARS OF HIGH STREAMFLOW

Years of high flow were positively correlated (in a quantitative sense only) with tree growth of upland red pine (site F,

table 1 and fig. 1), upland Scotch pine (site A), and red pine on a straight east-facing slope (site E). Basic ring-width data with extremes indicated are included in table 4. Years of large amount of tree growth for each tree (listed by Tree-Ring Laboratory number) for each of the three groups were as follows:

Sample group	TRL No.	Years of large amount of growth
Upland red pine	2599	1945, 1946
	2600	1945
	2601	1945, 1946, 1947, 1948, 1949, 1950
	2602	1945
	2603	1945
Upland Scotch pine . . .	2641	1945
	2642	1945
	2643	1945
	2644	1945, 1946, 1947
	2645	1946
East-facing red pine . . .	2594	1945, 1946
	2595	1945
	2596	1945, 1946
	2597	1945, 1946
	2598	1945, 1946
	High streamflow	

All three groups of trees grow on rather well-drained sites (table 1). In all three groups together, two out of 15 trees indicated 1947 as an extreme year, about half the 15 trees indicated 1946 as an extreme year, but 14 out of 15 trees indicated 1945 as a year of high streamflow. It is also interesting to note in passing that 1946 was the year of the second highest flow of the sample period record.

YEARS OF LOW PRECIPITATION

Years of large rings of European larch growing at streamside (site H) and small rings of Norway spruce growing on a flat upland (site A) corresponded with years of low precipitation (1954). Years of extreme rings of these two groups (see basic data, tables 3 and 4) were as follows:

Sample group	TRL No.	Years of extreme rings
Streamside European larch (large rings).	2589	1950, 1952, 1954, 1955
	2590	1955
	2591	1954
	2592	1954
	2593	1953, 1954
Upland Norway spruce (small rings).	2633	1952
	2634	1953, 1954
	2635	1957
	2636	1954
	2640	1953, 1954
Low precipitation		1954

Of all trees together, two out of 10 trees indicated 1955 as extreme, three out of 10 indicated 1953, while seven out of 10 indicated the year of least amount of precipitation, 1954.

Table 4.—Basic ring-width data, in millimeters, of trees from species-habitat combinations which indicated some correspondence between extremes in growth and extremes in precipitation and (or) runoff

[Extreme rings are noted with superscripts (+ = large; - = small)]

TRL No.	1957	1956	1955	1954	1953	1952	1951	1950	1949	1948	1947	1946	1945
Streamside European larch													
2589	4.30	4.75	6.90 ⁺	6.54 ⁺	5.96	6.44 ⁺	5.81	7.16 ⁺	3.91	2.79	3.48	2.14	1.47 ⁻
2590	6.39	4.39	7.14 ⁺	6.60	5.42	5.84	4.88	3.46	3.54	2.85	3.51	1.17 ⁻	1.87
2591	5.02	2.44	5.96	8.97 ⁺	6.05	5.99	5.96	4.82	4.74	2.82	3.44	1.52 ⁻	2.22
2592	8.29	7.32	8.44	10.30 ⁺	9.48	7.50	6.46	6.43	5.64	5.39	5.96	3.92 ⁻	5.11
2593	3.67	3.14	4.04	5.40 ⁺	5.20 ⁺	4.16	3.97	2.08	2.20	1.38 ⁻	2.13	1.55 ⁻	1.61 ⁻
East-facing slope red pine													
2594	3.54	2.90	3.54	2.02 ⁻	2.87	3.29	3.57	4.71	5.88	5.19	6.63	7.06 ⁺	7.06 ⁺
2595	2.92	2.60	3.56	1.91	.33 ⁻	2.55	3.12	2.55	3.21	2.56	2.81	3.19	5.99 ⁺
2596	1.08 ⁻	1.31 ⁻	2.45	2.14	2.15	3.13	2.66	2.53	3.27	3.75	4.33	5.56 ⁺	5.06 ⁺
2597	1.27 ⁻	1.23 ⁻	1.70 ⁻	1.51 ⁻	1.77 ⁻	1.82 ⁻	2.49	2.35	2.46	3.06	3.55	4.66 ⁺	4.37 ⁺
2598	3.16	2.66 ⁻	3.43	3.03	3.03	3.76	3.78	3.93	3.86	3.68	5.15	5.58 ⁺	5.76 ⁺
Upland red pine													
2599	1.90 ⁻	3.22	3.76	4.03	3.84	2.66	2.45	2.99	3.31	3.17	4.67	5.27 ⁺	5.23 ⁺
2600	1.66 ⁻	1.94 ⁻	2.27 ⁻	2.54 ⁻	3.25 ⁻	3.40 ⁻	2.85 ⁻	3.60 ⁻	3.76 ⁻	3.96 ⁻	4.53	7.67	8.36 ⁺
2601	.27 ⁻	.23 ⁻	.99	1.04	1.76	1.77	2.83	5.16 ⁺	5.21 ⁺	4.44 ⁺	4.57 ⁺	4.78 ⁺	5.25 ⁺
2602	1.58	1.25	2.03	1.54	.36 ⁻	1.46	1.59	1.44	2.11	2.42	2.81	3.71	5.12 ⁺
2603	1.21 ⁻	.86 ⁻	1.94 ⁻	1.82 ⁻	1.73 ⁻	.93 ⁻	1.47 ⁻	2.17 ⁻	3.07	2.81	3.16	4.33	6.08 ⁺
Upland Norway spruce													
2633	9.62 ⁺	6.63	6.24	5.78	5.50	3.95 ⁻	8.10	8.69	7.98	8.22	7.15	6.05	4.71
2634	9.34 ⁺	5.27	4.90	2.27 ⁻	2.81 ⁻	4.30	6.92	7.53	6.97	4.73	6.05	5.54	5.61
2635	.54 ⁻	1.67	2.09	1.93	2.35	2.56	4.01	4.58 ⁺	3.65	3.71	2.85	3.79	1.94
2636	5.74 ⁺	3.77	5.25 ⁺	3.52 ⁻	4.56	5.45 ⁺	5.95 ⁺	5.84 ⁺	4.07	4.08	5.23 ⁺	5.31 ⁺	5.64 ⁺
2640	3.47	2.30	2.28	1.19 ⁻	1.58 ⁻	2.37	4.83	5.52	4.51	5.05	6.84	6.68	7.61 ⁺
Upland Scotch pine													
2641	1.14 ⁻	.97 ⁻	1.54	2.52	1.86	2.19	2.81	2.64	3.73	3.66	3.90	4.36	5.07 ⁺
2642	2.43 ⁻	2.23 ⁻	3.31	3.68	2.76	4.01	4.48	5.25	5.77	5.29	5.18	5.35	6.16 ⁺
2643	1.56 ⁻	1.58 ⁻	1.69 ⁻	1.59 ⁻	1.33 ⁻	2.15	2.15	2.97	3.10	2.66	3.12	3.99	4.44 ⁺
2644	1.35 ⁻	1.16 ⁻	1.31 ⁻	1.47 ⁻	.94 ⁻	1.63 ⁻	3.53	3.47	3.99	4.74	5.13 ⁺	5.40 ⁺	5.56 ⁺
2645	3.08	2.58 ⁻	3.42	3.49	3.05	3.77	4.64	4.86	5.21	4.88	5.73	6.68 ⁺	6.03

While this is far from a perfect correspondence, 1954 stands out most consistently as the year of extreme size.

It might at first seem inconsistent that both small rings (Norway spruce) and large rings (European larch) would be correlated with small amounts of precipitation. The streamside European larch, which correlated with small amounts of precipitation, was growing in a low, very wet area. Though the planted larch has survived in this wet environment, it is most unlikely that it could have established itself there under natural conditions. Within the Shackham Brook watershed, larch seemed to have survived planting better, and was growing at a greater rate, in better drained areas. The streamside site might, during years of small amounts of precipitation, have been comparable to better drained areas during more typical years, and thus have resulted in greater amounts of growth. Further, during years of greater amounts of precipitation the streamside larch could be expected to exhibit even less growth than during drier years. Norway spruce, on the other hand, seemed to be doing better on the wetter, more poorly drained sites at Shackham Brook, thus in keeping with a positive correlation between growth and precipitation.

YEARS OF HIGH PRECIPITATION

Just as years of large rings of European larch growing at

streamside corresponded to years of small amounts of precipitation, years of small rings of the same trees corresponded to years of high precipitation. Years of large rings of red pine growing on a straight east-facing slope (the same trees that corresponded to greater amounts of runoff) also corresponded to years of high precipitation. Years of extreme growth of these two tree groups (table 4) are as follows:

Sample group	TRL No.	Years of extreme rings
Streamside European larch (small rings).	2589	1945
	2590	1946
	2591	1946
	2592	1946
	2593	1945, 1946, 1948
East-facing slope red pine (large rings).	2594	1945, 1946
	2595	1945
	2596	1945, 1946
	2597	1945, 1946
	2598	1945, 1946
High precipitation		1945, 1946, 1955

For both groups together, 1946 was indicated eight out of 10 times and 1945 seven out of 10 times. Both 1946 and 1945 were determined from the precipitation records (table 3) as being years of extremely high rainfall during the May-to-October growth season. However, no extreme growth rings

corresponded to the high precipitation of the 1955 growth season. Examination of precipitation distribution revealed the following:

	<i>Precipitation (inches)</i>	
	<i>Average, 1945-57</i>	<i>1955 only</i>
May-October	20	27
May-July	11	9
August-October	9	18

On the basis of measurements taken in southeastern Ohio (Phipps, 1961), it is most likely that the bulk of the tree growth at Shackham Brook takes place before the end of July. Thus, the high amount of precipitation received at Shackham Brook during August-October 1955 probably had very little effect on tree growth. Further, during the preceding year, 1954, growing-season precipitation and streamflow were at the lowest levels of the 13-year sample period (table 3). Though soil-moisture records are not available to confirm it, streamflow records suggest that soil-moisture values of the 1955 growing season were probably below "normal." And, as stated above, tree growth is more directly responsive to soil-moisture values than to precipitation. The trees used in this example, then, would appear to reflect high precipitation only so long as high precipitation also means high soil moisture. It may also be speculated, on the basis of studies of timing of tree growth, that a precipitation time period more correlative with tree growth at Shackham Brook might have been May-August rather than May-October.

CONCLUSIONS

The best correspondence between extremes in tree growth and extremes in stream runoff and precipitation may be summarized as follows:

Large amount of stream runoff:	Large rings, upland red pine. Large rings, upland Scotch pine. Large rings, east-facing slope red pine.
Small amount of stream runoff:	Insufficient data.
Large amount of precipitation:	Small rings, streamside European larch. Large rings, east-facing slope red pine.
Small amount of precipitation:	Large rings, streamside European larch. Small rings, upland Norway spruce.

If precipitation and streamflow were not known, selection of extremes in tree growth as described would have identified years of extremes in high streamflow, high precipitation, and low precipitation. The correspondence between years of

extreme growth and years of extreme precipitation or streamflow is strictly qualitative. It would not have been possible, for example, to determine which of two extreme precipitation years was the more extreme. During the short sample period used in analysis, no one or two years stood out as having had extremely low streamflow, and no correspondence between growth and low streamflow was found. Correspondence between years of extreme growth and years of extreme precipitation is assumed to apply only so long as a correlation between precipitation and soil moisture holds. Thus, 1955, a year of high growth-season precipitation, was not identified by extreme growth, presumably because 1955 followed a year of extremely dry conditions and was thus not characterized by either high streamflow or, it is assumed, high soil moisture. Also, a high percentage of the 1955 precipitation occurred during August-October when little or no growth took place.

Forest environment is much too complex a system of interrelated factors to expect a high year-to-year correlation between growth and only one or two environmental factors. Only sophisticated analyses employing complex computer programs have resulted in respectable correlations of tree growth with environment (Zahner and Stage, 1966; Fritts, 1966). The examination of extremes as described demonstrates that, notwithstanding complexities of environment, years of extremes of a single factor, such as precipitation or streamflow, can be identified from tree rings of certain species growing in certain habitats. It appears possible, then, in hydrologic investigations in which determination of years of extremes of some hydrologic factor is sought, that different species and habitat combinations can be used to identify years of extremes of hydrologic factors without employing the use of complex statistical analyses.

REFERENCES

- Fritts, H. C., 1966, Growth-rings of trees: their correlation with climate: *Science*, v. 154, p. 973-979.
- Kozlowski, T. T., 1964, *Water metabolism in plants*: New York, Harper and Row, 227 p.
- Phipps, R. L., 1961, A preliminary report concerning radial growth of selected trees at Neotoma: *Ohio Agr. Expt. Sta. Research Circ.* 102, 44 p.
- 1970, The potential use of tree rings in hydrologic investigations in eastern North America with some botanical considerations: *Water Resources Research*, v. 6, no. 6, p. 1634-1640.
- Schneider, W. J., and Ayer, G. R., 1961, Effect of reforestation on streamflow in central New York: *U.S. Geol. Survey Water-Supply Paper* 1602, 61 p.
- Schneider, W. J., and Conover, W. J., 1964, Tree growth proves nonsensitive indicator of precipitation in central New York, in *Geological Survey Research 1964*: U.S. Geol. Survey Prof. Paper 501-B, p. B185-B187.
- Wald, Abraham, 1947, *Sequential analysis*: New York, John Wiley and Sons, 212 p.
- Zahner, Robert, and Stage, Albert, 1966, A procedure for calculating daily moisture stress and its utility in regressions of tree growth on weather: *Ecology*, v. 47, p. 64-74.



TRITIUM IN PINE TREES FROM SELECTED LOCATIONS IN THE UNITED STATES, INCLUDING AREAS NEAR NUCLEAR FACILITIES

By G. L. STEWART¹, T. A. WYERMAN,
MAX SHERMAN, and ROBERT SCHNEIDER,
Amherst, Mass., Washington, D.C., Trenton, N.J., Washington, D.C.

Abstract.—Pine needles were sampled at several selected locations in the conterminous United States to determine if the natural tritium rainout pattern can be correlated with tritium in free water and in bound hydroxyls of new and old growth. Near nuclear facilities which are known to release tritium to the environment the objective was to obtain some information on the distribution pattern and fate of tritium in nearby vegetation. Excluding samples near the nuclear facilities, the tritium concentrations in pine needles followed a geographic pattern similar to that for the rainout of bomb-produced tritium—a general increase with latitude and distance from the ocean. However, tritium concentrations were greater in plant tissue than would be expected from natural rainout. At the Savannah River Plant, South Carolina, the data clearly indicate a decreasing concentration of tritium with distance from the release areas.

Prior to thermonuclear bomb testing, as a result of the interaction between cosmic rays and the atmosphere, tritium was present in nature at concentrations between 2 and 10 TU² (tritium units) (Kaufman and Libby, 1954; Libby, 1962). Since 1952 these relatively low natural tritium levels have been masked by bomb-produced tritium and by tritium from nuclear facilities. The testing of thermonuclear bombs has universally “tagged” modern precipitation with distinct seasonal and annual tritium pulses. In addition, nuclear facilities have added tritium to local precipitation.

The series of high-altitude thermonuclear detonations in 1961 and 1962 resulted in large quantities of tritium being hurled into the stratosphere. Today most of the tritium in precipitation is residual from these detonations. Because of meteorological phenomena, maximum mixing between the tritium-enriched stratosphere and the troposphere occurs in the late spring to early summer. Most of the annual tritium rainout occurs in the late spring to early summer and, since reaching a maximum in 1963, it has declined with time. Weighted-average concentrations of tritium in precipitation

have declined at the rate of about 40 percent of the preceding year's values (Stewart and Farnsworth, 1968; Stewart and Wyerman, 1970). Tritium rainout data for United States precipitation can be found in reports by Kaufman and Libby (1954), Libby (1962), Thatcher and Hoffman (1963), Stewart and Hoffman (1966), Stewart and Farnsworth (1968), and Stewart and Wyerman (1970).

Nuclear facilities such as the U.S. Atomic Energy Commission's Savannah River Plant (SRP) in South Carolina and the Western New York Nuclear Service Center (WNYNSC; subsidiary of W. R. Grace Co.) in New York are known to release tritium to their immediate environment. The release of tritium from nuclear facilities has scientific interest because this tritium provides a characteristic tag which may be potentially useful in tracing water through biological and hydrologic systems in the vicinity of these facilities.

In the spring of 1967 we conducted a preliminary study to obtain information about the occurrence of tritium in plants near the SRP and about isotopic fractionation in different kinds of plant tissue. The tritium concentrations in various kinds of plant tissue taken from loblolly pine and sweetgum trees and from corn were easily related to the proximity of nuclear facilities at the SRP. The tritium concentration of samples collected near Columbia, S.C., which is about 50 miles from the SRP, was in the range of that in local precipitation, whereas the concentration in samples collected near the SRP was considerably higher.

Although the data from the 1967 study were too limited to yield definitive conclusions, they provided interesting results and in fact were the basis for making the more thorough study discussed in this paper. The 1967 data suggested that future studies related to tritium released by the SRP should be restricted to areas close to the SRP and to one species of plant. From a hydrologic standpoint the most significant aspect of the preliminary study was the suggestion that the tritium distribution in plants could preserve the history of variations in the concentration of tritium rainout.

¹ University of Massachusetts.

² 1 TU equals 1 tritium atom in 10¹⁸ protium atoms; 1 TU is approximately equal to 3.2 picocuries/liter.

In view of the results from the 1967 study it was decided to restrict sampling to new and old growth of pine needles and to collect samples near nuclear facilities at the SRP, the WNYNSC, and the Hanford nuclear facilities, Washington. For comparative purposes, it was further decided to collect samples at several locations in the conterminous United States and to compare the results with tritium data from the U.S. Geological Survey's precipitation-sampling network. Specifically, the objectives of the investigation reported herein are:

1. To determine if natural tritium rainout distribution patterns can be correlated with tritium in free water and in bound hydroxyls of new and old growth of pine needles;
2. To detect and determine the distribution pattern and fate of tritium in vegetation near nuclear facilities which are known to release tritium to the environment; and
3. To obtain a better understanding of isotopic exchange and fractionation mechanisms in plants.

SAMPLE COLLECTION AND ANALYTICAL METHODS

Samples of pine needles (new and old growth) were collected from a single tree at each sampling location. Because most samples were collected during early May, newly formed buds had to be collected at a few locations. At locations where new growth was more advanced, newly formed pine needles were sampled. Because of the lack of pine trees in the vicinity of the Hanford nuclear facilities, downy brome grass (*Bromus tectorum* L.) samples were collected. The specific location, type of tree (or plant) and tissue sampled, and the date of collection are described in the following list:

Savannah River Plant and vicinity

Northwest traverse

- Site 1. About 10 miles northwest of the perimeter of the plant; loblolly pine (*Pinus taeda* L.) about 8 feet tall; needles of new growth up to about 1½ inches long and old growth 6 to 8 inches long. May 7, 1968.
- Site 2. About 3½ miles northwest of the perimeter of the plant; loblolly pine in about the same stage of growth as tree at site 1. May 7, 1968.
- Site 3. At the northwest perimeter of the plant; loblolly pine about 7 feet tall; new needles up to about 1 inch long; old needles 6 to 7 inches long. May 7, 1968.

On site

- Site 4. Between F and H separations areas, near the center of the plant; loblolly pine about 8 feet tall; new needles up to about 1½ inches long; old needles 6 to 8 inches long. May 7 and July 10, 1968.

Southeast traverse

- Site 5. At the southeast perimeter of the plant; loblolly pine about 10 feet tall; new needles up to about 2 inches long; old needles 7 to 8 inches long. May 8, 1968.
- Site 6. About 2 miles southeast of the perimeter of the plant; loblolly pine about 8 feet tall; new needles up to about 2 inches long; old needles 7 to 8 inches long. May 8, 1969.
- Site 7. About 9 miles southeast of the perimeter of the plant; loblolly pine about 7 feet tall; new needles up to about

1 inch long; old needles 6 to 7 inches long. May 8, 1968.

North perimeter

- Site 8. Near the north perimeter of the plant; loblolly pine about 8 feet tall; new needles up to about 1½ inches long; old needles 6 to 8 inches long. May 24, 1967, and May 7, 1968.

Western New York Nuclear Service Center

- Site 9. At the northeast perimeter, approximately 1.1 miles from main building; white pine (*Pinus strobus* L.) about 7 feet tall; bud growth and old needles sampled. May 14, 1968.
- Site 10. Approximately 2.5 miles northeast of the perimeter of the Center; white pine about 9 feet tall; bud growth and old needles. May 14, 1968.
- Site 11. Approximately 8.4 miles northeast of the perimeter of the Center; white pine about 9 feet tall; bud growth and old needles. May 14, 1968.

Hanford nuclear facilities

- Site 12. Near perimeter of Hanford Reservation, about 4 to 5 miles northeast of nuclear facilities on State Highway 24, 2.7 miles from Adams County line; downy brome grass (*Bromus tectorum* L.) 6 to 8 inches tall. May 14, 1968.
- Site 13. About 11.5 miles northeast of nuclear facilities and about 2 miles northeast of Taunton, Wash.; downy brome grass 6 to 8 inches tall. May 14, 1968.

North-central California

- Site 14. About 2 miles northeast of Colfax on Interstate Highway 80; ponderosa pine (*Pinus ponderosa* L.) about 10 feet tall; new needles up to about 2 inches long; old needles 8 to 10 inches long. May 16, 1968.

North-central Utah

- Site 15. About 15 miles southeast of Salt Lake City, in Big Cottonwood Canyon; ponderosa pine about 10 feet tall; only old needles sampled because new growth had not started. May 18, 1968.

Central New Mexico

- Site 16. Southeast of Albuquerque on State Highway 10, 1.1 miles south of Pine Flat recreation site; ponderosa pine about 10 feet tall; bud growth and old needles 5 to 6 inches long. May 20, 1968.

Northwest North Dakota

- Site 17. North Dakota State University Agricultural Experiment Station, Williston Branch; ponderosa pine about 10 feet tall; buds and old needles estimated to be from 1967, 1966, 1965, and 1964 growth. May 22, 1968.

Northwest Nebraska

- Site 18. Chadron State Park; ponderosa pine about 10 feet tall; bud growth and old needles. May 20, 1968.

Southeast Missouri

- Site 19. About 2 miles north of the intersection of State Highways 143 and 34 on State Highway 143; short leaf pine about 5 feet tall; new needles up to about 1 inch long; old needles 4 to 5 inches long. May 16, 1968.
- Site 20. North end of Sam A. Baker State Park on State Highway 143; loblolly pine about 25 feet tall; new needles up to about 1 inch long; old needles 6 to 7 inches long. May 16, 1968.

As soon as possible after removal of bud growth or pine needles from the tree, they were placed in large test tubes and sealed. About 30- to 35-g samples (wet weight) were collected. In the Geological Survey laboratory the test tubes containing

samples were connected to a vacuum line and placed in a furnace. A vacuum distillation technique was used to distill free water and bound hydroxyls from the plant tissue. If a plant sample is heated in a vacuum, considerable water is released in the temperature range from about 20°–100°C. Virtually no water is released between about 100°C and 200°C; but above 200°C (or 250°C) a little water is released which is probably associated with the bound hydroxyls. Free water as defined herein includes all interstitial, vacuole, and protoplasmic water and loosely held water in cell walls. A temperature of 110°C and a distillation time of 12 hours or more was used and determined sufficient to expel all free water from the sample. At the end of this time the free water (about 20 to 25 g) was removed from the trap where it had been collected over liquid nitrogen. Bound hydroxyl groups (sometimes referred to as bound water) represent tissue-bound hydroxyls that are an intimate part of the plant tissue. Most of these hydroxyls break down in a temperature range of 200°C to 400°C to form water and an oxide residue. After removal of the trap containing the free water, a clean trap was inserted and evacuated, and the furnace temperature was increased slowly to about 400°C. Four hours was found to be sufficient time to break down the plant structure and release the bound hydroxyls. Bound-hydroxyl water samples were vacuum distilled two additional times to remove dark hydrocarbons that distilled over at the higher temperature. Even with these additional distillations, the hydroxyl water samples contained some hydrocarbons (evident by the coloration of the samples); therefore, each sample was further treated with an ether washing. At the completion of the ether wash about 1 to 2 g of water was available for counting using a standard proportional gas counting technique.

The free-water samples believed to be high in tritium activity were counted using a liquid scintillation spectrometer. A proportional gas counting technique was used to count the free-water samples of lower activity and all bound-water samples. Because of the fluorescence caused by hydrocarbons in the hydroxyl water, the liquid scintillation counting could not be used for these samples.

Soil samples collected at a few of the sampling sites were taken from a depth of 0 to 8 inches in the root zone of the trees. Adsorbed water was distilled from these samples at a temperature of 110°C, using a vacuum distillation technique similar to the one described above. Depending upon the expected tritium activity of the sample, the adsorbed soil water was counted by either the liquid scintillation or the gas counting technique.

TRITIUM DERIVED FROM THERMONUCLEAR BOMB TESTING

With the use of tritium data collected by the U.S. Geological Survey during January to June 1968, weighted-average tritium concentration values for precipitation in the United States can

be roughly contoured to show geographical distribution patterns, as shown on maps in figures 1 to 3. These maps show that tritium concentrations increase with increase in latitude and with distance from the oceans. It is also characteristic for the greatest tritium rainout to occur in late spring to early summer—the same time period when new growth appears on trees and the same time period during which most of the vegetation sampling was done.

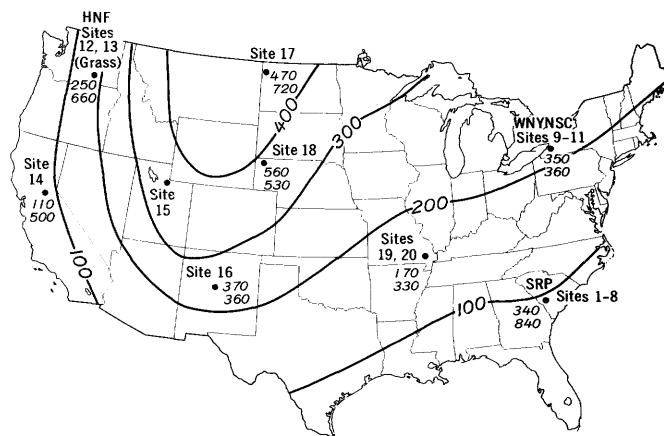


Figure 1.—Geographical distribution of weighted-average tritium concentration in precipitation (contours), in tritium units, for January through May 1968, and concentration in free water (top number) and bound water (bottom number) distilled from new pine needle growth. The values for the WNYNSC (Western New York Nuclear Service Center) and southeast of the SRP (Savannah River Plant) are for the sampling site most distant from the nuclear facilities; values at sites 19 and 20 are averaged. HNF, Hanford nuclear facilities.

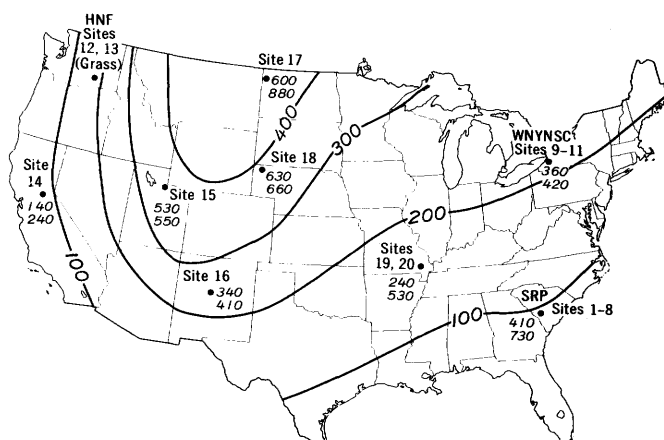


Figure 2.—Geographical distribution of weighted-average tritium concentration in precipitation (contours), in tritium units, for January through May 1968, and concentration in free water (top number) and bound water (bottom number) distilled from old pine needle growth. The values for the WNYNSC and southeast of the SRP are for the sampling site most distant from the nuclear facilities; values at sites 19 and 20 are averaged. See figure 1 for explanation of abbreviations.

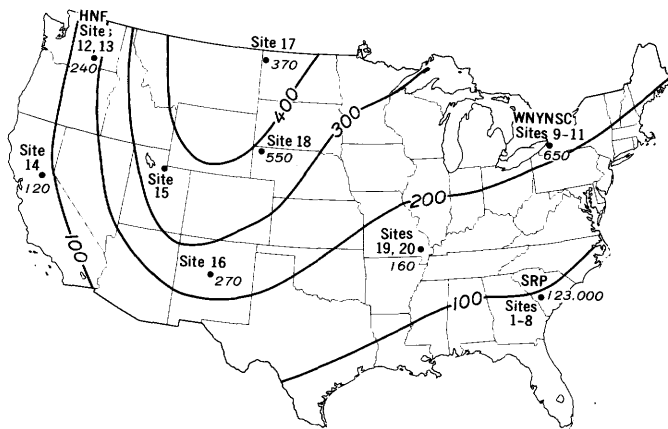


Figure 3.—Geographical distribution of weighted-average tritium concentration in precipitation (contours), in tritium units, for January through May 1968, and concentration in soil water (numbers). The values for the WNYNSC and SRP are for the sampling site nearest the nuclear facilities; values at sites 19 and 20 are averaged. See figure 1 for explanation of abbreviations.

The tritium concentration data collected for new and old growth and for soil water are presented in tables 1 and 2. When tritium concentrations in free water and bound hydroxyls for new and old pine needles are plotted on the maps in figures 1 and 2, respectively, it is observed that these values are generally higher than the extrapolated values for precipitation at the same location. The arithmetic mean tritium concentration in precipitation for 12 network stations in the United States during January to June 1968 was 220 TU (Stewart and Wyrman, 1970), and the arithmetic mean of the highest tritium concentrations in precipitation measured for each station during this period was 270 TU. The January–June average concentration (extrapolated values) of tritium in precipitation for six sites (sites 14, 16–20) falls between these two values (about 250 TU). Free water from new growth collected at these six locations had an average concentration of 310 TU; soil water averaged 270 TU, which correlates more

closely with tritium in precipitation (fig. 3). The average tritium concentration in the free water from new growth (310 TU) for the six sampling locations was 50 TU less than the tritium concentration in free water from old growth (360 TU).

The average tritium concentration in bound hydroxyls from new growth (460 TU) was 150 TU greater than that in free water from new growth (310 TU) for the six sites. It is often stated in the literature that new growth on trees at the beginning of each year depends to a large degree upon carbohydrates synthesized during the preceding year (Burger, 1962). Although many factors are involved in accounting for the concentration of tritium in plants, the data reported in table 1 appear to support this hypothesis. Some of the carbohydrates synthesized during 1967 could have been used to produce the bound hydroxyls of the new pine needles in 1968.

The difference between the arithmetic average tritium concentration in bound hydroxyls from new growth (460 TU) and old growth (490 TU) is only 30 TU. This difference is not as great as might be expected on the basis of the above-mentioned hypothesis. However, a reasonable explanation would be that new growth is produced primarily from stored carbohydrates synthesized during the previous year (or years), and a major part of the old growth may have come largely from carbohydrates synthesized during the same period, with only a small fraction from an earlier period. In future studies of this type it would be desirable to sample pine needles toward the end of the growing season. If new growth early in the season is dependent largely upon stored food materials, and if more carbohydrates are synthesized that season, then there may actually be a decrease in the concentration of tritium in bound water as the growing season progresses.

Bound hydroxyls from old growth at the six sites had an arithmetic average tritium concentration of 490 TU compared to 360 TU for free water. This large difference (130 TU) is expected because old growth undoubtedly contains some recent precipitation in its free water, whereas its bound hydroxyls may contain tritium derived mainly from precipita-

Table 1.—Tritium concentrations for new and old growth of pine needles and for soil water at selected locations in the conterminous United States

[Concentration values are in tritium units to the nearest 10 TU]

Sample location (see fig. 1)		Soil water	New growth		Old growth	
State	Site No.		Free water	Bound water	Free water	Bound water
California	14	120±10	110±10	500±20	140±10	240±10
Utah	15	270±10	370±40	360±10	530±40	550±20
New Mexico	16	270±10	370±40	360±10	340±40	410±10
North Dakota	17	370±10	¹ 470±40	¹ 720±30		
					² 550±40	² 550±30
					³ 390±40	³ 770±10
					⁴ 490±40	⁴ 830±20
					⁵ 990±50	⁵ 1,390±30
Nebraska	18	550±10	¹ 560±40	¹ 530±20	630±40	660±20
Missouri	19	150±10	170±10	280±10	250±10	680±50
	20	170±10	170±10	370±10	240±10	380±30

¹Bud growth.

²1967 growth.

³1966 growth.

⁴1965 growth.

⁵1964 growth.

Table 2.—Tritium concentrations for new and old growth of pine needles near the Savannah River Plant and the Western New York Nuclear Service Center, for grass near the Hanford nuclear facilities, and for soil water at the three locations

[Concentration values are in tritium units to the nearest 10 TU]

Sample location (see fig. 1)	Soil water	New growth		Old growth	
		Free water	Bound water	Free water	Bound water
Savannah River Plant					
Northwest traverse:					
Site 1	3,840±110	5,240±80	2,410±90	1,700±30
2	3,740±100	3,570±60	2,700±90	3,590±70
3	6,180±130	5,070±80	4,880±110	5,150±90
On site:					
Site ¹ 4	123,000±2,000	37,600±600	44,600±700	37,300±600	66,000±1,600
24	5,610±150	13,890±310	17,810±330	10,550±290	40,110±710
Southeast traverse:					
Site 5	1,200±80	2,480±70	1,120±70	2,820±80
6	750±70	1,890±60	900±80	2,320±70
7	340±60	840±20	410±70	730±10
North perimeter:					
Site ³ 8	920	2,420	770	4,420
48	1,500±70	2,450±70	1,230±70	3,700±60
Western New York Nuclear Service Center					
Site 9	650±50	⁵ 450±30	⁵ 710±80	420±40	600±10
10	⁵ 350±30	⁵ 280±30	330±30	380±10
11	⁵ 350±30	⁵ 360±30	360±30	420±10
Hanford nuclear facilities					
Site 12	340±30	260±40
13	240±10	250±10	660±60

¹ Collected May 7, 1968. ² Collected July 10, 1968. ³ Collected May 24, 1967. ⁴ Collected May 7, 1968. ⁵ Bud growth.

tion of previous years. The limited data of this study show a slightly greater difference (150 TU) between bound hydroxyls from new growth and its free water. The differences between tritium concentration in free water and bound hydroxyls from the two kinds of growth might be expected to be similar or slightly greater for the old growth. One possible explanation for the observed results is that residual tritium is present in the free water of old growth.

An attempt was made at the North Dakota site to sample pine needles of various ages. With the guidance of personnel of the North Dakota State Agricultural Experiment Station, pine needle growth dating back to 1964 was identified. Tritium data (table 1) for bound hydroxyls of a single tree suggest that the tritium content in old pine needles (growth of 1967, 1966, 1965, and 1964) follows a pattern similar to that in precipitation for this period—concentrations have decreased with time. The tritium concentration in free water collected from these pine needles does not follow this pattern, suggesting the possibility of incomplete isotopic exchange within the free water of pine needles.

TRITIUM DERIVED FROM NUCLEAR FACILITIES

Savannah River Plant

The existence of tritium concentration gradients as a function of distance from the nuclear facilities of the SRP is

clearly demonstrated by the data in table 2 and by the diagrammatic cross section shown in figure 4. Except for new growth at sampling sites 1 and 2, where concentrations are about the same, distinct tritium concentration gradients are present for all of the plant components sampled along both the northwest and southeast traverses. Tritium concentrations of samples from the northwest traverse are 10 or more times greater than would be expected for plants receiving only bomb-produced tritium from natural precipitation, and about three or more times greater for the southeast traverse samples (fig. 4). The tritium values in figures 1 and 2 are for the sampling site on the southeast traverse that is most distant from the nuclear facilities.

The concentrations in samples of the northwest traverse are expected to be greater than those of the southeast traverse because prevailing winds during April to August are out of the southeast. At other times of the year, prevailing winds are in a different direction. Because site 4 is close to areas where tritium is released operationally, its tritium concentration is considerably higher than at any other site.

The nature of the distribution of tritium released from the SRP is complicated because of variations in the amount of tritium released and the variability of factors related to its dispersion after release, particularly changes in the prevailing wind direction and other meteorological mechanisms. Thus, it is difficult to make meaningful comparisons between the tritium concentrations in the various kinds of plant tissue. The data for samples of free water from new growth and old

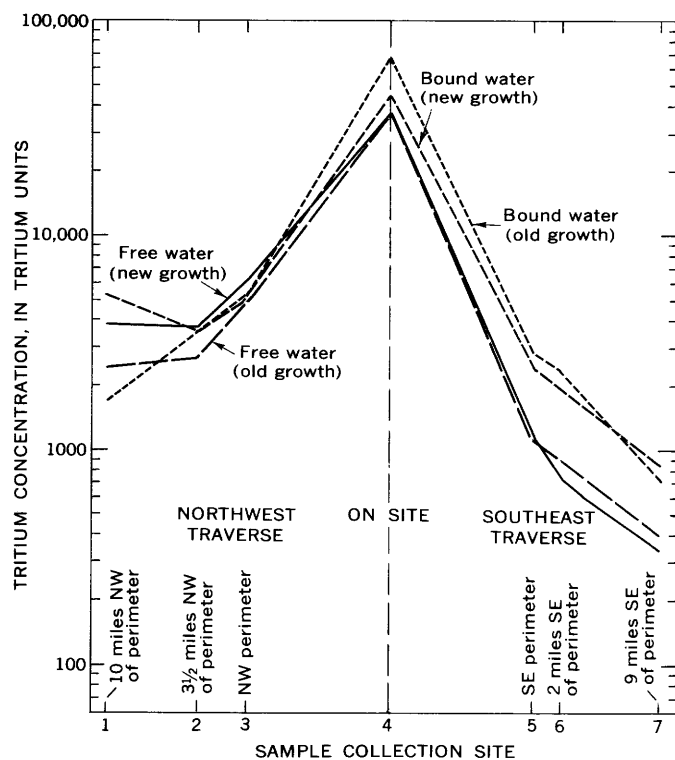


Figure 4.—Graph of tritium concentrations in pine needles with distance from the nuclear facilities of the Savannah River Plant.

growth collected along the northwest traverse suggest that just prior to the 1968 sampling a large deposition of tritium took place, as compared with the amount of deposition that occurred when tritium was being synthesized in the old pine needles.

The same pine tree at site 8 was sampled on May 24, 1967, and again on May 7, 1968. Free water of the 1967 samples contained less tritium than that of the 1968 samples, which may also suggest a relatively high release of tritium to the northwest just prior to the 1968 sampling.

Western New York Nuclear Service Center

The data in table 2 are too limited to determine if the nuclear facility in western New York releases an appreciable amount of tritium to its immediate surroundings. Although tritium concentration differences are relatively small, the concentration appears to be higher near the perimeter of the facility than at the more distant sampling points. The tritium concentration of free water in new growth (buds) was 450 TU and in old growth was 420 TU at 1.1 miles from the facility, compared to 350 TU and 330 TU at 3.7 miles, and 350 TU and 360 TU at 8.4 miles. Bound water at 1.1 miles was similarly higher in tritium than it was at the more distant stations.

Tritium values shown on the maps in figures 1 to 3 for the WNYNSC are for the sampling site most distant from the

nuclear facilities. Average values for the three sites would deviate even more from the contoured values for precipitation.

Hanford nuclear facilities

Because of the lack of pine trees (or other tree species) that depend upon natural precipitation for moisture in the vicinity of Hanford, Wash., downy brome grass was selected for sampling because it was prevalent in the area. The free water from the sample collected at about 4 to 5 miles from the nuclear facilities had a greater tritium concentration than that of the sample from the more distant point; the reverse was true for the bound water from the two samples. From these limited data it would appear that a measurable amount of tritium is not being discharged to the immediate surroundings, at least where the samples were collected. These data are generally consistent with tritium concentrations in vegetation at locations not influenced by nuclear facilities. The tritium values shown on the maps in figures 1 and 3 are for the sampling site most distant from the nuclear facilities.

SUMMARY AND DISCUSSION OF RESULTS

Rainout of bomb-produced tritium is universal, and because of the nature of global meteorological phenomena it occurs in an apparently consistent and characteristic pattern. Maximum rainout of bomb-produced tritium occurs in late spring and early summer, which is also the time when new plant growth has just started. Tritium rainout generally increases with latitude and distance from the ocean. Tritium in pine needles followed a similar geographic pattern, excluding sampling sites influenced by nuclear facilities releasing tritium. However, tritium concentrations were found to be greater in plant tissue than would be expected from natural rainout of bomb tritium. The following factors and observations are involved and may explain the observed concentrations of tritium in the soil water-plant system.

1. Within the root zone the soil contains water of various ages. Because tritium in precipitation has declined at the rate of about 40 percent per year, the soil water may, under many conditions, contain considerably more tritium than current precipitation. Some of these data suggest that the soil contains tritium from precipitation that infiltrated in previous years.

2. New growth is generally believed to contain a greater percentage of active water-conducting tissue than old growth. If all free water is equally mobile and exchangeable, then the tritium concentration of both new and old growth would be the same and characteristic of tritium in soil water. These data, although very limited, suggest that it is not equally exchangeable and that other plant factors such as age of the growth are involved. Remnants of tritium from water of previous years appeared to be present in free water of old growth, implying that different components of free water may be mobile and exchangeable to varying degrees. A portion of the water

distilled off at 110°C from old growth and counted as free water may actually be involved only passively in exchange reactions and (or) conduction of sap, whereas another portion may be more actively involved. The degree of mobility and exchange of water within plants may depend upon the age of the particular plant component.

3. Isotopic fractionation occurs during evapotranspiration and in metabolic and photosynthetic processes involving physical and chemical changes of water. Fractionation processes generally result in tritium becoming more concentrated relative to protium in phases where strong hydrogen bonds are formed. Although photosynthesis and metabolic processes are complicated, the isotopic effect is in the direction that could account for the observed difference between the concentration of tritium in free water and that in bound hydroxyls.

4. Exchange between tritium in bound hydroxyls and tritium in free water is possible, and if it occurs there would be an overall dilution of tritium in bound hydroxyls because of the continuing decline of bomb tritium in precipitation.

5. The tritium concentration in bound hydroxyls of new growth is likely to be greatest early in the growing season because (a) it is during this time that the tritium concentration in precipitation is high, and (b) stored food containing tritium from precipitation of previous years is used in the synthesis of new growth.

A meaningful interpretation of tritium concentrations in various kinds of plant tissue in the vicinity of nuclear facilities cannot be made without knowledge about operational releases

of tritium and detailed information on local meteorological factors which control the environmental distribution of these releases. The data collected near the SRP clearly showed that tritium released from the nuclear facilities is distributed throughout the surrounding area with concentration decreasing with distance from the release areas. Tritium in vegetation from the WYNSC and Hanford could not clearly be related to releases from these nuclear facilities.

REFERENCES

- Burger, H., 1962, Untersuchungen über das Hohenwachstum verschiedener Holzarten: Mitteilungen der Schweizerischen Anstalt für das Forstliche Versuchswesen, v. 14, p. 1-158.
- Kaufman, Sheldon, and Libby, W. F., 1954, The natural distribution of tritium: *Phys. Rev.*, v. 93, p. 1337.
- Libby, W. F., 1962, Tritium geophysics: Recent data and results, in *Tritium in the physical and biological sciences*, v. 1, A symposium in Vienna, Austria, May 3-10, 1961, Internat. Atomic Energy Agency, Vienna, p. 5-32.
- Stewart, G. L., and Farnsworth, R. K., 1968, United States tritium rainout and its hydrologic implications: *Water Resources Research*, v. 4, no. 2, p. 273-289.
- Stewart, G. L., and Hoffman, C. M., 1966, Tritium rainout over the United States in 1962 and 1963: *U.S. Geol. Survey Circ.* 520, 11 p.
- Stewart, G. L., and Wyerman, T. A., 1970, Tritium rainout in the United States during 1966, 1967, and 1968: *Water Resources Research*, v. 6, no. 1, p. 77-87.
- Thatcher, L. L., and Hoffman, C. M., 1963, Tritium fallout over North America from Soviet tests in 1961: *Jour. Geophys. Research*, v. 68, no. 20, p. 5899-5901.



THE UPPER BOUND OF A LOG-PEARSON TYPE III RANDOM VARIABLE WITH NEGATIVELY SKEWED LOGARITHMS

By E. J. GILROY, Arlington, Va.

Abstract.—When a negative skew coefficient is used in fitting a Pearson type III distribution to the logarithms of annual floods, the estimated annual floods are necessarily bounded from above. If Y_{\max} , μ_y , and σ_y denote the upper bound, the mean, and the standard deviation, respectively, of the annual floods, then the ratio $R = (Y_{\max} - \mu_y)/\sigma_y$ may be written as a function of the standard deviation, σ_x , and the skew coefficient γ of the logarithms of the annual floods. For values of σ_x between 0.1 and 1.0 and values of γ less than -1.8, R is less than 3.

The Hydrology Committee, Water Resources Council, has recommended the use of the log-Pearson type III distribution as a uniform technique for estimating the frequency distribution of annual floods. The committee also recommended the following method of determining the characteristics of the distribution. First transform the observed data to their corresponding common logarithms and then compute the mean, the standard deviation, and the skew coefficient of the logarithms. These sample values are then used to estimate logarithms of discharges corresponding to selected recurrence intervals under the assumption that the logarithms follow a Pearson type III distribution.

Now it sometimes happens that the sample skew coefficient of the logarithms is negative. In the presence of extreme outliers the sample skew of the logarithms often approaches a value of -3. If such a negative value of the sample skew coefficient of the logarithms is taken to be the population value of the skew coefficient, then it follows from the definition of the Pearson type III distribution that the logarithms of the annual floods—and hence the annual floods themselves—are bounded from above. Thus a numerical value of the upper bound, Y_{\max} , exists whereby no annual floods may exceed Y_{\max} . The implications of such a property of the annual floods could be serious depending on the magnitudes of the number Y_{\max} , the mean value of the annual floods, and the standard deviation of the annual floods.

Let Y_{\max} , μ_y , and σ_y^2 denote the upper bound, mean, and variance, respectively, of the annual floods. The ratio $R = (Y_{\max} - \mu_y)/\sigma_y$ is derived as a function of the standard deviation and skew coefficient of the logarithms of the annual

floods. The results are presented in the next section and the derivations are presented in the appendix.

RESULTS

Let Y denote the arithmetic magnitude of an annual flood event, and let X denote the common logarithm of Y . Thus

$$Y = 10^x. \tag{1}$$

Assume that X is distributed as a Pearson type III random variable and that the skew coefficient of X is negative. Let m denote the upper bound of X so that

$$-\infty < X \leq m \tag{2}$$

and

$$0 < Y \leq 10^m. \tag{3}$$

Let σ_x denote the standard deviation of the logarithms, X , and γ denote the skew of X . Then from the results given in the appendix the mean, μ_y , and the variance, σ_y^2 , of the annual floods are given in terms of the parameters m , σ_x , and γ of the logarithms, X , by

$$\mu_y = e^{cm} \left[1 - \frac{c\gamma\sigma_x}{2} \right]^{-4/\gamma^2} \tag{4}$$

and

$$\sigma_y^2 = e^{2cm} \left\{ (1 - c\gamma\sigma_x)^{-4/\gamma^2} - \left[1 - \frac{c\gamma\sigma_x}{2} \right]^{-8/\gamma^2} \right\} \tag{5}$$

where c is given by

$$c = \log_e 10. \tag{6}$$

Let D denote the distance between the upper bound, e^{cm} , of Y and the mean, μ_y , of Y . Then

$$D = e^{cm} \left[1 - \left(1 - \frac{c\gamma\sigma_x}{2} \right)^{-4/\gamma^2} \right] \tag{7}$$

The quantity of interest is the ratio, R , of D to the standard deviation, σ_y , of Y . Thus

$$R = \frac{1 - \left(1 - \frac{c\gamma\sigma_x}{2} \right)^{-4/\gamma^2}}{\left[(1 - c\gamma\sigma_x)^{-4/\gamma^2} - \left(1 - \frac{c\gamma\sigma_x}{2} \right)^{-8/\gamma^2} \right]^{1/2}} \tag{8}$$

Equation 8 gives the ratio R as a function only of the standard deviation, σ_x , of the logarithms and the skew coefficient, γ , of the logarithms.

Table 1 gives representative values of R for γ between -3.0 and zero and for σ_x between zero and 1.0. As γ approaches zero, the ratio R rapidly increases for all values of σ_x . For γ less than -1.8, R is less than 3 for all values of σ_x in the range 0.1-1.0.

APPENDIX

Let X denote a random variable following a Pearson type III probability distribution. The set of values which the random variable X may attain is bounded either from above or below and is unrestricted in the remaining direction (Kendall, 1952, p. 142; Elderton, 1953, p. 93). If the third moment about the mean is positive, the range of X is bounded from below, and if it is negative the range of X is bounded from above. To consider both of these conditions simultaneously the probability density function of the random variable X is given by

$$p(x) = \frac{1}{|a|\Gamma(b+1)} \left[\frac{x-m}{a} \right]^b \exp \left[-\frac{(x-m)}{a} \right], \tag{A-1}$$

with

$$0 \leq b < \infty, \tag{A-2}$$

$$-\infty < m < \infty, \tag{A-3}$$

$$|a| > 0, \text{ and} \tag{A-4}$$

$$0 \leq \frac{x-m}{a} < \infty. \tag{A-5}$$

If $a > 0$, equation A-5 gives

$$m \leq x < \infty \tag{A-5'}$$

as the range of x . If $a < 0$, equation A-5 gives

Table 1.—Values of the ratio R as a function of the skew coefficient γ and the standard deviation σ_x of the logarithms

γ	σ_x				
	0.2	0.4	0.6	0.8	1.0
-0.2	193	6,570	226×10 ⁶	677×10 ⁴	170×10 ⁶
-0.6	7.6	16.7	35.3	70.4	133
-1.0	3.3	4.9	6.9	9.3	12.1
-1.4	2.1	2.8	3.4	4.1	4.7
-1.8	1.6	1.9	2.3	2.6	2.8
-2.2	1.2	1.5	1.7	1.9	2.0
-2.6	1.0	1.2	1.4	1.5	1.6
-3.09	1.0	1.2	1.2	1.3

$$-\infty < x \leq m \tag{A-5''}$$

as the range of x .

The moment generating function, $\theta(t)$, associated with the random variable x is given by

$$\theta(t) = E(e^{tx}) = \int e^{tx} p(x) dx = e^{tm} (1 - ta)^{-(b+1)} \tag{A-6}$$

where the range of integration is determined by equation A-5' or equation A-5'' depending on the algebraic sign of the parameter a .

Let μ_x , σ_x^2 , μ_3 , and γ denote the mean, the variance, the third central moment, and the skew coefficient of X , respectively. Then

$$\mu_x = m + a(b+1), \tag{A-7}$$

$$\sigma_x^2 = a^2(b+1), \text{ and} \tag{A-8}$$

$$\mu_3 = 2a^3(b+1) = \gamma \sigma_x^3; \tag{A-9}$$

hence

$$b+1 = \frac{4}{\gamma^2}, \tag{A-10}$$

$$a = \frac{\gamma \sigma_x}{2}, \text{ and} \tag{A-11}$$

$$m = \mu_x - \frac{2\sigma_x}{\gamma}. \tag{A-12}$$

From equation A-9 it follows that a negative third central moment implies a negative skew and it also follows that the parameter a must be negative in order to have a negative skew coefficient. Hence a negative skew coefficient implies that X is bounded from above as in equation A-5''.

Consider the random variable Y defined as

$$Y = 10^x = e^{cx} \tag{A-13}$$

where $c = \log_e 10$. The random variable Y now corresponds to the magnitudes of the annual floods.

The moments of Y may then be written in terms of the moment generating function of X since

$$E(Y^k) = E(e^{ckx}) = \theta(ck). \quad (\text{A-16})$$

Therefore

$$\mu_y = E(y) = \theta(c) = e^{cm}(1 - ca)^{-(b+1)}, \quad (\text{A-17})$$

$$E(y^2) = \theta(2c) = e^{2cm}(1 - 2ca)^{-(b+1)}, \text{ and } (\text{A-18})$$

$$\sigma_y^2 = \text{var } Y = e^{2cm} [(1 - 2ca)^{-(b+1)} - (1 - ca)^{-2(b+1)}]. \quad (\text{A-19})$$

From inequalities A-5', A-5'', and equation A-15, the bounds on Y can be given as

$$e^{cm} \leq Y < \infty, \text{ for } a > 0, \text{ and } (\text{A-20})$$

$$0 < Y \leq e^{cm}, \text{ for } a < 0. \quad (\text{A-21})$$

The subject of this article is negatively skewed distributions, attention therefore has been restricted to the upper bound of equation A-21.

REFERENCES

- Elderton, W. P., 1953, Frequency curves and correlation, 4th ed.: Washington, D.C., Harren Press, 272 p.
 Kendall, M. G., 1952, The advanced theory of statistics, v. 1: New York, Hafner Publishing Co., 457 p.



SUBJECT INDEX

[For major headings such as "Economic geology," "Ground water," "Marine geology," see under State names or refer to table of contents]

A	Page	C	Page		Page
Acritarcha, Jurassic, Alaska	B17	Calderas, Utah, mineral potential . .	B67	Glacial deposits, Alaska, marine . . .	B9
Age determinations, Precambrian plutonic rocks, Arizona	191	California, petrology, Feather River area	85	Chazy, N. Y., geologic studies . .	35
Alaska, marine geology, southern coast	9	structural geology, northern coast	211	Granite, Idaho, thorium in	51
paleontology, northern part . .	17	northern White Mountains . .	195	Granite, Massachusetts, phase com- position	105
structural geology, southeast- ern part	211	tritium in pine trees	265	Gravity studies, San Juan Mountains, Colo.	183
Alluvium, particle-size discrimina- tion by radar	175	Cambrian, Kentucky, stratigraphy .	25	Green River Formation, Wyoming, mineralogy	121
Analyses. <i>See specific types:</i> Atomic absorption, Fac- tor, Fluid inclusion, Spec- trophotometric, X-ray fluorescence.		Chile, nitrate deposits, northern part	43	Gulf of Mexico, northeastern part, marine geology	1
Andover Granite, Massachusetts, petrology	105	Classification, genetic, igneous rocks	79		
Anorthosite, genetic classification . .	79	Clay, mineralogy and chemistry, Pennsylvania	57	H	
Antimony, X-ray fluorescence analysis	147	Colorado, gravity study, southwest- ern part	183	Hanson Creek Formation, Nevada, stratigraphy	21
Aquifers, contamination, southern Nassau County, N. Y.	225	Conodonts, Silurian, Nevada	21	Heavy minerals, in submarine sedi- ments, Alaska	9
recharge studies, Long Island, N. Y.	241	Contamination, aquifer, travel of bacteria in	237	High Bridge Group, Kentucky, stra- tigraphy	25
Argentina, structural geology, north- western part	205	Continental fragment, displaced from California to Alaska	211	Hurricane Camille, effect on reser- voir stages	253
Arizona, isotope studies, central part petrology, northern part	191 95	Continental margin, Gulf of Mexico, structural features	1		
remote sensing, northern part . .	175	Corrosion, metal well casings and screens	247	I	
Arsenic, X-ray fluorescence analysis .	147	Cretaceous, Florida, marine geology .	1	Idaho, thorium, east-central part . . .	51
Artificial recharge, use of purified sewage in	241			Igneous rocks, genetic classification .	79
Atacamite, new X-ray data	119	E		Impervious area, estimation from population-density data	219
Atomic absorption analysis, determi- nation of mercury in geologic materials	151	Electrolytic cleansing technique, crystal-surface impurities	141	Inclusions, in palagonite tuff, Ari- zona	95
		Eocene, Wyoming, mineralogy	121	Ingraham esker, Chazy, N. Y., glacial geology	35
B				Instruments and equipment, au- tomated spectrophotom- eter	137
Bacteria, as pollution indicator, travel in aquifer	237	F		electrolytic cleansing cells for crystals before fluid inclu- sion analysis	141
Basalt, California, Feather River area genetic classification	85 79	Factor analysis, geochemical, intru- sion breccia	125	Iron, in rutile, spectrophotometric determination	157
Batholith, postulated from gravity study, Colorado	183	Fission-track ages, Precambrian plu- tonic rocks, Arizona	191		
Belt Supergroup, Idaho, thorium- rich intrusions	51	Flexure, in structural trough, north- western Argentina	205	J	
Beryllium, Utah, potential deposits .	67	Floods, annual, estimating frequency by log-Pearson type III distribution	273	Jurassic, Alaska, paleontology	17
Boulder tracks, as indicators of bearing capacity of surface materials	165	Florida, marine geology, Gulf of Mexico	1	Argentina, structural geology . .	205
Breccia, Mule Ear diatreme, Utah . .	125	Fluid inclusion analysis, electrolytic cleansing technique	141	California-Nevada structural geology	195
		Fluorspar, Utah, potential deposits .	67		
		Fusulinids, use in correlating con- tinental fragment, western North America	211	K	
				Kentucky, stratigraphy, central part	25
		G		Kinnikinic Quartzite, Idaho, thori- um-rich intrusions	51
		Gabbro, genetic classification	79	Knox Group, Kentucky, stratigraphy	25

SUBJECT INDEX

B279

	Page
Utah, geochemistry, southeastern part	B125
tritium in pine trees	265

V

Vanadium, in rutile, spectrophotometric determination ...	157
X-ray fluorescence analysis ...	147

	Page
Virginia, surface water, northern part	B255

W

Washington, tritium in grass	265
Wells, corrosion of metal casings and screens	247
Wyoming, mineralogy, south-central part	121

X

	Page
X-ray data, new, atacamite	B119
X-ray fluorescence analyses, standard rocks	147

Z

Zeolites, Washakie Basin, Wyoming .	121
Zinc, X-ray fluorescence analysis ...	147

AUTHOR INDEX

B Page
 Boneham, R. F. B17
 Brown, W. E., Jr. 175
 Bunker, C. M. 51
 Bush, C. A. 51

C
 Cadigan, R. A. 125
 Castle, R. O. 105
 Connor, J. J. 25
 Cressman, E. R. 25
 Crowder, D. F. 195
 Cummings, David 95

D
 Denny, C. S. 35
 Dinnin, J. I. 151

E
 Ehlke, T. A. 237, 241
 Ehrlich, G. G. 237, 241
 Ericksen, G. E. 43
 Espos, L. F. 147

F
 Fabbi, B. P. 147

G
 Giaimo, A. A. 247
 Gilroy, E. J. 273

H
 Hietanen, Anna 85
 Hosterman, J. W. 57

I
 Irwin, W. P. 211

J Page
 Jackson, E. D. B79
 Jones, D. L. 211

K
 Koch, Ellis 225

L
 Larson, A. L. 119

M
 Marinenko, John 151
 Martin, G. L. 165
 Martin, R. G., Jr. 1
 Massoni, C. J. 137
 May, Irving 151
 Meyrowitz, Robert 157
 Moore, H. J. 165
 Mrose, M. E. 43
 Mullens, T. E. 21

N
 Naeser, C. W. 191

O
 Ovenshine, A. T. 211

P
 Pakiser, L. C. 183
 Perlmutter, N. M. 225
 Phipps, R. L. 259
 Pinckney, D. M. 141
 Plouff, Donald 183
 Pluhowski, E. J. 255
 Poole, F. G. 21

R Page
 Roehler, H. W. B121
 Ross, D. C. 195

S
 Schaber, G. G. 175
 Schneider, Robert 265
 Segerstrom, Kenneth 205
 Shapiro, Leonard 137
 Shawe, D. R. 67
 Sherman, Max 265
 Staatz, M. H. 51
 Stankowski, S. J. 219
 Stewart, G. L. 265
 Stuart-Alexander, D. E. 125
 Stuckless, J. S. 191

T
 Tailleur, I. L. 17
 Thayer, T. P. 79
 Theodore, T. G. 105
 Tripp, R. B. 119
 Turner, J. C. M. 205

V
 Vecchioli, John 237, 241, 247
 Vischer, W. A. 165

W
 Wilson, K. V. 253
 Wolcott, D. E. 25
 Wright, F. F. 9
 Wyerman, T. A. 265

